

# Peptide-Mediated Delivery of Antisense Oligonucleotides and Chemotherapeutics Across Biological Barriers

By

Colin MacLaine Fadzen

B.A. Physics and Biochemistry  
University of Pennsylvania, 2013

M.S. Chemistry  
University of Pennsylvania, 2013

Submitted to the Department of Chemistry  
in Partial Fulfillment of the Requirements for the

Degree of Doctor of Philosophy  
in Biological Chemistry

at the

Massachusetts Institute of Technology

June 2018

© 2018 Massachusetts Institute of Technology  
All rights reserved

Signature redacted

Signature of Author: \_\_\_\_\_

1 U Department of Chemistry  
May 11, 2018

Signature redacted

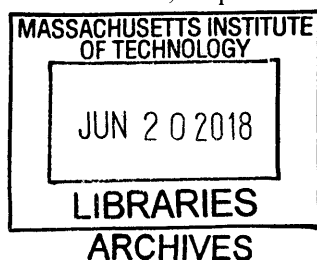
Certified by: \_\_\_\_\_

Bradley L. Pentelute  
Associate Professor of Chemistry  
Thesis Supervisor

Signature redacted

Accepted by: \_\_\_\_\_

Robert W. Field  
Haslam and Dewey Professor of Chemistry  
Chairman, Departmental Committee for Graduate Students







This doctoral thesis has been examined by a committee of the Department of Chemistry as follows:

Signature redacted

---

  
Pfizer-Laubach Career Development Assistant Professor  
Thesis Committee Chair

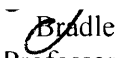
Alex K. Shalek

Pfizer-Laubach Career Development Assistant Professor

Thesis Committee Chair

Signature redacted

---

  
Associate Professor of Chemistry  
Thesis Supervisor

Bradley L. Pentelute

Associate Professor of Chemistry

Thesis Supervisor

Signature redacted

---

Alexander M. Klivanov  
Novartis Professor of Chemistry and Bioengineering  
Thesis Committee Member

Alexander M. Klivanov

Novartis Professor of Chemistry and Bioengineering

Thesis Committee Member



# Peptide-Mediated Delivery of Antisense Oligonucleotides and Chemotherapeutics Across Biological Barriers

By

Colin MacLaine Fadzen

Submitted to the Department of Chemistry on May 11, 2018  
in Partial Fulfillment of the Requirements for the  
Degree of Doctor of Philosophy in Chemistry

## Abstract

Many nucleic acids, peptides, and small molecules struggle to become clinically viable therapeutics as a result of poor delivery. Biological barriers such as the plasma membrane and the blood-brain barrier (BBB) contribute to this challenge as they can limit the passage of macromolecules. Cell-penetrating peptides (CPPs) that interact with membranes can improve the uptake of macromolecules across biological barriers. Here we explore methods for the peptide-mediated delivery of antisense oligonucleotides (ASOs) and chemotherapeutics.

First, we address the issue that the optimal peptide sequence for the delivery of a macromolecular cargo is often context-dependent and specific to that cargo. With one class of ASO, we develop a paradigm that combines systematic screening of known CPPs in a functional assay for ASO delivery with machine learning methods. Using our computational model, we identify five novel sequences that increase ASO activity at least three-fold. Next, we demonstrate that combining CPPs of different classes generates chimeric peptides with synergistic effects on ASO delivery. These chimeras improve ASO activity twenty-fold, which is greater than any literature-reported sequence. Then, we examine peptide cyclization with perfluoroaryl-cysteine  $S_NAr$  chemistry to improve the stability and delivery of peptide-ASO conjugates. We extend our  $S_NAr$  chemistry to the synthesis of arginine-rich bicyclic peptides, which are more stable to proteolysis than single cycles. Both perfluoroaryl cyclic and bicyclic arginine-rich peptides improve ASO activity fourteen-fold.

Consequently, we demonstrate that peptide cyclization with perfluoroaryl-cysteine  $S_NAr$  chemistry enhances the ability of peptides to cross the BBB. We prepare macrocyclic analogues of both a CPP and a therapeutic peptide. We show that a subset of the macrocycles cross the BBB in both a cellular spheroid model of the BBB, as well as after intravenous injection in mice. Finally, we conjugate a platinum (IV) prodrug of the chemotherapeutic cisplatin to a brain-penetrating perfluoroaryl macrocycle and show that the amount of platinum in the mouse brain is fifteen-fold greater than cisplatin after five hours.

In summary, we explore strategies to improve the peptide-mediated delivery of ASOs and small molecule chemotherapeutics across biological barriers. In the future, we envision extending these approaches to other macromolecular cargos of therapeutic interest.

Thesis Supervisor: Bradley L. Pentelute  
Associate Professor of Chemistry



## Acknowledgments

Graduate school has challenged me and pushed me to grow in ways I never could have imagined. It has forced me to question how I spend my time, how I see the world, and how to best advance my science based on the constraints in front of me. As someone who loves structure and predictability, it took me a while to grow comfortable with the fact I could not always predict where a result would lead, how long something would take, or what my project would look like a year down the road. I could not have made it through graduate school without the support of several people who contributed to my personal and professional development during this time.

First and foremost, thank you to Justin Wolfe. All of the work in this thesis is as much of a reflection of his ideas and creativity as my own. We have been a team throughout all of grad school and it is the greatest working partnership I have ever been a part of. He and I complement each other in many nuanced ways and our friendship has been a constant driving force for progress. Any time I am feeling anxious or obsessed with some small detail, he can always appreciate the bigger picture. I am also relatively risk-averse and default to tried and true methodologies, even if they are costly in terms of my own time. Justin loves tinkering with conditions and is always one to head into lab and try many different approaches to improve the status quo, just based on his own curiosity. He has definitely advanced my own intrinsic scientific curiosity.

Thank you to Prof. Bradley Pentelute, my thesis advisor. None of this research would have been possible without him. He was always one step ahead in terms of making sure I was set-up for success. From the moment I set foot in the lab, he helped guide me towards projects that aligned with my interests and my career path. He gave me tremendous freedom to pursue research in the directions I was passionate about and had an endless supply of enthusiasm and encouragement. As the first MD-PhD in the Chemistry department in recent years, he worked with me and the department to make it all feasible. He also created an incredible working environment in the lab filled with people who are talented, thoughtful, engaged, committed, and supportive.

The Pentelute lab has been the defining home for my PhD and I would not have made any scientific progress without my labmates. Thank you to Ethan, Alex M., and Surin for their friendship, scientific guidance and support since I first started in the lab as a rotation student in 2014. Thank you to Anthony Q. for being my partner-in-crime with second and third year orals. Thank you to Rebecca for making classes more fun and then joining our group and becoming one of my closest friends and scientific advisors in grad school. Thank you to Zi-Ning for wanting to work with me despite being a second semester senior and for all the incredible computer science expertise she brought to our science. I am also thankful to all the other Pentelute lab members past and present for everything they taught me and all the wonderful memories we shared in lab: Rachael, Katie, Jessie, Daniel, Amy, Zak, Alex L., Mike, Anthony R., Aaron, Carly, Dio, Azin, Faycal, Guillaume, Tuang, Chi, Kyle, Dan C., Mark, Mikael, Michael, Alex V., Mette, Peng, Vanessa, Yelim, Anupam, Nina, Nick, Lee, Heemal, and Andrei.

Thank you to Prof. Alex Shalek, my thesis chair for all of his help and support over the years. In addition to offering brilliant insight and being maximally efficient in meetings, it stood out to me that he started every meeting off asking me “how can I make your life in grad school better?” I also thank Prof. Alex Klivanov for serving on my committee the past three years.

Not only have I had support from the within the Department of Chemistry at MIT over my PhD, but I have also had all of the support from the MD-PhD program and from HST. Prof. Emery Brown never ceases to inspire me. Dr. Matthew Frosch has been an unwavering source of both academic and personal support throughout my entire time in the MD-PhD program so far. Anytime I have ever reached out with any concern, whether it be trying to figure out what direction to take

next with my science or how to handle exceptionally complex personal matters, he has always been a thoughtful listener and knows the exact right person to connect me with to help with the matter at hand. Thank you to Amy Cohen, Yi Shen, and Lisa Erickson in the MD-PhD office who went above and beyond to facilitate my NIH F30 fellowship application and for all random questions related to the program.

Thank you to Prof. Alan Beggs, who served as my co-sponsor for the F30 fellowship and who has provided phenomenal research mentorship, especially on the biological side and in considering potential applications of my work to muscle biology. I would also like to thank Dr. Gunnar Hanson and Monica Yao at Sarepta Therapeutics who collaborated with us on the PMO delivery work. I extend my gratitude to Dr. Fong Cho, Dr. Sean Lawler, Roscoe Wasserburg, and Dr. E. Antonio Chiocca at the Harvey-Cushing Neurooncology Laboratories at the Brigham and Women's Hospital. It was a pleasure to work closely with them on the blood-brain barrier project and they took me in with open arms to come spend time in the lab and learn more about animal work. I thank Prof. Steve Lippard and Dr. Wen Zhou for their contributions to the cisplatin work.

In addition to all the official support, I have also had many mentors and friends who have played an active role in my graduate school experience. Rebecca Wissner and Jake Goldberg were the people I looked up to most as scientists when I was an undergraduate in Prof. James Petersson's lab. I have tried to emulate Rebecca's passion for science throughout grad school. She is now working on protein delivery in her postdoctoral studies at Yale, so it has been incredibly fun to compare notes on intracellular delivery with her over the years. Jake did his postdoctoral studies at MIT so was always one staircase away, happy to chat about science at any time of day or night and always available to edit any scientific writing I sent his way.

I would not have survived grad school without Eriene Heidi-Sidhom and Ally Freedy. Both of them are the type of people that I can talk about anything with. We would go hiking, grab coffee, go for runs, eat dinner, or just mill around. Spending time with them was always restorative. They also are both brilliant scientists and given that they have other areas of scientific expertise, often had unique insights on my project. I also appreciate all the other MD/PhD and med school classmates who have been encouraging over the years including: David, Ditty, Jess, Emily, Nathan, Anna, Tim, Ben, Eve, and Kevin. MIT symphony orchestra (MITSO) has consistently been a positive outlet for me. My MITSO friends and I have amazing non-science conversations about music and life. Thanks to all my music friends past and present including: June, Sylvain, Taylor, Kelly, Kevin, Sabine, and Gabe.

Finally, I would like to thank my family. Ian McCurry's sense of humor never ceased to make me smile even on the worst days of grad school. He understands what makes me, me and I always feel most like myself around him. Ian's mom gave me a key pep talk at my lowest point in grad school that helped me to keep pushing forward. Robbie Berg is my person. He listens to every small detail of my life and is always there for me any time of day or night, no matter what else is going on. Robbie also makes me feel like the best version of myself. My grandma has always encouraged me to pursue education and at times made it financially possible. The Chitown crew, La, Dave, Ella and Ray, are a total blast and always offer a fun-filled Chicago retreat from life in Boston. My dad and brother have pushed me to be compassionate even when I am frustrated. And lastly, I would like to thank my mom. She is the coolest person I know, has supported every decision I have made, has always put things in perspective and is my role model in life. She has a phenomenal work ethic, can relate to absolutely anyone, and runs around with endless energy taking care of other people and being there to support them. I strive to be like her and have tried to approach graduate school with the same attitude she approaches life.



## **Table of Contents**

|  |    |
|--|----|
| <b>Abstract</b>  | 5  |
| <b>Acknowledgments</b>   | 7  |
| <b>Table of Contents</b>   | 10 |
| <b>List of Figures</b>   | 14 |
| <b>List of Tables</b>  | 17 |
| <b>Chapter 1: Background and Overview</b>  | 18 |
| <b>1.1 The Challenge of Biological Barriers</b>  | 19 |
| <b>1.2 Cell-Penetrating Peptides for Delivery</b>  | 21 |
| <b>1.3 Peptide Cyclization Strategies</b>  | 23 |
| <b>1.4 Antisense Oligonucleotide Therapeutics for Duchenne Muscular Dystrophy</b>              | 25 |
| <b>1.5 Blood-Brain Barrier</b>   | 27 |
| <b>1.6 Overview of Thesis</b>  | 29 |
| <b>1.7 References</b>  | 32 |
| <b>Chapter 2: Machine Learning to Predict Cell-Penetrating Peptides for Antisense Delivery</b> | 37 |
| <b>2.1 Introduction</b>  | 38 |
| <b>2.2 Results and Discussion</b>  | 40 |
| <b>2.3 Experimental</b>  | 50 |
| 2.3.1 Materials  | 50 |
| 2.3.2 Methods for LC-MS Analysis   | 50 |
| 2.3.3 General Method for Peptide Preparation   | 51 |
| 2.3.4 PMO Azide Synthesis  | 52 |
| 2.3.5 PMO-Peptide Conjugation with Cu(I)-Catalyzed Azide-Alkyne<br>Cycloaddition               | 52 |
| 2.3.6 Fluorophore Conjugation with Cu(I)-Catalyzed Azide-Alkyne<br>Cycloaddition               | 53 |
| 2.3.7 Computational Model Selection and Feature Importance                                     | 53 |
| 2.3.8 Flow Cytometry Assay for PMO-Peptide Conjugates  | 55 |
| 2.3.9 Flow Cytometry Assay for Cy5.5-Labeled Peptides  | 58 |



|   |     |
|---|-----|
| 2.3.10 Flow Cytometry Analysis with Endocytosis Inhibitors  | 58  |
| <b>2.4 Conclusions</b>  | 61  |
| <b>2.5 Acknowledgments</b>  | 63  |
| <b>2.6 Appendix of LC-MS Characterization</b>   | 64  |
| <b>2.7 References</b>   | 144 |
| <b>Chapter 3: Chimeras of Cell-Penetrating Peptides Demonstrate Synergistic Improvement in Antisense Efficacy</b> | 147 |
| <b>3.1 Introduction</b>   | 148 |
| <b>3.2 Results and Discussion</b>   | 150 |
| <b>3.3 Experimental</b>   | 162 |
| 3.3.1 Materials   | 162 |
| 3.3.2 Methods for LC-MS Analysis  | 162 |
| 3.3.3 General Method for Peptide Preparation  | 163 |
| 3.3.4 PMO Azide Synthesis   | 164 |
| 3.3.5 SulfoCy5-Maleimide Conjugation  | 164 |
| 3.3.6 PMO-Peptide Conjugation with Cu(I)-Catalyzed Azide-Alkyne Cycloaddition                                     | 164 |
| 3.3.7 Flow Cytometry Assay for PMO-Peptide Conjugates   | 165 |
| 3.3.8 Flow Cytometry Assay for SulfoCy5-Labeled PMO-Peptide Conjugates  | 165 |
| 3.3.9 Flow Cytometry Analysis with Endocytosis Inhibitors   | 166 |
| 3.3.10 Lactate Dehydrogenase (LDH) Assay  | 168 |
| 3.3.11 Live Cell Confocal Imaging   | 168 |
| <b>3.4 Acknowledgments</b>  | 170 |
| <b>3.5 Appendix of LC-MS Characterization</b>   | 171 |
| <b>3.6 Appendix of Confocal Images</b>  | 188 |
| <b>3.7 References</b>   | 198 |
| <b>Chapter 4: Perfluoroaryl Bicyclic Cell-Penetrating Peptides for Delivery of Antisense Oligonucleotides</b>     | 201 |
| <b>4.1 Introduction</b>   | 202 |
| <b>4.2 Results and Discussion</b>   | 204 |

|  |     |
|--|-----|
| <b>4.3 Experimental</b>  | 216 |
| 4.3.1 Materials  | 216 |
| 4.3.2 Methods for LC-MS Analysis   | 216 |
| 4.3.3 General Method for Peptide Preparation and Purification  | 217 |
| 4.3.4 Macrocyclization, Arylation, and Bicyclization   | 218 |
| 4.3.5 PMO-Peptide Conjugation  | 221 |
| 4.3.6 Proteolysis Assay  | 222 |
| 4.3.7 Comparison of <i>i, i+1</i> and <i>i, i+7</i> Cyclization  | 222 |
| 4.3.8 eGFP Exon Skipping Assay   | 223 |
| 4.3.9 eGFP Exon Skipping Assay with Varying Amounts of Serum   | 224 |
| 4.3.10 Lactate Dehydrogenase Assay   | 224 |
| <b>4.4 Acknowledgments</b>   | 227 |
| <b>4.5 Appendix of LC-MS Characterization</b>  | 228 |
| <b>4.6 References</b>  | 252 |
| <b>Chapter 5: Perfluoroarene-Based Peptide Macrocycles to Enhance Penetration Across the Blood-Brain Barrier</b> | 254 |
| <b>5.1 Introduction</b>  | 255 |
| <b>5.2 Results and Discussion</b>  | 257 |
| <b>5.3 Experimental</b>  | 268 |
| 5.3.1 Materials  | 268 |
| 5.3.2 Methods for LC-MS Analysis   | 268 |
| 5.3.3 General Method for Peptide Preparation   | 269 |
| 5.3.4 Macrocyclization, Alkylation, and Fluorophore Labeling Procedures  | 270 |
| 5.3.5 Flow Cytometry Assays  | 275 |
| 5.3.6 Proteolysis Assay  | 276 |
| 5.3.7 Lactate Dehydrogenase Assay  | 279 |
| 5.3.8 BBB Spheroid Assay   | 280 |
| 5.3.9 Serum Stability Assay  | 282 |
| 5.3.10 <i>In Vivo</i> Imaging System Analysis  | 282 |
| 5.3.11 Confocal Microscopy of <i>Ex Vivo</i> Brain Slices  | 285 |

|   |     |
|---|-----|
| <b>5.4 Acknowledgments</b>  | 287 |
| <b>5.5 Appendix of LC-MS Characterization</b>   | 288 |
| <b>5.6 References</b>   | 300 |
| <b>Chapter 6: A Pt(IV) Prodrug-Perfluoroaryl Macrocyclic Peptide Conjugate with Improved Stability and Brain Distribution</b> | 303 |
| <b>6.1 Introduction</b>   | 304 |
| <b>6.2 Results and Discussion</b>   | 306 |
| <b>6.3 Experimental</b>   | 312 |
| 6.3.1 Materials and Instrumentation   | 312 |
| 6.3.2 Method for LC-MS Analysis   | 312 |
| 6.3.3 Synthesis of Pt(IV) Prodrug   | 313 |
| 6.3.4 General Method for Peptide Preparation  | 315 |
| 6.3.5 Macrocyclization Procedure for PtIV-M13   | 317 |
| 6.3.6 Cytotoxicity Assays   | 317 |
| 6.3.7 Cell Uptake Assays  | 320 |
| 6.3.8 DNA Platination Assay   | 320 |
| 6.3.9 <i>In Vivo</i> Pharmacokinetics   | 321 |
| 6.3.10 <i>In Vivo</i> Biodistribution   | 321 |
| <b>6.4 Acknowledgments</b>  | 323 |
| <b>6.5 References</b>   | 324 |

## List of Figures

|   |     |
|---|-----|
| <b>Figure 2.1.</b> PMOs alter gene splicing.  | 41  |
| <b>Figure 2.2.</b> Cargo identity alters relative CPP efficacy.   | 44  |
| <b>Figure 2.3.</b> Random forest ensemble learning methods can be used to predict peptide sequences that facilitate PMO delivery.                   | 47  |
| <b>Figure 2.4.</b> Uptake of fluorophore-labeled PPCs.  | 48  |
| <b>Figure 2.5.</b> The PMO-PPC conjugates engage endocytic mechanisms in their uptake into cells.   | 48  |
| <b>Figure 2.6.</b> Mean decrease in accuracy due to removal of each feature in the final random forest ensemble.                                    | 54  |
| <b>Figure 2.7.</b> Representative histograms from the flow cytometry analysis of PMO-PPC conjugates.  | 57  |
| <b>Figure 2.8.</b> Effect of endocytosis inhibitors on PPC efficacy.  | 60  |
| <b>Figure 3.1.</b> Design and evaluation of PMO activity for PMO-Peptide chimera conjugates.  | 151 |
| <b>Figure 3.2.</b> Design principles of CPP chimeras.   | 153 |
| <b>Figure 3.3.</b> LDH Release from HeLa 654 cells upon treatment with 5 $\mu$ M PMO-peptide conjugate.   | 155 |
| <b>Figure 3.4:</b> Evaluation of mechanism of endocytosis for PMO-pVEC-Bpep conjugate.  | 156 |
| <b>Figure 3.5.</b> Study of mechanism of synergy with fluorophore-labeled conjugates.   | 159 |
| <b>Figure 3.6.</b> Comparison of PMO activity of unlabeled PMO-peptide conjugates with SulfoCy5-labeled PMO-peptide conjugates.                     | 161 |
| <b>Figure 3.7.</b> Effect of endocytosis inhibitors on PMO-Bpep, PMO-pVEC, and PMO-pVEC-Bpep efficacy.  | 167 |
| <b>Figure 4.1.</b> Multiple cysteine residues coupled to a perfluoroarene can be linked with 1,3,5-benzenetrithiol to enable peptide bicyclization. | 205 |
| <b>Figure 4.2.</b> The 1,3,5-benzenetrithiol linking strategy can be applied to smaller bicycles.   | 206 |
| <b>Figure 4.3.</b> Double macrocycle prepared through orthogonal protection.  | 206 |
| <b>Figure 4.4.</b> Kinetically controlled bicyclization enables high-yield synthesis of a double perfluoroaryl macrocyclic peptide.                 | 207 |
| <b>Figure 4.5.</b> Bicyclic peptides conjugated to PMO show increased exon-skipping activity.   | 209 |

|   |     |
|---|-----|
| <b>Figure 4.6.</b> Structures of cyclic controls.   | 209 |
| <b>Figure 4.7.</b> Effect of serum on level of PMO activity observed.   | 210 |
| <b>Figure 4.8.</b> Lactate dehydrogenase (LDH) release assay after treatment with PMO-Bicycle conjugates and controls.                              | 212 |
| <b>Figure 4.9.</b> Exon skipping activity of conjugates with R12 monocycles with different cyclization configurations.                              | 212 |
| <b>Figure 4.10.</b> Exon skipping activity of conjugates with Bpep monocycles with different cyclization configurations.                            | 213 |
| <b>Figure 4.11</b> Exon skipping activity of PMO conjugate to perfluoroaryl monocycles of cell-penetrating peptides.                                | 214 |
| <b>Figure 4.12.</b> Bicyclic peptides demonstrate enhanced proteolytic stability relative to monocyclic peptides.                                   | 215 |
| <b>Figure 5.1.</b> Macrocytic TP10 analogues prepared via $S_NAr$ .   | 258 |
| <b>Figure 5.2.</b> Perfluoroarene-based macrocytic TP10 analogues have increased uptake into HeLa and brain endothelial cells.                      | 258 |
| <b>Figure 5.3.</b> Perfluoroarene-based macrocytic TP10 analogues are resistant to proteolysis.   | 260 |
| <b>Figure 5.4.</b> Lactate dehydrogenase assay of perfluoroarene-based macrocytic TP10 analogues.   | 260 |
| <b>Figure 5.5.</b> Perfluoroarene-based macrocytic TP10 analogues display increased entry into BBB spheroids compared to their linear counterparts. | 261 |
| <b>Figure 5.6.</b> Example of fluorescence quantification for a sphere treated with 5 $\mu$ M BIM BH3 M4.   | 261 |
| <b>Figure 5.7.</b> Enhanced <i>in vivo</i> brain penetration of a perfluoroarene-based TP10 macrocycle.   | 263 |
| <b>Figure 5.8.</b> <i>In vivo</i> biodistribution of perfluoroarene-based macrocycles.  | 263 |
| <b>Figure 5.9.</b> Quantification of the <i>in vivo</i> biodistribution of perfluoroarene-based macrocycles.  | 264 |
| <b>Figure 5.10.</b> Serum stability of perfluoroarene-based TP10 analogue in mouse serum.   | 264 |
| <b>Figure 5.11.</b> Enhanced <i>in vivo</i> brain penetration of a perfluoroarene-based BIM BH3 macrocycle.   | 265 |

|  |     |
|--|-----|
| <b>Figure 5.12.</b> Comparison of perfluoroarene-cyclized BIM BH3 to hydrocarbon-cyclized BIM BH3.             | 266 |
| <b>Figure 5.13.</b> Schematic of perfluoroaryl macrocyclization reaction.                                      | 271 |
| <b>Figure 5.14.</b> Schematic of alkylation reaction.  | 271 |
| <b>Figure 5.15.</b> Histograms from flow cytometry experiments with HeLa cells.                                | 277 |
| <b>Figure 5.16.</b> Histograms from flow cytometry experiments with hCMEC/D3 brain endothelial cells.          | 278 |
| <b>Figure 5.17.</b> Confocal images of representative spheres treated with BIM BH3 analogues.                  | 281 |
| <b>Figure 5.18.</b> Total ion current (TIC) chromatograms of the serum stability assay with peptide TP10 M13.  | 283 |
| <b>Figure 5.19.</b> Total ion current (TIC) chromatograms of the serum stability assay with peptide TP10 Q*13. | 283 |
| <b>Figure 5.20.</b> IVIS images of mouse brains.   | 284 |
| <b>Figure 5.21.</b> IVIS images of TP10 analogues at lower concentration.                                      | 284 |
| <b>Figure 5.22.</b> Confocal images of brain slices after treatment with TP10 analogues.                       | 286 |
| <b>Figure 5.23.</b> Confocal images of brain slices after treatment with BIM analogues.                        | 286 |
| <b>Figure 6.1.</b> Synthetic route for preparing <b>4</b> from cisplatin.                                      | 307 |
| <b>Figure 6.2.</b> Synthesis and purification of PtIV-M13.   | 307 |
| <b>Figure 6.3.</b> PtIV-M13 has similar efficacy to cisplatin against patient-derived glioma initiating cells. | 308 |
| <b>Figure 6.4.</b> <i>In vitro</i> characterization of the PtIV-M13 conjugate compared with cisplatin.         | 308 |
| <b>Figure 6.5.</b> PtIV-M13 conjugate improves platinum stability and distribution of platinum to the brain.   | 310 |
| <b>Figure 6.6.</b> The perfluoroaryl moiety increases distribution to the brain, cerebellum, spleen and liver. | 310 |
| <b>Figure 6.7.</b> <sup>1</sup> H-NMR analysis of prodrug <b>4</b> .   | 314 |
| <b>Figure 6.8.</b> LC-MS analysis of PtIV-L13.   | 316 |
| <b>Figure 6.9.</b> LC-MS analysis of PtIV-M13 prior to macrocyclization.                                       | 316 |
| <b>Figure 6.10.</b> LC-MS analysis of PtIV-M13 after macrocyclization.   | 318 |
| <b>Figure 6.11.</b> DNA platination assay.   | 322 |

## List of Tables

|  |     |
|--|-----|
| <b>Table 2.1.</b> List of CPPs that were conjugated to PMO and tested in the eGFP assay.                             | 43  |
| <b>Table 2.2.</b> Variation in mean test accuracy according to selected hyperparameters.                             | 54  |
| <b>Table 4.1.</b> Arginine-rich peptides for bicyclization and control sequences.                                    | 205 |
| <b>Table 4.2.</b> Data from three individual experiments after treatment with each construct<br>at 5 $\mu\text{M}$ . | 226 |
| <b>Table 4.3.</b> Data from three individual experiments after treatment with each construct<br>at 2 $\mu\text{M}$ . | 226 |

## **Chapter 1: Background and Overview**



## 1.1. The Challenge of Biological Barriers

Over millennia, complex molecular mechanisms have evolved to protect organisms. These systems have been extraordinarily beneficial for the long-term survival of species such as humans. Yet, in an era in which scientists are gaining understanding of molecular mechanisms of disease and are designing molecules to modulate intracellular processes, natural defenses limit the development of new therapies. Natural defense mechanisms encompass several distinct biological processes. The immune system recognizes and clears foreign material from the body. The blood vessels in the brain, composed of several unique cell types, give rise to what is known as the blood-brain barrier and regulate which materials can access the brain. The phospholipid bilayer contains hundreds of embedded proteins that protect the cell from its surroundings. Whole scientific fields are devoted to each of these areas, as they are full of nuance and complexity. Designing methods to probe and selectively overcome these complex defense systems will be necessary for the advancement of macromolecular therapies.

When considering biological barriers such as the blood-brain barrier or the plasma membrane in relationship to therapeutic development, the lack of generalizable principles can be challenging. One framework for approaching this challenge is to ask: what is the molecule of interest, what is the target tissue within the body, and what delivery approach should be used. Useful macromolecular cargos of interest may include proteins, such as enzyme replacement therapies or Cas9 for *in vivo* gene editing,<sup>1-3</sup> oligonucleotides, such as antisense therapies or RNAi to modulate gene expression,<sup>4-7</sup> or peptides, such as protein-protein interaction inhibitors or proteolysis targeting chimeras.<sup>8,9</sup> These molecules vary in terms of size and chemical properties, and interact with biological barriers differently.

The second question of the target tissue within the body also governs which biological barriers must be considered. Does the molecule act extracellularly on a receptor or does it need to pass the plasma membrane and enter cells? Does the molecule need to access a poorly vascularized site? Does the molecule need to accumulate in a tumor? Does the molecule carry out its effect on the central nervous system? Some oligonucleotide therapeutics must cross the plasma membrane and enter the nucleus to mediate their effects. Chemotherapeutics for brain cancer must cross the blood-brain barrier and accumulate within the tumor if they are given intravenously.

Both the physicochemical properties of the molecule of interest and the target location impact the final consideration, the approach to delivery. For intracellular delivery, the methods

can be broken down into methods that rely on disrupting the cellular membrane and methods that utilize carriers to traverse the membrane, leaving the membrane intact.<sup>10</sup> Membrane-disruption techniques, as the name would suggest, typically involve the physical compromise of the plasma membrane through various mechanical, chemical, electrical, thermal, or optical means. While these methods allow the rapid delivery of diverse materials *ex vivo*, the non-specific physical disruption makes *in vivo* application difficult.

To cross biological barriers *in vivo*, carrier-mediated approaches to delivery drugs are safer and more effective. Carriers can include synthetic nanoparticles, viral vectors, micelles, liposomes, and peptides.<sup>11,12</sup> The path of carrier-drug conjugates involves uptake of the conjugate into cells through endocytosis. After endocytosis, the drug must escape the endosome and reach the desired subcellular compartment where it mediates its effect. In this thesis, we will specifically address peptide carriers and the peptide-mediated delivery of cargos across biological barriers. The rest of this introduction will cover detailed background information on the topics relevant to our approach.

## 1.2. Cell-Penetrating Peptides for Delivery

In 1988, back-to-back papers in *Cell* demonstrated that the *trans*-activator protein from HIV-1, tat, was rapidly taken up into cells.<sup>13,14</sup> The spontaneous cell entry of this protein fueled investigation over which part of the protein was necessary to observe cellular uptake.<sup>15</sup> Many deletion mutants were studied to identify the minimal peptide needed for cellular uptake, the nine residue sequence RKKRRQRRR.<sup>16</sup> In the same period of time, the *Antennapedia* gene homeobox from *Drosophila melanogaster* was synthesized and shown to enter differentiating nerve cells and drive morphological differentiation.<sup>17</sup> Eventually, it was determined that the third helix of the *Antennapedia* homeodomain was the portion responsible for cell entry; the peptide fragment corresponding to this helix was named “penetratin.”<sup>18</sup> Given their origins, these special peptide sequences that could cross biological barriers were initially termed protein transduction domains. Eventually, as more and more reports of peptide sequences with these capabilities emerged, the peptides became known as cell-penetrating peptides (CPPs).

Over the past few decades, several hundred CPPs have been described. An exact definition is difficult, but generally CPPs are peptide sequences of 5-40 amino acid residues that can enter cells. The lack of a cogent definition stems from the variations in the experiments performed to determine if a sequence is a CPP. Often, CPPs are evaluated through the covalent attachment of a fluorophore and the measurement of cellular fluorescence by flow cytometry and confocal microscopy. However, the devil can be in the details in these types of studies. Does a fluorescence measurement by flow cytometry confirm intracellular delivery or could the peptide be embedded in the cell membrane or trapped in endosomes? Does the fluorophore remain attached to the peptide? Does the fluorophore alter the physicochemical properties of the peptide? What concentrations are used? Are those concentrations physiologically relevant? Were the cells fixed prior to confocal imaging, as fixation can lead to artefactual results?<sup>19</sup> Fortunately, CPP sequences are often utilized in several contexts and for several applications over time, thus increasing confidence that a particular sequence is efficacious. Yet, the efficacy of a CPP for the delivery of a particular cargo will always be context-dependent.

CPP sequences can be grouped in several ways based on their origin or physicochemical properties. Many CPPs are derived from fragments of proteins, such as viral proteins, DNA- or RNA-binding proteins, or heparin-binding proteins. Others have come from rational design based on structure activity relationships, computational prediction based on the CPP literature,

antimicrobial peptides, or DNA-encoded libraries. In terms of physicochemical properties, the CPPs can be roughly broken down into cationic, amphipathic, and hydrophobic. However, even within these classifications there are gray areas of classification. For example, several cationic CPPs with net charges over +5 have amphipathic stretches that can adopt alpha helices.

The applications of CPPs to delivery are varied. CPPs have been used in the delivery of nanoparticles, proteins, peptides, antisense oligonucleotides, small molecules, small interfering RNA, and double stranded DNA. The CPP conjugates can have different properties from the parent CPP alone. Additionally, several mechanisms of cell entry exist for CPPs and CPP-cargo conjugates.<sup>20,21</sup> The mechanism is often highly dependent on the treatment concentrations and the type of cargo attached.<sup>22,23</sup> At low, physiologically-relevant concentrations, uptake is primarily endocytic. However, several different endocytic mechanisms can potentially be engaged including micropinocytosis, clathrin-mediated endocytosis, caveolae-mediated endocytosis and clathrin/caveolae-independent endocytosis.<sup>24</sup>

### 1.3. Peptide Cyclization Strategies

Macrocyclization is one attractive method to improve the *in vivo* stability of peptides and increase delivery across biological barriers. Linear peptides composed of natural amino acids are highly susceptible to proteolysis. Cyclizing the peptides improves stability by shielding the peptide backbone from endoproteases. Further, there is often the benefit of improved cellular uptake when a peptide is cyclized with a hydrophobic moiety. In several cases, this effect may be related to stabilizing an alpha-helical structure.<sup>25,26</sup> However, improved effects on intracellular delivery can be observed even with non-helical macrocyclic peptides, and therefore development of peptide macrocycles for delivery should not focus on helical promotion alone.

Most broadly, peptide macrocycles can be formed in four configurations: head to tail (N-terminus to C-terminus), head to side-chain, tail to side-chain, and side-chain to side-chain.<sup>27</sup> Macrocyclization reactions are typically performed under dilute conditions to favor intramolecular cyclization over intermolecular multimerization. The most common methods include lactamization,<sup>28</sup> lactonization,<sup>29</sup> and disulfide bridge formation, all of which use natural amino acid residues. Side-chain to side-chain lactamization can be performed by a condensation reaction between lysine and either aspartic or glutamic acid. Lactonization results from a condensation between a serine or threonine and either an aspartic or glutamic acid. Disulfide bridge formation simply requires two cysteine residues.

The unique nucleophilic reactivity of cysteine can be leveraged for macrocyclization using exogenous linkers. For example, a dibromide linker will react with a peptide containing two thiols and the bis-alkylation will yield a stable macrocycle.<sup>30-32</sup> Brown *et al.* have described a photoreversible macrocyclization between cysteines with *s*-tetrazine.<sup>33</sup> Wang *et al.* have shown that a diene can be used to macrocyclize two cysteine residues with thiol-ene chemistry.<sup>34</sup> The Pentelute and Buchwald groups have described palladium-mediated arylation of cysteine for macrocyclization.<sup>35,36</sup> Additionally, the Pentelute group has shown that nucleophilic aromatic substitution can be employed to generate a macrocycle between two cysteine residues with a perfluoroaromatic linker.<sup>37,38</sup> This perfluoroaryl macrocyclization represents a promising approach to improve delivery across biological barriers. In subsequent chapters, perfluoroaryl macrocyclized peptides are applied to the delivery of both oligonucleotides and chemotherapeutics.

The physicochemical properties of an ideal delivery vehicle differ based on the therapeutic cargo, and some macrocyclization techniques that employ unnatural amino acids yield distinct linkages with unique properties. If an azide and an alkyne are incorporated into a peptide, a copper-catalyzed 1,3-dipolar cycloaddition can be used to form a peptide macrocycle with a triazole.<sup>39</sup> An intramolecular oxime ligation can yield a macrocycle with a peptide containing an oxyamino and aldehyde pair.<sup>40</sup> Finally, ring closing metathesis with Grubbs catalyst is commonly employed to create macrocycles between two alpha-alpha disubstituted olefin-bearing amino acids.<sup>25,41</sup>

## 1.4. Antisense Oligonucleotide Therapeutics for Duchenne Muscular Dystrophy

One compelling application for peptide-mediated delivery is antisense oligonucleotides (ASOs). ASOs are single-stranded oligonucleotide analogues, 5-10 kDa in size, that hybridize to DNA and RNA via Watson-Crick base pairing. ASOs can be designed to target mRNA and form an ASO-mRNA heteroduplex. The heteroduplex can trigger mRNA degradation by RNase H,<sup>42</sup> translational arrest by sterically blocking ribosomal access, modulation of splicing affecting the spliceosome, or destabilization of pre-mRNA leading to downregulation of protein expression.<sup>4</sup>

If ASOs had an unmodified phosphodiester backbone, they would be rapidly degraded by nucleases. To increase nuclease resistance, several generations of backbone chemistries have been developed. The first-generation ASOs had a phosphorothioate backbone in which one of the non-bridging oxygen atoms of the phosphodiester bond was replaced by sulfur. The second-generation involved 2'-alkyl modifications of either a methyl (2'-OMe) or methoxyethyl (2'-MOE) to the ribose. Third-generation ASOs began modifying the furanose ring to further enhance target affinity, serum stability, and pharmacokinetics. The three most common third-generation chemistries are peptide nucleic acids, locked nucleic acids, and phosphorodiamidate morpholino oligonucleotides. Peptide nucleic acids have a *N*-(2-aminoethyl)glycine backbone and nucleobases are attached to the backbone via a methylene carbonyl linkage.<sup>43</sup> Locked nucleic acids are conformationally restricted with a 2'-O,4'-C-methylene bridge in the  $\beta$ -D-ribofuranosyl configuration.<sup>44,45</sup> Finally, phosphorodiamidate morpholino oligonucleotides (PMOs) contain a backbone consisting of methylenemorpholine rings instead of ribose and phosphorodiamidate linkages instead of phosphodiester linkages.

Eteplirsen, commercially marketed as Exondys 51, is a PMO from Sarepta Therapeutics designed to restore the reading frame of dystrophin in a subset of patients with Duchenne muscular dystrophy (DMD). DMD is an X-linked recessive genetic disorder affecting around 1 in 3500 boys that has a debilitating clinical phenotype of severe muscular degeneration. Typically, patients rely on wheelchairs for mobility by their early teens and die prematurely in their thirties due to either cardiomyopathy or respiratory infections.<sup>46,47</sup> DMD is caused by a variety of mutations that result in the truncation of the muscular variant of the dystrophin protein. The muscular variant of dystrophin is a 427 kDa protein consisting of four domains: an N-terminal domain, a rod domain with spectrin-like repeats, a cysteine-rich domain, and a C-terminal domain.<sup>48,49</sup> Approximately 80% of DMD mutations occur in the portion of the gene encoding the rod domain. The rod domain

contains repetitive sequences of limited individual functional importance but is cumulatively critical for dystrophin. The absence of an exon from the pre-mRNA encoding the rod domain still yields a functional protein product.<sup>50</sup> As a result, DMD is conducive to exon skipping, in which an exon is removed from the mature mRNA in order to eliminate a mutation or restore the reading frame.

Although PMOs are attractive molecules to trigger exon skipping and gene correction in DMD patients, their chemical properties impede effective delivery across the cell membrane and into the nucleus.<sup>51,52</sup> In fact, data from skeletal muscle cells in the mouse model of DMD suggest that most PMO entry into cells results from plasma membrane disruption in the absence of functional dystrophin.<sup>53</sup> In the case of Eteplirsen, systemic intravenous administration is inefficient and weekly dosing at 30 mg/kg of PMO is required. Even with this large dose, only moderate improvement in clinical phenotype is observed.<sup>54</sup> If the dose could be lowered by improving cellular delivery, additional clinical benefit may result.

Conjugating the PMO to a cell-penetrating peptide can improve cellular delivery.<sup>55-57</sup> PMOs conjugated to highly charged, arginine-rich peptides have been shown to restore dystrophin expression to ~50% of normal levels in skeletal muscle. While this level is sufficient for phenotypic improvement, these compounds have also been shown to have considerably increased toxicity.<sup>58</sup> Later chapters describe the development of PMO-CPP conjugates that ideally will lead to lower dosages for restoring dystrophin expression without conferring additional toxicity. The experiments described focus on a model PMO that has exon skipping activity in a facile *in vitro* assay. Using this assay, advancements were made in identifying peptide sequences apt for PMO delivery, as well as chemical modifications for improving uptake and stability. Hopefully these discoveries will be translated to Eteplirsen in the future.



## 1.5. Blood-Brain Barrier

Cell-penetrating peptides and macrocyclic peptides can also be applied to enhancing the transport of molecules, such as chemotherapeutics, across the blood-brain barrier. There are many parallels between intracellular delivery and delivery across the blood-brain barrier. Just as some delivery methods disrupt the plasma membrane and some methods leave the membrane intact, for penetration across BBB some methods temporarily disrupt the BBB, while others leave the BBB intact. Delivery methods that leave the BBB intact often rely on the process of transcytosis, in which molecules are actively transported through brain endothelial cells to the brain parenchyma. The first step in transcytosis across the BBB is intracellular uptake by brain endothelial cells, so carriers like cell-penetrating peptides that improve intracellular delivery are also potentially good delivery vehicles for crossing the BBB. However, for BBB penetration, the vehicle-cargo conjugate also needs to leave the endothelial cell on the other side and be trafficked to the brain.

The BBB arises from the complex interplay between three main components: the brain endothelial cells that line the lumen of the brain blood vessels, the pericytes that sit on the basal lamina, and the associating astrocytic end-feet and microglia.<sup>59</sup> The cellular architecture that develops between these different components tightly regulate molecular trafficking. The BBB is distinguished from the peripheral blood vessels by the upregulation of tight junctions that limit paracellular traffic and the upregulation of efflux pumps that actively extrude foreign substances from the brain into the blood.<sup>60,61</sup> Although the BBB most likely arose evolutionarily to protect our brains from harmful substances in the blood, the BBB also prevents most therapeutics from accessing the brain and limits treatment options for central nervous system diseases.

Strategies for delivery across the BBB can be clustered into those that disrupt the barrier and those that engage transcytosis. Osmotic disruption with mannitol is one disruption technique and allows for the nonspecific passage of molecules through based on size.<sup>62</sup> However, osmotic disruption can be difficult to perform in a confined way and has largely fallen out of favor. Another disruption technique is focused ultrasound, in which microbubbles are injected and then irradiated in a defined area with ultrasound to locally disrupt the barrier.<sup>63</sup> In transcytosis, the specific molecule of interest is endocytosed into brain endothelial cells and then exocytosed on the other side, leaving the barrier intact.

Transcytosis can be receptor-mediated or nonspecific, relying on a general adsorptive affinity for endothelial cells. Approaches that utilize receptor-mediated transcytosis involve the

conjugation of a therapeutic cargo to antibodies or nanobodies with affinity for a receptor, such as the transferrin or insulin receptors. While the insulin and transferrin receptors are not unique to the brain endothelial cell surface, they are two of the few targetable receptors.<sup>64</sup> A few peptides have been developed to bind to receptors on the endothelial surface, such as the peptide Angiopep-2 which binds to the lipoprotein receptor-related protein 1 (LRP1) receptor.<sup>65</sup> Other peptides have been described that cross the blood-brain barrier through adsorptive-mediated transcytosis, wherein peptides nonspecifically adsorb to the plasma membrane of brain endothelial cells and subsequently undergo transcytosis.<sup>66</sup> Several cell-penetrating peptides fall in this category.<sup>67</sup>

One challenge with BBB research is how to prove that a molecule has entered the brain. For example, some molecules are endocytosed into brain endothelial cells but remain trapped without undergoing exocytosis to the brain parenchyma. Many of the methodologies available to examine the amount of uptake into the brain are unable to distinguish between the brain endothelium and the brain parenchyma. When the molecule of interest is labeled with a radiotracer or a fluorophore, the analysis is still difficult. Brains must be removed from mice, cryosectioned *ex vivo*, and imaged (e.g. - confocal microscopy if fluorophore-labeled). However, the relative concentration of the molecule is typically quite low, especially if its localization is diffuse. This coupled with high amounts of autofluorescence in brain tissue from lipofuscins complicates analysis.<sup>68,69</sup> One approach to these challenges is to combine multiple different techniques that independently assess brain penetration.

## 1.6. Overview of Thesis

The unifying theme of this work is peptide-mediated delivery across biological barriers. Chapters 2-4 focus on improving the intracellular delivery of phosphorodiamidate morpholino oligonucleotides. Chapters 5-6 are devoted to developing methodology to increase the delivery of therapeutics to the brain. Each chapter looks to address a separate challenge in the field.

Chapter 2 addresses the question of how to select a cell-penetrating peptide sequence for a particular therapeutic cargo. When starting the project, we knew we wanted to improve the delivery of PMOs. However, only a fraction of CPPs in the literature have been tested in the context of PMO delivery. Further, the conditions under which researchers test CPPs can be highly variable in terms of concentration, whether or not a macromolecular cargo is attached, and whether or not there is serum in the media. In addition to these considerations, it is likely that the ideal peptide sequence for the delivery of a large protein with significant surface charge density is different from the ideal peptide sequence for the delivery of a charge-neutral 18-mer PMO. We propose one solution to this challenge in Chapter 2, in which 64 literature-reported CPPs are conjugated to PMO and tested in a cellular assay for PMO activity under standardized conditions. This systematic approach allows examination of trends in the CPPs that are optimal for PMO. From these data, we use ensemble learning methods to develop a predictive model for whether or not a given peptide sequence would improve PMO activity at least three-fold. The model is about 70% accurate using a held-out test set from the data. However, when we use the model to identify novel peptide sequences for PMO delivery, all five of the predicted positive sequences improve PMO activity in the assay. The combination of screening and predicting could be one way to engineer peptide delivery tools for a cargo of interest. One drawback of this approach is that the outputs are a result of the inputs and therefore the predictions are unlikely to exceed the range of PMO activity present in the input data set.

One trend in the data from Chapter 2 is that positive charge in the peptide is the single greatest predictor of CPP-PMO conjugate activity in the assay. However, we became curious why the amphipathic CPPs did not perform well. For a conjugate to have activity, it must associate with the cell membrane, be endocytosed, escape the endosome, enter the nucleus, bind to RNA, and alter splicing. It is possible that a peptide could be efficient for a few of these steps yet fail somewhere upstream of RNA binding. We hypothesize that if we combine CPPs of different classes, we could potentially leverage the benefits of each. In Chapter 3, we describe chimeras of

CPPs that synergistically promote PMO activity. We investigate the design principles of how to favorably combine CPPs and we examine the mechanism of uptake of these chimeras. Our best conjugates increased PMO activity around 20-fold compared with unconjugated PMO.

Both Chapters 2 and 3 utilize linear peptides composed of all L-amino acids. As a result, the peptides are relatively susceptible to proteolysis. In Chapter 4, we sought to improve the stability of CPPs for intracellular delivery with perfluoroaryl-cysteine cyclization chemistry. We also sought to move beyond single macrocycles to see if we could extend perfluoroaryl-cysteine cyclization chemistry to bicyclic structures. We hypothesized that the bicyclization of arginine-rich peptides would improve their stability and their ability to deliver PMO into the nucleus. Chapter 4 introduces two methods for the synthesis of arginine-rich bicyclic peptides using cysteine perfluoroarylation chemistry. The bicyclic peptides were covalently linked to PMO and assayed for exon skipping activity. The perfluoroaryl cyclic and bicyclic peptides improve PMO activity roughly 14-fold over the unconjugated PMO. The bicyclic peptides exhibited increased proteolytic stability relative to the monocycle, demonstrating that perfluoroaryl bicyclic peptides are potent and stable delivery agents.

Given our success with the perfluoroaryl cyclization as a means for improving intracellular delivery, we reasoned that perfluoroaryl cyclization could potentially enhance delivery across the BBB. As previously discussed, intracellular delivery to brain endothelial cells is the first step of transcytosis across the BBB. In Chapter 5, we describe the utility of perfluoroaryl macrocyclization to improve the ability of peptides to cross the BBB. Multiple macrocyclic analogues of the peptide transportan-10 were investigated that displayed increased uptake in brain endothelial cells and improved proteolytic stability. One of these analogues (TP10 M13) exhibited substantially increased delivery across a cellular spheroid model of the blood-brain barrier. Through *ex vivo* imaging of mouse brains, we demonstrated that this perfluoroarene-based macrocycle of TP10 exhibits increased penetration of the brain parenchyma following intravenous administration in mice. Finally, we evaluated macrocyclic analogues of the BH3 domain of the BIM protein to assess if our approach would be applicable to a peptide of therapeutic interest. We identified a BIM BH3 analogue that showed increased penetration of the brain tissue in mice.

In Chapter 5, all studies with TP10 M13 were completed with a fluorophore. However, we wished to extend our findings to a chemotherapeutic cargo of interest. We designed a conjugate between a platinum (IV) prodrug and TP10 M13 with glioblastoma therapy in mind. One of the

many factors that limits drug development for brain tumors is delivery to the brain and across the blood-brain barrier. We hypothesized that a conjugate between a platinum (IV) prodrug of cisplatin and TP10 M13 could overcome this challenge. We performed *in vitro* experiments illustrating the efficacy of our conjugate against two patient-derived glioma cell lines. Finally, we studied the pharmacokinetics and biodistribution of the conjugate after tail vein injection in mice. The amount of platinum in the brain after treatment with our conjugate is 15-fold greater than cisplatin at five hours.

Taken together, the ideas in this thesis offer different strategies for the advancement of peptide-mediated delivery. The three highlights are the combination of screening and computational methodology, the creation of chimeric sequences, and the cyclization of peptides with a perfluoroaryl linker. The studies contained within are among the first examples of using perfluoroaryl linkers for delivery applications and we are excited to see how this impacts drug design and delivery in the future.

## 1.7. References

- (1) Zuris, J. A.; Thompson, D. B.; Shu, Y.; Guilinger, J. P.; Bessen, J. L.; Hu, J. H.; Maeder, M. L.; Joung, J. K.; Chen, Z.-Y.; Liu, D. R. Cationic Lipid-Mediated Delivery of Proteins Enables Efficient Protein-Based Genome Editing in Vitro and in Vivo. *Nat. Biotechnol.* **2015**, *33* (1), 73–80.
- (2) Albadri, S.; Del Bene, F.; Revenu, C. Genome Editing Using CRISPR/Cas9-Based Knock-in Approaches in Zebrafish. *Methods San Diego Calif* **2017**, *121–122*, 77–85.
- (3) Fu, A.; Tang, R.; Hardie, J.; Farkas, M. E.; Rotello, V. M. Promises and Pitfalls of Intracellular Delivery of Proteins. *Bioconjug. Chem.* **2014**, *25* (9), 1602–1608.
- (4) Chan, J. H.; Lim, S.; Wong, W. F. Antisense Oligonucleotides: From Design to Therapeutic Application. *Clin. Exp. Pharmacol. Physiol.* **2006**, *33* (5–6), 533–540.
- (5) Dias, N.; Stein, C. A. Antisense Oligonucleotides: Basic Concepts and Mechanisms. *Mol. Cancer Ther.* **2002**, *1* (5), 347–355.
- (6) Crooke, S. T. Molecular Mechanisms of Antisense Oligonucleotides. *Nucleic Acid Ther.* **2017**, *27* (2), 70–77.
- (7) Kim, D. H.; Rossi, J. J. RNAi Mechanisms and Applications. *BioTechniques* **2008**, *44* (5), 613–616.
- (8) Buckley, D. L.; Crews, C. M. Small-Molecule Control of Intracellular Protein Levels through Modulation of the Ubiquitin Proteasome System. *Angew. Chem. Int. Ed Engl.* **2014**, *53* (9), 2312–2330.
- (9) Pelay-Gimeno, M.; Glas, A.; Koch, O.; Grossmann, T. N. Structure-Based Design of Inhibitors of Protein-Protein Interactions: Mimicking Peptide Binding Epitopes. *Angew. Chem. Int. Ed Engl.* **2015**, *54* (31), 8896–8927.
- (10) Stewart, M. P.; Sharei, A.; Ding, X.; Sahay, G.; Langer, R.; Jensen, K. F. In Vitro and Ex Vivo Strategies for Intracellular Delivery. *Nature* **2016**, *538* (7624), 183–192.
- (11) Torchilin, V. P. Recent Approaches to Intracellular Delivery of Drugs and Dna and Organelle Targeting. *Annu. Rev. Biomed. Eng.* **2006**, *8* (1), 343–375.
- (12) Stewart, M. P.; Lorenz, A.; Dahlman, J.; Sahay, G. Challenges in Carrier-Mediated Intracellular Delivery: Moving beyond Endosomal Barriers. *Wiley Interdiscip. Rev. Nanomed. Nanobiotechnol.* **2016**, *8* (3), 465–478.
- (13) Green, M.; Loewenstein, P. M. Autonomous Functional Domains of Chemically Synthesized Human Immunodeficiency Virus Tat Trans-Activator Protein. *Cell* **1988**, *55* (6), 1179–1188.
- (14) Frankel, A. D.; Pabo, C. O. Cellular Uptake of the Tat Protein from Human Immunodeficiency Virus. *Cell* **1988**, *55* (6), 1189–1193.
- (15) Green, M.; Ishino, M.; Loewenstein, P. M. Mutational Analysis of HIV-1 Tat Minimal Domain Peptides: Identification of Trans-Dominant Mutants That Suppress HIV-LTR-Driven Gene Expression. *Cell* **1989**, *58* (1), 215–223.
- (16) Vivès, E.; Brodin, P.; Lebleu, B. A Truncated HIV-1 Tat Protein Basic Domain Rapidly Translocates through the Plasma Membrane and Accumulates in the Cell Nucleus. *J. Biol. Chem.* **1997**, *272* (25), 16010–16017.
- (17) Joliot, A.; Pernelle, C.; Deagostini-Bazin, H.; Prochiantz, A. Antennapedia Homeobox Peptide Regulates Neural Morphogenesis. *Proc. Natl. Acad. Sci.* **1991**, *88* (5), 1864–1868.
- (18) Derossi, D.; Joliot, A. H.; Chassaing, G.; Prochiantz, A. The Third Helix of the Antennapedia Homeodomain Translocates through Biological Membranes. *J. Biol. Chem.* **1994**, *269* (14), 10444–10450.

- (19) Richard, J. P.; Melikov, K.; Vives, E.; Ramos, C.; Verbeure, B.; Gait, M. J.; Chernomordik, L. V.; Lebleu, B. Cell-Penetrating Peptides A REEVALUATION OF THE MECHANISM OF CELLULAR UPTAKE. *J. Biol. Chem.* **2003**, *278* (1), 585–590.
- (20) Thorén, P. E. G.; Persson, D.; Esbjörner, E. K.; Goksör, M.; Lincoln, P.; Nordén, B. Membrane Binding and Translocation of Cell-Penetrating Peptides. *Biochemistry (Mosc.)* **2004**, *43* (12), 3471–3489.
- (21) Lundin, P.; Johansson, H.; Guterstam, P.; Holm, T.; Hansen, M.; Langel, Ü.; EL Andaloussi, S. Distinct Uptake Routes of Cell-Penetrating Peptide Conjugates. *Bioconjug. Chem.* **2008**, *19* (12), 2535–2542.
- (22) Kosuge, M.; Takeuchi, T.; Nakase, I.; Jones, A. T.; Futaki, S. Cellular Internalization and Distribution of Arginine-Rich Peptides as a Function of Extracellular Peptide Concentration, Serum, and Plasma Membrane Associated Proteoglycans. *Bioconjug. Chem.* **2008**, *19* (3), 656–664.
- (23) Tünnemann, G.; Martin, R. M.; Haupt, S.; Patsch, C.; Edenhofer, F.; Cardoso, M. C. Cargo-Dependent Mode of Uptake and Bioavailability of TAT-Containing Proteins and Peptides in Living Cells. *FASEB J.* **2006**, *20* (11), 1775–1784.
- (24) Mayor, S.; Pagano, R. E. Pathways of Clathrin-Independent Endocytosis. *Nat. Rev. Mol. Cell Biol.* **2007**, *8* (8), 603.
- (25) Walensky, L. D.; Kung, A. L.; Escher, I.; Malia, T. J.; Barbuto, S.; Wright, R. D.; Wagner, G.; Verdine, G. L.; Korsmeyer, S. J. Activation of Apoptosis in Vivo by a Hydrocarbon-Stapled BH3 Helix. *Science* **2004**, *305* (5689), 1466–1470.
- (26) Chang, Y. S.; Graves, B.; Guerlavais, V.; Tovar, C.; Packman, K.; To, K.-H.; Olson, K. A.; Kesavan, K.; Gangurde, P.; Mukherjee, A.; et al. Stapled  $\alpha$ -helical Peptide Drug Development: A Potent Dual Inhibitor of MDM2 and MDMX for P53-Dependent Cancer Therapy. *Proc. Natl. Acad. Sci.* **2013**, 201303002.
- (27) White, C. J.; Yudin, A. K. Contemporary Strategies for Peptide Macrocyclization. *Nat. Chem.* **2011**, *3* (7), 509–524.
- (28) Herce, H. D.; Schumacher, D.; Schneider, A. F. L.; Ludwig, A. K.; Mann, F. A.; Fillies, M.; Kasper, M.-A.; Reinke, S.; Krause, E.; Leonhardt, H.; et al. Cell-Permeable Nanobodies for Targeted Immunolabelling and Antigen Manipulation in Living Cells. *Nat. Chem.* **2017**, *9* (8), 762–771.
- (29) Parenty, A.; Moreau, X.; Campagne, J.-M. Macrolactonizations in the Total Synthesis of Natural Products. *Chem. Rev.* **2006**, *106* (3), 911–939.
- (30) Timmerman, P.; Beld, J.; Puijk, W. C.; Meloen, R. H. Rapid and Quantitative Cyclization of Multiple Peptide Loops onto Synthetic Scaffolds for Structural Mimicry of Protein Surfaces. *Chembiochem Eur. J. Chem. Biol.* **2005**, *6* (5), 821–824.
- (31) Jo, H.; Meinhardt, N.; Wu, Y.; Kulkarni, S.; Hu, X.; Low, K. E.; Davies, P. L.; DeGrado, W. F.; Greenbaum, D. C. Development of  $\alpha$ -Helical Calpain Probes by Mimicking a Natural Protein–Protein Interaction. *J. Am. Chem. Soc.* **2012**, *134* (42), 17704–17713.
- (32) Peraro, L.; Zou, Z.; Makwana, K. M.; Cummings, A. E.; Ball, H. L.; Yu, H.; Lin, Y.-S.; Levine, B.; Kritzer, J. A. Diversity-Oriented Stapling Yields Intrinsically Cell-Penetrant Inducers of Autophagy. *J. Am. Chem. Soc.* **2017**, *139* (23), 7792–7802.
- (33) Brown, S. P.; Smith, A. B. Peptide/Protein Stapling and Unstapling: Introduction of s-Tetrazine, Photochemical Release, and Regeneration of the Peptide/Protein. *J. Am. Chem. Soc.* **2015**, *137* (12), 4034–4037.

- (34) Wang, Y.; Chou, D. H.-C. A Thiol-Ene Coupling Approach to Native Peptide Stapling and Macrocyclization. *Angew. Chem. Int. Ed Engl.* **2015**, *54* (37), 10931–10934.
- (35) Vinogradova, E. V.; Zhang, C.; Spokoyny, A. M.; Pentelute, B. L.; Buchwald, S. L. Organometallic Palladium Reagents for Cysteine Bioconjugation. *Nature* **2015**, *526* (7575), 687–691.
- (36) J. Rojas, A.; Zhang, C.; V. Vinogradova, E.; H. Buchwald, N.; Reilly, J.; L. Pentelute, B.; L. Buchwald, S. Divergent Unprotected Peptide Macrocyclisation by Palladium-Mediated Cysteine Arylation. *Chem. Sci.* **2017**, *8* (6), 4257–4263.
- (37) Spokoyny, A. M.; Zou, Y.; Ling, J. J.; Yu, H.; Lin, Y.-S.; Pentelute, B. L. A Perfluoroaryl-Cysteine SNAr Chemistry Approach to Unprotected Peptide Stapling. *J. Am. Chem. Soc.* **2013**, *135* (16), 5946–5949.
- (38) Zou, Y.; Spokoyny, A. M.; Zhang, C.; Simon, M. D.; Yu, H.; Lin, Y.-S.; Pentelute, B. L. Convergent Diversity-Oriented Side-Chain Macrocyclization Scan for Unprotected Polypeptides. *Org. Biomol. Chem.* **2013**, *12* (4), 566–573.
- (39) Bock, V. D.; Perciaccante, R.; Jansen, T. P.; Hiemstra, H.; van Maarseveen, J. H. Click Chemistry as a Route to Cyclic Tetrapeptide Analogues: Synthesis of Cyclo-[Pro-Val-Psi(Triazole)-Pro-Tyr]. *Org. Lett.* **2006**, *8* (5), 919–922.
- (40) Haney, C. M.; Loch, M. T.; Horne, W. S. Promoting Peptide  $\alpha$ -Helix Formation with Dynamic Covalent Oxime Side-Chain Cross-Links. *Chem. Commun.* **2011**, *47* (39), 10915–10917.
- (41) Miller, S. J.; Blackwell, H. E.; Grubbs, R. H. Application of Ring-Closing Metathesis to the Synthesis of Rigidified Amino Acids and Peptides. *J. Am. Chem. Soc.* **1996**, *118* (40), 9606–9614.
- (42) Wu, H.; Lima, W. F.; Zhang, H.; Fan, A.; Sun, H.; Crooke, S. T. Determination of the Role of the Human RNase H1 in the Pharmacology of DNA-like Antisense Drugs. *J. Biol. Chem.* **2004**, *279* (17), 17181–17189.
- (43) Nielsen, P. E.; Egholm, M.; Berg, R. H.; Buchardt, O. Sequence-Selective Recognition of DNA by Strand Displacement with a Thymine-Substituted Polyamide. *Science* **1991**, *254* (5037), 1497–1500.
- (44) Kurreck, J.; Wyszko, E.; Gillen, C.; Erdmann, V. A. Design of Antisense Oligonucleotides Stabilized by Locked Nucleic Acids. *Nucleic Acids Res.* **2002**, *30* (9), 1911–1918.
- (45) Petersen, M.; Wengel, J. LNA: A Versatile Tool for Therapeutics and Genomics. *Trends Biotechnol.* **2003**, *21* (2), 74–81.
- (46) Emery, A. E. H. The Muscular Dystrophies. *Lancet* **2002**, *359* (9307), 687–695.
- (47) Hoffman, E. P.; Brown, R. H.; Kunkel, L. M. Dystrophin: The Protein Product of the Duchenne Muscular Dystrophy Locus. *Cell* **1987**, *51* (6), 919–928.
- (48) Koenig, M.; Hoffman, E. P.; Bertelson, C. J.; Monaco, A. P.; Feener, C.; Kunkel, L. M. Complete Cloning of the Duchenne Muscular Dystrophy (DMD) cDNA and Preliminary Genomic Organization of the DMD Gene in Normal and Affected Individuals. *Cell* **1987**, *50* (3), 509–517.
- (49) Koenig, M.; Monaco, A. P.; Kunkel, L. M. The Complete Sequence of Dystrophin Predicts a Rod-Shaped Cytoskeletal Protein. *Cell* **1988**, *53* (2), 219–228.
- (50) Gregorevic, P.; Blankinship, M. J.; Allen, J. M.; Crawford, R. W.; Meuse, L.; Miller, D. G.; Russell, D. W.; Chamberlain, J. S. Systemic Delivery of Genes to Striated Muscles Using Adeno-Associated Viral Vectors. *Nat. Med.* **2004**, *10* (8), 828–834.



- (51) Alter, J.; Lou, F.; Rabinowitz, A.; Yin, H.; Rosenfeld, J.; Wilton, S. D.; Partridge, T. A.; Lu, Q. L. Systemic Delivery of Morpholino Oligonucleotide Restores Dystrophin Expression Bodywide and Improves Dystrophic Pathology. *Nat. Med.* **2006**, *12* (2), 175–177.
- (52) Wu, B.; Moulton, H. M.; Iversen, P. L.; Jiang, J.; Li, J.; Li, J.; Spurney, C. F.; Sali, A.; Guerron, A. D.; Nagaraju, K.; et al. Effective Rescue of Dystrophin Improves Cardiac Function in Dystrophin-Deficient Mice by a Modified Morpholino Oligomer. *Proc. Natl. Acad. Sci.* **2008**, *105* (39), 14814–14819.
- (53) Menke, A.; Jockusch, H. Decreased Osmotic Stability of Dystrophin-Less Muscle Cells from the Mdx Mouse. *Nature* **1991**, *349* (6304), 69–71.
- (54) Lu, Q.; Cirak, S.; Partridge, T. What Can We Learn From Clinical Trials of Exon Skipping for DMD? *Mol. Ther. — Nucleic Acids* **2014**, *3* (3), e152.
- (55) Jearawiriyapaisarn, N.; Moulton, H. M.; Buckley, B.; Roberts, J.; Sazani, P.; Fucharoen, S.; Iversen, P. L.; Kole, R. Sustained Dystrophin Expression Induced by Peptide-Conjugated Morpholino Oligomers in the Muscles of Mdx Mice. *Mol. Ther. J. Am. Soc. Gene Ther.* **2008**, *16* (9), 1624–1629.
- (56) Wu, B.; Lu, P.; Cloer, C.; Shaban, M.; Grewal, S.; Milazi, S.; Shah, S. N.; Moulton, H. M.; Lu, Q. L. Long-Term Rescue of Dystrophin Expression and Improvement in Muscle Pathology and Function in Dystrophic Mdx Mice by Peptide-Conjugated Morpholino. *Am. J. Pathol.* **2012**, *181* (2), 392–400.
- (57) Betts, C.; Saleh, A. F.; Arzumanov, A. A.; Hammond, S. M.; Godfrey, C.; Coursindel, T.; Gait, M. J.; Wood, M. J. Pip6-PMO, A New Generation of Peptide-Oligonucleotide Conjugates With Improved Cardiac Exon Skipping Activity for DMD Treatment. *Mol. Ther. Nucleic Acids* **2012**, *1* (8), e38.
- (58) Wu, B.; Li, Y.; Morcos, P. A.; Doran, T. J.; Lu, P.; Lu, Q. L. Octa-Guanidine Morpholino Restores Dystrophin Expression in Cardiac and Skeletal Muscles and Ameliorates Pathology in Dystrophic Mdx Mice. *Mol. Ther. J. Am. Soc. Gene Ther.* **2009**, *17* (5), 864–871.
- (59) Abbott, N. J.; Rönnbäck, L.; Hansson, E. Astrocyte-Endothelial Interactions at the Blood-Brain Barrier. *Nat. Rev. Neurosci.* **2006**, *7* (1), 41–53.
- (60) Wolburg, H.; Lippoldt, A. Tight Junctions of the Blood-Brain Barrier: Development, Composition and Regulation. *Vascul. Pharmacol.* **2002**, *38* (6), 323–337.
- (61) Schinkel, null. P-Glycoprotein, a Gatekeeper in the Blood-Brain Barrier. *Adv. Drug Deliv. Rev.* **1999**, *36* (2–3), 179–194.
- (62) Rapoport, S. I. Osmotic Opening of the Blood–Brain Barrier: Principles, Mechanism, and Therapeutic Applications. *Cell. Mol. Neurobiol.* **2000**, *20* (2), 217–230.
- (63) Etame, A. B.; Diaz, R. J.; Smith, C. A.; Mainprize, T. G.; Hynynen, K.; Rutka, J. T. Focused Ultrasound Disruption of the Blood-Brain Barrier: A New Frontier for Therapeutic Delivery in Molecular Neurooncology. *Neurosurg. Focus* **2012**, *32* (1), E3.
- (64) Jones, A. R.; Shusta, E. V. Blood-Brain Barrier Transport of Therapeutics via Receptor-Mediation. *Pharm. Res.* **2007**, *24* (9), 1759–1771.
- (65) Demeule, M.; Régina, A.; Ché, C.; Poirier, J.; Nguyen, T.; Gabathuler, R.; Castaigne, J.-P.; Béliveau, R. Identification and Design of Peptides as a New Drug Delivery System for the Brain. *J. Pharmacol. Exp. Ther.* **2008**, *324* (3), 1064–1072.

- (66) Oller-Salvia, B.; Sánchez-Navarro, M.; Giralt, E.; Teixidó, M. Blood–brain Barrier Shuttle Peptides: An Emerging Paradigm for Brain Delivery. *Chem. Soc. Rev.* **2016**, *45* (17), 4690–4707.
- (67) Schwarze, S. R.; Ho, A.; Vocero-Akbani, A.; Dowdy, S. F. In Vivo Protein Transduction: Delivery of a Biologically Active Protein into the Mouse. *Science* **1999**, *285* (5433), 1569–1572.
- (68) Mochizuki, Y.; Park, M. K.; Mori, T.; Kawashima, S. The Difference in Autofluorescence Features of Lipofuscin between Brain and Adrenal. *Zoolog. Sci.* **1995**, *12* (3), 283–288.
- (69) Spitzer, N.; Sammons, G. S.; Price, E. M. Autofluorescent Cells in Rat Brain Can Be Convincing Impostors in Green Fluorescent Reporter Studies. *J. Neurosci. Methods* **2011**, *197* (1), 48–55.

## **Chapter 2: Machine Learning to Predict Cell-Penetrating Peptides for Antisense Delivery**

The work presented in this chapter was published in the following manuscript and is reproduced with permission from the American Chemical Society:

Wolfe, J.M.,\* Fadzen, C.M.,\* Choo, Z-N., Holden, R.L., Yao, M., Hanson, G.J., & Pentelute, B.L. Machine Learning to Predict Cell-Penetrating Peptides for Antisense Delivery *ACS Central Science*. DOI: 10.1021/acscentsci.8b00098

\*: denotes authors contributed equally

## 2.1. Introduction

Although small molecules can generally diffuse through the plasma membrane, many large molecules have limited uptake into cells.<sup>1,2</sup> These macromolecules are unable to diffuse across the plasma membrane and, if endocytosed, often remain trapped in endosomes. For example, gene-editing proteins, antisense oligonucleotides, and peptide-based proteolysis targeting chimeras (PROTACS) all mediate their effects on intracellular targets, and poor delivery limits their therapeutic potential.<sup>3-5</sup> One promising solution to improve the intracellular delivery of these macromolecules is the covalent conjugation of cell-penetrating peptides.<sup>6</sup>

Over the past few decades, hundreds of cell-penetrating peptides (CPPs) have been documented in the literature and yet predicting which peptide sequences improve cytosolic delivery remains difficult. Due in part to the diverse nature of CPPs, the properties and characteristics that are necessary for cell penetration are not well understood. CPPs range from 5 to 40 residues in length, and the sequences can be highly cationic, amphipathic, or hydrophobic.<sup>6-8</sup> Many CPPs are derived from fragments of natural proteins, such as viral proteins, DNA- or RNA-binding proteins, heparin-binding proteins, or antimicrobial peptides.<sup>9</sup> Some sequences were rationally designed after recognizing that cationic residues or amphipathicity can improve cell-penetration, while others were discovered using DNA-encoded peptide libraries.<sup>10-13</sup> Taking advantage of machine learning techniques, one recent strategy to predict new CPPs combines experimental datasets of known CPPs with computational models, such as support vector machines or neural networks.<sup>14-17</sup>

Unfortunately, it is generally acknowledged that the existing computational models to predict CPPs are intrinsically limited.<sup>14,15,18</sup> These models were all trained on a similar heterogeneous dataset compiled from multiple experimental papers on CPPs.<sup>14-17</sup> Since the original papers investigated CPPs for different applications, different experimental parameters were employed. For example, CPP treatment concentrations ranged from 0.1-400  $\mu\text{M}$ , some included serum in the media and others did not, and different cell types were utilized including HeLa cells and primary rat cortex cells.<sup>10,19-21</sup> All of these variables affect cellular uptake, and therefore standardized treatment conditions should be used to improve model accuracy.

Additionally, there is a need for computational models that predict CPPs specifically for macromolecule delivery. Experiments to determine putative CPP sequences generally involve the conjugation of a small-molecule fluorophore to the CPP, and the uptake of the fluorophore-CPP is

then analyzed by flow cytometry or live-cell confocal imaging.<sup>22,23</sup> However, experiments with fluorophore-labeled CPPs do not assess whether or not the CPP is suitable for the delivery of macromolecular cargo. Further, it is likely that the optimal CPP for the delivery of one type of macromolecule is different from the optimal CPP for a different type of macromolecule. One approach to manage this cargo dependence is to evaluate CPPs in the context of a functional readout for a specific macromolecule. For example, several activity-based assays have been developed to evaluate successful delivery of peptides, proteins, and antisense oligonucleotides.<sup>24-</sup>  
27

Phosphorodiamidate morpholino oligonucleotides (PMOs) are one particular type of macromolecule that benefits from conjugation to CPPs. PMOs are a charge-neutral antisense oligonucleotide therapeutic in which the ribose sugar is replaced with a methylenemorpholine ring and the phosphodiester backbone is replaced with a phosphorodiamidate backbone (Figure 2.1A).<sup>28</sup> PMOs can be designed to bind to pre-mRNA and can alter gene splicing, resulting in the exclusion or inclusion of particular genetic fragments in the mature mRNA. To improve PMO delivery, arginine rich CPPs and their derivatives have been covalently conjugated to PMO and investigated using gene-splicing assays, where cellular fluorescence increases in the presence of PMO.<sup>29-32</sup> Other types of neutral antisense oligonucleotides, such as peptide nucleic acids, have also been investigated after conjugation to CPPs.<sup>33,34</sup>

Here, we seek to predict CPPs specifically for PMO delivery. We hypothesized that PMO-CPP conjugates evaluated in a functional assay with standardized conditions would provide a data set for training a computational model. We synthesize a library of 64 PMO-CPP conjugates, utilizing previously reported cell-penetrating peptides. To benchmark each CPP, we measure the amount of PMO activity in an exon-skipping assay. We test all PMO-CPP conjugates using the same concentration, cell-line, amount of serum in the media, and treatment time. Using select CPP sequences from our library, we directly compare the relative effectiveness of a given CPP for the delivery of small-molecule fluorophore to the delivery of PMO. We then develop a random forest classifier that can discriminate whether or not a given peptide sequences can improve PMO activity more than 3-fold. Lastly, we predict custom peptides for PMO delivery and experimentally validate the sequences for successful delivery.

## 2.2. Results and Discussion

We began by measuring the effectiveness of literature-reported CPPs specifically for PMO delivery. We synthesized a library of CPPs consisting of the sequences listed in the comprehensive review by Milleti in 2012.<sup>9</sup> All the CPPs were capped at the N-terminus with an alkyne for further conjugation. Peptides that synthesized poorly or exhibited limited solubility were discarded from the library. After purification using reverse-phase high-performance liquid chromatography (RP-HPLC), we used copper-catalyzed click chemistry to conjugate the peptides to a 6,212 Da, 18-mer PMO. The PMO we chose can trigger functional eGFP expression in a modified HeLa cell line (Figure 2.1B).<sup>27</sup> After another round of purification, we obtained a library of 64 PMO-CPP conjugates (Table 2.1). The library included all of the canonical CPPs, including TAT, pVEC, TP10, penetratin, and polyarginine. Other less commonly reported peptides, such as the heparin binding proteins (DPV3-15) and proline-rich CPPs such as Bac7, were also included. With regards to classes of CPPs, our library contained 25 sequences generally classified as cationic sequences, 8 classified as hydrophobic, and 23 classified as amphipathic.

For a functional readout, the PMO-CPP conjugates were tested in the eGFP HeLa PMO assay (Figure 2.1B). In this assay, HeLa-654 cells are stably transfected with an eGFP coding sequence interrupted by an intron from the human  $\beta$ -globin gene (IVS2-654) containing a mutation that alters the normal pre-mRNA splice site to a formerly cryptic splice site. The change in splicing leads to retention of an unnatural mRNA fragment in the spliced eGFP mRNA and the translation of a non-fluorescent form of eGFP. The PMO IVS2-654 hybridizes to the mutant  $\beta$ -globin exon in the stably transfected HeLa cells, altering gene splicing and leading to full-length eGFP expression. The amount of PMO delivered is therefore correlated to the amount of functional eGFP expressed. In the experiment, eGFP HeLa cells are incubated with 5  $\mu$ M of each PMO-CPP conjugate in media containing 10% fetal bovine serum (FBS) for 24 hours. Then the cellular fluorescence is analyzed by flow cytometry. Given that the effectiveness of CPPs can be sensitive to treatment conditions such as the amount of serum in the treatment media and the amount of time treated, we kept these variables constant, enabling us to directly compare all of the CPPs under similar conditions.

Testing the library under these unified conditions led to the observation that several literature CPPs had little effect on promoting PMO delivery (Table 1). While seven peptides increased PMO activity above five-fold, many peptides exhibited marginal improvement for PMO

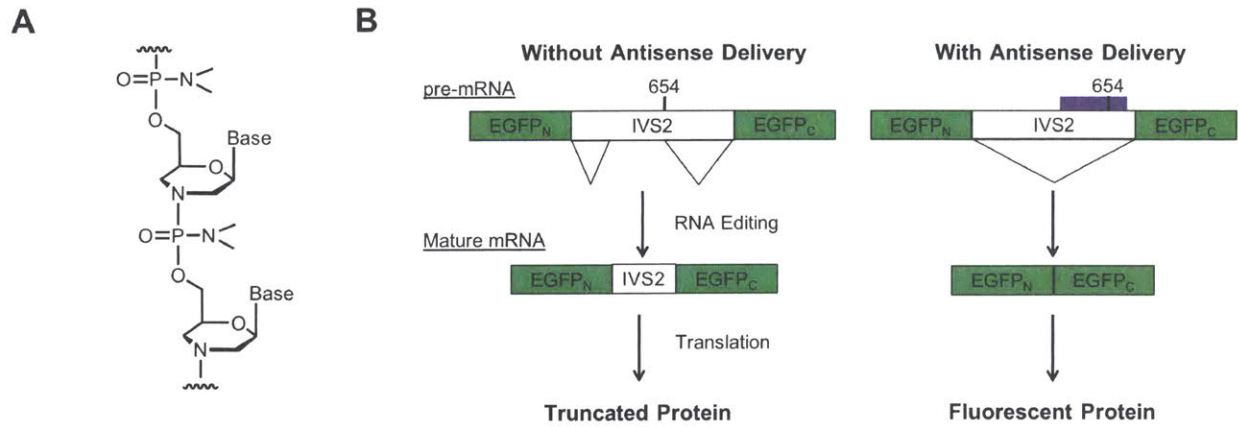


**Figure 2.1. PMOs alter gene splicing.** (A) The backbone structure of phosphorodiamidate morpholino oligonucleotides, a type of antisense oligonucleotide. (B) The exon-skipping assay used in this study. HeLa-654 cells are stably transfected with a split eGFP construct which contains a mutant intron. In the absence of PMO, a non-fluorescent truncated protein is expressed. If PMO IVS2-654 is present, it hybridizes to the mutant intron, alters pre-mRNA splicing, and produces functional message that is translated into fluorescent eGFP.

delivery. Twenty-seven CPPs (42% of library) led to under a two-fold increase in eGFP fluorescence and five CPPs actually decreased the amount of eGFP fluorescence compared to unconjugated PMO. In particular, the commonly used CPP transportan-10 (TP10) exhibited a negative effect on eGFP fluorescence, suggesting it is ineffective for PMO delivery under these conditions.

Additionally, we observed that net positive charge was one of the strongest predictors of a successful CPP. Cationic sequences represented 70% of the CPPs with over a three-fold improvement in PMO activity (19 out of 27 sequences). This trend is specific for the number arginine residues, with more arginine residues leading to more observed eGFP fluorescence. In particular, attachment of the Arginine-12 CPP led to the greatest enhancement of PMO activity. However, high net charge is by no means necessary – the CPP MPG has just one arginine residue and a relatively minor theoretical net charge of +5, yet it exhibited the second most activity of all the CPPs that we tested.

To understand if the trends in CPP effectiveness were specific for PMO delivery, we evaluated select members of our CPP library for fluorophore delivery (Figure 2.2A). The chosen CPPs cover the range of physiochemical properties present in our library, as well as the most commonly utilized CPP sequences. Again, we used copper-catalyzed click chemistry to conjugate the CPPs to cyanine 5.5 (Cy5.5 –  $\lambda_{\text{ex}}$  684 nm,  $\lambda_{\text{em}}$  710 nm). Next, eGFP HeLa cells were treated for 2 hours with 5  $\mu\text{M}$  of each Cy5.5-CPP conjugate in media containing 10% FBS and the cellular fluorescence was analyzed by flow cytometry. The amount of Cy5.5 fluorescence was normalized to mean fluorescence intensity of Cy5.5-YTA-4, the conjugate with the highest fluorescence intensity. Then, the amount of Cy5.5 fluorescence measured for each Cy5.5-CPP conjugate was compared to the relative amount of eGFP fluorescence for the equivalent PMO-CPP conjugate. We observed little correlation between the relative effectiveness of PMO and Cy5.5 delivery for a given CPP (Figure 2.2B). For example, Arginine-12 led to the highest eGFP fluorescence of the CPPs evaluated, yet only moderate Cy5.5 fluorescence. On the other hand, YTA4 and TP10 both led to substantial Cy5.5 fluorescence but demonstrated no practical improvement in PMO delivery.

It is important to note that the PMO assay does not distinguish between cellular uptake and other downstream effects that influence exon skipping (e.g. nuclear delivery or mRNA splicing). The amount of eGFP fluorescence is not a measure of intracellular concentration, even though they are correlated. We focused on an activity measurement because we believe that, in the context of



| CPP Name       | CPP Class    | Amino Acid Sequence        | Theoretical Net Charge | Activity Relative to PMO |
|----------------|--------------|----------------------------|------------------------|--------------------------|
| Arginine-12    | Cationic     | RRRRRRRRRRR                | 12                     | 10.4                     |
| MPG            | Amphipathic  | GLAFLGFLGAAGSTMGAWSQPKKRKY | 5                      | 7.5                      |
| Bac7           | Proline rich | RRIRPPRLPRPRPLPFPRPG       | 9                      | 6.1                      |
| TAT            | Cationic     | RKKRRQRRR                  | 8                      | 6.0                      |
| Arginine-10    | Cationic     | RRRRRRRRR                  | 10                     | 5.8                      |
| DPV6           | Cationic     | GRPRESGKKRKRKRLKP          | 9                      | 5.4                      |
| S413-PVrev     | Amphipathic  | ALWKTLLKKVLKAPKKRKY        | 9                      | 5.2                      |
| HRSV           | Cationic     | RRIPNRRPRR                 | 6                      | 4.9                      |
| HTLV-II Rex    | Cationic     | TRRQTRRRRRNR               | 8                      | 4.7                      |
| L-2            | Amphipathic  | HARIKPTFRRLKWKYKGFWD       | 9                      | 4.6                      |
| Melittin       | Amphipathic  | GIGAVLKVLTTGLPALISWIKRKRQQ | 5                      | 4.5                      |
| DPV15          | Cationic     | LRERQSLRRERQSR             | 6                      | 4.3                      |
| Arginine-9     | Cationic     | RRRRRRRRR                  | 9                      | 4.2                      |
| Penetratin     | Cationic     | RQIKIWFQNRMMKWK            | 7                      | 4.2                      |
| Yeast GCN4     | Cationic     | KRARNTEAARRSRARKLQRMKQ     | 9                      | 4.2                      |
| PDX-1          | Cationic     | RHIKIWFQNRMMKWK            | 8                      | 4.1                      |
| Arginine-8     | Cationic     | RRRRRRRRR                  | 8                      | 4.0                      |
| BMV Gag        | Cationic     | KMTRAQRRAAARRNRWTAR        | 8                      | 3.9                      |
| SynB1          | Amphipathic  | RGGLSYSRRRFTSTGR           | 6                      | 3.9                      |
| Knotted-1      | Cationic     | KQINWFINQRKRHWK            | 6                      | 3.8                      |
| IVV-14         | Hydrophobic  | KLWMRWYSPTRRYG             | 4                      | 3.7                      |
| W/R            | Amphipathic  | RRWWRWR                    | 6                      | 3.5                      |
| Engrailed-2    | Cationic     | SQIKIWFQNKRAKIK            | 6                      | 3.4                      |
| DPV15b         | Cationic     | GAYDLRRERQSLRRERQSR        | 7                      | 3.3                      |
| Yeast PrP6     | Cationic     | TRRNKRRIQEQLNRK            | 6                      | 3.3                      |
| DPV7           | Cationic     | GKRKKGKLGKGRDP             | 8                      | 3.2                      |
| HoxA-13        | Cationic     | RQVTIWFQNRVKEK             | 5                      | 3.1                      |
| AIP6           | Amphipathic  | RLRWR                      | 3                      | 2.9                      |
| (PPR)5         | Cationic     | PPRPPPPPPPPR               | 5                      | 2.7                      |
| CAYH           | -            | CAYHRLRC                   | 4                      | 2.6                      |
| DPV10          | Cationic     | SRRARRSPRHLGSG             | 6                      | 2.5                      |
| (PPR)4         | Amphipathic  | PPRPPPPPPR                 | 4                      | 2.4                      |
| P22 N          | Cationic     | NAKTRRHERRRKLAIER          | 7                      | 2.4                      |
| DPV1047        | Cationic     | VKRGKLRHVRPRVTRMDV         | 7                      | 2.4                      |
| SVM4           | Amphipathic  | LYKKGPAKGRPLRGWFH          | 7                      | 2.2                      |
| φ21N(12-29)    | Cationic     | TAKTRYKARRAELIERR          | 5                      | 2.1                      |
| SVM3           | Amphipathic  | KGTYKKLMRIPLKGT            | 6                      | 2.1                      |
| (PPR)3         | Amphipathic  | PPRPPPPR                   | 3                      | 1.9                      |
| SVM2           | -            | RASKRDGSWVKLHRILE          | 5                      | 1.9                      |
| Buforin 2      | Amphipathic  | TRSSRAGLQWPVGRVHLLRK       | 7                      | 1.9                      |
| SVM1           | -            | FKIYDKKVRTRVVKH            | 6                      | 1.7                      |
| SAP            | Amphipathic  | VRLPPPRLPPPRLPPP           | 3                      | 1.7                      |
| 435b           | Hydrophobic  | GPFFHYQFLFPV               | 1                      | 1.7                      |
| Pept1          | Hydrophobic  | PLILLRLLRGQF               | 2                      | 1.7                      |
| YTA2           | -            | YTAIAWVKAFIRKLRK           | 5                      | 1.5                      |
| Pep-1          | Amphipathic  | KETVWETWWTWWSQPKRKY        | 2                      | 1.4                      |
| EB-1           | Amphipathic  | LIRLWSHLIHWQNRRLKWKK       | 9                      | 1.4                      |
| Pyrrhocoricin  | Proline rich | VDKGSYLPRTPPRPIYNRN        | 3                      | 1.4                      |
| ΔN(1-22)       | Cationic     | MDAQRTRRRERRAEQAQWKAAN     | 4                      | 1.4                      |
| 439a           | Hydrophobic  | GSPWGLQHPPRT               | 3                      | 1.3                      |
| MAP            | Amphipathic  | KLALKALKALKAAKLA           | 5                      | 1.3                      |
| Bip            | Hydrophobic  | IPALK                      | 1                      | 1.3                      |
| Bip            | Hydrophobic  | VPALR                      | 1                      | 1.3                      |
| pVEC           | Amphipathic  | LLIILRRRIRKQAHASK          | 8                      | 1.2                      |
| YTA4           | -            | IAWVKAFIRKLRKGPLG          | 5                      | 1.2                      |
| K-FGF + NLS    | Amphipathic  | AAVLLPVLLAAPVQRKRQLP       | 4                      | 1.2                      |
| HN-1           | Hydrophobic  | TSPLNIHNGQKL               | 2                      | 1.2                      |
| Bip            | Hydrophobic  | VPTLK                      | 1                      | 1.2                      |
| Bip            | Hydrophobic  | VSALK                      | 1                      | 1.1                      |
| VT5            | Amphipathic  | DPKGDPKGVTVTVTVTGKGDPKPD   | 0                      | 0.8                      |
| Transportan 10 | Amphipathic  | AGYLLGKINLKALAALAKIL       | 4                      | 0.8                      |
| SAP(E)         | Amphipathic  | VELPPPVELPPPVELPPP         | -3                     | 0.8                      |
| CADY           | Amphipathic  | GLWRALWRLRSLWRLLWRA        | 5                      | 0.6                      |
| PreS2-TLM      | Amphipathic  | PLSSIFSRIGDP               | 0                      | 0.6                      |

**Table 2.1. List of CPPs that were conjugated to PMO and tested in the eGFP assay.** Each previously reported CPP was synthesized, purified, and conjugated to PMO IVS2-654. The conjugates were tested for functional PMO activity in the HeLa-654 cell assay. Individual CPPs are ranked by their activity relative to unconjugated PMO.

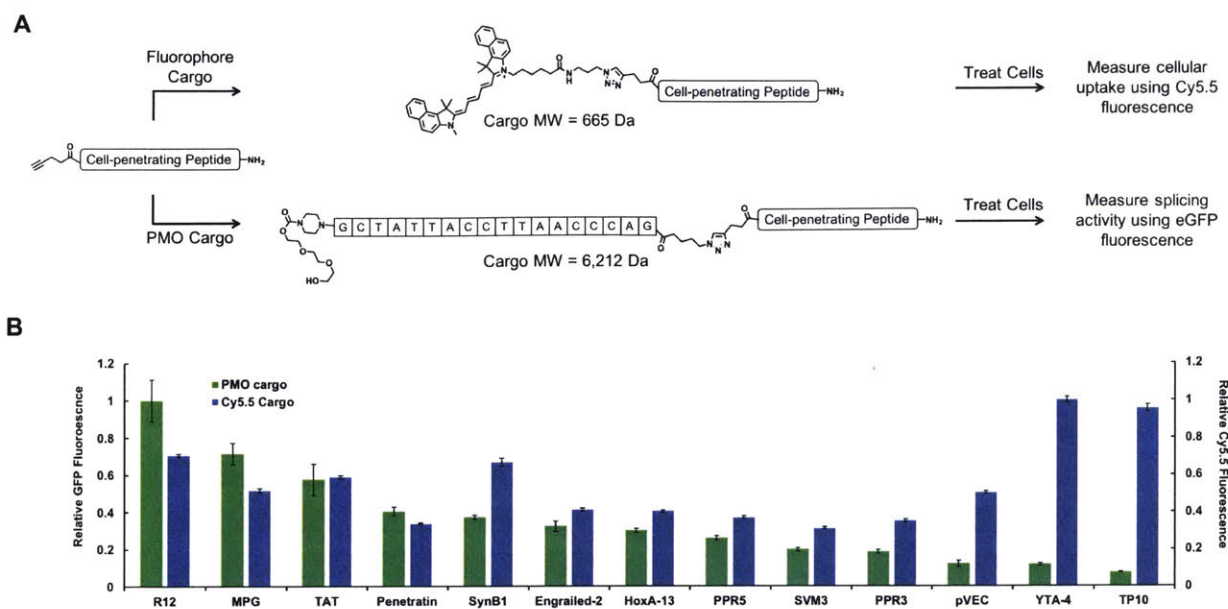


**Figure 2.2. Cargo identity alters relative CPP efficacy.** (A) Each CPP sequence analyzed for delivery of both a fluorophore (Cy5.5, MW=665 Da) and a PMO (IVS2-654, MW=6212 Da). For Cy5.5-CPP conjugates, HeLa-654 cells were treated with 5  $\mu$ M of the conjugate in media containing 10% FBS. After two hours, the Cy5.5 fluorescence was measured by flow cytometry. For PMO-CPP conjugates, HeLa-654 cells were treated with 5  $\mu$ M of the conjugate in media containing 10% FBS. After twenty-two hours, the eGFP fluorescence was measured by flow cytometry. (B) The cargo dependency of a given CPP, normalized to the activity of the highest-performing CPP for each type of cargo. There is little relationship between the CPPs that led to the most cellular Cy5.5 fluorescence and the CPPs that led to the most eGFP fluorescence.

macromolecule delivery, the final functional output of a cargo represents the most relevant criterion for judging a CPP.

After benchmarking literature CPPs and noting the cargo dependency, we sought to develop a method to identify efficacious CPPs for PMO delivery. We hypothesized that we could leverage the consistency of our data set (identical concentrations, treatment times, serum-containing media, and assay) along with techniques from machine learning to build a predictive computational model for PMO delivery. While the algorithms we employed are standard in the computer science field, this is the first time they have been applied to the prediction task of peptides for antisense oligonucleotide delivery.

We chose to train a random forest classifier to select CPPs specific to PMO delivery (Figure 2.3A). Random forests are sets of decision trees, each fit to a randomly selected subset of features and training examples, and we selected this ensemble learning method due to its scalability and robustness to overfitting.<sup>35</sup> We calculated twenty-three features for each peptide sequence. Two features were peptide molecular weight and sequence length (total number of residues). The theoretical net charge of the sequence was averaged across the five N-terminal residues, the five C-terminal residues, and the entire peptide sequence to give three features. The remaining eighteen features were derived from six previously described amino acid physicochemical descriptors. These six descriptors were produced by factor analysis of 384 molecular properties calculated for 22 natural and 593 non-natural amino acids.<sup>36</sup> For each peptide sequence, the six descriptors were also averaged across five N-terminal residues, five C-terminal residues, and the entire peptide sequence.

The CPP sequences were classified as either positive or negative examples based on whether or not they exhibited above a three-fold change in eGFP fluorescence with respect to the unconjugated PMO. Forty-four sequences were used as the training set for the random forest model. The other twenty sequences were held out to serve as a test set to evaluate the degree to which the model properly fit the data and could successfully predict the exon skipping activity of a sequence. The performance metrics of the model are shown in Figure 2.3A.

After testing our model computationally, we sought to validate it experimentally. Random peptide sequences were generated by selecting a peptide length and amino acid composition with probability proportional to the distribution observed in the training data set from the CPP library. Of the random peptides, we selected five positive sequences predicted to lead to above a three-

fold increase in eGFP fluorescence and two negative sequences (NSs). We selected more positive sequences as our goal was to develop novel peptide sequences for PMO delivery, which we have termed predicted PMO carriers (PPCs). These PPCs were synthesized by solid-phase peptide synthesis, conjugated to PMO IVS2-654, and purified by RP-HPLC.

We tested the PPCs in the eGFP assay and all five PPCs had a greater than three-fold change in cellular fluorescence with respect to unconjugated PMO (Figure 2.3B and 2.3C). In fact, PMO-PPC3 increased fluorescence 4.4-fold, which is a larger increase than 80% of the literature CPPs. The negative sequences demonstrated less than a three-fold change, indicating that our model could accurately discriminate between positive and negative sequences.

To demonstrate that our model is sensitive to the effects of cargo on CPP effectiveness, we next assessed whether or not our novel PPCs were CPPs with regards to small-molecule fluorophore delivery. We prepared variants of our PPCs labeled with Cy5.5, rather than the PMO, and measured the uptake by flow cytometry (Figure 2.4). Here, the trends were completely different, as Cy5.5-labeled NS2 treated cells exhibited fluorescence similar to cells treated with our positive control Cy5.5-YTA-4 and twice the fluorescence of Cy5.5-PPC1. These data parallel our observations of the literature CPPs and suggest that our computational model is truly specific for PMO-based cargo, providing further evidence that CPPs must be chosen in the context of the cargo of interest.

Next, we sought to characterize the mechanisms by which our PMO-PPC conjugates are internalized into cells, focusing on PPC3 and PPC5. All mechanistic studies were conducted at concentrations of 5  $\mu$ M to remain consistent with the conditions with which we evaluated our PMO-PPC library. The experiments were performed in a pulse-chase format, in which the cells were pre-incubated in a particular treatment condition for thirty minutes followed by addition of PMO-PPC. After three hours, the media was exchanged for fresh media that did not contain the conjugate and the cells were allowed to incubate for an additional 22 hours at 37 °C.

First, we compared eGFP fluorescence after three hours of treatment at 4 °C vs. 37 °C. We found that for PMO alone and both PMO-PPC conjugates, eGFP fluorescence decreased when treatment occurred at 4 °C, suggesting that energy-dependent mechanisms play a role in the uptake of our conjugates (Figure 2.5A). One plausible explanation for the residual fluorescence in the 4 °C condition is that the cells incubate for an additional 22 hours at 37 °C after treatment, so any

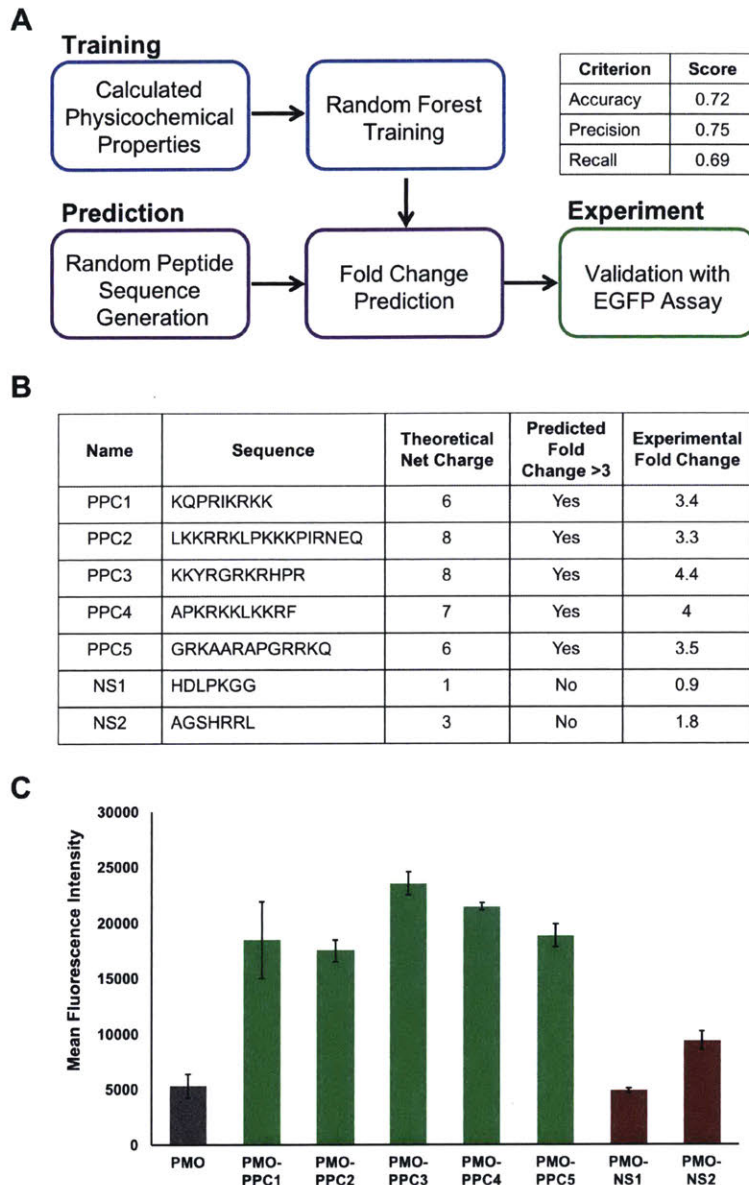


**Figure 2.3. Random forest ensemble learning methods can be used to predict peptide sequences that facilitate PMO delivery.** (A) Scheme of the workflow for the development of computationally derived peptide sequences for antisense delivery. One component of the workflow was random forest training using the properties of the CPPs in the library to build a model. Another component was randomly generating peptide sequences and using the model to predict the predicted PMO carrier (PPC) activity. Lastly, select sequences were synthesized for experimental validation. Performance metrics for the model based on the test set are given in the table. (B) Table of five PPCs and two predicted negative sequences (NS). All five PMO-PPC conjugates exhibited above a three-fold improvement in eGFP fluorescence, whereas both PMO-NS conjugates exhibited less than a three-fold change with respect to PMO. (C) The mean fluorescence intensity of eGFP HeLa cells treated at a concentration of 5  $\mu$ M with each of the PMO-PPCs and PMO-NSs in serum-containing media. Each individual experiment consisted of the average of three different wells with the same treatment conditions, and the experiment was repeated three times. The error bars represent the standard deviation across the experimental replicates.



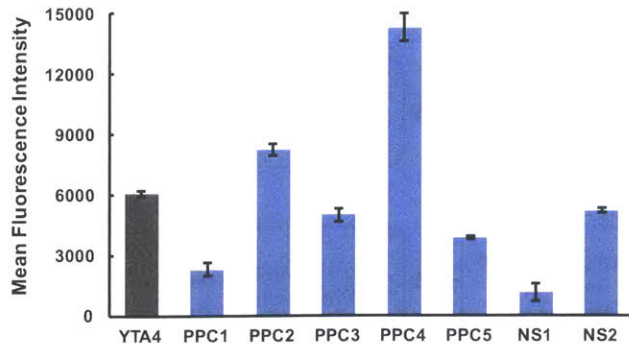


**Figure 2.4. Uptake of fluorophore-labeled PPCs.** The seven novel sequences were conjugated to Cy5.5. YTA-4 was used as a positive control, since it is a known CPP sequence that we tested as part of our library. HeLa-654 cells were treated with 5  $\mu$ M of each conjugate in media containing 10% FBS. After two hours, the fluorescence was measured by flow cytometry. There is little correlation between PMO delivery with the PPCs and uptake of Cy5.5-labeled PPCs. For example, PPC1, PPC3, and PPC5 all had the same or lower mean fluorescence intensity than NS2.

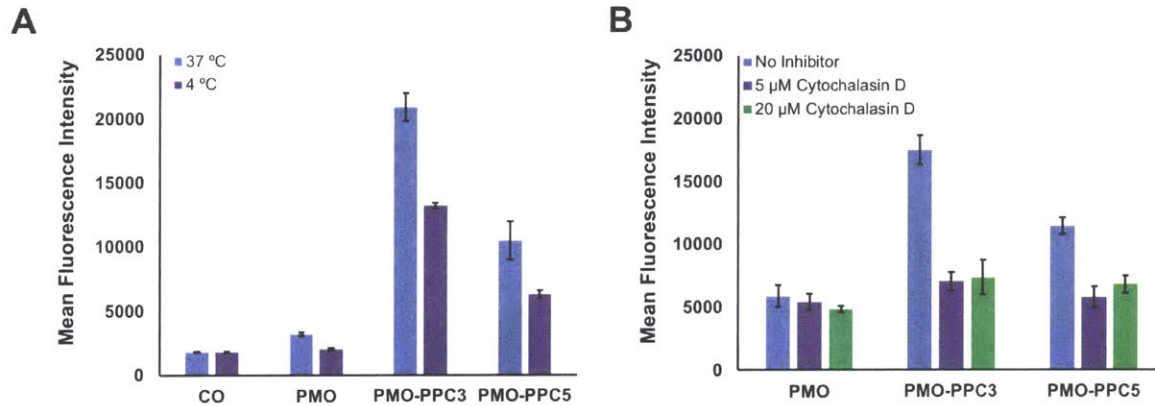


**Figure 2.5. The PMO-PPC conjugates engage endocytic mechanisms in their uptake into cells.** (A) Effect of temperature on PMO-PPC activity. eGFP HeLa cells were incubated at 4 °C for 30 minutes before incubation with either PMO or PMO-PPC conjugates at 4 °C at a concentration of 5  $\mu$ M. After 3 hours, the treatment media was replaced with fresh, untreated media and the cells were allowed to grow for an additional 22 hours at 37 °C. CO refers to cell-only. (B) Effect of cytochalasin D on PMO-PPC activity. eGFP HeLa cells were treated with cytochalasin D for 30 minutes in serum-containing media before the addition of either PMO or PMO-PPC conjugates at a concentration of 5  $\mu$ M. After 3 hours, the treatment media was replaced with fresh, untreated media and the cells were allowed to grow for an additional 22 hours. The cells were analyzed for eGFP fluorescence by flow cytometry and the results are shown in terms of the mean fluorescence intensity. These experiments were conducted on a plate alongside several other inhibitors and the full results are in section 2.4.

conjugate that binds to the surface of the cells during treatment at 4 °C may be subsequently internalized and trigger eGFP expression.

We also treated the HeLa eGFP cells with a panel of endocytosis disruptors and assessed the effects on internalization (Figure 2.5B). While eGFP fluorescence was relatively unchanged after pre-incubation with many of the inhibitors, pre-incubation with cytochalasin D led to a notable decrease in eGFP fluorescence. Cytochalasin D binds to the barbed, fast growing ends of actin microfilaments, which prevents assembly and disassembly of actin monomers.<sup>37</sup> This affects not only the cytoskeleton of the cell, but also the ability of the membrane to ruffle and reorganize to facilitate macropinocytosis. While it is possible that the decrease in eGFP fluorescence is due to effects downstream in the exon skipping pathway, these results suggest that macropinocytosis plays a significant role in the internalization of our conjugates.

## 2.3. Experimental

### 2.3.1. Materials

H-Rink Amide-ChemMatrix resin was obtained from PCAS BioMatrix Inc. (St-Jean-sur-Richelieu, Quebec, Canada). 1-[Bis(dimethylamino)methylene]-1H-1,2,3-triazolo[4,5-b]pyridinium-3-oxid-hexafluorophosphate (HATU), 4-pentynoic acid, 5-azidopentanoic acid, Fmoc- $\beta$ -Ala-OH, Fmoc-6-aminohexanoic acid, Fmoc-L-Arg(Pbf)-OH, Fmoc-L-His(Trt)-OH, Fmoc-L-Lys(Boc)-OH, Fmoc-L-Asp(tBu)-OH, Fmoc-L-Glu(tBu)-OH, Fmoc-L-Ser(tBu)-OH, Fmoc-L-Thr(tBu)-OH, Fmoc-L-Asn(Trt)-OH, Fmoc-L-Gln(Trt)-OH, Fmoc-L-Cys(Trt)-OH, Fmoc-L-Gly-OH, Fmoc-L-Ala-OH, Fmoc-L-Val-OH, Fmoc-L-Leu-OH, Fmoc-L-Ile-OH, Fmoc-L-Met-OH, Fmoc-L-Phe-OH, Fmoc-L-Pro-OH, Fmoc-L-Tyr(tBu)-OH, and Fmoc-L-Trp(Boc)-OH were purchased from Chem-Impex International (Wood Dale, IL). PyAOP was purchased from P3 BioSystems (Louisville, KY). Cy5.5-azide was purchased from Lumiprobe Corporation (Hallandale Beach, FL). Peptide synthesis-grade N,N-dimethylformamide (DMF), CH<sub>2</sub>Cl<sub>2</sub>, diethyl ether, *t*-butanol and HPLC-grade acetonitrile were obtained from VWR International (Radnor, PA). Cytochalasin D was obtained from Santa Cruz Biotech. All other reagents were purchased from Sigma-Aldrich (St. Louis, MO). Milli-Q water was used exclusively. The PMO-CPP library was tested at Sarepta Therapeutics and follow-up experiments with the PMO-PPC conjugates were performed at MIT using HeLa-654 cells obtained from the University of North Carolina Tissue Culture Core facility.

### 2.3.2. Methods for LC-MS Analysis

The following methods were used on an Agilent 6520 ESI-Q-TOF mass spectrometer equipped with a C<sub>3</sub> Zorbax column (300SB C3, 2.1 x 150 mm, 5  $\mu$ m). Mobile phases were: 0.1% formic acid in water (solvent A) and 0.1% formic acid in acetonitrile (solvent B). The following LC-MS methods were used for characterization:

Method A: 5% B from 0 to 2 min, linear ramp from 5% B to 65% B from 2 to 11 min, 65% B from 11 to 12 min and finally 3 min of post-time at 5% B for equilibration, flow rate: 0.8 mL/min.

Method B: 1% B from 0 to 2 min, linear ramp from 1% B to 61% B from 2 to 11 min, 61% B to 99% B from 11 to 12 min and finally 3 min of post-time at 1% B for equilibration, flow rate: 0.8 mL/min.

Additionally, some chromatograms were acquired using an Agilent 6550 ESI-Q-TOF mass spectrometer equipped with a C<sub>3</sub> Zorbax column (Poroshell 300SB C3, 1.0 x 75 mm, 5  $\mu$ m).



Mobile phases were: 0.1% formic acid in water (solvent A) and 0.1% formic acid in acetonitrile (solvent B).

Method C: 5% B from 0 to 1 min, linear ramp from 5% B to 65% B from 1 to 11 min, 65% B from 11 to 12 min and finally 2 min of post-time at 5% B for equilibration, flow rate: 0.4 mL/min.

All data were processed using Agilent MassHunter software package. Y-axis in all chromatograms shown represents total ion current (TIC) unless noted.

### **2.3.3. General Method for Peptide Preparation**

*Fast-flow Peptide Synthesis*: Peptides were synthesized on a 0.1-mmol scale using an automated flow peptide synthesizer.<sup>38</sup> A 200 mg portion of ChemMatrix Rink Amide HYR resin was loaded into a reactor maintained at 90 °C. All reagents were flowed at 80 mL/min with HPLC pumps through a stainless-steel loop maintained at 90 °C before introduction into the reactor. For each coupling, 10 mL of a solution containing 0.2 M amino acid and 0.17 M HATU in DMF were mixed with 200  $\mu$ L diisopropylethylamine and delivered to the reactor. Fmoc removal was accomplished using 10.4 mL of 20% (v/v) piperidine. Between each step, DMF (15 mL) was used to wash out the reactor. Special coupling conditions were used for arginine, in which the flow rate was reduced to 40 mL/min and 10 mL of a solution containing 0.2 M Fmoc-L-Arg(Pbf)-OH and 0.17 M PyAOP in DMF were mixed with 200  $\mu$ L diisopropylethylamine and delivered to the reactor. To cap the peptide with 4-pentynoic acid, the resin was incubated for 30 min at room temperature with 4-pentynoic acid (1 mmol) dissolved in 2.5 mL 0.4 M HATU in DMF with 500  $\mu$ L diisopropylethylamine. After completion of the synthesis, the resins were washed 3 times with DCM and dried under vacuum.

*Peptide Cleavage and Deprotection*: Each peptide was subjected to simultaneous global side-chain deprotection and cleavage from resin by treatment with 5 mL of 94% trifluoroacetic acid (TFA), 2.5% 1,2-ethanedithiol (EDT), 2.5% water, and 1% triisopropylsilane (TIPS) (v/v) for 7 min at 60 °C. For arginine-rich sequences, the resin was treated with a cleavage cocktail consisting of 82.5% TFA, 5% phenol, 5% thioanisole, 5% water, and 2.5% EDT (v/v) for 14 hours at room temperature. The TFA was evaporated by bubbling N<sub>2</sub> through the mixture. Then ~40 mL of cold ether (chilled at -80°C) was added to precipitate and wash the peptide. The crude product was pelleted through centrifugation for three minutes at 4,000 rpm and the ether decanted. The ether precipitation and centrifugation was repeated two more times. After the third wash, the pellet

was redissolved in 50% water and 50% acetonitrile containing 0.1% TFA, filtered through a fritted syringe to remove the resin and lyophilized.

*Peptide Purification:* The peptides were redissolved in water and acetonitrile containing 0.1% TFA, filtered through a 0.22  $\mu\text{m}$  nylon filter and purified by mass-directed semi-preparative reversed-phase HPLC. Solvent A was water with 0.1% TFA additive and Solvent B was acetonitrile with 0.1% TFA additive. A linear gradient that changed at a rate of 0.5%/min was used. Most of the peptides were purified on an Agilent Zorbax SB C3 column: 9.4 x 250 mm, 5  $\mu\text{m}$ . Extremely hydrophilic peptides, such as the arginine-rich sequences were purified on an Agilent Zorbax SB C18 column: 9.4 x 250 mm, 5  $\mu\text{m}$ . Using mass data about each fraction from the instrument, only pure fractions were pooled and lyophilized. The purity of the fraction pool was confirmed by LC-MS.

#### **2.3.4. PMO Azide Synthesis**

PMO IVS-654 (200 mg, 32  $\mu\text{mol}$ ) was dissolved in 600  $\mu\text{L}$  DMSO. To the solution was added a solution containing 4 equivalents of 5-azidopentanoic acid (13.6  $\mu\text{L}$ , 128  $\mu\text{mol}$ ) activated with HBTU (320  $\mu\text{L}$  of 0.4 M HBTU in DMF, 128  $\mu\text{mol}$ ) and DIEA (22.3  $\mu\text{L}$ , 128  $\mu\text{mol}$ ) in 244  $\mu\text{L}$  DMF (Final reaction volume = 1.2 mL). The reaction proceeded for 25 minutes before being quenched with 1 mL of water and 2 mL of ammonium hydroxide. The ammonium hydroxide will hydrolyze any ester formed during the course of the reaction. After 1 hour, the solution was diluted to 40 mL and purified using reversed-phase HPLC (Agilent Zorbax SB C3 column: 21.2 x 100 mm, 5  $\mu\text{m}$ ) and a linear gradient from 2 to 60% B (solvent A: water; solvent B: acetonitrile) over 58 minutes (1% B / min). Using mass data about each fraction from the instrument, only pure fractions were pooled and lyophilized. The purity of the fraction pool was confirmed by LC-MS.

#### **2.3.5. PMO-Peptide Conjugation with Cu(I)-Catalyzed Azide-Alkyne Cycloaddition**

PMO-peptide conjugates were synthesized using Cu(I)-catalyzed azide-alkyne 1,3-dipolar cycloaddition using copper(I) bromide in DMF. PMO-azide (0.95  $\mu\text{mol}$ ), Peptide-alkyne (1.1  $\mu\text{mol}$ ), and copper(I) bromide (0.05 mmol) powders were added to a septum vial (note: the amount of PMO-azide ranged from 0.63-0.95  $\mu\text{mol}$ ). The vial was flushed with  $\text{N}_2$  for 2 minutes, 1 mL dry DMF was added, and the vial was vortexed. The reaction was allowed to proceed for 1 hour. The reaction was quenched with the addition of 10 mL of 50 mM Tris (pH 8).

Our optimized purification procedure was using reversed-phase HPLC with a linear gradient from 5-45% B over 20 minutes (Agilent Zorbax SB C3 9.4 x 50 mm, 5  $\mu\text{m}$ ). Mobile phase

A: 100 mM ammonium acetate pH 7.2 in water. Mobile phase B: acetonitrile. Using mass data about each fraction from the instrument, only pure fractions were pooled and lyophilized. The purity of the fraction pool was confirmed by LC-MS. Prior to optimization, the mobile phases were slightly different. Mobile phase A: 5 mM ammonium acetate pH 8 in water. Mobile phase B: 5 mM ammonium acetate pH = 8 in 90% acetonitrile 10% water.

The first set of PMO-peptide conjugates was worked-up by solid phase extraction rather than purification by reversed-phase HPLC. This method requires accurate reaction stoichiometry, as it is difficult to purify away any excess PMO or peptide. The conjugates purified by solid phase extraction are denoted with a \* in the appendix. Disposable columns were packed with Amberchrom CG300 and conditioned. After the click reaction was quenched with 10 mL of 50 mM Tris (pH 8), the reaction mixture was loaded onto the column by gravity. Next, the column was rinsed with 1 M sodium chloride (3 mL), followed by three successive washes with water (3 x 12 mL). Then, the column was rinsed once with 90:10 water:acetonitrile (3 mL). Finally, the product was eluted with two successive treatments with 50:50 water:acetonitrile (2 x 3 mL) and collected. The eluant was analyzed by LC-MS, flash frozen in liquid N<sub>2</sub> and lyophilized.

For chromatograms and mass spectra of all PMO-peptide conjugates, please see Section 2.6.

### **2.3.6. Fluorophore Conjugation with Cu(I)-Catalyzed Azide-Alkyne Cycloaddition**

Cy5.5 azide was conjugated to peptide alkyne by copper-catalyzed azide alkyne cycloaddition using copper sulfate and ascorbic acid. Briefly, 0.5 μmol of peptide alkyne was dissolved in 200 μL 50:50 *t*-butanol:water in a 1.7 mL microcentrifuge tube. The following solutions were added in order: 10 μL of 50 mM Cy5.5 azide in DMSO, 100 μL of 500 mM Tris pH 8 in water, 50 μL of 100 mM copper(II) sulfate in water, 10 μL of 10 mM Tris(benzyltriazolylmethyl)amine (TBTA) in DMSO, 530 μL 50:50 *t*-butanol:water, and 100 μL of 1 M ascorbic acid in water. After 1 hour, the reactions were purified by reverse-phase HPLC using a linear gradient from 5-45% B over 80 minutes. Mobile phase A: water with 0.1% TFA. Mobile phase B: acetonitrile with 0.1% TFA. For LC-MS characterization of Cy5.5-PPC conjugates, please see Section 2.6.

### **2.3.7. Computational Model Selection and Feature Importance**

Random forest classifier hyperparameters were optimized through grid search with classification accuracy estimated with three-fold cross validation. The selected number of features

| Number of features | Number of estimators | Maximum tree depth | Mean test accuracy |
|--------------------|----------------------|--------------------|--------------------|
| 0.75               | 50                   | 20                 | 0.72               |
| <b>0.5</b>         | <b>50</b>            | <b>20</b>          | <b>0.72</b>        |
| 0.25               | 50                   | 20                 | 0.69               |
| 0.5                | 10                   | 20                 | 0.71               |
| 0.5                | 250                  | 20                 | 0.69               |
| 0.5                | 1000                 | 20                 | 0.70               |
| 0.5                | 50                   | 5                  | 0.69               |
| 0.5                | 50                   | 10                 | 0.69               |

**Table 2.2. Variation in mean test accuracy according to selected hyperparameters.** The number of features (as a fraction of total available features), the number of estimators in the random forest, and the maximum tree depth were varied and mean test accuracy was computed through three-fold cross validation to select a final random forest model. Test accuracy was not very sensitive to hyperparameters and the bolded model was selected for the classification test.

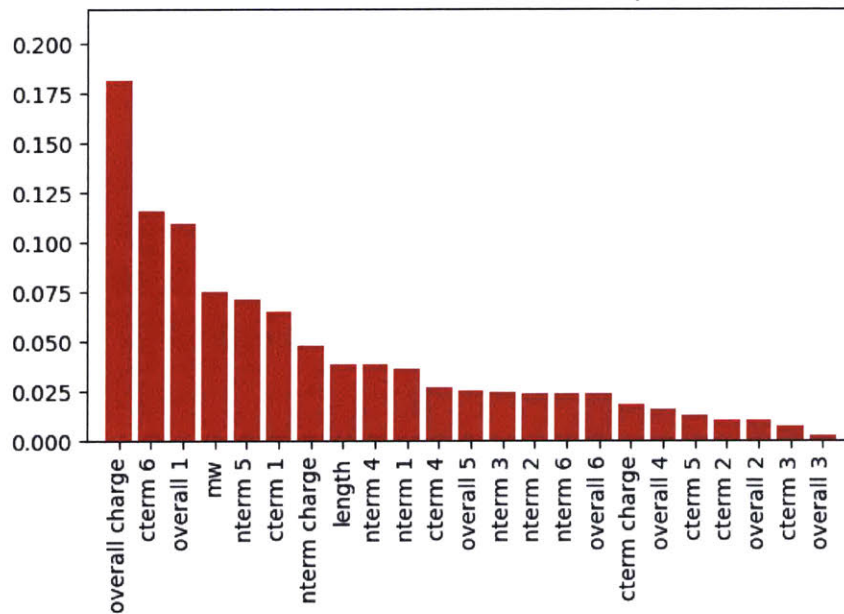


**Figure 2.6. Mean decrease in accuracy due to removal of each feature in the final random forest ensemble.** “nterm” and “cterm” refer to a feature derived from principal component analysis averaged across the five N-terminal and C-terminal amino acids, respectively. The numbers 1-6 refer to the principal component number as described in Liang *et al.*<sup>36</sup>

per tree, number of trees, and maximum tree depth were eleven, fifty, and twenty respectively. The change in accuracy from varying select hyperparameters is shown in Table 2.2. Performance metrics from classifier evaluation on a held-out test set of twenty sequences are given in Figure 2.2A. The performance metrics are defined below, where TP refers to true positive, TN refers to true negative, FP refers to false positive, and FN refers to false negative.

$$Accuracy = \frac{TP + TN}{TP + TN + FP + FN}$$

$$Precision = \frac{TP}{TP + FP}$$

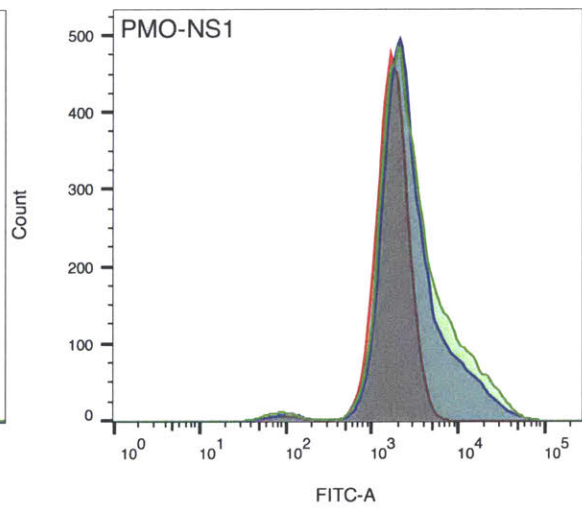
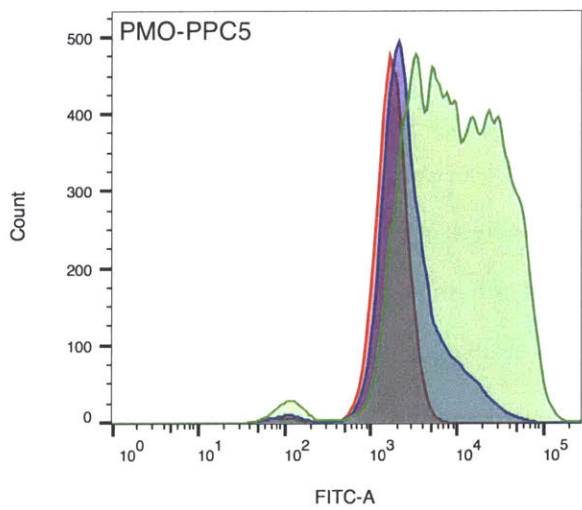
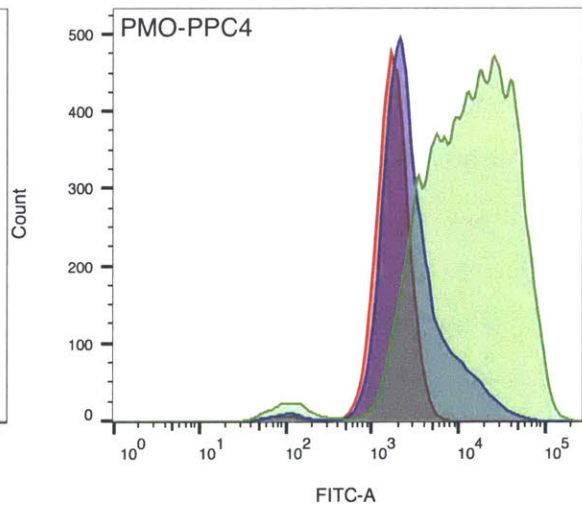
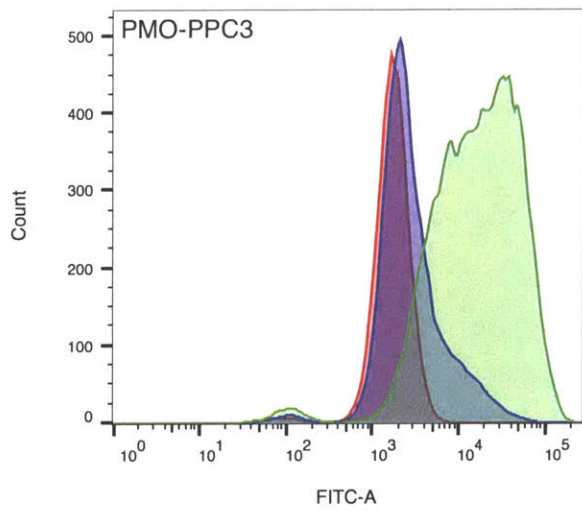
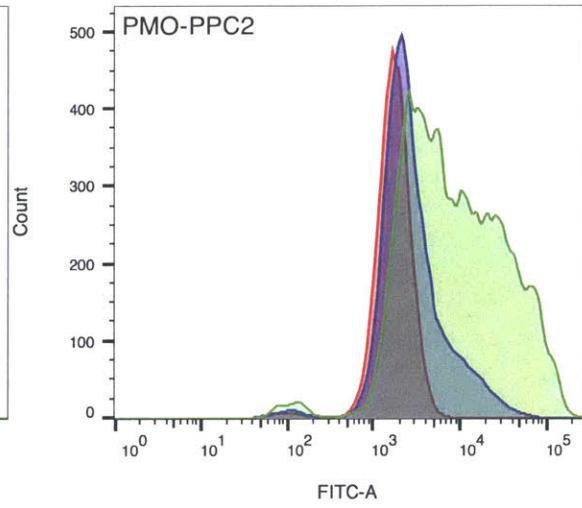
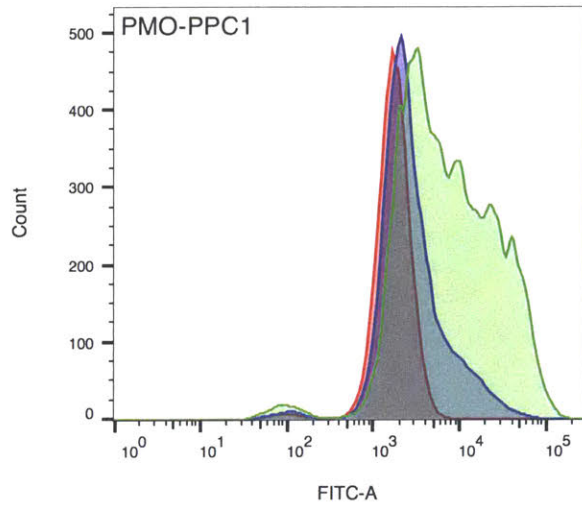
$$Recall = \frac{TP}{TP + FN}$$

The importance of each feature in our selected random forest classifier is shown in Figure 2.6. Feature importance is defined as the mean decrease in accuracy of an estimator in the random forest ensemble after the feature is removed. The model was implemented in Python 2.7.6 with the scikit-learn library.<sup>39</sup> All the code used for the model has been uploaded to Github: [https://github.com/zining01/cpp\\_classification](https://github.com/zining01/cpp_classification)

### 2.3.8. Flow Cytometry Assay for PMO-Peptide Conjugates

For testing the library of PMO-CPP conjugates, flow cytometry analysis of GFP fluorescence was conducted as previously described.<sup>27</sup> For testing the PMO-PPC conjugates, HeLa 654 cells were maintained in MEM supplemented with 10% (v/v) fetal bovine serum (FBS) and 1% (v/v) penicillin-streptomycin at 37 °C and 5% CO<sub>2</sub>. Stocks of each PMO-PPC conjugate were prepared in phosphate-buffered saline (PBS). The concentration of the stocks was determined by measuring the absorbance at 260 nm and using an extinction coefficient of 168,700 L mol<sup>-1</sup> cm<sup>-1</sup>. Cells were incubated with each respective conjugate at a concentration of 5 μM in MEM supplemented with 10% FBS and 1% penicillin-streptomycin for 22 hours at 37 °C and 5% CO<sub>2</sub>. Next, the treatment media was aspirated. The cells were incubated with Trypsin-EDTA 0.25 % for 15 min at 37 °C and 5% CO<sub>2</sub>, washed 1x with PBS, and resuspended in PBS with 2% FBS and 2 μg/mL propidium iodide.

Flow cytometry analysis was carried out on a BD LSRII flow cytometer. Gates were applied to the data to ensure that cells that were highly positive for propidium iodide or exhibited



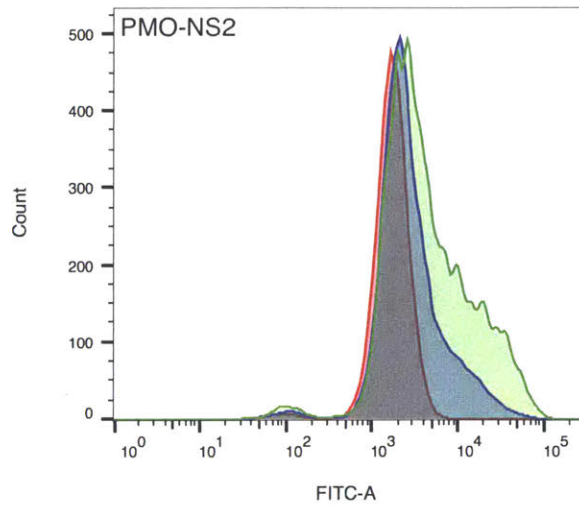


**Figure 2.7. Representative histograms from the flow cytometry analysis of PMO-PPC conjugates.** The red histogram is the cell-only control, the blue histogram is the PMO control, and the green is the PMO conjugate. Each histogram is the result from one treatment well. Each experiment contained three treatment wells for each construct, and the experiment was repeated three times.

forward/side scatter readings that were sufficiently different from the main cell population were excluded. Each histogram contained at least 10,000 gated events. Representative histograms are shown in Figure 2.7.

### **2.3.9. Flow Cytometry Assay for Cy5.5-Labeled Peptides**

HeLa-654 cells were maintained in MEM supplemented with 10% (v/v) fetal bovine serum and 1% (v/v) Pen Strep at 37 °C and 5% CO<sub>2</sub>. Twelve hours before treatment, HeLa cells were plated at a density of 50,000 cells per well in a 24-well plate. 1 mM stocks of each of the peptides were prepared in DMSO. Concentration of the stocks was quantified by absorbance using a UV/Vis spectrophotometer after dilution into 95:5 water:acetonitrile containing 0.1% TFA. A Cy5.5 extinction coefficient of  $\epsilon \approx 60,000 \text{ M}^{-1}\text{cm}^{-1}$  at  $\lambda=680 \text{ nm}$  was used (determined experimentally by creating a standard curve of Cy5.5 azide dissolved in 95:5 water:acetonitrile containing 0.1% TFA. The extinction coefficient is sensitive to the amount of acetonitrile in solution). Then, each peptide was diluted to a final concentration of 5  $\mu\text{M}$  in MEM supplemented with 10% (v/v) fetal bovine serum and 1% (v/v) Pen Strep. To treat the cells, the overnight growth media was aspirated from each well and 250  $\mu\text{L}$  of a given 5  $\mu\text{M}$  peptide stock was applied to each well. Cells were incubated for 2 hours at 37 °C and 5% CO<sub>2</sub> with the peptide treatment, and then the treatment media was aspirated. Trypsin-EDTA 0.25 % (150  $\mu\text{L}$ ) was added to the cells and incubated for 10 min at 37 °C and 5% CO<sub>2</sub>. To quench the trypsin, 600  $\mu\text{L}$  of MEM supplemented with 10% (v/v) fetal bovine serum and 1% (v/v) Pen Strep was added to each well. The dissociated cells in media were transferred to microcentrifuge tubes and spun at 500 ref for 3 min. The supernatant was removed and the pellets were each washed with 1 mL of phosphate-buffered saline (PBS), and the tubes were spun again. The supernatant was again removed and the pellets were resuspended in 500  $\mu\text{L}$  PBS with 2% FBS (v/v) and 2  $\mu\text{g}/\text{mL}$  propidium iodide in water. Flow cytometry analysis was carried out on a BD LSRII flow cytometer. Gates were applied to the data to ensure that only data from healthy, living cells were taken into account. Cells that were highly positive for propidium iodide or had forward/side scatter readings that were sufficiently different from the main cell population were excluded. Each histogram contains at least 10,000 gated events.

### **2.3.10. Flow Cytometry Analysis with Endocytosis Inhibitors**

To inhibit a variety of endocytic mechanisms, a pulse-chase experiment was performed. Cells were treated using stock solutions of each inhibitor dissolved in the following solutions: chlorpromazine - 10 mM in water; cytochalasin D - 10 mM in DMSO; wortmannin - 2 mM in



DMSO; MBCD - 5 mM in cell culture media; EIPA - 10 mM in DMSO; dynasore - 10 mM in DMSO. Briefly, HeLa 654 cells were plated at a density of 5,000 cells per well in a 96-well plate in MEM supplemented with 10% FBS and 1% penicillin-streptomycin. The next day, the cells were treated with each inhibitor at the indicated concentration. After 30 minutes, PMO-peptide conjugate was added to each well at a concentration of 5  $\mu$ M. After incubation at 37 °C and 5% CO<sub>2</sub> for 3 hours, the treatment media was replaced with fresh media (containing neither inhibitor nor PMO-peptide) and the cells were allowed to grow for another 22 hours at 37 °C and 5% CO<sub>2</sub>. For the 4 °C experiments, the day after plating, the cells were pre-incubated for 30 minutes at 4 °C, followed by the addition of PMO-peptide conjugate to each well at a concentration of 5  $\mu$ M. After incubation at 4 °C for 3 hours, the treatment media was replaced with fresh media and the cells were allowed to grow for another 22 hours at 37 °C and 5% CO<sub>2</sub>. Sample preparation and flow cytometry were then performed as described above. Each histogram contains at least 2,000 gated events, with the exception of treatment with 20  $\mu$ M cytochalasin D and 200 nM wortmannin.

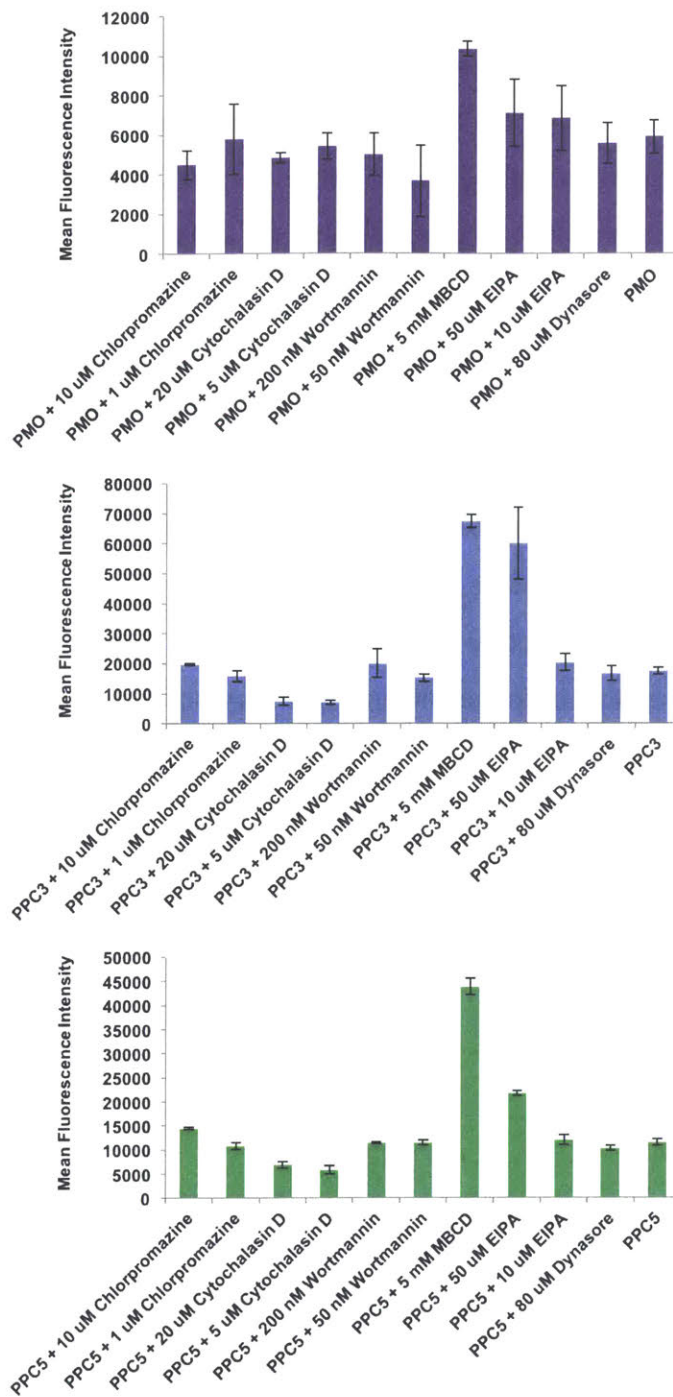


**Figure 2.8. Effect of endocytosis inhibitors on PPC efficacy.** HeLa-654 cells were treated with each inhibitor in a pulse-chase experiment. After treatment, the mean fluorescence intensity of eGFP is measured by flow cytometry. PMO is the unconjugated PMO, and here PPC3 and PPC5 are used as shorthand for the PPC3-PMO and PPC5-PMO conjugates. (MBCD = methyl- $\beta$ -cyclodextrin and EIPA = 5-(N-Ethyl-N-isopropyl)amiloride)

## 2.4. Conclusions

Serendipity is not necessary to discover new cell-penetrating peptide sequences for macromolecule delivery. Although many CPPs have been discovered using peptide fragments from natural proteins, computational models challenge the notion that CPP sequences must be found in nature. Here, we generated a random forest classifier that could accurately predict whether or not conjugation of a given peptide sequence would increase PMO activity 3-fold. Our model enabled the discovery of five completely novel sequences that increased PMO activity, and accurately discriminated between active and inactive sequences. A BLAST search revealed that these new sequences are not found in nature.

One key component of our computational model is the standardized assay conditions used in the data set for training. Multiple experimental variables influence cellular uptake, including treatment concentration and the presence of serum. To enable the accurate classification of multiple CPPs, the peptides must be tested under similar conditions. Additionally, as noted previously in the CPP field, the computational models are only as valuable as the data used to train a given model. By testing a PMO-CPP library under standardized conditions, we obtained a high-quality training set to improve the accuracy of the predictions from the model.

The second key component of our model is the type of cargo utilized to assess cell penetration. Functional macromolecules have diverse chemical structures, mechanisms of action, and sites of activity inside of cells. Although many CPPs are investigated using only an attached fluorophore as a metric of their efficacy, our experiments indicated that fluorophore studies have little predictive value with regards to the optimal CPP for macromolecular delivery. Therefore, to develop an optimal computational model, the training set should involve CPPs tested in the appropriate context. For our experiments, we investigated a library of PMO-CPP conjugates to focus on the context of improving PMO delivery and promoting exon skipping.

Combining these two components leads to a computational model that enables exploration of the design space for cell-penetrating peptides. Although many, potentially infinite, peptide sequences may facilitate PMO delivery, our model can be employed to select sequences based on certain desirable parameters. For example, peptide sequences with a large number of arginine residues can lead to toxicity *in vivo* and so, in our computational model, sequence space can be restricted to sequences containing fewer than 3 arginine residues. Similar approaches can be utilized for identifying and avoiding peptide sequences that are immunogenic (e.g. by referencing

a database of immunogenic sequences), or peptide sequences that will be synthetically challenging (e.g. peptides with multiple  $\beta$ -branched residues). We envision that using our computational model, vast numbers of putative sequences can be tested *in silico*, reducing experimental burden and drastically increasing the chemical space that can be investigated. Then, only the optimized sequences that meet the desired criteria can be evaluated experimentally.

Moving forward, we seek to understand the generalizability of our current computational model. If our model extends to clinically-relevant PMO sequences, it could serve as a valuable resource to optimize therapeutic PMO-peptide conjugates. Additionally, we will investigate the utility of our computational model for improving the delivery of different classes of antisense oligonucleotides. Understanding the strengths and limitations of computational prediction will be critical for applying machine learning to the challenge of intracellular delivery. We envision that careful experimental design coupled with the appropriate machine learning algorithm will significantly increase the portfolio of CPPs for macromolecule delivery.

## **2.5. Acknowledgments**

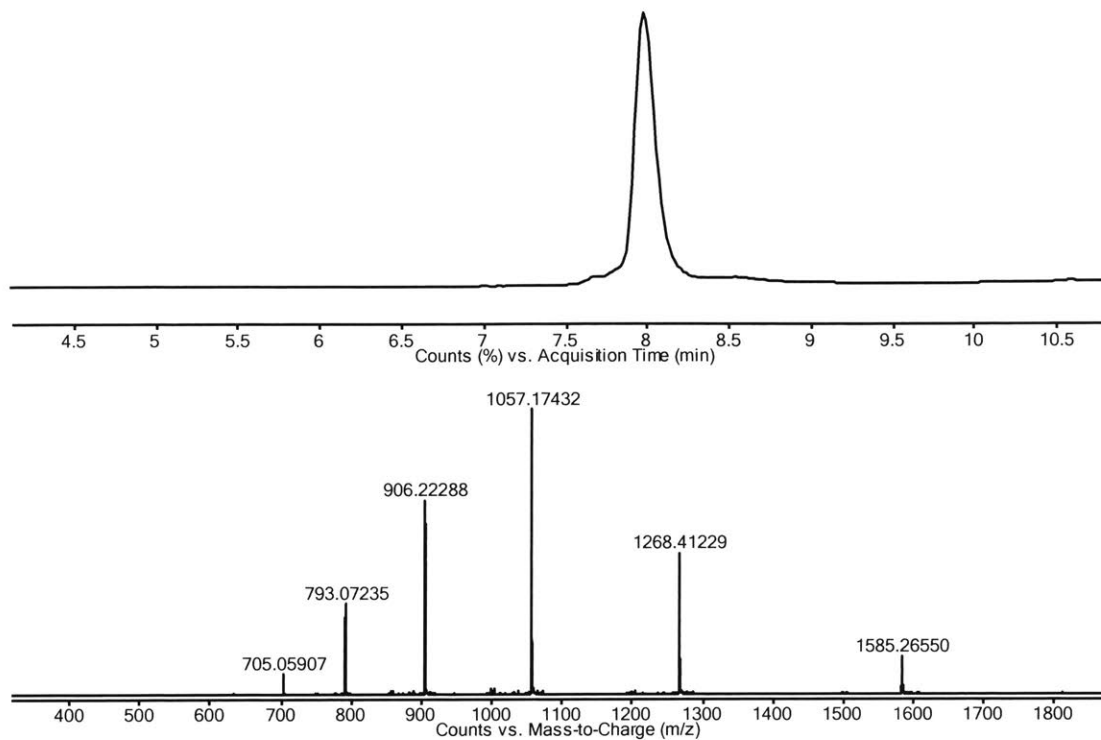
This work was supported by Sarepta Therapeutics, Cambridge MA. J.M.W. and R.L.H are supported by the National Science Foundation Graduate Research Fellowship under Grant No. 1122374. C.M.F. is supported by the David H. Koch Graduate Fellowship Fund and by the Eunice Kennedy Shriver National Institute of Child Health and Human Development of the National Institutes of Health under award number F30HD093358. The authors acknowledge the Swanson Biotechnology Center Flow Cytometry Facility at the Koch Institute for advice and the use of their flow cytometers. We thank Mark Simon, Dan Dunkelmann, and Alex Mijalis for assistance with peptide synthesis. We also thank Ethan Evans, Dr. Alan Beggs, and Dr. Guriq Basi for helpful discussions and comments during manuscript preparation.

## 2.6. Appendix of LC-MS Characterization

PMO-azide: LC-MS chromatogram obtained using Method A

Mass expected: 6337.5 Da

Mass observed: 6337.9 Da



PMO-CPP Conjugate Library: All chromatograms obtained with Method A unless otherwise noted.

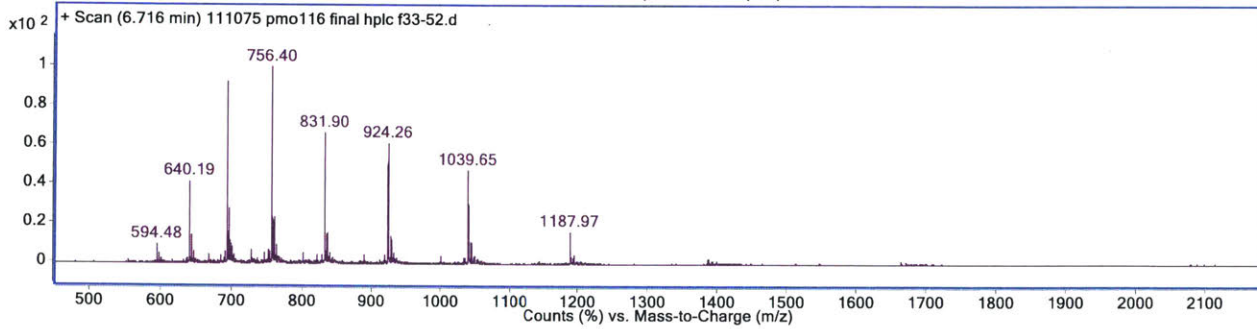
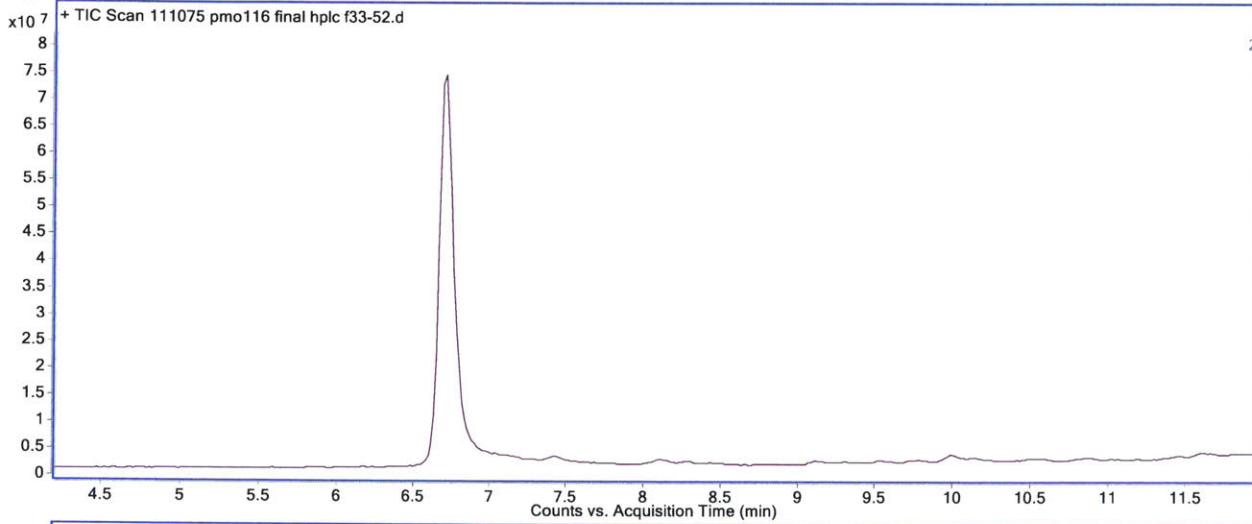
PMO-R12

Mass expected: 8307.7 g/mol

Mass observed: 8309.6 g/mol

Amount: 4.8 mg (61%)

Peptide Sequence: RRRRRRRRRRRR



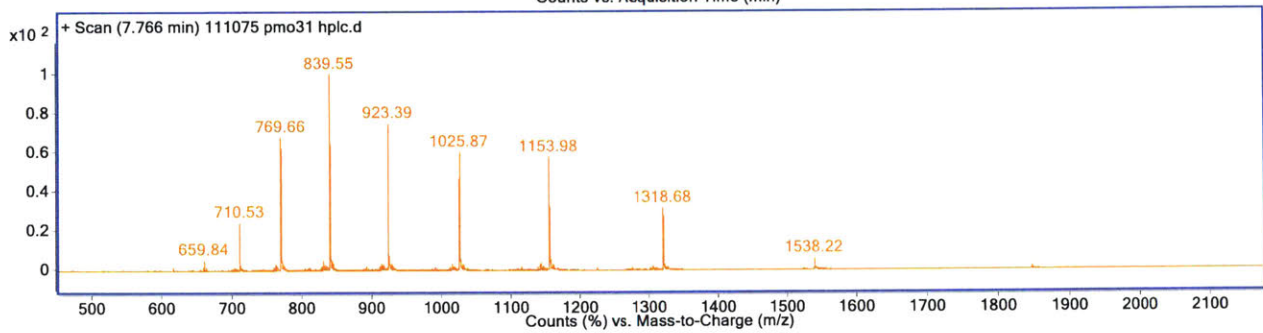
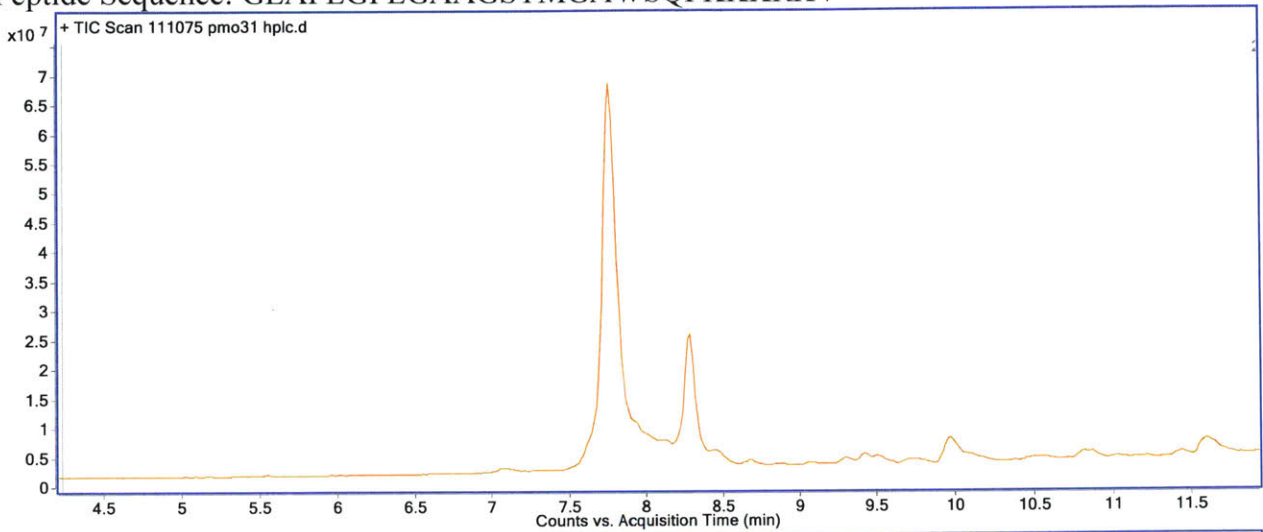
PMO-MPG

Mass expected: 9223.9 g/mol

Mass observed: 9224.3 g/mol

Amount: 4.0 mg (55%)

Peptide Sequence: GLAFLGFLGAAGSTMGAWSQPKKKRKV



Note: The smaller peak at 8.3 minutes is unreacted peptide



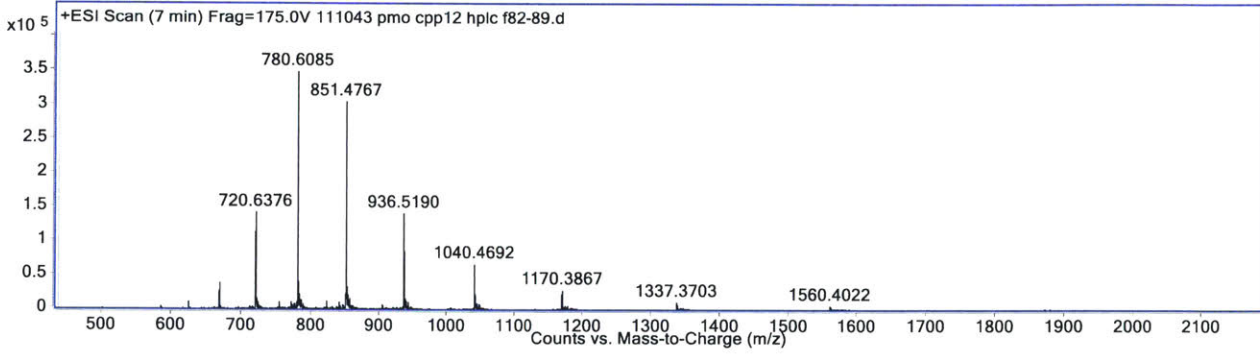
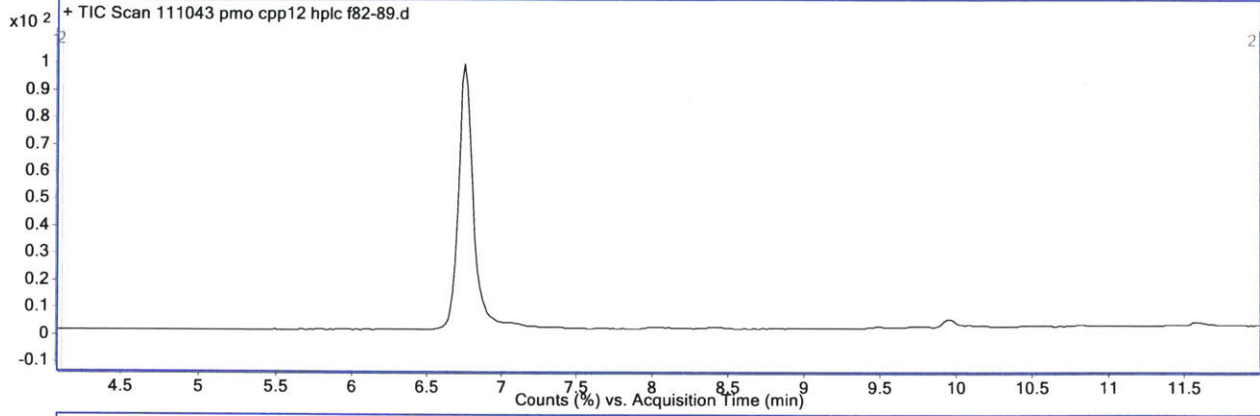
PMO-Bac7

Mass expected: 9355.2 g/mol

Mass observed: 9355.6 g/mol

Amount: 7.2 mg (81%)

Peptide Sequence: RRIRPRPPRLPRPRRPLPFPRPG



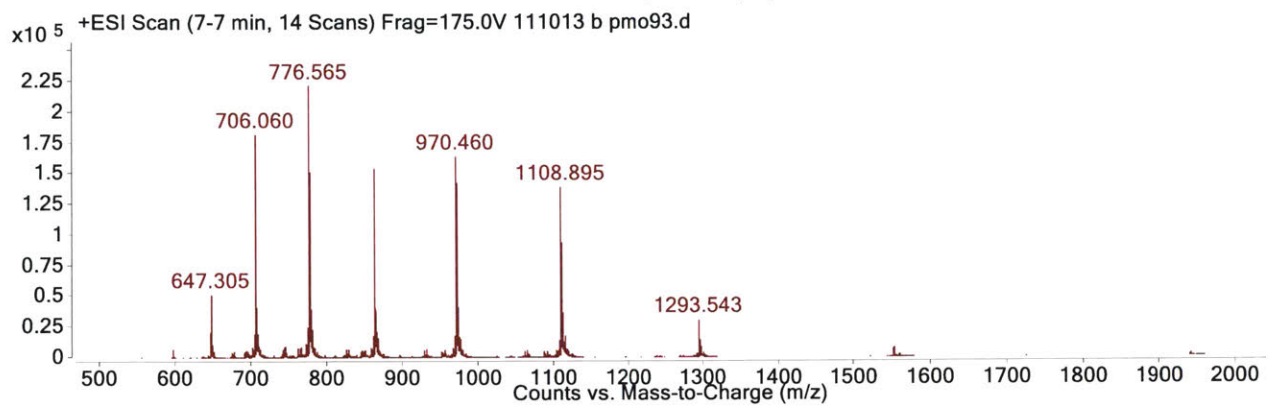
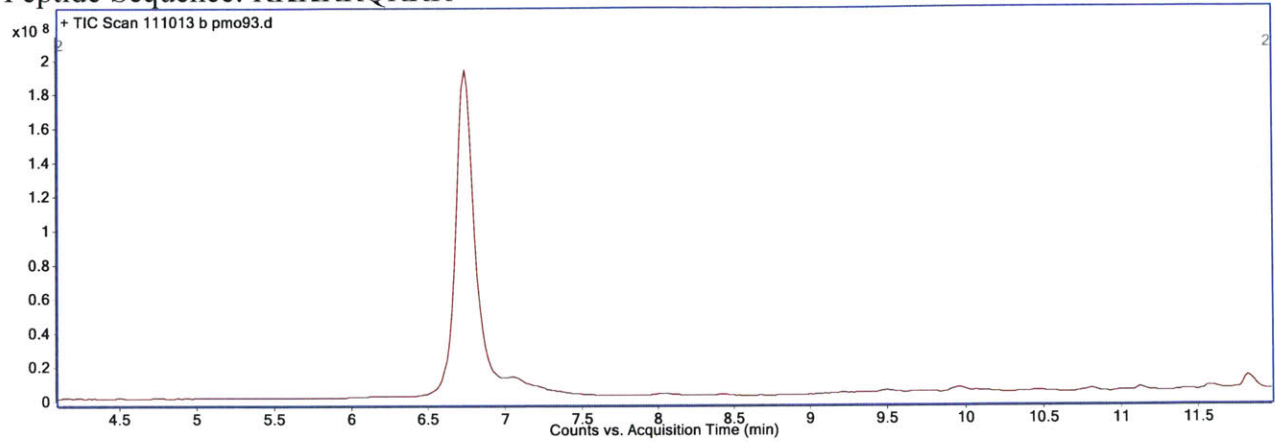
PMO-TAT

Mass expected: 7756.2 g/mol

Mass observed: 7756.4 g/mol

Amount: 4.7 mg (64%)\*

Peptide Sequence: RKKRRQRRR



PMO-R10

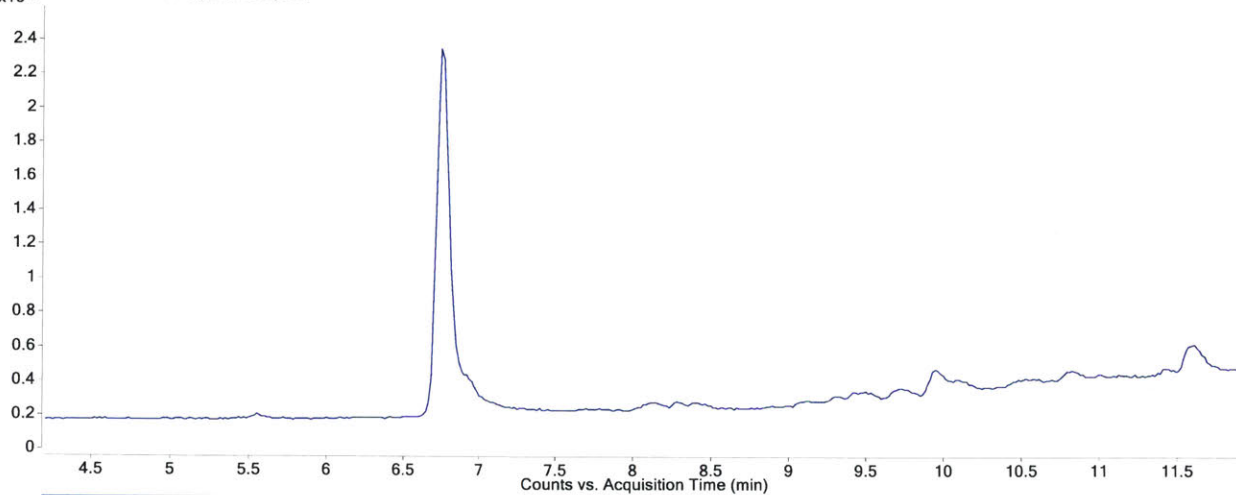
Mass expected: 7996.4 g/mol

Mass observed: 7996.7 g/mol

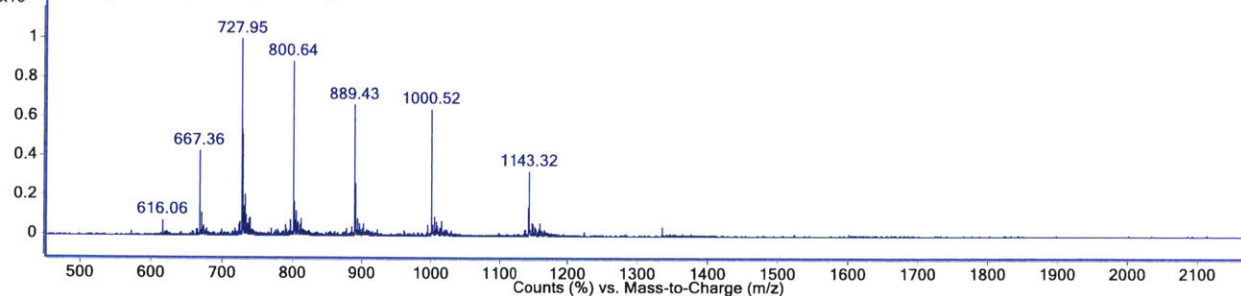
Amount: 2.8 mg (74%)

Peptide Sequence: RRRRRRRRRR

x10<sup>7</sup> + TIC Scan 111075 pmo115 hplc.d



x10<sup>2</sup> + Scan (6.761 min) 111075 pmo115 hplc.d



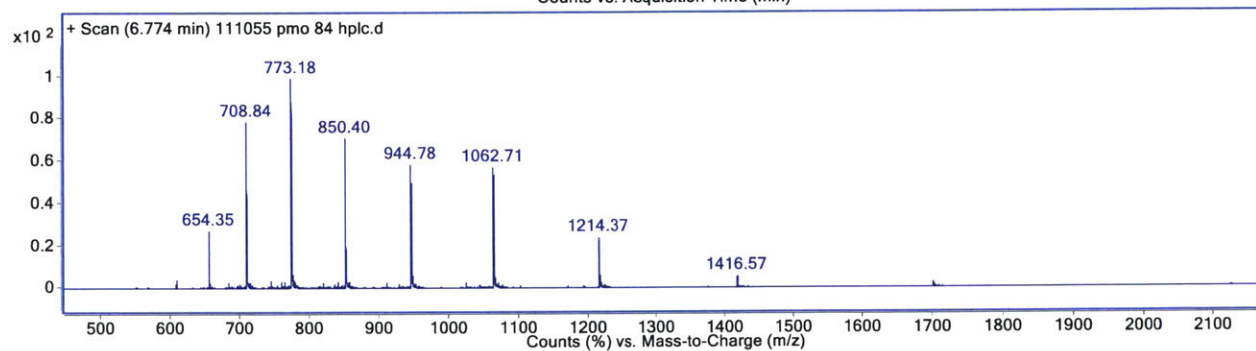
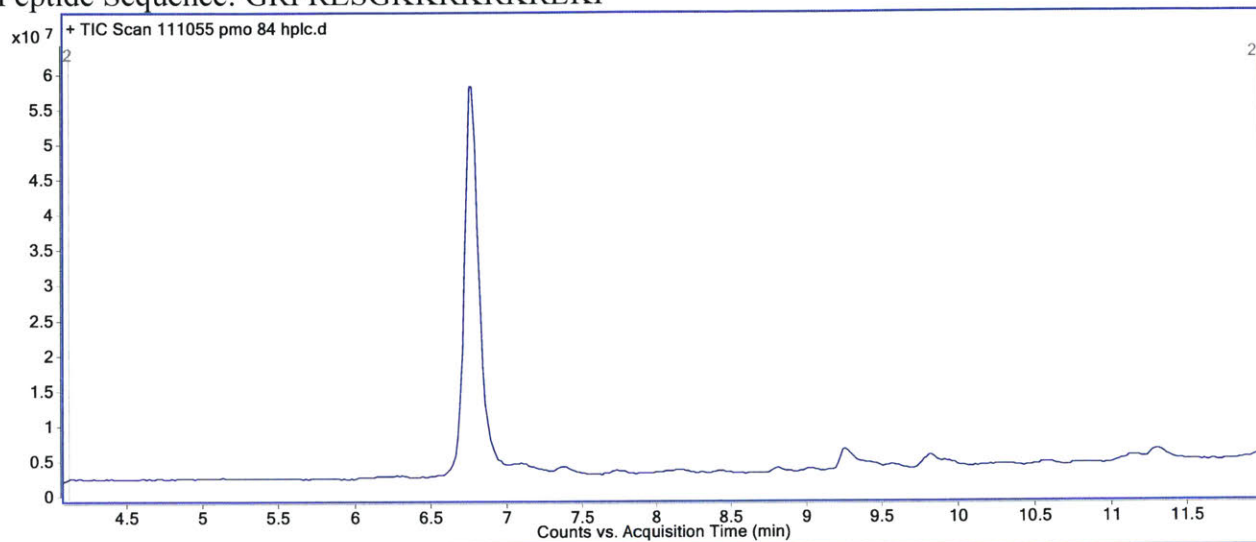
PMO-DPV6

Mass expected: 8494.0 g/mol

Mass observed: 8494.6 g/mol

Amount: 6.8 mg (84%)

Peptide Sequence: GRPRESGKKRKRKRLKP



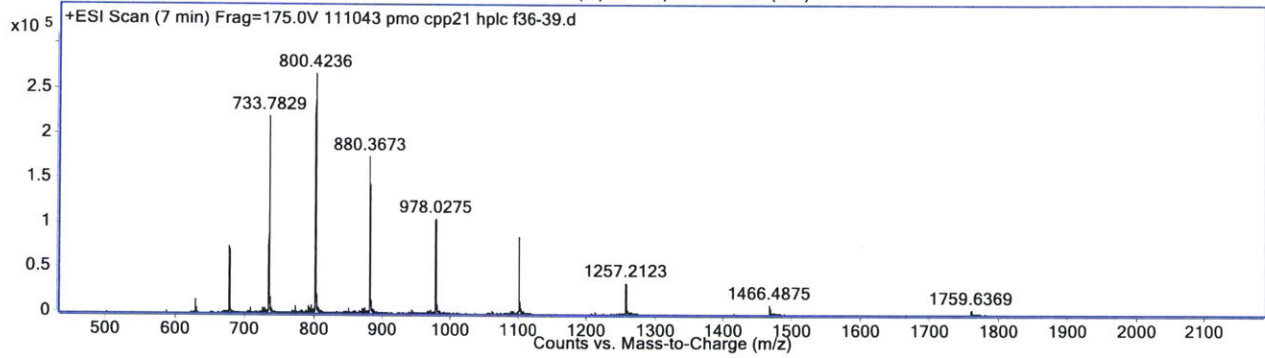
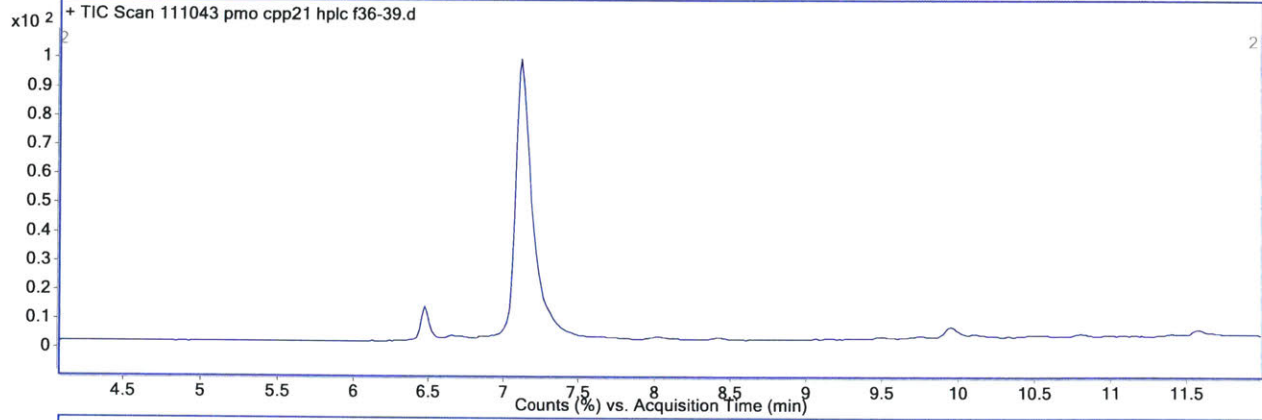
PMO-S413-PVrev

Mass expected: 8793.7 g/mol

Mass observed: 8793.9 g/mol

Amount: 2.8 mg (33.5%)

Peptide Sequence: ALWKTLKKVLKAPKKRKV



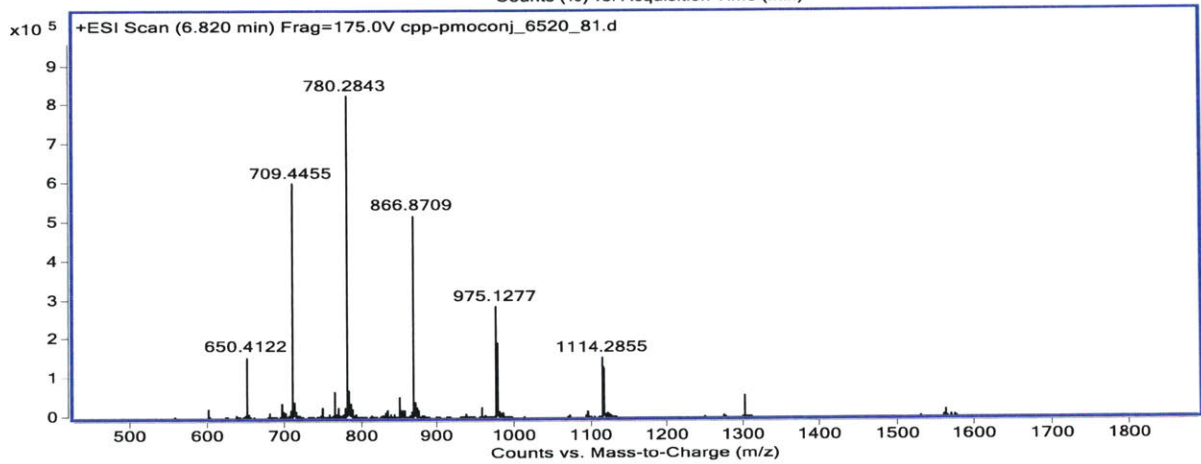
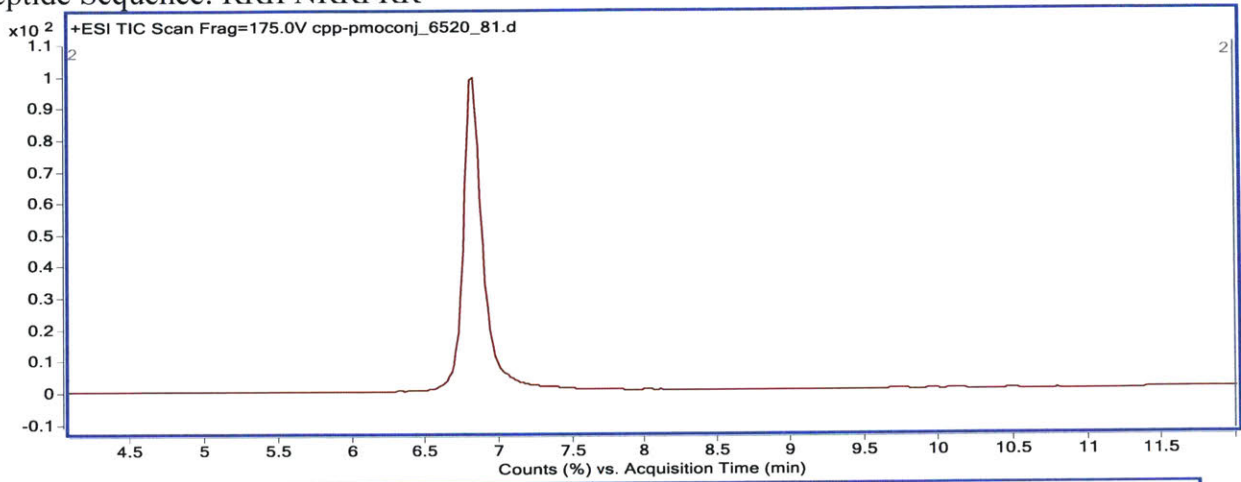
PMO-HRSV

Mass expected: 7793.1 g/mol

Mass observed: 7793.7 g/mol

Amount: 1.4 mg (19%)

Peptide Sequence: RRIPNRRPRR



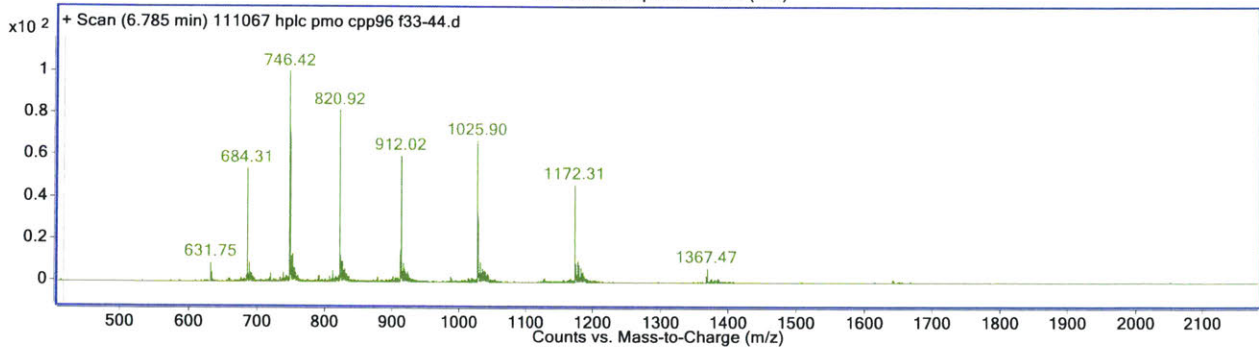
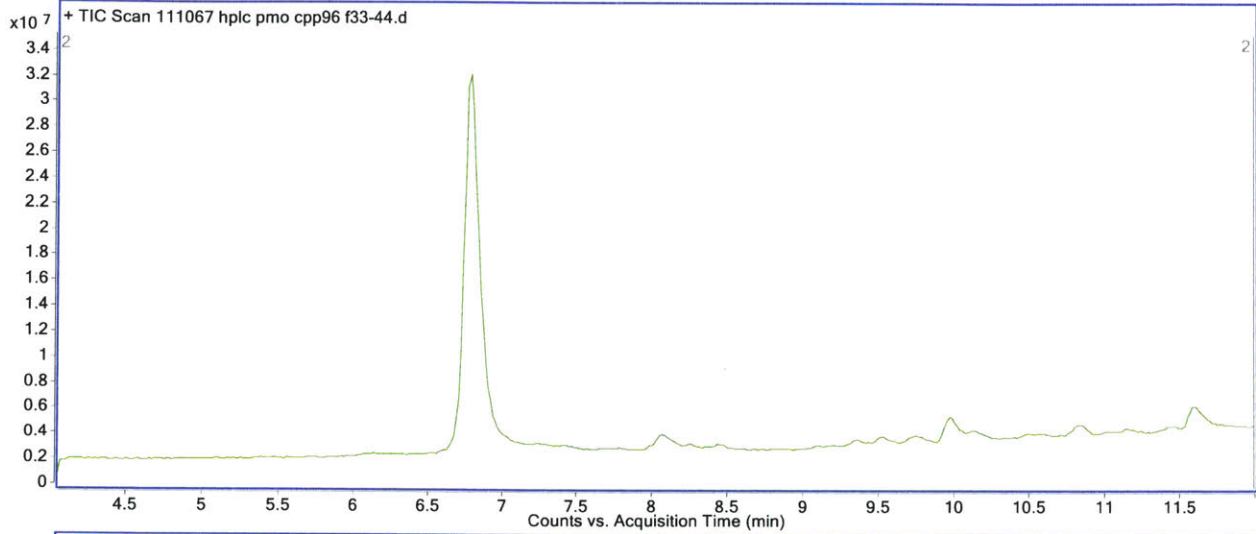
PMO-HTLV-II Rex

Mass expected: 8199.5 g/mol

Mass observed: 8200.0 g/mol

Amount: 3.8 mg (98%)

Peptide Sequence: TRRQRTRRARRNR



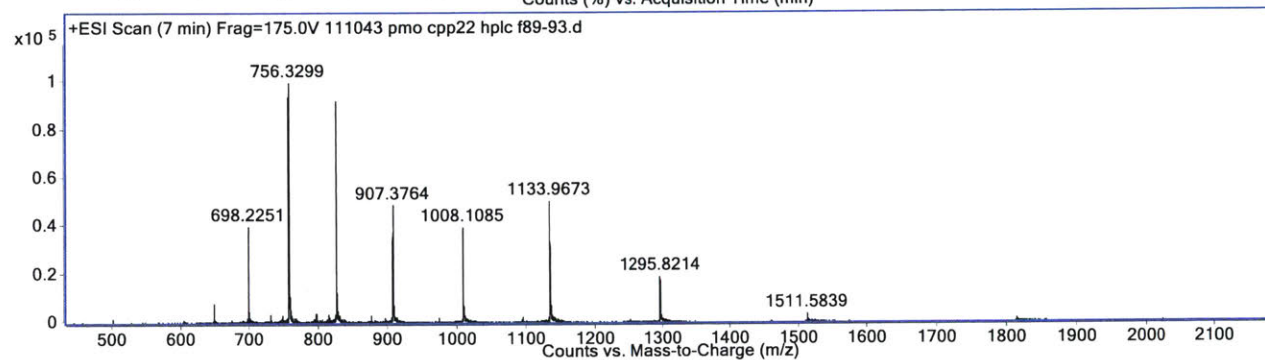
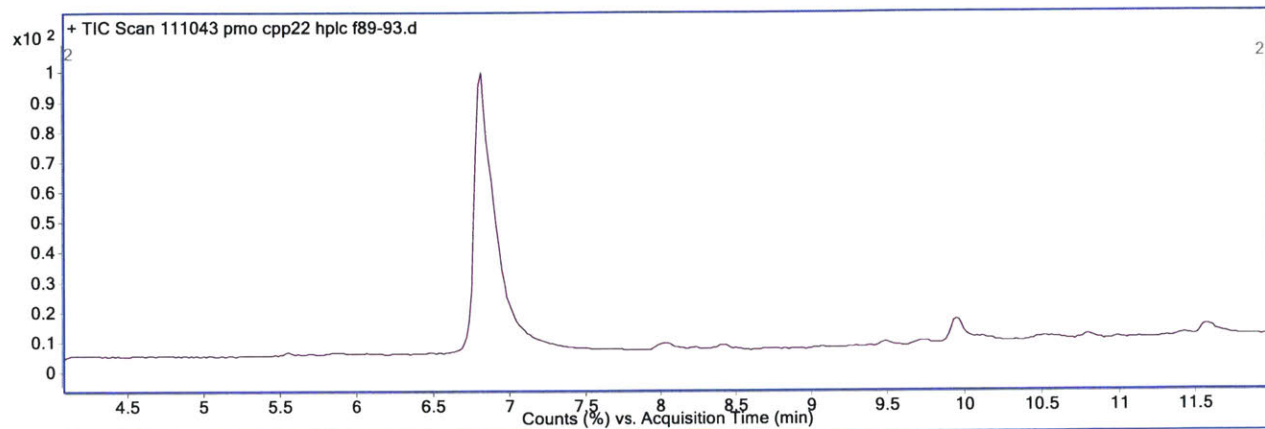
PMO-L-2

Mass expected: 9063.8 g/mol

Mass observed: 9064.1 g/mol

Amount: 2.6 mg (30.2%)

Peptide Sequence: HARIKPTFRRLKWKYKGFW





PMO-Melittin

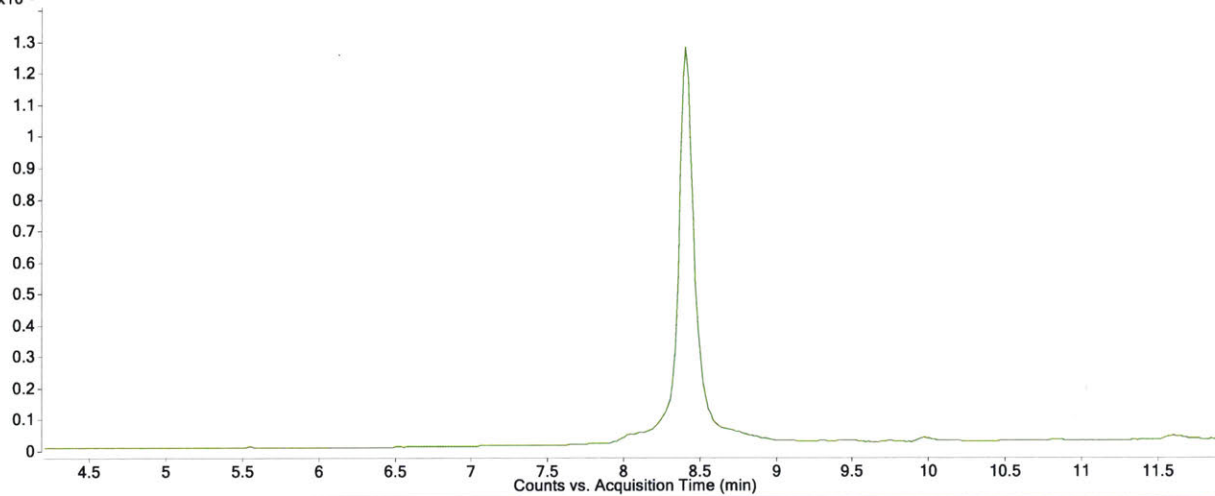
Mass expected: 9264.1 g/mol

Mass observed: 9265.1 g/mol

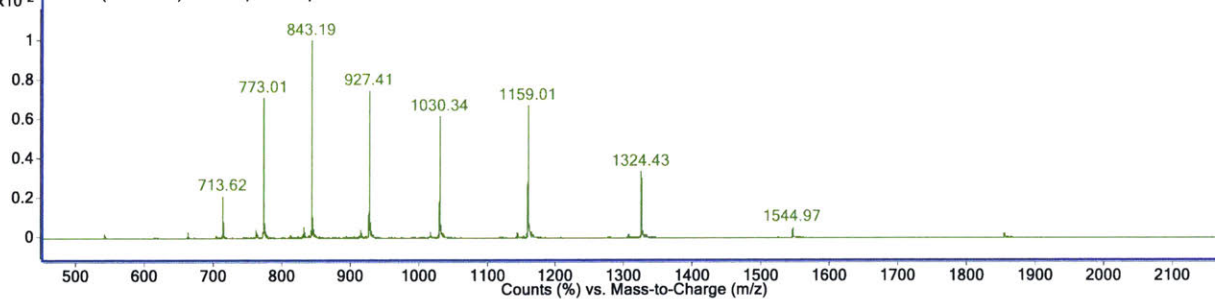
Amount: 7.6 mg (86%)

Peptide Sequence: GIGAVLKVLTTGLPALISWIKRKRQQ

x10<sup>8</sup> + TIC Scan 111075 pmo16 hplc.d



x10<sup>2</sup> + Scan (8.399 min) 111075 pmo16 hplc.d



PMO-DPV15

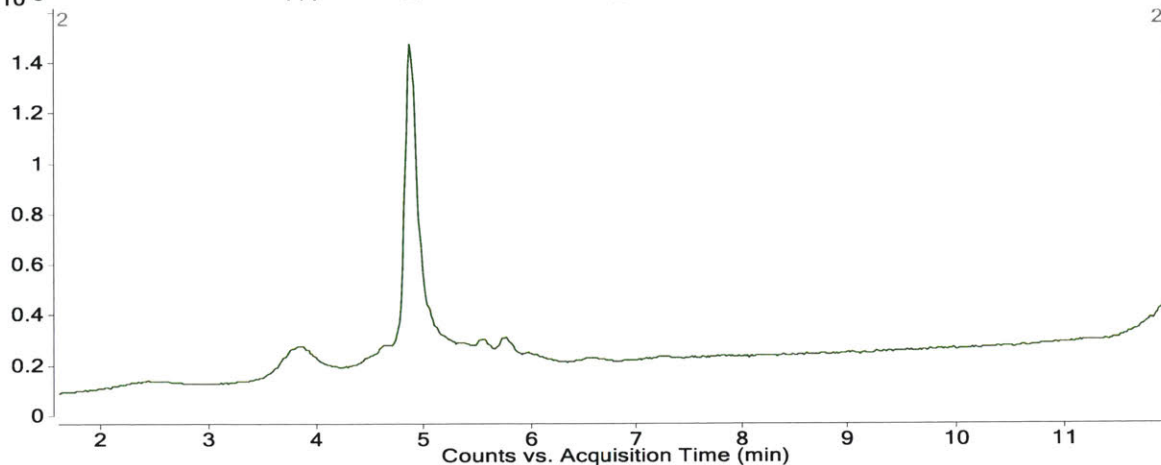
Mass expected: 8599.0 g/mol

Mass observed: 8599.6 g/mol

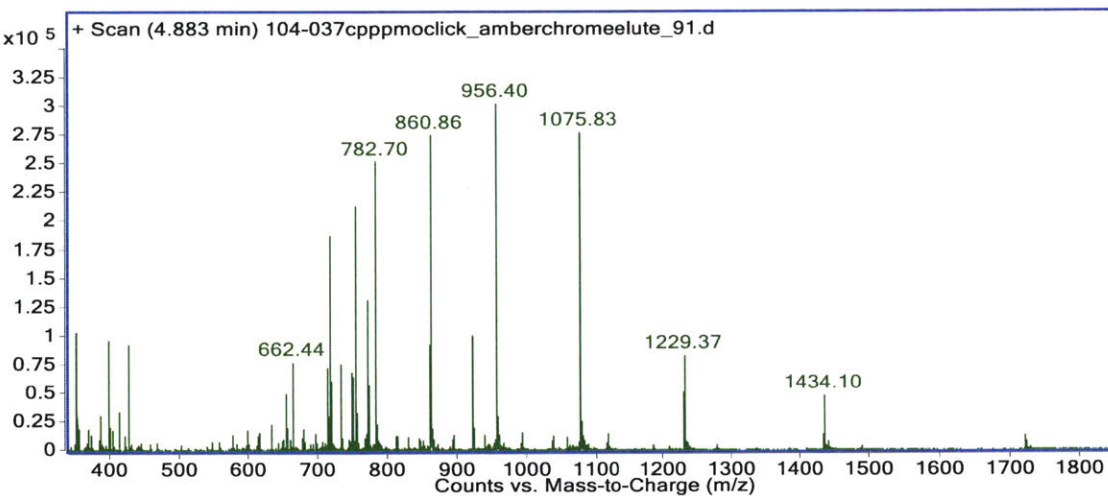
Amount: 6 mg (73%)\*

Peptide Sequence: LRRERQSRLRRERQSR

x10<sup>8</sup> + TIC Scan 104-037cpppmoclick\_amberchromeelute\_91.d



x10<sup>5</sup> + Scan (4.883 min) 104-037cpppmoclick\_amberchromeelute\_91.d



Note: LC-MS Method C

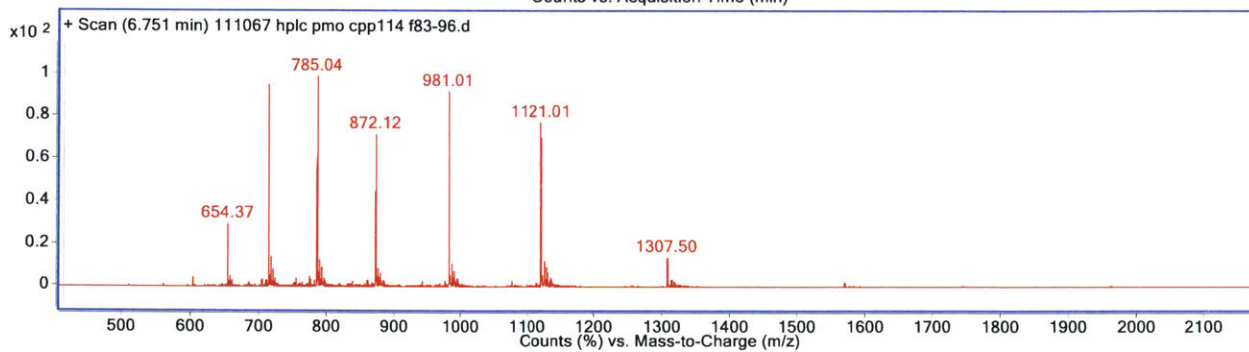
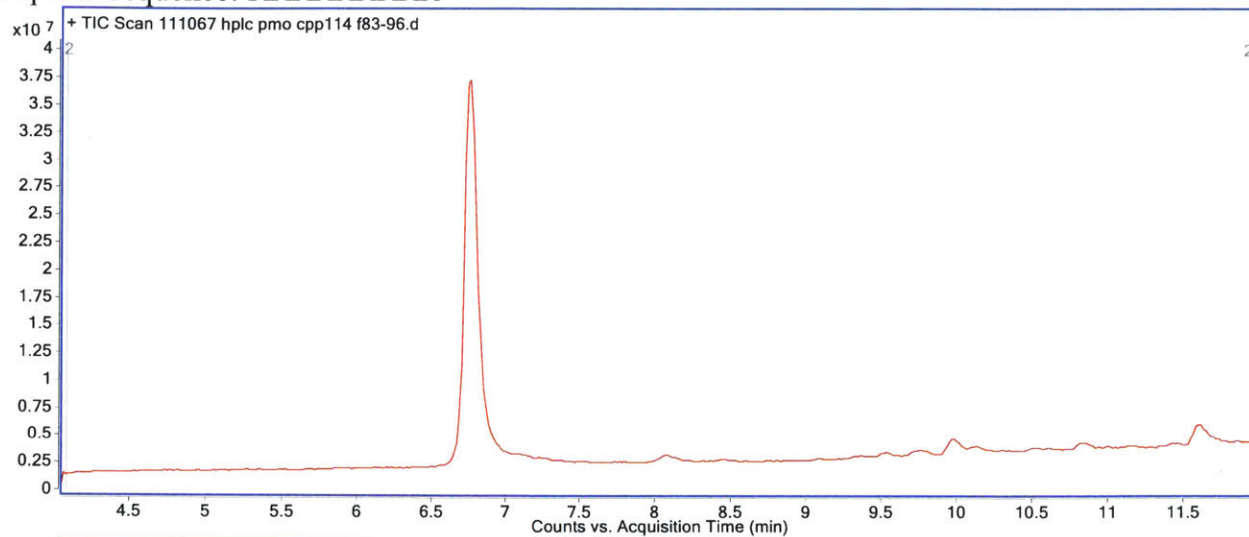
PMO-R9

Mass expected: 7840.2 g/mol

Mass observed: 7840.8 g/mol

Amount: 5.4 mg (73%)

Peptide Sequence: RRRRRRRRRR



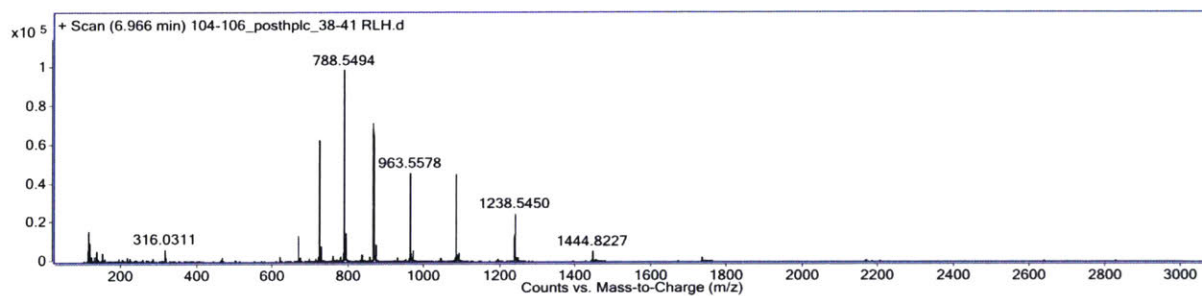
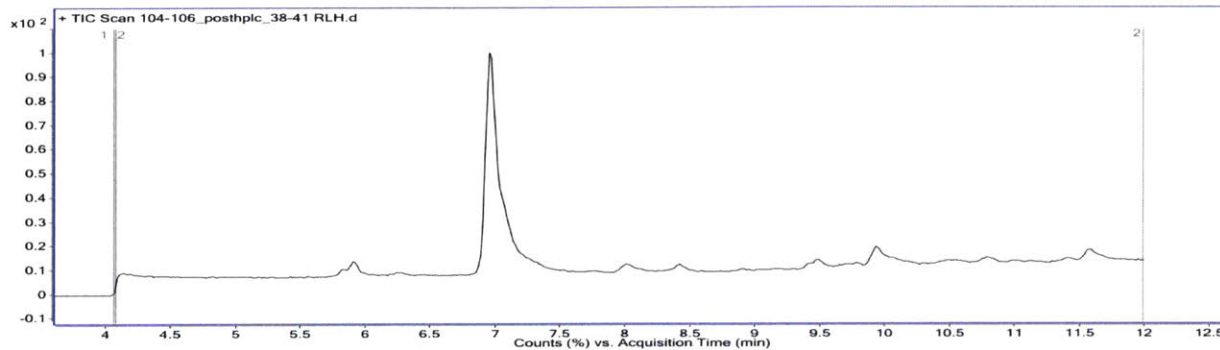
PMO-Penetratin

Mass Expected: 8663.3 g/mol

Mass Observed: 8663.9 g/mol

Amount: 1.3 mg (16%)

Peptide Sequence: RQIKIWFQNRRMKWKK



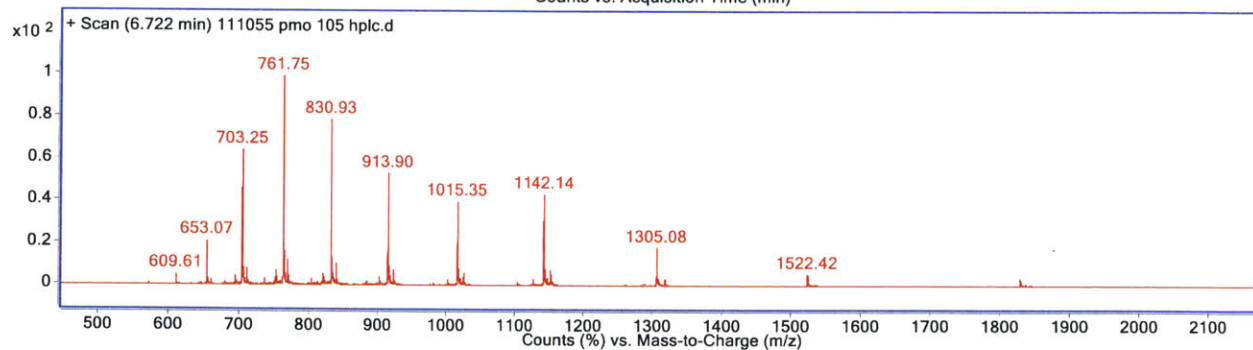
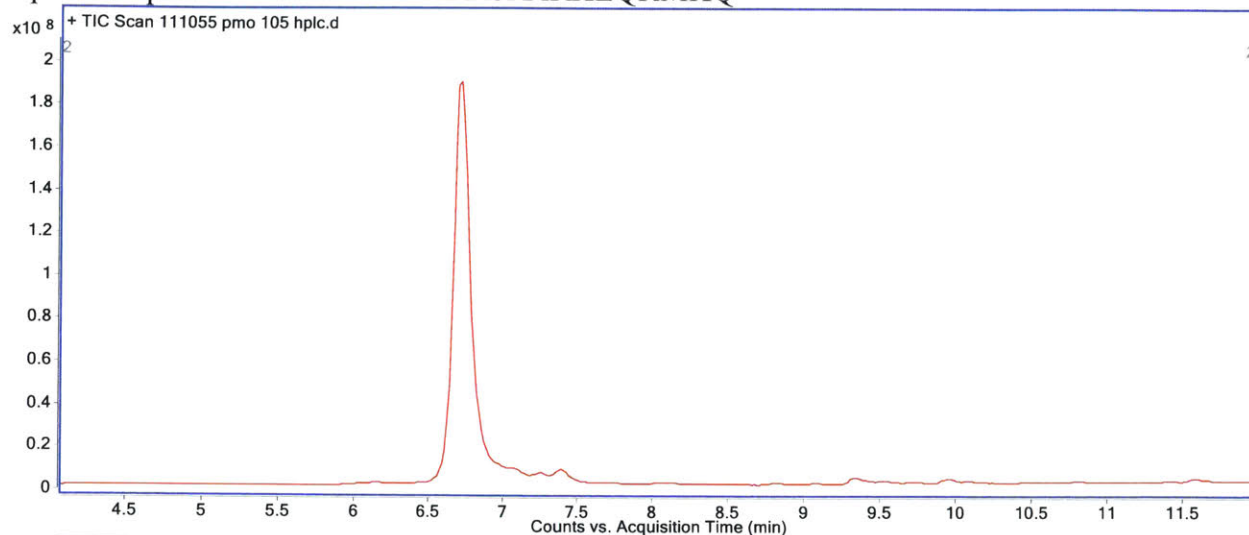
PMO-Yeast GCN4

Mass expected: 9128.6 g/mol

Mass observed: 9129.6 g/mol

Amount: 7.4 mg (85%)

Peptide Sequence: KRARNTEAARRSRARKLQRMKQ



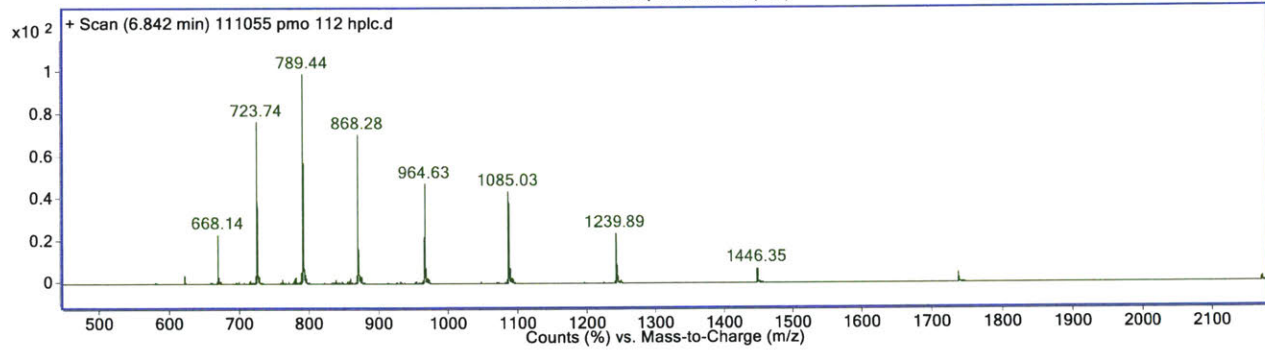
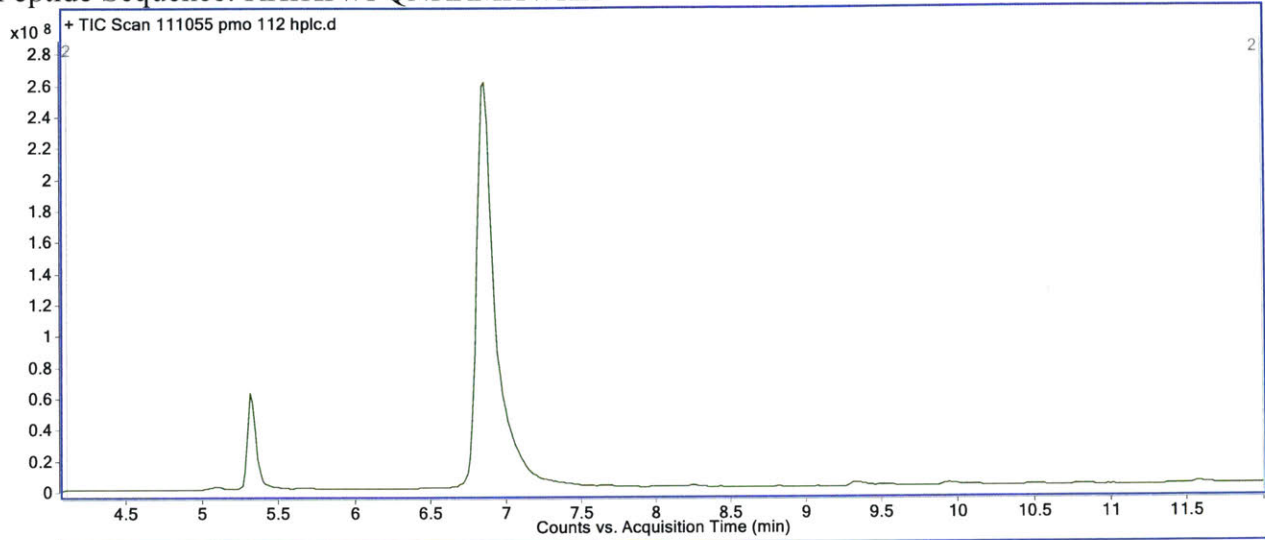
PMO-PDX-1

Mass expected: 8672.3 g/mol

Mass observed: 8673.0 g/mol

Amount: 5.4 mg (66%)

Peptide Sequence: RHIKIWFQNRRMKWKK



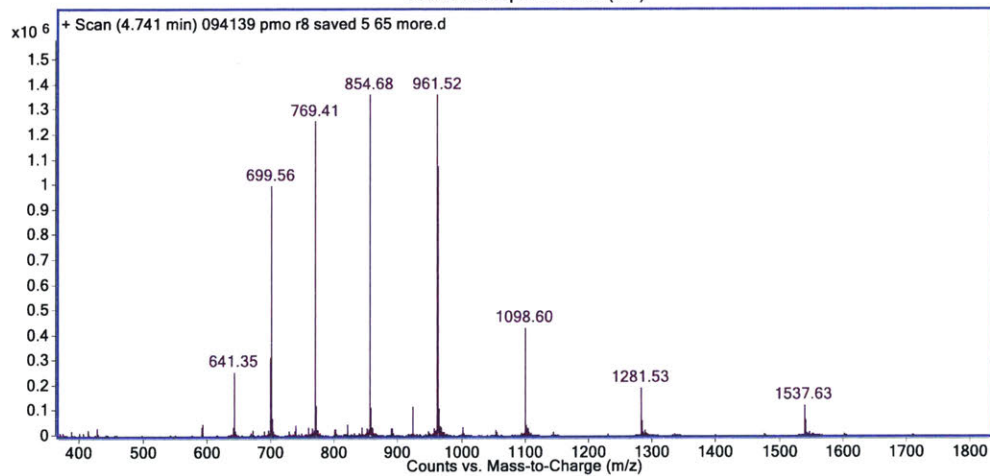
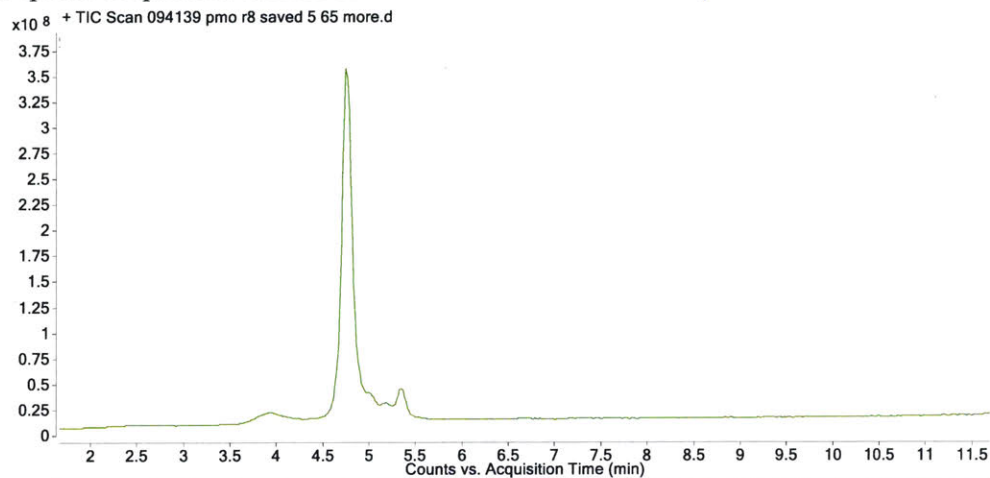
PMO-R8

Mass expected: 7684.0 g/mol

Mass observed: 7684.2 g/mol

Amount: 5.0 mg (68%)\*

Peptide Sequence: RRRRRRRR



Note: LC-MS Method C

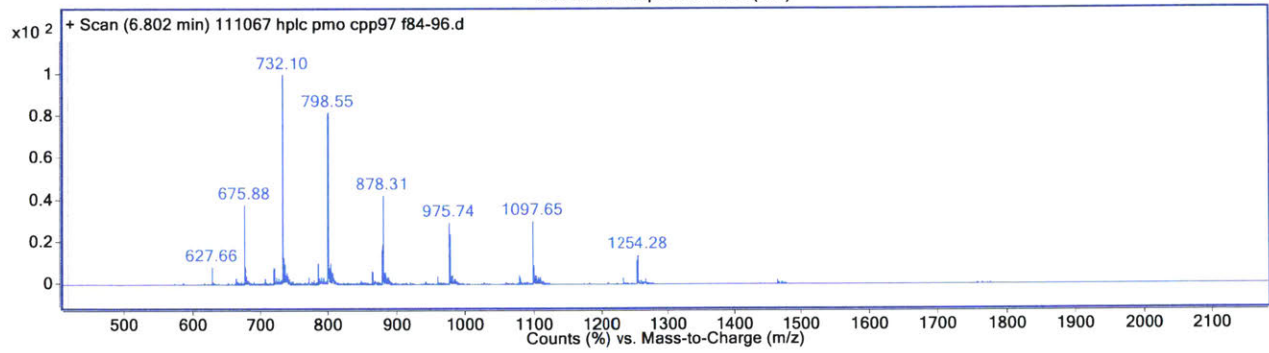
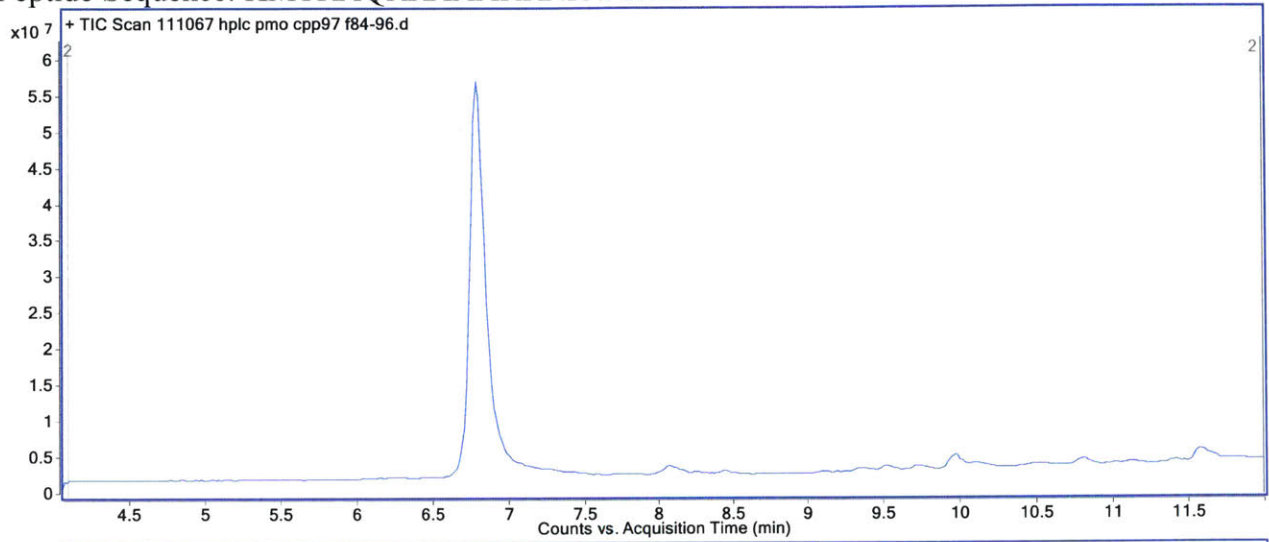
PMO-BMV Gag

Mass expected: 8773.2 g/mol

Mass observed: 8773.8 g/mol

Amount: 7.5 mg (90%)

Peptide Sequence: KMTRAQRRAAARRNRWTAR





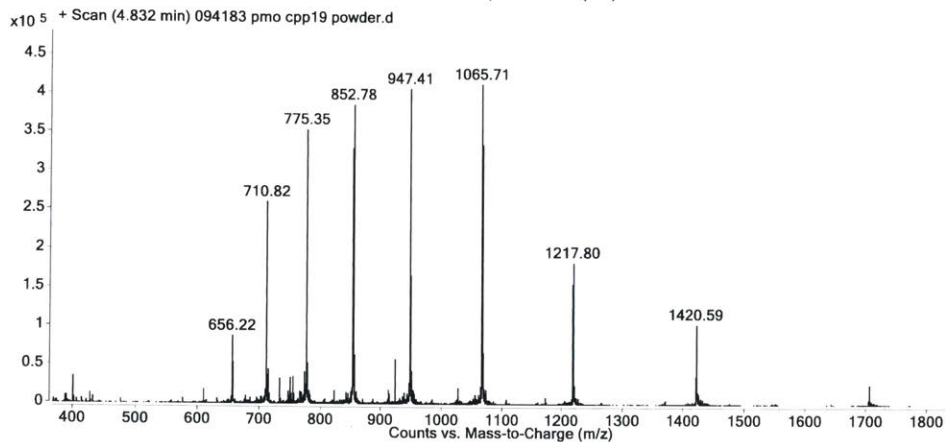
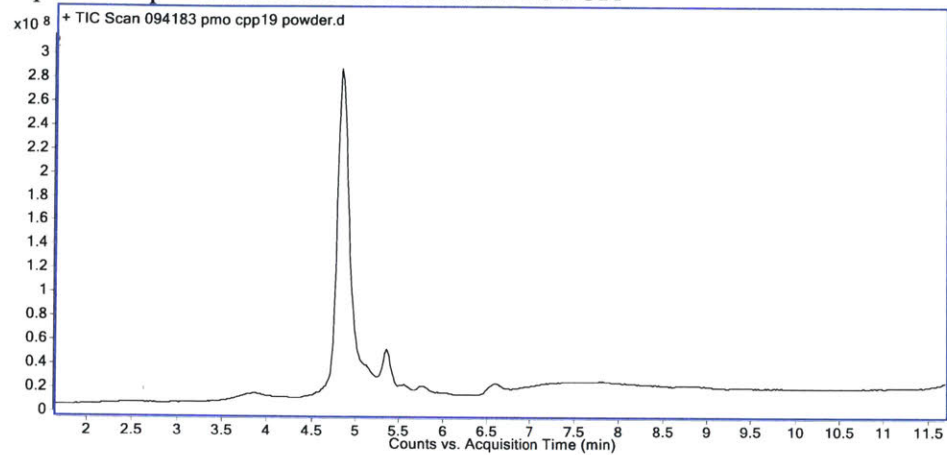
PMO-SynB1

Mass expected: 8516.9 g/mol

Mass observed: 8517.5 g/mol

Amount: 3.8 mg (47%)\*

Peptide Sequence: RGGRLSYSRRRFSTSTGR



Note: LC-MS Method C

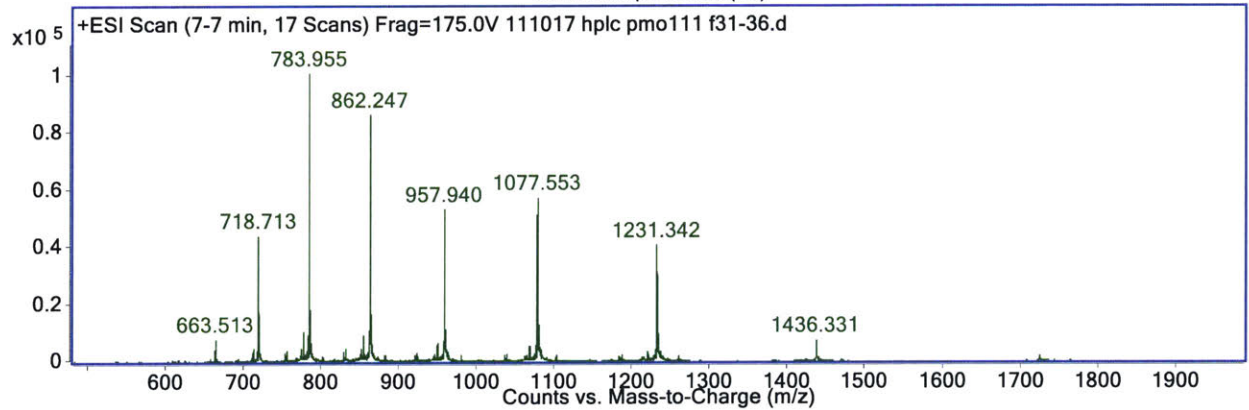
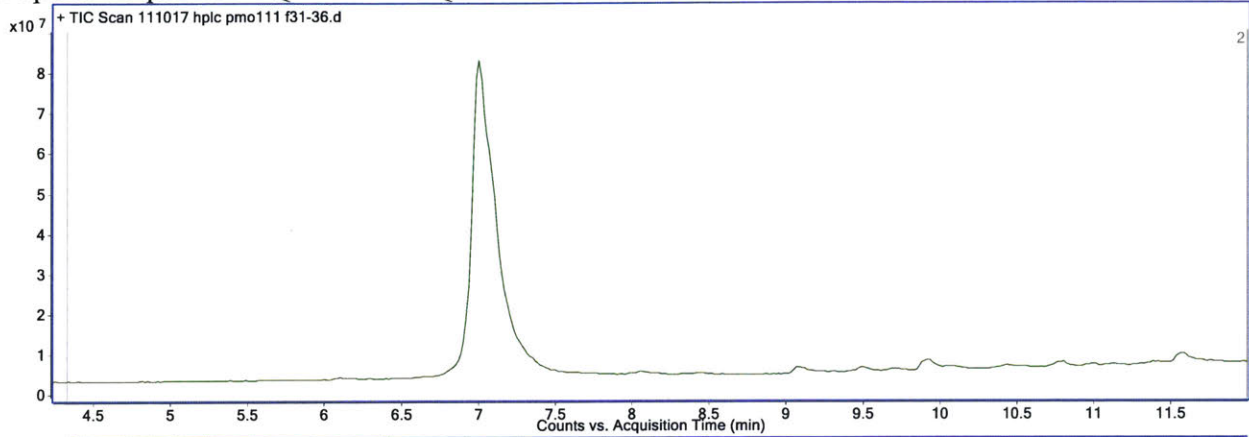
PMO-Knotted-1

Mass expected: 8613.1 g/mol

Mass observed: 8612.3 g/mol

Amount: 6.8 mg (83%)

Peptide Sequence: KQINNWFINQRKRWK



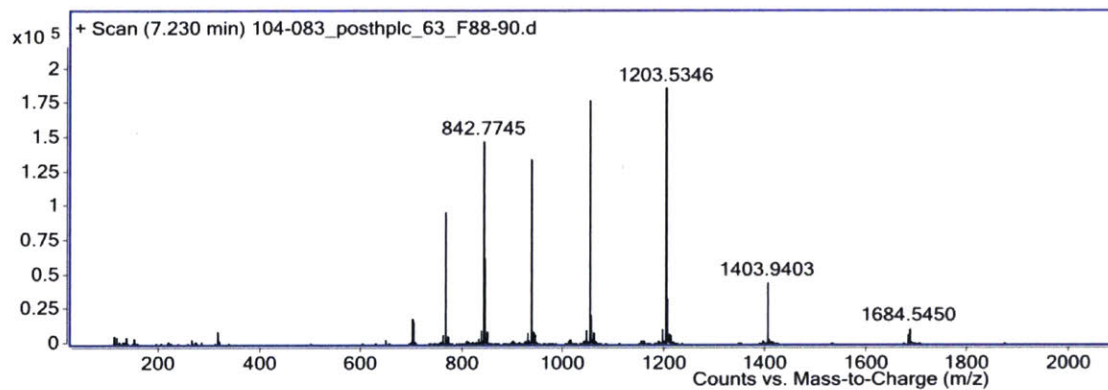
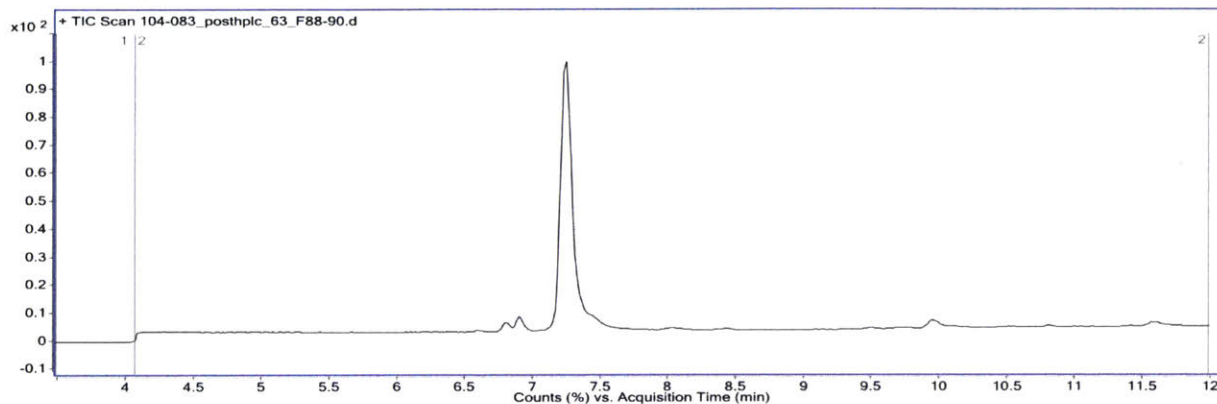
PMO-IVV14

Mass Expected: 8417.8

Mass Observed: 8418.4

Amount: 2.7 mg (34%)

Peptide Sequence: KLWMRWYSPTRRYG



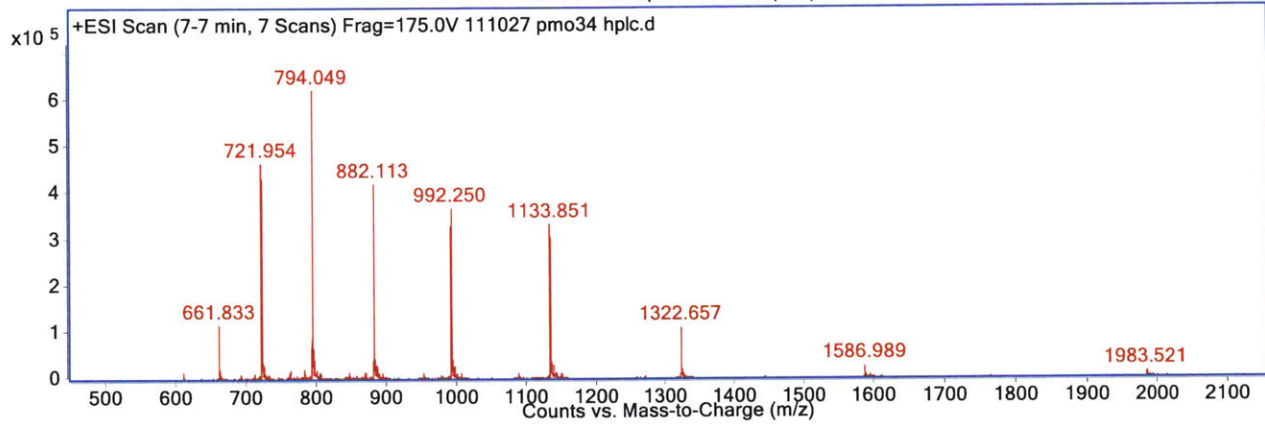
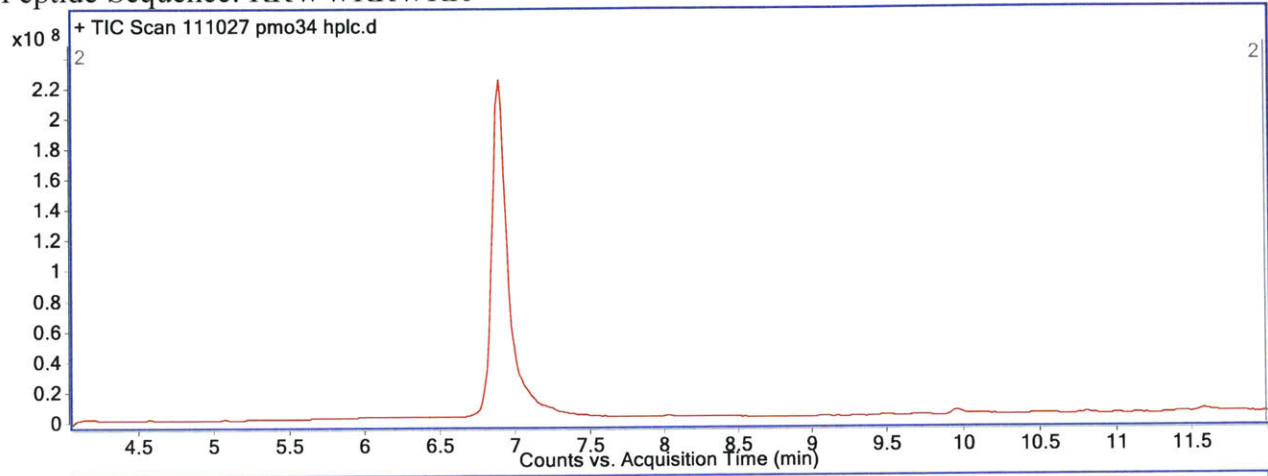
PMO-W/R

Mass expected: 7930.4 g/mol

Mass observed: 7930.8 g/mol

Amount: 6.7 mg (89%)

Peptide Sequence: RRWRRWRR



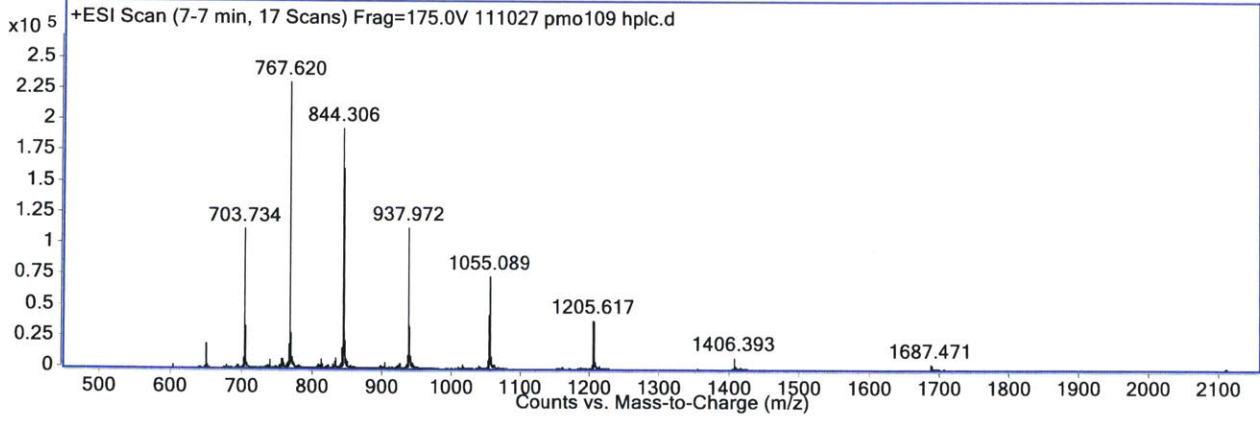
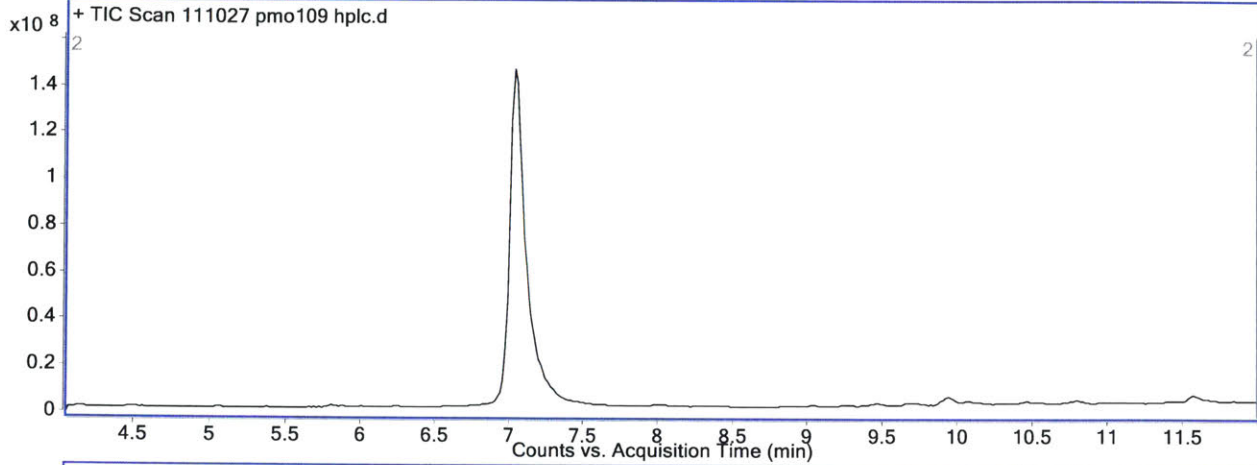
PMO-Engrailed-2

Mass expected: 8433.1 g/mol

Mass observed: 8433.4 g/mol

Amount: 5.6 mg (70%)

Peptide Sequence: SQIKIWFQNKRAKIKK



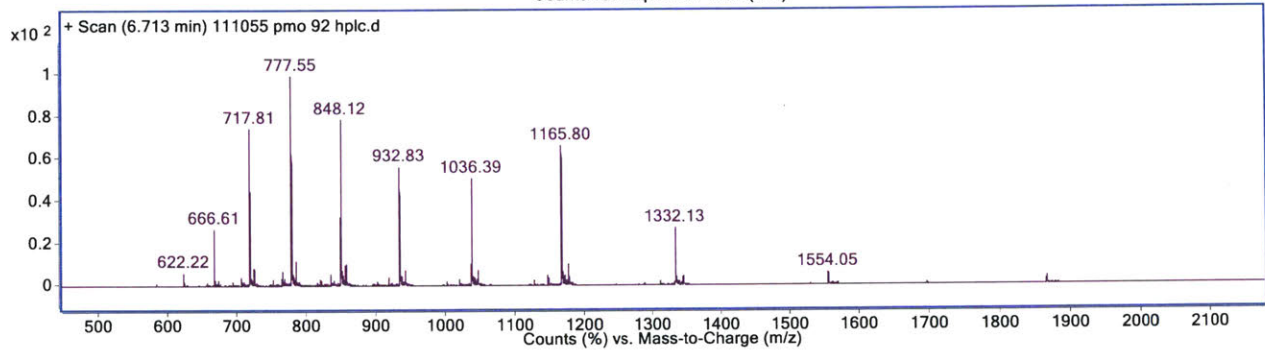
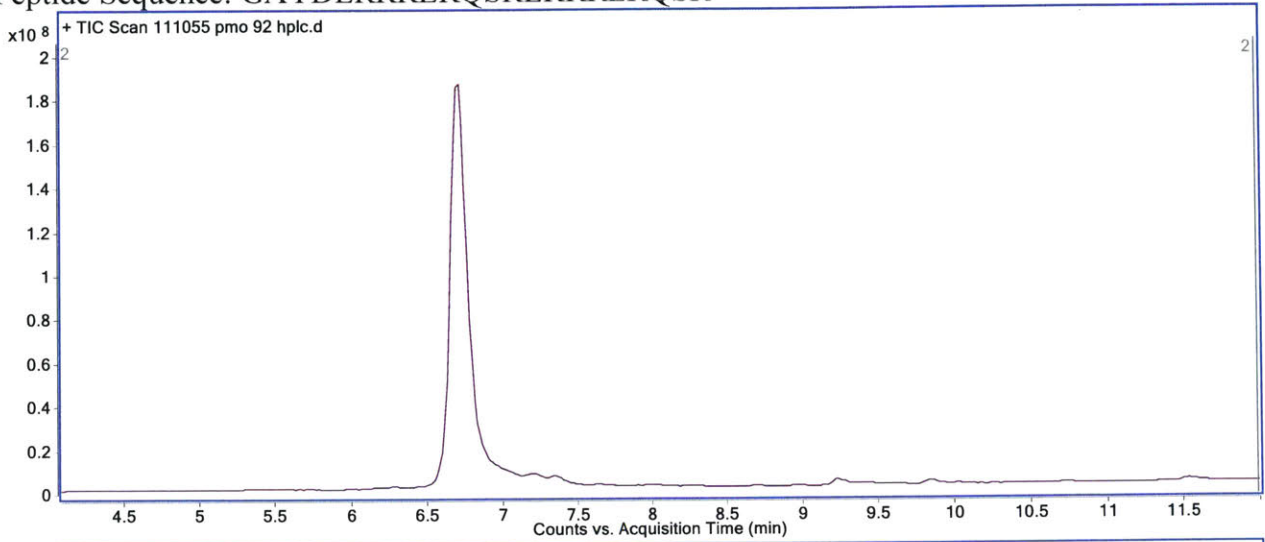
PMO-DPV15b

Mass expected: 9317.7g/mol

Mass observed: 9318.8 g/mol

Amount: 7.7 mg (87%)

Peptide Sequence: GAYDLRRRERQSRLRRRERQSR



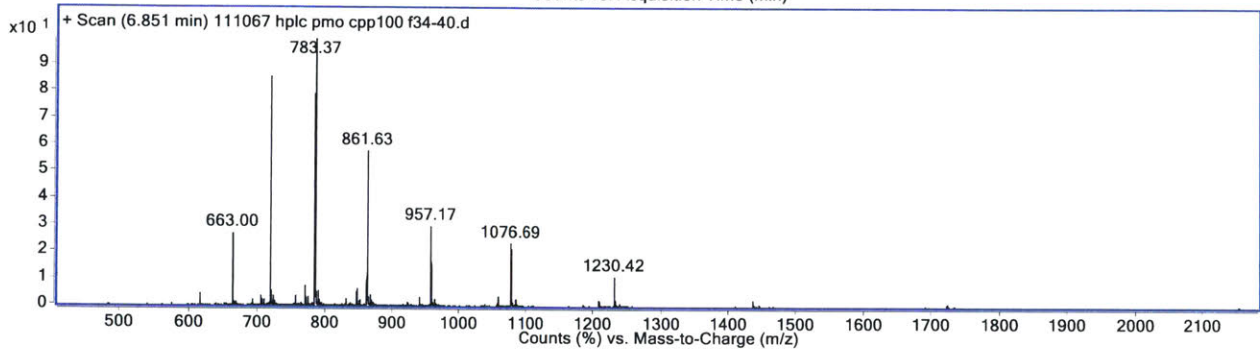
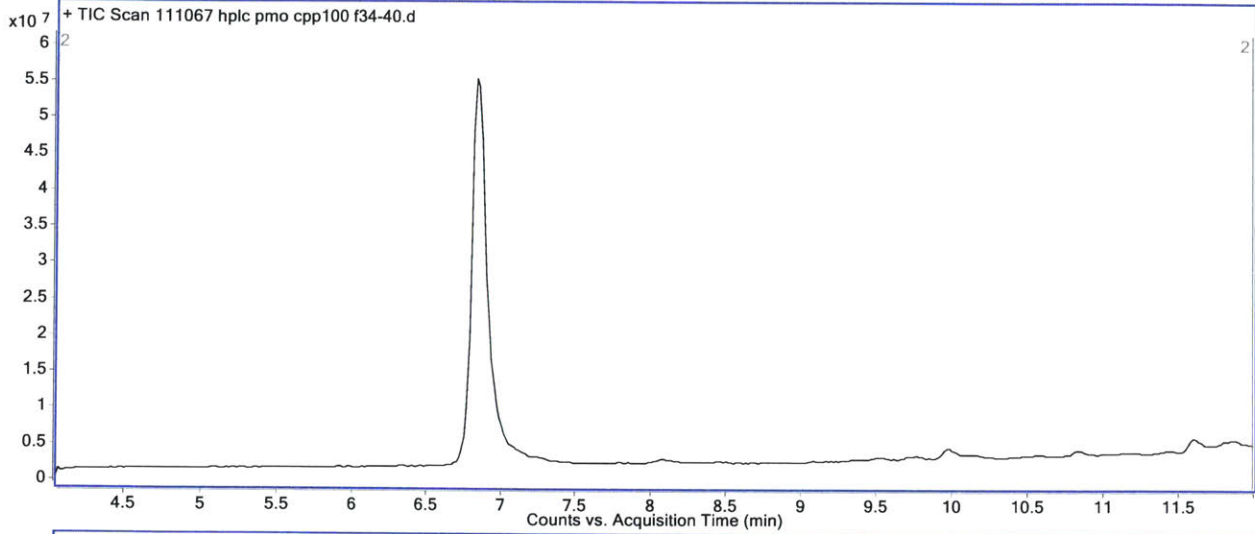
PMO-Yeast PrP6

Mass expected: 8526.9 g/mol

Mass observed: 8527.6 g/mol

Amount: 6.8 mg (84%)

Peptide Sequence: TRRNKRNRIQEQLNRK



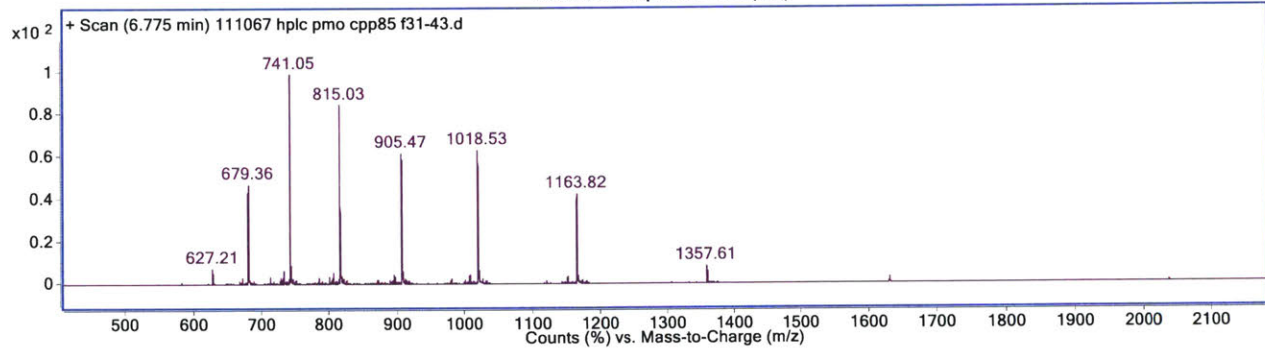
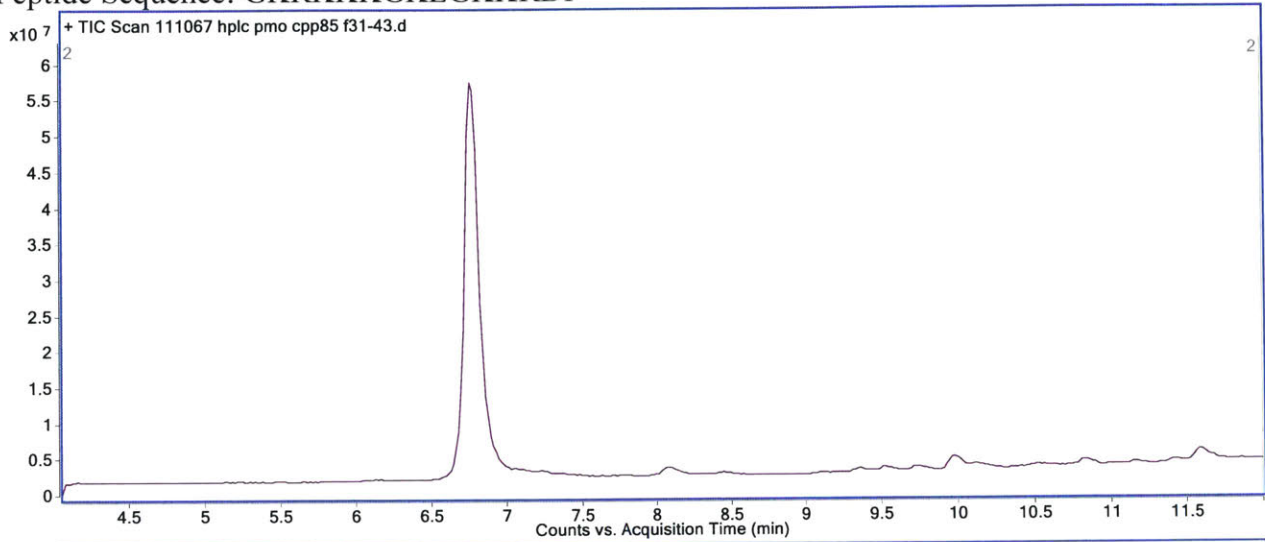
PMO-DPV7

Mass expected: 8140.6 g/mol

Mass observed: 8141.0 g/mol

Amount: 6.1 mg (79%)

Peptide Sequence: GKRKKKGKLGKKRDP





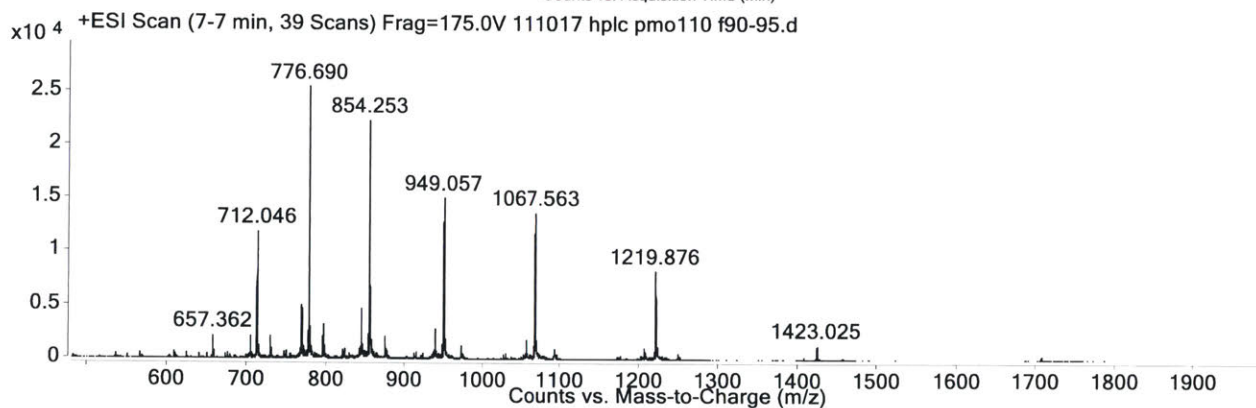
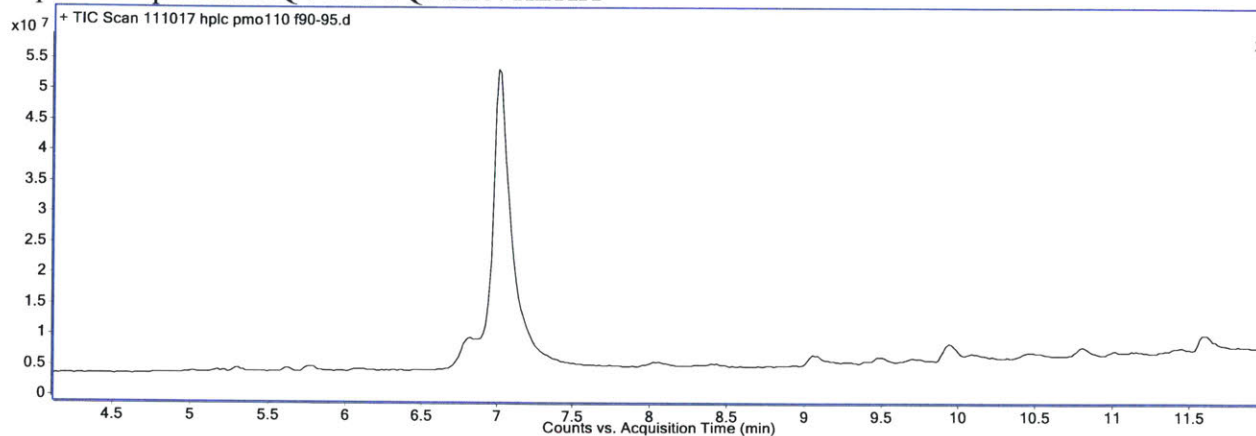
PMO-HoxA-13

Mass expected: 8533.1 g/mol

Mass observed: 8533.0 g/mol

Amount: 3.6 mg (44%)

Peptide Sequence: RQVTIWFQNRRRVKEKK



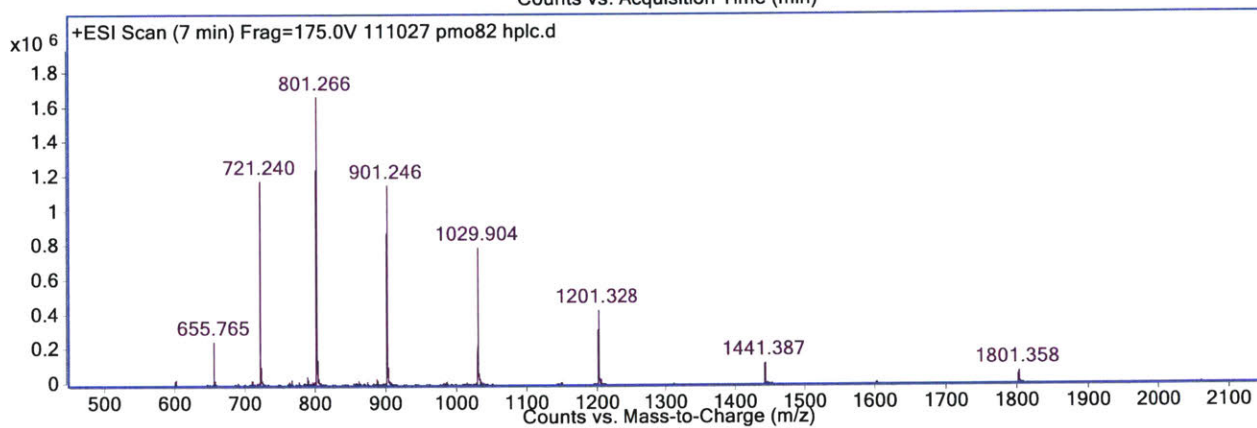
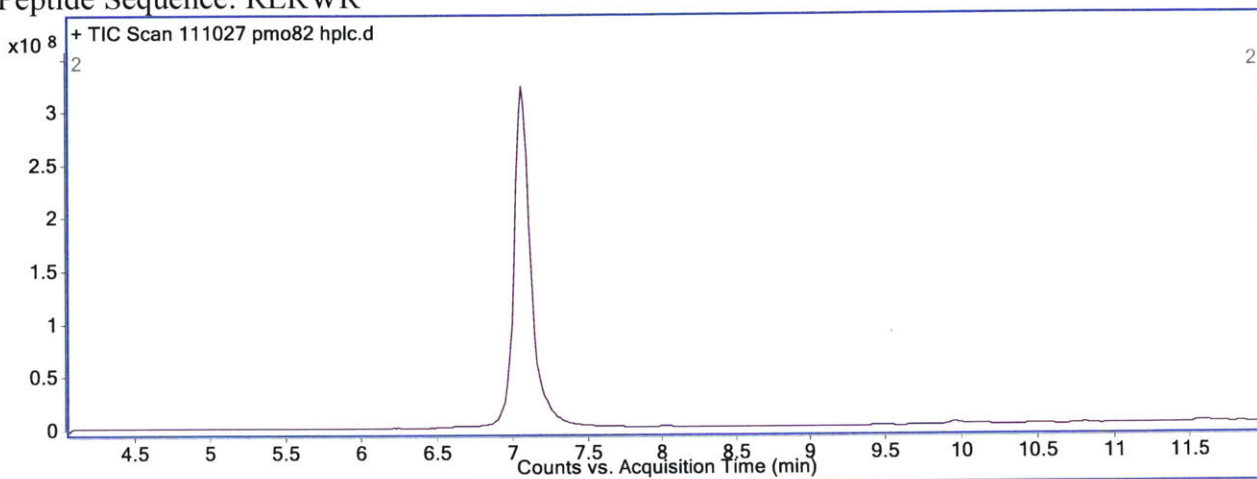
PMO-AIP6

Mass expected: 7202.5 g/mol

Mass observed: 7203.0 g/mol

Amount: 5.3 mg (77%)

Peptide Sequence: RLRWR



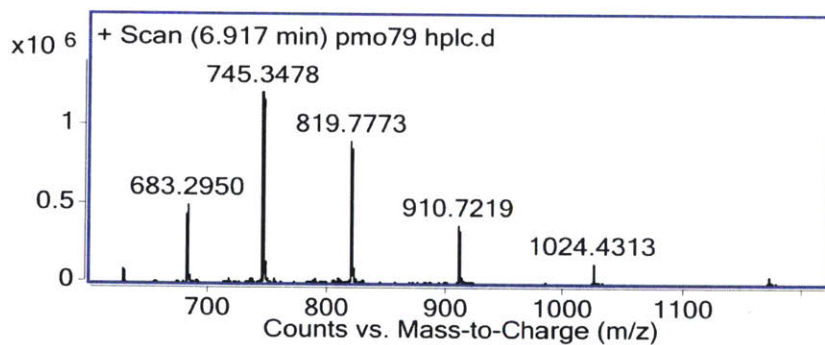
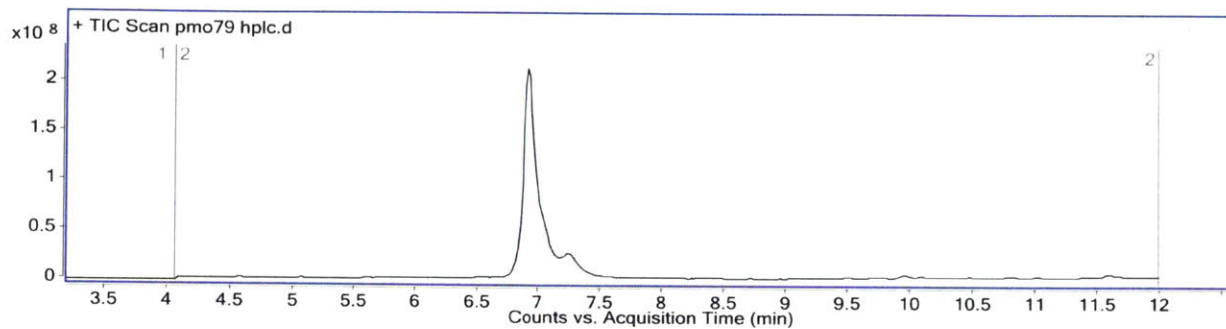
PMO-(PPR)<sub>5</sub>

Mass Expected: 8186.7

Mass Observed: 8188.2

Amount: 6.8 mg (87%)

Peptide Sequence: PPRPPRPPRPPRPPR



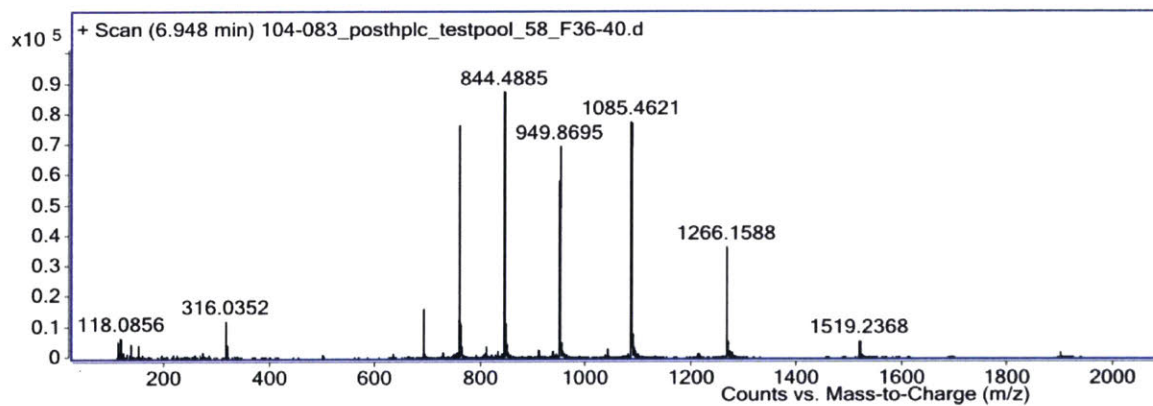
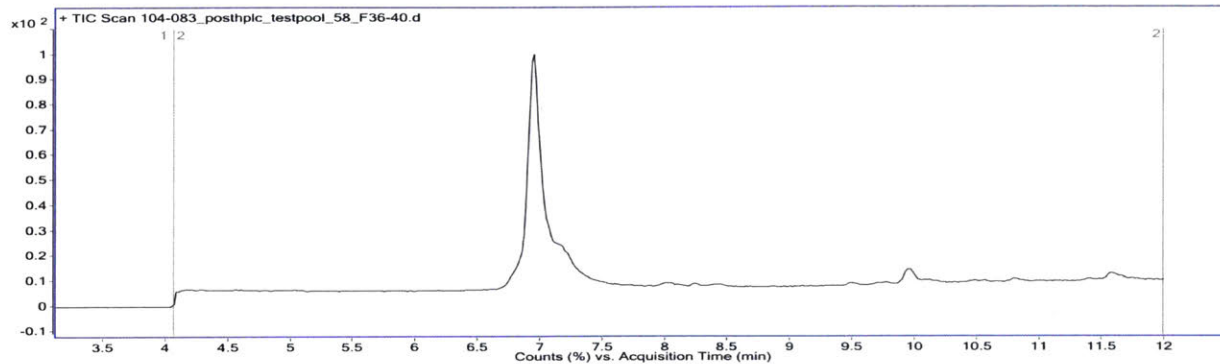
PMO-CAYH

Mass Expected: 7591.9

Mass Observed: 7592.0

Amount: 4.9 mg (68%)

Peptide Sequence: CAYHRLRRC (oxidized disulfide)



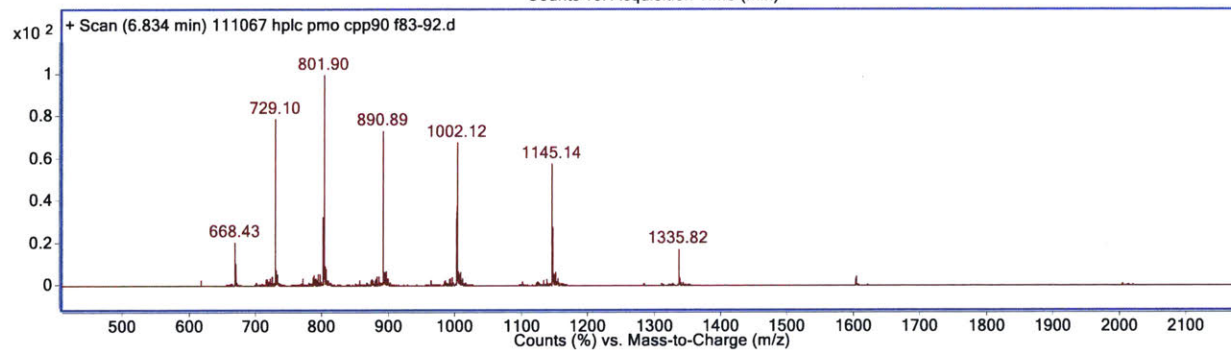
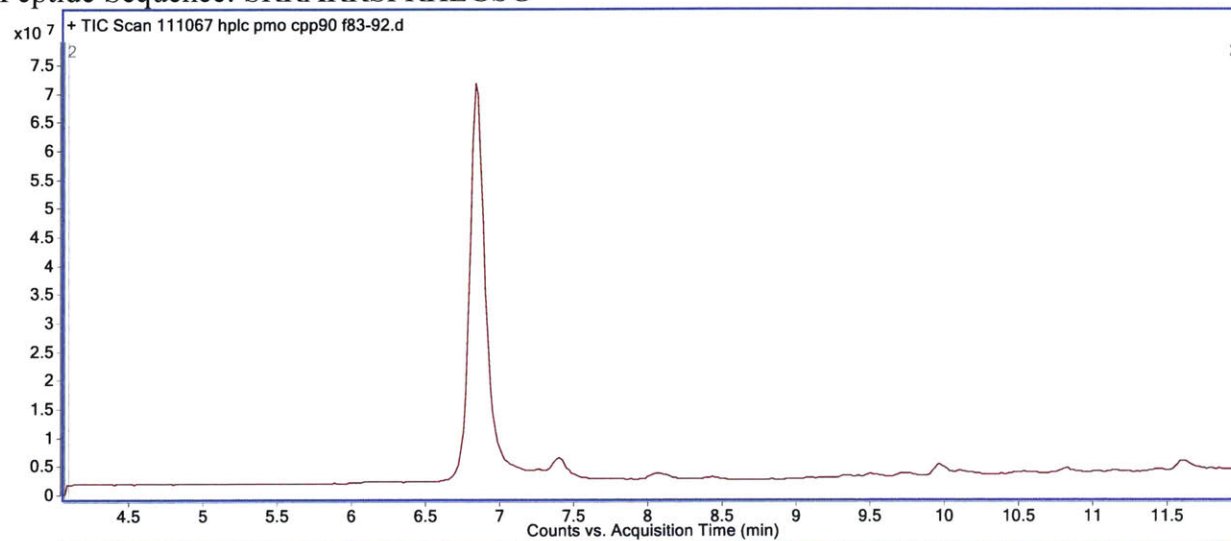
PMO-DPV10

Mass expected: 8009.3 g/mol

Mass observed: 8009.7 g/mol

Amount: 7.5 mg (99%)

Peptide Sequence: SRRARRSPRHLGSG



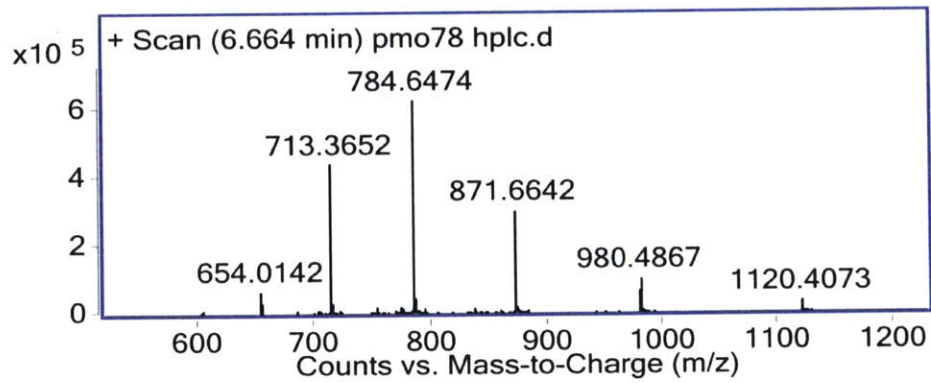
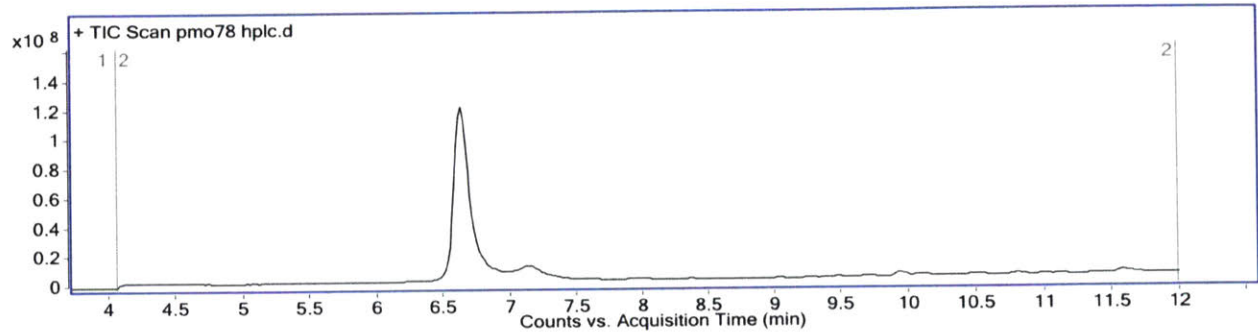
PMO-(PPR)<sub>4</sub>

Mass Expected: 7836.3

Mass Observed: 7836.8

Amount: 6.0 mg (81%)

Peptide Sequence: PPRPPRPPRPPR



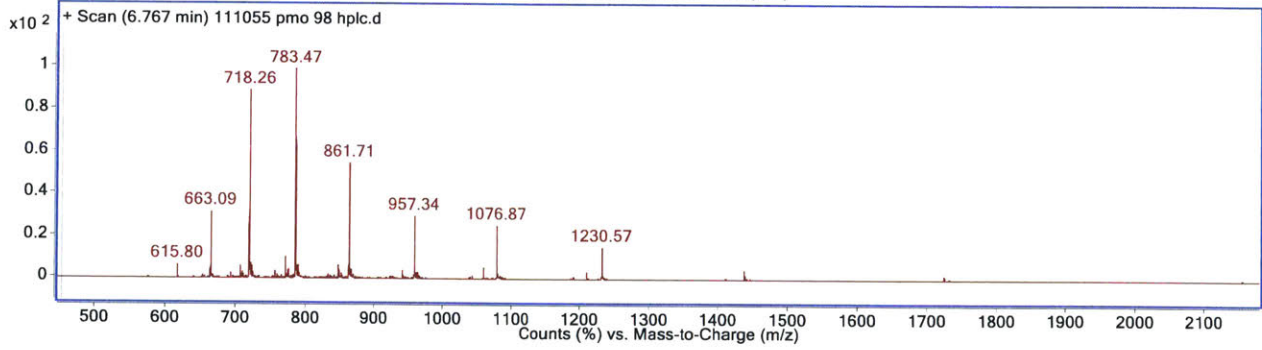
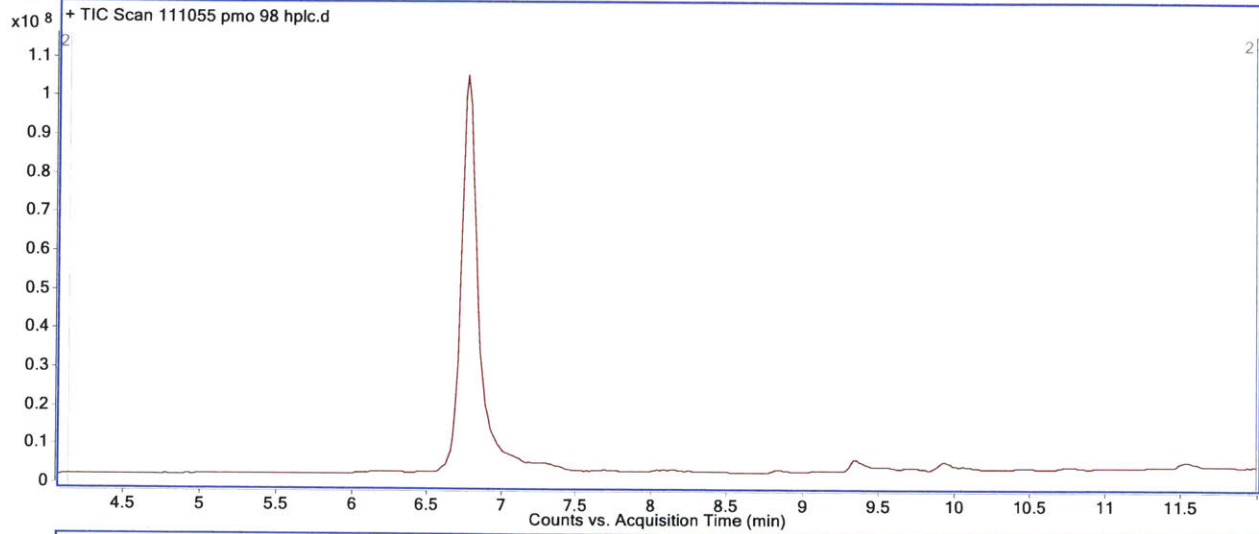
PMO-P22 N

Mass expected: 8607.0 g/mol

Mass observed: 8607.7 g/mol

Amount: 3.8 mg (87%)

Peptide Sequence: NAKTRRHERRRKLAIER



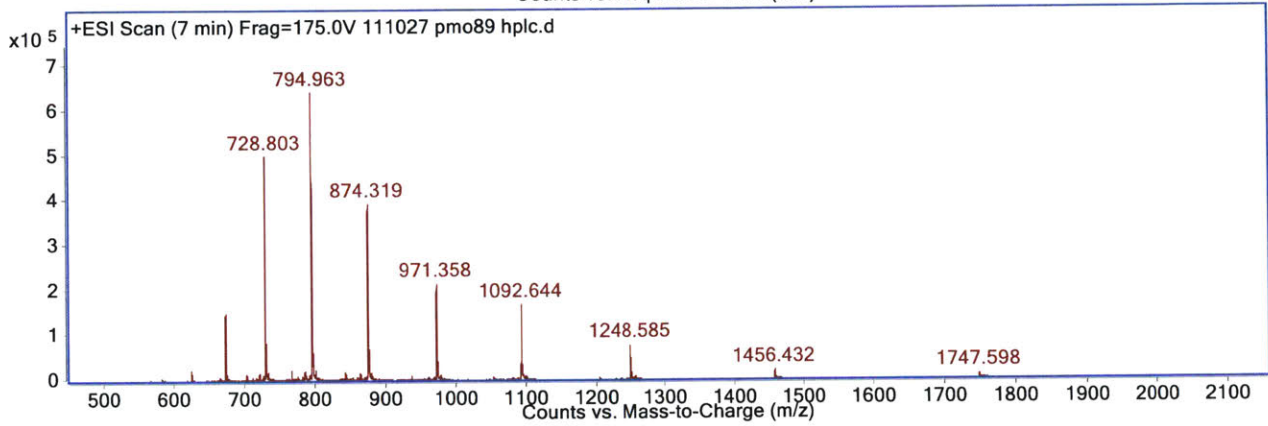
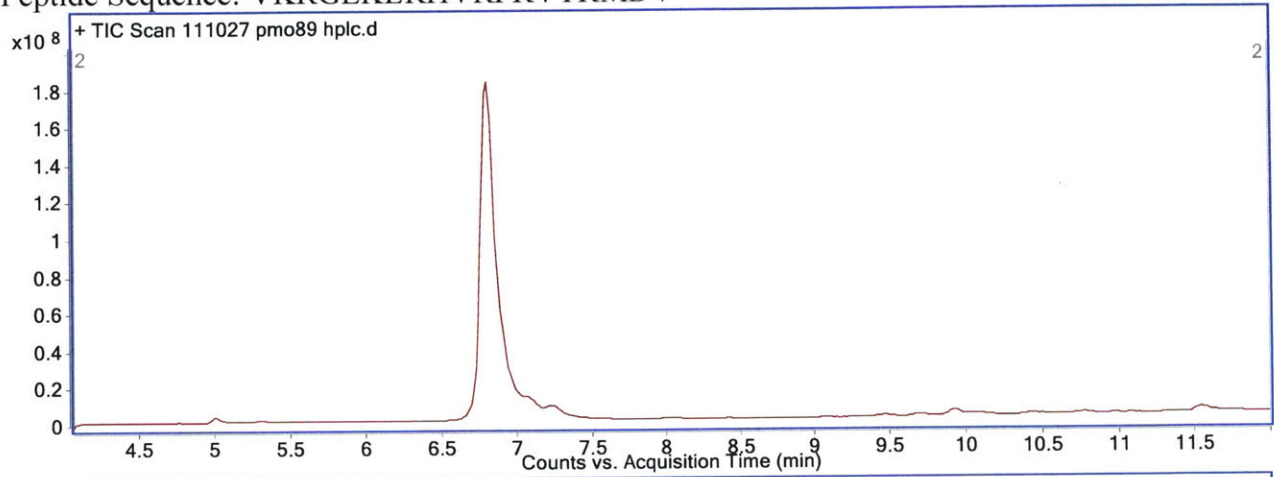
PMO-DPV1047

Mass expected: 8733.4 g/mol

Mass observed: 8733.8 g/mol

Amount: 8.1 mg (98%)

Peptide Sequence: VKRGLKLRHVRPRVTRMDV





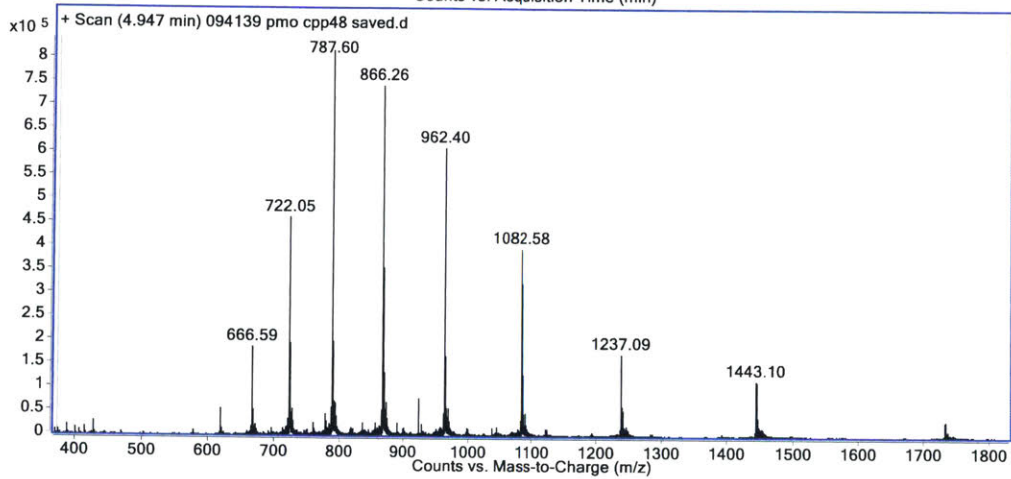
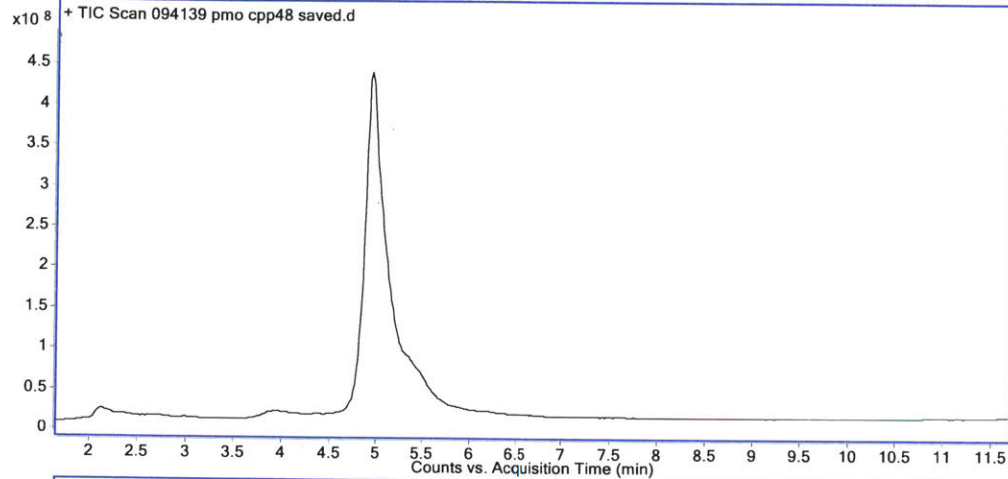
PMO-SVM4

Mass expected: 8653.2 g/mol

Mass observed: 8653.6 g/mol

Amount: 4.5 mg (55%)\*

Peptide Sequence: LYKKG PAKKG RPPLR GWFH



Note: LC-MS Method C

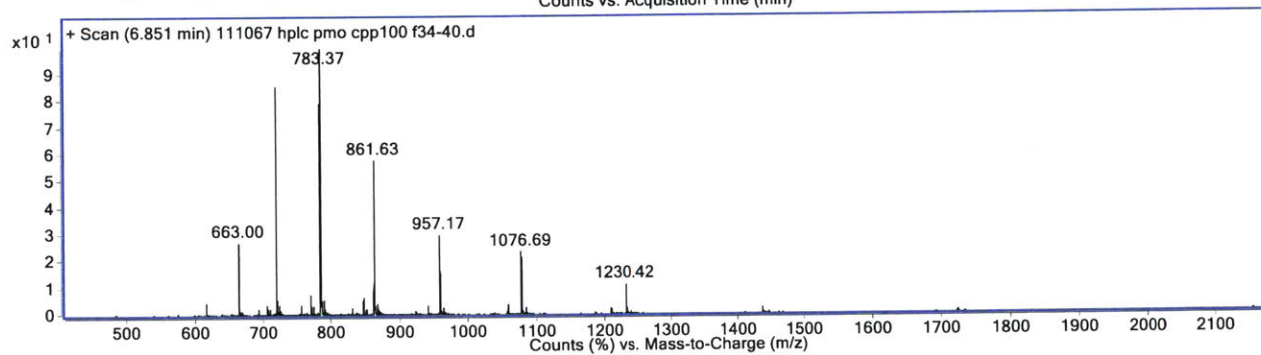
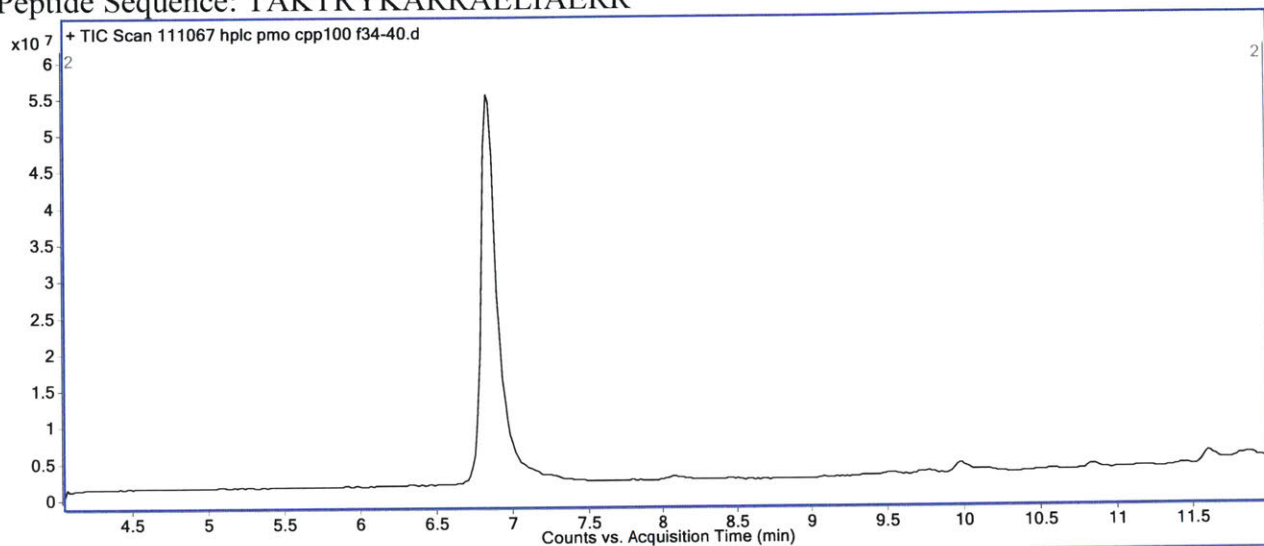
PMO-φ21N(12-29)

Mass expected: 8606.0 g/mol

Mass observed: 8606.7 g/mol

Amount: 5.0 mg (61%)

Peptide Sequence: TAKTRYKARRAELIAERR



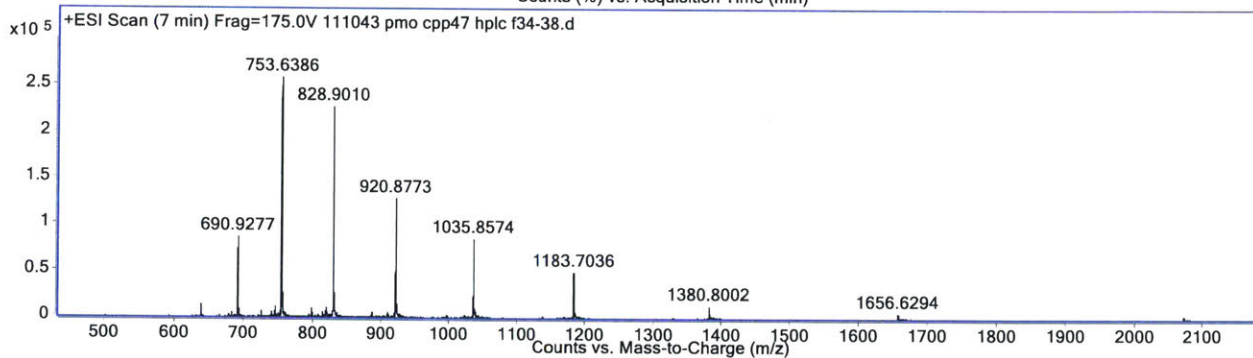
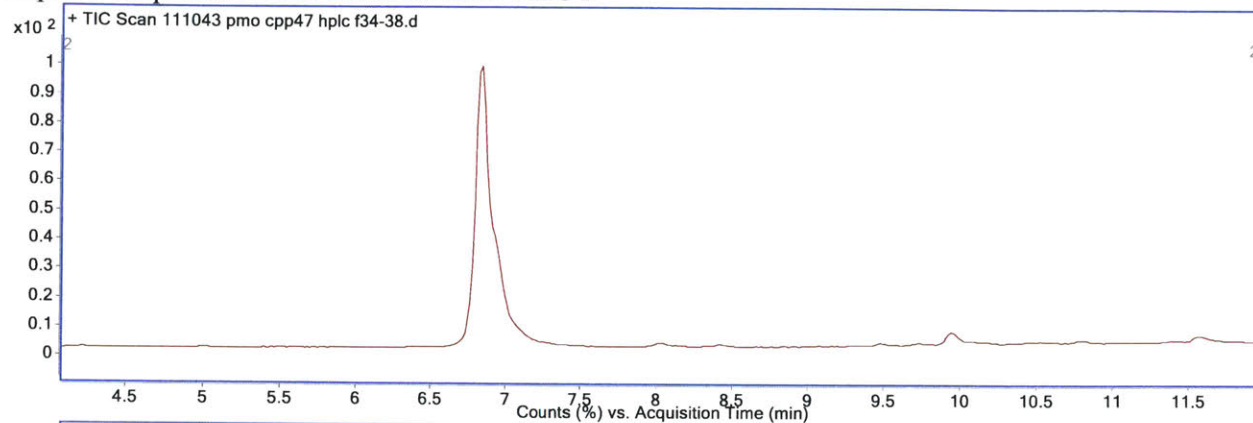
PMO-SVM3

Mass expected: 8278.9 g/mol

Mass observed: 8279.4 g/mol

Amount: 3.5 mg (45%)

Peptide Sequence: KGTYKKKLMRIPLKGT



PMO-PPR3

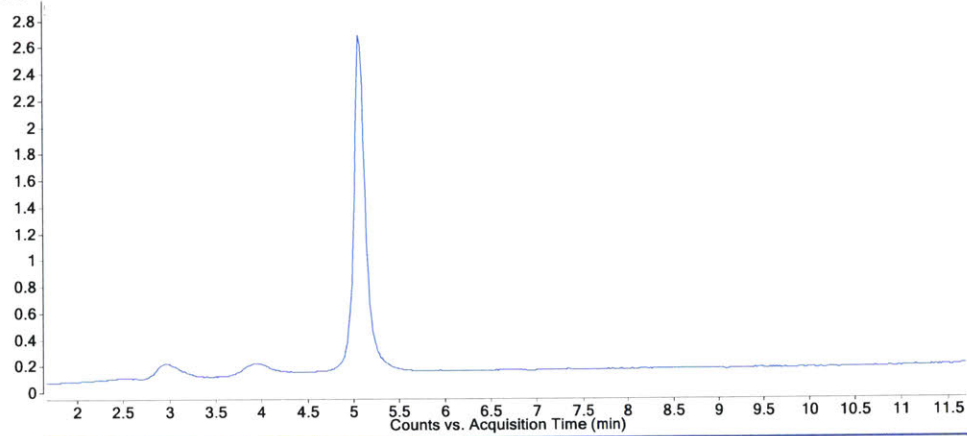
Mass expected: 7485.9 g/mol

Mass observed: 7486.2 g/mol

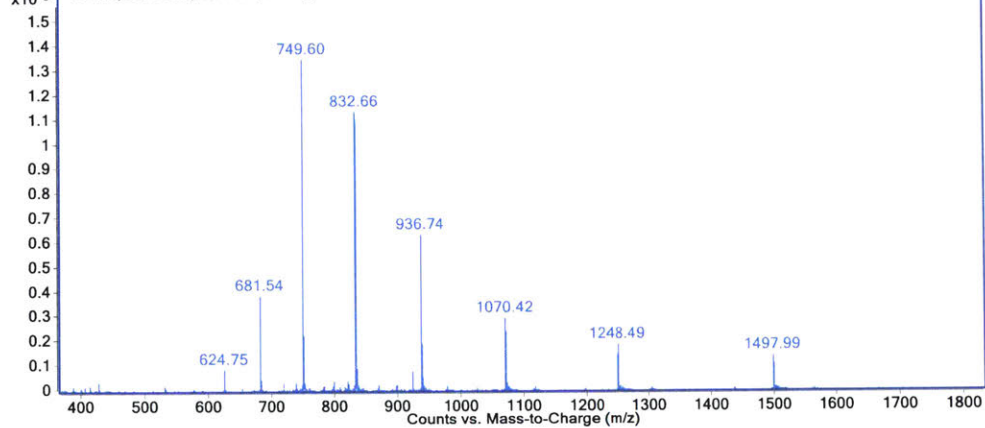
Amount: 2.8 mg (39%)\*

Peptide Sequence: PPRPPRPPR

x10<sup>8</sup> + TIC Scan 094139 pmo cpp77 saved.d



x10<sup>6</sup> + Scan (5.073 min) 094139 pmo cpp77 saved.d



Note: LC-MS Method C

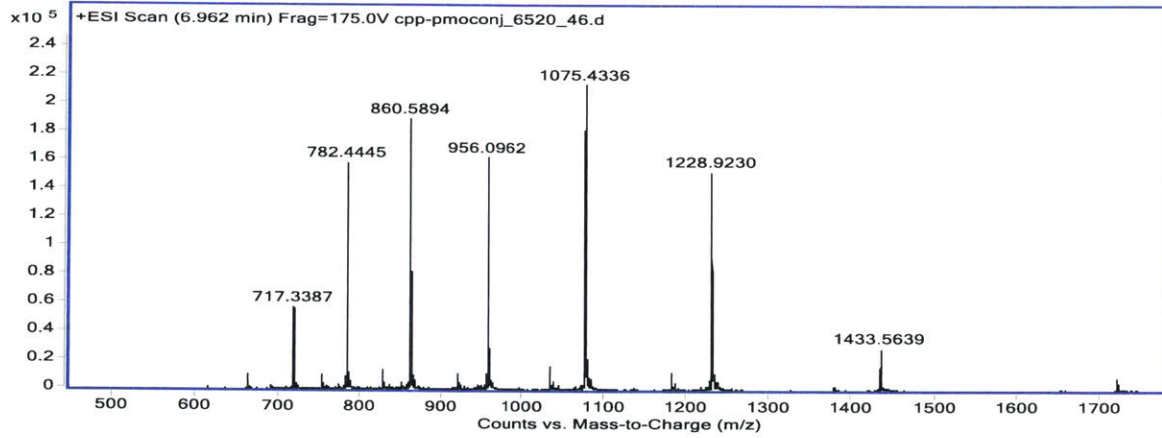
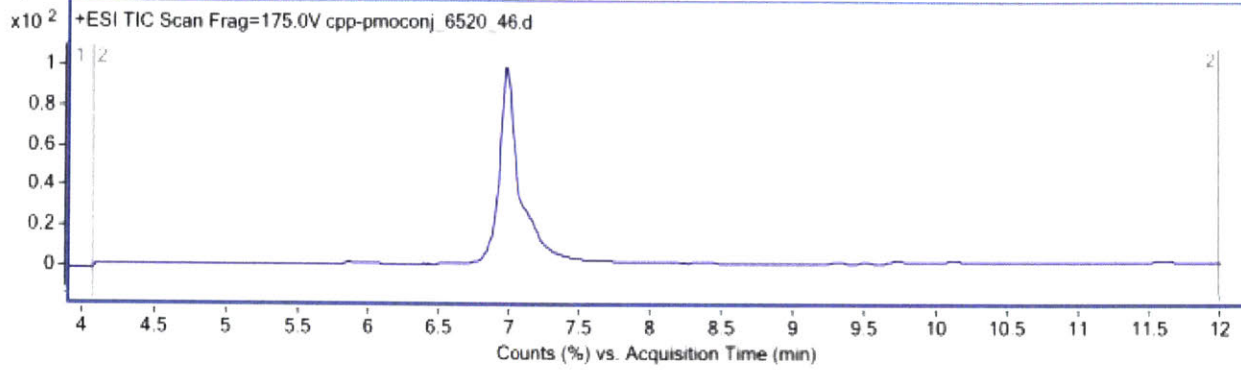
PMO-SVM2

Mass expected: 8596.1 g/mol

Mass observed: 8596.5 g/mol

Amount: 4.8 mg (59%)

Peptide Sequence: RASKRDGSWVKKLHRILE



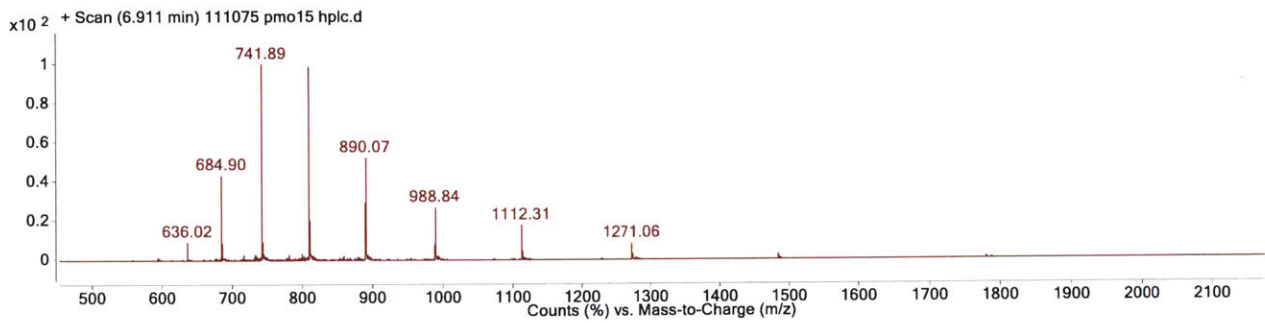
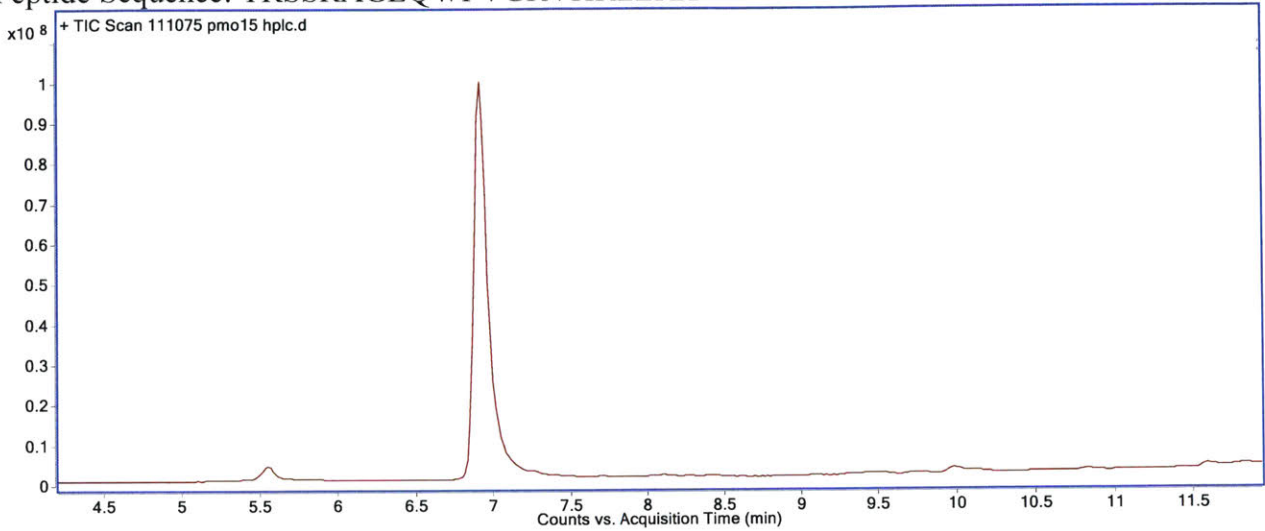
PMO-Buforin 2

Mass expected: 8890.5 g/mol

Mass observed: 8891.1 g/mol

Amount: 7.6 mg (90%)

Peptide Sequence: TRSSRAGLQWPVGRVHRLLRK



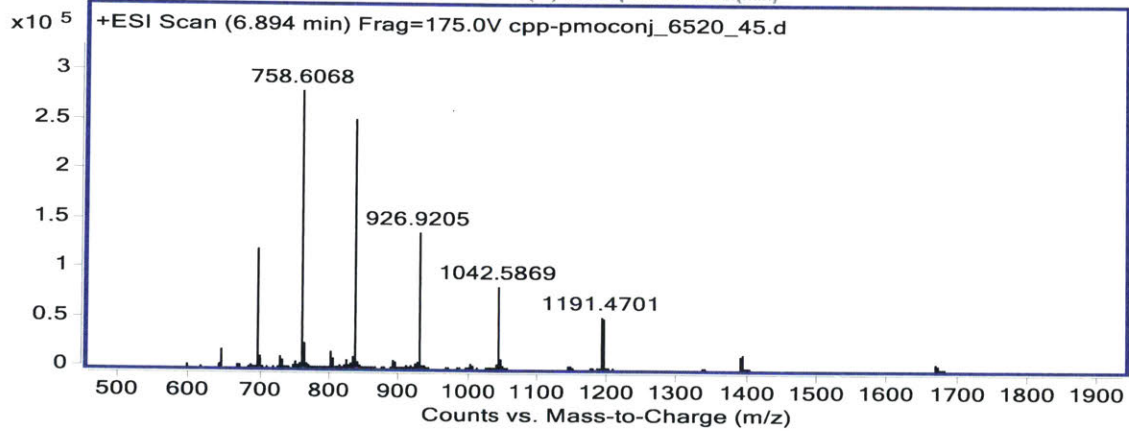
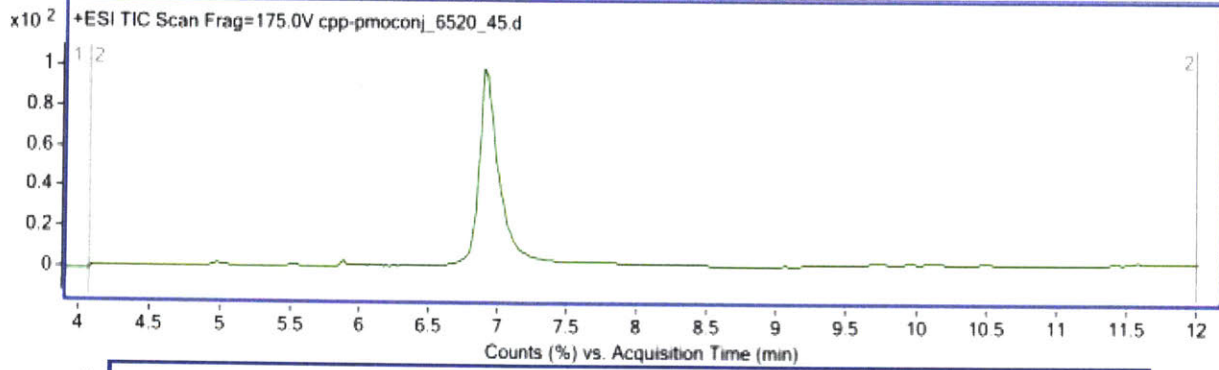
PMO-SVM1

Mass expected: 8333.8 g/mol

Mass observed: 8329.3 g/mol

Amount: 4.4 mg (56%)

Peptide Sequence: FKIIYDKKVRTRVVKH



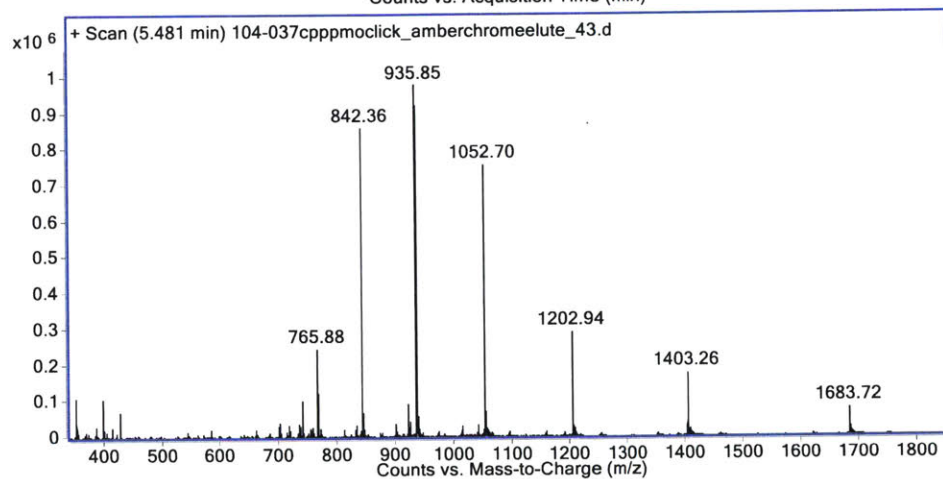
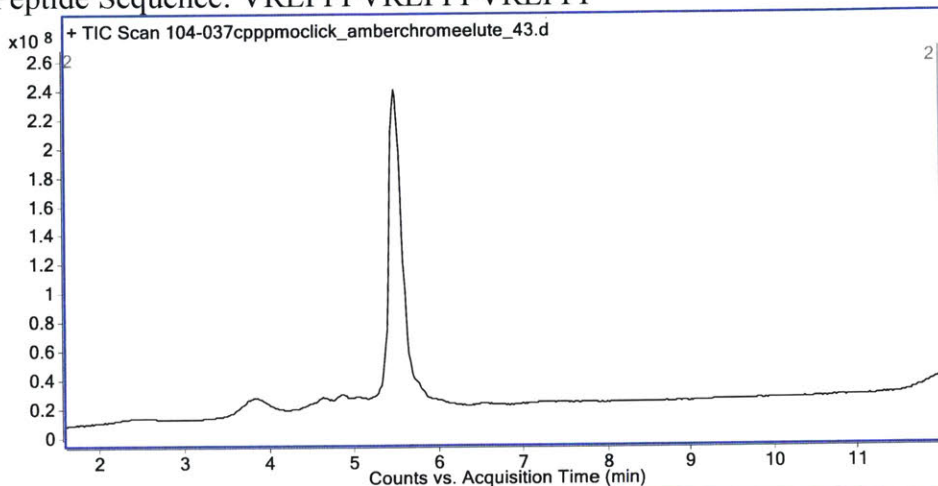
PMO-SAP

Mass expected: 8414.0 g/mol

Mass observed: 8414.6 g/mol

Amount: 7 mg (88%)\*

Peptide Sequence: VRLPPPVRLPPPVRLPPP



Note: LC-MS Method C



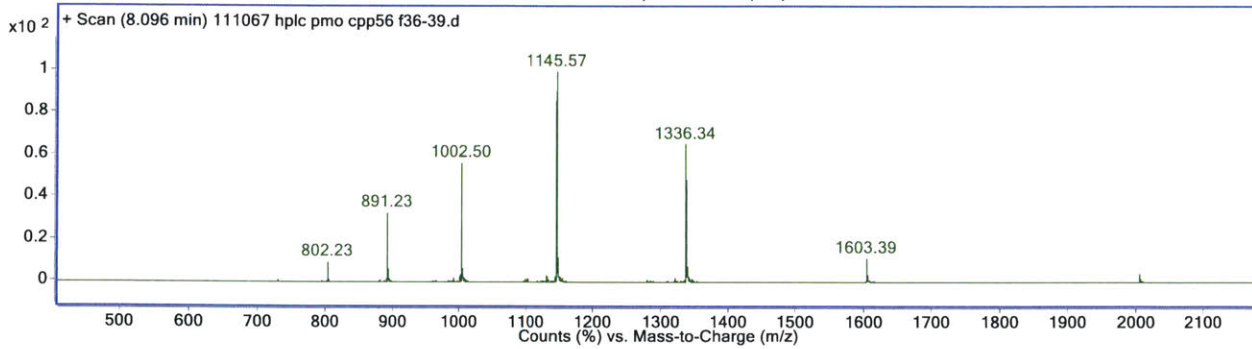
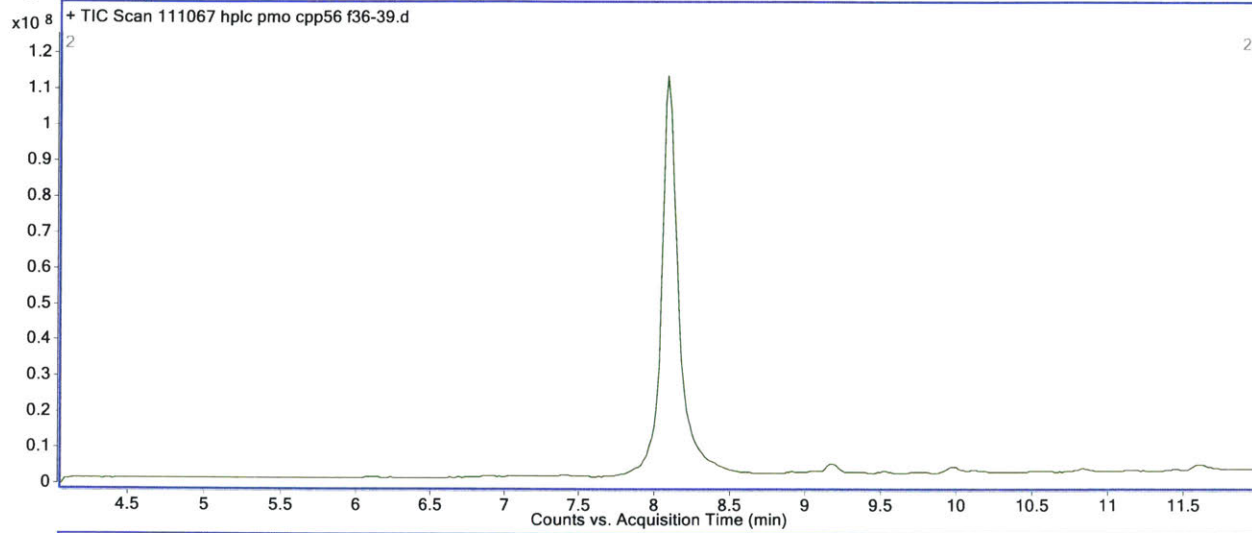
PMO-435b

Mass expected: 8012.4 g/mol

Mass observed: 8012.8 g/mol

Amount: 3.4 mg (45%)

Peptide Sequence: GPFHFYQFLFPPV



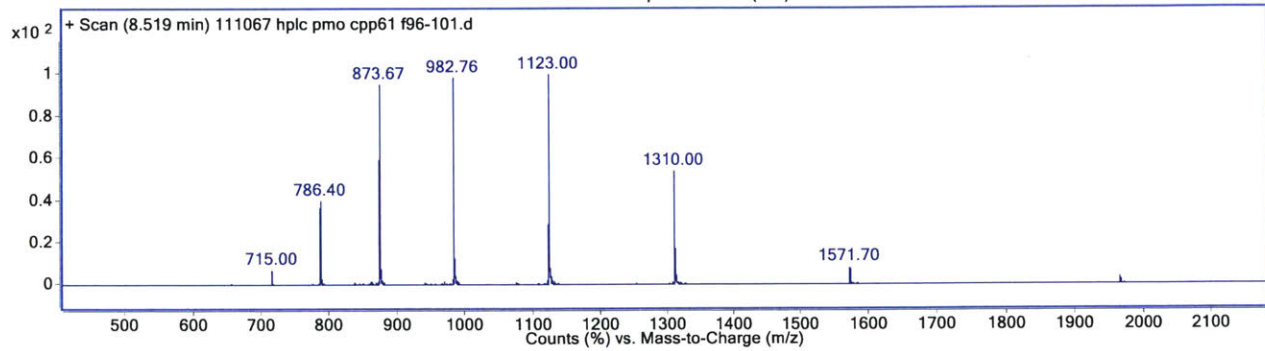
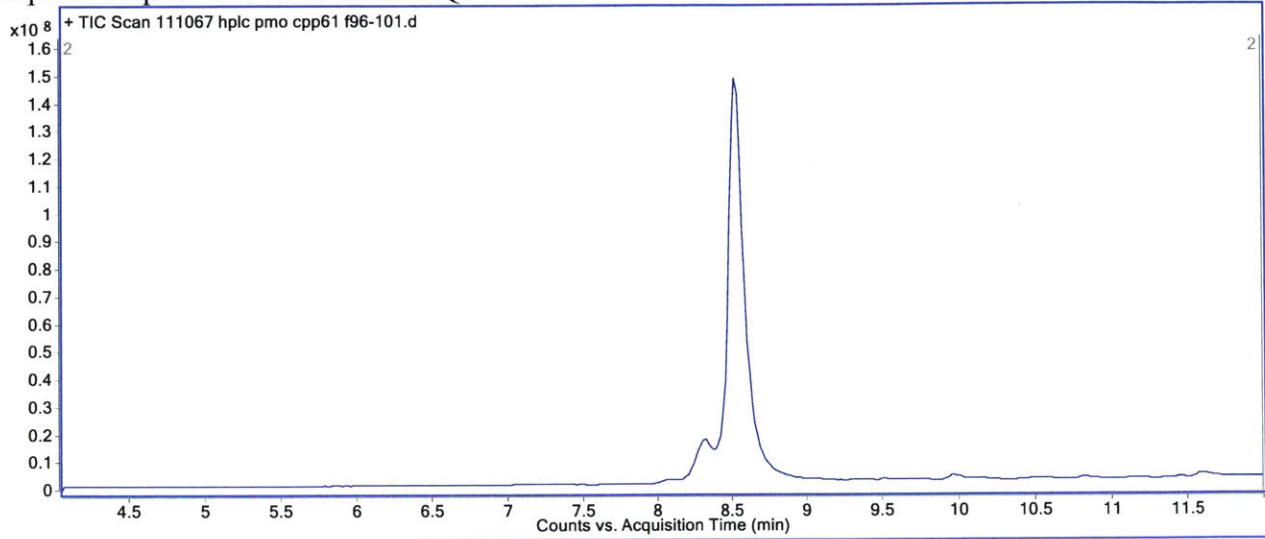
PMO-Pept1

Mass expected: 7855.3 g/mol

Mass observed: 7854.8 g/mol

Amount: 6.0 mg (80%)

Peptide Sequence: PLILLRLLRGQF



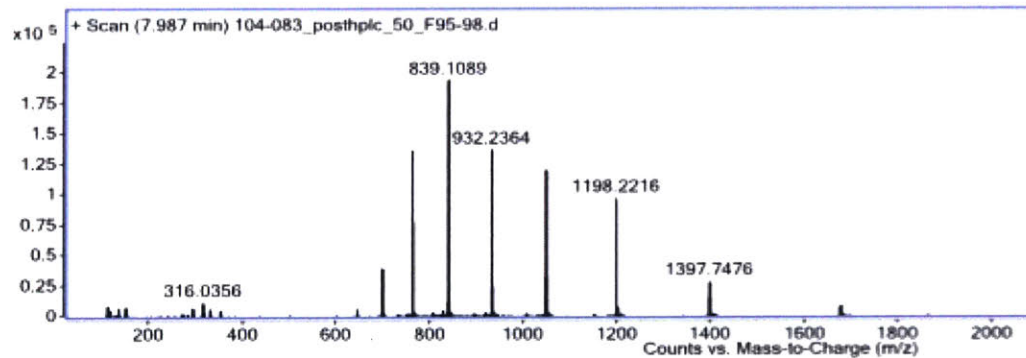
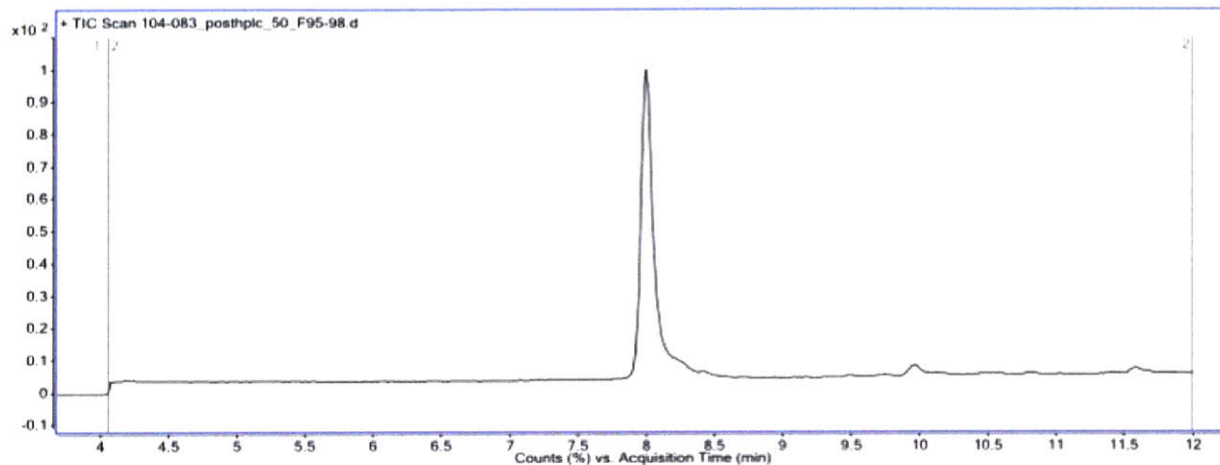
PMO-YTA2

Mass Expected: 8380.9

Mass Observed: 8381.6

Amount: 3 mg (38%)

Peptide Sequence: YTAIAWVKAFIRKLRK



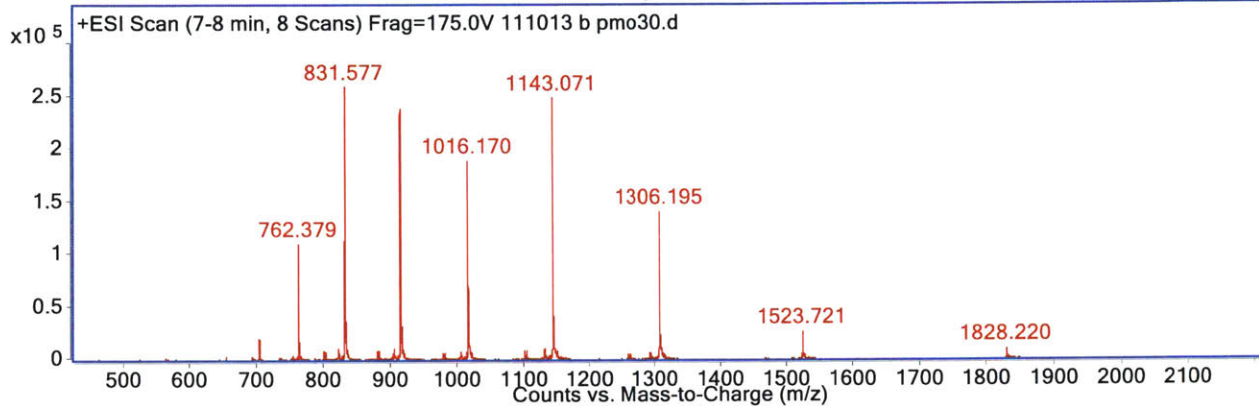
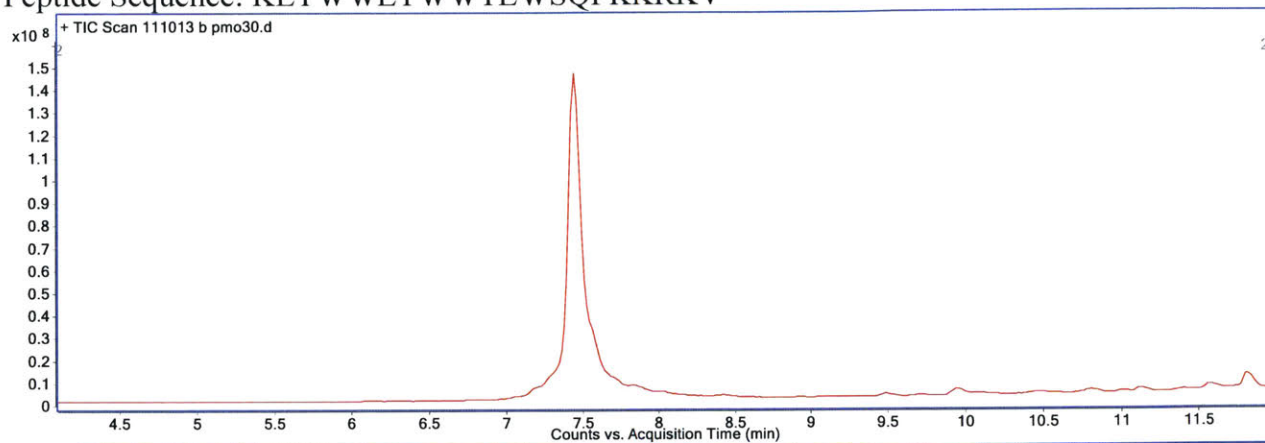
PMO-Pep-1

Mass expected: 9136.7 g/mol

Mass observed: 9136.8 g/mol

Amount: 3.6 mg (30%)\*

Peptide Sequence: KETWWETWWTEWSQP~~K~~RKRV



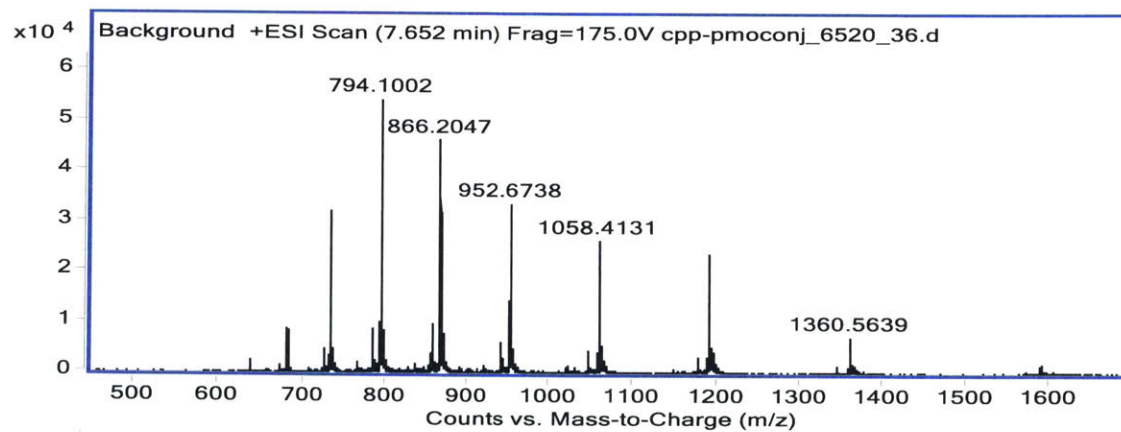
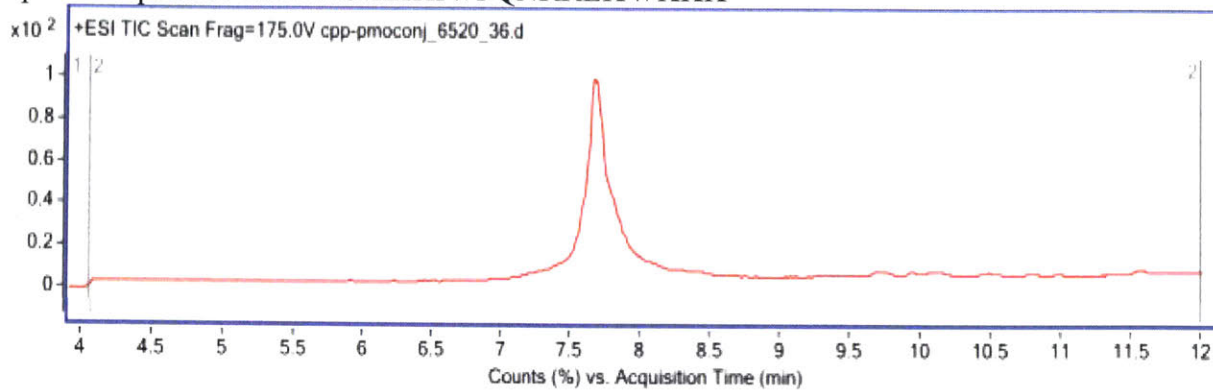
PMO-EB-1

Mass expected: 9517.4 g/mol

Mass observed: 9517.8 g/mol

Amount: 2.6 mg (29%)

Peptide Sequence: LIRLWSHLIHIWFQNRRLKWKKK



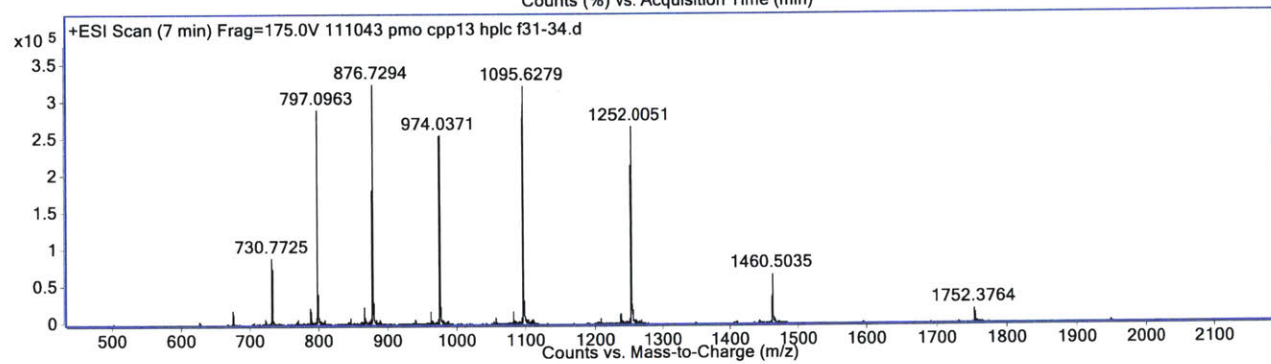
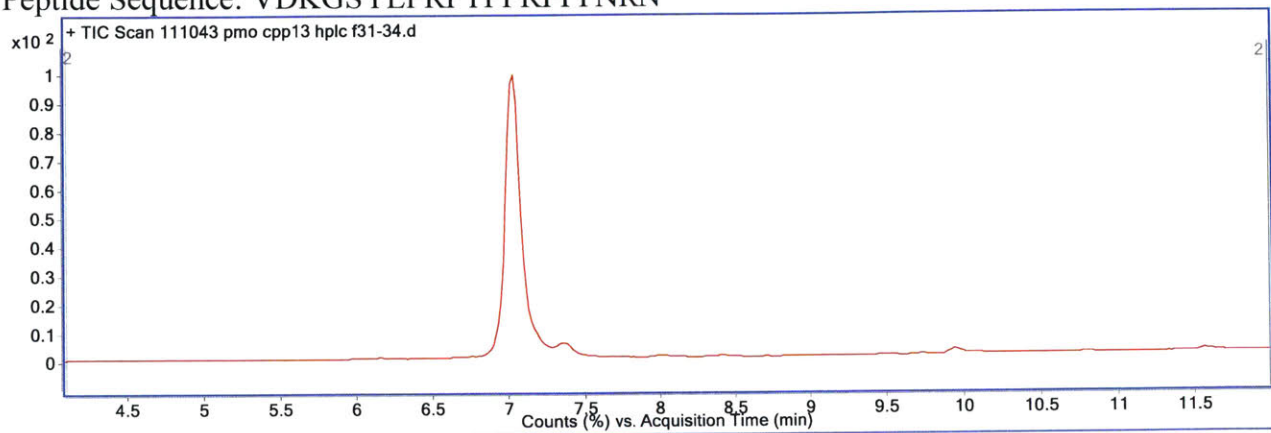
PMO-Pyrrhocoricin

Mass expected: 8757.3 g/mol

Mass observed: 8757.7 g/mol

Amount: 6.3 mg (76%)

Peptide Sequence: VDKGSYLPRPTPPRPIYNRN



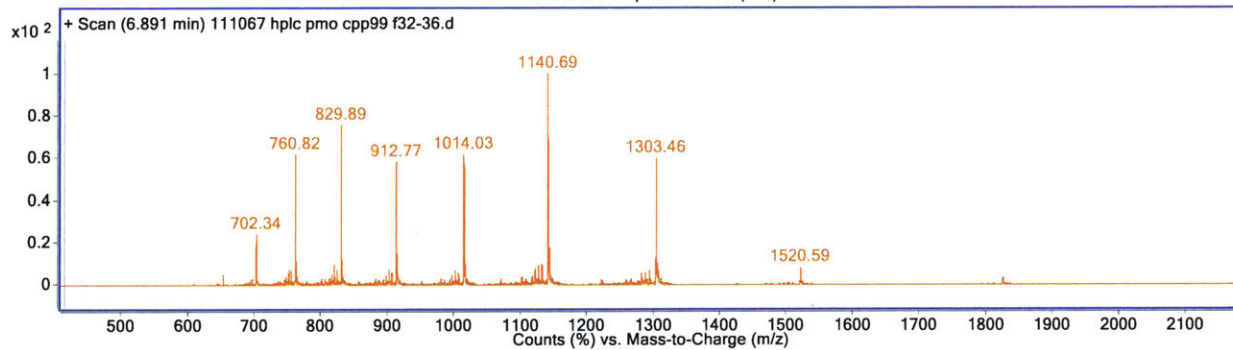
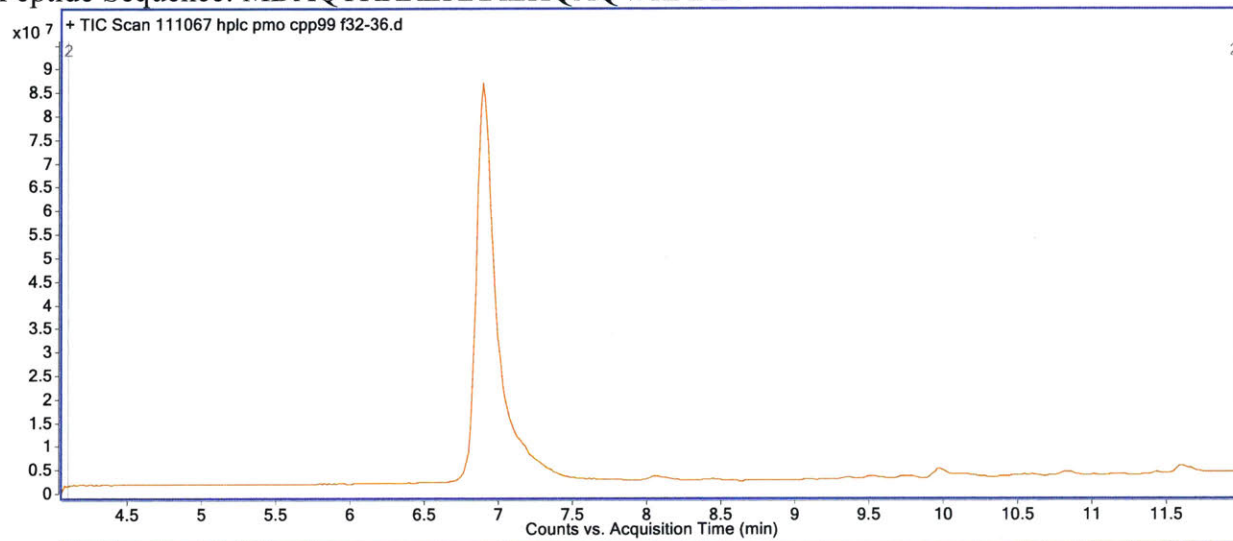
PMO-λN(1-22)

Mass expected: 9117.5 g/mol

Mass observed: 9117.9 g/mol

Amount: 4.9 mg (75%)

Peptide Sequence: MDAQTRRRERRAEKQAQWKAAN



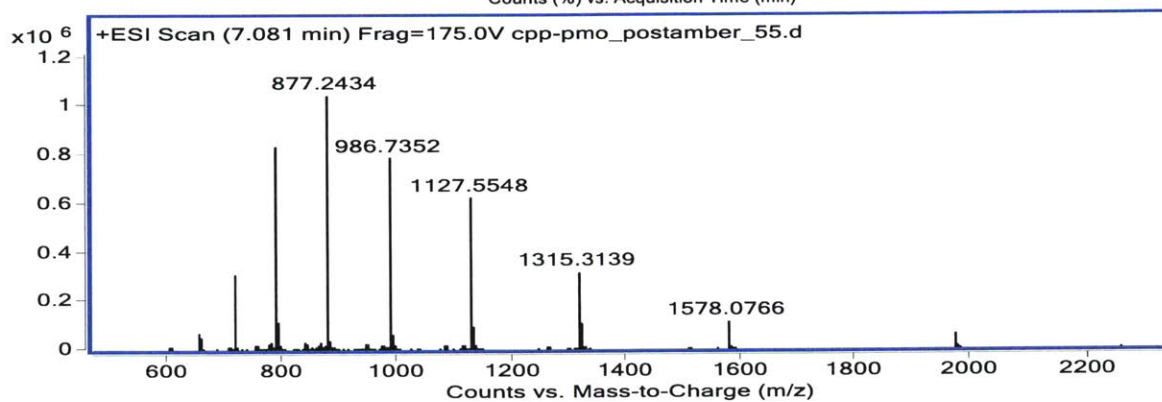
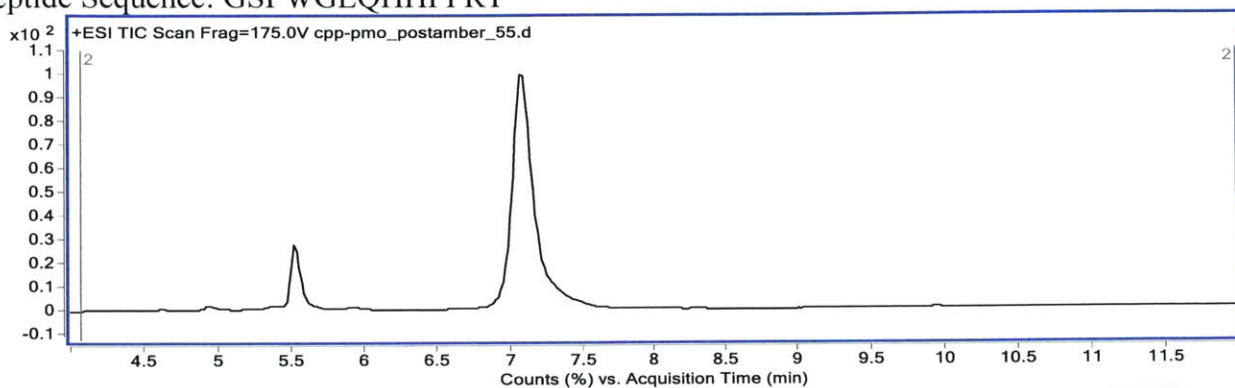
PMO-439a

Mass expected: 7886.1 g/mol

Mass observed: 7886.9 g/mol

Amount: 8.3 mg (111%)\*

Peptide Sequence: GSPWGLQHHPRT



\*Peak at 5.5 minutes is unreacted peptide



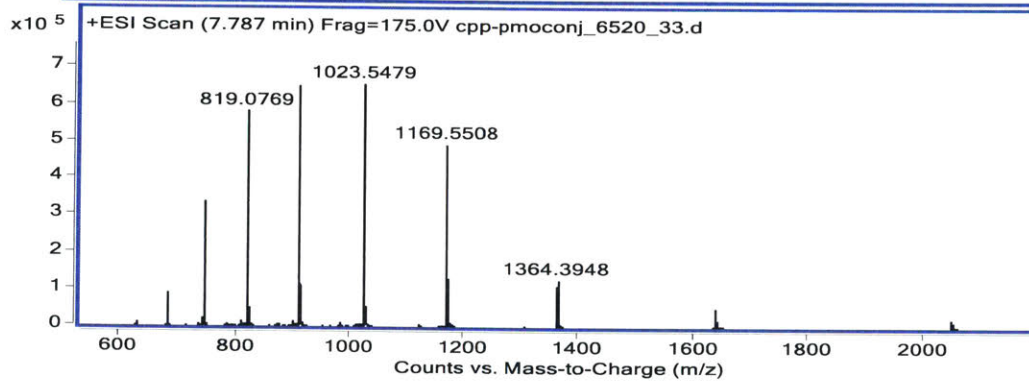
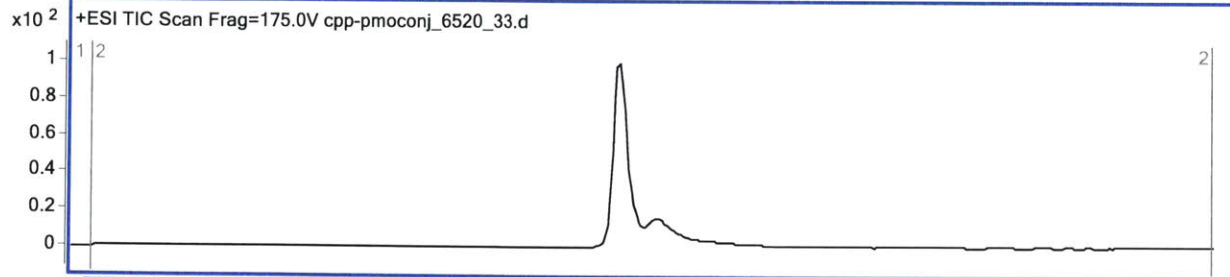
PMO-MAP

Mass expected: 8180.9 g/mol

Mass observed: 8181.6 g/mol

Amount: 3.6 mg (46%)

Peptide Sequence: KLALKALKALKAALKLA



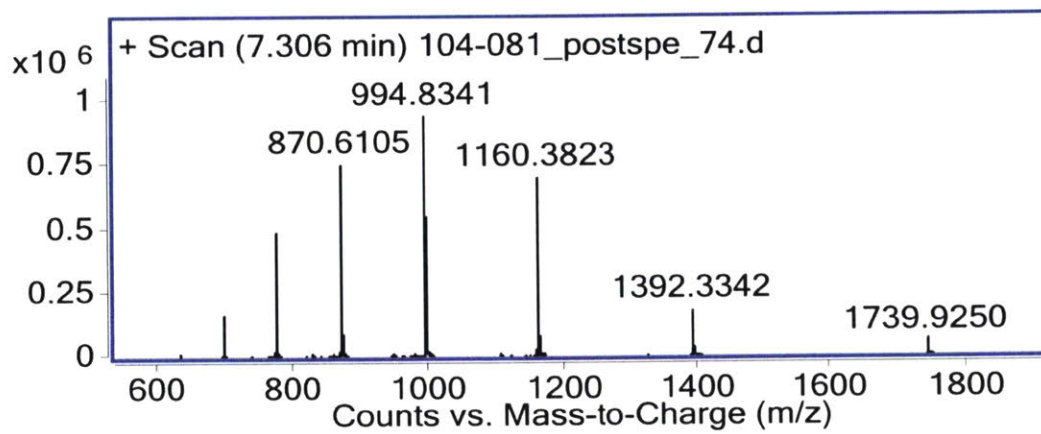
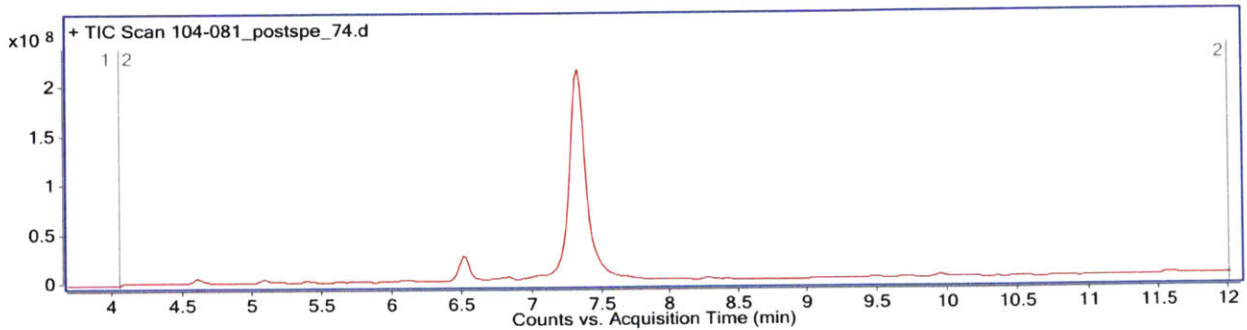
PMO-Bip

Mass Expected: 6957.3

Mass Observed: 6957.8

Amount: 5.5 mg (83%)\*

Peptide Sequence: IPALK



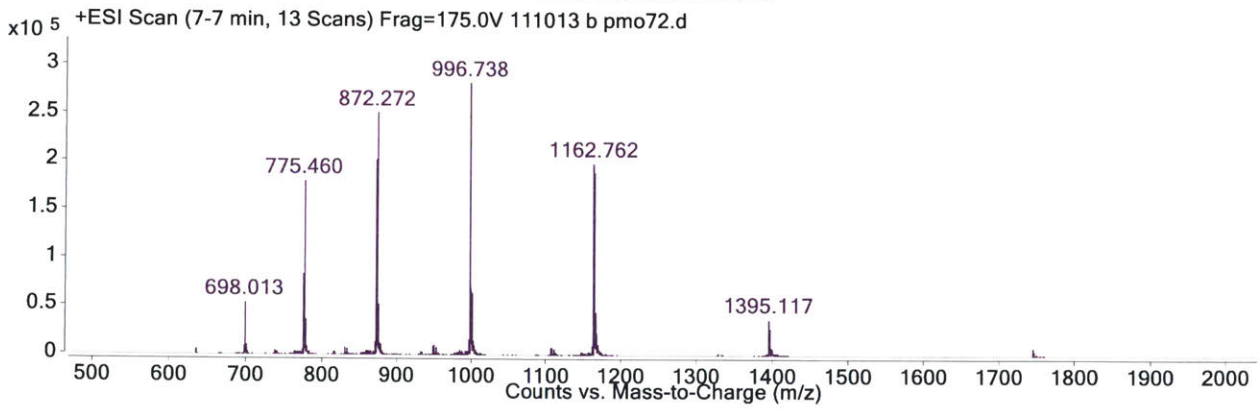
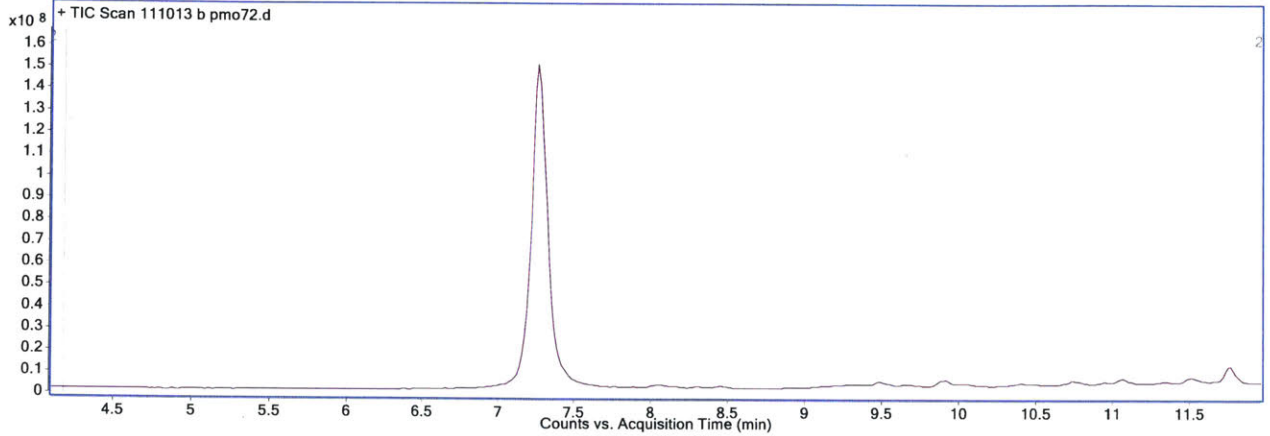
PMO-Bip

Mass expected: 6971.3 g/mol

Mass observed: 6971.6 g/mol

Amount: 2.5 mg (38%)\*

Peptide Sequence: VPALR



PMO-pVEC

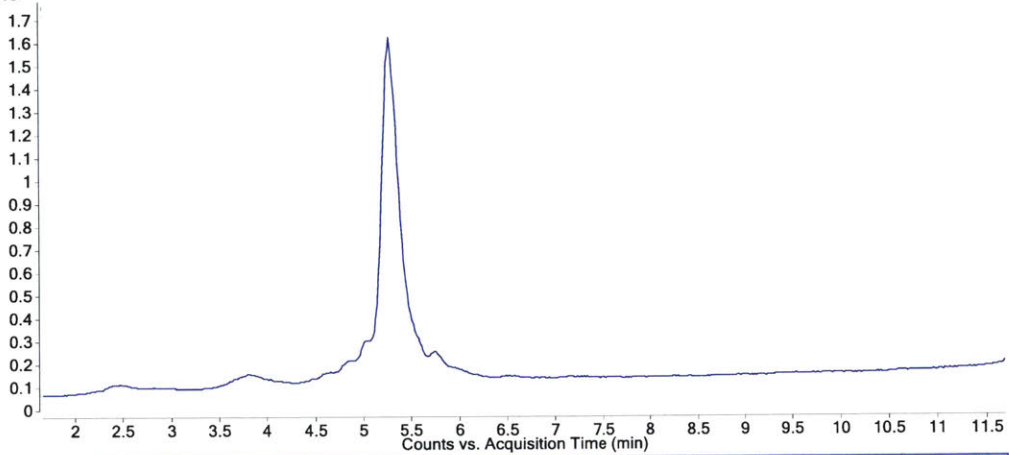
Mass expected: 8626.2 g/mol

Mass observed: 8624.9 g/mol

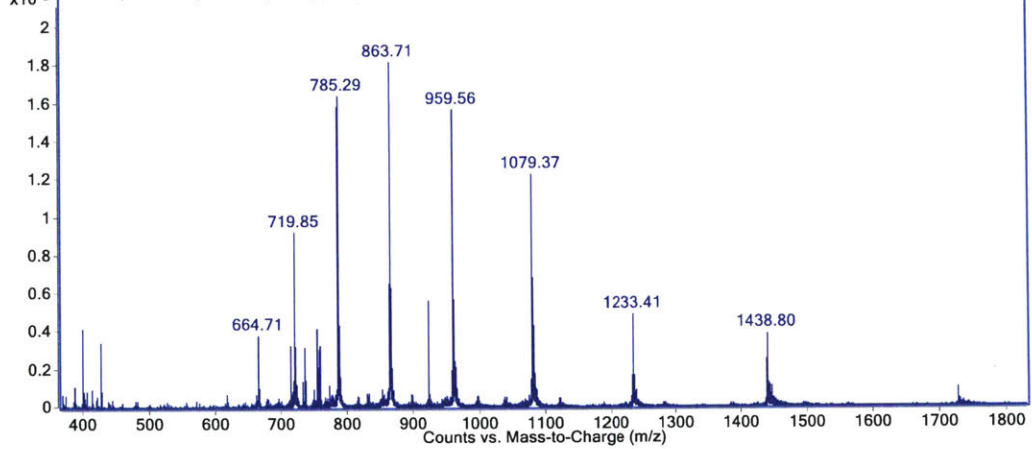
Amount: 1.3 mg (16%)\*

Peptide Sequence: LLILRRRIRKQAHHSK

x10<sup>8</sup> + TIC Scan 094183 pmo cpp66 powder more.d



x10<sup>5</sup> + Scan (5.251 min) 094183 pmo cpp66 powder more.d



Note: LC-MS Method C

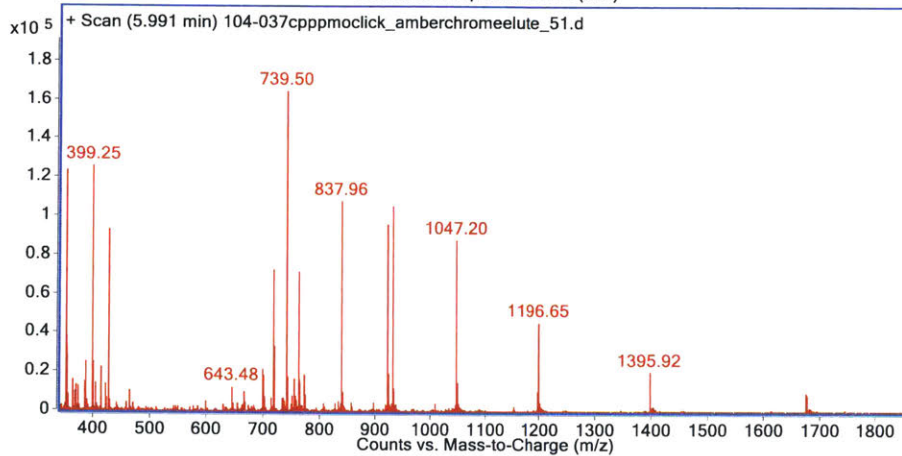
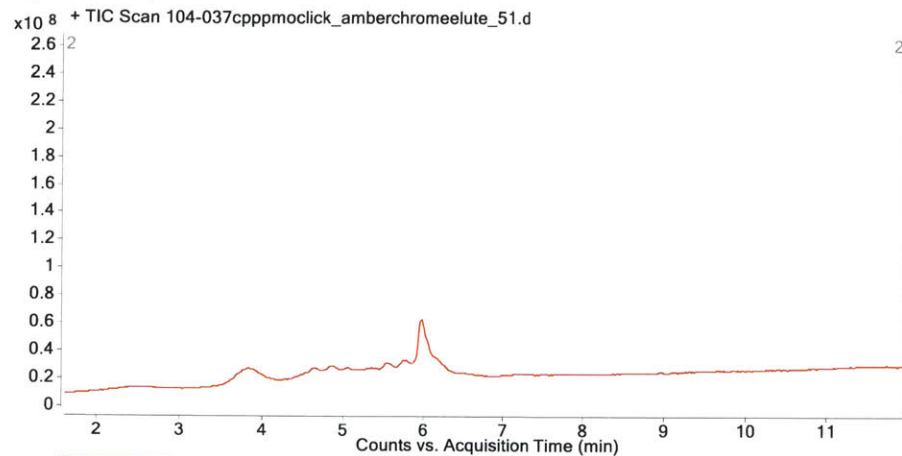
PMO-YTA-4

Mass expected: 8369.9 g/mol

Mass observed: 8370.1 g/mol

Amount: 4 mg (50%)\*

Peptide Sequence: IAWVKAFIRKLRKGPLG



Note: LC-MS Method C

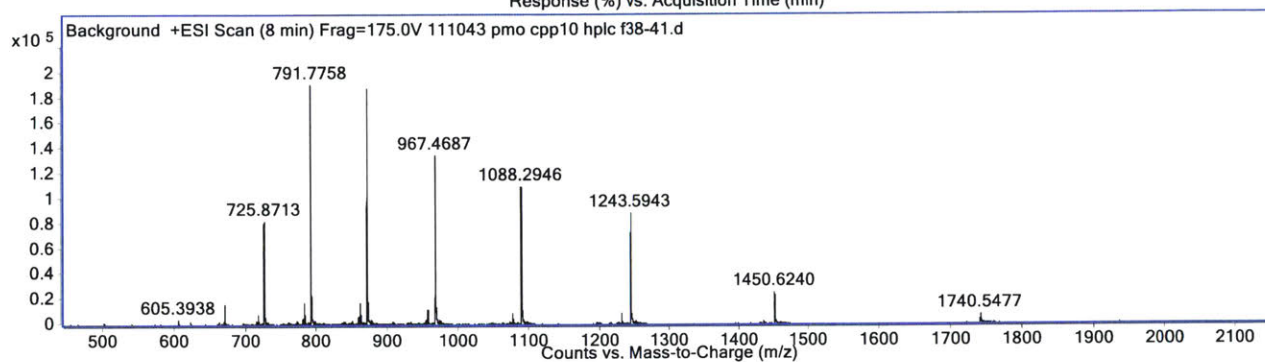
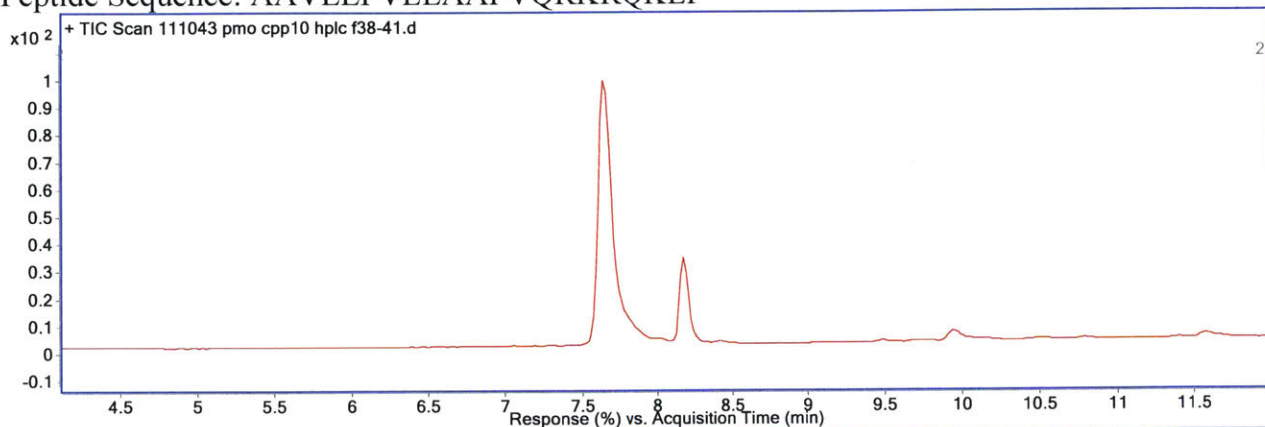
PMO-K-FGF+NLS

Mass expected: 8698.4 g/mol

Mass observed: 8698.8 g/mol

Amount: 2.5 mg (30%)

Peptide Sequence: AAVLLPVLLAAPVQRKRQKLP



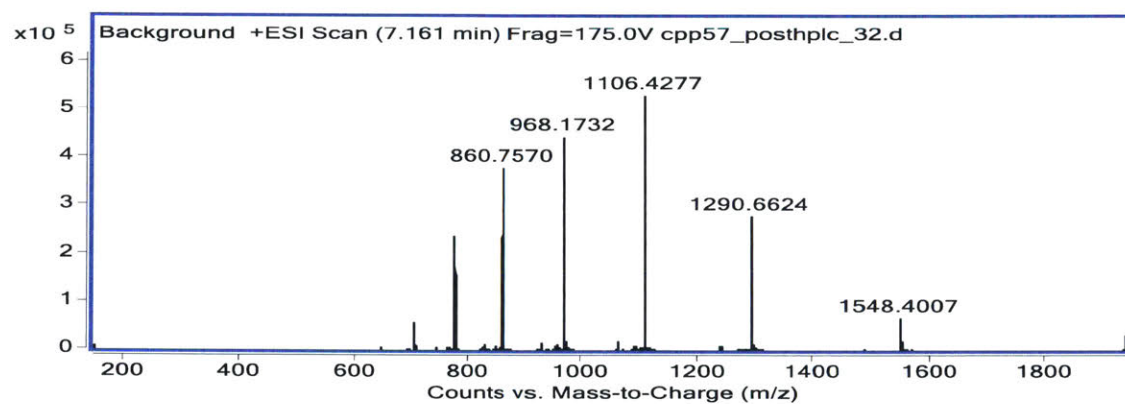
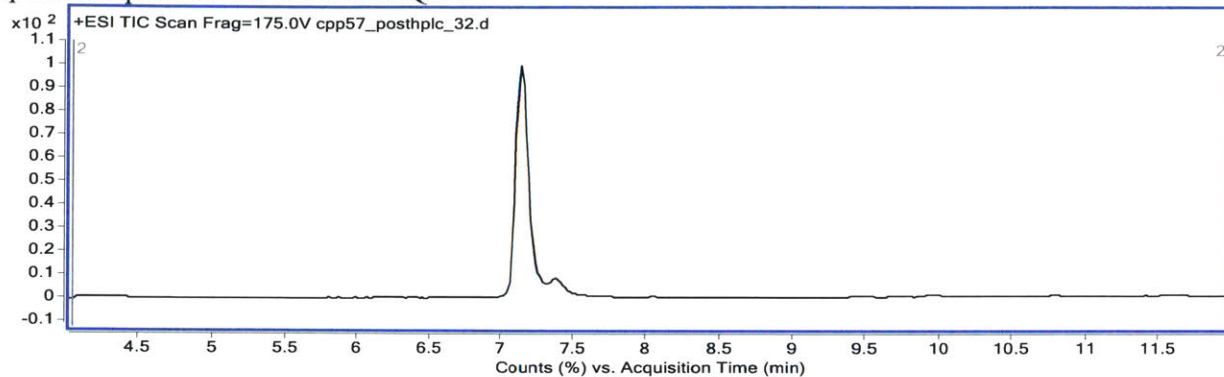
PMO-HN-1

Mass expected: 7738.0 g/mol

Mass observed: 7738.6 g/mol

Amount: 1.4 mg (19%)

Peptide Sequence: TSPLNIHNGQKL



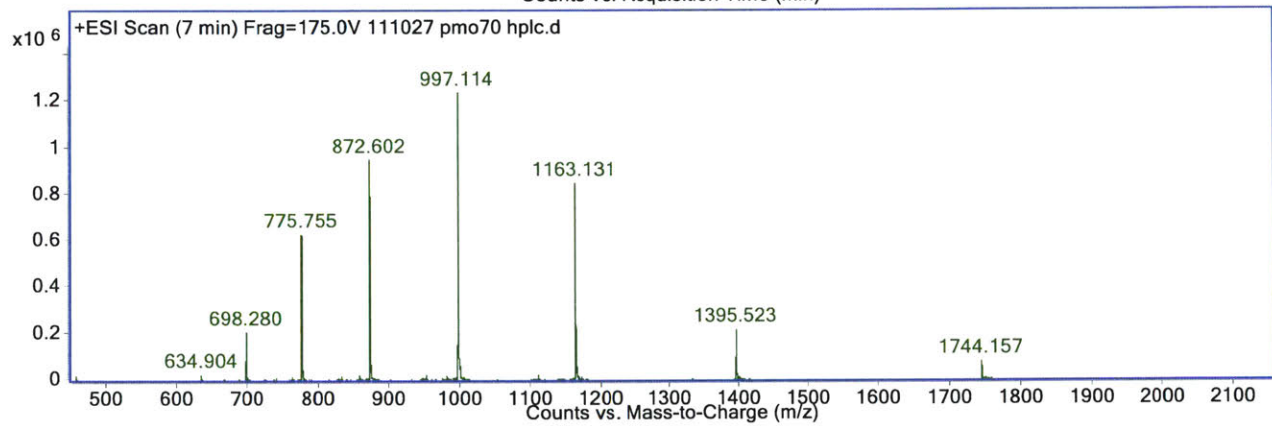
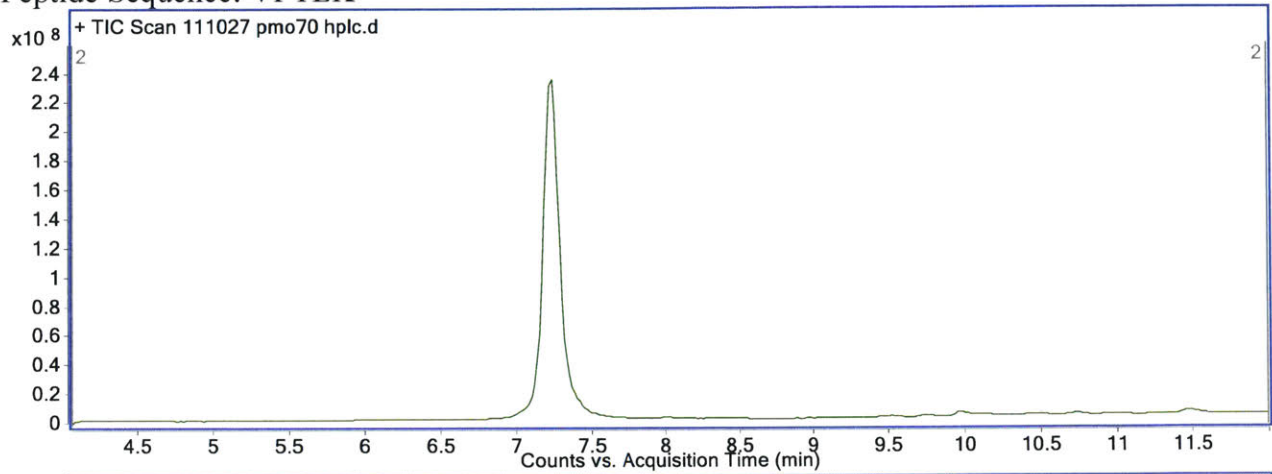
PMO-Bip

Mass expected: 6973.3 g/mol

Mass observed: 6973.8 g/mol

Amount: 5.4 mg (81%)

Peptide Sequence: VPTLK





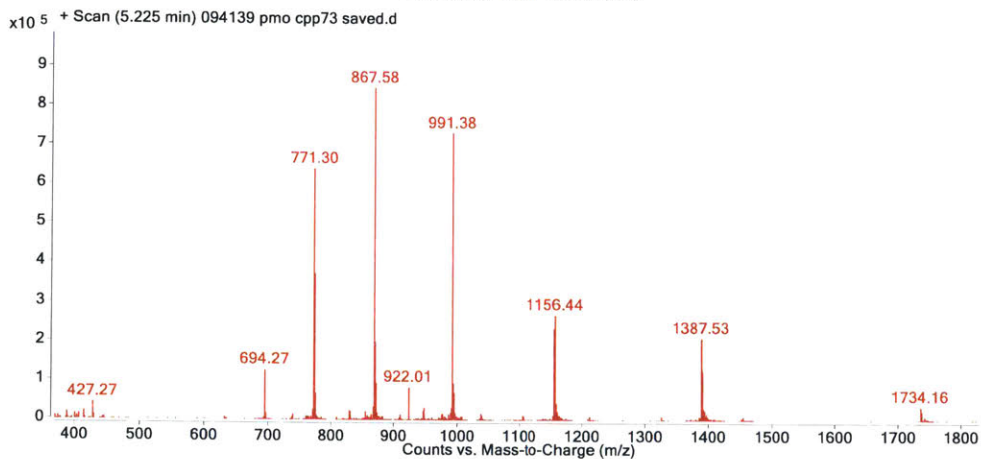
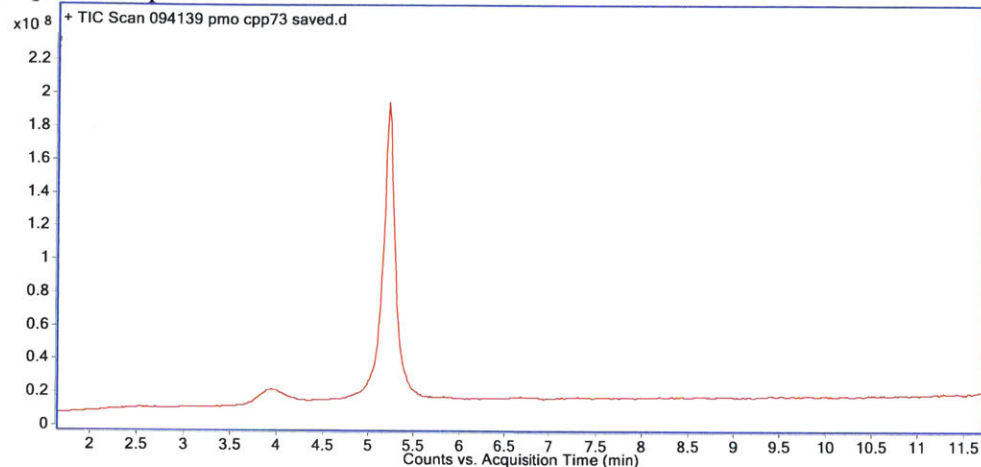
PMO-Bip

Mass expected: 6933.2 g/mol

Mass observed: 6933.7 g/mol

Amount: 3.2 mg (49%)\*

Peptide Sequence: VSALK



Note: LC-MS Method C

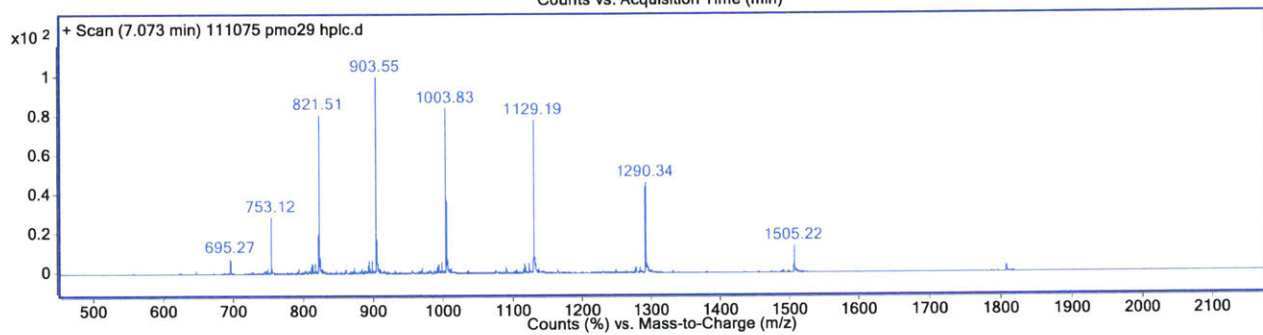
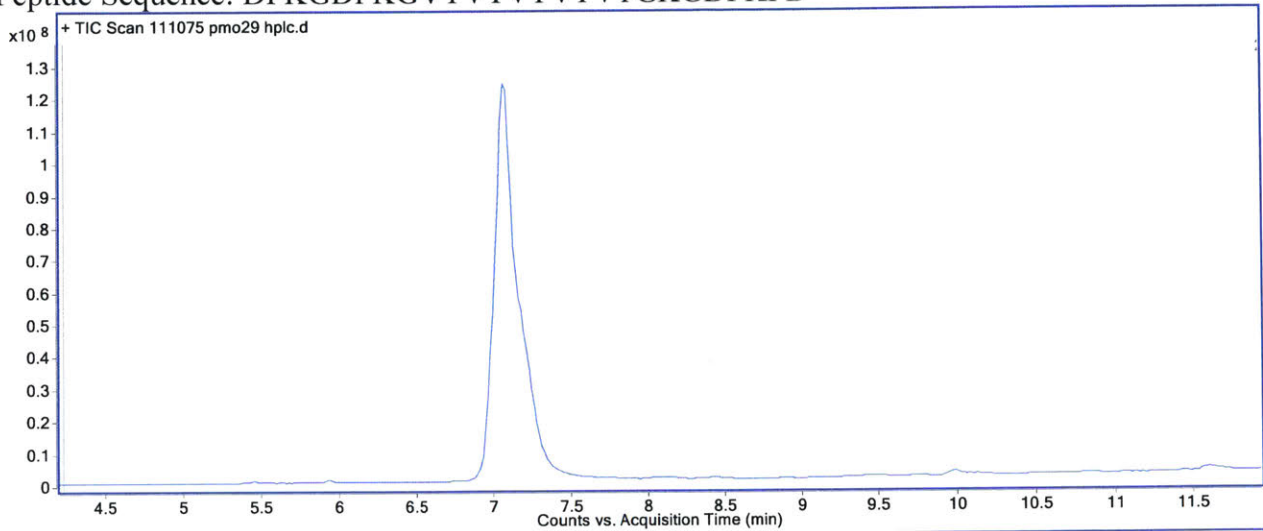
PMO-VT5

Mass expected: 9025.5 g/mol

Mass observed: 9026.0 g/mol

Amount: 5.5 mg (64%)

Peptide Sequence: DPKGDPKGVTVTVTVTVTGKGDPKPD



PMO-TP10

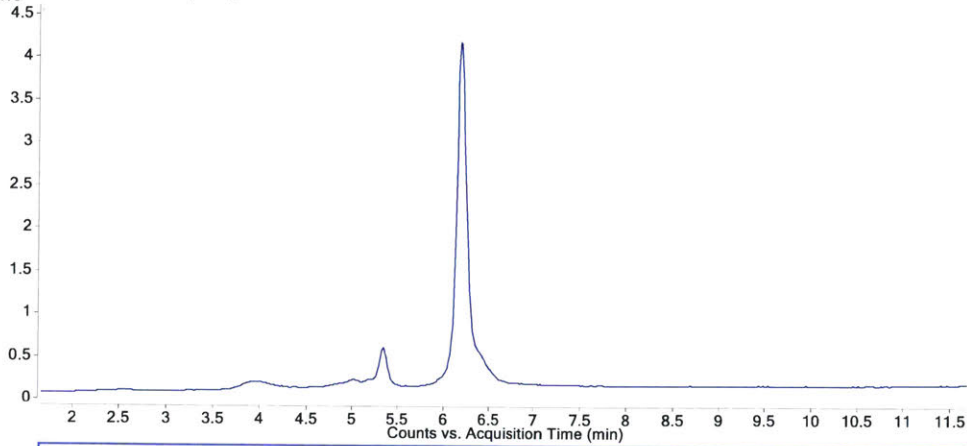
Mass expected: 8599.4 g/mol

Mass observed: 8599.7 g/mol

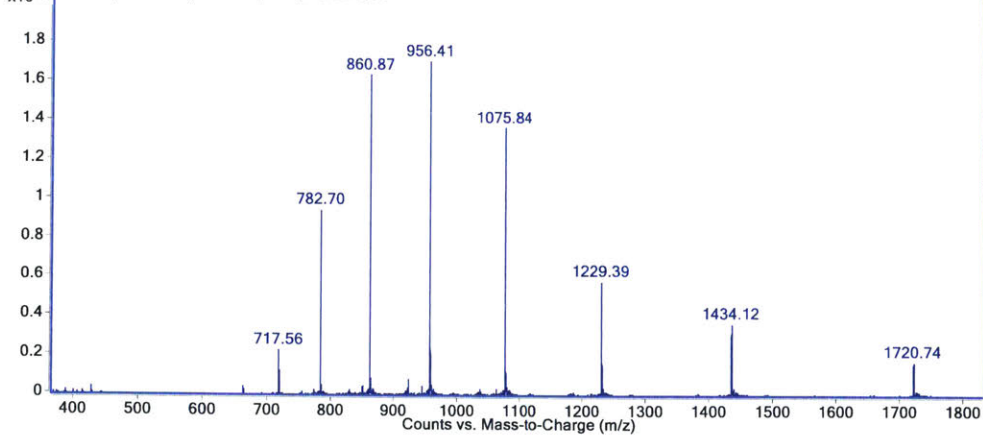
Amount: 9.0 mg (110%)\*

Peptide Sequence: AGYLLGKINLKALAALAKKIL

x10<sup>8</sup> + TIC Scan 094139 pmo tp10 saved.d



x10<sup>6</sup> + Scan (6.195 min) 094139 pmo tp10 saved.d



Note: LC-MS Method C

PMO-SAP(E)

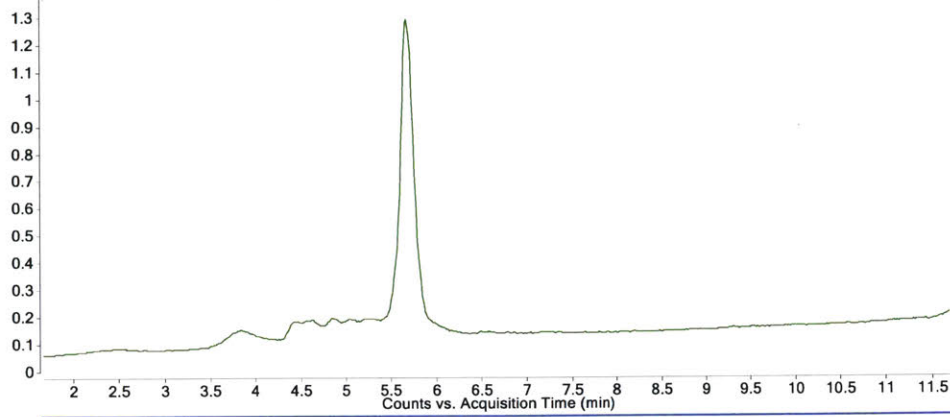
Mass expected: 8332.8 g/mol

Mass observed: 8331.6 g/mol

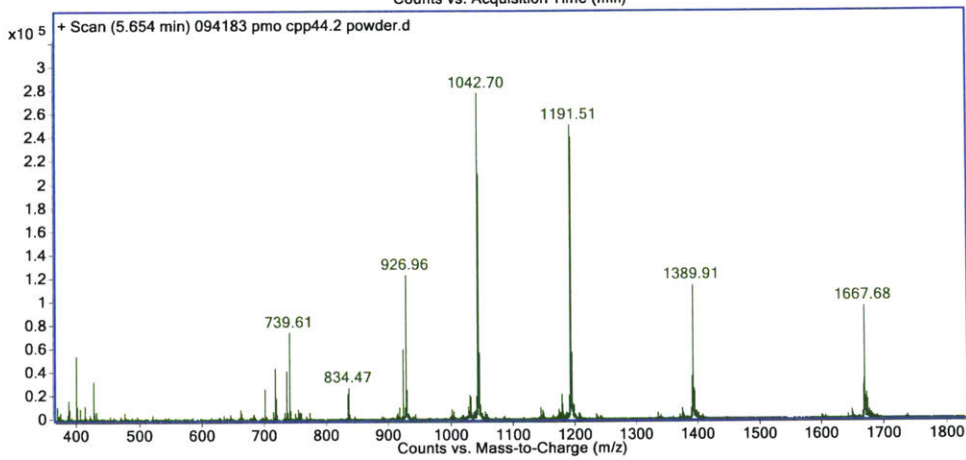
Amount: 3.4 mg (43%)\*

Peptide Sequence: VELPPPVELPPPVELPPP

x10<sup>8</sup> + TIC Scan 094183 pmo cpp44.2 powder.d



x10<sup>5</sup> + Scan (5.654 min) 094183 pmo cpp44.2 powder.d



Note: LC-MS Method C

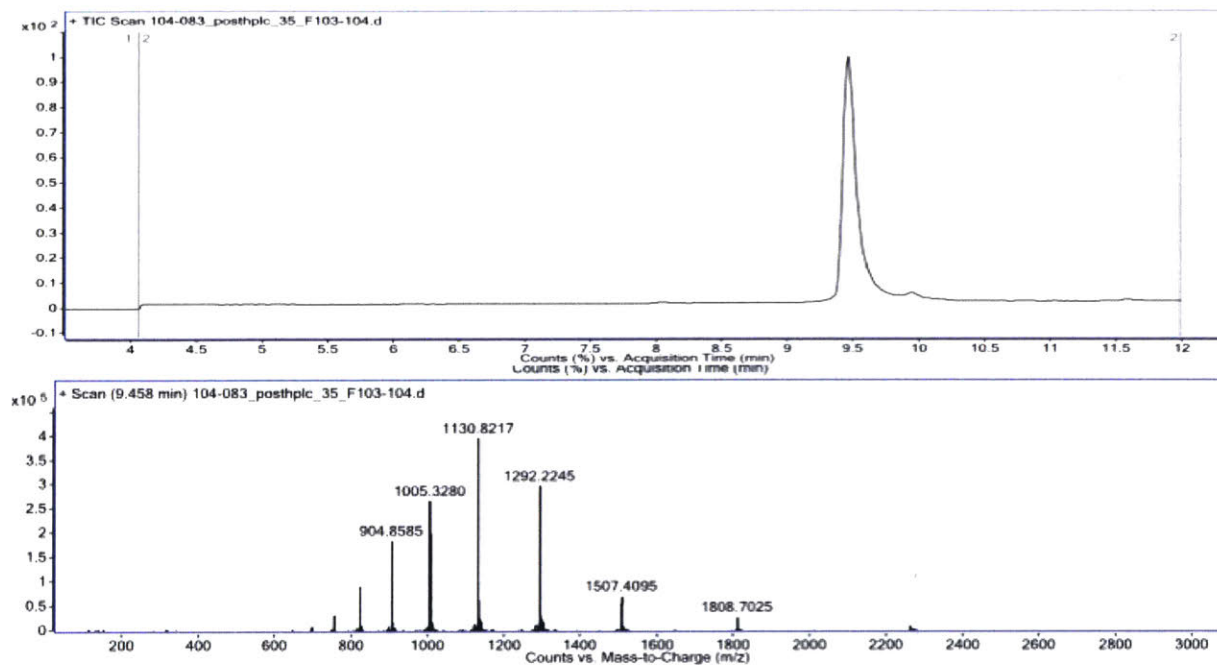
PMO-CADY

Mass Expected: 9038.8

Mass Observed: 9039.3

Amount: 3.3 mg (38%)

Peptide Sequence: GLWRALWLLRSLWLLWRA



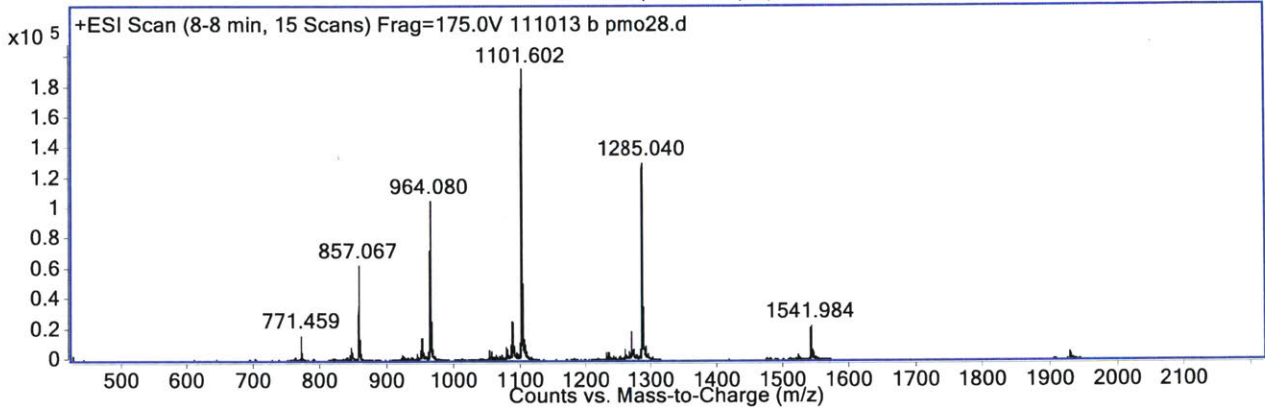
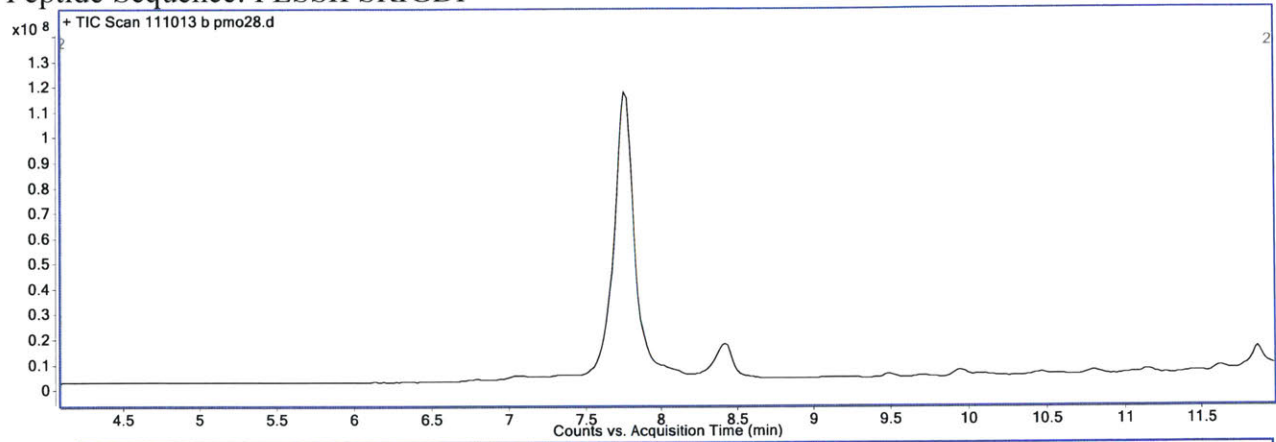
PMO-PreS2-TLM

Mass expected: 7705.1 g/mol

Mass observed: 7705.5 g/mol

Amount: 8.4 mg (115%)\*

Peptide Sequence: PLSSIFSRIGDP



*PMO-PPC and PMO-NS Conjugates*: All chromatograms obtained with Method B.

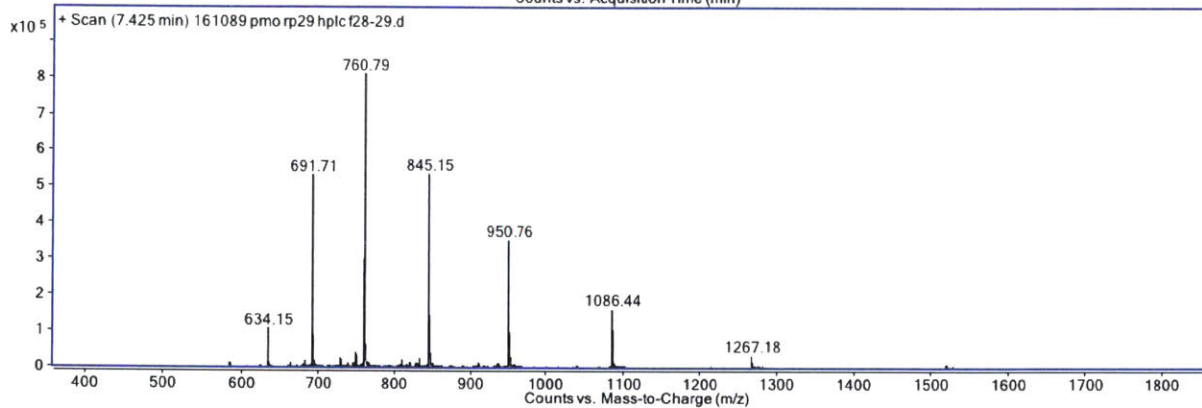
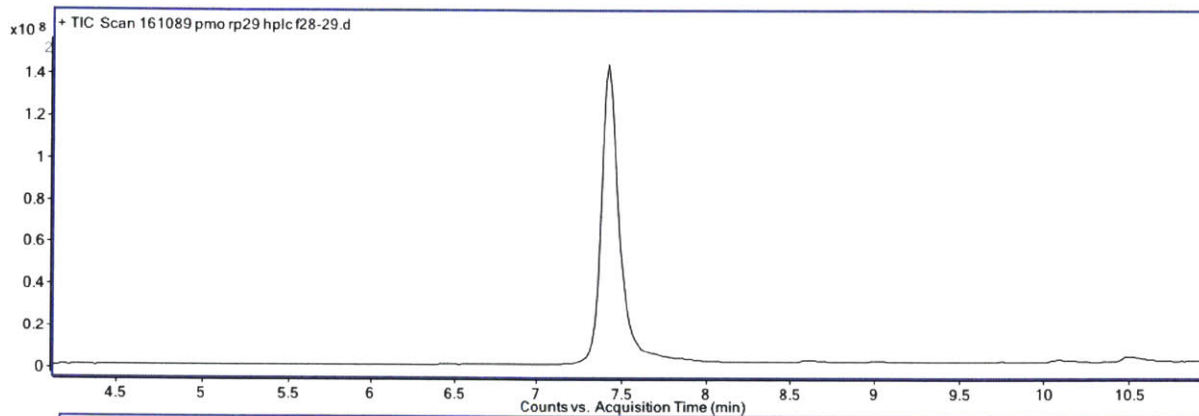
PMO-PPC1

Mass expected: 7598.3

Mass observed: 7598.6

Amount: 1.4 mg (23%)

Peptide Sequence: KQPRIKRKK



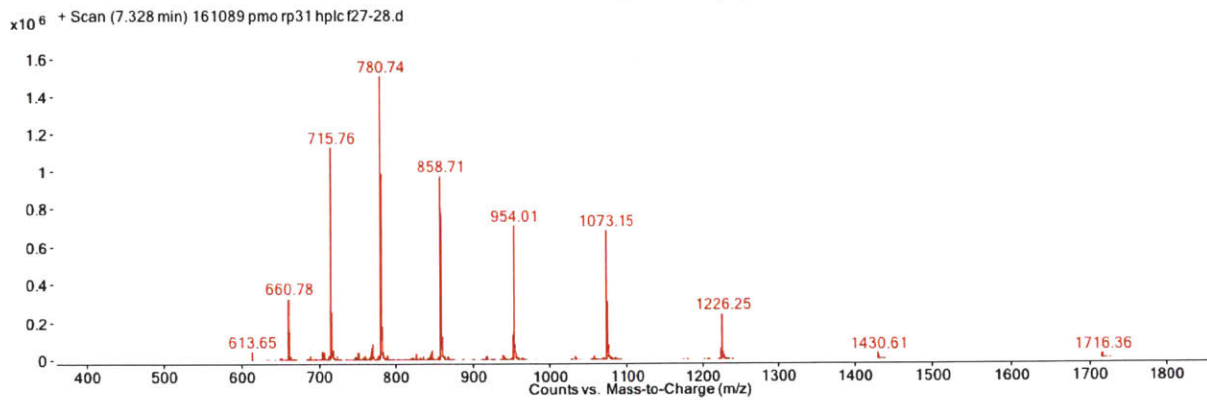
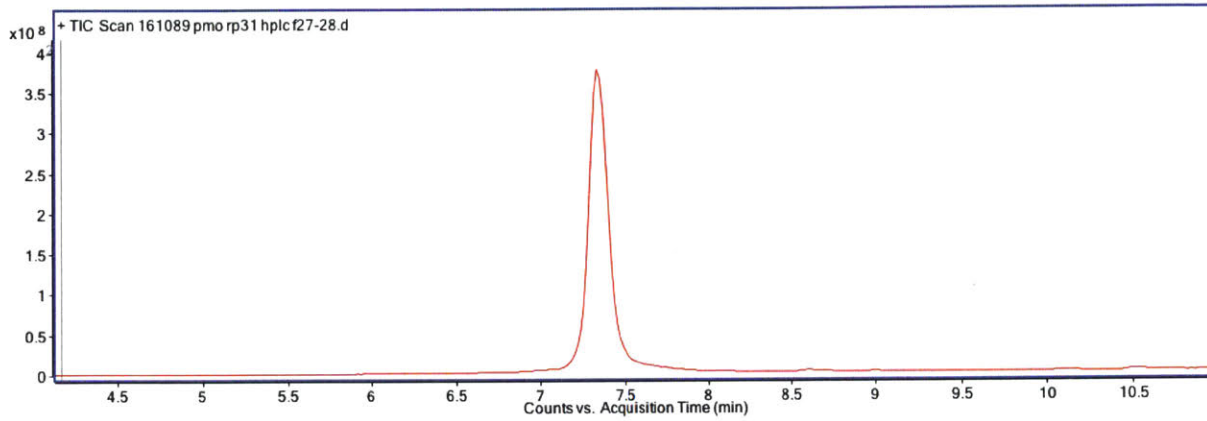
PMO-PPC2

Mass expected: 8577.2

Mass observed: 8577.8

Amount: 4.1 mg (61%)

Peptide Sequence: LKKRRKLPKKKPIRNEQ





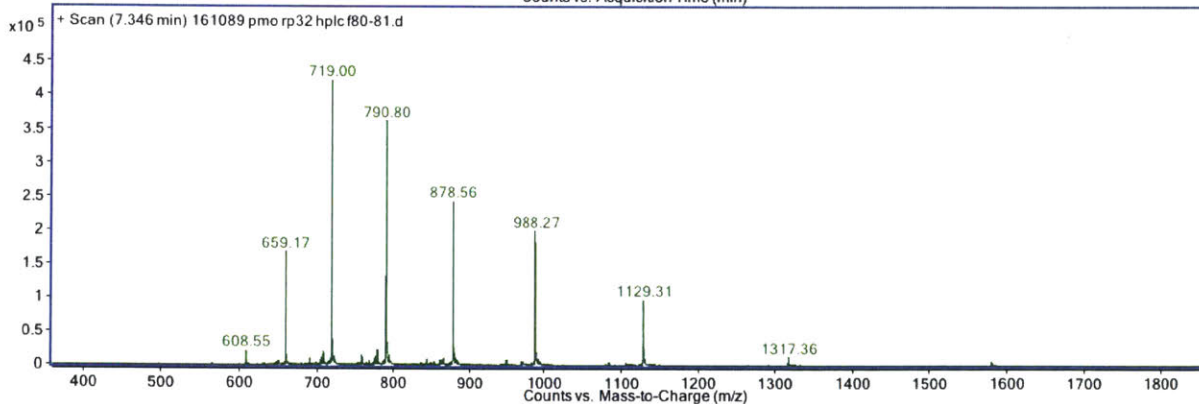
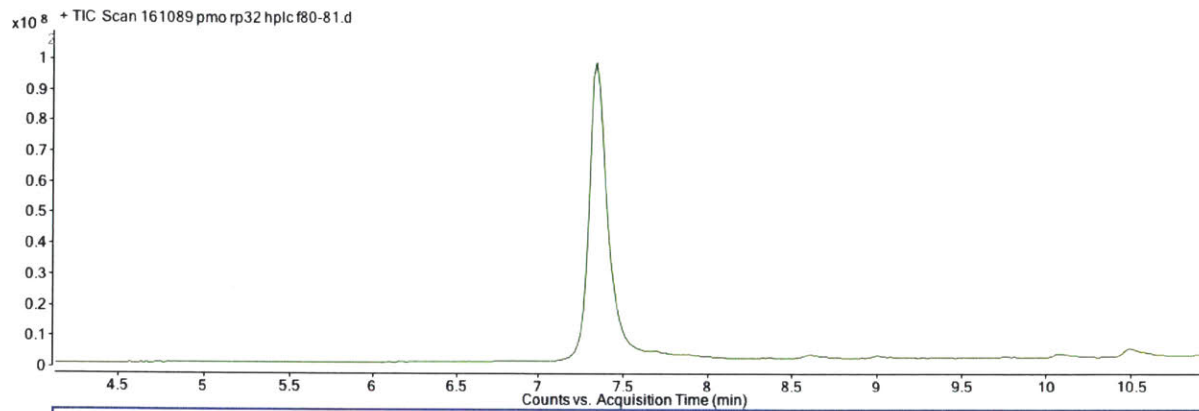
PMO-PPC3

Mass expected: 7898.3

Mass observed: 7898.7

Amount: 2.9 mg (47%)

Peptide Sequence: KKYRGRKRHPR



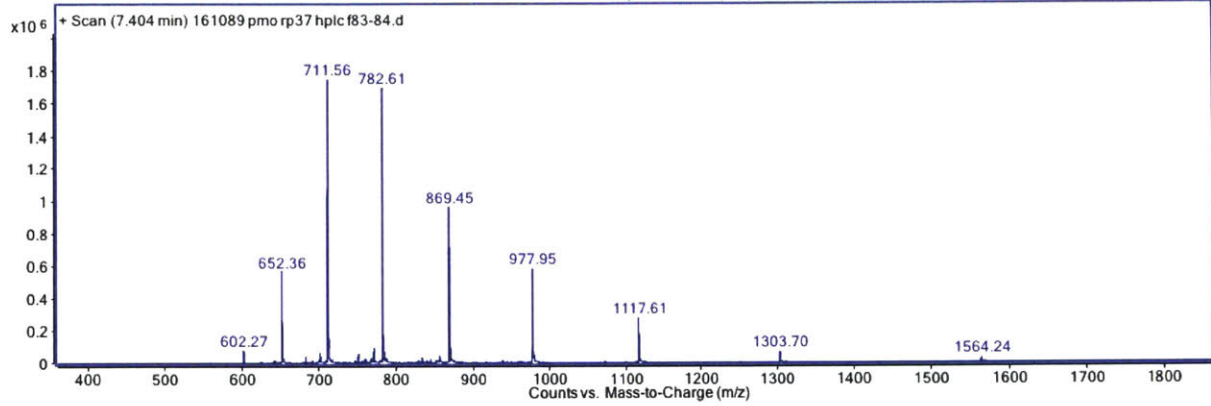
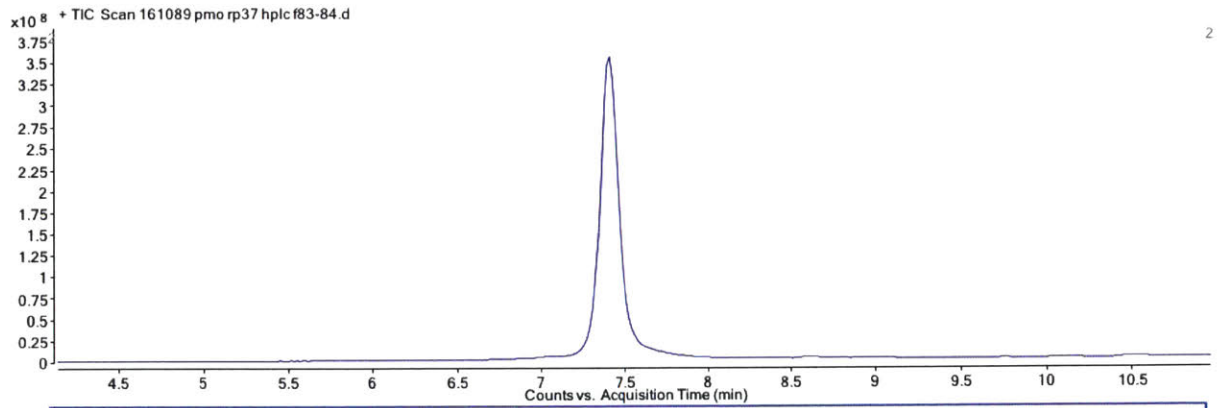
PMO-PPC4

Mass expected: 7816.3

Mass observed: 7816.8

Amount: 3.4 mg (55%)

Peptide Sequence: APKRKKLKKRF



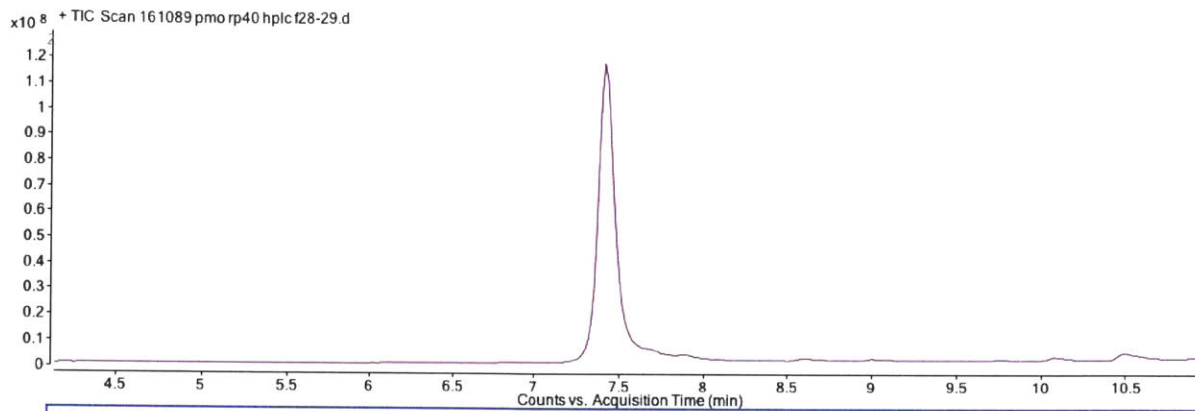
PMO-PPC5

Mass expected: 7868.2

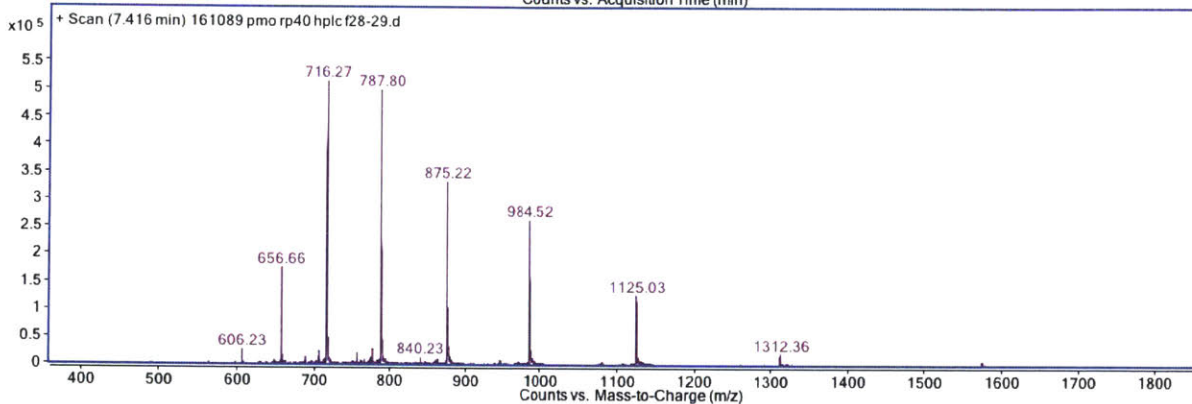
Mass observed: 7868.7

Amount: 3.4 mg (55%)

Peptide Sequence: GRKAARAPGRRKQ



2



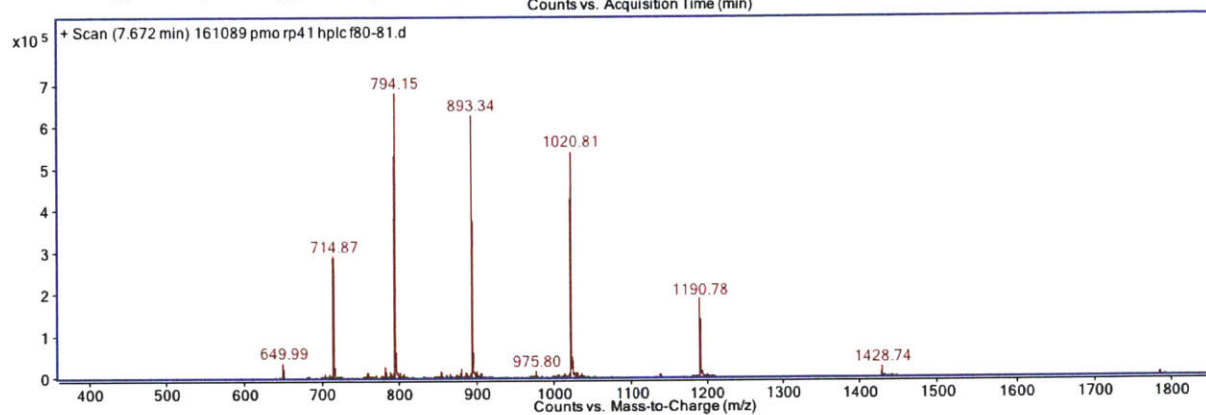
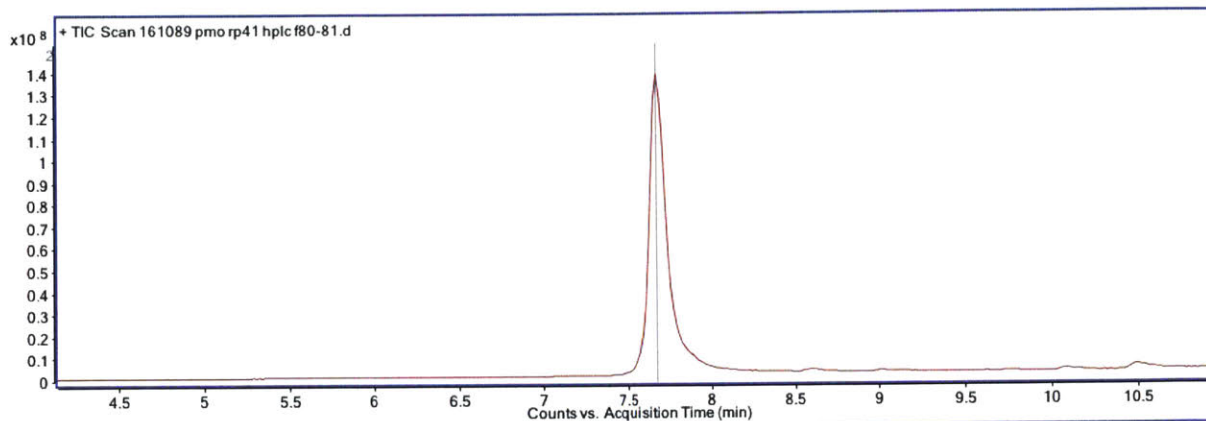
PMO-NS1

Mass expected: 7139.3

Mass observed: 7139.8

Amount: 4.0 mg (71%)

Peptide Sequence: HDLPKGG



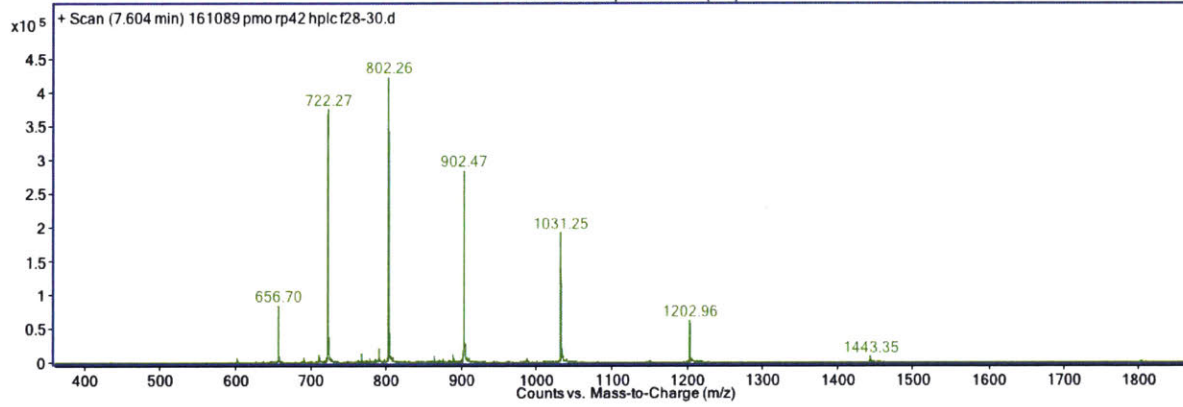
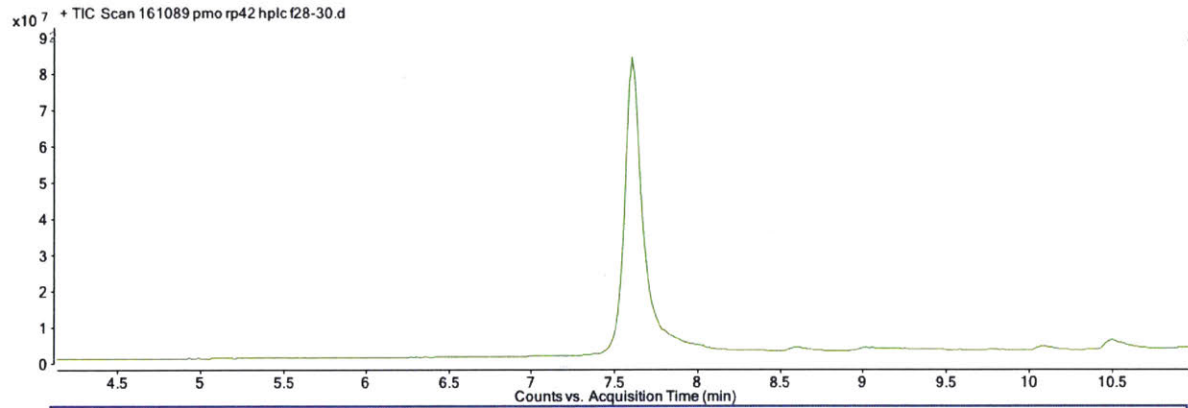
PMO-NS2

Mass expected: 7212.4

Mass observed: 7212.9

Amount: 3.7 mg (65%)

Peptide Sequence: AGSHRRL



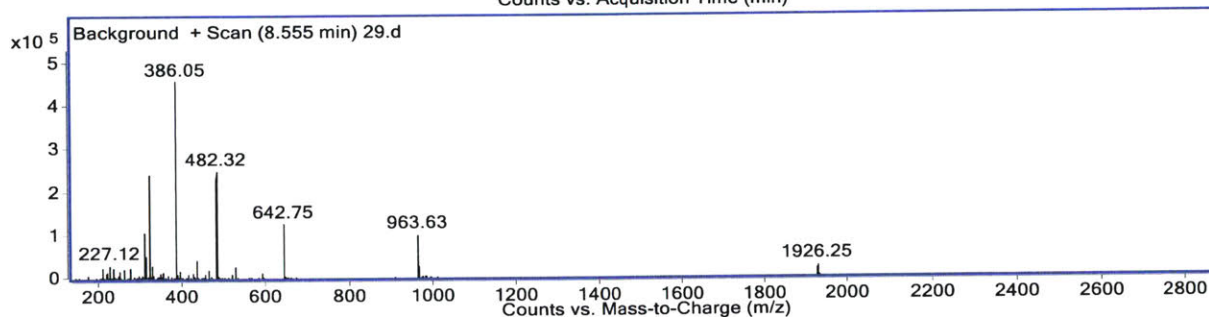
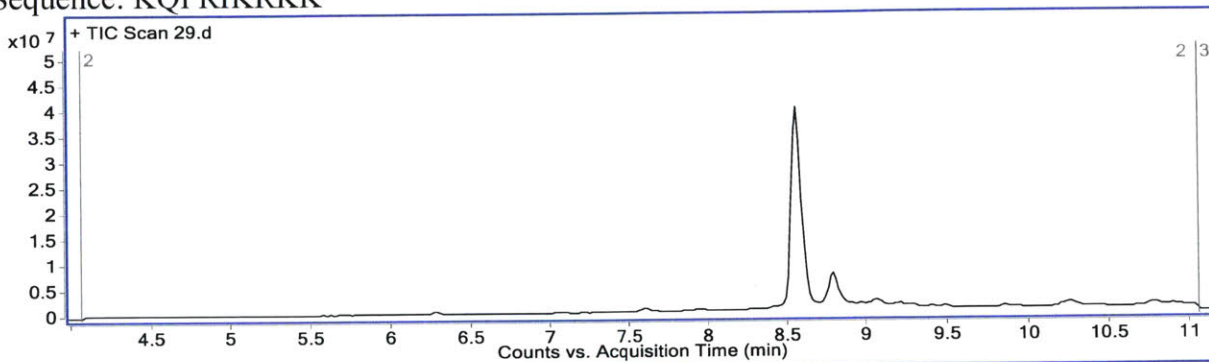
Cy5.5-PPC and Cy5.5-NS Conjugates: All chromatograms obtained with Method B.

Cy5.5-PPC1

Mass expected: 1925.2

Mass observed: 1925.3

Sequence: KQPRIKRKK



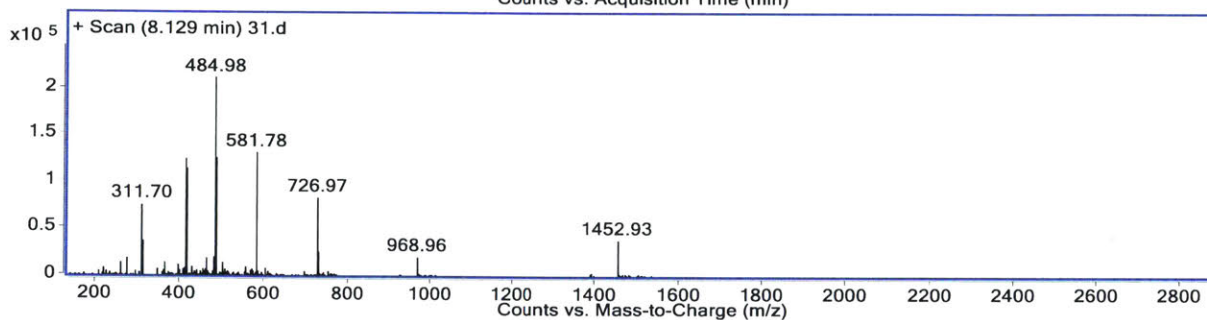
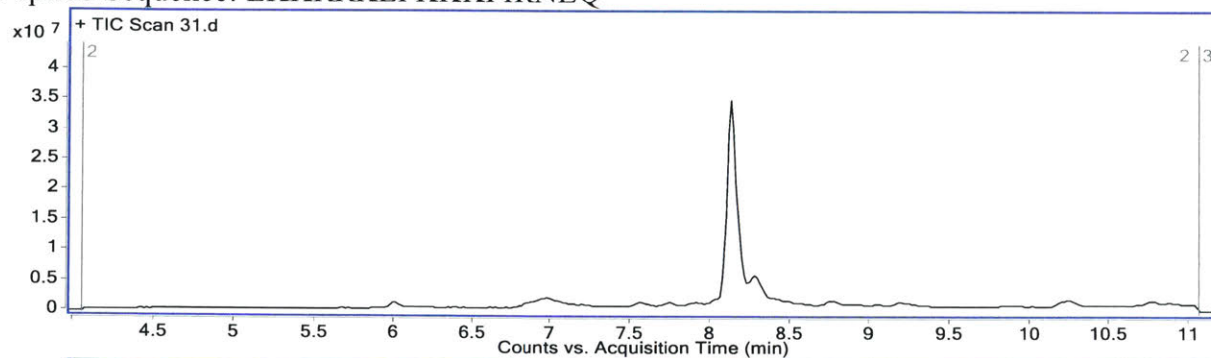
Note: the minor peak has a mass of 1796.1, which represents a single lysine deletion.

Cy5.5-PPC2

Mass expected: 2903.8

Mass observed: 2903.8

Peptide Sequence: LKKRRKLPKKKPIRNEQ



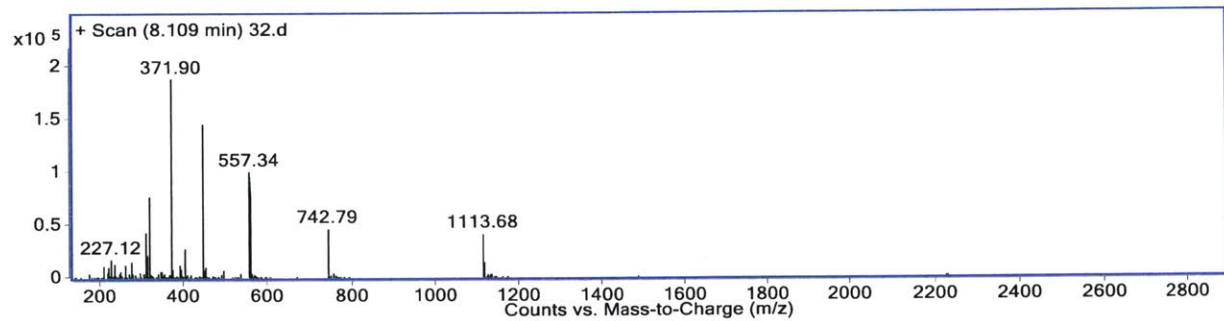
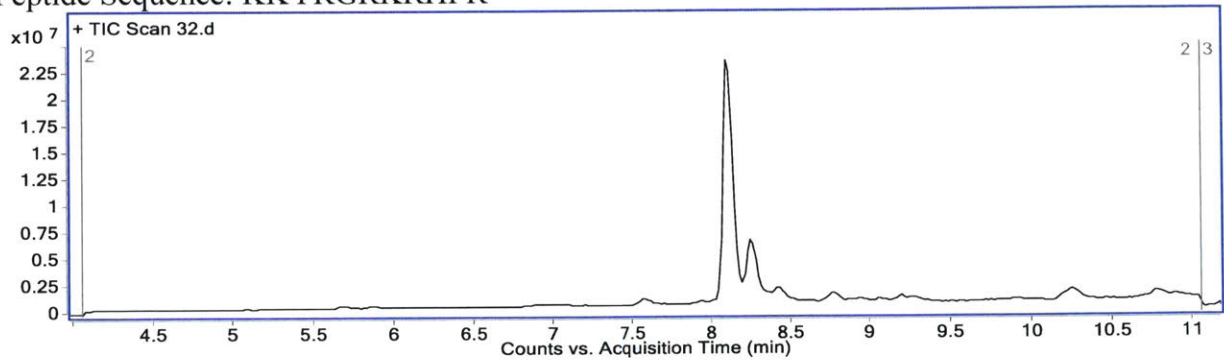
Note: the small shoulder has a mass of 2774.8, which represents a single lysine deletion.

Cy5.5-PPC3

Mass expected: 2225.3

Mass observed: 2225.4

Peptide Sequence: KKYRGRKRHPR



Note: the minor peak has multiple masses of +47 and -10 compared to the desired mass of the major peak.

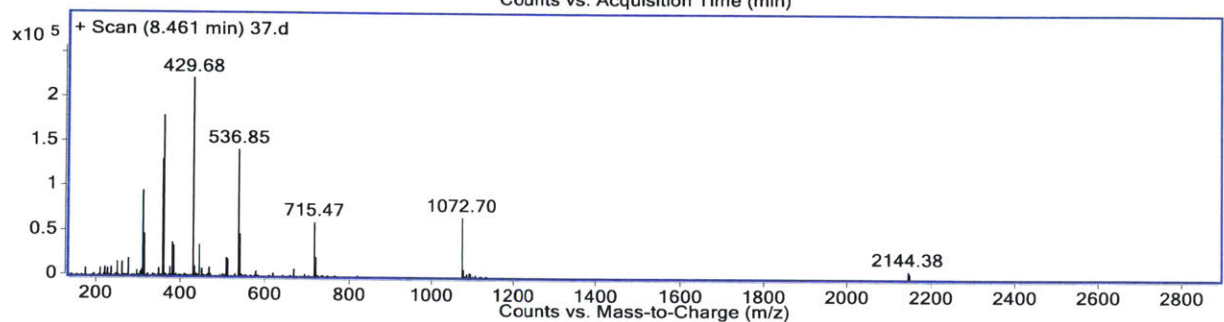
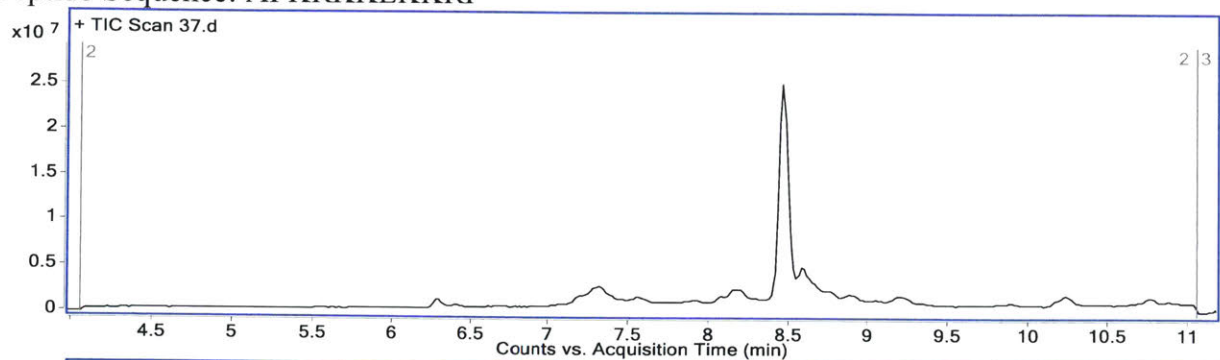


Cy5.5-PPC4

Mass expected: 2143.4

Mass observed: 2143.4

Peptide Sequence: APKRKKLKKRF

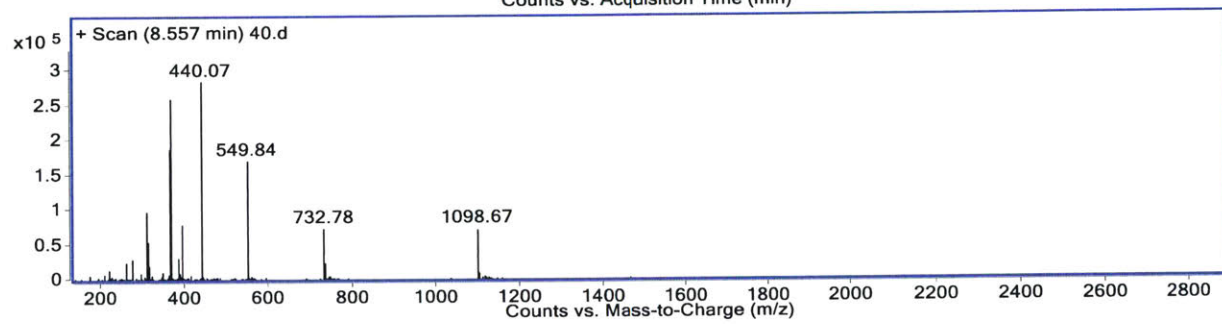
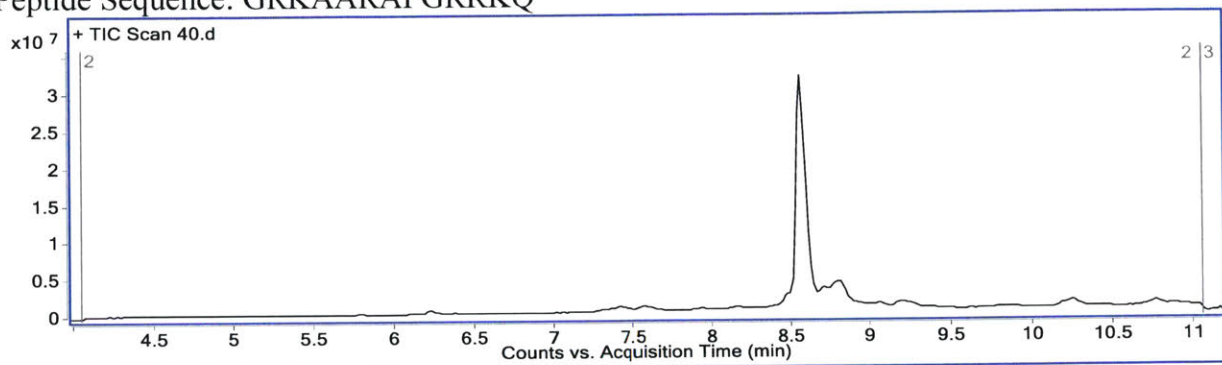


Cy5.5-PPC5

Mass expected: 2195.3

Mass observed: 2195.4

Peptide Sequence: GRKAARAPGRRKQ

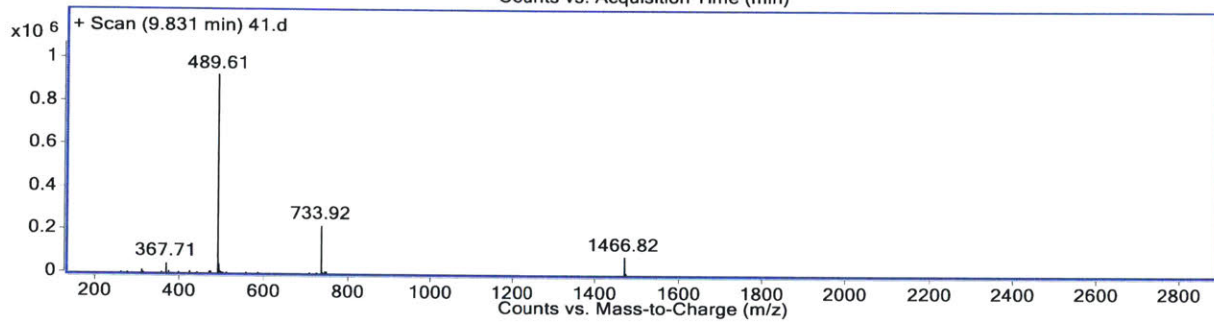
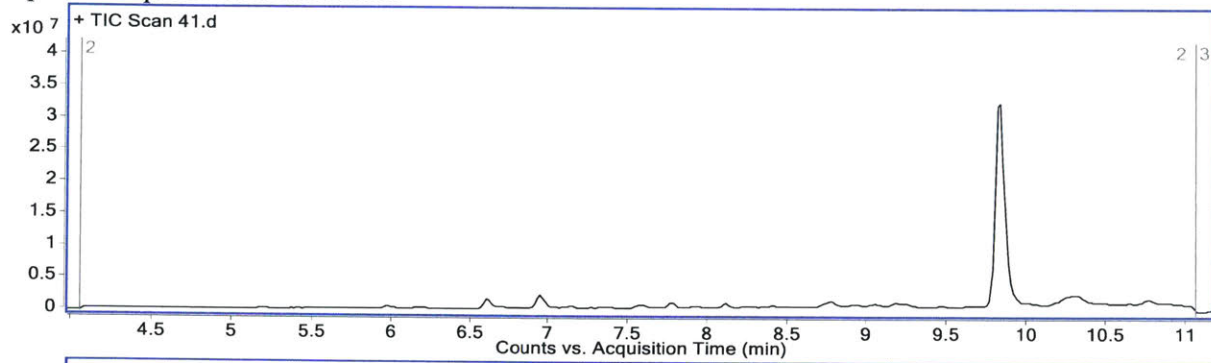


Cy5.5-NS1

Mass expected: 1466.8

Mass observed: 1466.8

Peptide Sequence: HDLPKGG

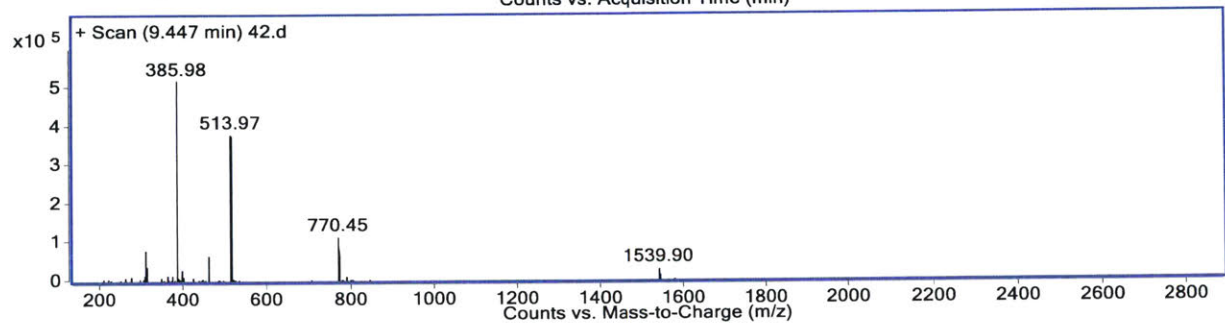
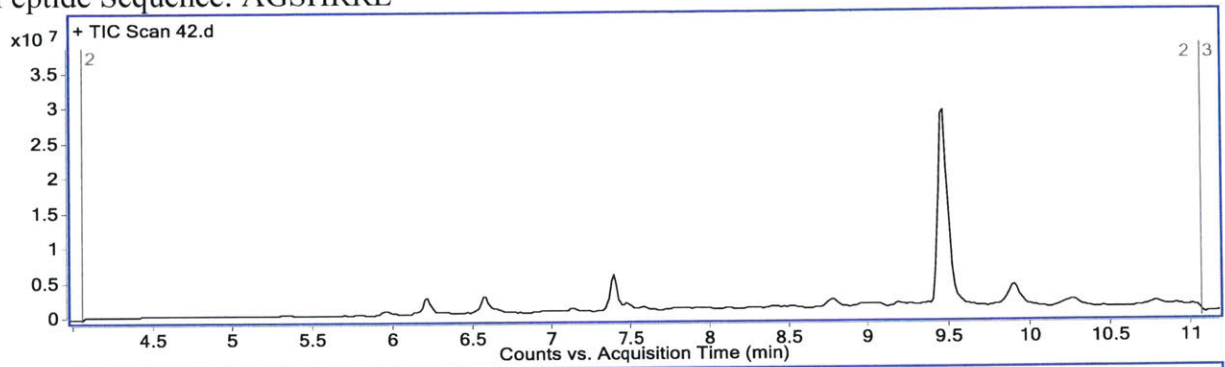


Cy5.5-NS2

Mass expected: 1539.9

Mass observed: 1539.9

Peptide Sequence: AGSHRRL

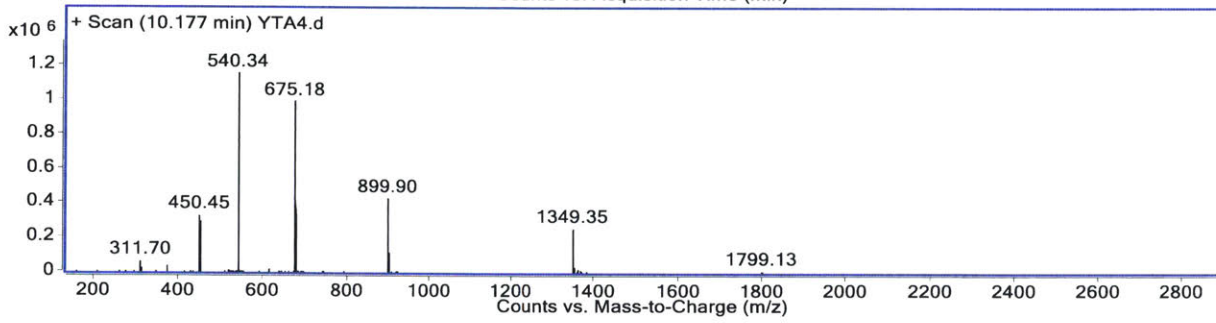
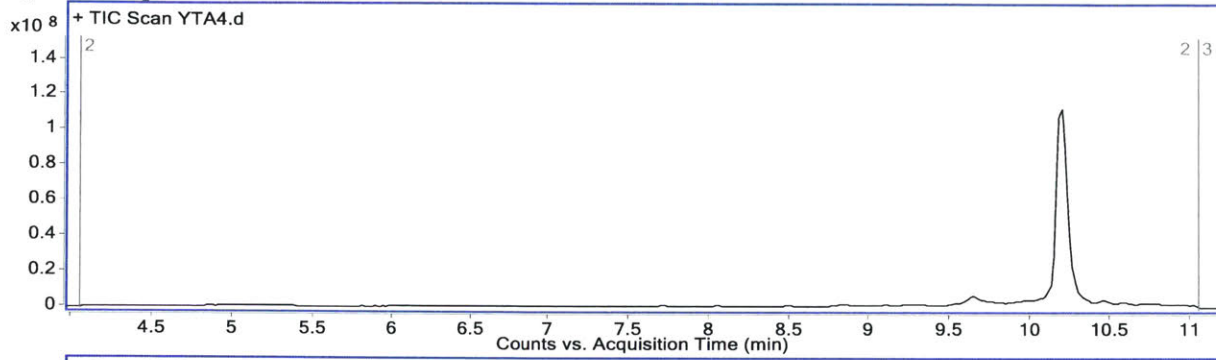


Cy5.5-YTA4

Mass expected: 2696.6

Mass observed: 2696.7

Peptide Sequence: IAWVKAFIRKLRKGPLG



## 2.7. References

- (1) Fu, A.; Tang, R.; Hardie, J.; Farkas, M. E.; Rotello, V. M. Promises and Pitfalls of Intracellular Delivery of Proteins. *Bioconjug. Chem.* **2014**, *25* (9), 1602–1608.
- (2) Stewart, M. P.; Sharei, A.; Ding, X.; Sahay, G.; Langer, R.; Jensen, K. F. In Vitro and Ex Vivo Strategies for Intracellular Delivery. *Nature* **2016**, *538* (7624), 183–192.
- (3) Buckley, D. L.; Crews, C. M. Small-Molecule Control of Intracellular Protein Levels through Modulation of the Ubiquitin Proteasome System. *Angew. Chem. Int. Ed.* **2014**, *53* (9), 2312–2330.
- (4) Juliano, R. L. The Delivery of Therapeutic Oligonucleotides. *Nucleic Acids Res.* **2016**, *44* (14), 6518–6548.
- (5) Anderson, D. G.; Yin, H.; Kauffman, K. J. Delivery Technologies for Genome Editing. *Nat. Rev. Drug Discov.* **2017**, *16* (6), nrd.2016.280.
- (6) Copolovici, D. M.; Langel, K.; Eriste, E.; Langel, Ü. Cell-Penetrating Peptides: Design, Synthesis, and Applications. *ACS Nano* **2014**, *8* (3), 1972–1994.
- (7) *Cell-Penetrating Peptides*; Langel, Ü., Ed.; Methods in Molecular Biology; Humana Press: Totowa, NJ, 2011; Vol. 683.
- (8) Agrawal, P.; Bhalla, S.; Usmani, S. S.; Singh, S.; Chaudhary, K.; Raghava, G. P. S.; Gautam, A. CPPsite 2.0: A Repository of Experimentally Validated Cell-Penetrating Peptides. *Nucleic Acids Res.* **2016**, *44* (Database issue), D1098–D1103.
- (9) Milletti, F. Cell-Penetrating Peptides: Classes, Origin, and Current Landscape. *Drug Discov. Today* **2012**, *17* (15–16), 850–860.
- (10) Soomets, U.; Lindgren, M.; Gallet, X.; Hällbrink, M.; Elmquist, A.; Balaspiri, L.; Zorko, M.; Pooga, M.; Brasseur, R.; Langel, Ü. Deletion Analogues of Transportan. *Biochim. Biophys. Acta BBA - Biomembr.* **2000**, *1467* (1), 165–176.
- (11) Morris, M. C.; Vidal, P.; Chaloin, L.; Heitz, F.; Divita, G. A New Peptide Vector for Efficient Delivery of Oligonucleotides into Mammalian Cells. *Nucleic Acids Res.* **1997**, *25* (14), 2730–2736.
- (12) Daniels, D. S.; Schepartz, A. Intrinsically Cell-Permeable Miniature Proteins Based on a Minimal Cationic PPII Motif. *J. Am. Chem. Soc.* **2007**, *129* (47), 14578–14579.
- (13) Tünnemann, G.; Ter-Avetisyan, G.; Martin, R. M.; Stöckl, M.; Herrmann, A.; Cardoso, M. C. Live-Cell Analysis of Cell Penetration Ability and Toxicity of Oligo-Arginines. *J. Pept. Sci.* **2008**, *14* (4), 469–476.
- (14) Sanders, W. S.; Johnston, C. I.; Bridges, S. M.; Burgess, S. C.; Willeford, K. O. Prediction of Cell Penetrating Peptides by Support Vector Machines. *PLOS Comput. Biol.* **2011**, *7* (7), e1002101.
- (15) Gautam, A.; Chaudhary, K.; Kumar, R.; Sharma, A.; Kapoor, P.; Tyagi, A.; Raghava, G. P. S. In Silico Approaches for Designing Highly Effective Cell Penetrating Peptides. *J. Transl. Med.* **2013**, *11*, 74.
- (16) Holton, T. A.; Pollastri, G.; Shields, D. C.; Mooney, C. CPPpred: Prediction of Cell Penetrating Peptides. *Bioinformatics* **2013**, *29* (23), 3094–3096.
- (17) Dobchev, D. A.; Mager, I.; Tulp, I.; Karelson, G.; Tamm, T.; Tamm, K.; Janes, J.; Langel, U.; Karelson, M. Prediction of Cell-Penetrating Peptides Using Artificial Neural Networks. *Curr. Comput. Aided Drug Des.* **2010**, *6* (2), 79–89.
- (18) Hansen, M.; Kilk, K.; Langel, Ü. Predicting Cell-Penetrating Peptides. *Adv. Drug Deliv. Rev.* **2008**, *60* (4), 572–579.

- (19) Derossi, D.; Calvet, S.; Trembleau, A.; Brunissen, A.; Chassaing, G.; Prochiantz, A. Cell Internalization of the Third Helix of the Antennapedia Homeodomain Is Receptor-Independent. *J. Biol. Chem.* **1996**, *271* (30), 18188–18193.
- (20) Fischer, P. m.; Zhelev, N. z.; Wang, S.; Melville, J. e.; Fåhraeus, R.; Lane, D. p. Structure–activity Relationship of Truncated and Substituted Analogues of the Intracellular Delivery Vector Penetratin. *J. Pept. Res.* **2000**, *55* (2), 163–172.
- (21) Gomez, J. A.; Gama, V.; Yoshida, T.; Sun, W.; Hayes, P.; Leskov, K.; Boothman, D.; Matsuyama, S. Bax-Inhibiting Peptides Derived from Ku70 and Cell-Penetrating Pentapeptides. *Biochem. Soc. Trans.* **2007**, *35* (4), 797–801.
- (22) Richard, J. P.; Melikov, K.; Vives, E.; Ramos, C.; Verbeure, B.; Gait, M. J.; Chernomordik, L. V.; Lebleu, B. Cell-Penetrating Peptides A Reevaluation of the Mechanism of Cellular Uptake. *J. Biol. Chem.* **2003**, *278* (1), 585–590.
- (23) LaRochelle, J. R.; Cobb, G. B.; Steinauer, A.; Rhoades, E.; Schepartz, A. Fluorescence Correlation Spectroscopy Reveals Highly Efficient Cytosolic Delivery of Certain Penta-Arg Proteins and Stapled Peptides. *J. Am. Chem. Soc.* **2015**, *137* (7), 2536–2541.
- (24) Wadia, J. S.; Stan, R. V.; Dowdy, S. F. Transducible TAT-HA Fusogenic Peptide Enhances Escape of TAT-Fusion Proteins after Lipid Raft Macropinocytosis. *Nat. Med.* **2004**, *10* (3), 310–315.
- (25) Schmidt, S.; Adjobo-Hermans, M. J. W.; Wallbrecher, R.; Verdurmen, W. P. R.; Bovée-Geurts, P. H. M.; van Oostrum, J.; Milletti, F.; Enderle, T.; Brock, R. Detecting Cytosolic Peptide Delivery with the GFP Complementation Assay in the Low Micromolar Range. *Angew. Chem. Int. Ed.* **2015**, *54* (50), 15105–15108.
- (26) Kang, S.-H.; Cho, M.-J.; Kole, R. Up-Regulation of Luciferase Gene Expression with Antisense Oligonucleotides: Implications and Applications in Functional Assay Development†. *Biochemistry (Mosc.)* **1998**, *37* (18), 6235–6239.
- (27) Sazani, P.; Kang, S.-H.; Maier, M. A.; Wei, C.; Dillman, J.; Summerton, J.; Manoharan, M.; Kole, R. Nuclear Antisense Effects of Neutral, Anionic and Cationic Oligonucleotide Analogs. *Nucleic Acids Res.* **2001**, *29* (19), 3965–3974.
- (28) Summerton, J.; Weller, D. Morpholino Antisense Oligomers: Design, Preparation, and Properties. *Antisense Nucleic Acid Drug Dev.* **1997**, *7* (3), 187–195.
- (29) Moulton, H. M.; Nelson, M. H.; Hatlevig, S. A.; Reddy, M. T.; Iversen, P. L. Cellular Uptake of Antisense Morpholino Oligomers Conjugated to Arginine-Rich Peptides. *Bioconjug. Chem.* **2004**, *15* (2), 290–299.
- (30) Wu, R. P.; Youngblood, D. S.; Hassinger, J. N.; Lovejoy, C. E.; Nelson, M. H.; Iversen, P. L.; Moulton, H. M. Cell-Penetrating Peptides as Transporters for Morpholino Oligomers: Effects of Amino Acid Composition on Intracellular Delivery and Cytotoxicity. *Nucleic Acids Res.* **2007**, *35* (15), 5182–5191.
- (31) Abes, R.; Moulton, H. M.; Clair, P.; Yang, S.-T.; Abes, S.; Melikov, K.; Prevot, P.; Youngblood, D. S.; Iversen, P. L.; Chernomordik, L. V.; et al. Delivery of Steric Block Morpholino Oligomers by (R-X-R)<sub>4</sub> Peptides: Structure–activity Studies. *Nucleic Acids Res.* **2008**, *36* (20), 6343–6354.
- (32) Yin, H.; Saleh, A. F.; Betts, C.; Camelliti, P.; Seow, Y.; Ashraf, S.; Arzumanov, A.; Hammond, S.; Merritt, T.; Gait, M. J.; et al. Pip5 Transduction Peptides Direct High Efficiency Oligonucleotide-Mediated Dystrophin Exon Skipping in Heart and Phenotypic Correction in Mdx Mice. *Mol. Ther.* **2011**, *19* (7), 1295–1303.

- (33) Deuss, P. J.; Arzumanov, A. A.; Williams, D. L.; Gait, M. J. Parallel Synthesis and Splicing Redirection Activity of Cell-Penetrating Peptide Conjugate Libraries of a PNA Cargo. *Org. Biomol. Chem.* **2013**, *11* (43), 7621–7630.
- (34) Lee, S. H.; Moroz, E.; Castagner, B.; Leroux, J.-C. Activatable Cell Penetrating Peptide–Peptide Nucleic Acid Conjugate via Reduction of Azobenzene PEG Chains. *J. Am. Chem. Soc.* **2014**, *136* (37), 12868–12871.
- (35) Breiman, L. Random Forests. *Mach. Learn.* **2001**, *45* (1), 5–32.
- (36) Liang, G.; Liu, Y.; Shi, B.; Zhao, J.; Zheng, J. An Index for Characterization of Natural and Non-Natural Amino Acids for Peptidomimetics. *PLOS ONE* **2013**, *8* (7), e67844.
- (37) Carlier, M. F.; Criquet, P.; Pantaloni, D.; Korn, E. D. Interaction of Cytochalasin D with Actin Filaments in the Presence of ADP and ATP. *J. Biol. Chem.* **1986**, *261* (5), 2041–2050.
- (38) Mijalis, A. J.; Thomas III, D. A.; Simon, M. D.; Adamo, A.; Beaumont, R.; Jensen, K. F.; Pentelute, B. L. A Fully Automated Flow-Based Approach for Accelerated Peptide Synthesis. *Nat. Chem. Biol.* **2017**, *13* (5), 464–466.
- (39) Pedregosa, F.; Varoquaux, G.; Gramfort, A.; Michel, V.; Thirion, B.; Grisel, O.; Blondel, M.; Prettenhofer, P.; Weiss, R.; Dubourg, V.; et al. Scikit-Learn: Machine Learning in Python. *J. Mach. Learn. Res.* **2011**, *12*, 2825–2830.



### **Chapter 3: Chimeras of Cell-Penetrating Peptides Demonstrate Synergistic Improvement in Antisense Efficacy**

The work presented in this chapter has been submitted for publication:

Fadzen, C.M.,\* Holden, R.L.,\* Wolfe, J.M.,\* Choo, Z-N., Yao, M., Hanson, G.J., & Pentelute, B.L. “Chimeras of Cell-Penetrating Peptides Demonstrate Synergistic Improvement in Antisense Efficacy”

\*: denotes authors contributed equally

### 3.1. Introduction

Phosphorodiamidate morpholino oligonucleotides (PMOs) are attractive therapeutic molecules for genetic diseases. Designed to recognize targets by Watson-Crick base pairing, PMOs exhibit a high level of specificity for their complementary nucleotide sequence. Depending on the type of sequence targeted, PMOs can mediate a variety of effects, including blocking protein translation or modifying gene splicing. Eteplirsen, a PMO conditionally approved by the FDA to treat Duchenne muscular dystrophy, causes a mutation-containing exon in the pre-mRNA encoding for dystrophin to be excluded from the final protein transcript, restoring protein functionality.<sup>1</sup>

In terms of structure, PMOs are neutral oligonucleotide analogues in which the ribosyl ring has been replaced with a morpholino ring and the negatively-charged phosphodiester backbone has been replaced with the uncharged phosphorodiamidate.<sup>2</sup> The altered backbone structure prevents degradation in both serum and by intracellular nucleases.<sup>3,4</sup> Yet the relatively large size and neutral charge of PMOs can lead to inefficient delivery to the cytosol and nucleus.<sup>5</sup>

Cell-penetrating peptides (CPPs) are a promising strategy to improve the delivery of PMO to the nucleus.<sup>6-11</sup> CPPs are relatively short sequences of 5-40 amino acids that ideally access the cytosol and can promote the intracellular delivery of cargo.<sup>12,13</sup> CPPs can be classified into different groups based on their physicochemical properties. One common CPP class consists of repetitive, arginine-based peptides such as R<sub>12</sub> and Bpep (RXRRβRRXRRβR, in which X is aminohexanoic acid and β is β-alanine). These oligoarginine peptides are often random coils.<sup>14</sup> When conjugated to PMO, the oligoarginine peptides have been some of the most effective peptides in promoting PMO delivery.<sup>7-9</sup> Other CPPs, such as Penetratin, pVEC, and melittin, are more amphipathic in nature. While these sequences do contain cationic residues, the defined separation of charged and hydrophobic residues can promote amphipathic helix formation. However, amphipathic CPPs have not been demonstrated to significantly improve PMO efficacy.

No universal mechanism of cell entry exists for CPPs or CPP-PMO conjugates.<sup>15,16</sup> The mechanism is often highly dependent on the treatment concentrations and the type of cargo attached.<sup>17,18</sup> Above a certain threshold concentration (generally low micromolar), energy-independent cytosolic uptake can be observed faster than the time scale of endocytosis and cell surface recycling.<sup>17,19</sup> The fast uptake rate provides evidence for a direct translocation mechanism similar to what is observed for a small molecule. However, at low, physiologically-relevant

concentrations, uptake is primarily endocytic. Even within the category of endocytosis, CPPs and CPP-PMO conjugates can enter cells using one or multiple endocytic mechanisms.<sup>16,20</sup> These endocytic mechanisms include micropinocytosis, clathrin-mediated endocytosis, caveolae-mediated endocytosis and clathrin/caveolae-independent endocytosis.<sup>21</sup> CPP-PMO conjugates are primarily endocytosed at low concentrations, and the CPPs that are poor for PMO delivery are likely trapped in endosomes or excluded from the nuclear compartment.

Given that different CPPs can engage different endocytic mechanisms and that some CPPs are better at escaping endosomes than others, each individual CPP has strengths and weaknesses. One way to harness the benefits of various peptides is to combine them into chimeric peptides and leverage the strengths of each component. Yin and coworkers created covalent chimeras between a muscle targeting peptide and Bpep to combine muscle targeting with cell-penetration for PMO delivery.<sup>22</sup> Abes *et al.* utilized one chimera composed of penetratin and a polyarginine peptide to improve the delivery of peptide nucleic acids, a different class of antisense oligonucleotide.<sup>23</sup> However, there has yet to be an extensive examination of the design space of chimeras composed of two CPPs. A thorough understanding of this space is necessary in order to apply these hybrid molecules to improve PMO delivery.

To begin our investigations, we envisioned that chimeric peptides composed of a random-coil, oligoarginine CPP with an amphipathic CPP could improve PMO activity. If each CPP utilizes distinct mechanisms of endocytosis, the chimera may be able to access multiple mechanisms of cellular entry. Further the different CPPs may have beneficial effects on processes downstream of uptake, such as endosomal escape or nuclear entry. Here, we present several amphipathic/oligoarginine CPP chimeras that exhibited a synergistic, rather than additive, gain in PMO efficacy in a biological assay. The CPP chimeras outperform the potent CPP standard (Bpep) for PMO activity in this assay. We investigate several of the design principles for the success of these conjugates and probe the mechanism of uptake for one particular conjugate.

### 3.2. Results and Discussion

Our initial proof-of-concept experiments were aimed at determining if chimeric CPPs could improve PMO efficacy. We designed a set of three constructs that combine an arginine-rich CPP with an amphipathic CPP. Each construct has three components: the two CPPs and the PMO. The two CPPs were linked through an amide bond to generate one long, linear peptide. The C-terminal peptide for each construct was Bpep, an arginine-rich CPP that has consistently been one of the highest performing CPPs for PMO delivery.<sup>9,11,24</sup> For the N-terminal peptide, we chose three known amphipathic CPPs: pVEC, penetratin, and mellitin.<sup>25-27</sup> One additional construct was generated with Bpep as the N-terminal peptide to serve as a standard of comparison in which the chimera is two arginine-rich peptides (Figure 3.1A). The PMO cargo employed was a 6 kDa, 18-base pair PMO that can trigger increased eGFP expression in a HeLa cell line stably transfected with a split eGFP construct (Figure 3.1B).

To synthesize the constructs, the two-component, chimeric peptide was prepared by automated fast-flow solid-phase peptide synthesis.<sup>28</sup> The N-terminus of the peptide was capped with 4-pentynoic acid to provide a click chemistry handle. The PMO was provided by Sarepta Therapeutics and functionalized at the 3'-amine with 5-azidopentanoic acid. The PMO was conjugated to the chimeric peptide using copper-catalyzed click chemistry and the PMO-chimera conjugates were purified by reversed-phase high-performance liquid chromatography (RP-HPLC)(Figure 3.1B).

Next, the conjugates were evaluated in the HeLa-654 eGFP assay to assess if the chimeric CPPs would improve PMO efficacy. In this assay, the HeLa cells are stably transfected with an eGFP sequence that is interrupted with a mutated intron of the human  $\beta$ -globin gene (IVS2-654). The mutation creates a cryptic splice site that leads to retention of a  $\beta$ -globin fragment in the eGFP mRNA sequence. Upon translation, the eGFP is nonfluorescent. The IVS2-654 PMO utilized in the conjugates hybridizes to the mutated intron and prevents the aberrant gene splicing, leading to an eGFP mRNA sequence that encodes for functional, fluorescent eGFP. The amount of PMO delivered is therefore correlated to the amount of functional eGFP expressed.

The HeLa-654 eGFP cells were treated with 5  $\mu$ M of each conjugate in serum-containing media. After 22 hours, the fluorescence of the cells was analyzed by flow cytometry (Figure 3.1C). All four CPP chimeras performed better than Bpep, the consistently high-performing CPP for PMO delivery. Our top chimera, PMO-Penetratin-Bpep had an approximately 70-fold increase in

|                 |            |            |                     |
|-----------------|------------|------------|---------------------|
| Penetratin-Bpep | RQIKIWFQNR | RJKWKKRXRR | BRRXRRBR            |
| pVEC-Bpep       | LLIILRRRIR | KQAHHSKRX  | RRBRRXRRBR          |
| Melittin-Bpep   | GIGAVLKVLT | TGLPALISWI | KRKRQQRXRR BRRXRRBR |
| Bpep-Bpep       | RXRRBRRXRR | BRRXRRBRRX | RRBR                |

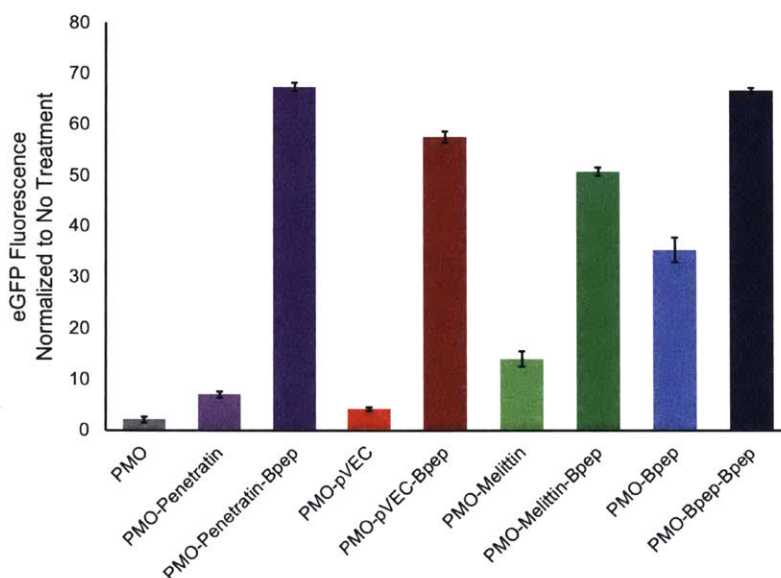
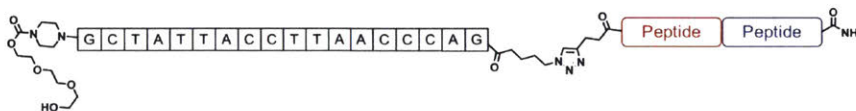


**Figure 3.1. Design and evaluation of PMO activity for PMO-Peptide chimera conjugates.** A) Amino acid sequences of the four cell-penetrating peptide chimeras used in this work. Each chimera includes one cell-penetrating peptide on the N-terminus followed by Bpep on the C-terminus. X = aminohexanoic acid, B = beta-alanine and J = norleucine. B) General scheme of a PMO-chimera conjugate. C) Plot showing mean eGFP fluorescence of a population of stably transfected HeLa 654 cells after continuous treatment for 22 hours with 5  $\mu$ M of each PMO-peptide conjugate (n=3). The mean eGFP fluorescence was normalized to the eGFP fluorescence of untreated cells. Both PMO-Penetratin-Bpep and PMO-pVEC-Bpep demonstrated synergistic improvement in activity over the base PMO-peptide conjugates.

eGFP fluorescence compared to the background fluorescence of untreated cells. For reference, this is over a 20-fold improvement with respect to the unconjugated PMO and a two-fold improvement with respect to PMO-Bpep.

Both PMO-Penetratin-Bpep and PMO-pVEC-Bpep displayed synergy, in which the activity of the PMO-chimeric CPP was greater than the sum of the expected activities from each of the PMO-CPPs individually. For example, PMO-Penetratin demonstrated a 7-fold increase and PMO-Bpep demonstrated a 35-fold increase in eGFP fluorescence. An additive effect would lead to a 42-fold increase in eGFP fluorescence for PMO-Penetratin-Bpep. However, the PMO-Penetratin-Bpep chimera had an almost 70-fold increase in eGFP fluorescence, meaning it performed approximately 1.5 times better than an additive effect. A similar synergy was also observed for PMO-pVEC-Bpep, in which the measured eGFP fluorescence was also 1.5 times greater than the sum of the parts.

The existence of a synergistic effect in two of the chimeras supports the notion that combining an arginine-rich CPP with an amphipathic CPP can improve PMO efficacy. However, other variables could be responsible for the observed effects. In the context of the design space, the order of the individual peptides may influence PMO activity. Therefore, for each construct, we synthesized the peptide sequences with the order reversed where Bpep is on the N-terminal end and the other CPP is on the C-terminal end. After conjugation to PMO and purification by RP-HPLC, these conjugates were tested in the eGFP assay along with their counterparts that had Bpep on the C-terminal end. Interestingly, for both synergistic chimeras (PMO-Penetratin-Bpep and PMO-pVEC-Bpep), switching the order of the peptides decreased the mean fluorescence observed (Figure 3.2A). This observation suggests that it is critical to have Bpep as the C-terminal component to observe synergy.

One consequence of this result is that it raises the question of whether or not the N-terminal peptide has functional significance. Alternatively, the N-terminal peptide could serve as a spacer between the PMO and Bpep that amplifies the effect of Bpep. If this were true, it would explain why all four chimeras with Bpep on the C-terminal end performed similarly. To address this question, we prepared a chimera in which the N-terminal peptide was a polyproline spacer of similar length to the amphipathic CPPs (15 residues). PMO-P15-Bpep was evaluated in the eGFP assay, along with PMO-P15 and PMO-Bpep (Figure 3.2B). PMO-P15 exhibited lower efficacy than unconjugated PMO and PMO-P15-Bpep performed approximately the same as PMO-Bpep.

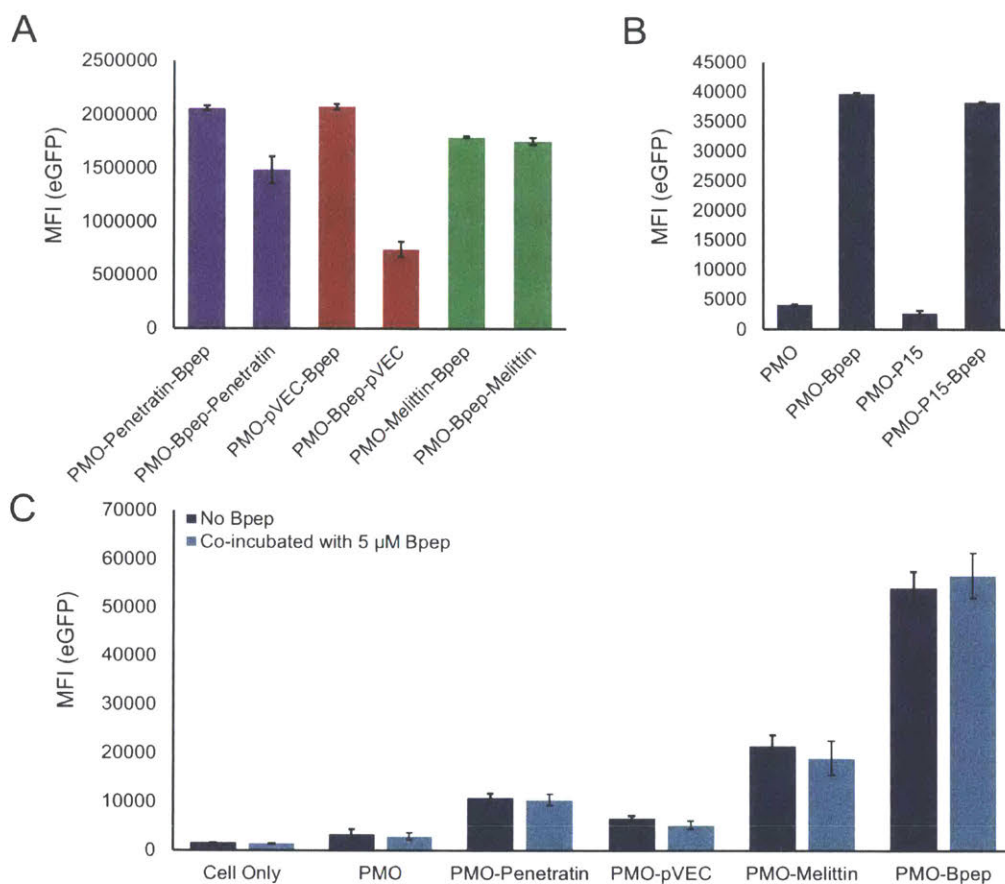


**Figure 3.2. Design principles of CPP chimeras.** A) For each chimera, the order of the sequences was reversed and the activity of the PMO-peptide conjugate was measured in the eGFP assay. The plot shows the mean fluorescence intensity of eGFP (n=3). B) Plot of the mean fluorescence intensity of eGFP for cells treated with 5  $\mu$ M of PMO, PMO-P15, PMO-Bpep or PMO-P15-Bpep for 22 hours (n=3). C) Comparison of eGFP mean fluorescence intensity for HeLa 654 cells treated with 5  $\mu$ M of each base PMO-CPP for 22 hours in the presence or absence of 5  $\mu$ M Bpep (n=3).

Given that the P15 spacer did not improve the effect of Bpep at all, these results support the notion that the identity of the N-terminal peptide has a functional consequence on the outcome of the chimeric CPP.

Next, we investigated the necessity of covalent attachment. The increase in PMO activity may or may not require the two component peptides of the chimera to be covalently attached. The eGFP assay was repeated with PMO-Penetratin, PMO-pVEC, PMO-Melittin and PMO-Bpep in the presence and absence of 5  $\mu$ M Bpep (Figure 3.2C). In all cases, the PMO-CPP conjugates performed identically in the presence and absence of Bpep. This result demonstrates that covalently linking the two CPPs is necessary to observe an improvement in activity. Co-incubation with Bpep did not result in any change in eGFP fluorescence.

Given concerns over the size and net charge of the constructs, a lactate dehydrogenase assay was performed to assess if the plasma membrane of the cells had been compromised in any way during treatment with the chimeric constructs (Figure 3.3). None of the constructs except for the PMO-Melittin-Bpep construct caused additional lactate dehydrogenase release compared to untreated cells, suggesting the majority of our chimeras do not disrupt the cell membrane.

We probed the mechanism by which these chimeric CPPs improve PMO efficacy. The eGFP HeLa cells provide a functional assay for PMO activity, yet many mechanistic steps contribute to this final read-out. Any of the PMO conjugates must be internalized into cells, escape endosomes if endocytosed, localize to the nucleus, and bind to pre-mRNA to generate any effect. The different parts of the chimera may be aiding in one or many of these steps. While it is challenging to conclusively demonstrate the exact mechanism given the complexity of the biological processes involved, we chose one model chimera to thoroughly study to gain additional insight. We chose to use PMO-pVEC-Bpep for this purpose, since it demonstrated synergy and did not disrupt the plasma membrane. Additionally, the poor performance of PMO-pVEC made the strong performance of PMO-pVEC-Bpep a surprising and intriguing result.

We commenced these mechanistic studies with experiments to assess cellular uptake pathways. To examine if energy-dependent pathways are involved, PMO activity was measured after treatment at 4 °C vs. 37 °C. The experiments were performed in a pulse-chase format in which the HeLa eGFP cells were incubated with 5  $\mu$ M PMO-pVEC, PMO-Bpep, or PMO-pVEC-Bpep for 3 hours at either 4 °C or 37 °C (Figure 3.4A). Then, the treatment media was exchanged for fresh media and the cells were allowed to grow for an additional 22 hours. For all compounds



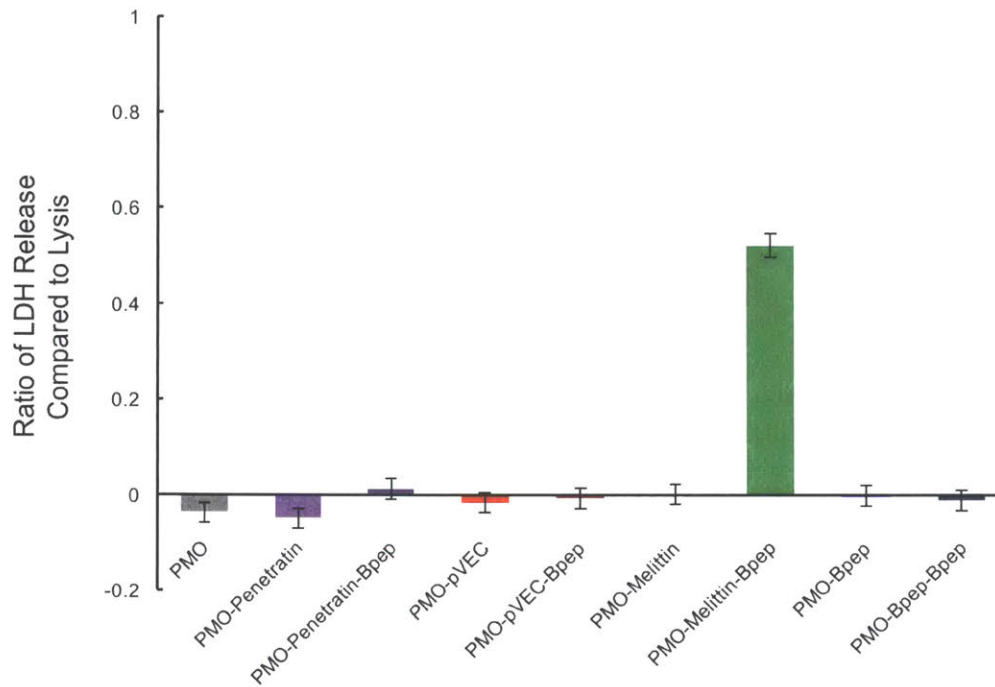


**Figure 3.3. LDH release from HeLa 654 cells upon treatment with 5  $\mu$ M PMO-peptide conjugate.** HeLa-654 cells were treated with each construct at 5  $\mu$ M for twenty-two hours. The y-axis is the ratio of LDH release compared with the cell lysis control. The only construct that demonstrated compromise of the cell membrane and early signs of cytotoxicity was PMO-Melittin-Bpep.

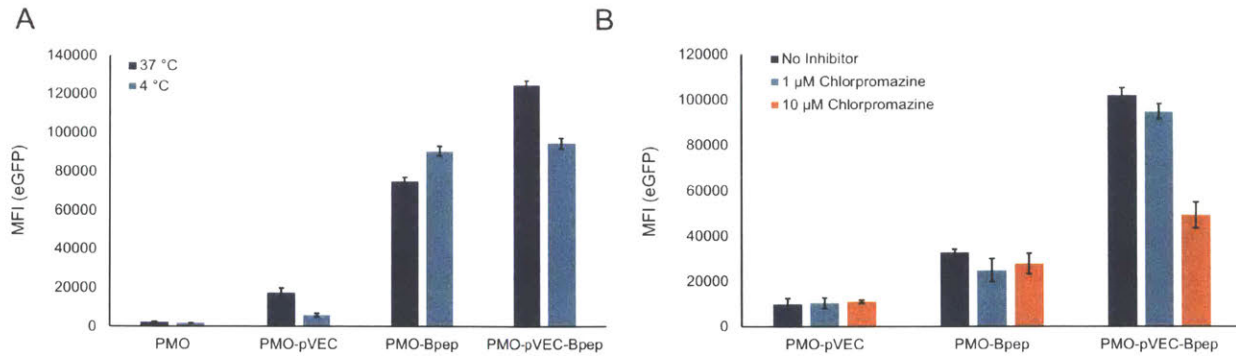


**Figure 3.4: Evaluation of mechanism of endocytosis for PMO-pVEC-Bpep conjugate.** A) Plot of eGFP mean fluorescence intensity for cells treated at either 37 °C and 4 °C (n=3). The cells were allowed to equilibrate to their respective temperatures for 30 minutes prior to treatment with 5 μM PMO, PMO-pVEC, PMO-Bpep, or PMO-pVEC-Bpep. After treatment with the constructs for 3 hours, the media was exchanged for fresh, untreated media and the cells from both conditions were incubated for another 22 hours at 37 °C. Both PMO-pVEC and PMO-pVEC-Bpep exhibited a reduction in uptake at 4 °C, suggesting that energy-dependent processes are relevant for uptake. B) Plot of eGFP mean fluorescence intensity for cells treated with different concentrations of chlorpromazine (n=3). The cells were pre-incubated for 30 minutes with chlorpromazine and then 5 μM PMO, PMO-pVEC, PMO-Bpep, or PMO-pVEC-Bpep was added. After treatment with the constructs for 3 hours, the media was exchanged for fresh, untreated media and the cells from both conditions were incubated for another 22 hours at 37 °C. At 10 μM chlorpromazine, eGFP fluorescence decreased only in the cells treated with the PMO-pVEC-Bpep chimera, suggesting that clathrin-mediated endocytosis plays a unique role in the uptake of the chimera.

except PMO-Bpep, there was a decrease in eGFP fluorescence when treated at 4 °C. This result suggests that energy-dependent mechanisms are relevant to the uptake of the PMO-pVEC-Bpep chimera. Of note particularly to the PMO-Bpep results is that any conjugate that binds to the surface of the cells during treatment at 4 °C could be subsequently internalized and trigger eGFP expression when the cells are incubated for an additional 22 hours at 37 °C after treatment.

In addition, we studied the effect of multiple endocytosis inhibitors on the internalization of PMO-pVEC, PMO-Bpep, and PMO-pVEC-Bpep into cells (Figure 3.4B). The experiments were performed in a pulse-chase format in which the eGFP HeLa cells were pre-incubated with the inhibitors. After thirty minutes of pre-incubation, the peptide was added and after three hours, the treatment media was exchanged with fresh media and the cells were left to grow for another 22 hours. The majority of the inhibitors had no effect. However, at high concentrations of chlorpromazine, eGFP fluorescence decreased in the cells treated with the PMO-pVEC-Bpep chimera. While chlorpromazine is considered an inhibitor of clathrin-mediated endocytosis, it may possibly affect downstream components of the process too. Beyond the possible role of clathrin-mediated endocytosis in the uptake of the chimera, these data demonstrate that the chimera is accessing a unique internalization mechanism since no appreciable decrease was observed with either PMO-pVEC or PMO-Bpep.

Finally, the constructs were labeled with a small molecule organic dye orthogonal to eGFP to allow simultaneous monitoring of the uptake of the compounds and functional exon-skipping activity. Experiments of this format could help deconvolute cellular internalization from PMO efficacy. To prepare these compounds, pVEC, Bpep and pVEC-Bpep were synthesized with a cysteine residue on the N-terminus of the sequence and the terminus was then capped with 4-pentynoic acid as before. After purification by RP-HPLC, the peptides were dissolved in water with equimolar Sulfo-Cyanine5 maleimide and purified again by RP-HPLC. Finally, the SulfoCy5-labeled peptides were all conjugated to the PMO-azide through copper-catalyzed click chemistry and purified by RP-HPLC.

Using the SulfoCy5-labeled constructs, we performed a flow cytometry experiment with the eGFP HeLa cells. The cells were treated with 5  $\mu$ M of each conjugate in serum-containing media for 22 hours and then analyzed by flow cytometry (Figure 3.5A). For eGFP fluorescence, the 488 nm excitation laser and 530 nm emission filter were used, and for the SulfoCy5, the 561 nm excitation laser and 695 nm emission filter were used. The separation of channels enabled

fluorescence from both fluorophores to be simultaneously recorded. We also treated with unlabeled PMO-pVEC, PMO-Bpep, and PMO-pVEC-Bpep to determine if the fluorophore was perturbing the effect of a given conjugate. In all cases, eGFP fluorescence was slightly decreased with the fluorophore attached suggesting that while the fluorophore may affect the efficacy of the conjugate, it does so uniformly (Figure 3.6).

In terms of SulfoCy5 fluorescence, PMO-SulfoCy5-Bpep exhibited less fluorescence than PMO-SulfoCy5-pVEC or PMO-SulfoCy5-pVEC-Bpep. However, PMO-SulfoCy5-Bpep had a relatively high ability to facilitate eGFP expression. This result suggests that while the overall cellular uptake of PMO-Bpep is less than PMO-pVEC, Bpep has a beneficial downstream effect. Perhaps improved endosomal escape, nuclear entry, RNA binding, or splice-modification results in the relatively high eGFP fluorescence for PMO-Bpep. On the other hand, PMO-SulfoCy5-pVEC had high SulfoCy5 fluorescence, but poor eGFP expression, which indicates that the compound has good cellular uptake but has limitations elsewhere downstream. The pVEC-Bpep chimera exhibited both the highest eGFP expression and the highest SulfoCy5 fluorescence, though the SulfoCy5 fluorescence was on a similar scale to pVEC. Therefore, our hypothesis for the basis of the chimera's synergy is that the pVEC component is improving cellular uptake without interfering with the beneficial downstream effects of Bpep.

To further test this hypothesis and examine to what extent the material localized to endosomes, we did live cell confocal microscopy imaging experiments on the HeLa eGFP cells. The same treatment conditions as the flow cytometry assay were used except that a Rab5a-RFP fusion protein was used to label early endosomes. After treatment and sixteen hours prior to imaging, the HeLa eGFP cells were transiently transfected with a Rab5a-RFP fusion construct utilizing a baculovirus vector. We reasoned that if PMO-SulfoCy5-pVEC had poor efficacy in triggering eGFP expression due to endosomal entrapment, the RFP signal would be co-localized with the SulfoCy5 signal.

The imaging data correlate very well with the flow cytometry data (Figure 3.5B). With both PMO-SulfoCy5-pVEC and PMO-SulfoCy5-pVEC-Bpep, the bright SulfoCy5 signal is concentrated in punctae. Some SulfoCy5 signal is co-localized with RFP signal, demonstrating localization to the early endosome, while other SulfoCy5 punctae are likely late endosomes and lysosomes. These images provide further evidence that the primary mechanism of internalization

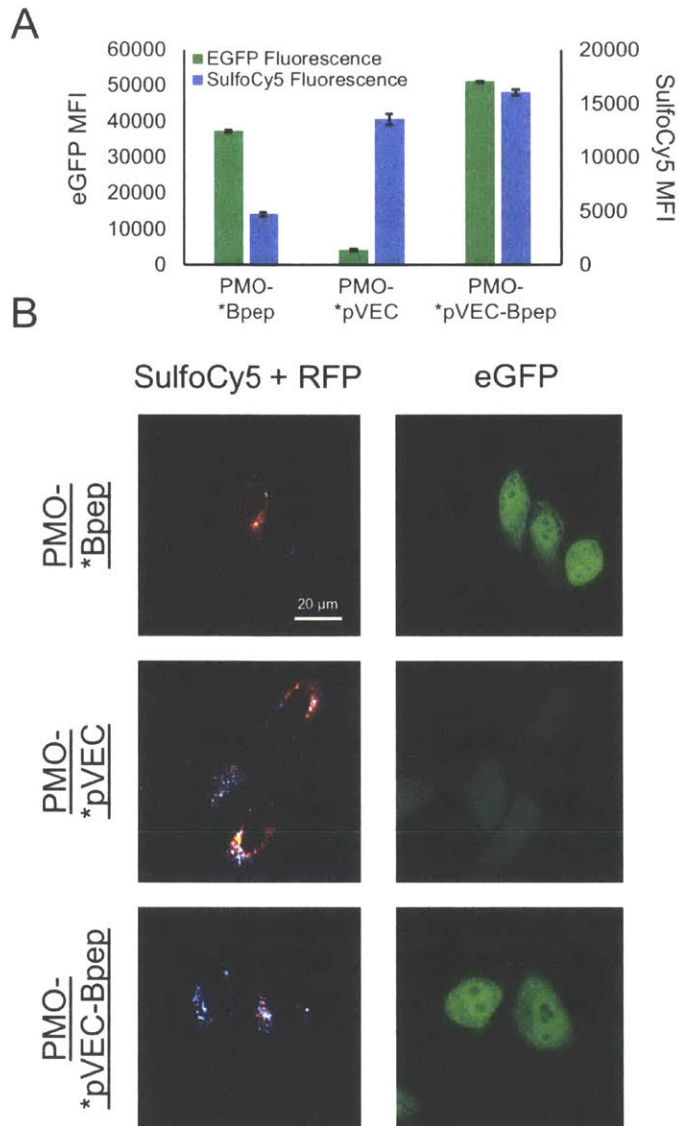


**Figure 3.5. Study of mechanism of synergy with fluorophore-labeled conjugates.** A) Plot showing the mean fluorescence intensity in each respective channel for eGFP and SulfoCy5 for HeLa 654 cells treated with 5  $\mu$ M PMO-SulfoCy5-pVEC, PMO-SulfoCy5-Bpep, or PMO-SulfoCy5-pVEC-Bpep for 22 hours at 37  $^{\circ}$ C (n=3). The left axis pertains to eGFP fluorescence and the right axis pertains to SulfoCy5 fluorescence. \*Peptide is a figure abbreviation for a PMO-SulfoCy5-Peptide construct. B) Live-cell confocal microscopy images of HeLa 654 cells after treatment with the same conditions as the flow cytometry experiments. The cells were also transiently transfected with an RFP-Rab5a fusion construct to label early endosomes (green - eGFP - PMO activity, red - RFP - early endosomes, cyan - SulfoCy5 - conjugates). For visualization of nuclei and brightfield images, see Section 3.6.

is endocytosis and that endosomal entrapment can limit PMO activity for certain constructs, despite significant cellular uptake.

Further experiments will be necessary to precisely define the effects downstream of internalization that are involved in the synergistic performance of the chimeras. However, here we show with our mechanistic studies that individual CPPs may be helpful with different elements of macromolecule delivery. We show that chimeric peptides composed of CPPs can exhibit synergistic improvements in PMO delivery and exon skipping efficiency. We show that the relative position of the sequences affects the degree of uptake, that both peptides must be CPPs, and that they must be covalently attached to observe the effect. One issue with this strategy is the large molecular weight of the resultant conjugates. One way to overcome this would be to create deletion analogues to identify the minimal necessary sequence to observe synergy. This will be the subject of future investigations with the Penetratin-Bpep and pVEC-Bpep chimeras.

Given that poor intracellular delivery has largely limited the therapeutic application of antisense oligonucleotides, we believe this strategy could help improve conjugate therapies for the treatment of several genetic diseases, such as Duchenne muscular dystrophy. More generally, we envision that the approach of combining CPPs from different classes can be applied to the intracellular delivery of a variety of macromolecular cargoes.

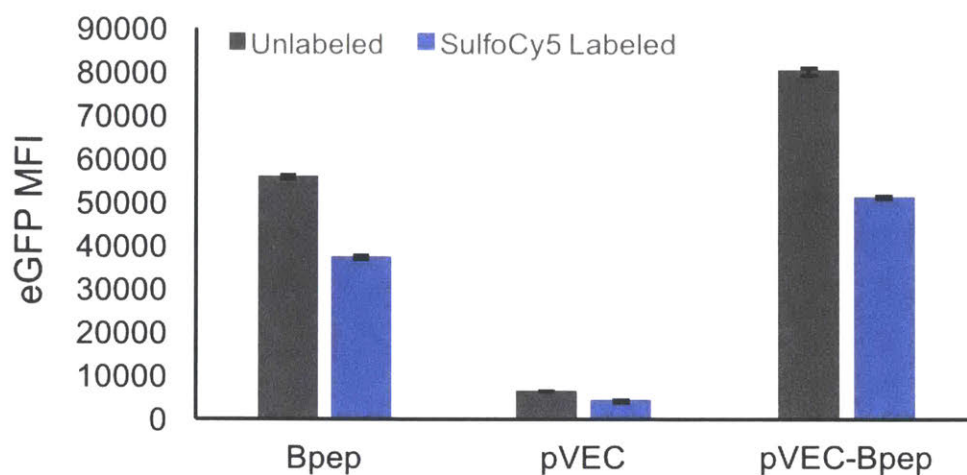


**Figure 3.6. Comparison of PMO activity of unlabeled PMO-peptide conjugates with SulfoCy5-labeled PMO-peptide conjugates.** The original unlabeled PMO-peptide conjugates were run side-by-side in the flow cytometry assay with the Sulfo-Cy5-labeled PMO-peptide conjugates to determine the extent to which SulfoCy5 perturbs the effect of the conjugates. In all cases, eGFP fluorescence was slightly decreased with SulfoCy5 attached, suggesting that while the fluorophore may affect the efficacy of the conjugate, it does so in a relatively uniform fashion.

### 3.3. Experimental

#### 3.3.1. Materials

H-Rink Amide-ChemMatrix resin was obtained from PCAS BioMatrix Inc. (St-Jean-sur-Richelieu, Quebec, Canada). 1-[Bis(dimethylamino)methylene]-1H-1,2,3-triazolo[4,5-b]pyridinium-3-oxid-hexafluorophosphate (HATU), 4-pentynoic acid, 5-azidopentanoic acid, Fmoc- $\beta$ -Ala-OH, and Fmoc-6-aminohexanoic acid were purchased from Chem-Impex International (Wood Dale, IL). Fmoc-L-Arg(Pbf)-OH, Fmoc-L-His(Trt)-OH, Fmoc-L-Lys(Boc)-OH, Fmoc-L-Asp(tBu)-OH, Fmoc-L-Glu(tBu)-OH, Fmoc-L-Ser(tBu)-OH, Fmoc-L-Thr(tBu)-OH, Fmoc-L-Asn(Trt)-OH, Fmoc-L-Gln(Trt)-OH, Fmoc-L-Cys(Trt)-OH, Fmoc-L-Gly-OH, Fmoc-L-Ala-OH, Fmoc-L-Val-OH, Fmoc-L-Leu-OH, Fmoc-L-Ile-OH, Fmoc-L-Met-OH, Fmoc-L-Phe-OH, Fmoc-L-Pro-OH, Fmoc-L-Tyr(tBu)-OH, and Fmoc-L-Trp(Boc)-OH were purchased from Advanced ChemTech (Louisville, KY). PyAOP was purchased from P3 BioSystems (Louisville, KY). Sulfo-Cy5-Maleimide was purchased from Lumiprobe Corporation (Hallandale Beach, FL). Peptide synthesis-grade N,N-dimethylformamide (DMF), CH<sub>2</sub>Cl<sub>2</sub>, diethyl ether, and HPLC-grade acetonitrile were obtained from VWR International (Radnor, PA). Cytochalasin D was obtained from Santa Cruz Biotech. The LDH Assay kit was purchased from Promega (Madison, WI). All other reagents were purchased from Sigma-Aldrich (St. Louis, MO). Milli-Q water was used exclusively. HeLa-654 cells were obtained from the University of North Carolina Tissue Culture Core facility.

#### 3.3.2. Methods for LC-MS Analysis

LC-MS analyses were performed on an Agilent 6520 ESI-Q-TOF mass spectrometer equipped with a C<sub>3</sub> Zorbax column (300SB C3, 2.1 x 150 mm, 5  $\mu$ m). Mobile phases were: 0.1% formic acid in water (solvent A) and 0.1% formic acid in acetonitrile (solvent B). The following LC-MS methods were used for characterization:

**Method A:** 5% B from 0 to 2 min, linear ramp from 5% B to 65% B from 2 to 11 min, 65% B from 11 to 12 min and finally 3 min of post-time at 5% B for equilibration, flow rate: 0.8 mL/min.

**Method B:** 1% B from 0 to 2 min, linear ramp from 1% B to 61% B from 2 to 11 min, 61% B to 99% B from 11 to 12 min and finally 3 min of post-time at 1% B for equilibration, flow rate: 0.8 mL/min.



Chromatograms were obtained using Method B unless otherwise noted. All data were processed using Agilent MassHunter software package. Y-axis in all chromatograms shown represents total ion current (TIC) unless noted.

### 3.3.3. General Method for Peptide Preparation

*Fast-flow Peptide Synthesis:* Peptides were synthesized on a 0.1-mmol scale using an automated flow peptide synthesizer.<sup>28</sup> A 200 mg portion of ChemMatrix Rink Amide HYR resin was loaded into a reactor maintained at 90 °C. All reagents were flowed at 80 mL/min with HPLC pumps through a stainless-steel loop maintained at 90 °C before introduction into the reactor. For each coupling, 10 mL of a solution containing 0.2 M amino acid and 0.17 M HATU in DMF were mixed with 200  $\mu$ L diisopropylethylamine and delivered to the reactor. Fmoc removal was accomplished using 10.4 mL of 20% (v/v) piperidine. Between each step, DMF (15 mL) was used to wash out the reactor. Special coupling conditions were used for arginine, in which the flow rate was reduced to 40 mL/min and 15 mL of a solution containing 0.2 M Fmoc-L-Arg(Pbf)-OH and 0.17 M PyAOP in DMF were mixed with 200  $\mu$ L diisopropylethylamine and delivered to the reactor. To cap the peptide with 4-pentynoic acid, the resin was incubated for 30 min at room temperature with 4-pentynoic acid (1 mmol) dissolved in 2.5 mL 0.4 M HATU in DMF with 500  $\mu$ L diisopropylethylamine. After completion of the synthesis, the resins were washed 3 times with DCM and dried under vacuum.

*Peptide Cleavage and Deprotection:* Each peptide was subjected to simultaneous global side-chain deprotection and cleavage from resin by treatment with 5 mL of 94% trifluoroacetic acid (TFA), 2.5% 1,2-ethanedithiol (EDT), 2.5% water, and 1% triisopropylsilane (TIPS) (v/v) for 7 min at 60 °C. For arginine-rich sequences, the resin was treated with a cleavage cocktail consisting of 82.5% TFA, 5% phenol, 5% thioanisole, 5% water, and 2.5% EDT (v/v) for 14 hours at room temperature. The TFA was evaporated by bubbling N<sub>2</sub> through the mixture. Then ~40 mL of cold ether (chilled at -80°C) was added to precipitate and wash the peptide. The crude product was pelleted through centrifugation for 3 min at 4,000 rpm and the ether decanted. The ether precipitation and centrifugation was repeated two more times. After the third wash, the pellet was redissolved in 50% water and 50% acetonitrile containing 0.1% TFA, filtered through a fritted syringe to remove the resin and lyophilized.

*Peptide Purification:* The peptides were redissolved in water and acetonitrile containing 0.1% TFA, filtered through a 0.22  $\mu$ m nylon filter and purified by mass-directed semi-preparative

reversed-phase HPLC. Solvent A was water with 0.1% TFA additive and Solvent B was acetonitrile with 0.1% TFA additive. A linear gradient that changed at a rate of 0.5%/min was used. Most of the peptides were purified on an Agilent Zorbax SB C3 column: 9.4 x 250 mm, 5  $\mu$ m. Extremely hydrophilic peptides, such as the arginine-rich sequences were purified on an Agilent Zorbax SB C18 column: 9.4 x 250 mm, 5  $\mu$ m. Using mass data about each fraction from the instrument, only pure fractions were pooled and lyophilized. The purity of the fraction pool was confirmed by LC-MS.

#### **3.3.4. PMO Azide Synthesis**

PMO IVS-654 (200 mg, 32  $\mu$ mol) was dissolved in 600  $\mu$ L DMSO. To the solution was added a solution containing 4 equivalents of 5-azidopentanoic acid (13.6  $\mu$ L, 128  $\mu$ mol) activated with HBTU (320  $\mu$ L of 0.4 M HBTU in DMF, 128  $\mu$ mol) and DIEA (22.3  $\mu$ L, 128  $\mu$ mol) in 244  $\mu$ L DMF (Final reaction volume = 1.2 mL). The reaction proceeded for 25 min before being quenched with 1 mL of water and 2 mL of ammonium hydroxide. The ammonium hydroxide will hydrolyze any ester formed during the course of the reaction. After 1 hour, the solution was diluted to 40 mL and purified using reversed-phase HPLC (Agilent Zorbax SB C3 column: 21.2 x 100 mm, 5  $\mu$ m) and a linear gradient from 2 to 60% B (solvent A: water; solvent B: acetonitrile) over 58 min (1% B / min). Using mass data about each fraction from the instrument, only pure fractions were pooled and lyophilized. The purity of the fraction pool was confirmed by LC-MS.

#### **3.3.5. SulfoCy5-Maleimide Conjugation**

For fluorophore-labeled PMO-peptide conjugates, the organic dye was attached prior to conjugation to PMO. Equimolar SulfoCy5-maleimide was conjugated to cysteine-containing peptides in 1 mL of H<sub>2</sub>O. After 30 minutes, the reactions were purified by reversed-phase HPLC using a linear gradient from 5-45% B over 80 minutes for pVEC and pVEC-Bpep and a linear gradient from 1-31% B over 60 minutes for Bpep. Mobile phase A: water with 0.1% TFA. Mobile phase B: acetonitrile with 0.1% TFA. For LC-MS characterization of SulfoCy5-peptide conjugates, please see Section 3.5.

#### **3.3.6. PMO-Peptide Conjugation with Cu(I)-Catalyzed Azide-Alkyne Cycloaddition**

PMO-peptide conjugates were synthesized using Cu(I)-catalyzed azide-alkyne 1,3-dipolar cycloaddition using copper(I) bromide in DMF. PMO-azide (0.95  $\mu$ mol), Peptide-alkyne (1.1  $\mu$ mol), and copper(I) bromide (0.05 mmol) powders were added to a septum vial (note: the amount of PMO-azide ranged from 0.63-0.95  $\mu$ mol). The vial was flushed with N<sub>2</sub> for 2 min, 1 mL dry

DMF was added, and the vial was vortexed. The reaction was allowed to proceed for 1 hour. The reaction was quenched with the addition of 10 mL of 50 mM Tris in water (pH 8).

Our optimized purification procedure was using reversed-phase HPLC with a linear gradient from 5-45% B over 20 min (Agilent Zorbax SB C3 9.4 x 50 mm, 5  $\mu$ m). Mobile phase A: 100 mM ammonium acetate pH 7.2 in water. Mobile phase B: acetonitrile. Using mass data about each fraction from the instrument, only pure fractions were pooled and lyophilized. The purity of the fraction pool was confirmed by LC-MS.

### **3.3.7. Flow Cytometry Assay for PMO-Peptide Conjugates**

HeLa 654 cells were maintained in MEM supplemented with 10% (v/v) fetal bovine serum (FBS) and 1% (v/v) penicillin-streptomycin at 37 °C and 5% CO<sub>2</sub>. Eighteen hours prior to treatment, the cells were plated at a density of 5,000 cells per well in a 96-well plate in MEM supplemented with 10% FBS and 1% penicillin-streptomycin. The day of the experiment, stocks of each PMO-peptide conjugate were prepared in phosphate-buffered serum (PBS). The concentration of the stocks was determined by measuring the absorbance at 260 nm and using an extinction coefficient of 168,700 L mol<sup>-1</sup> cm<sup>-1</sup>. Cells were incubated with each respective conjugate at a concentration of 5  $\mu$ M in MEM supplemented with 10% FBS and 1% penicillin-streptomycin for 22 hours at 37 °C and 5% CO<sub>2</sub>. Next, the treatment media was aspirated the cells were incubated with Trypsin-EDTA 0.25 % for 15 min at 37 °C and 5% CO<sub>2</sub>, washed 1x with PBS, and resuspended in PBS with 2% FBS and 2  $\mu$ g/mL propidium iodide. Flow cytometry analysis was carried out on a BD LSRII flow cytometer. Gates were applied to the data to ensure that cells that were highly positive for propidium iodide or had forward/side scatter readings that were sufficiently different from the main cell population were excluded. Each histogram contains at least 3,000 gated events, with the exception of cells treated with PMO-Melittin-Bpep.

### **3.3.8. Flow Cytometry Assay for SulfoCy5-Labeled PMO-Peptide Conjugates**

HeLa-654 cells were maintained in MEM supplemented with 10% (v/v) fetal bovine serum and 1% (v/v) penicillin-streptomycin at 37 °C and 5% CO<sub>2</sub>. Twenty-four hours before treatment, HeLa cells were plated at a density of 5,000 cells per well in a 96-well plate. The next day, fresh 1 mM stocks of each of the SulfoCy5-PMO-peptide conjugates in DMSO, as well as the respective unlabeled PMO-peptide controls in DMSO, were prepared. The concentration of the stocks was determined by measuring the absorbance at 260 nm and using an extinction coefficient of 168,700 L mol<sup>-1</sup> cm<sup>-1</sup>. The growth media was aspirated from the cells and treatment media consisting of

each respective conjugate 5  $\mu$ M concentration in MEM supplemented with 10% FBS and 1% penicillin-streptomycin was added. The cells were incubated with treatment-containing media for 22 hours at 37 °C and 5% CO<sub>2</sub>. Next, the treatment media was aspirated. Trypsin-EDTA 0.25 % (20  $\mu$ L) was added to the cells and incubated for 15 min at 37 °C and 5% CO<sub>2</sub>. To quench the trypsin, 80  $\mu$ L of MEM supplemented with 10% (v/v) fetal bovine serum and 1% (v/v) Pen Strep was added to each well. The dissociated cells in media were transferred with a multichannel pipet to a polypropylene v-bottom 96-well plate (Falcon) and centrifuged at 500 rcf for 3 min. The supernatant was removed, the cell pellets were resuspended with 200  $\mu$ L of phosphate-buffered saline (PBS), and the plate was centrifuged again. The supernatant was again removed and the pellets were resuspended in 300  $\mu$ L PBS with 2% FBS (v/v) and 2  $\mu$ g/mL propidium iodide in water. Flow cytometry analysis was carried out on a BD LSRII flow cytometer. For eGFP fluorescence, the 488 nm excitation laser and 530 nm emission filter were used, and for the SulfoCy5, the 561 nm excitation laser and 695 nm emission filter were used. The separation of channels enabled fluorescence from both fluorophores to be simultaneously recorded. Gates were applied to the data to ensure that only data from healthy, living cells were taken into account. Cells that were highly positive for propidium iodide or had forward/side scatter readings that were sufficiently different from the main cell population were excluded. Each histogram contained at least 3,000 gated events.

### **3.3.9. Flow Cytometry Analysis with Endocytosis Inhibitors**

To inhibit a variety of endocytic mechanisms, a pulse-chase experiment was performed. Cells were treated using stock solutions of each inhibitor dissolved in the following solutions: chlorpromazine - 10 mM in water; cytochalasin D - 10 mM in DMSO; wortmannin - 2 mM in DMSO; MBCD - 5 mM in cell culture media; EIPA - 10 mM in DMSO; dynasore - 10 mM in DMSO. Briefly, HeLa 654 cells were plated at a density of 5,000 cells per well in a 96-well plate in MEM supplemented with 10% FBS and 1% penicillin-streptomycin. The next day, the cells were treated with each inhibitor at the indicated concentration. After 30 minutes, PMO-peptide conjugate was added to each well at a concentration of 5  $\mu$ M. After incubation at 37 °C and 5% CO<sub>2</sub> for 3 hours, the treatment media was replaced with fresh media (containing neither inhibitor nor PMO-peptide) and the cells were allowed to grow for another 22 hours at 37 °C and 5% CO<sub>2</sub>. For the 4 °C experiments, the day after plating, the cells were pre-incubated for 30 minutes at 4 °C, followed by the addition of PMO-peptide conjugate to each well at a concentration of 5  $\mu$ M.

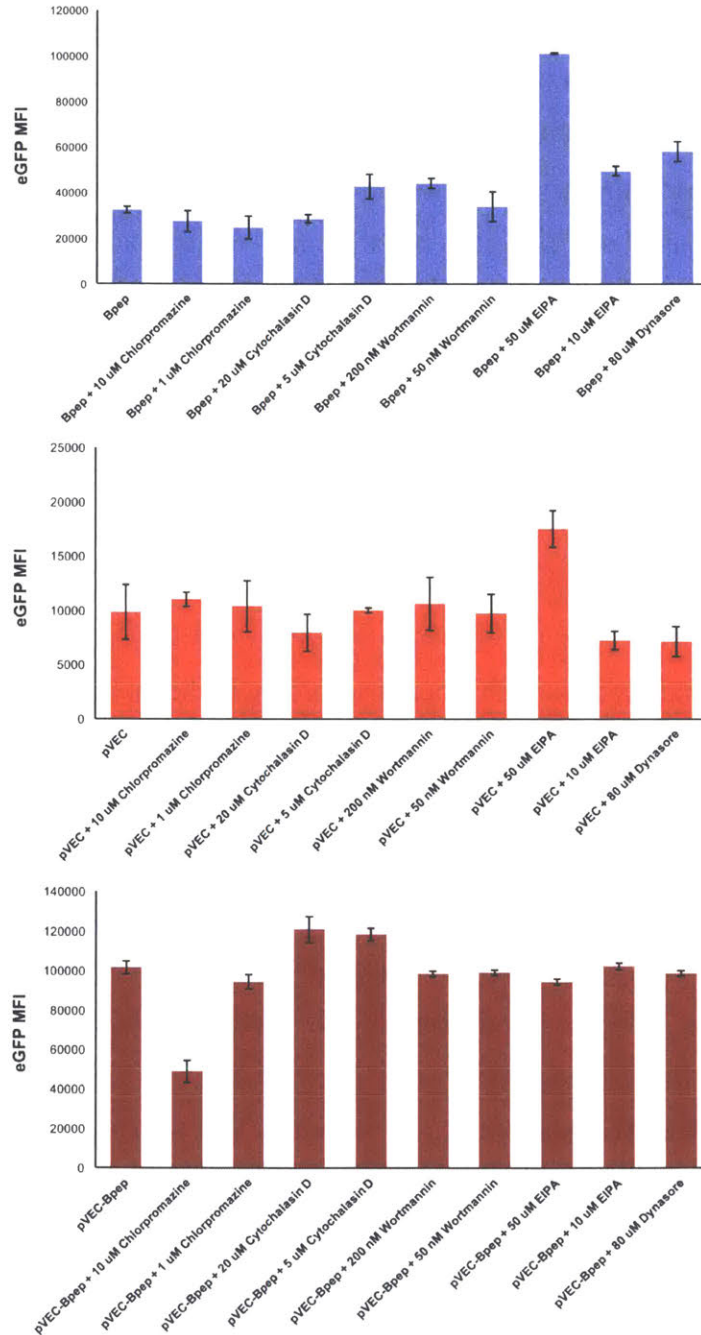


**Figure 3.7. Effect of endocytosis inhibitors on PMO-Bpep, PMO-pVEC, and PMO-pVEC-Bpep efficacy.** HeLa-654 cells were treated with each inhibitor in a pulse-chase experiment as described in the main text. After treatment, the mean fluorescence intensity of eGFP is measured by flow cytometry. Bpep, pVEC, and pVEC-Bpep are used as shorthand for the PMO-Bpep, PMO-pVEC and PMO-pVEC-Bpep conjugates. EIPA is 5-(N-Ethyl-N-isopropyl)amiloride.

After incubation at 4 °C for 3 hours, the treatment media was replaced with fresh media and the cells were allowed to grow for another 22 hours at 37 °C and 5% CO<sub>2</sub>. Sample preparation and flow cytometry was then performed as described above. Each histogram contains at least 3,000 gated events, with the exception of treatment with 20 μM cytochalasin D.

### **3.3.10. Lactate Dehydrogenase (LDH) Assay**

HeLa-654 cells were maintained in MEM supplemented with 10% (v/v) fetal bovine serum and 1% (v/v) penicillin-streptomycin at 37 °C and 5% CO<sub>2</sub>. Eighteen hours before treatment, HeLa cells were plated at a density of 5,000 cells per well in a 96-well plate. The next day, fresh 1 mM stocks of each of PMO-peptide conjugate were prepared in PBS. The concentration of the stocks was determined by measuring the absorbance at 260 nm and using an extinction coefficient of 168,700 L mol<sup>-1</sup> cm<sup>-1</sup>. The growth media was aspirated from the cells and treatment media was added with each respective conjugate at a concentration of 5 μM in MEM supplemented with 10% FBS and 1% penicillin-streptomycin. The cells were incubated with treatment-containing media for 22 hours at 37 °C and 5% CO<sub>2</sub>. Next, the supernatant treatment media was transferred to another clear-bottom 96-well plate for the assay. The assay was performed using the CytoTox 96® Non-Radioactive Cytotoxicity Assay (Promega) according to the included technical bulletin. After completion of the assay, the final solution in each well was diluted 1:4 with PBS such that the measured absorbance was in the linear range of the instrument. The absorbance was measured on a BioTek Epoch Microplate Spectrophotometer at 490 nm. The positive control is a cell lysis and the negative control is untreated cells. The data are worked up by subtracting the absorbance of untreated cells from all of the treatment conditions, including the cell lysis, and then dividing by the corrected lysis value. A value of 0 reflects no additional LDH release over cell baseline and a value of 1 reflects total LDH release.

### **3.3.11. Live Cell Confocal Imaging**

HeLa-654 cells were plated at a density of 5,000 cells per well in a #1.5 coverslip glass-bottom 96-well plate in MEM supplemented with 10% (v/v) fetal bovine serum and 1% (v/v) penicillin-streptomycin. The next day, fresh 1 mM stocks of each PMO-SulfoCy5-peptide conjugate were prepared in DMSO. The concentration of the stocks was determined by measuring the absorbance at 260 nm and using an extinction coefficient of 168,700 L mol<sup>-1</sup> cm<sup>-1</sup>. Twenty-four hours after plating, the growth media was aspirated and the cells were treated with media containing each PMO-SulfoCy5-peptide conjugate at a concentration of 5 μM in MEM

supplemented with 10% FBS and 1% penicillin-streptomycin. Six hours after that (sixteen hours prior to imaging), 3  $\mu\text{L}$  of CellLight™ Early Endosomes-RFP, BacMam 2.0 was added to each well (corresponding to 30 particles per cell). After 22 hours of total PMO treatment, the treatment media was aspirated, the cells were washed twice with PBS (5 min for each wash), and the cells were stained for 10 min with 2  $\mu\text{g}/\text{mL}$  Hoescht in PBS followed by two more PBS washes (5 min for each wash). Finally, the cells were imaged in PBS on a spinning disk confocal microscope composed of a Yokogawa CSU-22 spinning disk confocal scan head with Borealis modification, Zeiss AxioVert 200M inverted microscope stand with DIC optics, six lasers, a Hamamatsu Orca-ER cooled CCD camera, and MetaMorph acquisition software. The images were acquired with the 63x objective and processed using FIJI.

### **3.4. Acknowledgments**

This work was supported by Sarepta Therapeutics, Cambridge MA. J.M.W. and R.L.H are supported by the National Science Foundation Graduate Research Fellowship under Grant No. 1122374. C.M.F. is supported by the David H. Koch Graduate Fellowship Fund and by the Eunice Kennedy Shriver National Institute of Child Health and Human Development of the National Institutes of Health under award number F30HD093358. The authors acknowledge the Swanson Biotechnology Center Flow Cytometry Facility at the Koch Institute for advice and the use of their flow cytometers. The authors also acknowledge Wendy Salmon and the W.M. Keck Biological Imaging Facility at the Whitehead Institute for advice and the use of their confocal microscope. We thank Ethan Evans and Dr. Alan Beggs for helpful discussions.



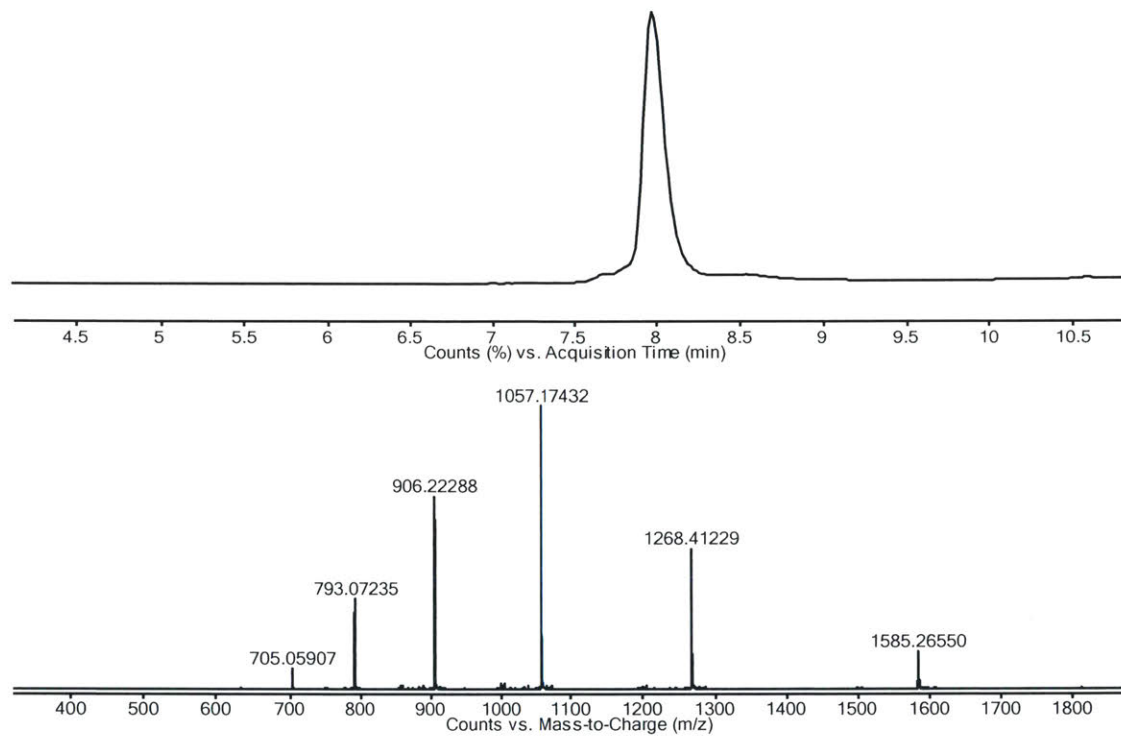
### 3.5. Appendix of LC-MS Characterization

*Note:* Chromatograms were obtained using Method B unless otherwise noted.

PMO-Azide

Mass expected: 6337.5 Da

Mass observed: 6337.9 Da

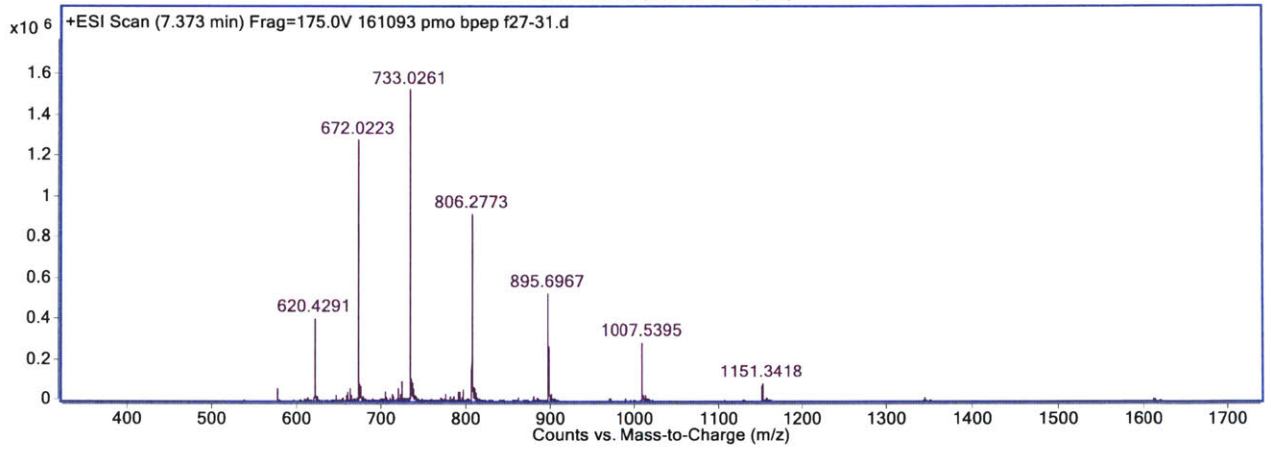
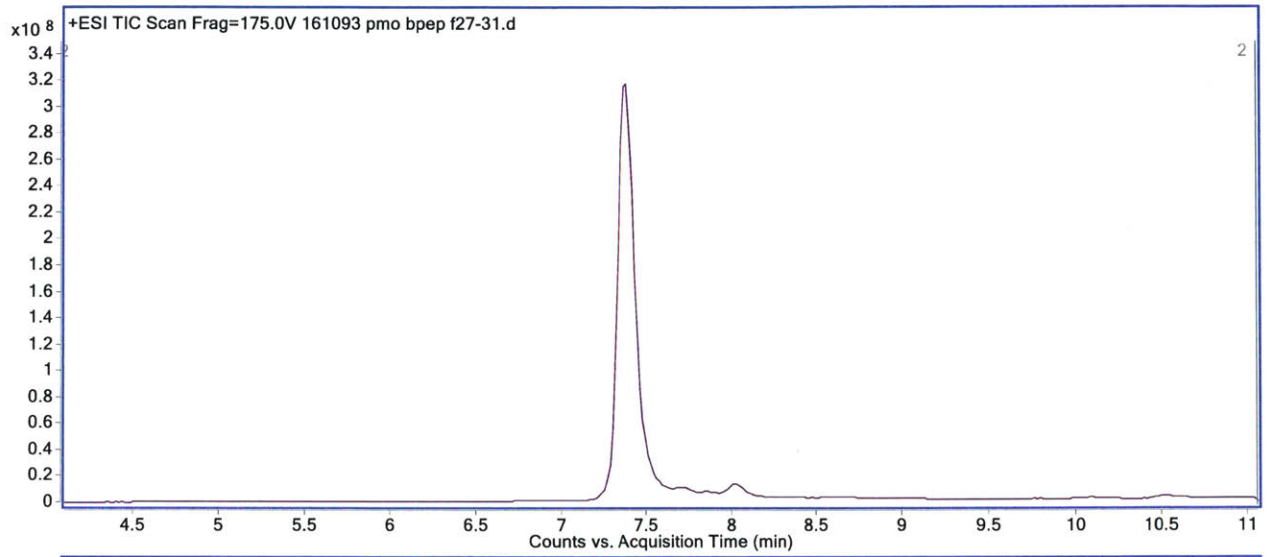


PMO-Bpep

Mass Expected: 8052.5 Da

Mass Observed: 8053.0 Da

Peptide Sequence: RXRRBRRXRRBR

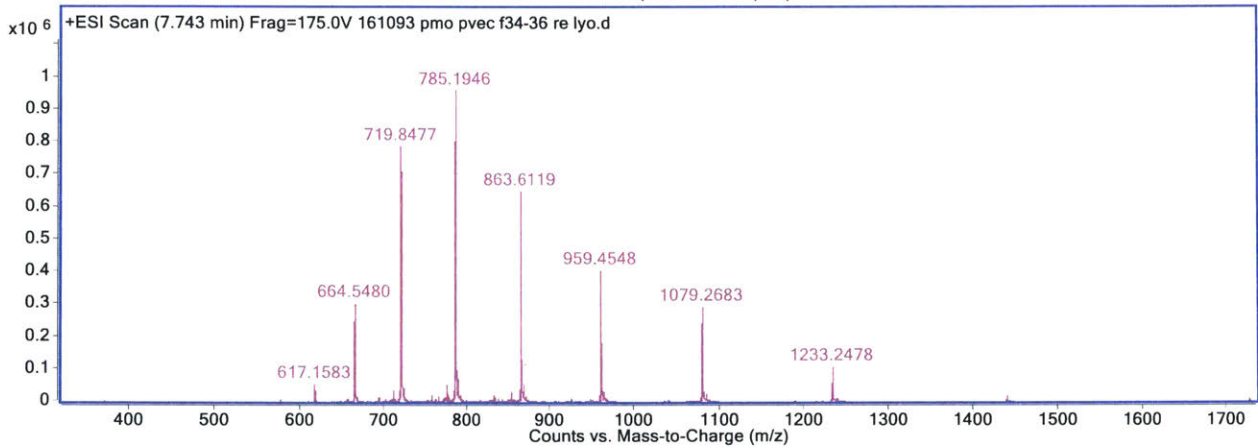
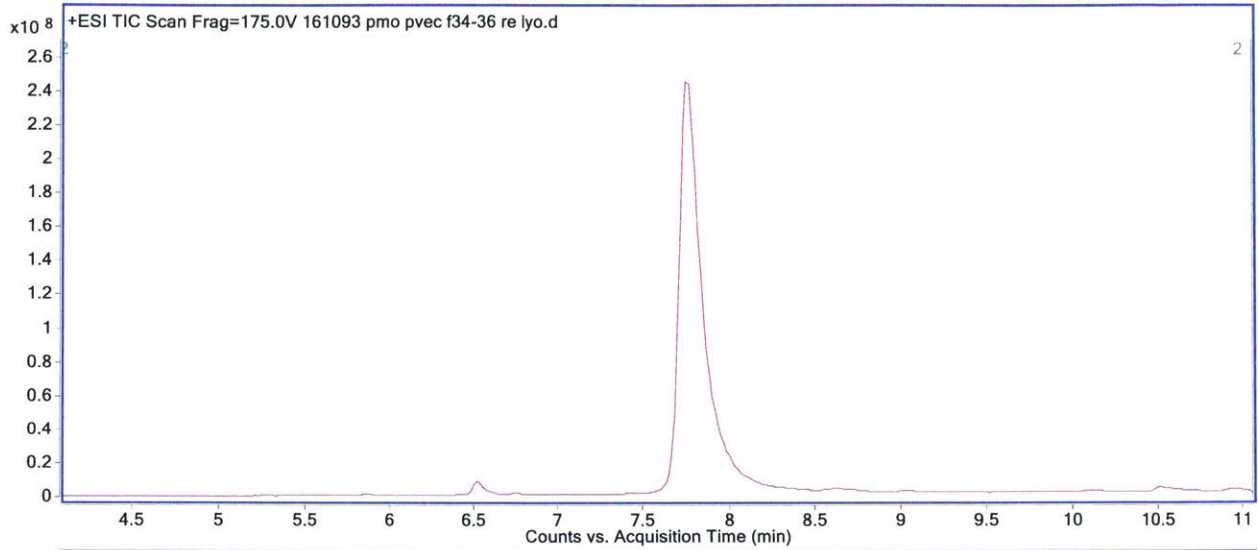


PMO-pVEC

Mass Expected: 8626.3 Da

Mass Observed: 8626.8 Da

Peptide Sequence: LLILRRRIRKQAHHSK

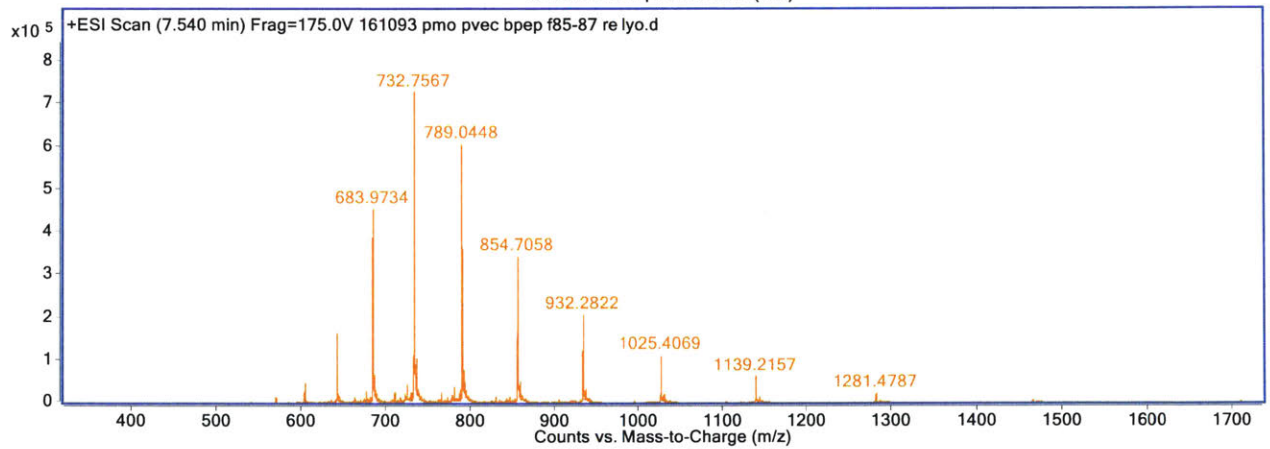
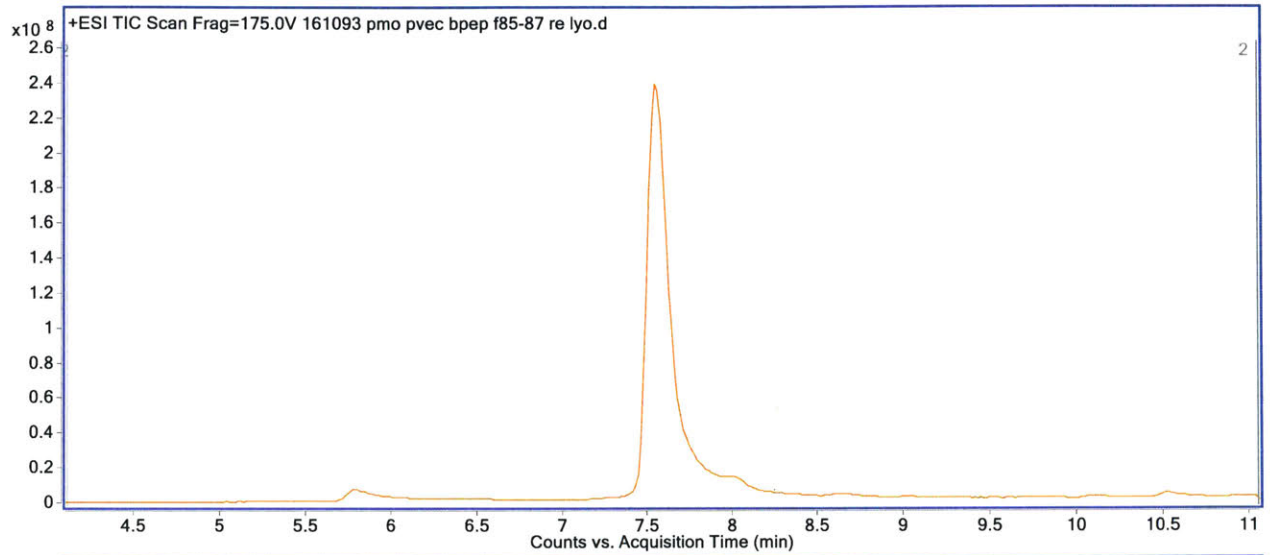


PMO-pVEC-Bpep

Mass Expected: 10244.3 Da

Mass Observed: 10244.7 Da

Peptide Sequence: LLILRRRIRKQAHHSKRXXRRBRRXRBR



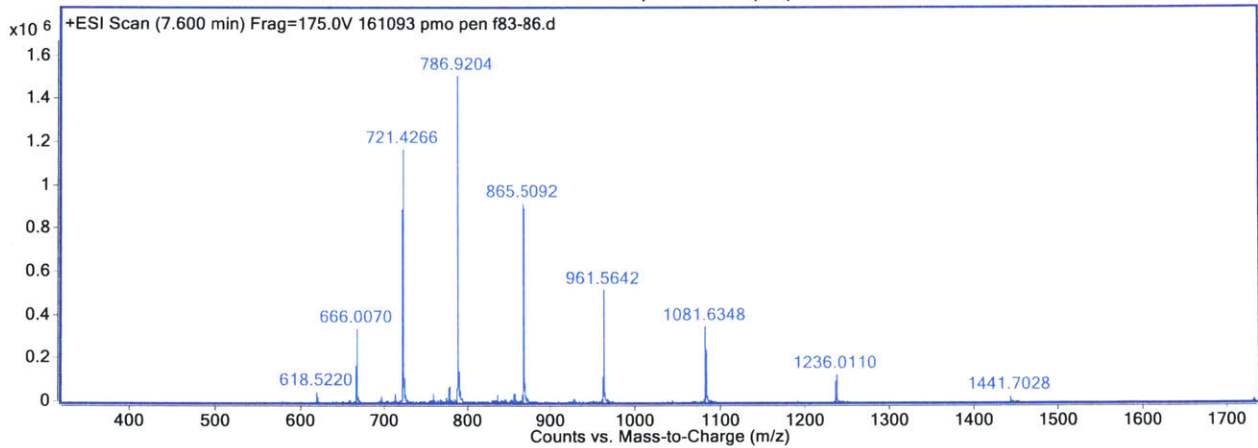
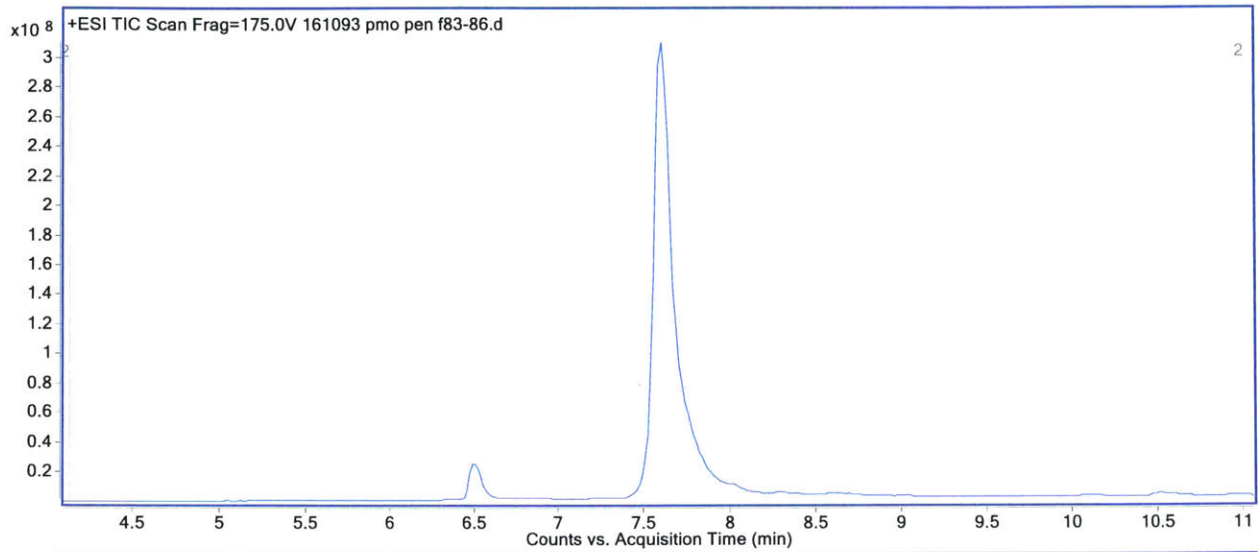
PMO-Penetratin

Mass Expected: 8645.3 Da

Mass Observed: 8645.8 Da

Peptide Sequence: RQIKIWFQNRRJKWKK

*J* = norleucine

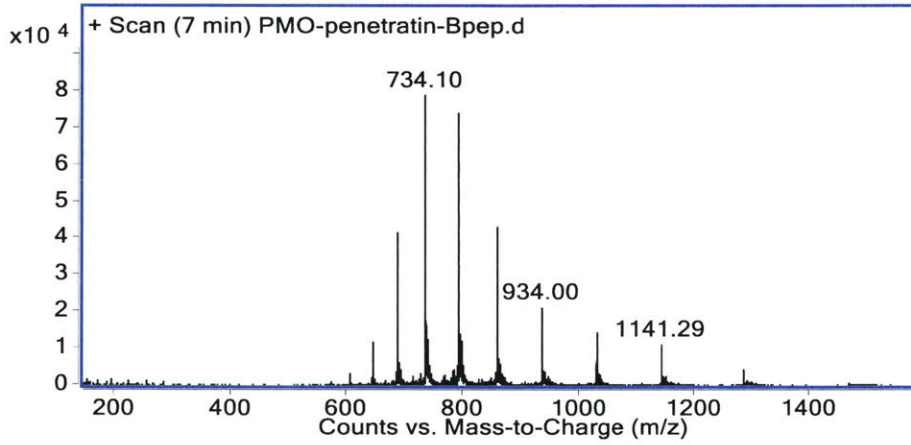
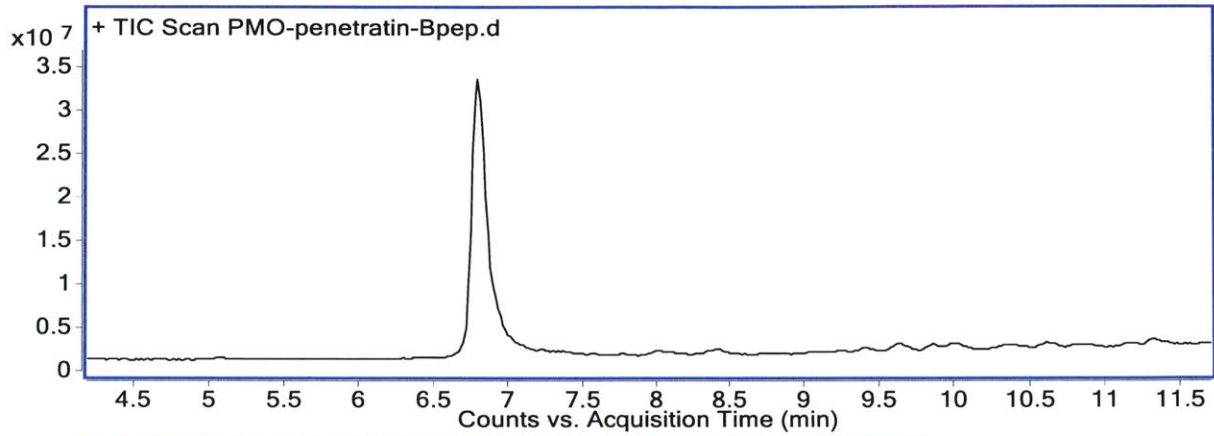


PMO-Penetratin-Bpep

Mass Expected: 10263.3 Da

Mass Observed: 10263.6 Da

Peptide Sequence: RQIKIWFQNRRJKWKKR<sup>+</sup>RRBRRXRRBR

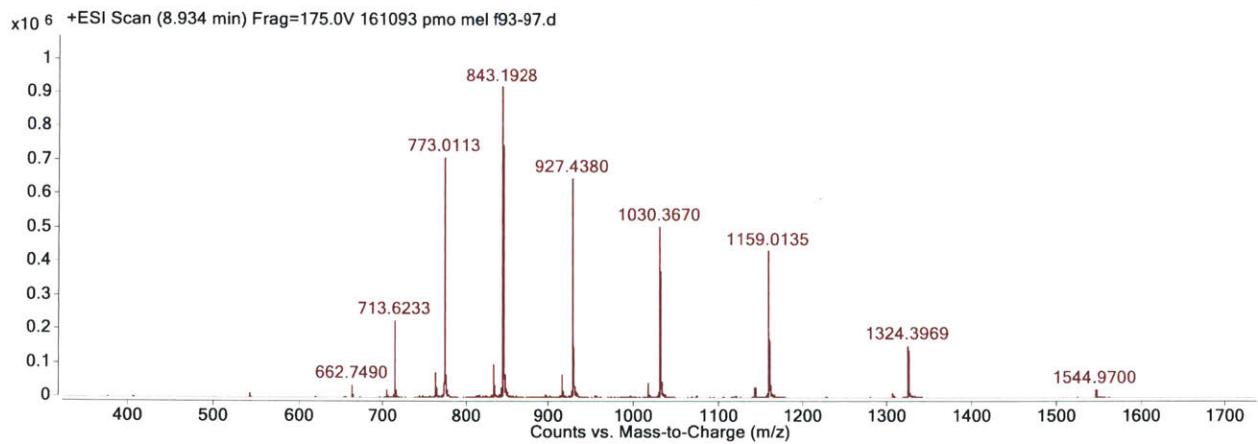
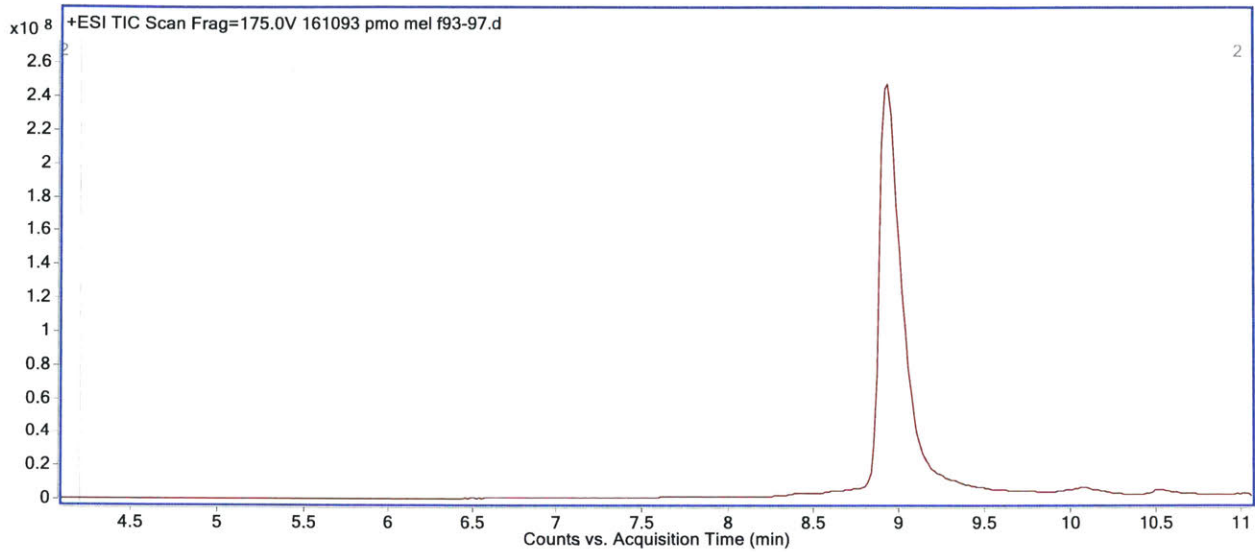


PMO-Melittin

Mass Expected: 9264.1 Da

Mass Observed: 9264.6 Da

Peptide Sequence: GIGAVLKVLTTGLPALISWIKRKRQQ

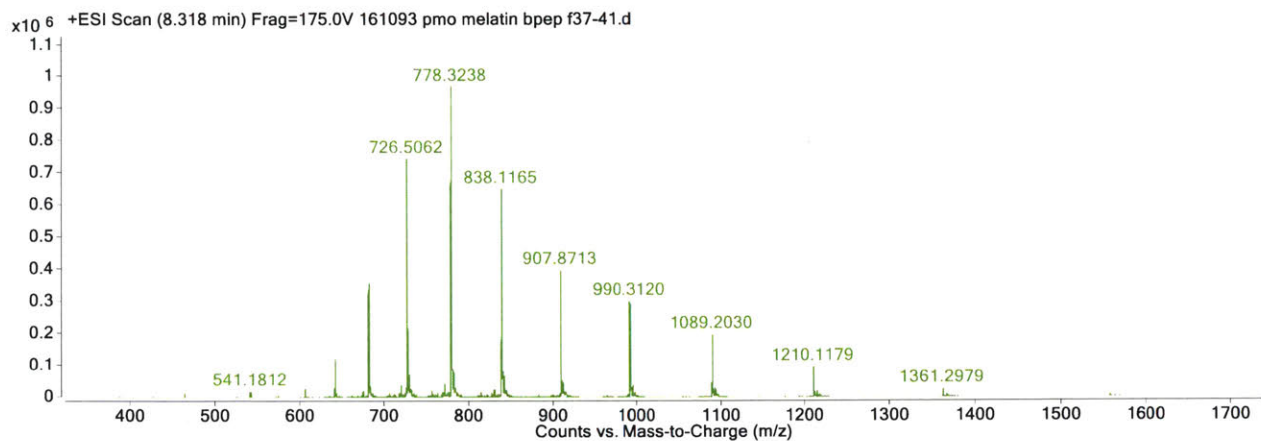
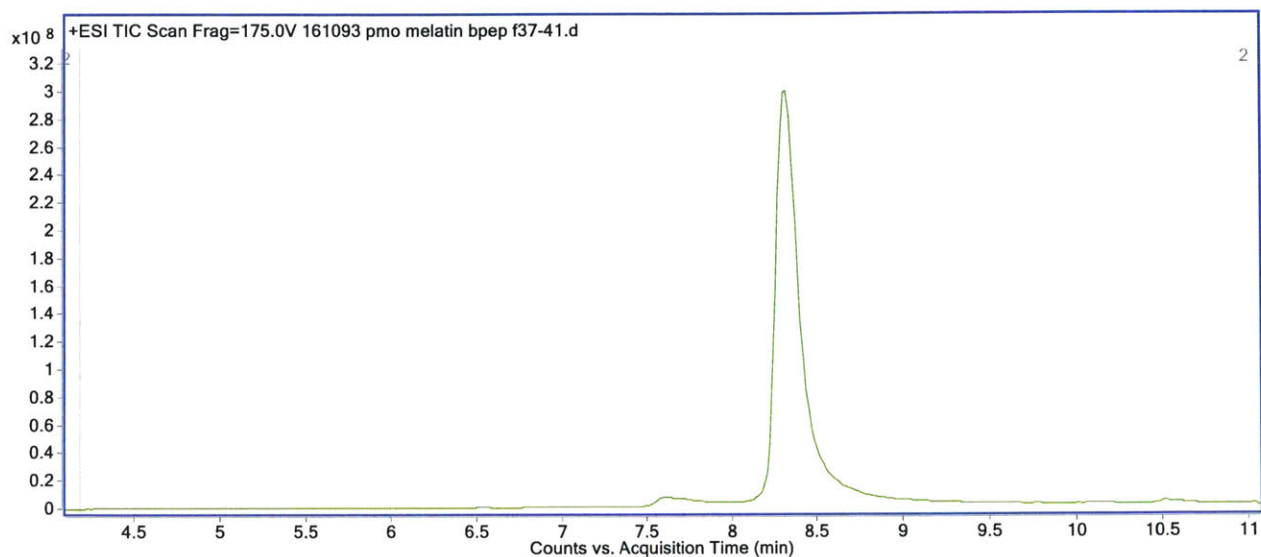


PMO-Melittin-Bpep

Mass Expected: 10882.1 Da

Mass Observed: 10882.7 Da

Peptide Sequence: GIGAVLKVLTTGLPALISWIKRKRQQRXRRBRXRBR



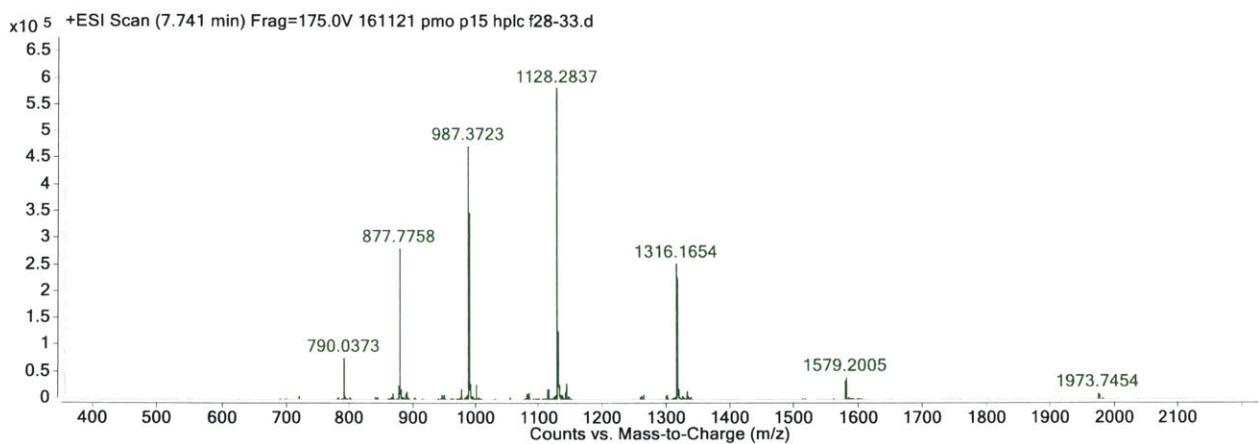
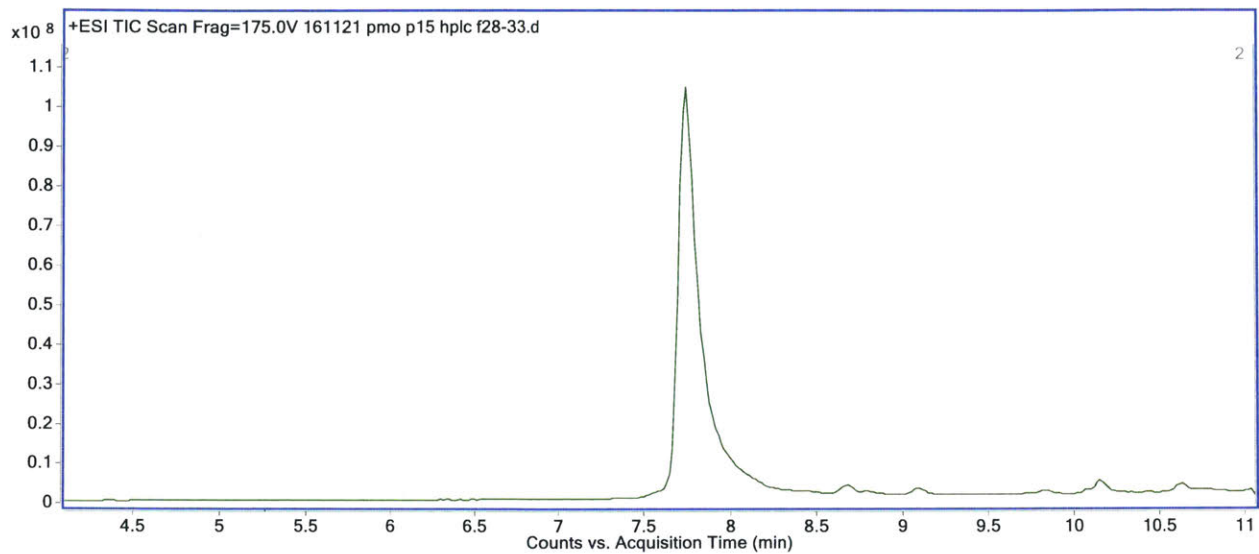


PMO-P15

Mass Expected: 7891.3 Da

Mass Observed: 7891.7 Da

Peptide Sequence: PPPPPPPPPPPPPPP

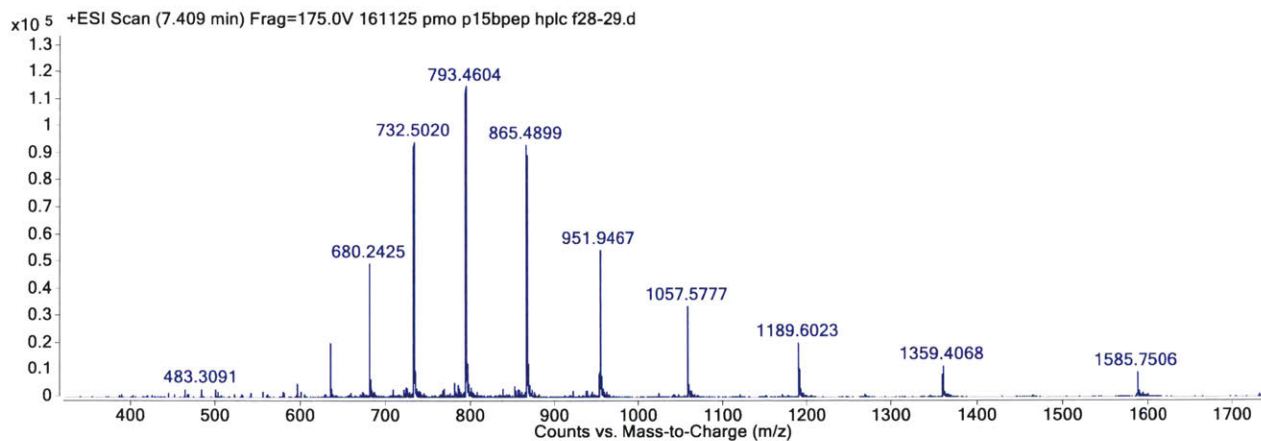
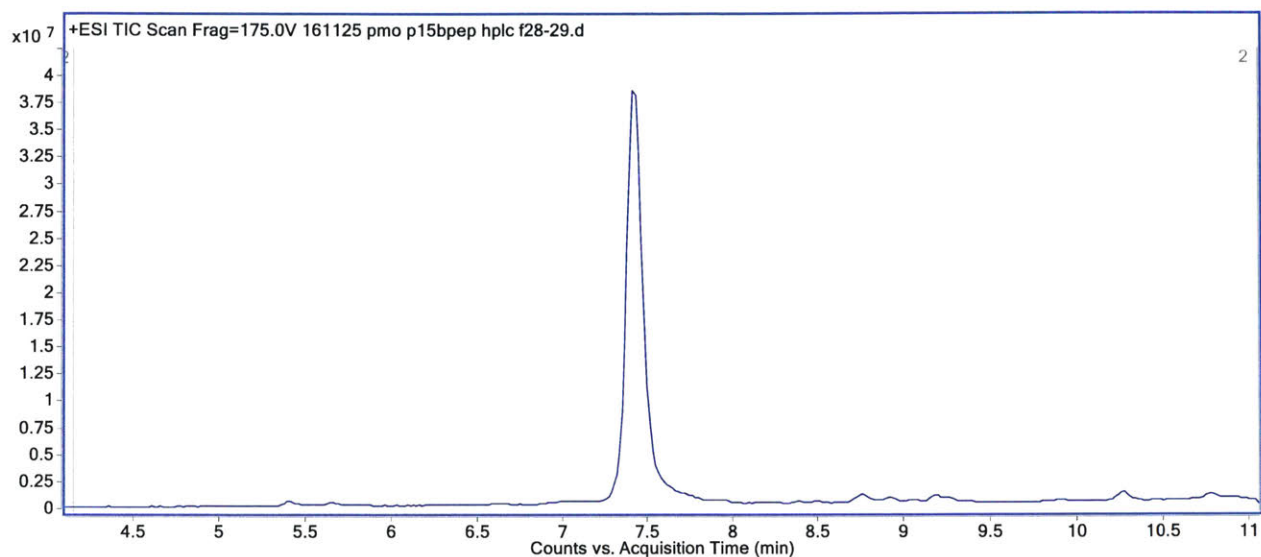


PMO-P15-Bpep

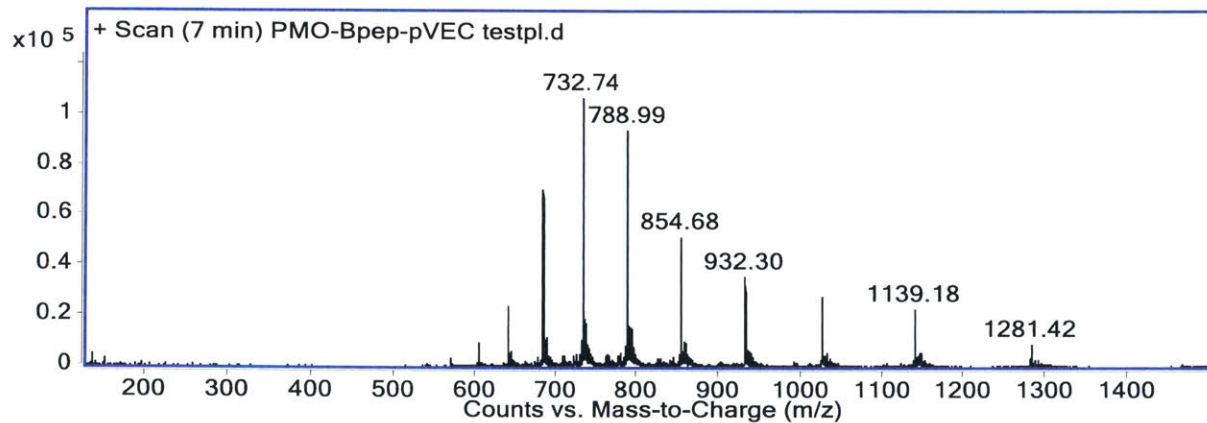
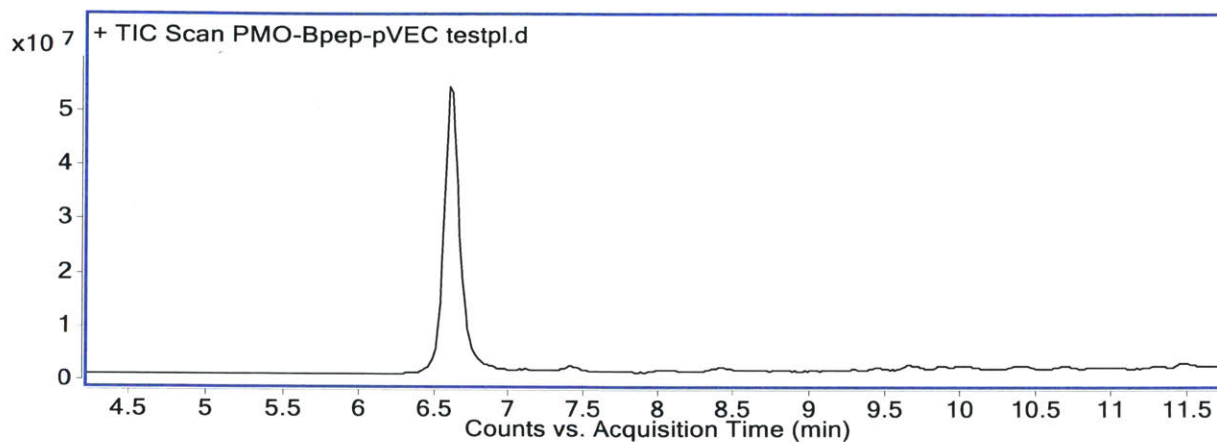
Mass Expected: 9509.2 Da

Mass Observed: 9509.7 Da

Peptide Sequence: P15BPPPPPPPPPPRXXRRBRRXRRBR



PMO-Bpep-pVEC  
Mass Expected: 10244.3 Da  
Mass Observed: 10244.6 Da  
Peptide Sequence: RXRRBRRXRRBLLIILRRRIRKQAHASK  
LC-MS Method A



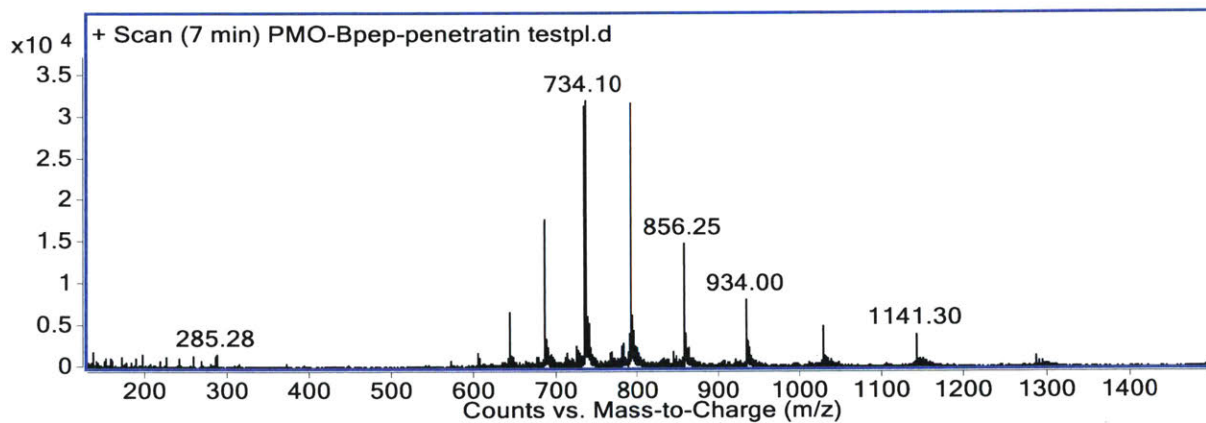
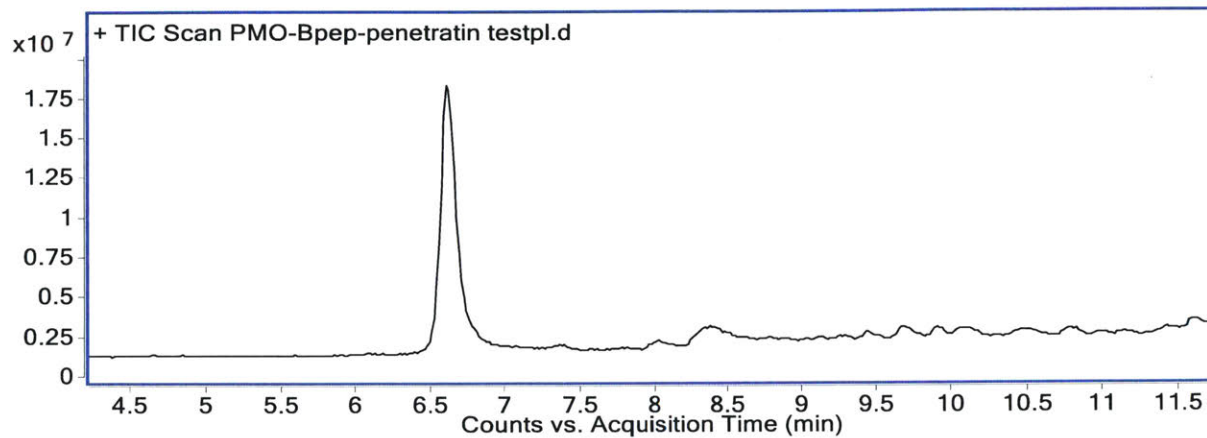
PMO-Bpep-Penetratin

Mass Expected: 10263.3 Da

Mass Observed: 10263.7 Da

Peptide Sequence: RXRRBRRXRRBRRQIKIWFQNRRJKWKK

LC-MS **Method A**



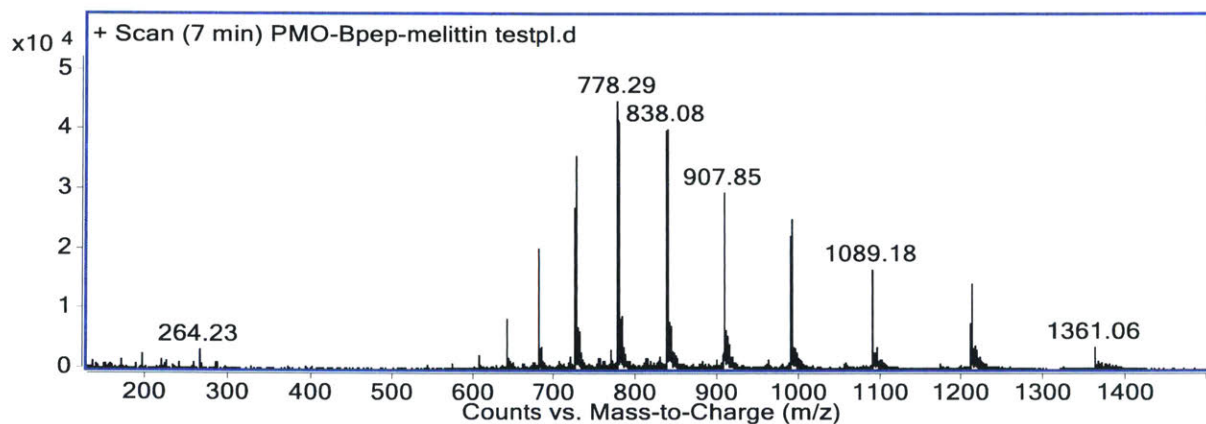
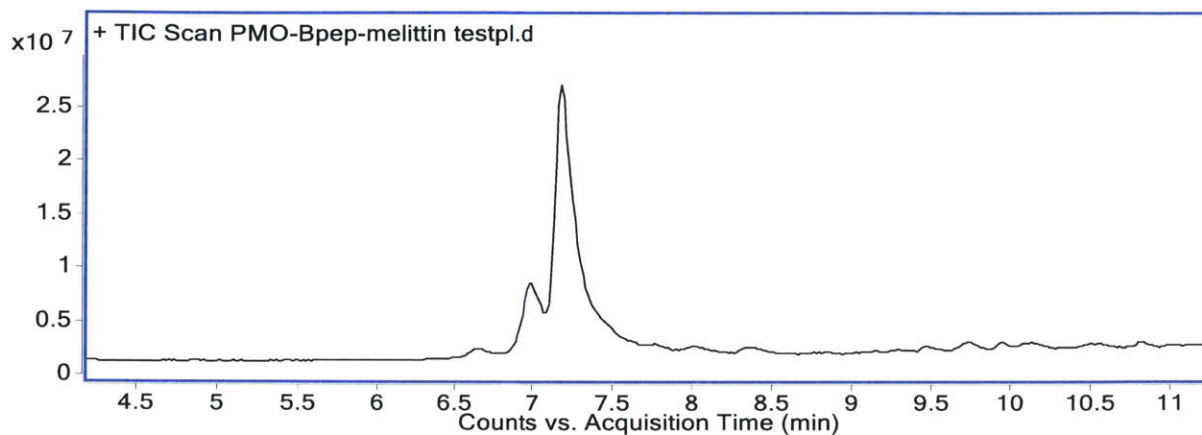
PMO-Bpep-Melittin

Mass Expected: 10882.1 Da

Mass Observed: 10882.5 Da

Peptide Sequence: RXRRBRRXRRBRGIGAVLKVLTTGLPALISWIKRKRQQ

LC-MS Method A



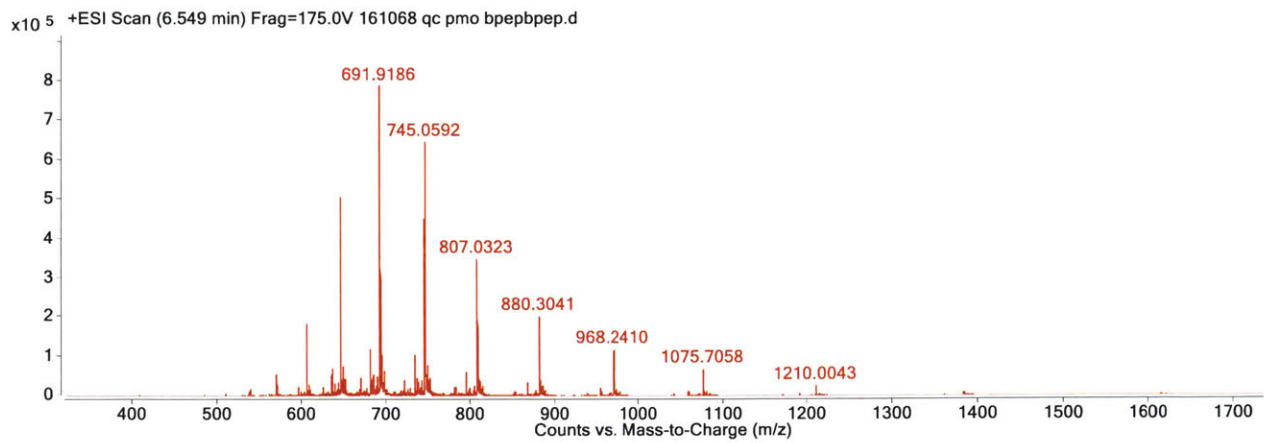
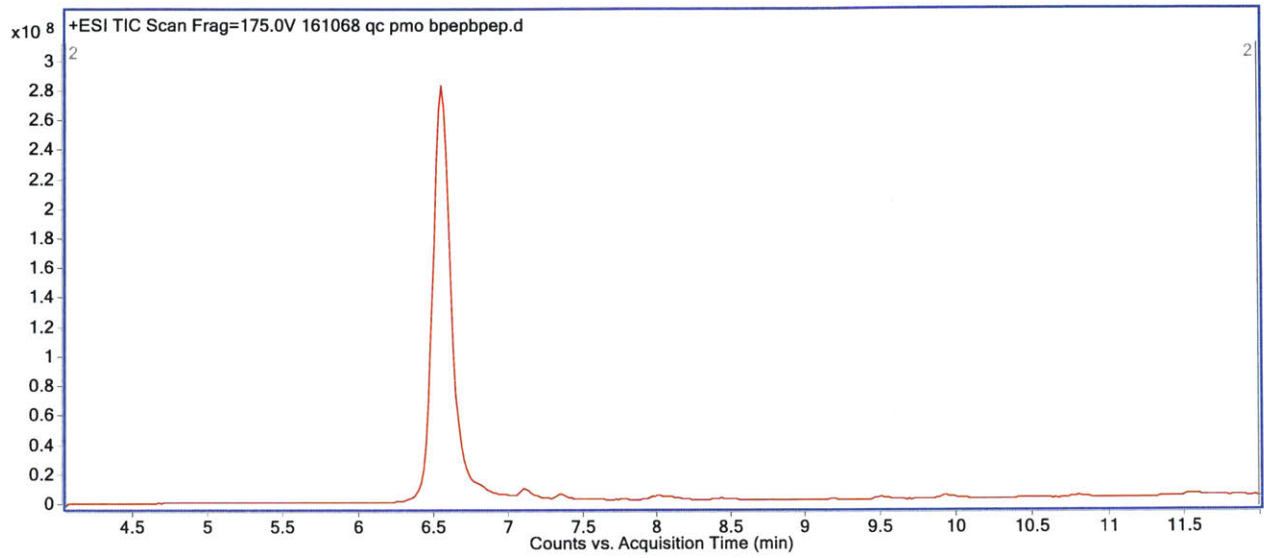
PMO-Bpep-Bpep

Mass Expected: 9670.5 Da

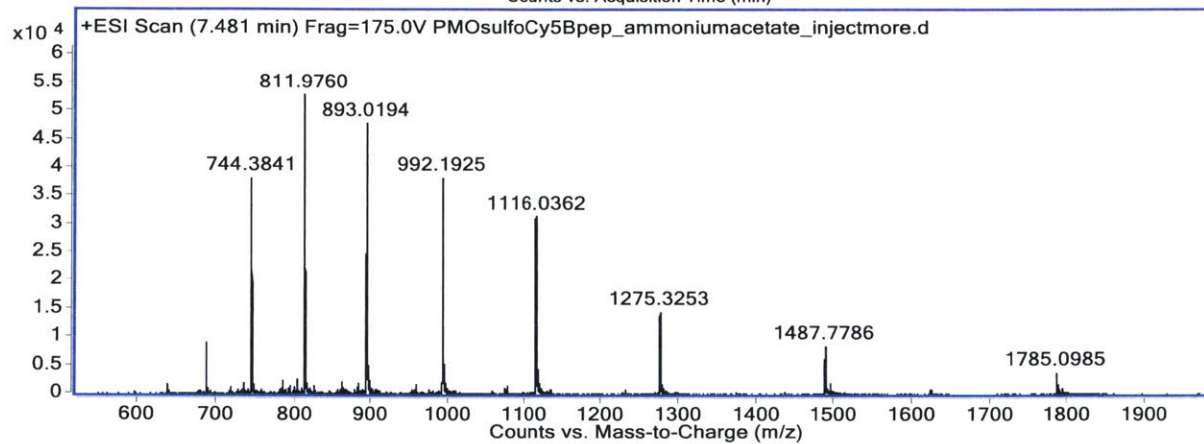
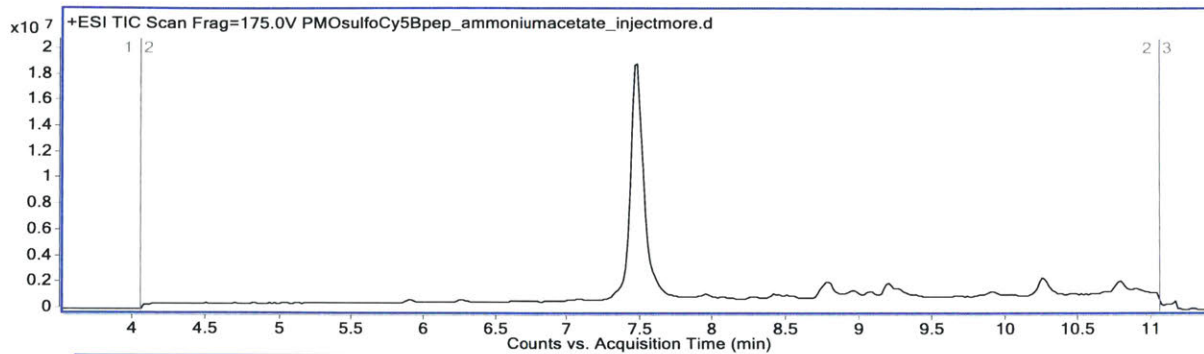
Mass Observed: 9672.9 Da

Peptide Sequence: RXRRBRRXRRBRRXRRBRRXRRBR

LC-MS Method A



PMO-SulfoCy5-Bpep  
Mass Expected: 8921.7  
Mass Observed: 8921.6  
Peptide Sequence: C(SulfoCy5)RXRRBRRXRRBR

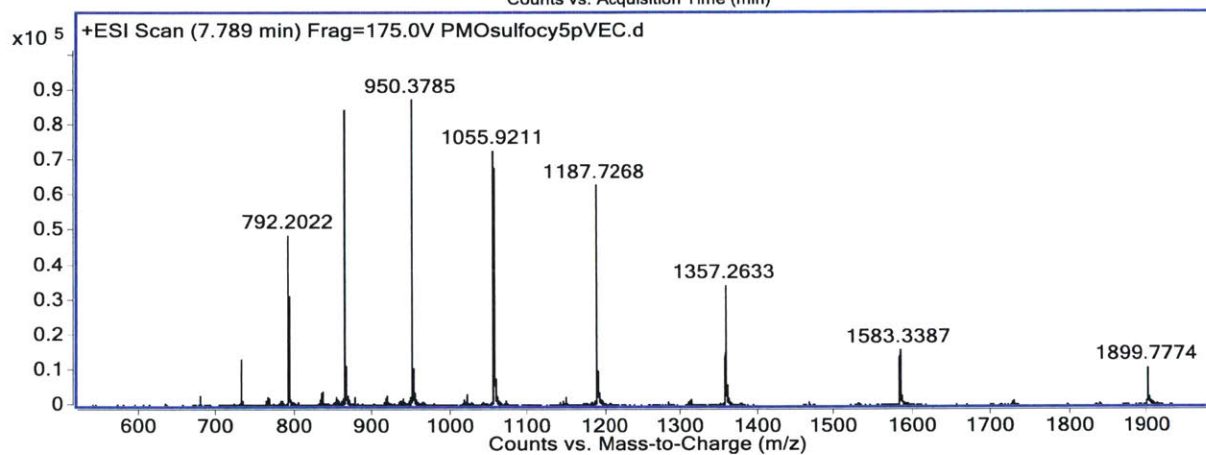
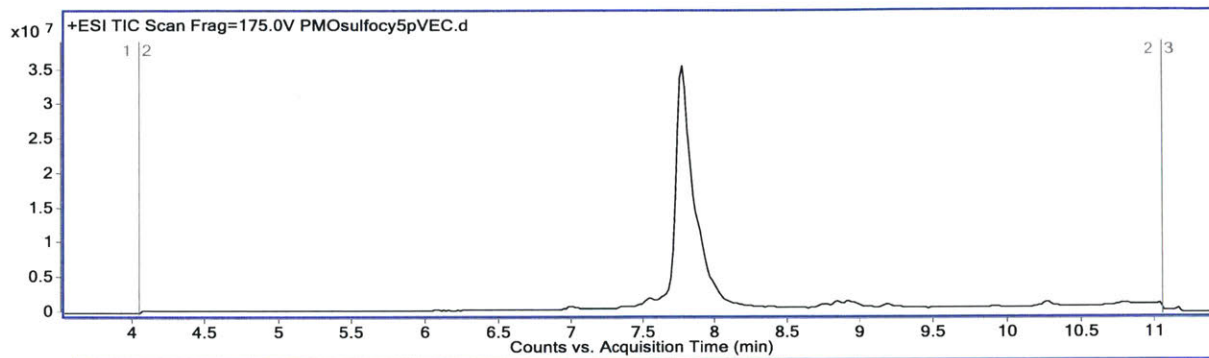


PMO-SulfoCy5-pVEC

Mass Expected: 9495.4

Mass Observed: 9495.0

Peptide Sequence: C(SulfoCy5)LLIILRRRIRKQAHASK



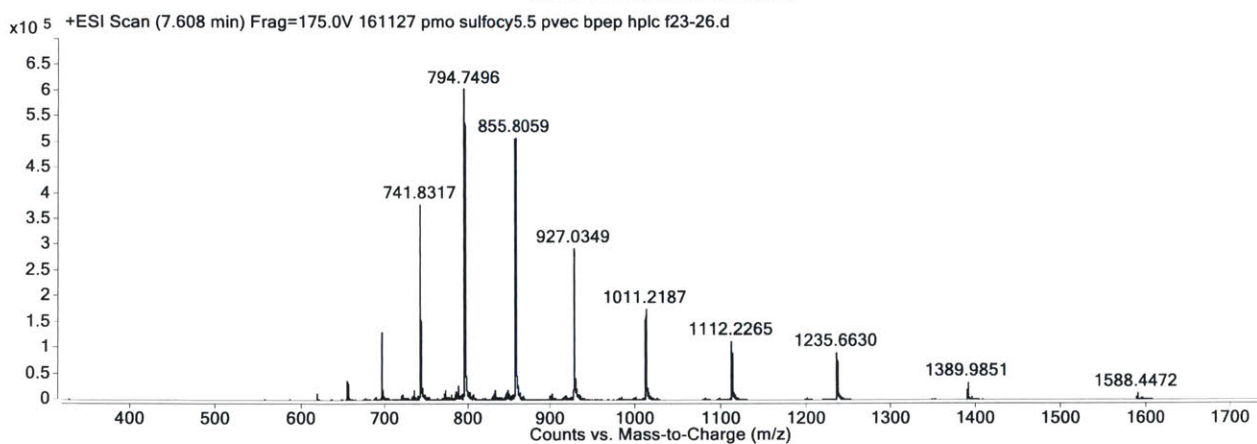
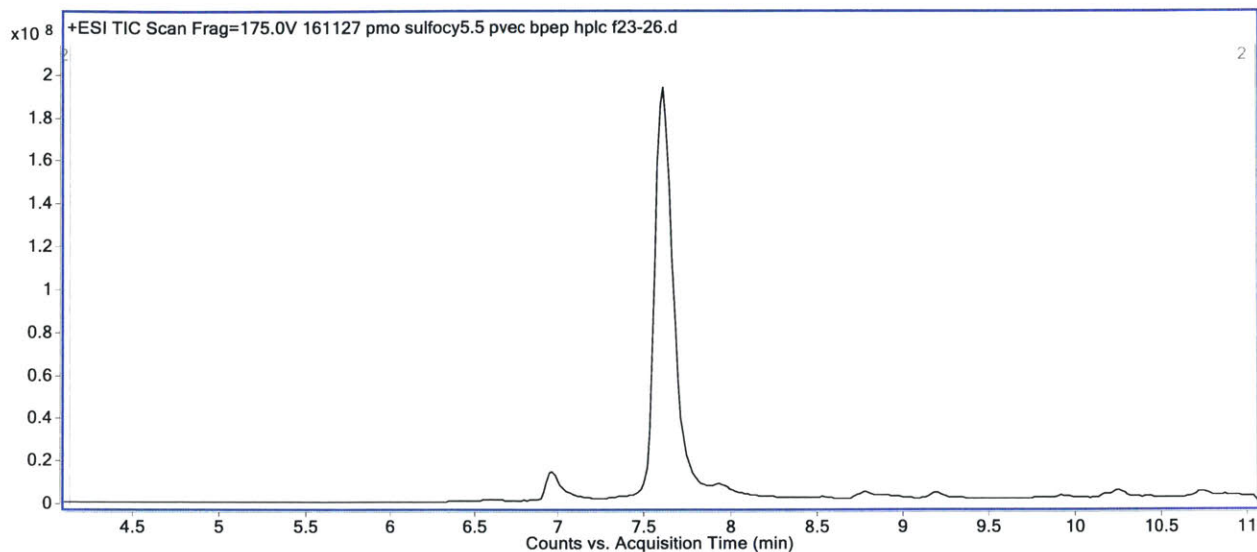


PMO-SulfoCy5-pVEC-Bpep

Mass Expected: 11112.8 Da

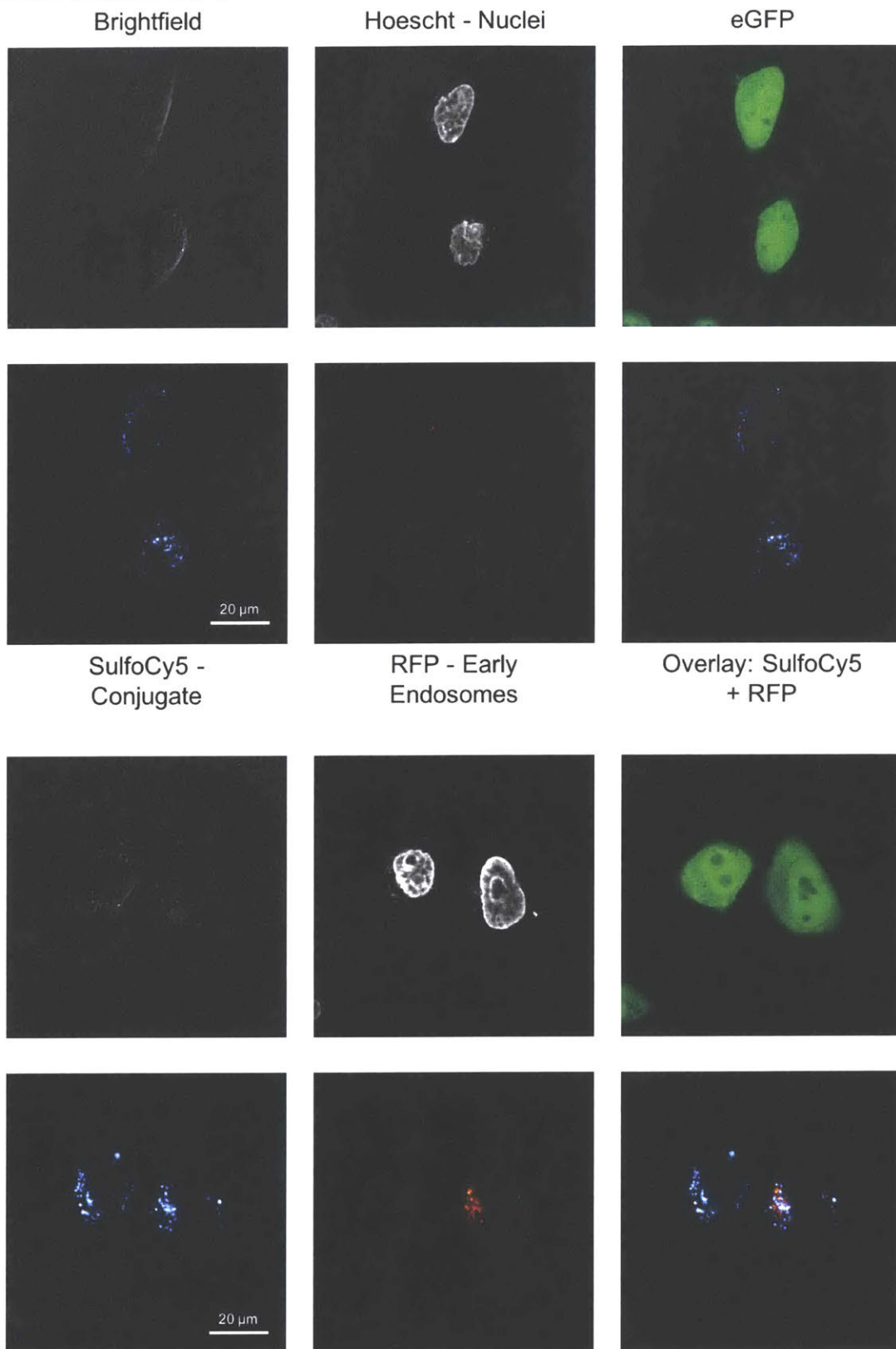
Mass Observed: 11112.6 Da

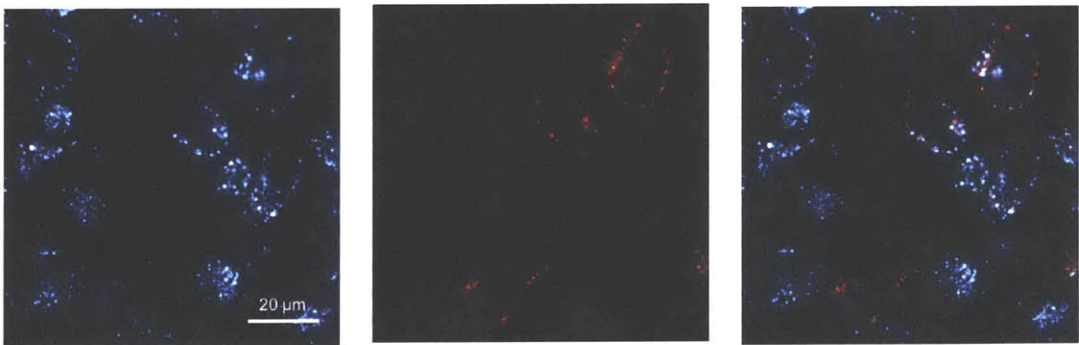
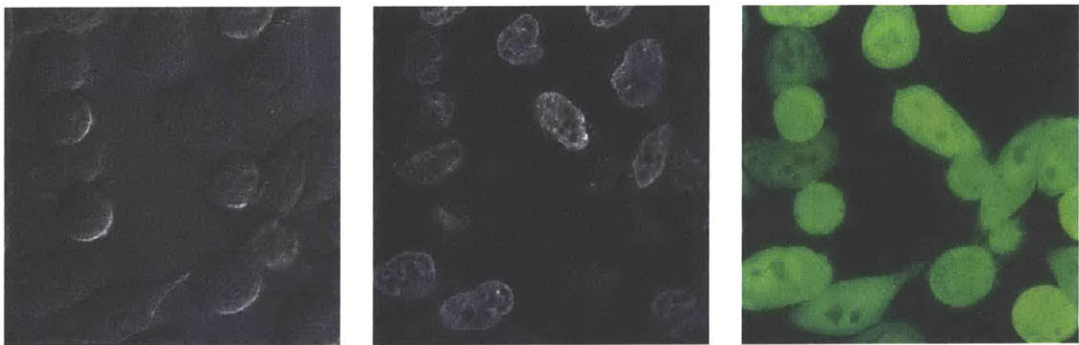
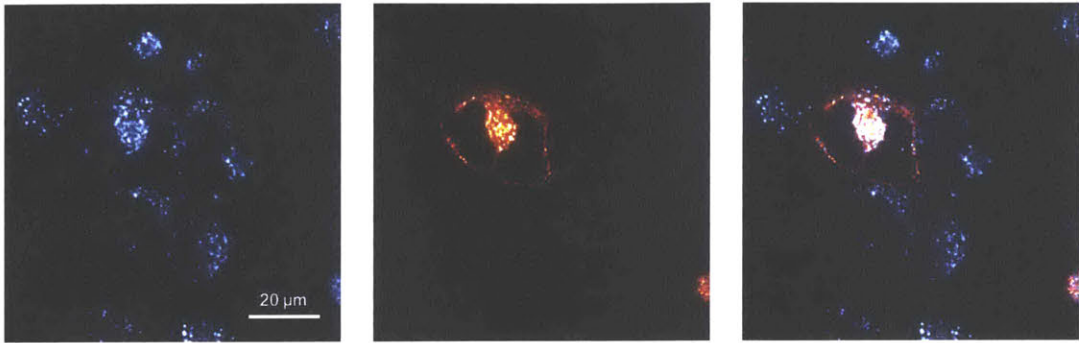
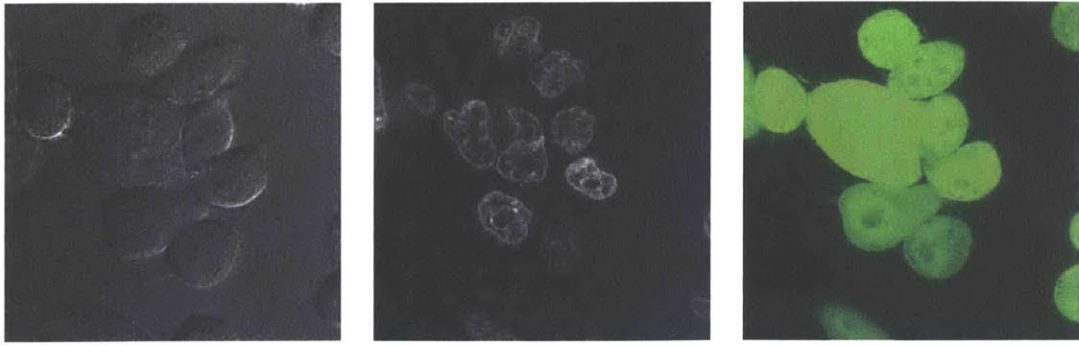
Peptide Sequence: C(SulfoCy5)LLILRRRIRKQAHAAHSKRXRBRBRXRBR

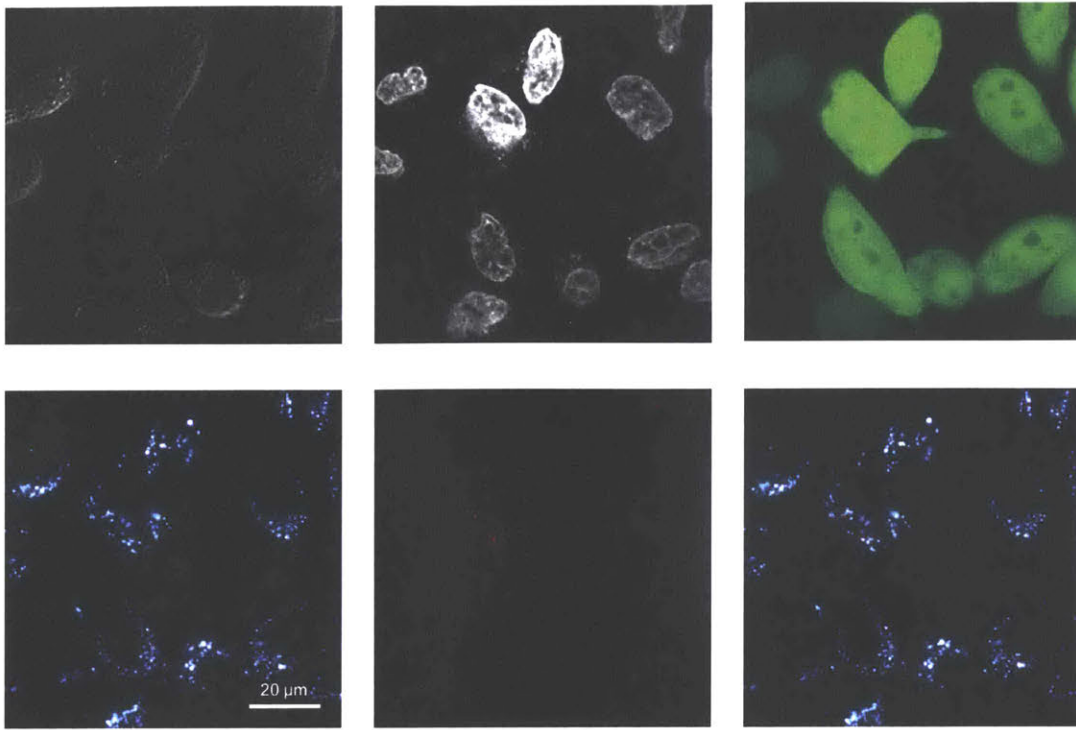


### 3.6. Appendix of Confocal Images

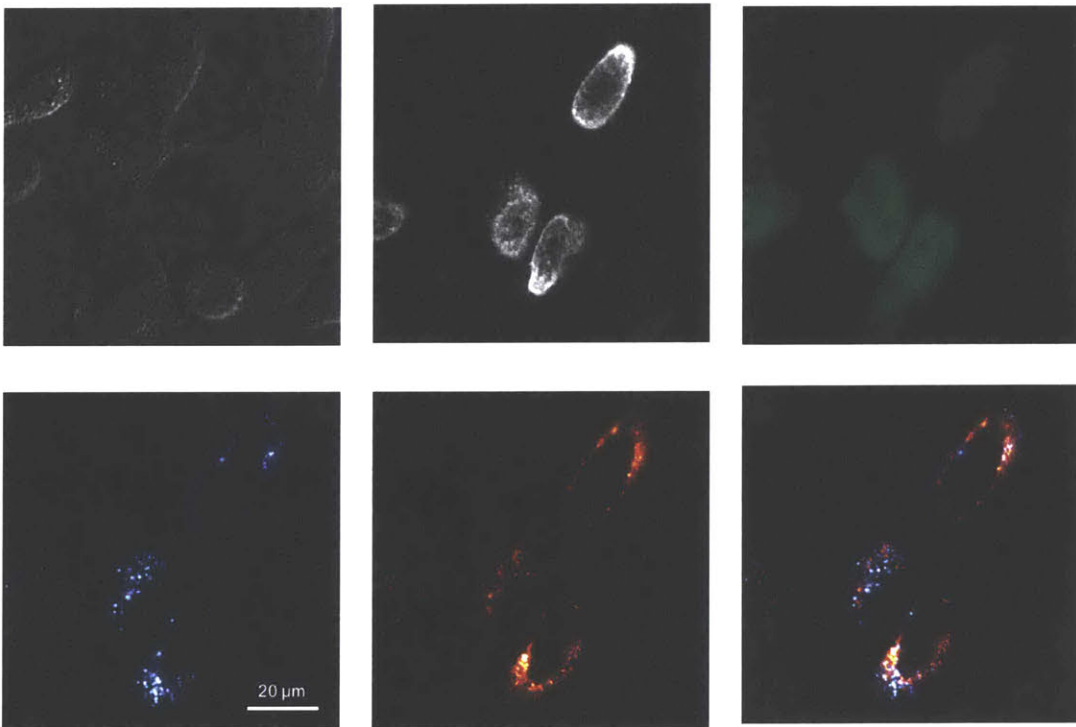
*PMO-SulfoCy5-pVEC-Bpep*

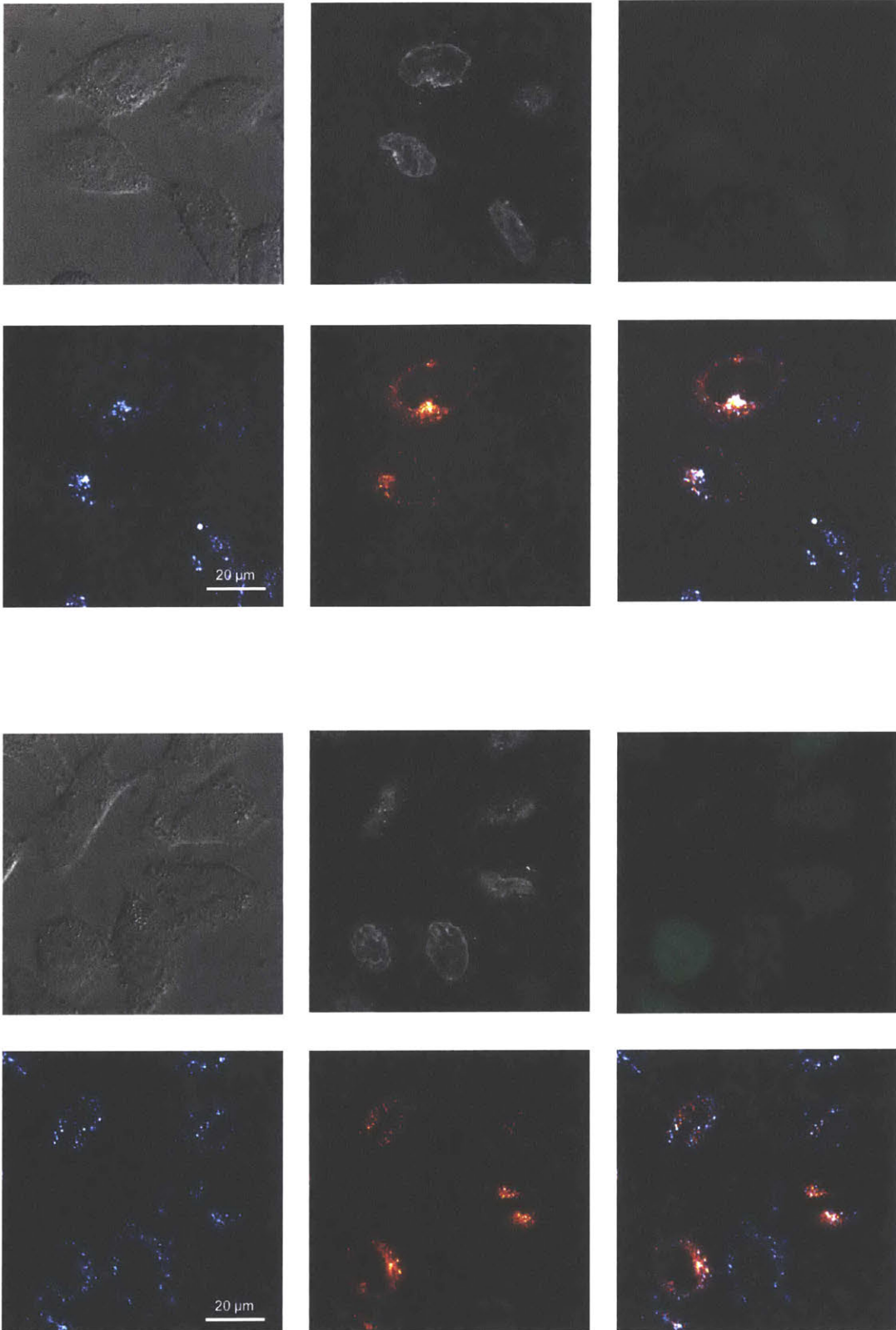


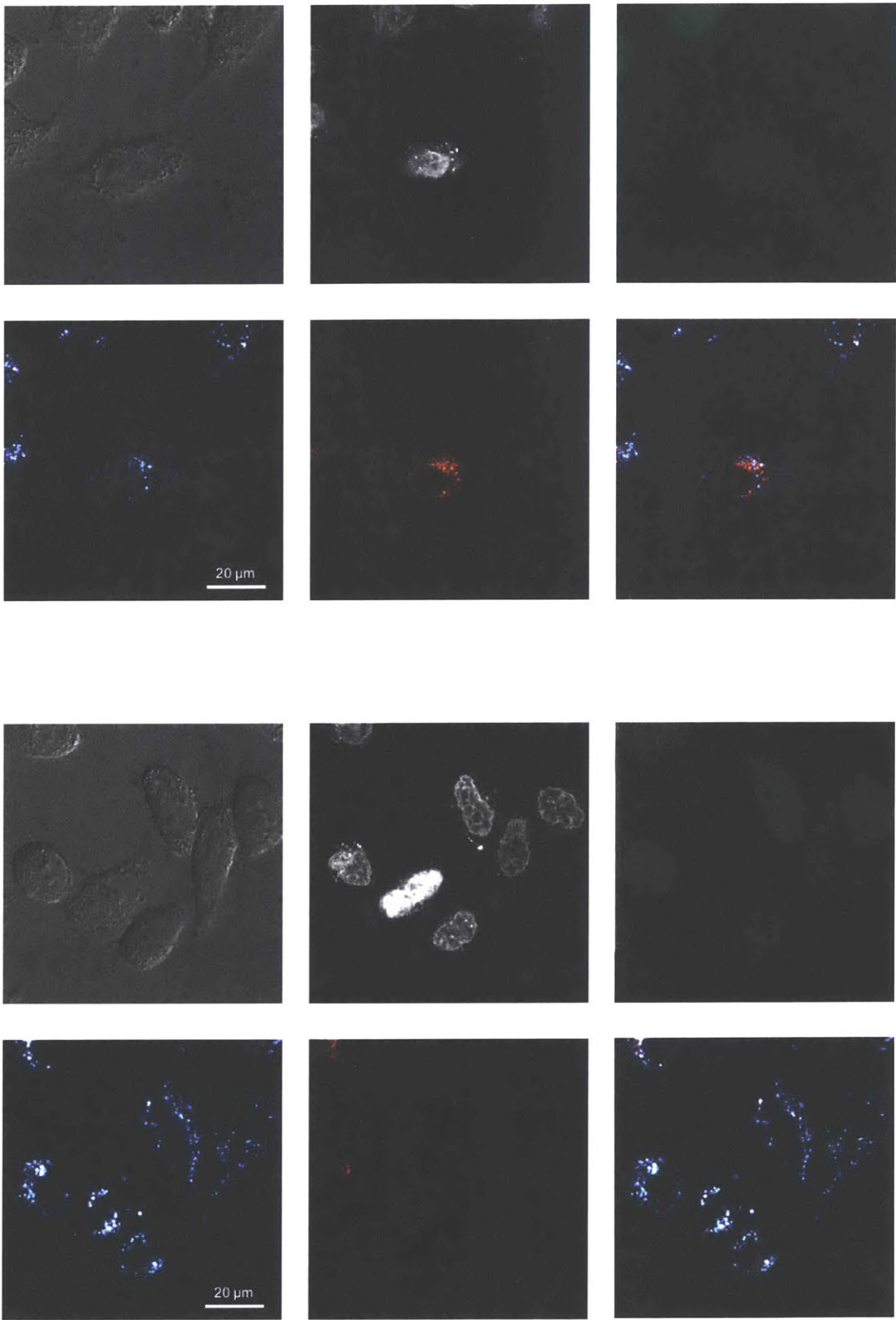




*PMO-SulfoCy5-pVEC*

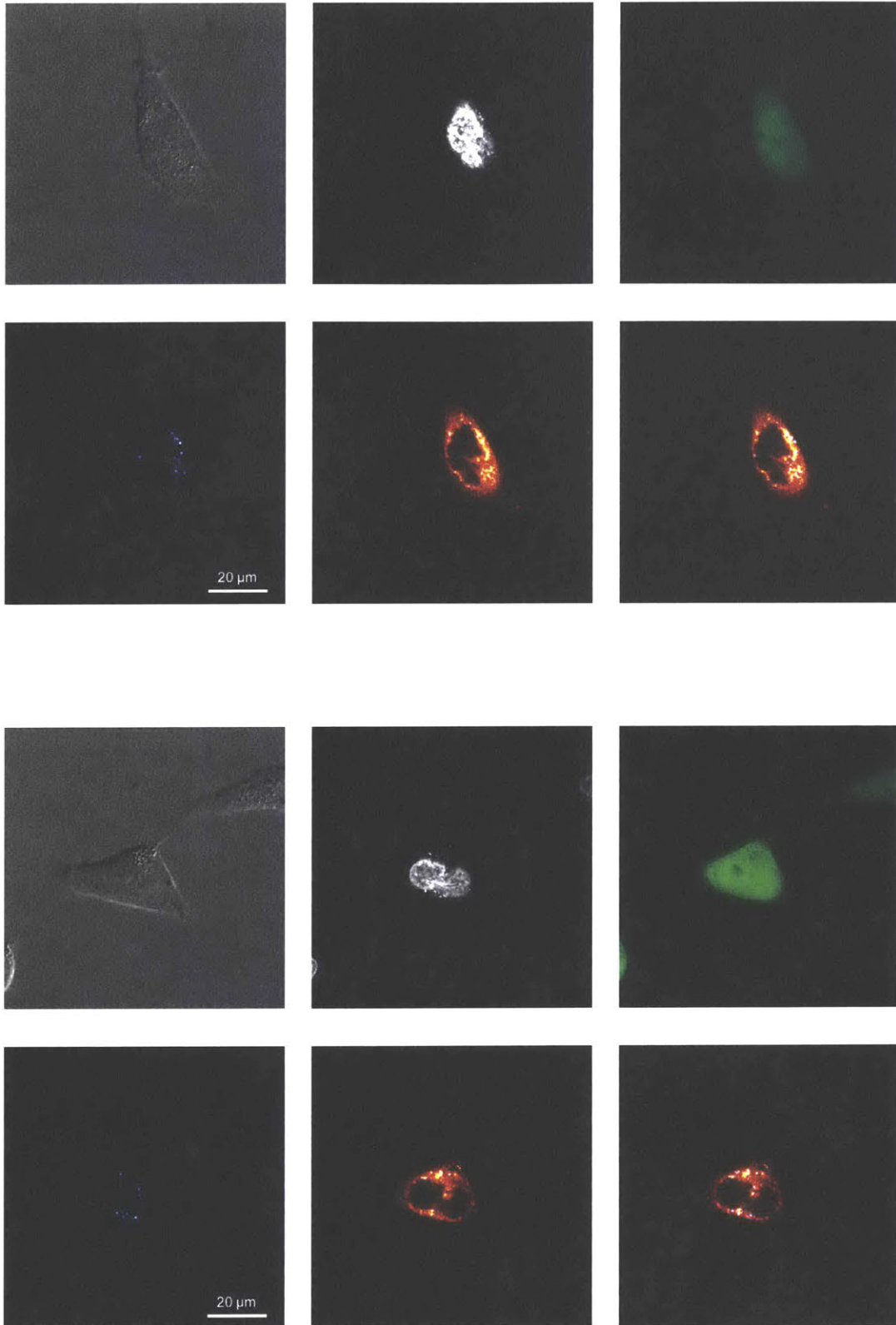


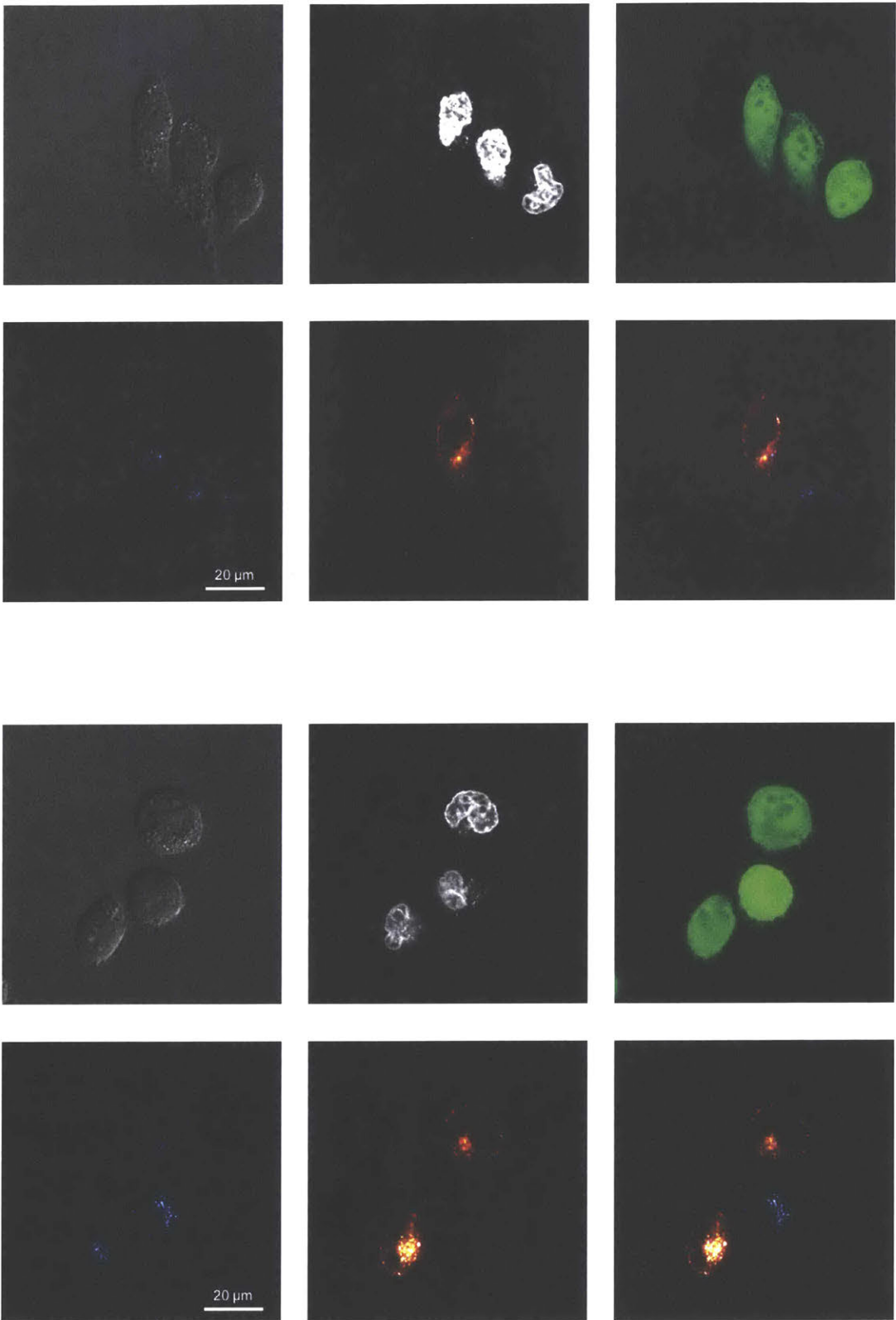




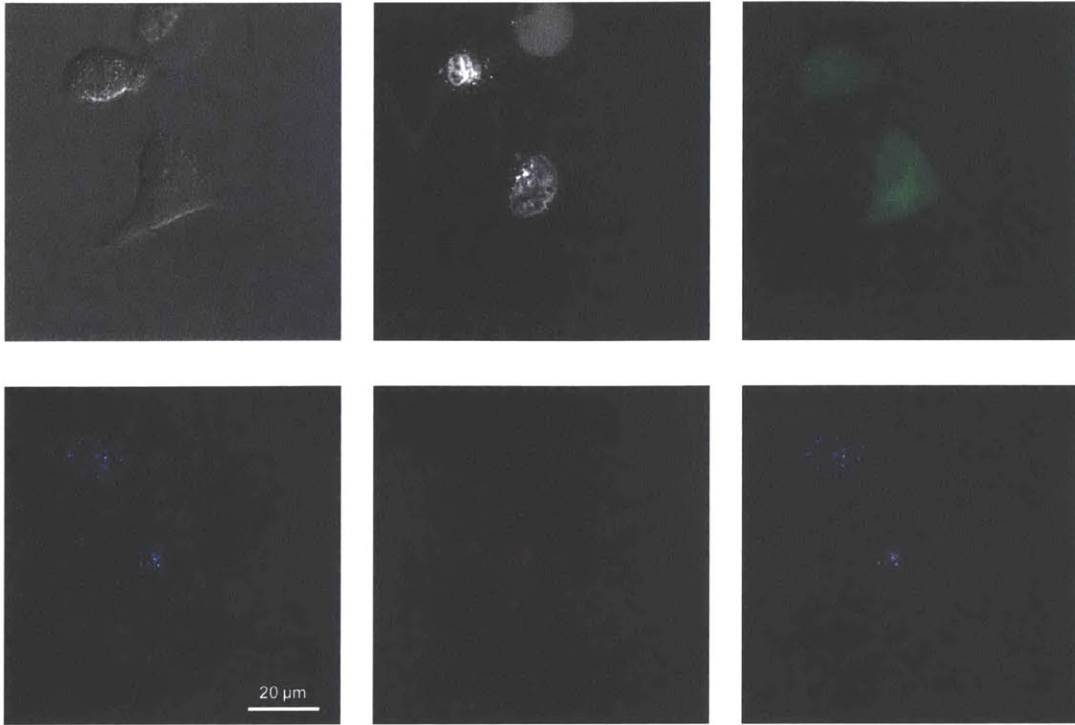


*PMO-SulfoCy5-Bpep*

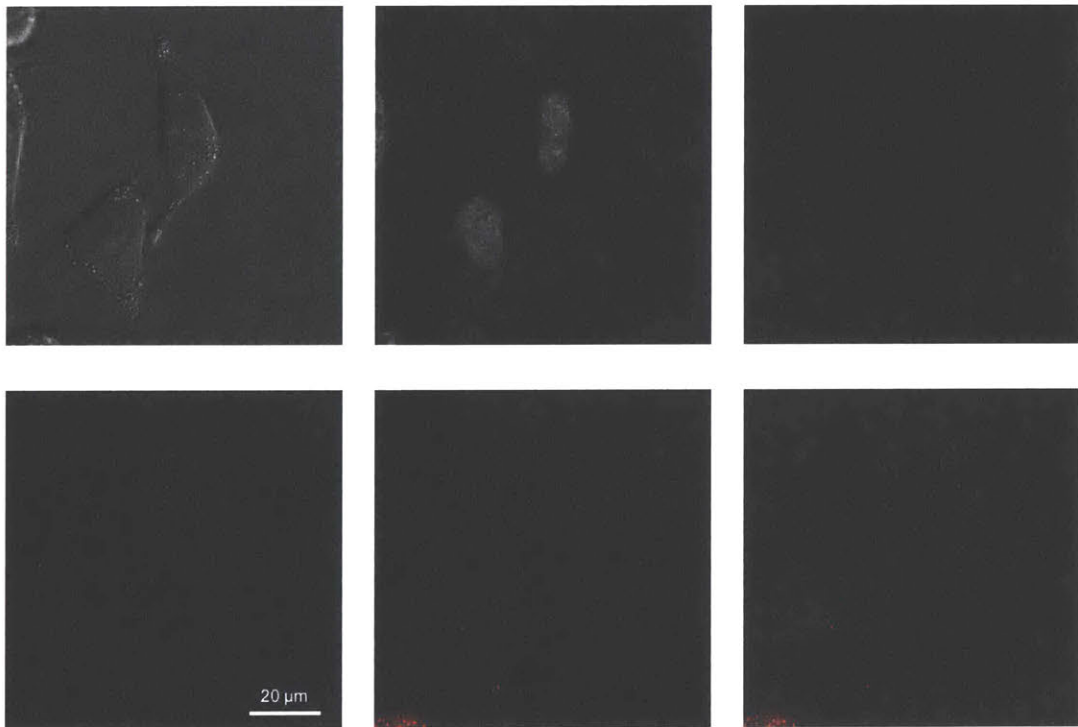


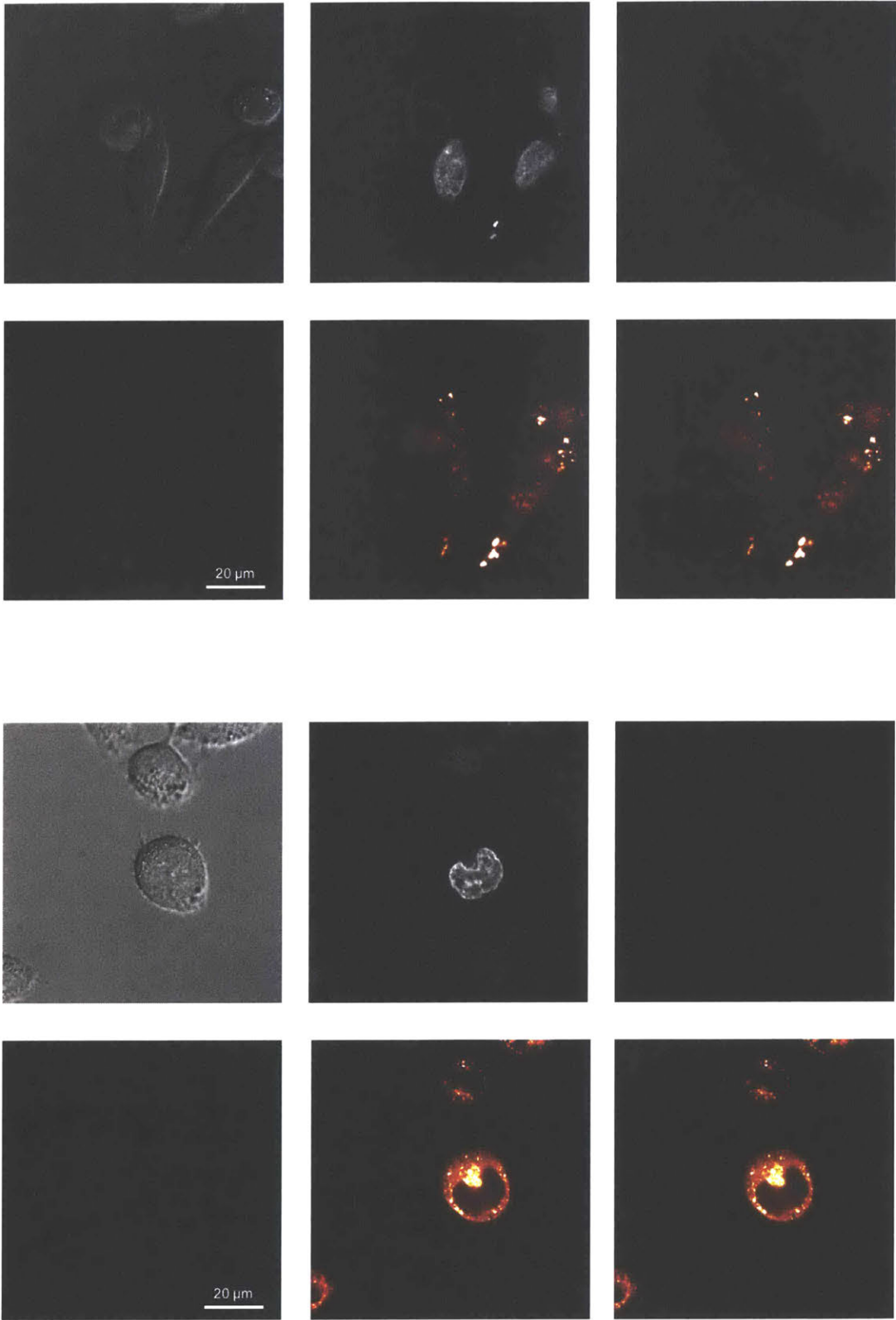


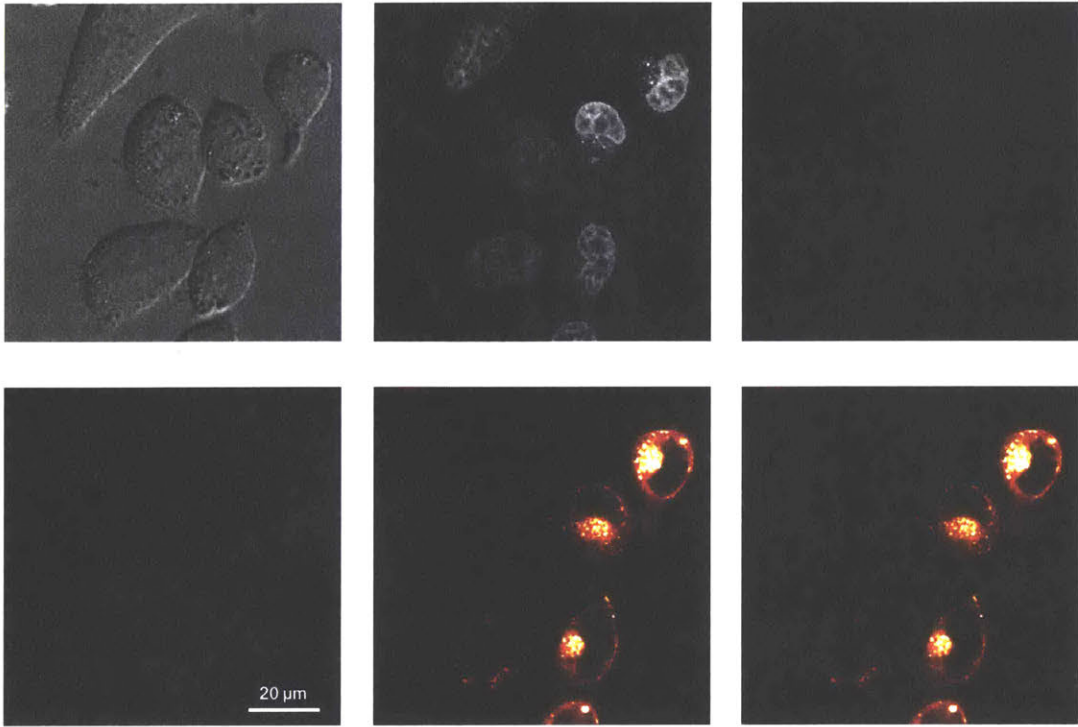




*Untreated Cells*







### 3.7. References

- (1) Lim, K. R. Q.; Maruyama, R.; Yokota, T. Eteplirsen in the Treatment of Duchenne Muscular Dystrophy. *Drug Des. Devel. Ther.* **2017**, *11*, 533–545.
- (2) Summerton, J.; Weller, D. Morpholino Antisense Oligomers: Design, Preparation, and Properties. *Antisense Nucleic Acid Drug Dev.* **1997**, *7* (3), 187–195.
- (3) Youngblood, D. S.; Hatlevig, S. A.; Hassinger, J. N.; Iversen, P. L.; Moulton, H. M. Stability of Cell-Penetrating Peptide–Morpholino Oligomer Conjugates in Human Serum and in Cells. *Bioconjug. Chem.* **2007**, *18* (1), 50–60.
- (4) Hudziak, R. M.; Barofsky, E.; Barofsky, D. F.; Weller, D. L.; Huang, S.-B.; Weller, D. D. Resistance of Morpholino Phosphorodiamidate Oligomers to Enzymatic Degradation. *Antisense Nucleic Acid Drug Dev.* **1996**, *6* (4), 267–272.
- (5) Chan, J. H.; Lim, S.; Wong, W. F. Antisense Oligonucleotides: From Design to Therapeutic Application. *Clin. Exp. Pharmacol. Physiol.* **2006**, *33* (5–6), 533–540.
- (6) Hammond, S. M.; Hazell, G.; Shabanpoor, F.; Saleh, A. F.; Bowerman, M.; Sleigh, J. N.; Meijboom, K. E.; Zhou, H.; Muntoni, F.; Talbot, K.; et al. Systemic Peptide-Mediated Oligonucleotide Therapy Improves Long-Term Survival in Spinal Muscular Atrophy. *Proc. Natl. Acad. Sci. U. S. A.* **2016**, *113* (39), 10962–10967.
- (7) Betts, C.; Saleh, A. F.; Arzumanov, A. A.; Hammond, S. M.; Godfrey, C.; Coursindel, T.; Gait, M. J.; Wood, M. J. Pip6-PMO, A New Generation of Peptide-Oligonucleotide Conjugates With Improved Cardiac Exon Skipping Activity for DMD Treatment. *Mol. Ther. Nucleic Acids* **2012**, *1* (8), e38.
- (8) Moulton, H. M.; Nelson, M. H.; Hatlevig, S. A.; Reddy, M. T.; Iversen, P. L. Cellular Uptake of Antisense Morpholino Oligomers Conjugated to Arginine-Rich Peptides. *Bioconjug. Chem.* **2004**, *15* (2), 290–299.
- (9) Wu, R. P.; Youngblood, D. S.; Hassinger, J. N.; Lovejoy, C. E.; Nelson, M. H.; Iversen, P. L.; Moulton, H. M. Cell-Penetrating Peptides as Transporters for Morpholino Oligomers: Effects of Amino Acid Composition on Intracellular Delivery and Cytotoxicity. *Nucleic Acids Res.* **2007**, *35* (15), 5182–5191.
- (10) Moulton, H. M.; Moulton, J. D. Morpholinos and Their Peptide Conjugates: Therapeutic Promise and Challenge for Duchenne Muscular Dystrophy. *Biochim. Biophys. Acta BBA - Biomembr.* **2010**, *1798* (12), 2296–2303.
- (11) Wu, B.; Moulton, H. M.; Iversen, P. L.; Jiang, J.; Li, J.; Li, J.; Spurney, C. F.; Sali, A.; Guerron, A. D.; Nagaraju, K.; et al. Effective Rescue of Dystrophin Improves Cardiac Function in Dystrophin-Deficient Mice by a Modified Morpholino Oligomer. *Proc. Natl. Acad. Sci.* **2008**, *105* (39), 14814–14819.
- (12) *Cell-Penetrating Peptides*; Langel, Ü., Ed.; Methods in Molecular Biology; Humana Press: Totowa, NJ, 2011; Vol. 683.
- (13) Copolovici, D. M.; Langel, K.; Eriste, E.; Langel, Ü. Cell-Penetrating Peptides: Design, Synthesis, and Applications. *ACS Nano* **2014**, *8* (3), 1972–1994.
- (14) Eiríksdóttir, E.; Konate, K.; Langel, Ü.; Divita, G.; Deshayes, S. Secondary Structure of Cell-Penetrating Peptides Controls Membrane Interaction and Insertion. *Biochim. Biophys. Acta BBA - Biomembr.* **2010**, *1798* (6), 1119–1128.
- (15) Thorén, P. E. G.; Persson, D.; Esbjörner, E. K.; Goksör, M.; Lincoln, P.; Nordén, B. Membrane Binding and Translocation of Cell-Penetrating Peptides. *Biochemistry (Mosc.)* **2004**, *43* (12), 3471–3489.

- (16) Lundin, P.; Johansson, H.; Guterstam, P.; Holm, T.; Hansen, M.; Langel, Ü.; EL Andaloussi, S. Distinct Uptake Routes of Cell-Penetrating Peptide Conjugates. *Bioconjug. Chem.* **2008**, *19* (12), 2535–2542.
- (17) Kosuge, M.; Takeuchi, T.; Nakase, I.; Jones, A. T.; Futaki, S. Cellular Internalization and Distribution of Arginine-Rich Peptides as a Function of Extracellular Peptide Concentration, Serum, and Plasma Membrane Associated Proteoglycans. *Bioconjug. Chem.* **2008**, *19* (3), 656–664.
- (18) Tünnemann, G.; Martin, R. M.; Haupt, S.; Patsch, C.; Edenhofer, F.; Cardoso, M. C. Cargo-Dependent Mode of Uptake and Bioavailability of TAT-Containing Proteins and Peptides in Living Cells. *FASEB J.* **2006**, *20* (11), 1775–1784.
- (19) Madani, F.; Lindberg, S.; Langel, Ü.; Futaki, S.; Gräslund, A. Mechanisms of Cellular Uptake of Cell-Penetrating Peptides <https://www.hindawi.com/archive/2011/414729/> (accessed Dec 11, 2017).
- (20) Duchardt, F.; Fotin-Mleczek, M.; Schwarz, H.; Fischer, R.; Brock, R. A Comprehensive Model for the Cellular Uptake of Cationic Cell-Penetrating Peptides. *Traffic* **2007**, *8* (7), 848–866.
- (21) Mayor, S.; Pagano, R. E. Pathways of Clathrin-Independent Endocytosis. *Nat. Rev. Mol. Cell Biol.* **2007**, *8* (8), 603.
- (22) Yin, H.; Boisguerin, P.; Moulton, H. M.; Betts, C.; Seow, Y.; Boutilier, J.; Wang, Q.; Walsh, A.; Lebleu, B.; Wood, M. J. Context Dependent Effects of Chimeric Peptide Morpholino Conjugates Contribute to Dystrophin Exon-Skipping Efficiency. *Mol. Ther. Nucleic Acids* **2013**, *2* (9), e124.
- (23) Abes, S.; Turner, J. J.; Ivanova, G. D.; Owen, D.; Williams, D.; Arzumanov, A.; Clair, P.; Gait, M. J.; Lebleu, B. Efficient Splicing Correction by PNA Conjugation to an R6-Penetratin Delivery Peptide. *Nucleic Acids Res.* **2007**, *35* (13), 4495–4502.
- (24) Yin, H.; Moulton, H. M.; Seow, Y.; Boyd, C.; Boutilier, J.; Iverson, P.; Wood, M. J. A. Cell-Penetrating Peptide-Conjugated Antisense Oligonucleotides Restore Systemic Muscle and Cardiac Dystrophin Expression and Function. *Hum. Mol. Genet.* **2008**, *17* (24), 3909–3918.
- (25) Elmquist, A.; Lindgren, M.; Bartfai, T.; Langel, U. null. VE-Cadherin-Derived Cell-Penetrating Peptide, PVEC, with Carrier Functions. *Exp. Cell Res.* **2001**, *269* (2), 237–244.
- (26) Derossi, D.; Joliot, A. H.; Chassaing, G.; Prochiantz, A. The Third Helix of the Antennapedia Homeodomain Translocates through Biological Membranes. *J. Biol. Chem.* **1994**, *269* (14), 10444–10450.
- (27) Terwilliger, T. C.; Eisenberg, D. The Structure of Melittin. II. Interpretation of the Structure. *J. Biol. Chem.* **1982**, *257* (11), 6016–6022.
- (28) Mijalis, A. J.; Thomas III, D. A.; Simon, M. D.; Adamo, A.; Beaumont, R.; Jensen, K. F.; Pentelute, B. L. A Fully Automated Flow-Based Approach for Accelerated Peptide Synthesis. *Nat. Chem. Biol.* **2017**, *13* (5), 464–466.
- (29) Liang, G.; Liu, Y.; Shi, B.; Zhao, J.; Zheng, J. An Index for Characterization of Natural and Non-Natural Amino Acids for Peptidomimetics. *PLOS ONE* **2013**, *8* (7), e67844.
- (30) Pedregosa, F.; Varoquaux, G.; Gramfort, A.; Michel, V.; Thirion, B.; Grisel, O.; Blondel, M.; Prettenhofer, P.; Weiss, R.; Dubourg, V.; et al. Scikit-Learn: Machine Learning in Python. *J. Mach. Learn. Res.* **2011**, *12*, 2825–2830.

- (31) Sazani, P.; Kang, S.-H.; Maier, M. A.; Wei, C.; Dillman, J.; Summerton, J.; Manoharan, M.; Kole, R. Nuclear Antisense Effects of Neutral, Anionic and Cationic Oligonucleotide Analogs. *Nucleic Acids Res.* **2001**, *29* (19), 3965–3974.

## Chapter 4: Perfluoroaryl Bicyclic Cell-Penetrating Peptides for Delivery of Antisense Oligonucleotides

The work presented in this chapter was published in the following manuscript and is reproduced with permission from Wiley-VCH:

Wolfe, J.M.,\* Fadzen, C.M.,\* Holden, R.L., Yao, M, Hanson, G.J., & Pentelute, B.L.  
Perfluoroaryl Bicyclic Cell-Penetrating Peptides for Delivery of Antisense Oligonucleotides.  
*Angew. Chem. Int. Ed.* **57**(17), 4756-4759 (2018).

\*: denotes authors contributed equally. J.M.W. devised and performed synthesis of bicyclic peptides. C.M.F. performed cellular assays for exon skipping activity.

## 4.1. Introduction

Exon-skipping antisense oligonucleotides have been developed into successful therapeutic molecules for debilitating genetic diseases, such as Duchenne muscular dystrophy (DMD).<sup>1-3</sup> To promote exon-skipping, these molecules bind to pre-mRNA in the nucleus and sterically block splice junctions or intraexonic ribonucleoprotein binding motifs. The steric blocking alters the spliceosomal processing of pre-mRNA, and results in the exclusion of one or more exons from the mature mRNA transcript. Thus, the oligonucleotide restores the in-frame mRNA and leads to translation of a functional protein.<sup>1</sup>

Phosphorodiamidate morpholino oligonucleotides (PMOs) are one type of exon-skipping oligonucleotide. PMOs are uncharged nucleic acid polymers in which the ribosyl ring is replaced with a morpholino ring and the natural phosphodiester backbone is replaced with phosphorodiamidate.<sup>4</sup> PMOs readily hybridize to DNA and RNA, and their altered backbone structure prevents degradation by serum and intracellular nucleases.<sup>5,6</sup> Eteplirsen, a PMO designed to restore functional dystrophin, recently became the only FDA-approved therapy to address the underlying genetic cause of DMD.

Unfortunately, PMOs, like all antisense oligonucleotides, exhibit limited delivery into the nucleus of cells. To improve PMO delivery, multiple strategies have been explored, such as the covalent attachment of cationic dendrimers or side-chains.<sup>7-9</sup> Arginine-rich cell-penetrating peptides have been widely utilized to improve cargo delivery, and these peptides are one of the most promising strategies for PMO delivery.<sup>10-14</sup> However, arginine-rich sequences suffer from proteolytic instability.<sup>6</sup> Delivery tools with enhanced proteolytic stability and delivery efficiency are therefore widely desired.

Bicyclic peptides are a unique class of peptides characterized by two intramolecular linkages. Excluding disulfide-linked peptides, methods to bicyclize unprotected peptides include bromomethylated aromatics, thiol-ene chemistry, tetrafluoroterephthalonitrile, or multiple orthogonal reactions.<sup>15-19</sup> The constrained conformation of bicyclic peptides can lead to reduced flexibility, improved binding properties, and protease resistance. Additionally, in the context of cellular delivery, bicyclic peptides with certain sequences show robust uptake into cells.<sup>20,21</sup> However, bicyclic peptides have not been explored as tools to promote the intracellular delivery of a large, covalently-attached cargo such as PMOs.



We recently developed a new method for peptide macrocyclization which joins the cysteine side-chains of unprotected peptides with perfluoroaromatic linkers.<sup>22,23</sup> These perfluoroaryl macrocyclic peptides have increased uptake into cells and increased proteolytic stability. Because the synthesis of multiple sizes of macrocycles is facile, we envisioned this perfluoroarylation chemistry could be extended towards the synthesis of bicyclic peptides. We anticipated that these bicyclic peptides would have enhanced stability, and that when covalently attached to oligonucleotides, would promote intracellular delivery.

## 4.2. Results and Discussion

Our first peptide bicyclization strategy used a trithiol to link together three perfluoroarenes covalently attached to an unprotected peptide (Figure 4.1). We began with R<sub>12</sub> peptide **1**. The purified peptide was incubated with an excess of decafluorobiphenyl in dimethylformamide (DMF) with *N,N*-diisopropylethylamine (DIEA) to generate the perfluoroarylated peptide **1a** (35% isolated yield). After purification of **1a**, 1,3,5-benzenetrithiol (1 mM) was added to the peptide (1 mM) in DMF and after 2 hours the bicyclic peptide **1b** was observed. The reaction was quenched and the peptide was purified by high-performance liquid chromatography (HPLC) (62% isolated yield). This strategy also enables the bicyclization of smaller peptides, demonstrated by its applicability to R<sub>6</sub> peptide **2**. This peptide was reacted with excess decafluorobiphenyl and then bicyclized under similar conditions to generate peptide **2b** (35% isolated yield) (Figure 4.2).

For a second bicyclization strategy, we performed a double macrocyclization of a linear peptide. Initially, we synthesized the R<sub>12</sub> peptide **3** and utilized orthogonal protection to install two macrocycles sequentially (Figure 4.3). However, after final purification, the bicyclic peptide **3b** was obtained in an overall yield of 4.5%.

To improve the synthesis of **3b** by eliminating deprotection and purification steps, we developed an alternative method, which we refer to as kinetically controlled bicyclization (Figure 4.4A). Given the slow rates of *i, i+1* cyclization with decafluorobiphenyl,<sup>23</sup> we anticipated unlinked perfluoroarenes could be pre-installed on resin and peptide cyclization would be favored at specific sites after the addition of base. Peptide **3** was synthesized with two trityl-protected cysteine residues and two *tert*-butylthiol-protected cysteine residues. The *tert*-butylthiol protected cysteines were placed at positions 1 and 9 and deprotected on resin. Then, decafluorobiphenyl was introduced and allowed to react with the free thiol. Cleavage and HPLC purification provided peptide **3a**. Next, the peptide was simply dissolved in DMF with 50 mM DIEA. Complete conversion to the double cycle product **3b** occurred in under 5 minutes (Figure 4.4B). HPLC purification led to the isolation of **3b** in 81% yield.

Importantly, both methods to synthesize **3b** provided products with identical retention times (Figure 4.4C), suggesting that a bicycle with two *i, i+7* macrocycles is favored over the bicycle with *i, i+15* and *i, i+1* macrocycles. To confirm our hypothesis that the *i, i+1* reaction is slow, we synthesized the control peptide **4a** containing one cysteine residue adjacent to a cysteine residue linked to decafluorobiphenyl. When treated with 50 mM DIEA in DMF, less than 5% of

| Peptide | Sequence                                     | Cyclic Form   |
|---------|--|---|
| 1       | Z <u>C</u> RRRRRRR <u>C</u> RRRRRR <u>C</u>  | <b>1b</b> – Trithiol bicycle<br><b>1nfb</b> – Non-fluorinated bicycle |
| 2       | Z <u>C</u> RRR <u>C</u> RRR <u>C</u>         | <b>2b</b> – Trithiol bicycle  |
| 3       | Z <u>C</u> RRRRRRR <u>C</u> RRRRRRR <u>C</u> | <b>3b</b> – Double macrocycle   |
| 4       | ZRRRRRRR <u>C</u> RRRRRR                     | <b>4c</b> – Monocycle   |
| 5       | ZRRRRRRRRRRRR                                | None  |
| 6       | Z <u>C</u> RRRRRRRRRRRRR <u>C</u>            | <b>6c</b> – Monocycle   |
| 7       | X <u>K</u> RrRrRrRrRrRr <u>E</u>             | <b>7c</b> – Lactam monocycle  |

**Table 4.1. Arginine-rich peptides for bicyclization and control sequences.** Z = 4-pentynoyl, X = 5-azidopentyl, and all peptides are C-terminal amides.

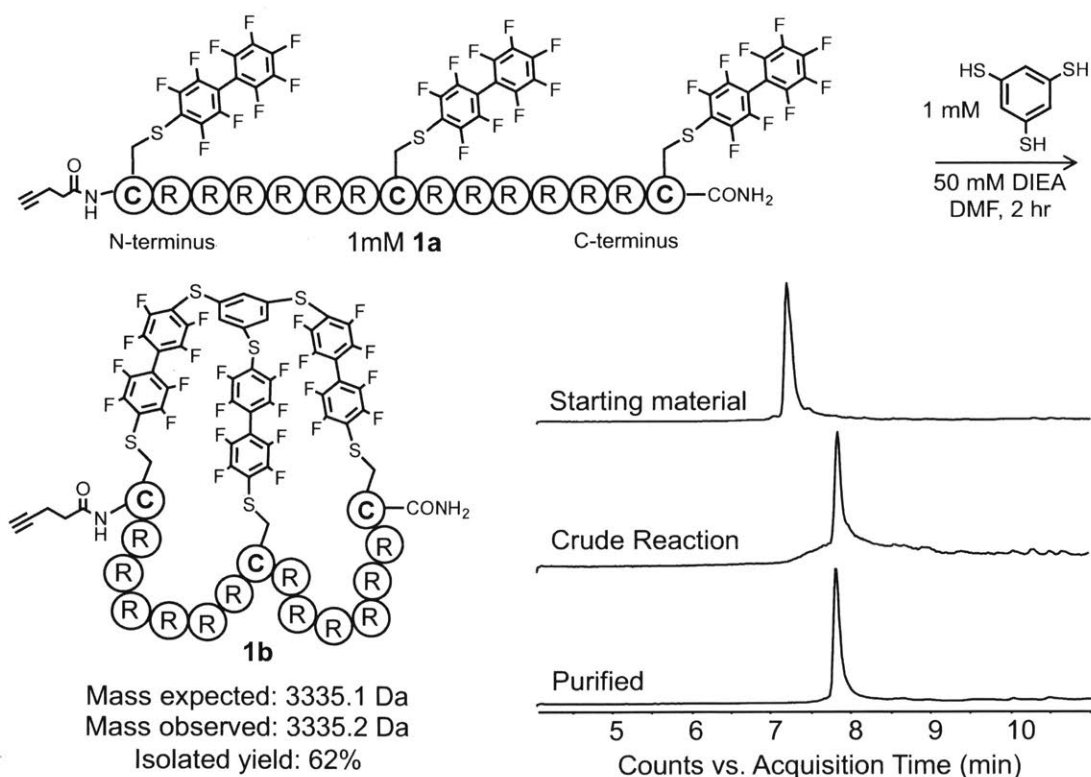


**Figure 4.1. Multiple cysteine residues coupled to a perfluoroarene can be linked with 1,3,5-benzenetrithiol to enable peptide bicyclization.** Peptide **1** is perfluoroarylated to give peptide **1a**. Incubating **1a** (1 mM) with equimolar 1,3,5-benzenetrithiol for 2 hours generates the bicyclic peptide **1b**. LC-MS analysis confirms complete conversion. All chromatograms are total ion currents (TIC). HPLC purification affords **1b** in 62% yield.

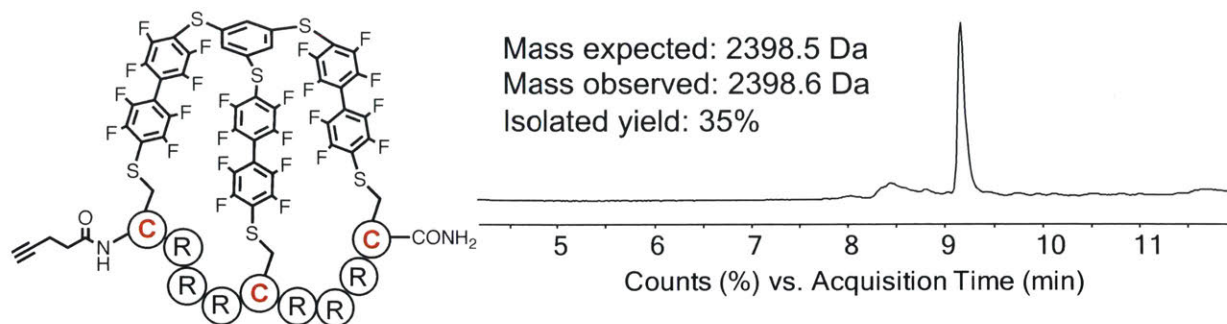


**Figure 4.2.** The 1,3,5-benzenetrithiol linking strategy can be applied to smaller bicycles. Structure and LC-MS analysis of bicyclic peptide **2b**. HPLC purification affords **2b** in 35% yield.

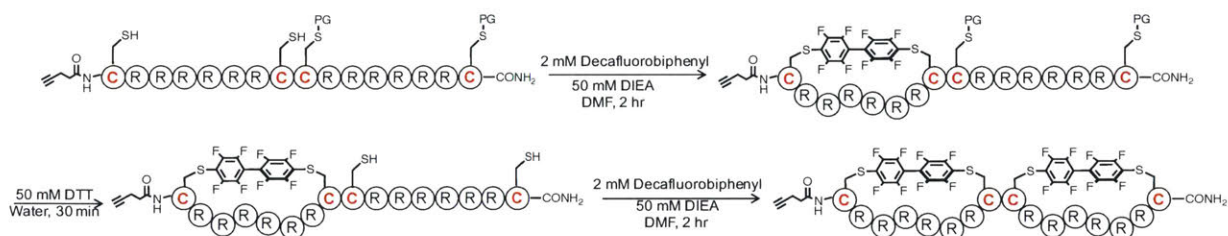


**Figure 4.3.** Double macrocycle prepared through orthogonal protection. Synthetic scheme of bicyclic peptide **3b** using orthogonal protection. PG refers to the *tert*-butylthiol protecting group.

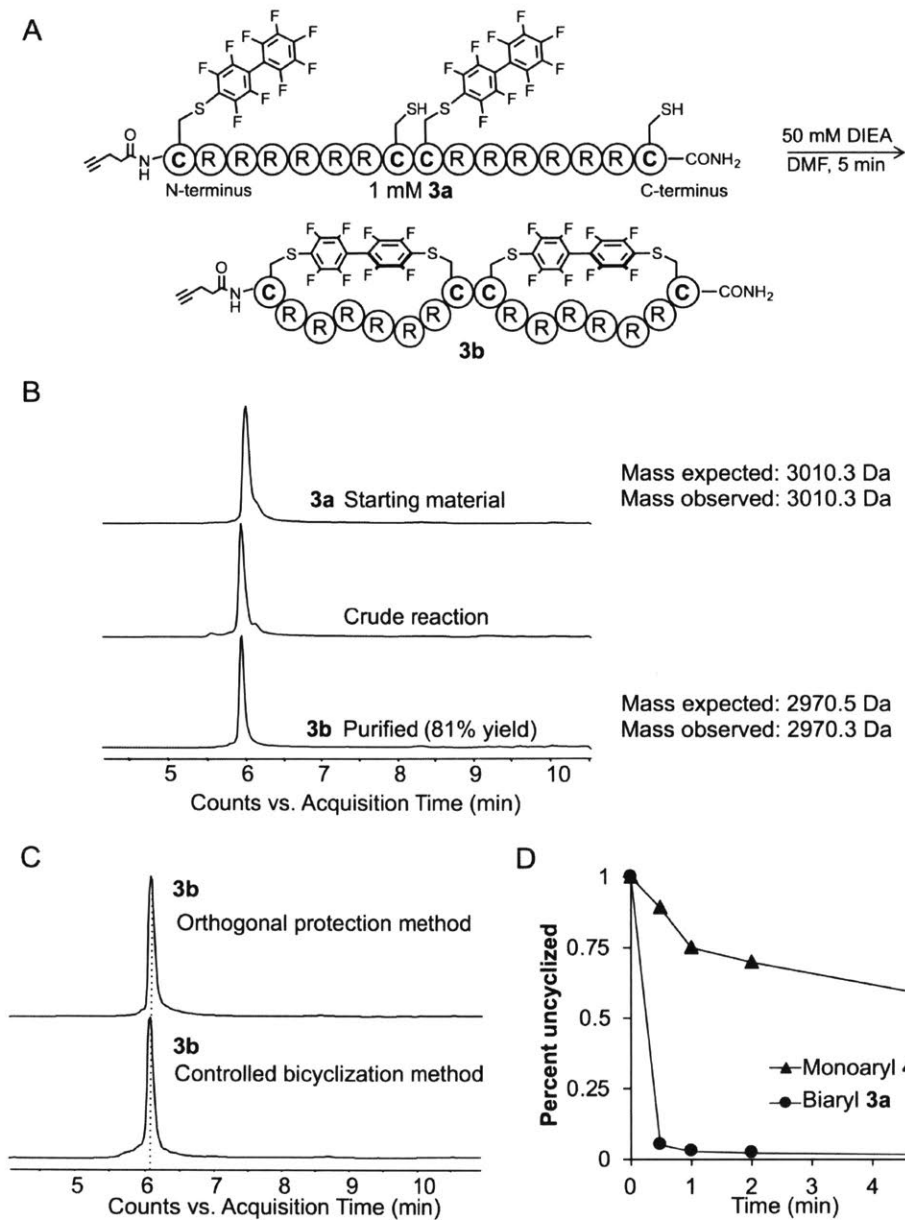


**Figure 4.4. Kinetically controlled bicyclization enables high-yield synthesis of a double perfluoroaryl macrocyclic peptide.** (A) Two perfluoroarenes are selectively installed on the peptide on resin. Peptide **3a** undergoes intramolecular  $S_NAr$  after addition of base to preferentially form two  $i, i+7$  cycles, due to the slow rate of linking adjacent  $i, i+1$  residues. (B) LC-MS analysis and TIC chromatogram demonstrating the conversion of **3a** to **3b** with the appropriate change of mass. (C) TIC chromatogram for peptide **3b** synthesized using orthogonal protection is identical to the chromatogram of peptide **3b** synthesized using kinetically controlled bicyclization. (D) The rate of  $i, i+1$  cyclization of peptide **4a** was compared to cyclization of peptide **3a**. Just 5% of peptide **4a** cyclized in the first 30 seconds, while peptide **3a** shows 95% cyclization in 30 seconds, indicating that the favored regioisomer for peptide **3b** contains two  $i, i+7$  cycles.

**4a** cyclized in the first 30 seconds and less than 30% cyclized after 5 minutes (Figure 4.4D). In comparison, peptide **3a** shows 95% conversion in 30 seconds. The slow rate for *i, i+1* cyclization indicates that the favored regioisomer for peptide **3b** contains two *i, i+7* cycles.

Next, we tested our bicyclic compounds for their ability to promote the intracellular delivery of an 18-mer, 6 kDa PMO. The PMO-peptide conjugates were synthesized using copper-catalyzed “click” chemistry (Figure 4.5A). In addition to the bicyclic peptides, the PMO was conjugated to a monocyclic R12 peptide **6c**, linear R12 peptide **5**, a non-fluorinated bicyclic peptide **1nfb**, and a recently-reported lactam-cyclized R10 peptide **7c** (Figure 4.6).<sup>24</sup>

We measured the activity of the conjugates in the HeLa-654 cell assay.<sup>25</sup> The HeLa-654 cells are stably transfected with an eGFP coding sequence interrupted by a mutant intron from the human  $\beta$ -globin gene (IVS2-654). This intron contains a mutation that alters the normal pre-mRNA splice site to a cryptic splice site, leading to retention of an unnatural exon fragment in the spliced eGFP mRNA. This aberrant mRNA leads to the translation of a *non-fluorescent* form of eGFP. The cargo PMO has a nucleobase sequence complementary to IVS2-654. When the PMO hybridizes to the mutant  $\beta$ -globin exon, it prevents the aberrant gene splicing from occurring and leads to functional eGFP expression. Successful nuclear delivery of PMO leads to the observation of green fluorescence.

To determine if bicyclic peptides improve PMO delivery, the cells were incubated with each PMO-peptide conjugate at 2 and 5  $\mu$ M in media containing 10% serum. After 22 hours, cellular fluorescence was analyzed by flow cytometry (Figure 4.5B). At 5  $\mu$ M treatment, the perfluoroaryl cyclic and bicyclic peptide conjugates all led to an approximately 14-fold increase in eGFP fluorescence relative to PMO. Both the lactam cyclized R10 and the non-fluorinated bicycle exhibited lower fluorescence, demonstrating that the perfluoroarenes contribute to the gains in PMO activity. Additionally, at 2  $\mu$ M concentration, the bicyclic conjugate PMO-**3b** outperformed all of the other conjugates.

To investigate the role of serum, the PMO conjugates were tested in the eGFP assay using media containing 0, 5, and 10% fetal bovine serum. All conjugates exhibited only a mild reduction in activity at higher serum concentrations, suggesting that the hydrophobic perfluoroarenes are not sequestered by serum proteins (Figure 4.7). Additionally, a lactate dehydrogenase (LDH) assay was performed to determine if these compounds disrupt the plasma membrane. For PMO-**1b**, LDH

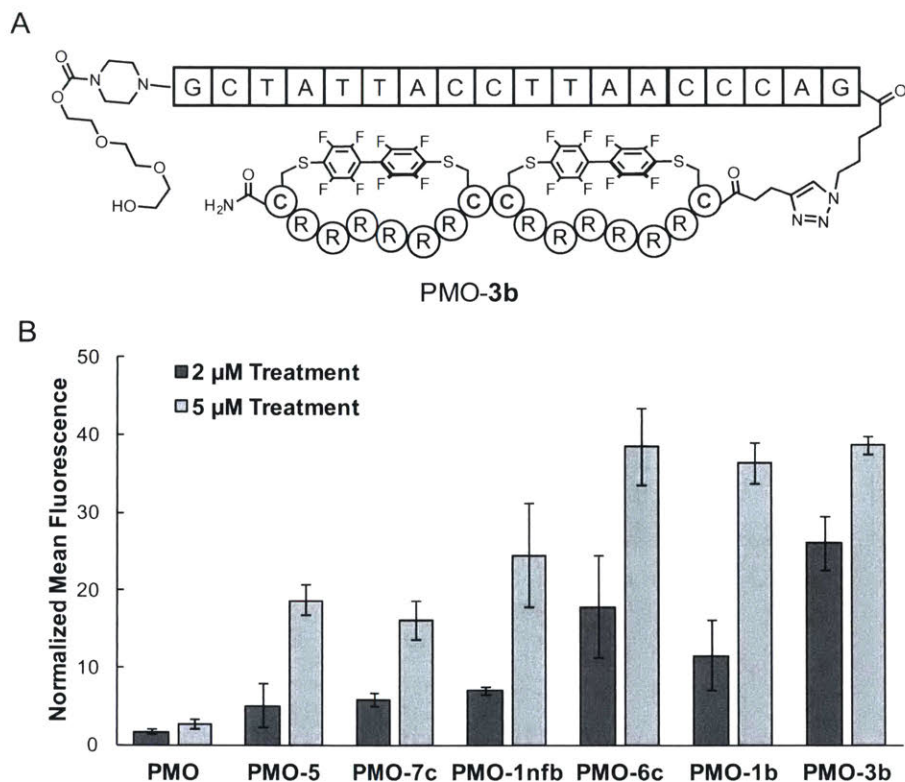


**Figure 4.5. Bicyclic peptides conjugated to PMO show increased exon-skipping activity.** (A) Depiction of bicyclic peptide conjugate **PMO-3b**. (B) Conjugates between PMO and perfluoroaryl cyclic or bicyclic peptides (**6c**, **1b**, and **3b**) lead to more cellular fluorescence than conjugates to linear R12 (**5**), an established cyclic peptide cR10 (**7c**), or a non-fluorinated bicyclic peptide (**1nfb**). The PMO corrects eGFP splicing in a modified HeLa cell line. Cells were incubated with 2  $\mu$ M or 5  $\mu$ M of each PMO-peptide conjugate for 22 hours and the mean fluorescence intensity was analyzed by flow cytometry. Error bars are standard deviation ( $n=3$  independent replicates).

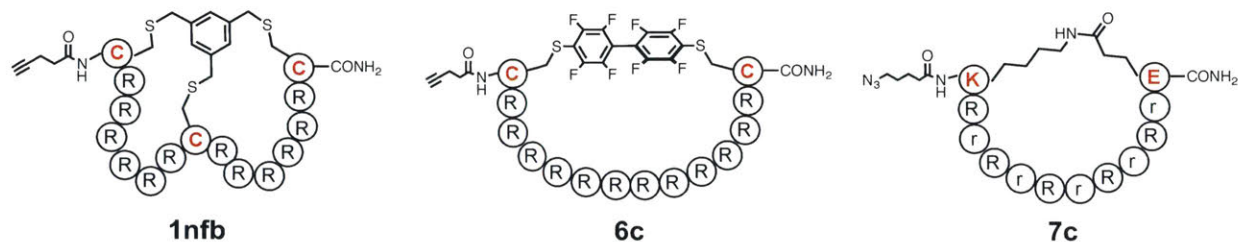


**Figure 4.6. Structures of cyclic controls.** Structures of peptide **1nfb**, **6c**, and **7c**. The non-fluorinated bicyclic peptide **1nfb** was synthesized through the reaction between peptide **1** and tris(bromomethyl)benzene. The cyclic peptide **6c** was synthesized through the reaction between peptide **6** and decafluorobiphenyl. The lactam-cyclized peptide **7c** was cyclized on-resin using standard active-ester chemistry.



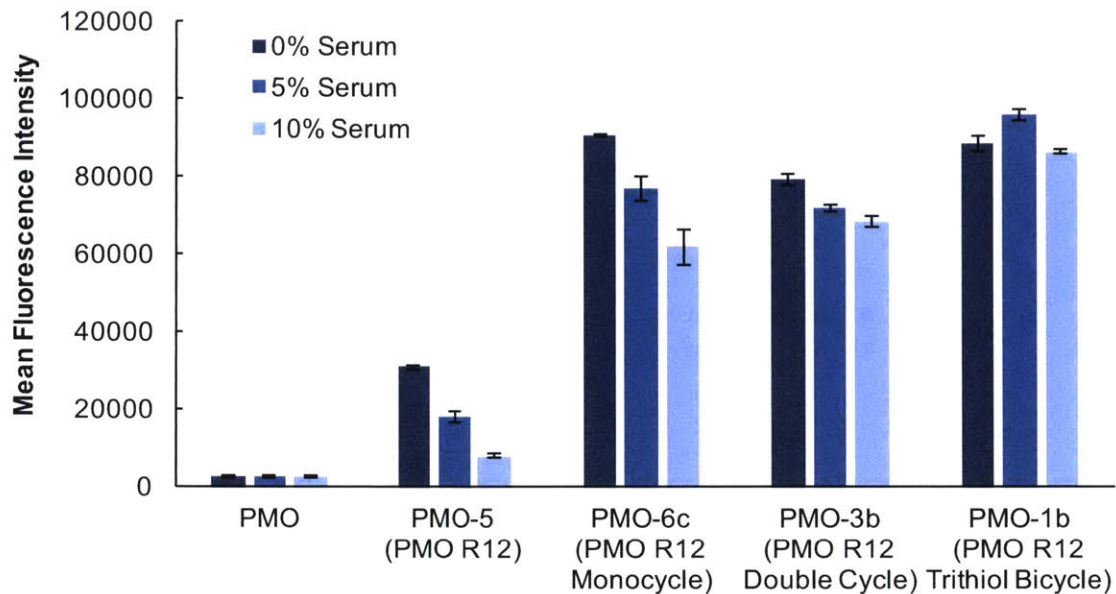


**Figure 4.7. Effect of serum on level of PMO activity observed.** Treatment of HeLa-654 cells using media with different amounts of serum. HeLa-654 cells were treated in a pulse-chase style experiment using 5  $\mu$ M of each PMO conjugate in media containing 0, 5, or 10% fetal bovine serum. After three hours, the treatment media was removed and replaced with untreated media containing 10% FBS. The cells were allowed to grow for 22 hours, and then eGFP fluorescence was analyzed by flow cytometry. Errors bars are standard deviation (n=3 biological replicates). Both PMO-5 and PMO-6c showed a reduction in activity with increasing amounts of serum, while PMO-3b and PMO-1b showed less reduction in activity.



release was observed at both 5  $\mu\text{M}$  and 2  $\mu\text{M}$ , indicating early signs of cytotoxicity. At 2  $\mu\text{M}$ , PMO-**3b** exhibited no signs of LDH release while remaining highly active (Figure 4.8).

We examined if the increase in PMO activity resulted from structural characteristics of the peptides or solely from the combination of arginine residues with a perfluoroarene. PMO-**6c** was tested along with R12 variants cyclized along either the 6 N-terminal residues or the 6 C-terminal residues. The C-terminal cyclized R12 led to less eGFP fluorescence than the fully cyclic peptide **6c**, demonstrating that macrocycle position affects activity (Figure 4.9). Similarly, for the related arginine-rich peptide Bpep, the fully cyclic peptide led to more activity than the N- and C-terminal cyclic variants (Figure 4.10). However, investigations with other peptide transporters confirmed the importance of arginine residues (Figure 4.11).

Lastly, anticipating the peptide bicycles would exhibit enhanced stability, we measured the proteolytic stability of bicyclic *versus* monocyclic peptides (Figure 4.12). The peptides (100  $\mu\text{M}$ ) were incubated with trypsin (0.05  $\mu\text{g}/\text{mL}$ ) at 37  $^{\circ}\text{C}$ . After one hour, less than 5% of the cyclic compound **6c** remained, while 45% of bicycle **3b** remained and nearly 70% of trithiol linked bicycle **1b** remained. Ultimately, both bicyclic peptides demonstrated greater stability than the monocyclic peptide, and this stability could be necessary in therapeutic applications.

Here, we demonstrate multiple strategies for peptide bicyclization using cysteine  $\text{S}_{\text{N}}\text{Ar}$  chemistry. A trithiol can link three perfluoroarenes on a single peptide together into a bicycle, or two thiol pairs can be selectively crosslinked to synthesize a double macrocyclic peptide. In these studies, our cysteine arylation chemistry is shown to modulate the biological properties of arginine-rich peptides. The bicyclic peptides exhibit substantial protease resistance, and PMO-conjugated **3b** does not display signs of cytotoxicity at 2  $\mu\text{M}$  concentration. The exon-skipping activity of PMOs conjugated to perfluoroaryl cyclic or bicyclic peptides is greater than the activity of PMOs conjugated to other cyclic or bicyclic peptides. Moving towards *in vivo* applications, this control over stability, toxicity, and activity will enable the optimization of our lead compounds. Given these results, we envision that perfluoroaryl CPPs represent next-generation delivery agents for macromolecular cargo.

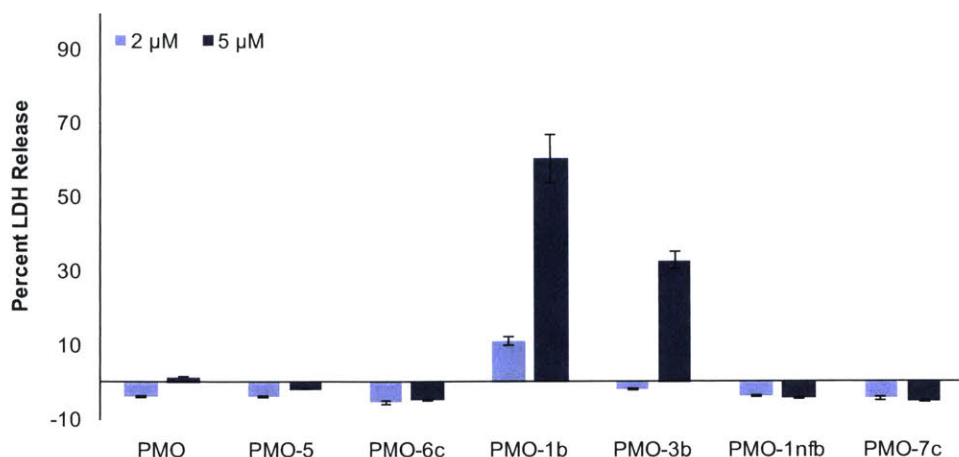


**Figure 4.8. Lactate dehydrogenase (LDH) release assay after treatment with PMO-Bicycle conjugates and controls.** HeLa-654 cells were incubated with 2 or 5  $\mu\text{M}$  of each PMO-peptide conjugate for 22 hours. The media was removed and analyzed for the amount of LDH present. The plot shows the percent of LDH released, compared to total cell lysis as 100% and untreated cells as 0%. PMO-1b showed LDH release at both concentrations, suggesting membrane disruption and early signs of cytotoxicity, while PMO-3b only showed LDH release at 5  $\mu\text{M}$  concentration.

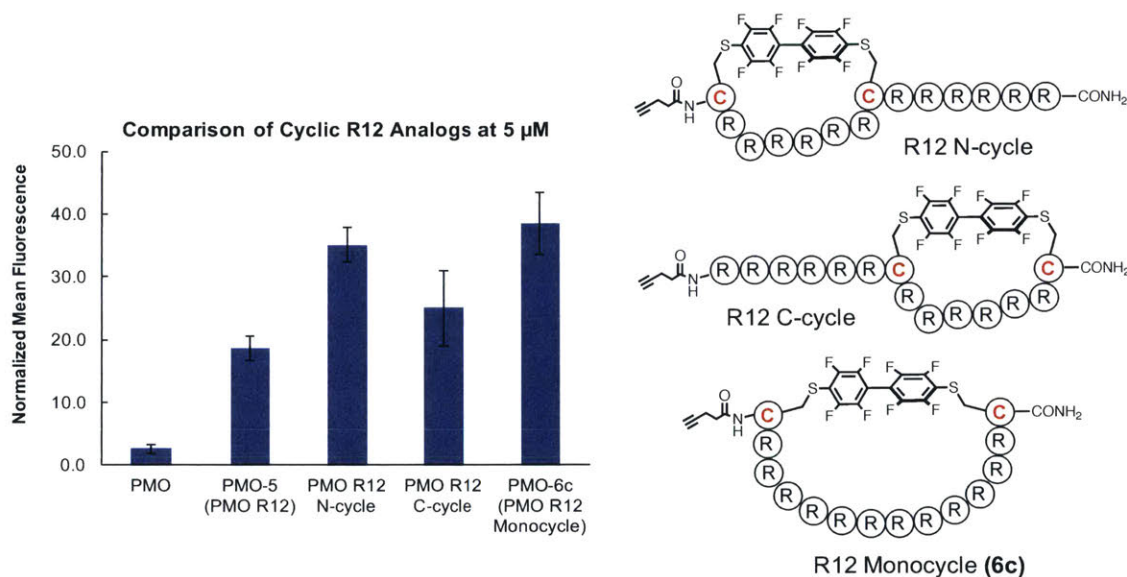


**Figure 4.9. Exon skipping activity of conjugates with R12 monocycles with different cyclization configurations.** The peptides were conjugated to the IVS2-654 PMO and assayed for exon-skipping activity in HeLa-654 cells. Cells were treated with 5  $\mu\text{M}$  of each PMO conjugate for 22 hours and the cellular fluorescence was analyzed by flow cytometry. Each sample was normalized to the background fluorescence of untreated cells. Error bars are standard deviation (three independent experimental replicates, each with  $n=3$  biological replicates). The PMO R12 C-cycle conjugate exhibited reduced cellular fluorescence, suggesting that the increase in activity for PMO-6c is not solely a result of hydrophobicity and cationic nature.

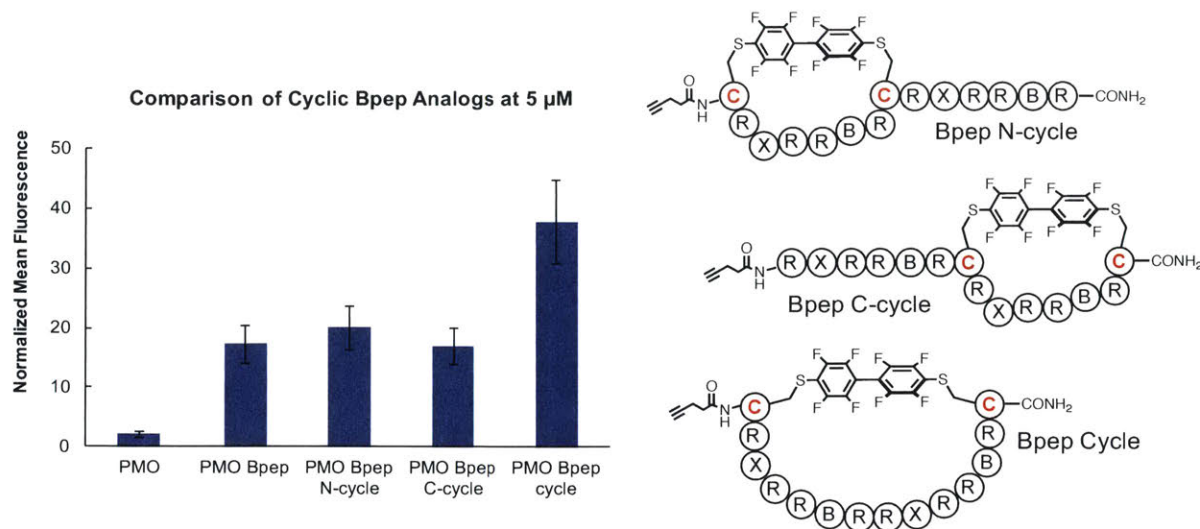


**Figure 4.10. Exon skipping activity of conjugates with Bpep monocycles with different cyclization configurations.** The effect of cyclization for Bpep, another arginine-rich peptide. Bpep was either cyclized across the entire sequence or cyclized on the 6 N-terminal or C-terminal residues. Next, the peptides were conjugated to the IVS2-654 PMO and assayed for exon-skipping activity in HeLa-654 cells. Cells were treated with  $5\mu\text{M}$  of each PMO conjugate for 22 hours and the cellular fluorescence was analyzed by flow cytometry. Each sample was normalized to the background fluorescence of untreated cells. Error bars are standard deviation ( $n=3$  biological replicates). The PMO Bpep cycle conjugate exhibited a two-fold increase in cellular fluorescence relative to Bpep, Bpep N-cycle, and Bpep C-cycle. X = aminohexanoic acid; B = beta-alanine.

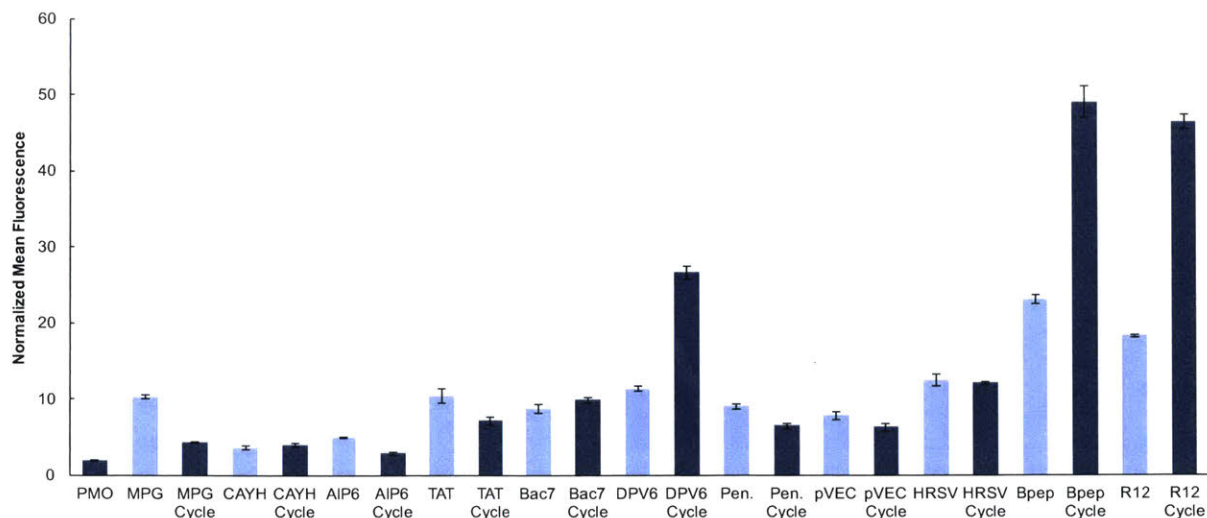


**Figure 4.11 Exon skipping activity of PMO conjugate to perfluoroaryl monocycles of cell-penetrating peptides.** Linear and perfluoroaryl-cyclic cell-penetrating peptides (CPPs) were compared for PMO delivery. For 11 known CPPs, each peptide was synthesized both as a linear peptide and as a cyclic variant with cysteine residues on the N and C-termini of the peptide and linked across the sequence using decafluorobiphenyl. The peptides were conjugated to PMO and assayed for activity in HeLa-654 cells. Cells were treated with 5 $\mu$ M of each PMO conjugate for 22 hours and the cellular fluorescence was analyzed by flow cytometry. Each sample was normalized to the background fluorescence of untreated cells. Error bars are standard deviation (n=3 biological replicates). Many decafluorobiphenyl-cyclized CPPs did not improve PMO activity relative to their linear counterparts. However, cyclic arginine-rich sequences (DPV6, Bpep, and R12) all demonstrated roughly a 2-fold increase in activity relative to the linear sequences. Amino acid sequences and LC-MS analysis in section 4.5. Notes for this figure: R12 is identical to PMO-5 and R12 cycle is identical to PMO-6c. Penetratin is abbreviated as Pen. The linear PMO-CPP conjugate control data shown here are from the library screen in Chapter 2.

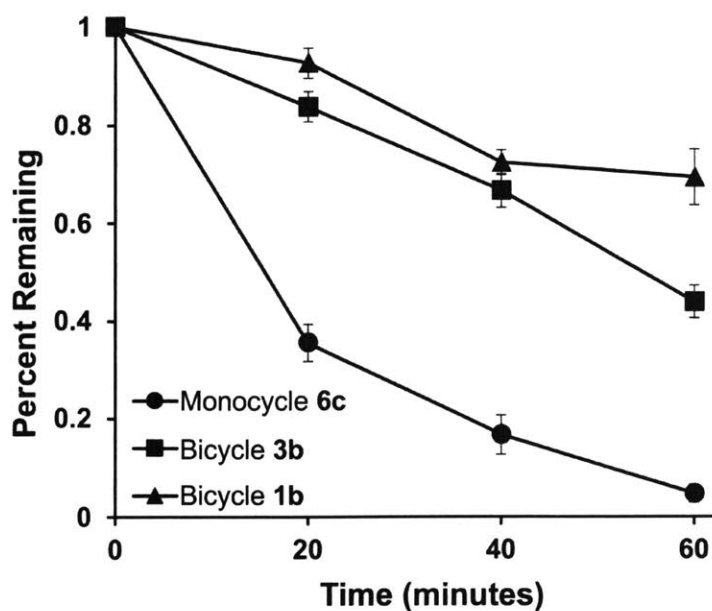


**Figure 4.12. Bicyclic peptides demonstrate enhanced proteolytic stability relative to monocyclic peptides.** The bicyclic peptides **1b** and **3b** and monocyclic peptide **6c** (100  $\mu$ M) were incubated with trypsin (0.05  $\mu$ g/mL) at 37  $^{\circ}$ C. After 1 hour, less than 5% of **6c** remained, while 45% of **3b** and 70% of **1b** remained, demonstrating that bicyclization improves proteolytic stability relative to monocyclization.

## 4.3. Experimental

### 4.3.1. Materials

H-Rink Amide-ChemMatrix resin was obtained from PCAS BioMatrix Inc. (St-Jean-sur-Richelieu, Quebec, Canada). 1-[Bis(dimethylamino)methylene]-1*H*-1,2,3-triazolo[4,5-*b*]pyridinium-3-oxid-hexafluorophosphate (HATU), Fmoc-L-Cys(StBu)-OH, 4-pentynoic acid, and 5-azidopentanoic acid were purchased from Chem-Impex International (Wood Dale, IL). All other Fmoc-protected amino acids were purchased from Advanced ChemTech (Louisville, KY). Peptide synthesis-grade *N,N*-dimethylformamide (DMF), dichloromethane (DCM), diethyl ether, and HPLC-grade acetonitrile were obtained from VWR International (Philadelphia, PA). Decafluorobiphenyl was purchased from Oakwood Products, Inc. (Estill, SC). IVS-654 PMO was provided by Sarepta Therapeutics. All other reagents were purchased from Sigma-Aldrich (St. Louis, MO), water was deionized before use, and reactions were conducted in open-air on bench. For experiments performed at MIT, HeLa-654 cells were obtained from the University of North Carolina Tissue Culture Core facility.

### 4.3.2. Methods for LC-MS Analysis

For all experiments except for the proteolysis assays, LC-MS chromatograms and associated mass spectra were acquired using an Agilent 6520 ESI-Q-TOF mass spectrometer equipped with a C<sub>3</sub> Zorbax column. Mobile phases were: 0.1% formic acid in water (solvent A) and 0.1% formic acid in acetonitrile (solvent B). Column: Zorbax SB C3 column: 2.1 x 150 mm, 5 μm.

General Method: 1% B from 0 to 2 min, linear ramp from 1% B to 61% B from 2 to 11 min, 61% B to 99% B from 11 to 12 min and 3 min of post-time at 1% B for equilibration, flow rate: 0.8 mL/min.

PMO Library method: 5% B from 0 to 2 min, linear ramp from 5% B to 65% B from 2 to 11 min, 65% B from 11 to 12 min and 3 min of post-time at 5% B for equilibration, flow rate: 0.8 mL/min

All data were processed using Agilent MassHunter software package. Y-axis in all chromatograms shown represents total ion current (TIC) unless noted. For the proteolysis assays and bicyclization comparison assay, LC-MS chromatograms and associated mass spectra were acquired using an Agilent 6550 iFunnel Q-TOF mass spectrometer equipped with a Jupiter C<sub>4</sub> Phenomenex column. The following LC-MS method was used: Phenomenex Jupiter C<sub>4</sub>: 150 x 1.0



mm ID, 5  $\mu\text{m}$ , linear gradient from 1% B to 61% B over 10 minutes, pre- and post-time: 2 minutes. Flow rate: 0.1 mL/min.

### 4.3.3. General Method for Peptide Preparation and Purification

*Fast-flow Peptide Synthesis:* Peptides were synthesized on a 0.1-mmol scale using an automated flow peptide synthesizer as previously described.<sup>26</sup> ChemMatrix Rink Amide HYR resin (200 mg) was loaded into a reactor maintained at 90 °C. All reagents were flowed at 80 mL/min with HPLC pumps through a stainless-steel loop maintained at 90 °C before introduction into the reactor. For each coupling, 10 mL of a solution containing 0.2 M amino acid and 0.17 M HATU in DMF were mixed with 200  $\mu\text{L}$  diisopropylethylamine and delivered to the reactor. Fmoc removal was accomplished using 10.4 mL of 20% (v/v) piperidine. Between each step, DMF (15 mL) was used to wash out the reactor. Special coupling conditions were used for arginine, in which the flow rate was reduced to 40 mL/min and 10 mL of a solution containing 0.2 M Fmoc-L-Arg(Pbf)-OH and 0.17 M PyAOP in DMF were mixed with 200  $\mu\text{L}$  diisopropylethylamine and delivered to the reactor. The final coupling was with 4-pentynoic acid, rather than an amino acid, but using the same conditions for activation. After completion of the synthesis, the resins were washed 3 times with DCM and dried under vacuum.

*Peptide Cleavage and Deprotection:* Each peptide was subjected to simultaneous global side-chain deprotection and cleavage from resin by treatment with 6 mL of Reagent K (82.5% trifluoroacetic acid, 5% phenol, 5% water, 5% thioanisole, and 2.5% 1,2-ethanedithiol (EDT)). For arginine-rich peptides, cleavages were left at room temperature for 16 hours to ensure complete removal of the Pbf protecting group. The cleavage cocktail was filtered to remove the resin and the TFA was evaporated by bubbling  $\text{N}_2$  through the mixture. Then ~35 mL of cold ether was added and the crude product was pelleted through centrifugation for three minutes. This ether trituration and centrifugation was repeated two more times. After the third wash, the pellet was redissolved in 50% water and 50% acetonitrile and lyophilized.

*Peptide Purification:* Solvent A: water containing 0.1% TFA and Solvent B: acetonitrile containing 0.1% TFA. Lyophilized peptide was dissolved into a minimum volume of mobile phase (95% A, 5% B). The solution was loaded onto a reversed-phase HPLC column (Agilent Zorbax SB C18 column: 9.4 x 250 mm, 5  $\mu\text{m}$  or Agilent Zorbax SB C3 column: 9.4 x 250 mm, 5  $\mu\text{m}$ ) attached to a mass-based purification system. A linear gradient was run at 0.5% B / min from 5%

B to 55% B. Using mass data about each fraction from the instrument, only pure fractions were pooled and lyophilized. The purity of the fraction pool was confirmed by LC-MS.

#### 4.3.4. Macrocyclization, Arylation, and Bicyclization

*General Conditions for Peptide Macrocyclization:* To the purified peptide dissolved in DMF, decafluorobiphenyl and diisopropylethylamine (DIEA) were added such that the final concentration in the reaction vessel was 1 mM peptide, 2 mM decafluorobiphenyl, and 50 mM DIEA. After two hours, DMF was removed by rotary evaporation to a final volume of 1 mL and the reaction was quenched by adding 39 mL of water containing 2% TFA. The crude reaction was purified by mass-directed semi-preparative reversed-phase HPLC.

*Procedure for Synthesis of **1a**, **2a**:* Peptides **1** (28 mg, 10  $\mu$ mol) or **2** (20 mg, 12  $\mu$ mol) were dissolved in DMF, and stock solutions of decafluorobiphenyl in DMF and diisopropylethylamine (DIEA) were added for a final concentration in the reaction vessel of 1 mM peptide, 100 mM decafluorobiphenyl, and 50 mM DIEA. After two hours, DMF was removed by rotary evaporation to a final volume of 1 mL and the reaction was quenched by adding 39 mL of 85:15 water:acetonitrile containing 2% TFA. The crude reaction was centrifuged, filtered, and purified by mass-directed semi-preparative reversed-phase HPLC (C3 column) to provide **1a** (13 mg, 35%) or **2a** (11 mg, 35%).

*Procedure for Synthesis of Bicycles **1b**, **2b**:* Purified peptides **1a** (10 mg, 2.56  $\mu$ mol) or **2a** (5 mg, 1.9  $\mu$ mol) were dissolved in DMF, and stock solutions of 1,3,5-benzenetrithiol in DMF and DIEA were added such that the final concentration in the reaction vessel was 1 mM peptide, 1 mM 1,3,5-benzenetrithiol, and 50 mM DIEA. After two hours, DMF was removed by rotary evaporation to a final volume of 1 mL and the reaction was quenched by adding 39 mL of 85:15 water:acetonitrile containing 2% TFA. The crude reaction was purified by mass-directed semi-preparative reversed-phase HPLC (C3 column) to provide **1b** (6.4 mg, 62%) or **2b** (1.8 mg, 35%).

*Procedure for Synthesis of Non-fluorinated Bicyclic Peptide **1infb**:* Purified peptide **1** (5 mg, 2.2  $\mu$ mol) was dissolved in 2.2 mL of a degassed solution containing 50 mM Tris buffer pH=8 in 2:1 water:acetonitrile. Then 23  $\mu$ L of a 100 mM solution of tris(bromomethyl)benzene in acetonitrile was added (2.3  $\mu$ mol). After 1 hour, the reaction was diluted to 20 mL with water containing 0.1% TFA and purified by mass-directed semi-preparative reversed-phase HPLC (C18 column) to provide **1infb** (4.7 mg, 89% yield)



*Procedure for Synthesis of bicycle 3b using Orthogonal Deprotection (Figure 4.3):* Peptide **3** was synthesized using standard automated flow chemistry. *Tert*-butyl thiol protected cysteine was incorporated for cysteine residues 1 and 2 and trityl protected cysteine was incorporated for cysteine residues 3 and 4. After cleavage and deprotection, the peptide was purified by reversed-phase HPLC. The peptide was macrocyclized using the above procedure for macrocyclization with a decafluorobiphenyl using 29 mg of peptide (9.5 mg, 30.3% yield). Next, *tert*-butylthiol protected cysteine residues 1 and 2 were deprotected by incubating the peptide (1 mM) with DTT (50 mM) and Tris (25 mM pH 8) in water for 30 minutes, followed by solid-phase extraction (SPE) to remove residual DTT (6.5 mg, 73% yield). The remaining two free cysteine residues were macrocyclized using the general procedure and purified by reversed-phase HPLC (C3 column) (1.5 mg, 21% yield). Overall yield 4.5%.

*Procedure for Synthesis of 3a:* Peptide **3** was synthesized using standard automated flow chemistry using 200 mg of resin. *Tert*-butyl thiol protected cysteine was incorporated for cysteine residues 1 and 3 and trityl protected cysteine was incorporated for cysteine residues 2 and 4. The *tert*-butyl thiol groups were deprotected on resin using 3.8 mmol DTT in 2.5 mL DMF with 0.25 mL DIEA. The reaction proceeded at 60 °C for 20 minutes. The resin was washed 3 times with DMF, followed by the addition of decafluorobiphenyl (1 mmol) with 2.5 mL DMF and 0.25 mL DIEA. The reaction proceeded at room temperature for 2 hours, and then the resin was washed with DMF (3x) and DCM (3x). The peptide was then cleaved from the resin and purified by reversed-phase HPLC (C3 column) to afford **3a**.

*Procedure for Synthesis of Bicycle 3b using Kinetically Controlled Bicyclization:* Peptide **3a** (15 mg, 4  $\mu$ mol, assuming 6 coordinated TFA salts) was suspended in 4 mL DMF. Neat DIEA (35.4  $\mu$ L) was added to achieve a concentration of 50 mM. The reaction was allowed to proceed for 5 minutes, after which complete conversion is observed. DMF was removed by rotary evaporation to a final volume of 1 mL and the reaction was quenched by adding 39 mL of water containing 2% TFA. The reaction was purified by mass-directed semi-preparative reversed-phase HPLC (C3 column) to provide peptide **3b** (12.0 mg, 81% yield).

*Procedure for Synthesis of Arylated Control Peptide 4a:* Peptide **4** was synthesized using standard automated flow chemistry using 200 mg of resin except *tert*-butyl thiol protected cysteine was incorporated for cysteine residue 1 and trityl protected cysteine was incorporated for cysteine residue 2. The *tert*-butyl groups were deprotected on resin using 3.8 mmol DTT in 2.5 mL DMF

with 0.25 mL DIEA. The reaction proceeded at 60 °C for 20 minutes. The resin was washed 3x with DMF, followed by the addition of decafluorobiphenyl (1 mmol) with 2.5 mL DMF and 0.25 mL DIEA. The reaction proceeded at room temperature for 2 hours, and then the resin was washed with DMF (3x) and DCM (3x). The peptide was then cleaved from the resin and purified using mass-directed semi-preparative reversed-phase HPLC (C3 column) to afford **4a**.

*Procedure for Synthesis of Cyclic Peptide 6c:* Peptide **6** was synthesized using standard automated flow chemistry using 200 mg of resin. *Tert*-butyl thiol protected cysteine was incorporated for cysteine residue 1 and trityl protected cysteine was incorporated for cysteine residue 2. The *tert*-butyl groups were deprotected on resin using 3.8 mmol DTT in 2.5 mL DMF with 0.25 mL DIEA. The reaction proceeded at 60 °C for 20 minutes. The resin was washed with DMF (3x), followed by the addition of decafluorobiphenyl (1 mmol) with 2.5 mL DMF and 0.25 mL DIEA. The reaction proceeded at room temperature for 2 hours, and then the resin was washed with DMF (3x) and DCM (3x). The peptide was then cleaved from the resin and purified using mass-directed semi-preparative reversed-phase HPLC (C3 column) to afford the monoaryl **6a**.

Peptide **6a** was macrocyclized by suspending the peptide (12 mg, 3.9 μmol, assuming 6 coordinated TFA salts) in 3.9 mL DMF. Neat DIEA (33.8 μL) was added to achieve a concentration of 50 mM. The reaction was allowed to proceed for 5 minutes, after which complete conversion was observed. DMF was removed by rotary evaporation to a final volume of 1 mL and the reaction was quenched by adding 39 mL of water containing 2% TFA. The reaction was purified by mass-directed semi-preparative reversed-phase HPLC (C3 column) to provide peptide **6c** (8.4 mg, 88% yield).

*Procedure for Synthesis of Cyclic Peptide 7c:* Peptide **7**, XK(Alloc)RrRrRrRrRrE(OAll) was synthesized using a combination of standard manual flow solid-phase peptide synthesis and published protocols synthesis of cR10 as detailed below.<sup>24,27</sup> “R” refers to Fmoc-L-Arg(Pbf) while “r” refers to Fmoc-D-Arg(Pbf). Lysine was Alloc-protected and Glu was OAll-protected to enable selective side-chain deprotection on resin for lactam cyclization. “X” is 5-azidopentanoic acid, which was incorporated instead of 4-pentynoic acid to avoid side-reactions between palladium and alkynes.

Synthesis proceeded as follows: 140 mg of H-Rink-Amide PEG resin was downloaded to 0.1667 mmol/g using a 1:2 mixture of Fmoc-Glu(OAll)-OH and Boc-Glu(OBnzl)-OH. The remaining amino-acids were coupled using manual flow peptide synthesis conditions, as

previously described.<sup>27</sup> To remove Alloc- and OAll- protecting groups, the peptidyl resin was mixed with 0.01 mmol tetrakis(triphenylphosphine) palladium and 2.5 mmol phenylsilane in dry DCM. After 30 minutes, the resin was washed with DCM (3x), with 20% DIEA in DMF (3x), and with DMF (3x). To cyclize, 1 eq. of HBTU (0.023 mmol, based upon resin loading) was diluted into 6 mL of DMF with 8  $\mu$ L DIEA and added to the resin. After 2 hours, the resin was washed with DMF (3x) and with DCM (3x). The peptide was then cleaved from the resin and purified using mass-directed semi-preparative reversed-phase HPLC (C18 column) to afford the cyclic peptide **7c**.

#### 4.3.5. PMO-Peptide Conjugation

*Procedure for Coupling 5-azidopentanoic to PMO:* PMO IVS2-654 (200 mg, 32  $\mu$ mol) was dissolved in 600  $\mu$ L DMSO. To the DMSO solution was added a solution containing 4 equivalents of 5-azidopentanoic acid (13.6  $\mu$ L, 128  $\mu$ mol) activated with HBTU (320  $\mu$ L of 0.4 M HBTU in DMF, 128  $\mu$ mol) and DIEA (22.3  $\mu$ L, 128  $\mu$ mol) in 244  $\mu$ L DMF (Final reaction volume = 1.2 mL). The reaction proceeded for 25 minutes before being quenched with 1 mL of water and 2 mL of ammonium hydroxide. The ammonium hydroxide will hydrolyze any ester formed during the course of the reaction. After 1 hour, the solution was diluted to 40 mL and purified using reversed-phase HPLC (Agilent Zorbax SB C3 column: 21.2 x 100 mm, 5  $\mu$ m) and a linear gradient from 2 to 60% B (solvent A: water; solvent B: acetonitrile) over 58 minutes (1 %B / min). Using mass data about each fraction from the instrument, only pure fractions were pooled and lyophilized. The purity of the fraction pool was confirmed by LC-MS. Lyophilization afforded 171 mg of dry powder (84% yield).

*Procedure for Coupling 4-pentynoic acid to PMO:* PMO IVS2-654 (200 mg, 32  $\mu$ mol) was dissolved in 600  $\mu$ L DMSO. To the DMSO solution was added a solution containing 4 equivalents of 4-pentynoic acid (128  $\mu$ mol) activated with HBTU (320  $\mu$ L of 0.4 M HBTU in DMF, 128  $\mu$ mol) and DIEA (22.3  $\mu$ L, 128  $\mu$ mol) in 244  $\mu$ L DMF (Final reaction volume = 1.2 mL). The reaction proceeded for 25 minutes before being quenched with 1 mL of water and 2 mL of ammonium hydroxide. The ammonium hydroxide will hydrolyze any ester formed during the course of the reaction. After 1 hour, the solution was diluted to 40 mL and purified using reversed-phase HPLC (Agilent Zorbax SB C3 column: 21.2 x 100 mm, 5  $\mu$ m) and a linear gradient from 2 to 60% B (solvent A: water; solvent B: acetonitrile) over 58 minutes (1 %B / min). Using mass data about

each fraction from the instrument, only pure fractions were pooled and lyophilized. The purity of the fraction pool was confirmed by LC-MS.

*General Procedure for PMO-peptide conjugation by azide/alkyne Huisgen Cycloaddition:*

A 20 mL scintillation vial with a septum cap was charged with peptide alkyne (1.1  $\mu\text{mol}$ ), ISV2-654 azide (0.95  $\mu\text{mol}$ ), and copper bromide (0.05 mmol). The vial was purged with nitrogen for 5 minutes to ensure the removal of oxygen before the addition of  $\sim 1$  mL of degassed DMF through the septum. The reaction mixture was vortexed for 1 minute. After 2 hours, the reaction mixture was diluted with 10 mL of 50 mM Tris (pH 8), and loaded onto a reversed-phase HPLC column (Agilent Zorbax SB C3 9.4 x 50 mm, 5  $\mu\text{m}$ ). Chromatography was performed using a linear gradient from 5-45 %B over 20 minutes. Solvent A: 100 mM ammonium acetate, pH = 8 in water; solvent B: acetonitrile. Using mass data about each fraction from the instrument, only pure fractions were pooled and lyophilized. The purity of the fraction pool was confirmed by LC-MS.

Because peptide **7c** contained an azide group, for the synthesis of PMO-**7c** an identical protocol was followed using ISV2-654-alkyne.

PMO-**3b** and PMO-**6c** were purified a second time to remove co-eluting PMO, except now using solvent A: water containing 0.1% formic acid and solvent B: acetonitrile containing 0.1% formic acid. After lyophilization, the conjugates were then resuspended in water containing 100 mM ammonium acetate and lyophilized again.

#### **4.3.6. Proteolysis Assay**

For each peptide, 19.6  $\mu\text{L}$  of PBS, 0.2  $\mu\text{L}$  of Trypsin (0.005 mg/mL stock solution in 1 mM HCl), and 0.2  $\mu\text{L}$  of peptide (1 mM DMSO stock solution) were combined in a PCR tube. The resulting reaction mixture was capped and incubated at 37  $^{\circ}\text{C}$ . At each time point, 1.0  $\mu\text{L}$  of the crude reaction was transferred to a LC-MS vial and quenched by addition of 99  $\mu\text{L}$  of 50:50 water:acetonitrile containing 0.1% TFA. 1.0  $\mu\text{L}$  of the quenched reaction was injected onto the Agilent 6550 iFunnel Q-TOF MS. Time points were taken at  $t = 0$  min, 20 min, 40 min, and 60 min. An extracted ion current (EIC) for the +5 charge state  $m/z$  was analyzed using the MassHunter software. The EIC peak was integrated and percent peptide intact was determined by  $(\text{EIC}_{t_1}/\text{EIC}_{t_0}) * 100$  in which  $\text{EIC}_{t_1}$  is the peak integration at a given time point and  $\text{EIC}_{t_0}$  is the peak integration at time  $t = 0$ .

#### **4.3.7. Comparison of *i*, *i+1* and *i*, *i+7* Cyclization**

A 0.5 mL microcentrifuge tube was charged with 1 mM **3a** in DMF. The cyclization reaction began with the addition of DIEA (50 mM) and the reaction vessel was vortexed for 30 seconds. After 0, 30, 60, 120, and 300 seconds, a 1  $\mu$ L aliquot was quenched with 19  $\mu$ L of 50:50 water:acetonitrile containing 0.1% TFA and subjected to LC-MS analysis on an Agilent 6550 iFunnel Q-TOF MS. An extracted ion current (EIC) for the +5 charge state  $m/z$  was analyzed using the MassHunter software. The EIC peak was integrated and percent peptide intact was determined by  $(EIC_{t_1}/EIC_{t_0}) * 100$  in which  $EIC_{t_1}$  is the peak integration at a given time point and  $EIC_{t_0}$  is the peak integration at time  $t = 0$ . The process was repeated exactly for **4a**.

#### 4.3.8. eGFP Exon Skipping Assay

HeLa-654 cells were maintained in MEM supplemented with 10% (v/v) fetal bovine serum (FBS) and 1% (v/v) penicillin-streptomycin at 37 °C and 5% CO<sub>2</sub>. Each PMO-peptide conjugate stock solution was freshly prepared on the same day as the experiment using phosphate-buffered serum (PBS). The concentration of the stocks was determined by measuring the absorbance at  $\lambda=260$  nm (PMO extinction coefficient of  $\epsilon=168,700$  L mol<sup>-1</sup> cm<sup>-1</sup>). One day before treatment, cells were plated in a 96-well plate at a density of 5,000 cells/well. For treatment, cells were incubated with 100  $\mu$ L of each respective conjugate at a concentration of either 2 or 5  $\mu$ M in MEM supplemented with 10% FBS and 1% penicillin-streptomycin at 37 °C and 5% CO<sub>2</sub> for 22 hours. Next, the treatment media was aspirated and each well was incubated with 20  $\mu$ L Trypsin-EDTA 0.25% for 15 min at 37 °C and 5% CO<sub>2</sub>. To quench the trypsin, 80  $\mu$ L of media was added to each well. The dissociated cells were transferred to a 96-well plate and spun at 500 *ref* for 3 min. The supernatant was removed and the pellets were each washed with 200  $\mu$ L of phosphate-buffered saline (PBS), and the 96-well plate was centrifuged again. The supernatant was again removed and the pellets were resuspended in 300  $\mu$ L PBS with 2% FBS (v/v) and 2  $\mu$ g/mL propidium iodide in water.

Flow cytometry analysis was carried out on a BD LSRII flow cytometer. Gates were applied to the data to ensure that cells that were highly positive for propidium iodide or exhibited forward/side scatter readings that were sufficiently different from the main cell population were excluded. The gated cell population for each sample well contains at least 2,000 events, with the exception of PMO-**1b** which contains 100-2,600 events for 5  $\mu$ M treatment and 1,300-5,000 events for 2  $\mu$ M treatment.

The mean fluorescence intensity was calculated for each sample and normalized to the background cellular fluorescence of untreated cells. For each PMO-peptide conjugate, the mean fluorescence intensity was averaged across the biological replicates (n=3). The experiment was then repeated on 3 different days. The average normalized fluorescence data for each experiment are shown in Tables 4.2 and 4.3.

All HeLa-654 experiments were performed in the Pentelute lab, with the exception of experiments testing the additional linear and cyclic peptides shown in Figures 4.10 and 4.11. These experiments were performed at Sarepta Therapeutics as part of a library screen. In these cases, the mean fluorescence intensity was calculated for each sample and normalized to the background cellular fluorescence of untreated cells. Then, for each PMO-peptide conjugate, the mean fluorescence intensity was averaged across the biological replicates (n=3). The experiment was not repeated.

#### **4.3.9. eGFP Exon Skipping Assay with Varying Amounts of Serum**

To test the role of serum in the treatment media, a pulse-chase experiment was performed. Briefly, HeLa 654 cells were plated at a density of 5,000 cells per well in a 96-well plate in MEM supplemented with 10% FBS and 1% penicillin-streptomycin. The next day, PMO-peptide conjugate stocks were prepared in PBS and added to media supplemented with 0%, 5%, or 10% (v/v) FBS to a final concentration of 5  $\mu$ M. After preparation, the culture media was aspirated and the treatment media was added to each well. After incubation at 37 °C and 5% CO<sub>2</sub> for 3 hours, the treatment media was replaced with fresh untreated media (containing 10% serum and no PMO-peptide conjugate) and the cells were allowed to grow for another 22 hours at 37 °C and 5% CO<sub>2</sub>. Sample preparation and flow cytometry was then performed as described above. The gated cell population for each sample well contains at least 2,000 events, with the exception of PMO-1b which contained between 500 and 2500 events per sample.

#### **4.3.10. Lactate Dehydrogenase Assay**

This experiment was performed using the treatment media from the eGFP exon-skipping assay experiment. After the 22-hour treatment, the supernatant treatment media was transferred to another clear-bottom 96-well plate for the assay. The assay was performed using the CytoTox 96® Non-Radioactive Cytotoxicity Assay (Promega) according to the included technical bulletin. After completion of the assay, the final solution in each well was diluted 5x with PBS such that the measured absorbance was in the linear range of the instrument. The absorbance was measured on

a BioTek Epoch Microplate Spectrophotometer. Two sets of cell only wells were used as controls - one set was the negative control and the other was a positive control in which the cells were lysed using the assay lysis buffer to provide data for total LDH release. The results are expressed as a ratio of (Absorbance of sample – absorbance of negative control)/(Absorbance of total lysis - absorbance of negative control).

| <b>Construct at 5<math>\mu</math>M</b> | <b>Experiment 1<br/>Average<br/>Normalized Mean<br/>Fluorescence</b> | <b>Experiment 2<br/>Average<br/>Normalized Mean<br/>Fluorescence</b> | <b>Experiment 3<br/>Average<br/>Normalized Mean<br/>Fluorescence</b> |
|--|--|--|--|
| PMO                                    | 2.6  | 3.4  | 2.0  |
| PMO-5                                  | 18.4   | 16.9   | 20.7   |
| PMO-6c                                 | 33.2   | 39.2   | 43.1   |
| PMO-1b                                 | 38.8   | 36.7   | 33.6   |
| PMO-3b                                 | 39.5   | 37.3   | 39.3   |
| PMO-1nfb                               | 17.4   | 25.2   | 30.9   |
| PMO-7c                                 | 13.3   | 17.8   | 17.3   |
| PMO-R12 N-cycle                        | 36.6   | 31.9   | 36.8   |
| PMO-R12 C-cycle                        | 18.7   | 25.9   | 30.6   |

**Table 4.2. Data from three individual experiments after treatment with each construct at 5  $\mu$ M.**

| <b>Construct at 2 <math>\mu</math>M</b> | <b>Experiment 1<br/>Average<br/>Normalized Mean<br/>Fluorescence</b> | <b>Experiment 2<br/>Average<br/>Normalized Mean<br/>Fluorescence</b> | <b>Experiment 3<br/>Average<br/>Normalized Mean<br/>Fluorescence</b> |
|---|--|--|--|
| PMO                                     | 2.0  | 1.3  | 1.7  |
| PMO-5                                   | 3.5  | 3.3  | 8.3  |
| PMO-6c                                  | 11.6   | 17.1   | 24.9   |
| PMO-1b                                  | 9.2  | 8.8  | 16.8   |
| PMO-3b                                  | 22.2   | 28.7   | 27.5   |
| PMO-1nfb                                | 6.9  | 7.6  | 6.6  |
| PMO-7c                                  | 5.7  | 5.0  | 6.6  |

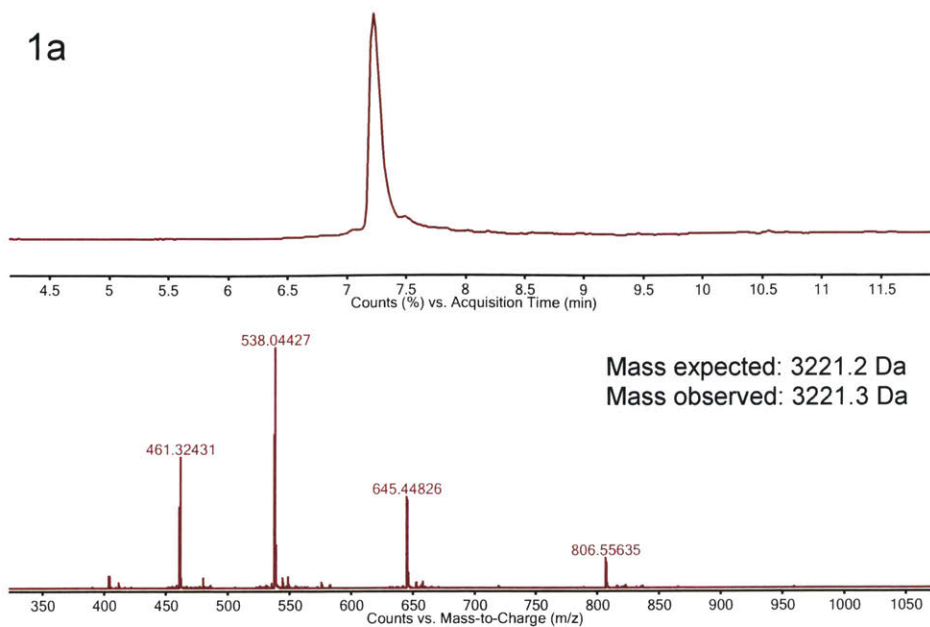
**Table 4.3. Data from three individual experiments after treatment with each construct at 2  $\mu$ M.**



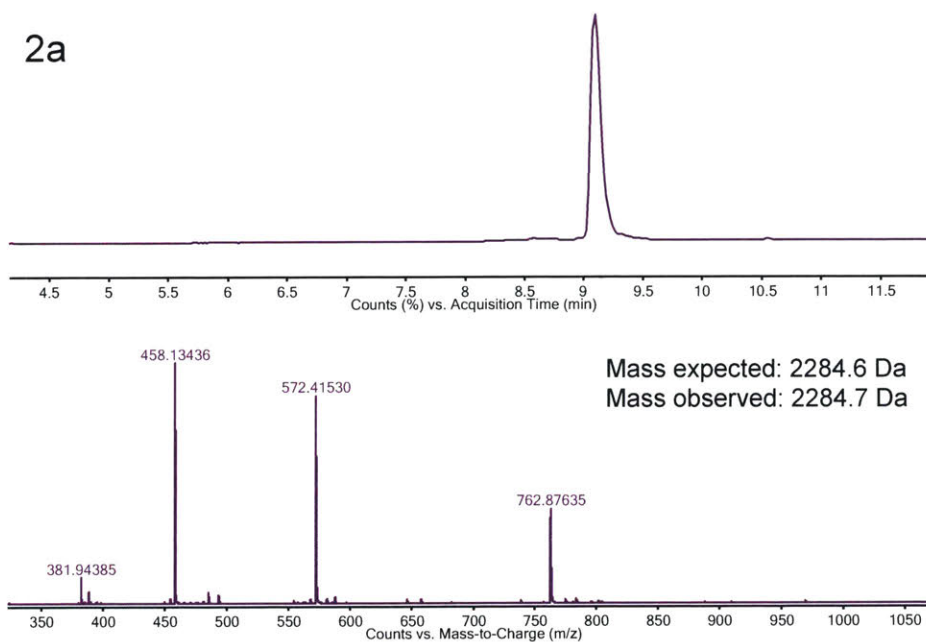
#### **4.4. Acknowledgments**

This work was supported by Sarepta Therapeutics, Cambridge MA. J.M.W. and R.L.H are supported by the National Science Foundation Graduate Research Fellowship under Grant No. 1122374. C.M.F. is supported by the David H. Koch Graduate Fellowship Fund and by the Eunice Kennedy Shriver National Institute of Child Health and Human Development of the National Institutes of Health under award number F30HD093358.

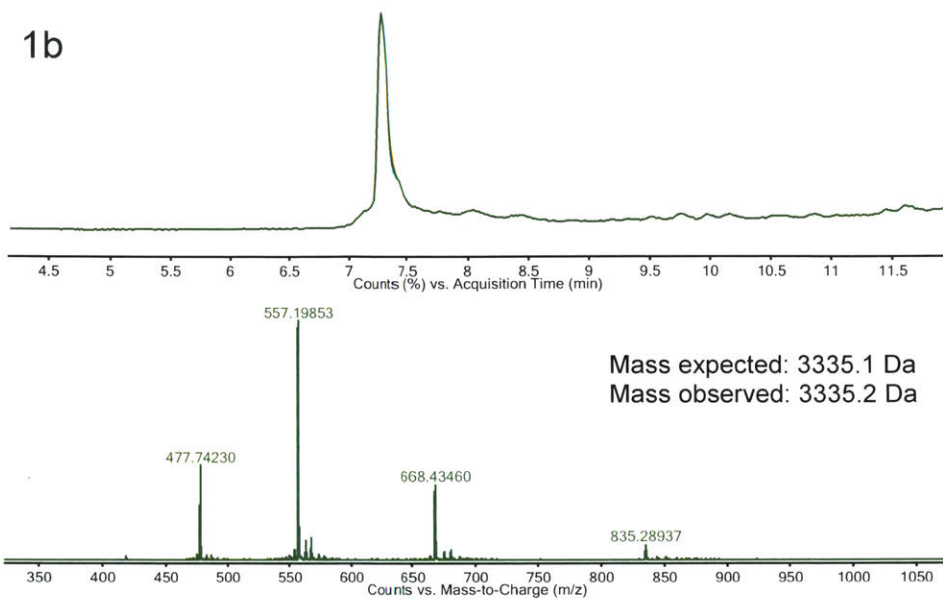
## 4.5. Appendix of LC-MS Characterization



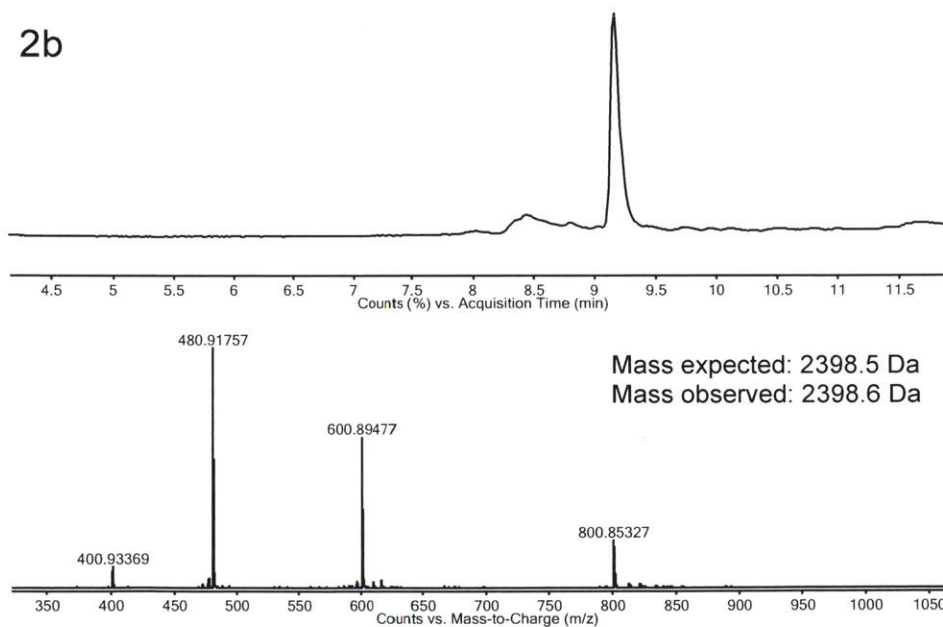
LC-MS characterization of peptide **1a** (perfluoroarylated). TIC and mass spectrum of major peak.



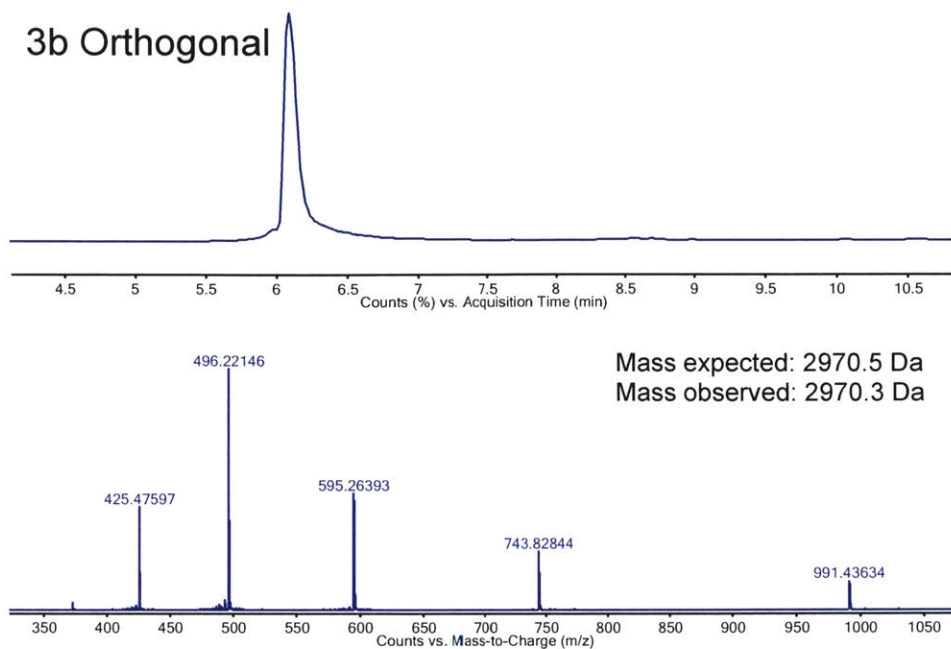
LC-MS characterization of peptide **2a** (perfluoroarylated). TIC and mass spectrum of major peak.



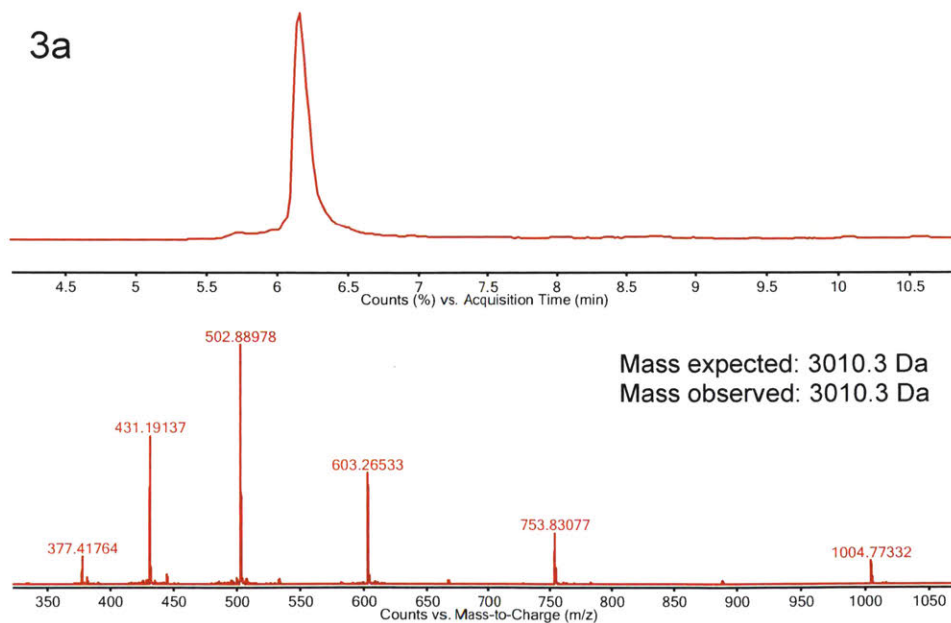
LC-MS characterization of peptide **1b** (bicycle). TIC and mass spectrum of major peak.



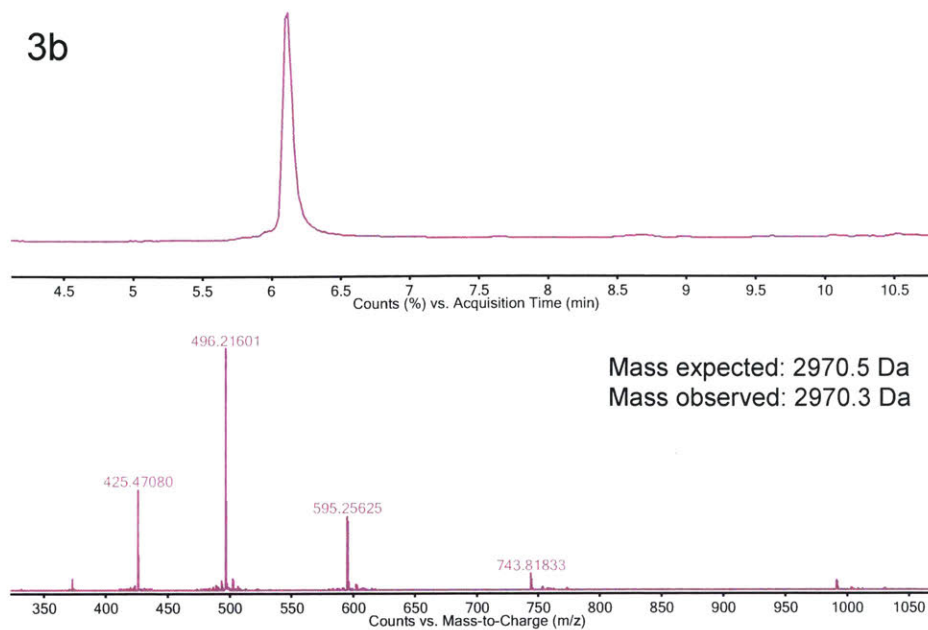
LC-MS characterization of peptide **2b** (bicycle). TIC and mass spectrum of major peak.



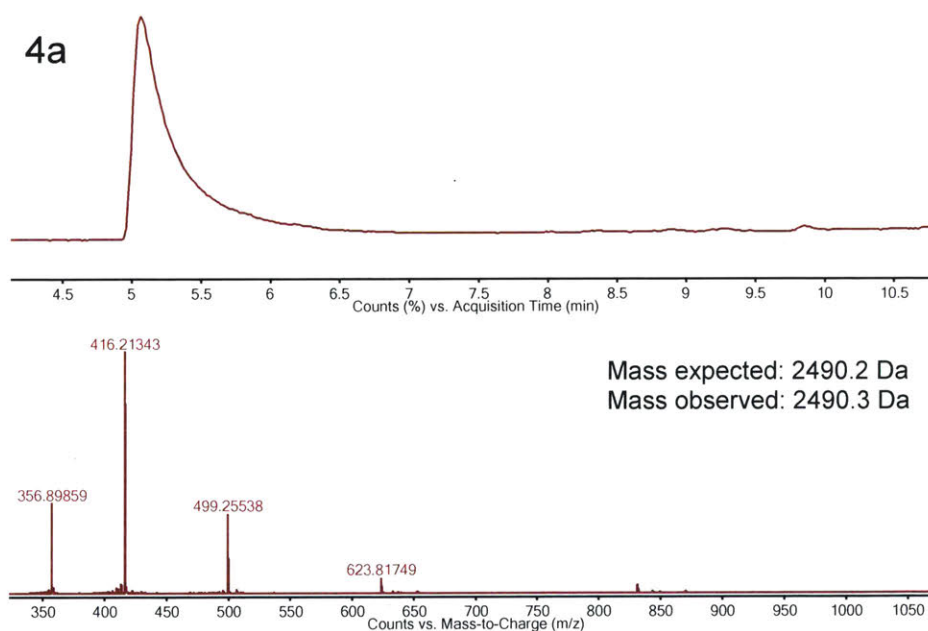
LC-MS characterization of peptide **3b** (double macrocycle prepared through orthogonal deprotection). TIC and mass spectrum of major peak.



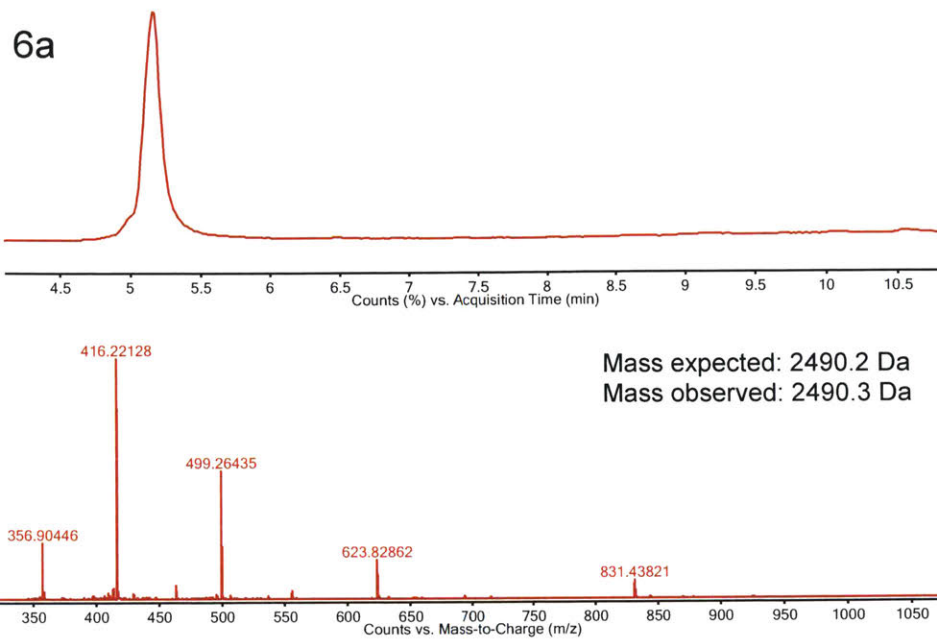
LC-MS characterization of peptide **3a** (peptide 3 with decafluorobiphenyl at positions 1 and 9). TIC and mass spectrum of major peak.



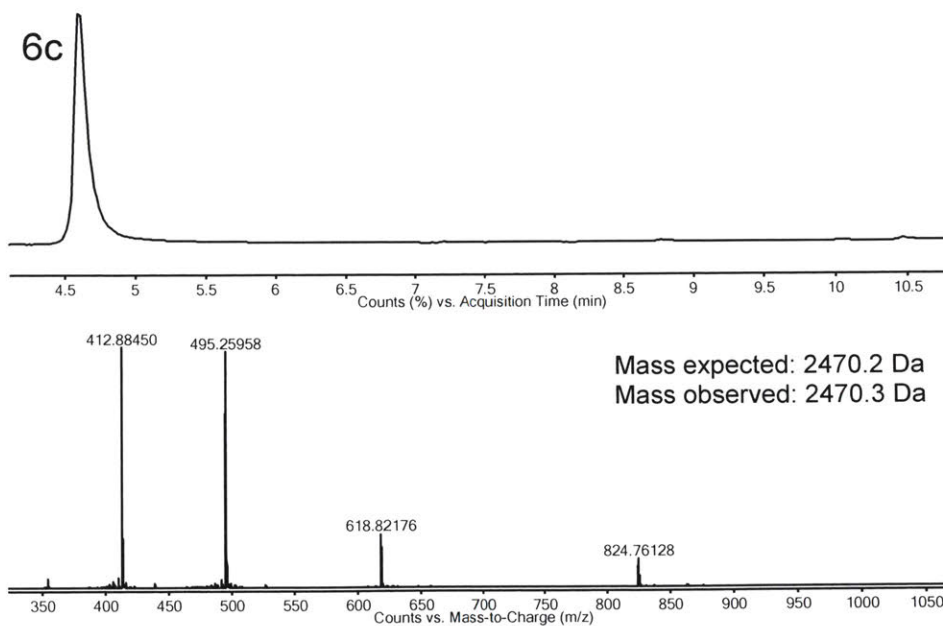
LC-MS characterization of peptide **3b** (double macrocycle prepared through kinetic control). TIC and mass spectrum of major peak.



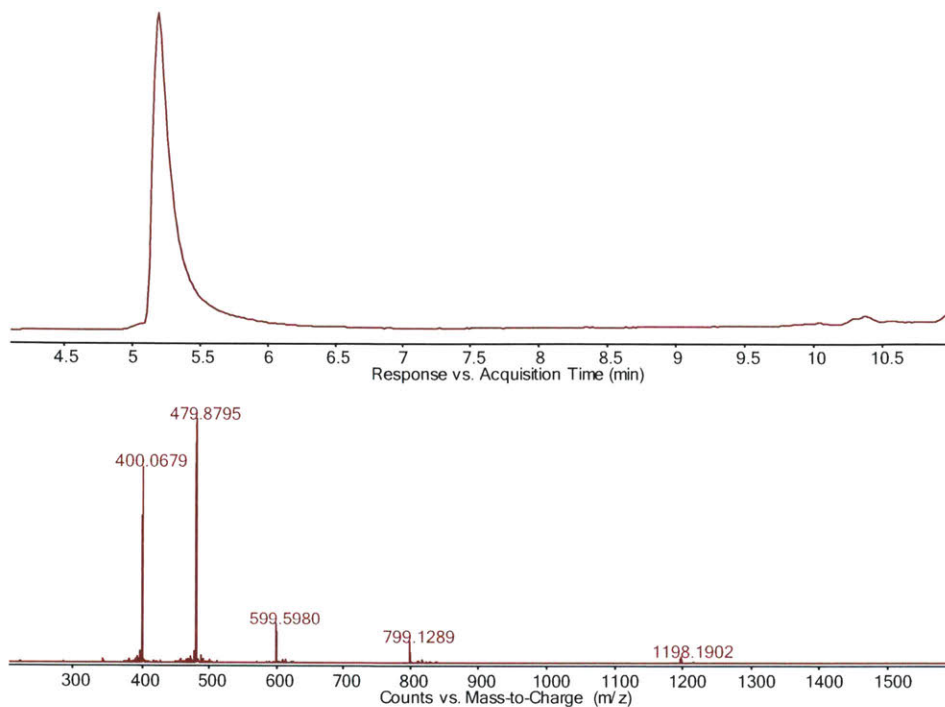
LC-MS characterization of peptide **4a** (peptide 4 with decafluorobiphenyl at position 9). TIC and mass spectrum of major peak.



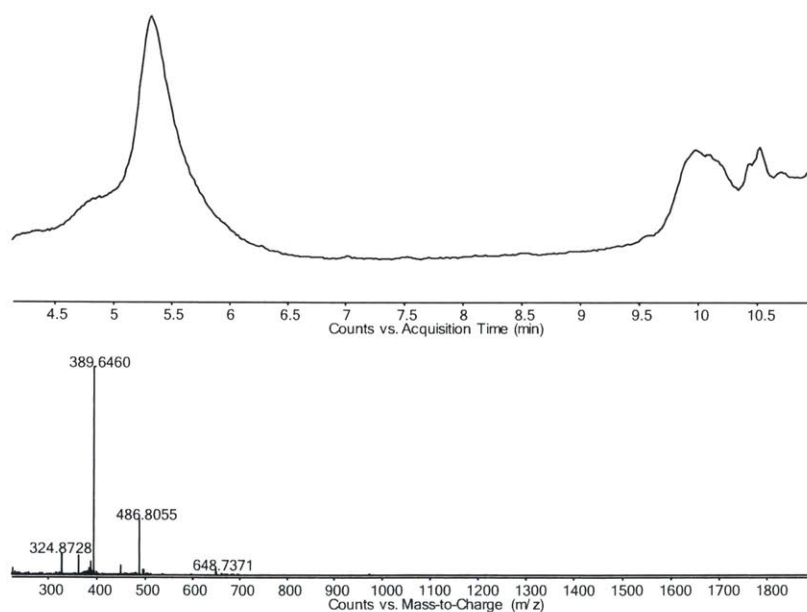
LC-MS characterization of peptide **6a**. TIC and mass spectrum of major peak.



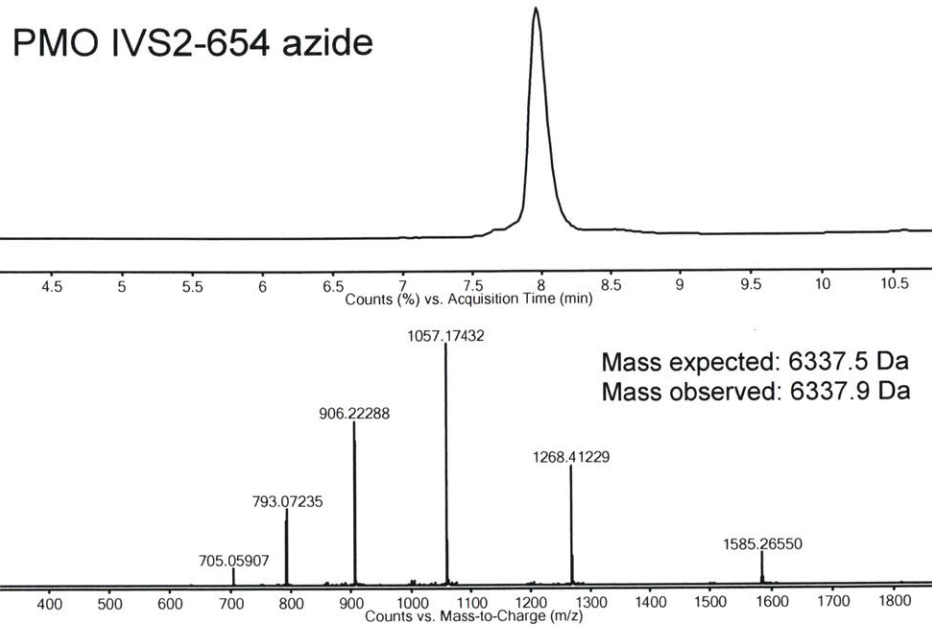
LC-MS characterization of peptide **6c** (R12 Monocycle). TIC and mass spectrum of major peak.



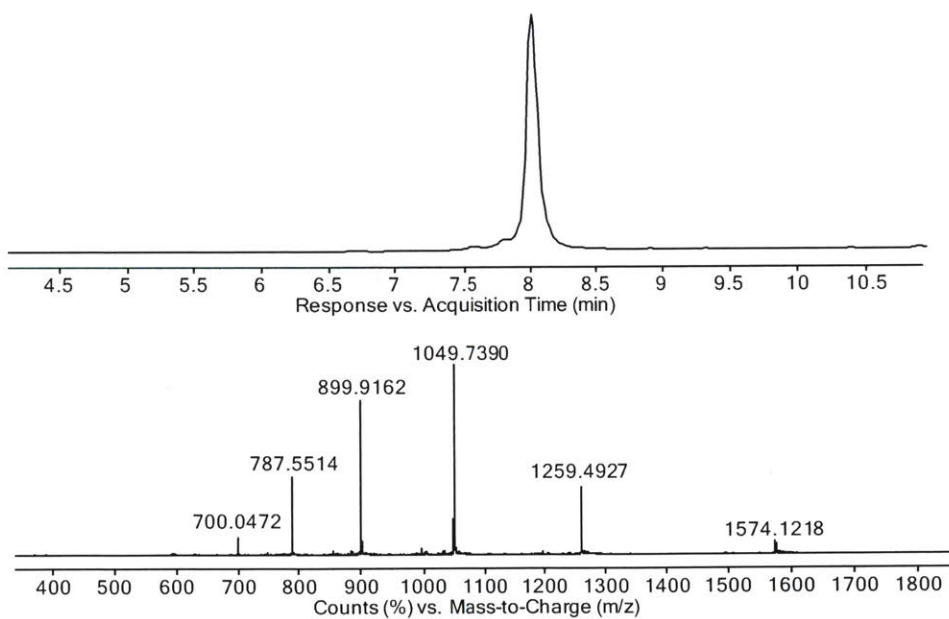
LC-MS characterization of peptide **1nfb** (R12 non-fluorinated bicycle). TIC and mass spectrum of major peak. Mass expected: 2393.3 Da. Mass observed: 2393.4 Da.



LC-MS characterization of peptide **7c** (cR10). TIC and mass spectrum of major peak. Mass expected: 1942.2 Da. Mass observed: 1942.3 Da. The peaks after 9 minutes result from column background. The hydrophilic nature of peptide **7c** requires a C18 column.

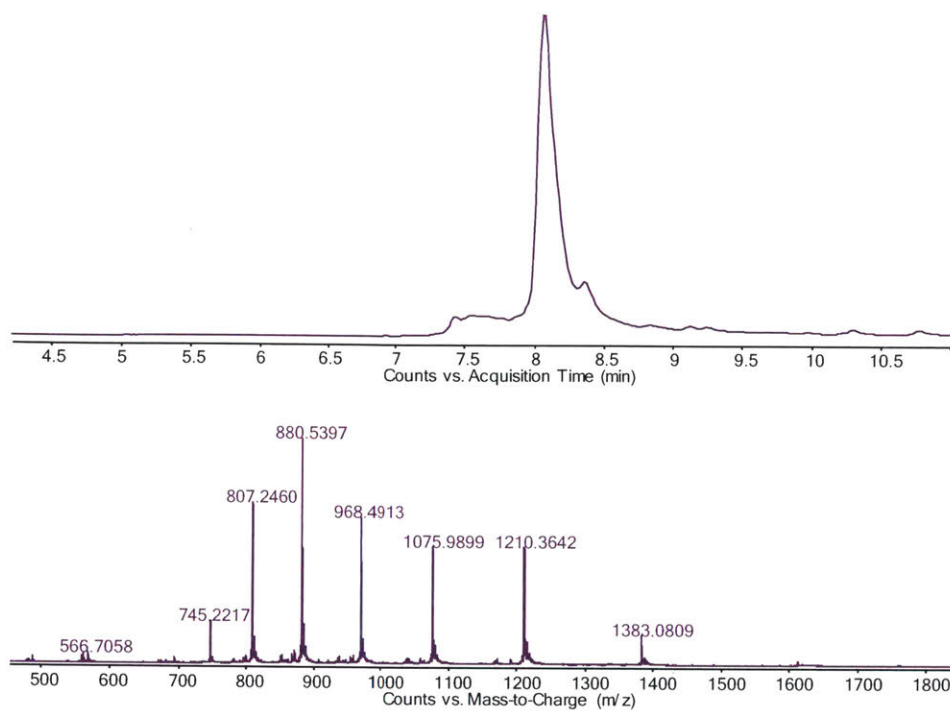


LC-MS characterization of PMO-Azide. TIC and mass spectrum of major peak.

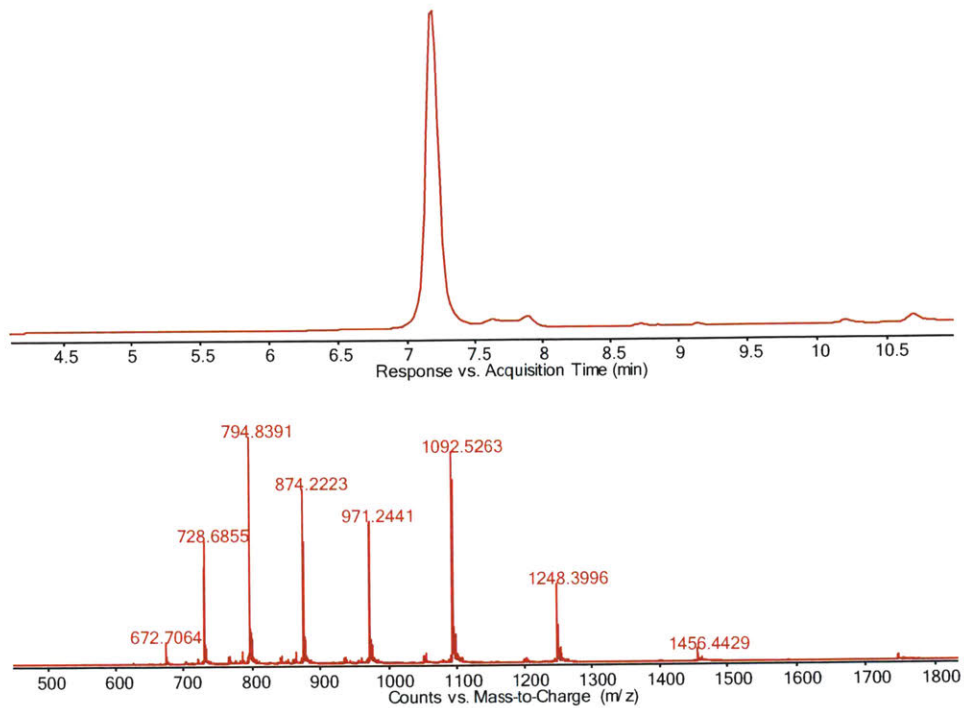


LC-MS characterization of PMO-Alkyne. TIC and mass spectrum of major peak. Mass expected: 6292.5 Da. Mass observed: 6293.6 Da

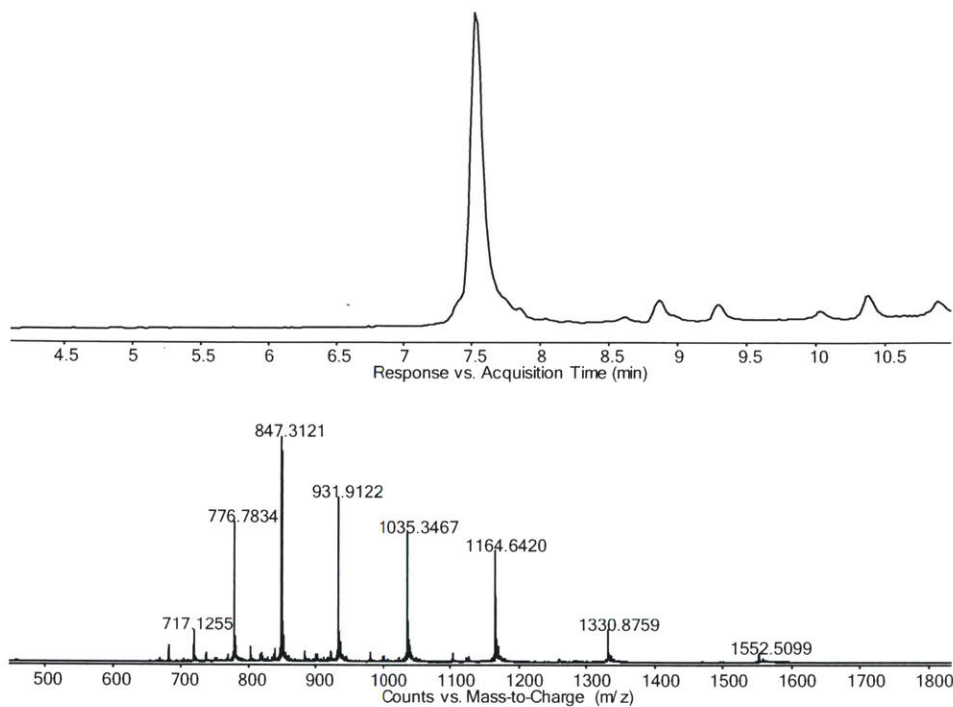




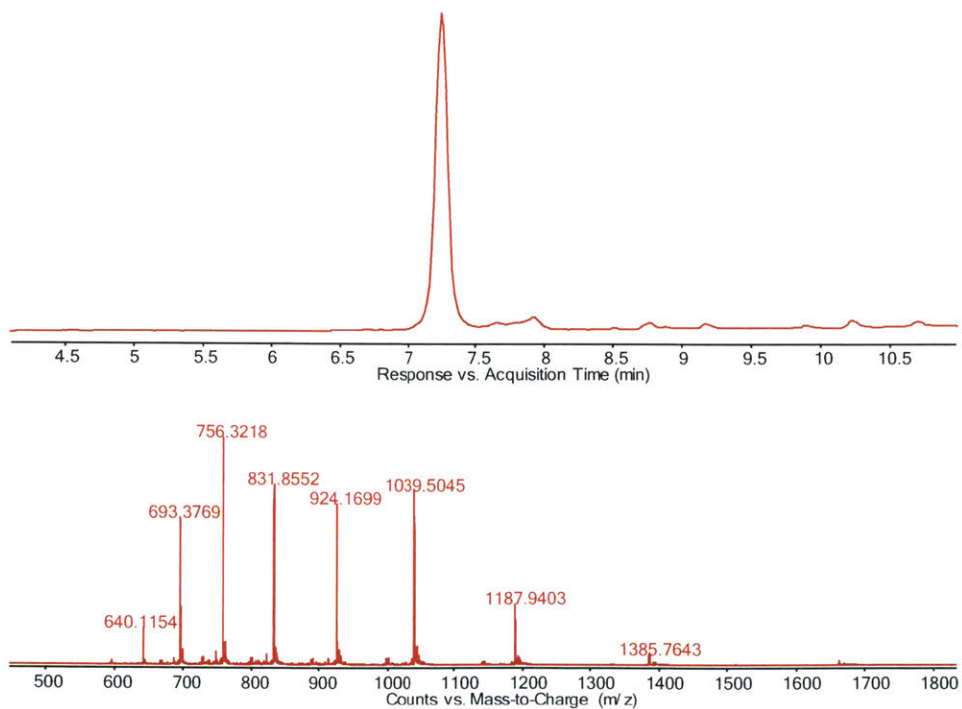
LC-MS characterization of PMO-1b (PMO-R12 trithiol bicycle). TIC and mass spectrum of major peak. Mass expected: 9674.9 Da. Mass observed: 9675.3 Da.



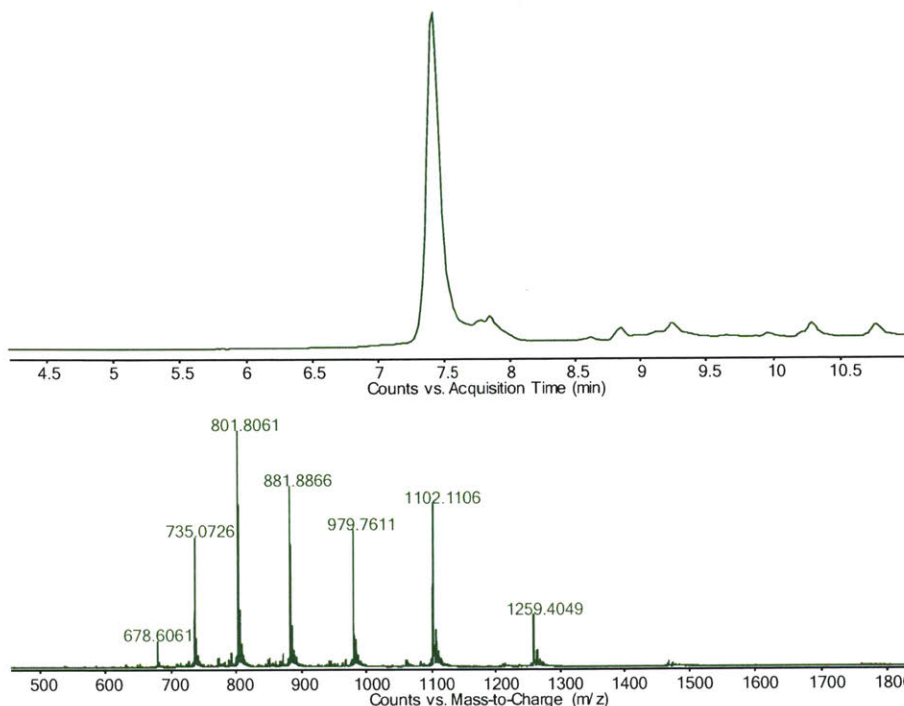
LC-MS characterization of PMO-1nfb (PMO-R12 non-fluorinated bicycle). TIC and mass spectrum of major peak. Mass expected: 8732.5 Da. Mass observed: 8732.9 Da.



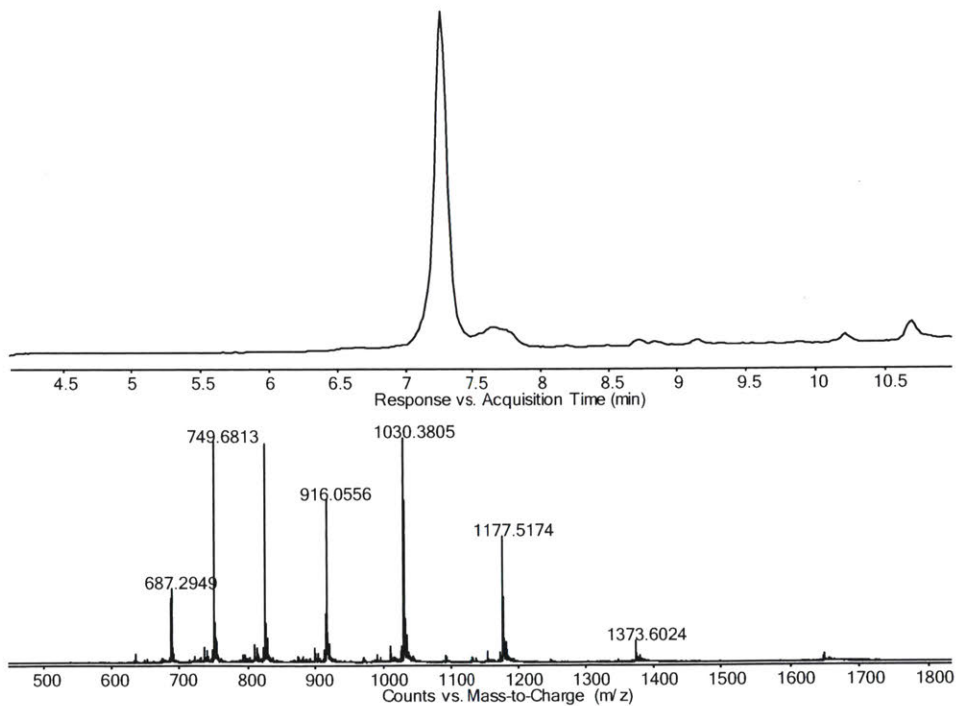
LC-MS characterization of PMO-**3b** (PMO-R12 double macrocycle). TIC and mass spectrum of major peak. Mass expected: 9309.6 Da. Mass observed: 9309.8 Da.



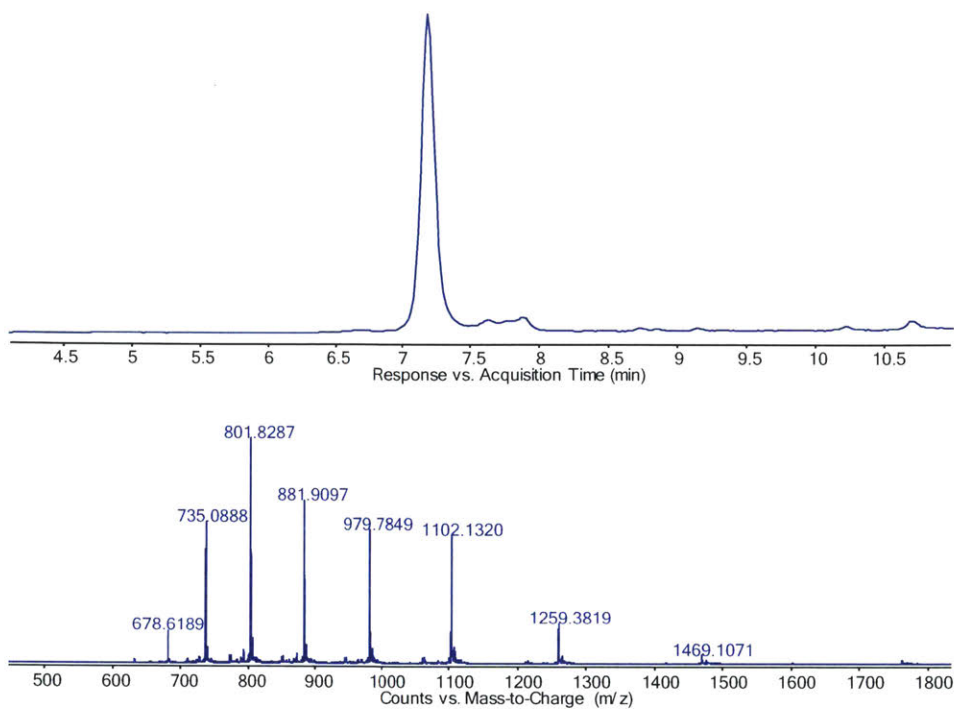
LC-MS characterization of PMO-**5** (PMO-R12). TIC and mass spectrum of major peak. Mass expected: 8309.0 Da. Mass observed: 8309.5 Da.



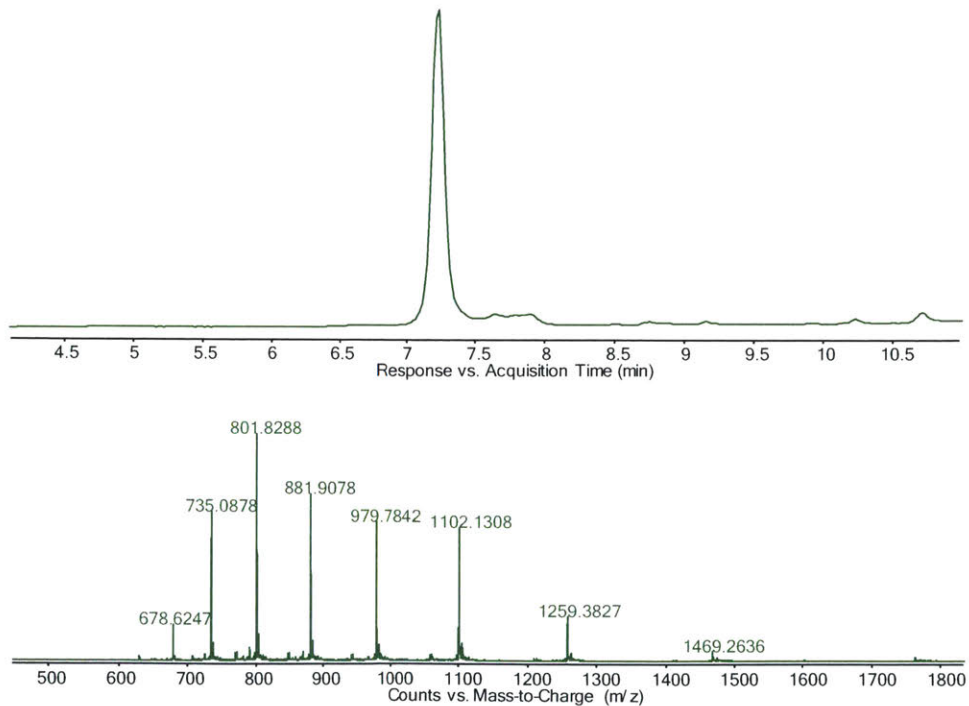
LC-MS characterization of PMO-**6c** (PMO-R12 monocycle). TIC and mass spectrum of major peak. Mass expected: 8809.2 Da. Mass observed: 8809.6 Da.



LC-MS characterization of PMO-**7c** (PMO-cR10). TIC and mass spectrum of major peak. Mass expected: 8235.8 Da. Mass observed: 8236.3 Da.



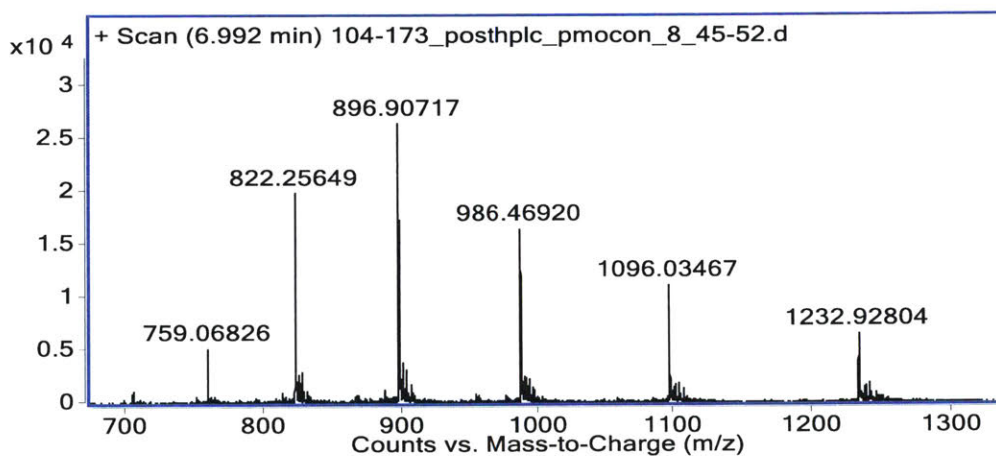
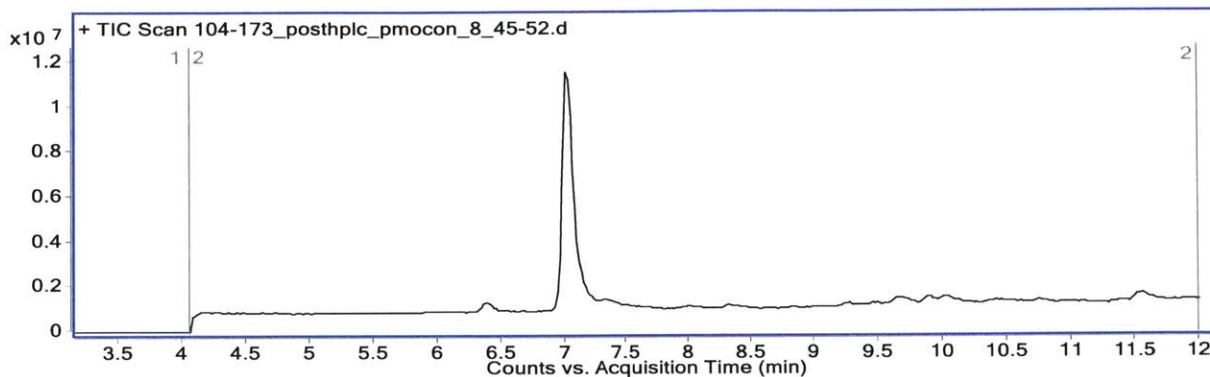
LC-MS characterization of PMO-R12 cyclized with decafluorobiphenyl across N-terminal 6 residues. TIC and mass spectrum of major peak. Mass expected: 8809.2 Da. Mass observed: 8809.7 Da.



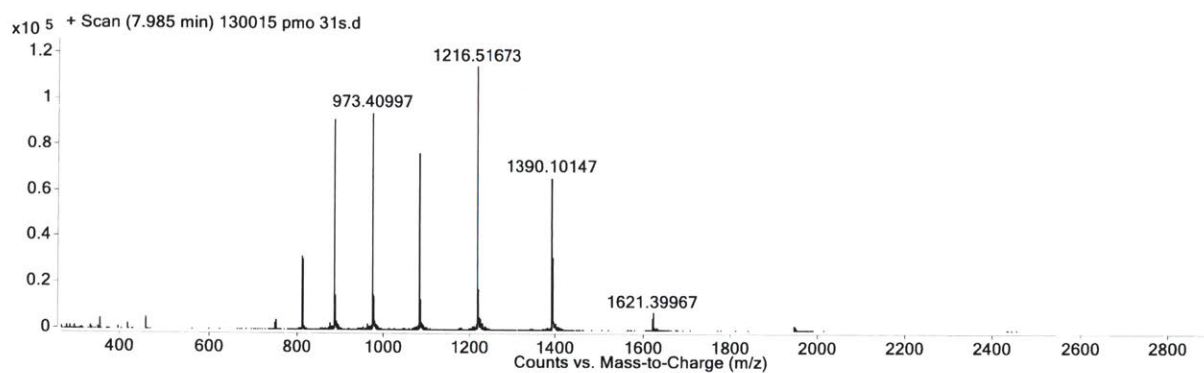
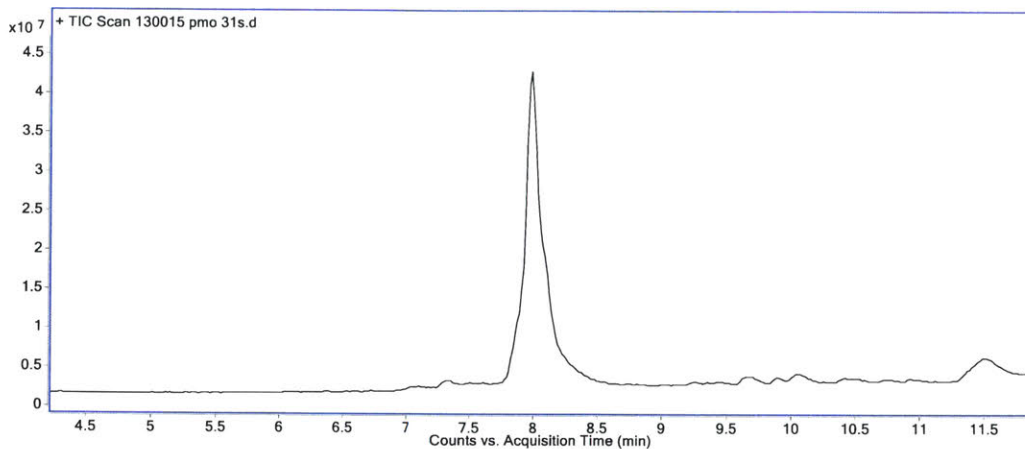
LC-MS characterization of PMO-R12 cyclized with decafluorobiphenyl across C-terminal 6 residues. TIC and mass spectrum of major peak. Mass expected: 8809.2 Da. Mass observed: 8809.7 Da.

*PMO-cyclic Cell-Penetrating Peptide Conjugates:*

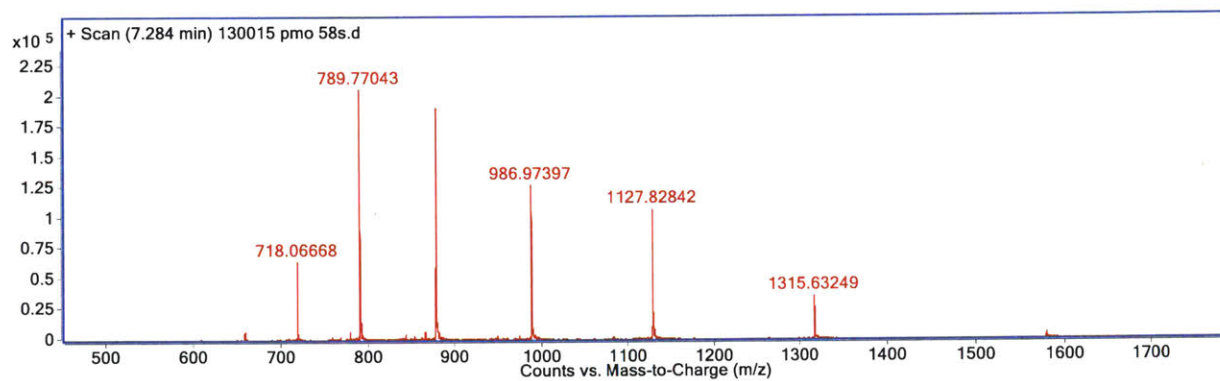
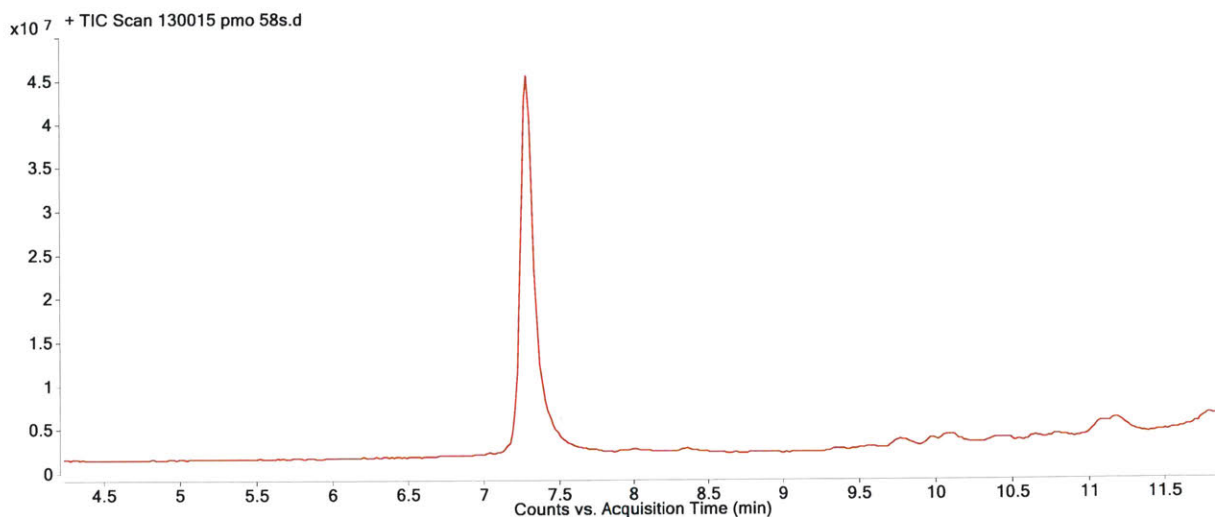
Bolded cysteines are linked with decafluorobiphenyl. All peptides had an N-terminal 4-pentanoyl for conjugation to PMO. Note: the linear cell-penetrating peptide conjugate chromatograms can be found in Chapter 2. The sequences of the linear peptide do not contain the cysteine residues.



LC-MS characterization of PMO-Bac7 cyclized with decafluorobiphenyl. TIC and mass spectrum of major peak. Peptide Sequence: CRRI**R**PRPPRLPRPRPRPLPFPRPGC. Mass expected: 9855.6 Da. Mass observed: 9856.0 Da.

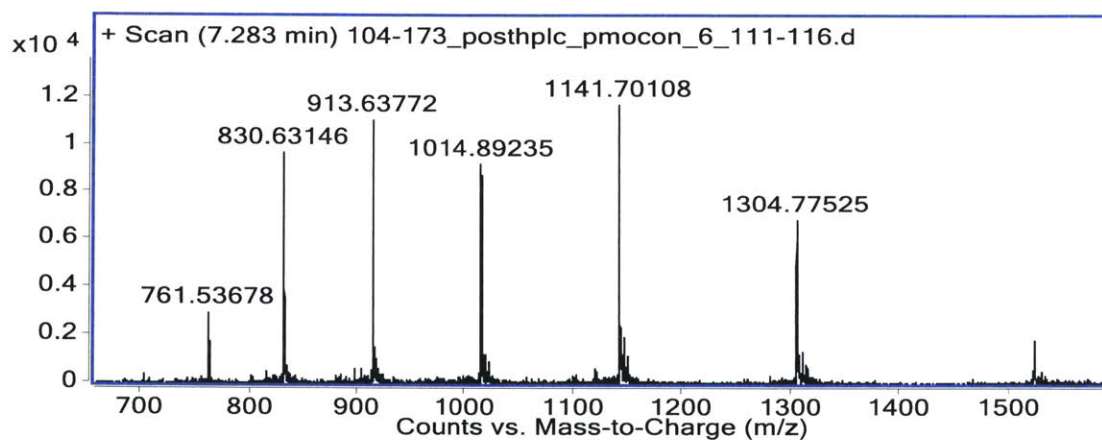
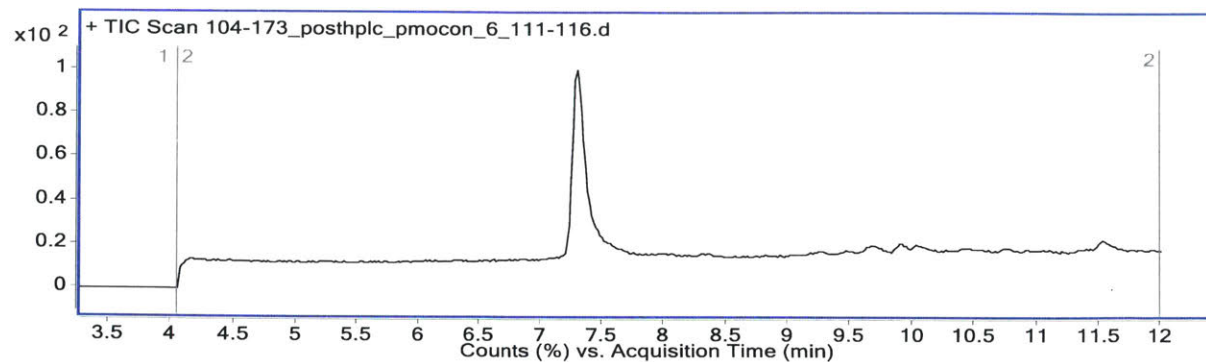


LC-MS characterization of PMO-MPG cyclized with decafluorobiphenyl. TIC and mass spectrum of major peak. Peptide Sequence: CGLAFLGFLGAAGSTMGAWSQPKKKRKVC. Mass expected: 9724.3 Da. Mass observed: 9724.7 Da.

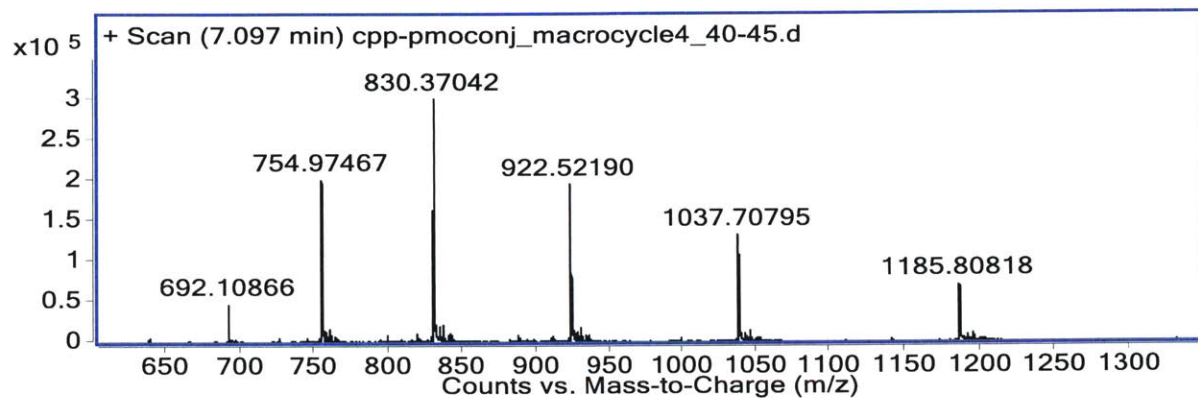
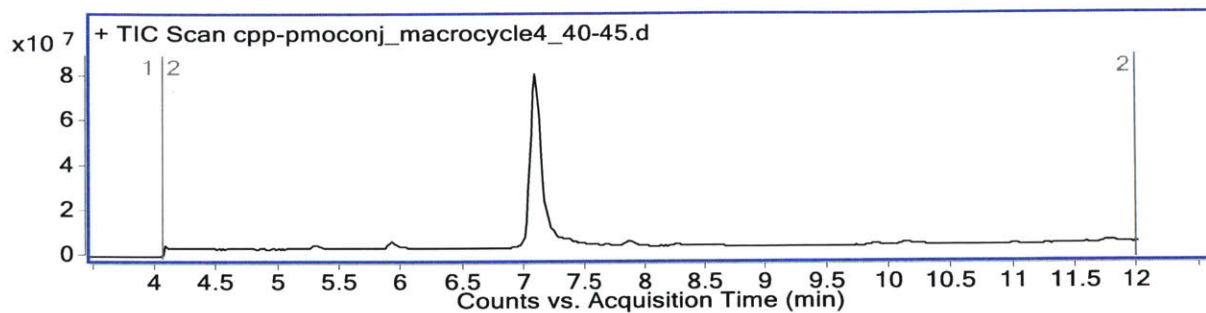


LC-MS characterization of PMO-CAYH cyclized with decafluorobiphenyl. TIC and mass spectrum of major peak. Peptide Sequence: CAYHRLRRC. Mass expected: 7888.0 Da. Mass observed: 7888.6 Da.

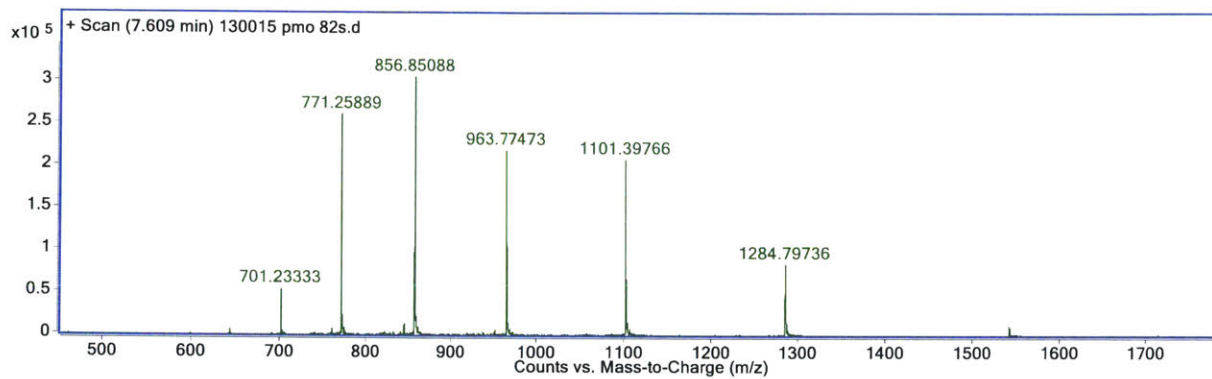
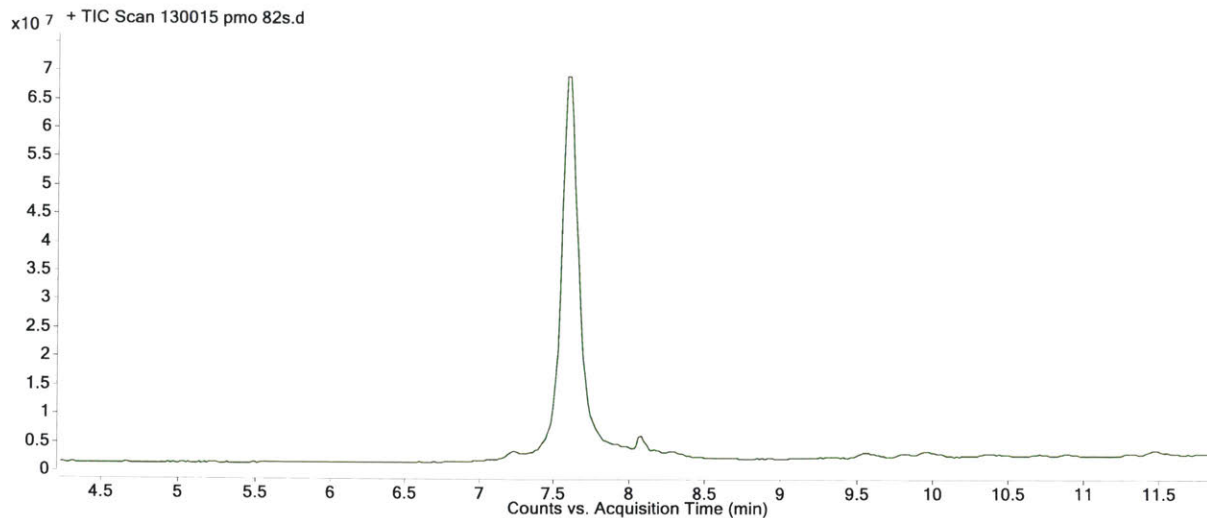




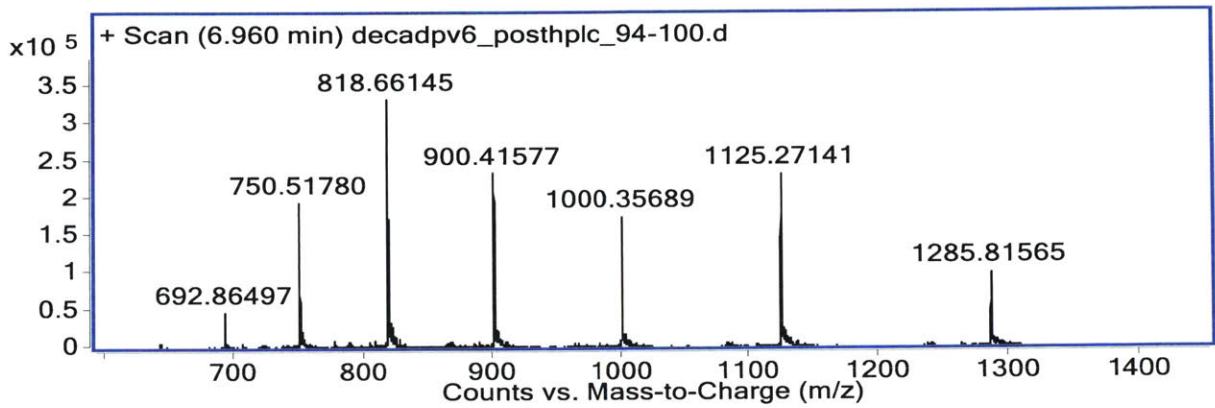
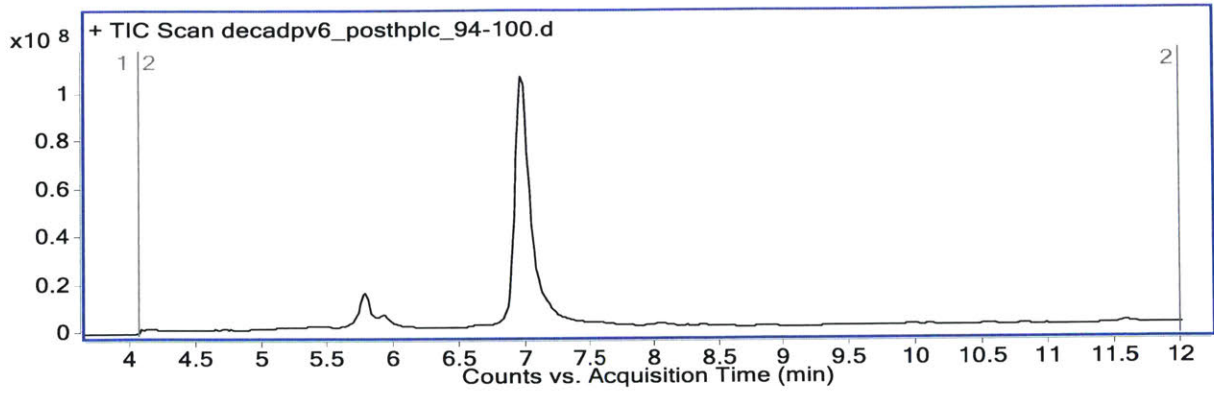
LC-MS characterization of PMO-pVEC cyclized with decafluorobiphenyl. TIC and mass spectrum of major peak. Peptide Sequence: CLLILRRRIRKQAHHSKC. Mass expected: 9126.7 Da. Mass observed: 9127.1 Da.



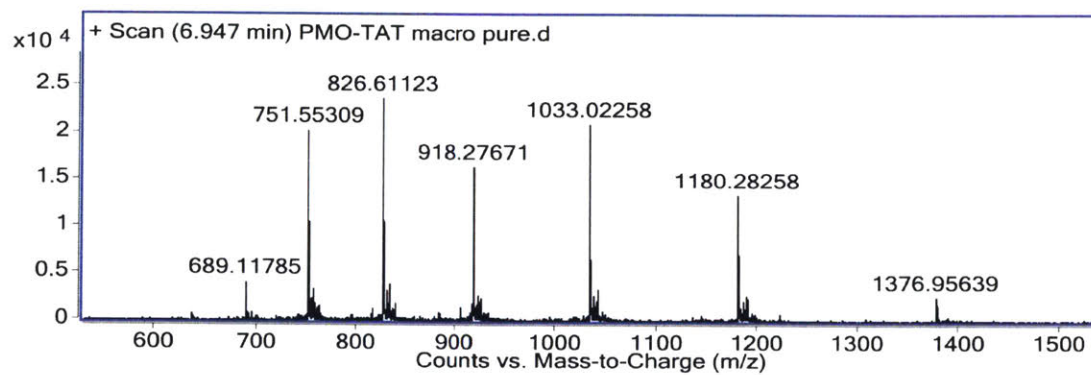
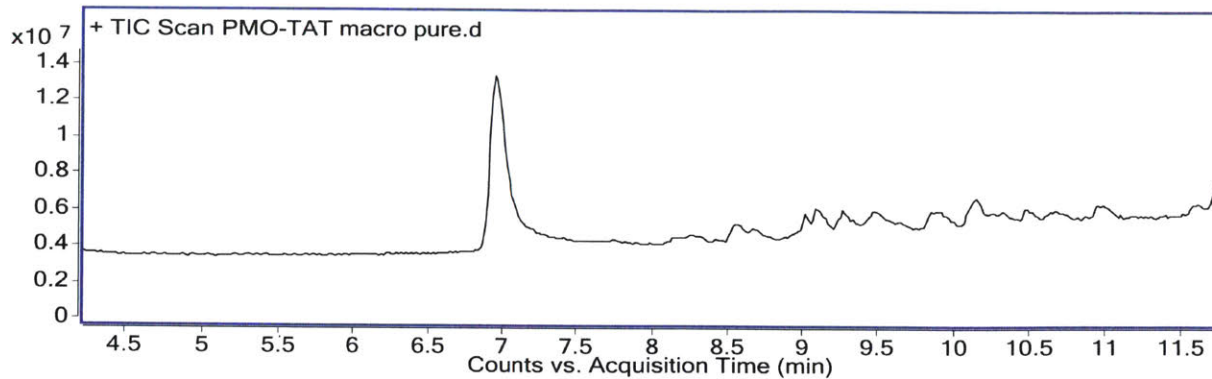
LC-MS characterization of PMO-HRSV cyclized with decafluorobiphenyl. TIC and mass spectrum of major peak. Peptide Sequence: CRRI PNRRPRRC. Mass expected: 8293.7 Da. Mass observed: 8293.7 Da.



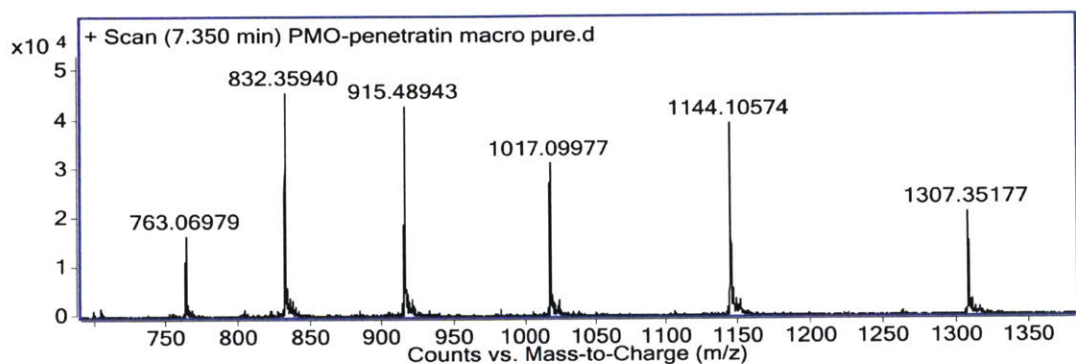
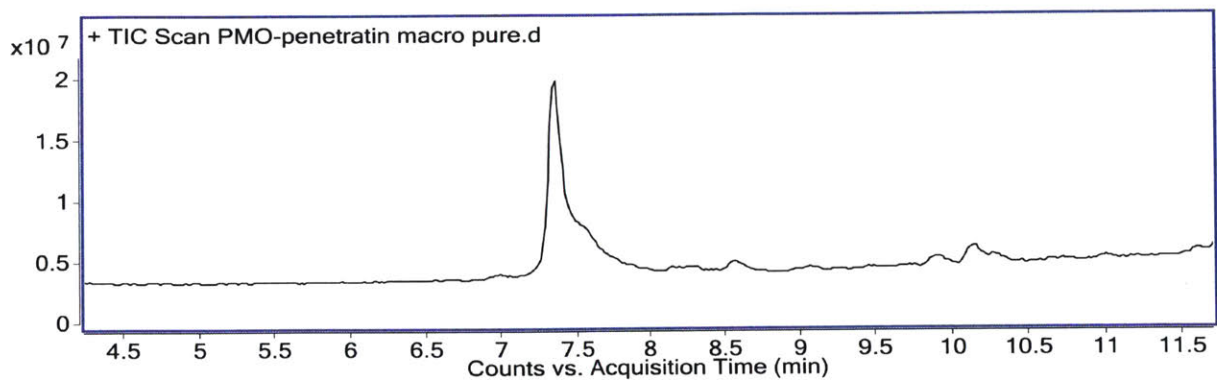
LC-MS characterization of PMO-AIP6 cyclized with decafluorobiphenyl. TIC and mass spectrum of major peak. Peptide Sequence: CRLRWRC. Mass expected: 7702.8 Da. Mass observed: 7704.0 Da.



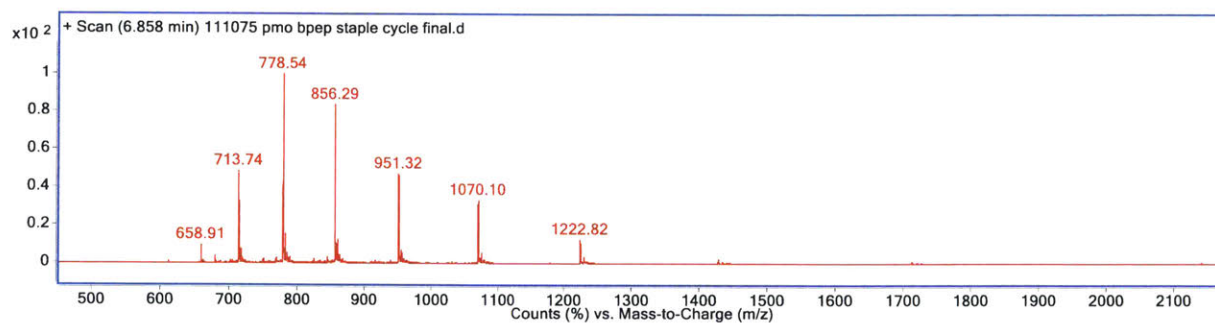
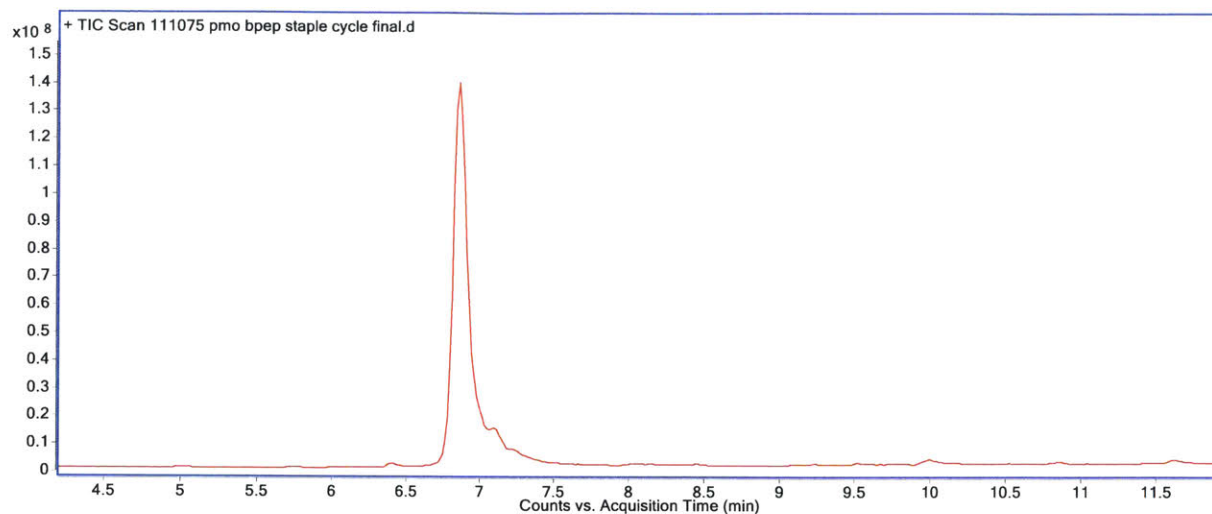
LC-MS characterization of PMO-DPV6 cyclized with decafluorobiphenyl. TIC and mass spectrum of major peak. Peptide Sequence: CGRPRESGKKRKRRLKPC. Mass expected: 8994.6 Da. Mass observed: 8995.1 Da.



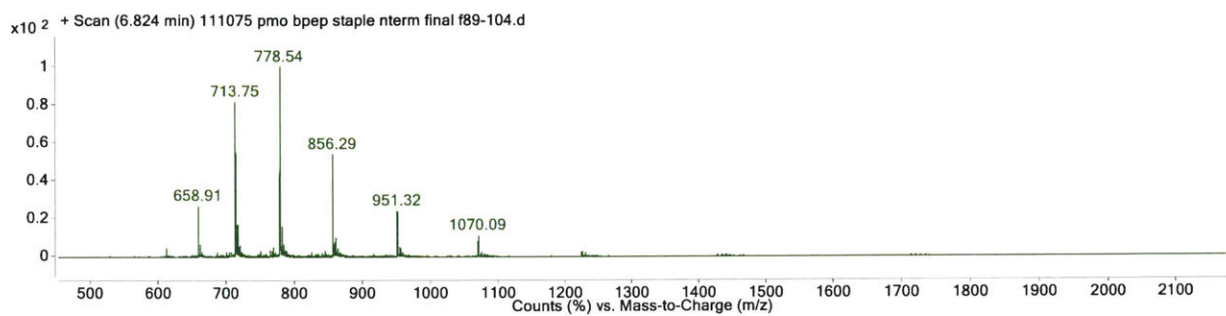
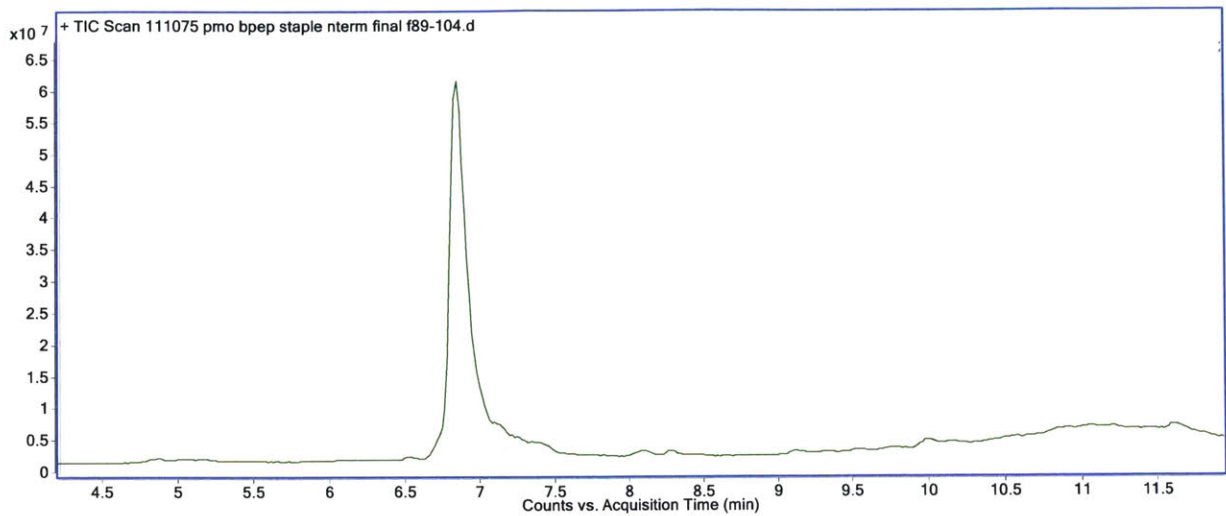
LC-MS characterization of PMO-TAT cyclized with decafluorobiphenyl. TIC and mass spectrum of major peak. Peptide Sequence: CRKKRRQRRCC. Mass expected: 8255.4 Da. Mass observed: 8257.0 Da



LC-MS characterization of PMO-Penetratin cyclized with decafluorobiphenyl. TIC and mass spectrum of major peak. Peptide Sequence: CRQIKIWFQNRRMKWKKC. Mass expected: 9143.9 Da. Mass observed: 9145.7 Da. The shoulder in the LC-MS trace corresponds to minor spontaneous oxidation products.

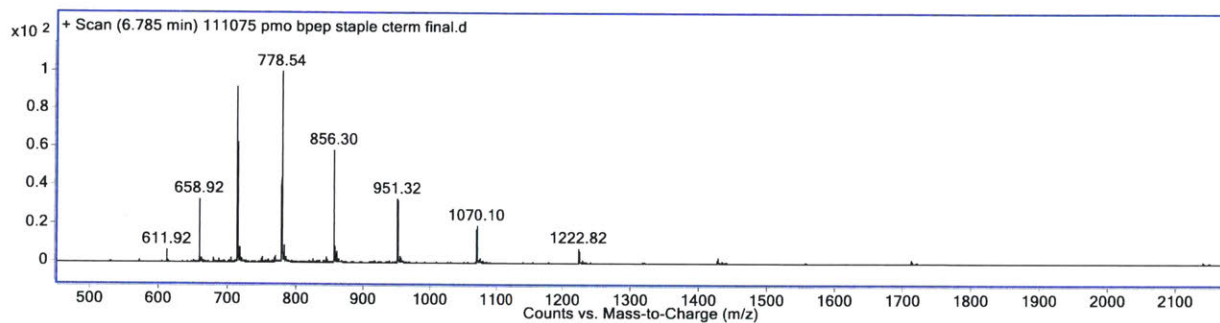
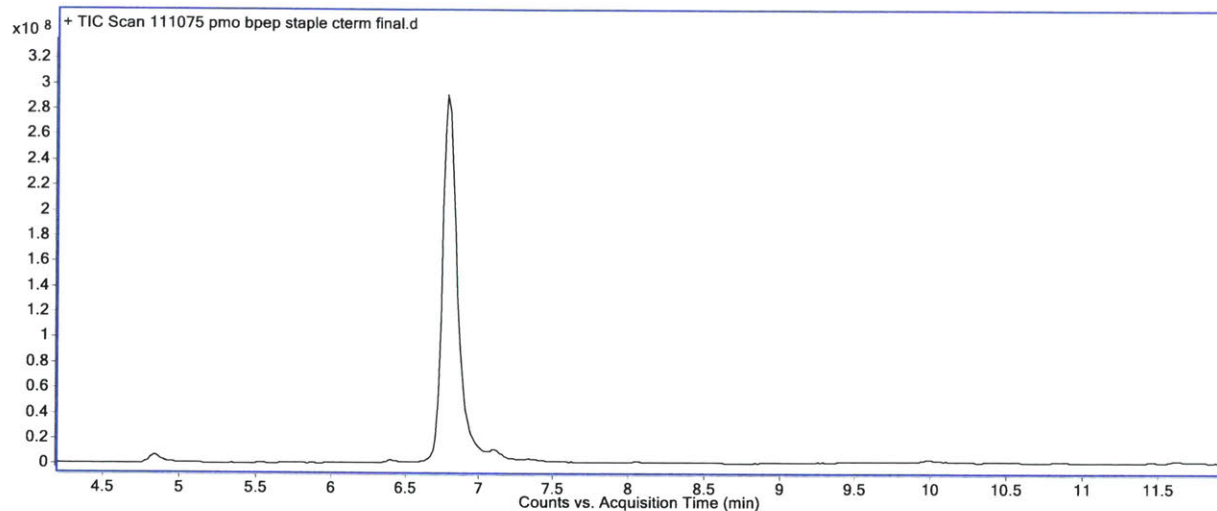


LC-MS characterization of PMO-Bpep cyclized with decafluorobiphenyl across the entire sequence. TIC and mass spectrum of major peak. Peptide Sequence: CRXRRBRRXRRBRC. Mass expected: 8553.0 Da. Mass observed: 8552.4 Da.



LC-MS characterization of PMO-Bpep cyclized with decafluorobiphenyl across the N-terminal six residues. TIC and mass spectrum of major peak. Peptide Sequence: CRXRRBCRXRRBR. Mass expected: 8553.0 Da. Mass observed: 8553.0 Da.





LC-MS characterization of PMO-Bpep cyclized with decafluorobiphenyl across the C-terminal six residues. TIC and mass spectrum of major peak. Peptide Sequence: RXRRBRCRXRRBR. Mass expected: 8553.0 Da. Mass observed: 8551.1 Da.

## 4.6. References

- (1) Kole, R.; Krainer, A. R.; Altman, S. RNA Therapeutics: Beyond RNA Interference and Antisense Oligonucleotides. *Nat. Rev. Drug Discov.* **2012**, *11* (2), 125–140.
- (2) van Roon-Mom, W. C.; Aartsma-Rus, A. Overview on Applications of Antisense-Mediated Exon Skipping. In *Exon Skipping*; Aartsma-Rus, A., Ed.; Methods in Molecular Biology; Humana Press, 2012; pp 79–96.
- (3) Siva, K.; Covello, G.; Denti, M. A. Exon-Skipping Antisense Oligonucleotides to Correct Missplicing in Neurogenetic Diseases. *Nucleic Acid Ther.* **2014**, *24* (1), 69–86.
- (4) Summerton, J.; Weller, D. Morpholino Antisense Oligomers: Design, Preparation, and Properties. *Antisense Nucleic Acid Drug Dev.* **1997**, *7* (3), 187–195.
- (5) Hudziak, R. M.; Barofsky, E.; Barofsky, D. F.; Weller, D. L.; Huang, S.-B.; Weller, D. D. Resistance of Morpholino Phosphorodiamidate Oligomers to Enzymatic Degradation. *Antisense Nucleic Acid Drug Dev.* **1996**, *6* (4), 267–272.
- (6) Youngblood, D. S.; Hatlevig, S. A.; Hassinger, J. N.; Iversen, P. L.; Moulton, H. M. Stability of Cell-Penetrating Peptide–Morpholino Oligomer Conjugates in Human Serum and in Cells. *Bioconjug. Chem.* **2007**, *18* (1), 50–60.
- (7) Li, Y.-F.; Morcos, P. A. Design and Synthesis of Dendritic Molecular Transporter That Achieves Efficient in Vivo Delivery of Morpholino Antisense Oligo. *Bioconjug. Chem.* **2008**, *19* (7), 1464–1470.
- (8) Wu, B.; Li, Y.; Morcos, P. A.; Doran, T. J.; Lu, P.; Lu, Q. L. Octa-Guanidine Morpholino Restores Dystrophin Expression in Cardiac and Skeletal Muscles and Ameliorates Pathology in Dystrophic Mdx Mice. *Mol. Ther.* **2009**, *17* (5), 864–871.
- (9) Hanson, G. J.; Weller, D. D.; Cai, B. Z.; Zhou, M. Functionally-Modified Oligonucleotides and Subunits Thereof. US9278987 B2, March 8, 2016.
- (10) Stanzl, E. G.; Trantow, B. M.; Vargas, J. R.; Wender, P. A. Fifteen Years of Cell-Penetrating, Guanidinium-Rich Molecular Transporters: Basic Science, Research Tools, and Clinical Applications. *Acc. Chem. Res.* **2013**, *46* (12), 2944–2954.
- (11) Moulton, H. M.; Nelson, M. H.; Hatlevig, S. A.; Reddy, M. T.; Iversen, P. L. Cellular Uptake of Antisense Morpholino Oligomers Conjugated to Arginine-Rich Peptides. *Bioconjug. Chem.* **2004**, *15* (2), 290–299.
- (12) Abes, S.; Moulton, H. M.; Clair, P.; Prevot, P.; Youngblood, D. S.; Wu, R. P.; Iversen, P. L.; Lebleu, B. Vectorization of Morpholino Oligomers by the (R-Ahx-R)<sub>4</sub> Peptide Allows Efficient Splicing Correction in the Absence of Endosomolytic Agents. *J. Controlled Release* **2006**, *116* (3), 304–313.
- (13) Lebleu, B.; Moulton, H. M.; Abes, R.; Ivanova, G. D.; Abes, S.; Stein, D. A.; Iversen, P. L.; Arzumanov, A. A.; Gait, M. J. Cell Penetrating Peptide Conjugates of Steric Block Oligonucleotides. *Adv. Drug Deliv. Rev.* **2008**, *60* (4), 517–529.
- (14) Hanson, G. J. Peptide Oligonucleotide Conjugates. US 9,161,948, October 20, 2015.
- (15) Timmerman, P.; Beld, J.; Puijk, W. C.; Meloen, R. H. Rapid and Quantitative Cyclization of Multiple Peptide Loops onto Synthetic Scaffolds for Structural Mimicry of Protein Surfaces. *ChemBioChem* **2005**, *6* (5), 821–824.
- (16) Heinis, C.; Rutherford, T.; Freund, S.; Winter, G. Phage-Encoded Combinatorial Chemical Libraries Based on Bicyclic Peptides. *Nat. Chem. Biol.* **2009**, *5* (7), 502–507.
- (17) Chen, S.; Morales-Sanfrutos, J.; Angelini, A.; Cutting, B.; Heinis, C. Structurally Diverse Cyclisation Linkers Impose Different Backbone Conformations in Bicyclic Peptides. *ChemBioChem* **2012**, *13* (7), 1032–1038.

- (18) Wang, J.; Zha, M.; Fei, Q.; Liu, W.; Zhao, Y.; Wu, C. Peptide Macrocycles Developed from Precisely Regulated Multiple Cyclization of Unprotected Peptides. *Chem.* **2017**, *23* (60), 15150-15155.
- (19) Sako, Y.; Morimoto, J.; Murakami, H.; Suga, H. Ribosomal Synthesis of Bicyclic Peptides via Two Orthogonal Inter-Side-Chain Reactions. *J. Am. Chem. Soc.* **2008**, *130* (23), 7232–7234.
- (20) Wallbrecher, R.; Depré, L.; Verdurmen, W. P. R.; Bovée-Geurts, P. H.; van Duinkerken, R. H.; Zekveld, M. J.; Timmerman, P.; Brock, R. Exploration of the Design Principles of a Cell-Penetrating Bicyclic Peptide Scaffold. *Bioconjug. Chem.* **2014**, *25* (5), 955–964.
- (21) Lian, W.; Jiang, B.; Qian, Z.; Pei, D. Cell-Permeable Bicyclic Peptide Inhibitors against Intracellular Proteins. *J. Am. Chem. Soc.* **2014**, *136* (28), 9830–9833.
- (22) Spokoyny, A. M.; Zou, Y.; Ling, J. J.; Yu, H.; Lin, Y.-S.; Pentelute, B. L. A Perfluoroaryl-Cysteine SNAr Chemistry Approach to Unprotected Peptide Stapling. *J. Am. Chem. Soc.* **2013**, *135* (16), 5946–5949.
- (23) Zou, Y.; Spokoyny, A. M.; Zhang, C.; Simon, M. D.; Yu, H.; Lin, Y.-S.; Pentelute, B. L. Convergent Diversity-Oriented Side-Chain Macrocyclization Scan for Unprotected Polypeptides. *Org. Biomol. Chem.* **2013**, *12* (4), 566–573.
- (24) Herce, H. D.; Schumacher, D.; Schneider, A. F. L.; Ludwig, A. K.; Mann, F. A.; Fillies, M.; Kasper, M.-A.; Reinke, S.; Krause, E.; Leonhardt, H.; et al. Cell-Permeable Nanobodies for Targeted Immunolabelling and Antigen Manipulation in Living Cells. *Nat. Chem.* **2017**, *9* (8), 762.
- (25) Sazani, P.; Kang, S.-H.; Maier, M. A.; Wei, C.; Dillman, J.; Summerton, J.; Manoharan, M.; Kole, R. Nuclear Antisense Effects of Neutral, Anionic and Cationic Oligonucleotide Analogs. *Nucleic Acids Res.* **2001**, *29* (19), 3965–3974.
- (26) Mijalis, A. J.; Thomas III, D. A.; Simon, M. D.; Adamo, A.; Beaumont, R.; Jensen, K. F.; Pentelute, B. L. A Fully Automated Flow-Based Approach for Accelerated Peptide Synthesis. *Nat. Chem. Biol.* **2017**, *13* (5), 464–466.
- (27) Simon, M. D.; Heider, P. L.; Adamo, A.; Vinogradov, A. A.; Mong, S. K.; Li, X.; Berger, T.; Policarpo, R. L.; Zhang, C.; Zou, Y.; et al. Rapid Flow-Based Peptide Synthesis. *ChemBioChem* **2014**, *15* (5), 713–720.

## Chapter 5: Perfluoroarene-Based Peptide Macrocycles to Enhance Penetration Across the Blood-Brain Barrier

The work presented in this chapter was published in the following manuscript and is reproduced with permission from the American Chemical Society:

Fadzen, C.M.,\* Wolfe, J.M.,\* Cho, C-F., Chiocca, E.A., Lawler, S.E., & Pentelute, B.L. Perfluoroarene-Based Peptide Macrocycles to Enhance Penetration Across the Blood-Brain Barrier. *J. Am. Chem. Soc.* **139**, 15628-15631 (2017).

\*: denotes authors contributed equally

## 5.1. Introduction

The blood-brain barrier (BBB) poses a significant challenge to delivering therapeutics to the brain, which limits treatment options for various central nervous system diseases, including primary tumors, brain metastases, autoimmune diseases and infections.<sup>1-4</sup> The brain endothelial layer that comprises the BBB is highly specialized, containing continuous tight junctions, a high electrical resistance, and many efflux pumps that extrude drugs from the brain into the blood. Previous efforts to deliver therapeutics across the BBB have focused on temporary chemical or mechanical disruption of the barrier, or inhibition of efflux pumps.<sup>5-8</sup> Both of these techniques have significant limitations. Even when successful in mediating delivery across the BBB, these approaches are nonspecific and thus may also enhance the delivery of unwanted substances into the brain and cause neurotoxicity.<sup>3</sup>

Significant work to overcome the challenge of specificity has been devoted to molecular delivery vectors, also called “BBB shuttles.”<sup>9</sup> These delivery vectors have classically targeted receptors on the surface of brain endothelial cells, such as the insulin and transferrin receptors.<sup>10,11</sup> In addition to antibody-based BBB-shuttles, peptide shuttles have shown promise for cargo delivery across the BBB.<sup>12-14</sup> Peptides are easier to characterize than antibodies and can be prepared by chemical synthesis, enabling the incorporation of diverse chemical moieties to modulate the shuttle’s properties.

Many peptides, however, do not possess an intrinsic ability to cross the BBB and are susceptible to proteolytic degradation. Over the past 25 years, many chemical strategies have been developed for peptide macrocyclization<sup>15-21</sup> which can confer favorable biological properties to the peptide, such as increased uptake into cells or resistance to proteolysis.<sup>21-25</sup> We recently reported methodology that allows for the macrocyclization of an unprotected peptide between two cysteine residues with a perfluoroaryl linker through  $S_NAr$  chemistry in the presence of a mild base.<sup>26,27</sup> We demonstrated that these perfluoroarene-based peptide macrocycles had increased cellular uptake and increased resistance to proteolytic degradation compared with their linear counterparts.

Here we show that our  $S_NAr$  macrocyclization chemistry can be utilized to facilitate peptide crossing of the BBB. We observed that several perfluoroarene-based, macrocyclic analogues of transportan-10 (TP10) have enhanced uptake into two different cell types, including brain endothelial cells. Therefore, we hypothesized that these macrocycles may serve as important

delivery tools for transport across the BBB. To this end, we tested TP10 analogues in a culture-based spheroid model of the BBB that recapitulates many of the important known barrier functions of the BBB. We also tested the top TP10 analogue in mice to demonstrate the applicability of our technology to *in vivo* brain penetration. Finally, we examined the generalizability of this technology to a peptide of therapeutic interest both in the BBB spheres and in mice. This work highlights the potential of perfluoroarene-based peptide macrocycles as brain-penetrating agents.

## 5.2. Results and Discussion

Our initial experiments were designed to determine the extent to which macrocyclization through our perfluoroaryl-cysteine  $S_NAr$  chemistry could modulate the biological properties of a model peptide known for its ability to translocate across membranes.<sup>28,29</sup> Analogues of this model peptide, TP10, were prepared containing two cysteine residues in a variety of *i, i+7* configurations (Figure 5.1). Cysteines were substituted rather than inserted into the sequence in an effort to maintain the spatial relationships between the other amino acids of the peptide. In addition to the macrocyclic aryl variants (denoted M), linear controls (denoted Q\*) were also prepared in which the cysteines were alkylated with 2-bromoacetamide in order to account for changes in behavior that may arise from the cysteine mutation. To facilitate conjugation of a fluorophore via copper-catalyzed click chemistry, 4-pentynoic acid was coupled to the N-terminus of all peptides using standard solid-phase peptide synthesis conditions.

For our initial experiments, 5-carboxytetramethylrhodamine (5-TAMRA) was conjugated to the N-terminal alkyne of all analogues. To examine these fluorophore-labeled constructs in a biological context, we treated HeLa cells with 2.5  $\mu$ M of each construct for 2 hours in serum-free media. After washing with trypsin and buffer to remove any cell surface-adherent peptide, we observed that all macrocyclic variants of TP10 demonstrated increased mean fluorescence intensity compared with their respective alkyl control by flow cytometry (Figure 5.2). Encouraged by these results, we sought to determine if this observation was recapitulated in hCMEC/D3 endothelial cells - an immortalized cell line that has been extensively characterized for brain endothelial cell phenotype and is used in models of the BBB.<sup>30,31</sup> Identical treatment conditions were used except the treatment media for the hCMEC/D3 cells was supplemented with 2% human serum. All macrocyclic variants of TP10 displayed an increase in mean fluorescence intensity with respect to both the native TP10 sequence and their respective alkyl control (Figure 5.2), indicating increased uptake into hCMEC/D3 cells. Given that brain endothelial cells are a key component of the BBB, we hypothesized that perfluoroarene-based macrocycles may also have increased ability to cross the BBB and accumulate in the brain.

The stability of the macrocyclic TP10 analogues was assayed by incubating 100  $\mu$ M of each construct, with 1.75 nM Proteinase k at 37 °C. After 2 h of incubation with the protease, all macrocyclic variants were still >90% intact, while <40% of the native TP10 remained (Figure 5.3). Taken with the observation that the linear alkyl controls were no more stable than the native

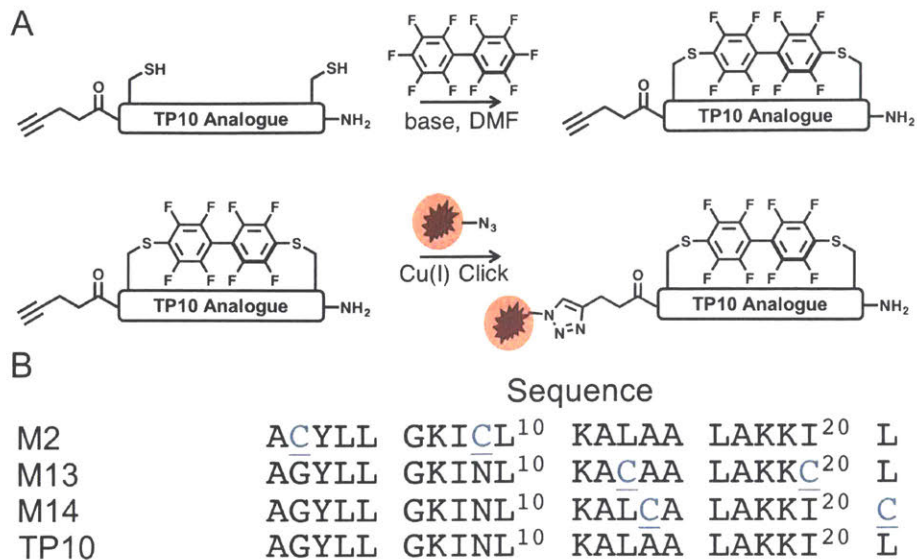


**Figure 5.1. Macrocyclic TP10 analogues prepared via  $S_NAr$ .** (A) Workflow for generating fluorophore-containing perfluoroarene-based macrocyclic TP10 analogues. (B) Peptide sequences for the TP10 macrocycles. The N-terminus is capped with 4-pentynoic acid to provide a click handle for labeling.

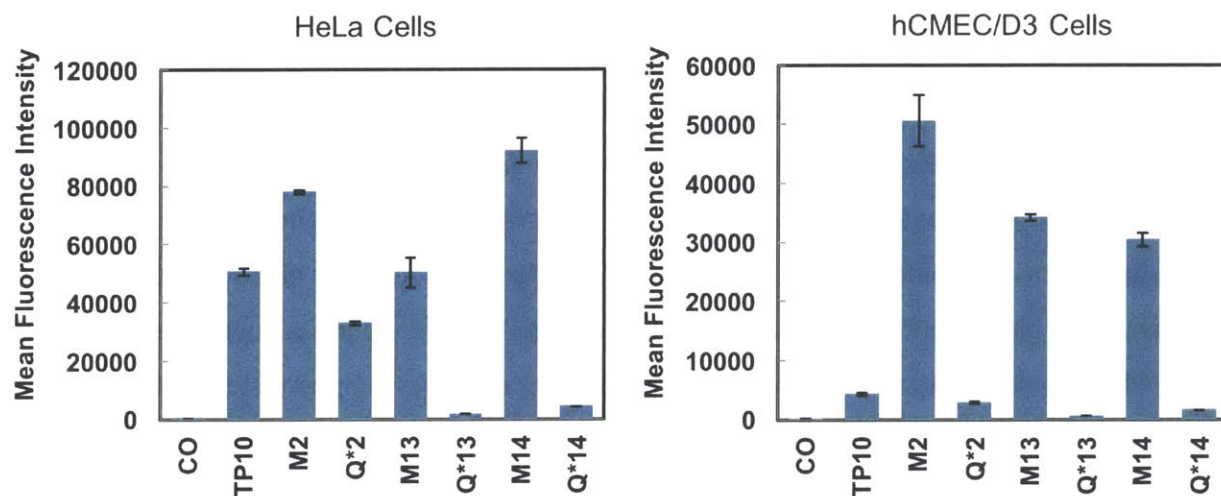


**Figure 5.2. Perfluoroarene-based macrocyclic TP10 analogues have increased uptake into HeLa and brain endothelial cells.** Flow cytometry analysis of HeLa and hCMEC/D3 cells treated with 2.5  $\mu$ M of each peptide for 2 h at 37  $^{\circ}$ C. The macrocyclic variants display up to a 12-fold increase in mean fluorescence intensity relative to native TP10 (n = 3).



TP10 (Figure 5.3), these data suggest that the perfluoroarene macrocycle confers beneficial proteolytic stability. Finally, to ensure that the macrocyclic TP10 analogues did not compromise the plasma membrane, a lactate dehydrogenase (LDH) assay was performed using HeLa cells. Neither M13 nor M14 showed appreciable LDH leakage at concentrations of 5  $\mu$ M or below, indicating that at biologically-relevant concentrations, the plasma membrane of the cells was not compromised (Figure 5.4).

Our next set of experiments was designed to test if our macrocyclic peptides could potentially cross the BBB using the cellular BBB spheroid model.<sup>32</sup> The spheroid model employed in this work consists of a 1:1:1 ratio of human brain microvascular endothelial cells (hCMEC/D3), human brain vascular pericytes (HBVPs), and human astrocytes that spontaneously self-organize into spheres when co-cultured. In the brain, the blood vessels are lined with endothelial cells, which associate closely with pericytes and astrocytes to form the BBB.<sup>33</sup> In the spheres, endothelial cells interact with pericytes to line the outermost surface of the sphere, while astrocytes make up the spheroid core (Figure 5.5). The ability of a molecule to penetrate the surface of the sphere and accumulate in the core represents delivery into the brain. Importantly, previous work has shown that these spheres display several of the key properties of the BBB, including high expression of tight junction proteins, upregulation of drug efflux pumps, and receptor-mediated transport across the barrier.<sup>34</sup>

The spheres were treated with 5  $\mu$ M of each TP10 analogue for 3.5 hours at 37 °C. After treatment, the spheres were imaged by confocal microscopy. Quantification of spheroid entry was performed by measuring the mean 5-TAMRA fluorescence intensity at a depth of 90  $\mu$ m into the core of the spheroid (Figure 5.6). Of the three macrocyclic analogues, both M13 and M14 displayed increased penetration of the sphere with respect to both native TP10 and their alkyl analogues (Figure 5.5). M13 showed the greatest increase with an 8-fold change over TP10. These data suggest that both M13 and M14 may have increased ability to cross the BBB. Intriguingly, the location of the perfluoroarene within the sequence significantly affected the ability of a given analogue to enter the sphere, despite all analogues having increased uptake into brain endothelial cells.

Next, we assessed whether or not the enhanced spheroid penetration we observed could be translated to *in vivo* BBB penetration in a living system. Given the superior influx of M13 into the spheres, M13 was chosen for further evaluation in mice. Cy5.5 was attached to the N-terminal

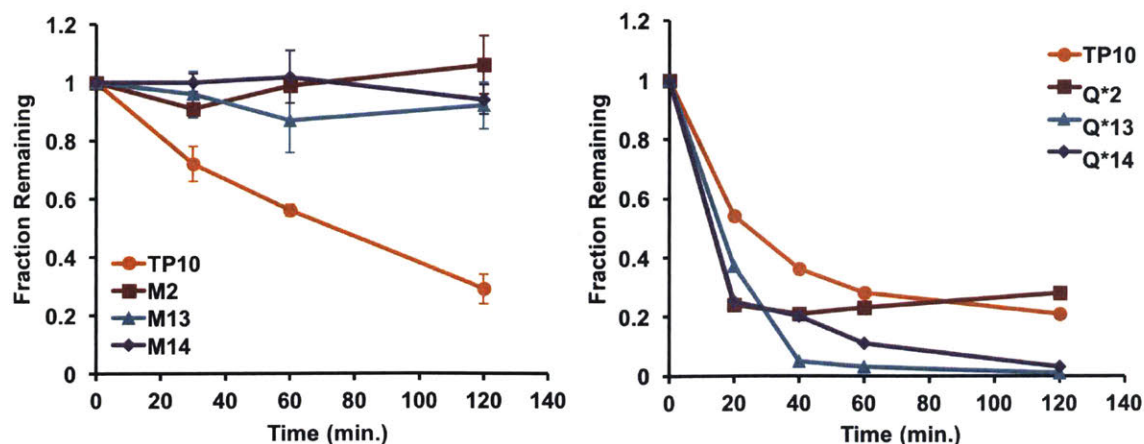


**Figure 5.3. Perfluoroarene-based macrocyclic TP10 analogues are resistant to proteolysis.** Over 2 h at 37 °C, the macrocyclic analogues are all stable to Proteinase K, while native TP10 is degraded. All alkylated controls were degraded to the same or greater extent than the native TP10 peptide.

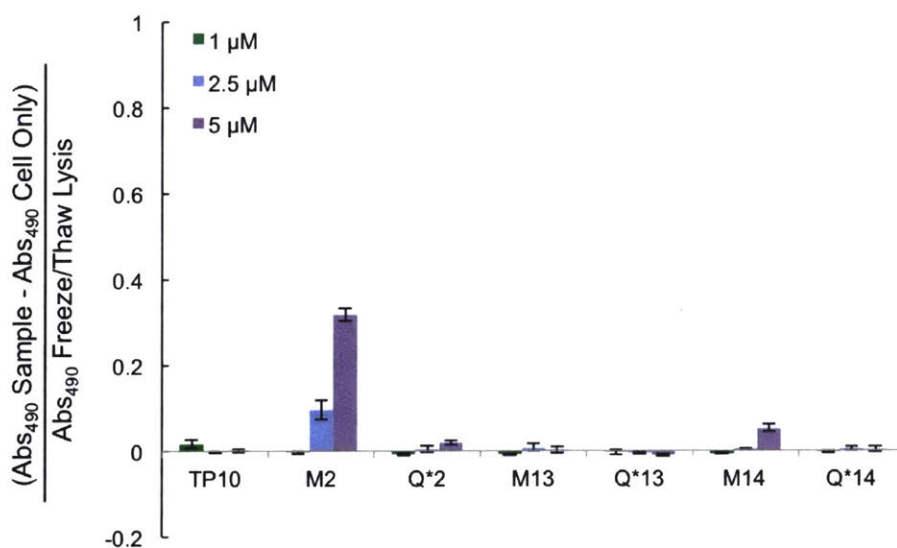


**Figure 5.4. Lactate dehydrogenase assay of perfluoroarene-based macrocyclic TP10 analogues.** Release of lactate dehydrogenase (LDH) from HeLa cells after incubation with varying concentrations of the macrocycles and controls for 2 h at 37 °C. TP10 M2 did induce some LDH leakage and early signs of cytotoxicity, especially with increasing concentration. However, TP10 M13 and M14 did not display LDH release, which suggests the cell membrane remains intact.

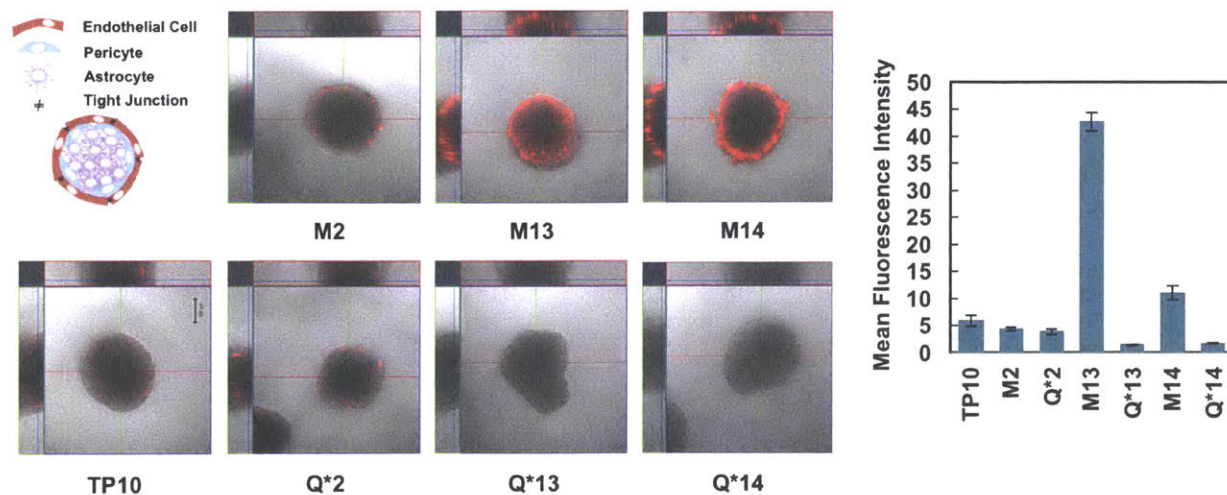


**Figure 5.5. Perfluoroarene-based macrocyclic TP10 analogues display increased entry into BBB spheroids compared to their linear counterparts.** A schematic illustrating the cellular composition of the spheres (not to scale). The confocal microscopy images display a representative spheroid after incubation with 5  $\mu\text{M}$  of each construct showing an overlay of both fluorescence (5-TAMRA) and brightfield (scale bar = 100  $\mu\text{m}$ ). The images are at a z-depth of 90  $\mu\text{m}$  into the core of the sphere. The plot shows the mean fluorescence intensity of a 100  $\mu\text{m}$  diameter circular region that excludes fluorescence on the spheroid exterior (n=3-5).

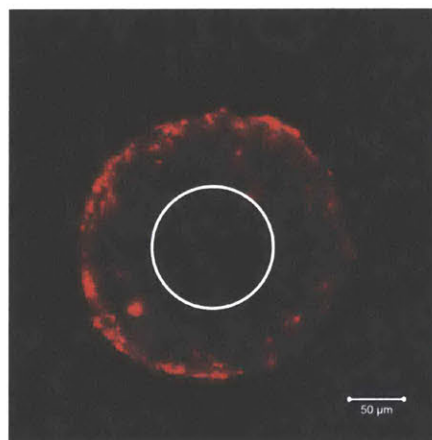


**Figure 5.6. Example of fluorescence quantification for a sphere treated with 5  $\mu\text{M}$  BIM BH3 M4.** For each sphere, a z-stack is collected. The image corresponding to a z-depth of 85-90  $\mu\text{m}$  into the sphere is extracted for quantification. The mean fluorescence intensity of the circle shown above is quantified using ImageJ. This is to ensure that the results are reflective of fluorescent material in the core of the sphere, rather than on the outside in the endothelial cells.

alkyne of M13 and Q\*13. First, 100  $\mu\text{L}$  of a 100  $\mu\text{M}$  solution of each peptide was injected into the tail vein (corresponding to  $\sim 1.5$  mg/kg at time  $t = 0$ ). Mice either received M13 or the alkyl control, Q\*13. After 4 hours, the mice were infused intravenously with 50  $\mu\text{L}$  of 50 mg/mL TRITC-dextran, which allows visualization of highly perfused blood vessels. At 4.5 hours, the mice were sacrificed. The brain, spleen, kidneys, lungs, heart, and liver were excised, flash frozen, and imaged on an *in vivo* imaging system (IVIS) (Figures 5.7A, 5.8). The total radiant efficiency from Cy5.5 in each organ was quantified (Figure 5.9). The liver and kidneys were brightest for both M13 and Q\*13 – although the amount of signal was similar between the macrocycle and control. However, in the brains of mice treated with the macrocycle, the total radiant efficiency was over double that of the linear control, suggesting increased uptake of the macrocycle into the brain.

Given the resolution of the IVIS instrument, distinguishing fluorescence in the actual brain tissue from fluorescence in the blood vessels of the brain can be challenging. Therefore, we performed a more detailed analysis by *ex vivo* brain imaging using high-resolution confocal microscopy to confirm the peptide was actually entering the brain parenchyma. The frozen brains were cryosectioned into 30  $\mu\text{m}$  slices after IVIS imaging and the slices were imaged by confocal microscopy. M13 can be observed outside of the vessel and in the brain parenchyma, providing evidence that the macrocyclic peptide is crossing the BBB and entering the brain tissue (Figures 5.7B, 5.7C). Additionally, a serum stability assay was performed by incubating each peptide in 5% mouse serum and measuring degradation over 24 hours (Figure 5.10). M13 displayed greater serum stability, suggesting that the increase in brain penetration is likely due to both increased stability in serum and increased ability to cross the BBB.

Finally, we wanted to see if our findings could be generalized to a peptide of therapeutic interest. We chose the BH3 domain of the pro-apoptotic BIM protein, as Bird *et al.* have conducted an exhaustive staple scan of the peptide and demonstrated which positions are amenable to mutation.<sup>35</sup> We synthesized two BIM BH3 peptide sequences, but substituted cysteine residues for the  $\alpha,\alpha$ -disubstituted olefin-bearing amino acids previously employed (Figure 5.11A). To evaluate the ability of our perfluoroarene-based macrocyclic BIM BH3 variants to cross the BBB, we performed the same sequence of experiments under the same conditions as we did with TP10. First, TAMRA-labeled BIM BH3 analogues were tested in BBB spheres. BIM M4 had significantly increased fluorescence in the core of the sphere, compared to both its linear alkyl control and to a hydrocarbon-cyclized control (Figures 5.11B, 5.12). Conversely, although bright



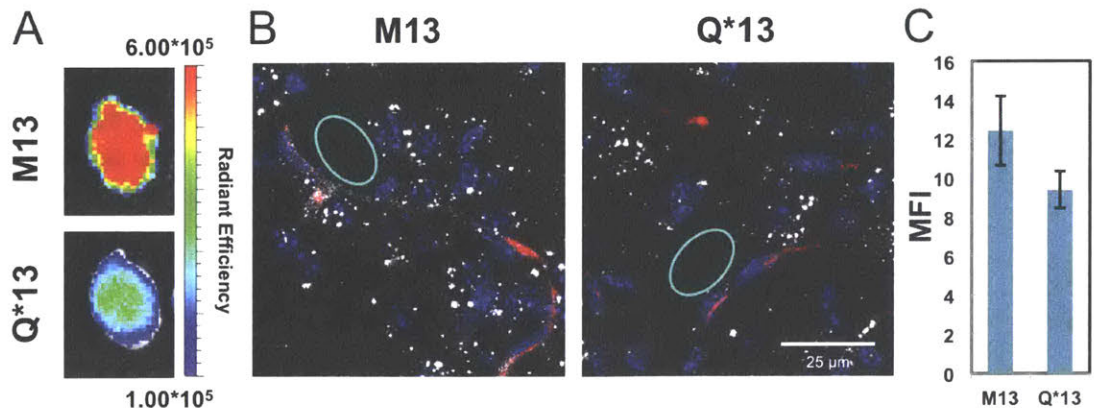


**Figure 5.7. Enhanced *in vivo* brain penetration of a perfluoroarene-based TP10 macrocycle.** (A) IVIS imaging of mouse brains treated with Cy5.5-labeled TP10 analogues. One representative brain in each group after excitation at 640 nm ( $n=2$ ). (B) Confocal microscopy images of brain cryosections showing a square area around a capillary. For full confocal images, see Figure xxx (nuclei – Hoechst – blue, dextran – TRITC – red, peptide – Cy5.5 – white). (C) Quantification of the diffuse Cy5.5 signal in the brain parenchyma from the confocal images, suggesting accumulation of the TP10 analogues in the brain. The quantification was performed by selecting regions (such as the cyan circles) outside the vessels that did not contain bright puncta and averaging the mean fluorescence intensities from each region ( $n=10$ ). M13 had a statistically significant increase in mean fluorescence intensity compared with Q\*13 by a Student's *t*-test ( $P<0.001$ ).

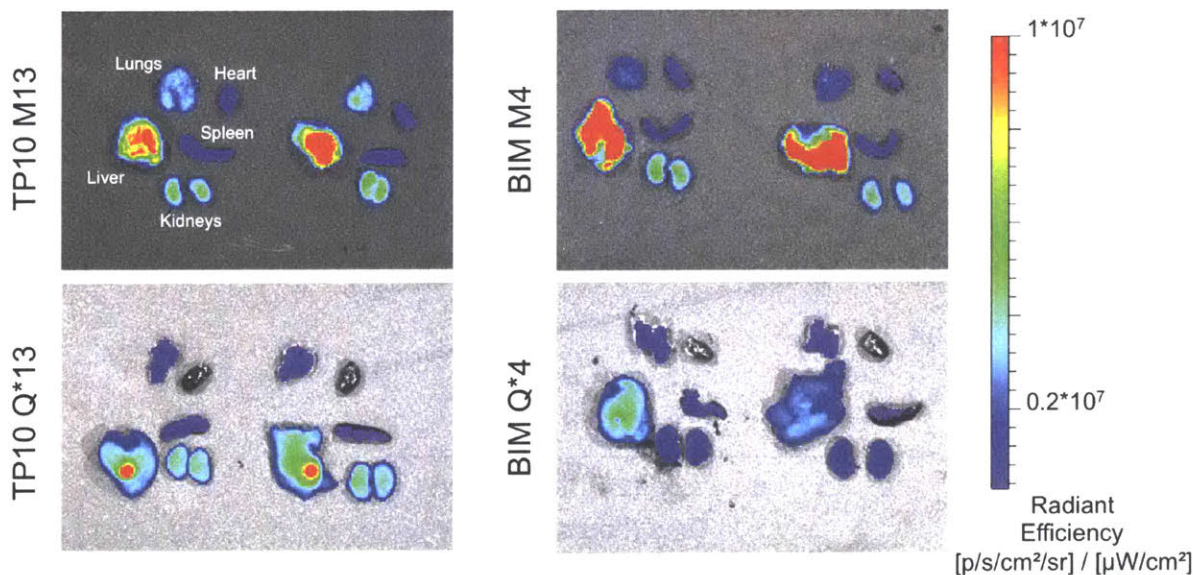


**Figure 5.8. *In vivo* biodistribution of perfluoroarene-based macrocycles.** Radiant efficiency of Cy5.5 in each set of mouse organs after treatment with Cy5.5-labeled versions of TP10 M13, TP10 Q\*13, BIM M4, and BIM Q\*4. For imaging, the excitation wavelength was at 640 nm and the emission was monitored through the Cy5.5 filter on the instrument.

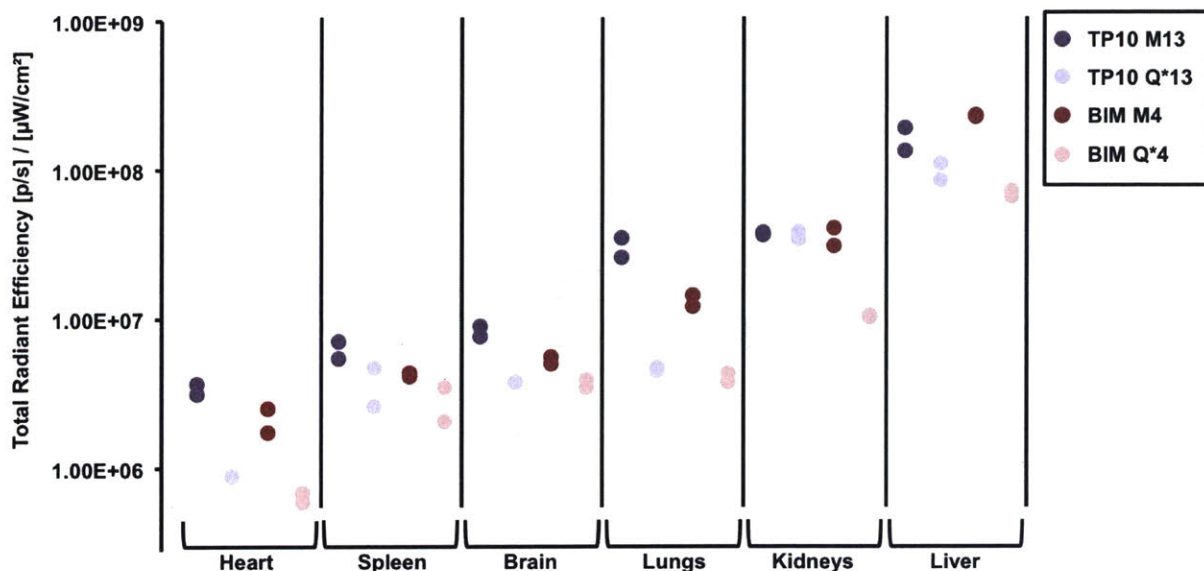


**Figure 5.9. Quantification of the *in vivo* biodistribution of perfluoroarene-based macrocycles.** Total Cy5.5 radiant efficiency of organs from mice treated with Cy5.5-labeled versions of TP10 M13, TP10 Q\*13, BIM M4, and BIM Q\*4. Two mice were in each treatment group and the data points from each mouse organ are plotted individually. The fluorescent material primarily ends up in the liver and kidneys for both the macrocyclic analogues and the alkyl analogues. The macrocycles have increased accumulation in the brain, heart, and lungs compared to their respective alkyl controls.

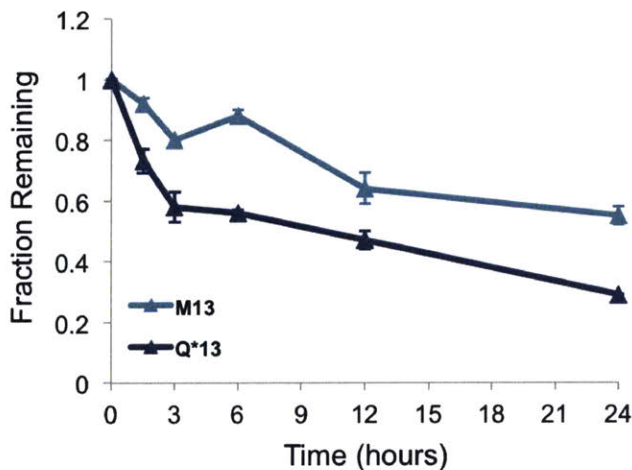


**Figure 5.10. Serum stability of perfluoroarene-based TP10 analogue in mouse serum.** Serum stability data (in triplicate) obtained from incubating M13 and Q\*13 with 5% mouse serum. While degradation of both peptides was seen over time, there was a greater fraction remaining of M13 at time  $t = 24$  h.

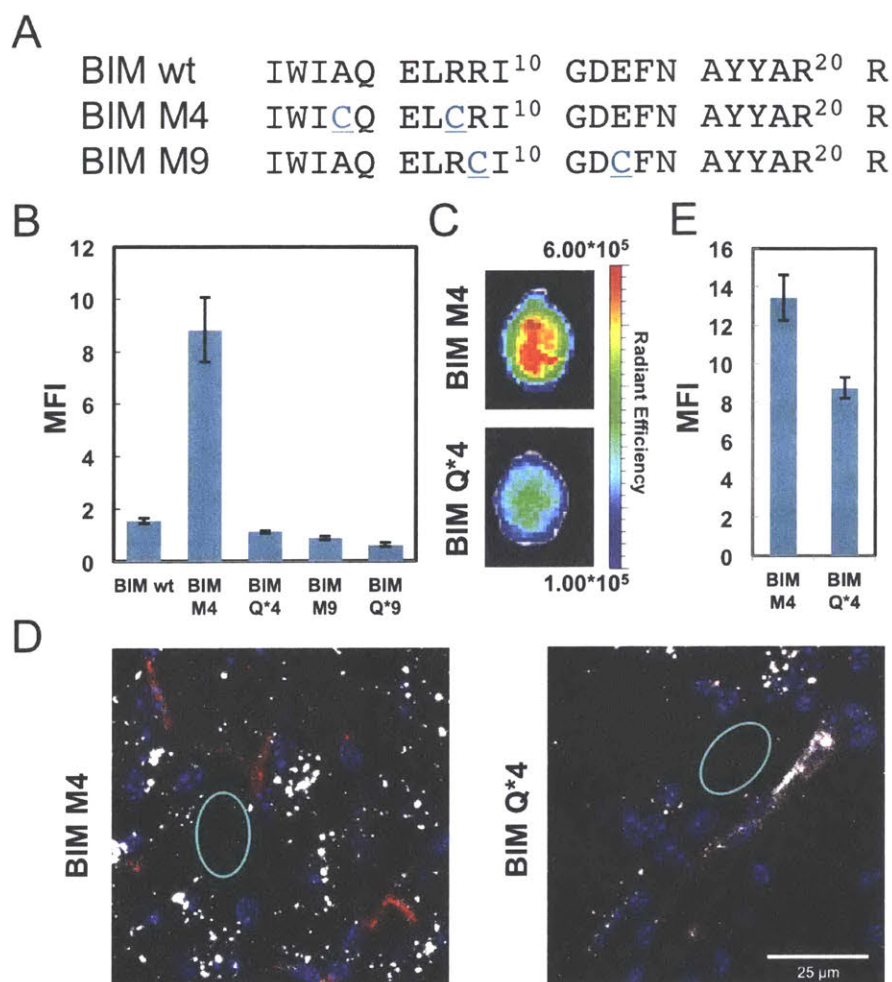


**Figure 5.11. Enhanced *in vivo* brain penetration of a perfluoroarene-based BIM BH3 macrocycle.** (A) Sequences of the BIM BH3 analogues prepared. (B) A plot of the mean fluorescence intensity in the core of the sphere for TAMRA-labeled BIM BH3 analogues (n=6). (C) IVIS imaging of mouse brains treated with Cy5.5-labeled analogues. One representative brain in each group after excitation at 640 nm (n=2). (D) Confocal microscopy images of brain cryosections showing a square area around a capillary. For full confocal images, see Figure xxx (nuclei – Hoechst – blue, dextran – TRITC – red, peptide – Cy5.5 – white). (E) A plot showing quantification of the diffuse Cy5.5 signal in the brain parenchyma from the confocal images, suggesting accumulation of the BIM BH3 analogues in the brain. The quantification was performed by selecting regions (such as the cyan circles) outside the vessels that did not contain bright puncta and averaging the mean fluorescence intensities from each region (n=10). BIM M4 had a statistically significant increase in mean fluorescence intensity compared with BIM Q\*4 by a Student's *t*-test ( $P < 0.0001$ ).



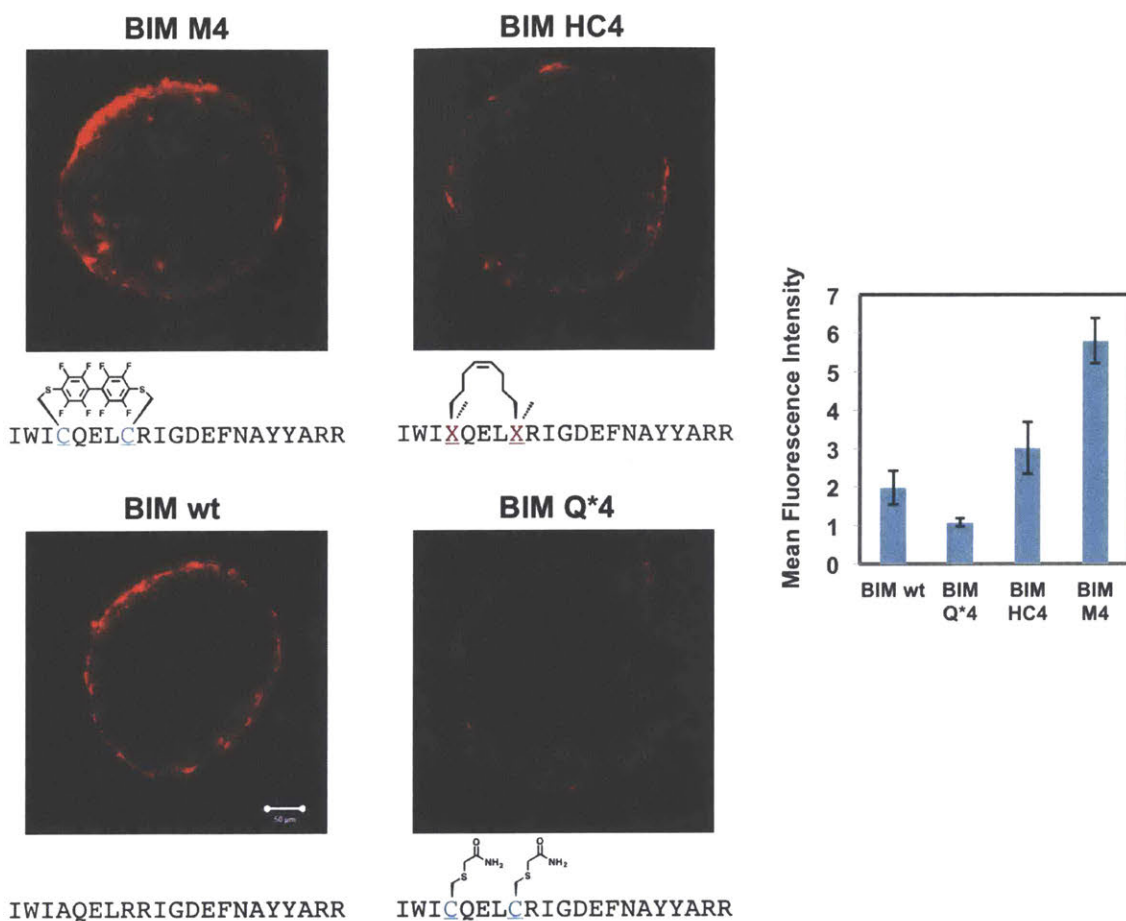


**Figure 5.12. Comparison of perfluoroarene-cyclized BIM BH3 to hydrocarbon-cyclized BIM BH3.** The confocal microscopy images display a representative spheroid after incubation in a solution of BBB media with 5 μM of each BIM BH3 analogue. The images show fluorescence (5-TAMRA) and are at a z-depth of 85 μm into the core of the sphere. The plot shows quantification of the mean fluorescence intensity in the core of the sphere for all BIM BH3 analogues (n=8).



on the sphere surface, M9 had little fluorescence in the sphere core. As a result, we carried Cy5.5-BIM M4 and its alkyl control Cy5.5-BIM Q\*4 forward for *in vivo* evaluation. The perfluoroarene macrocycle had a modest increase in total radiant efficiency in the brain by IVIS relative to the alkyl control (Figure 5.11C). When the brain was sectioned and imaged by confocal microscopy, significantly more Cy5.5 fluorescence was observed in the brain parenchyma for BIM M4 than BIM Q\*4 (Figures 5.11D, E). Altogether, these data suggest that the perfluoroarene macrocycle improves the ability of the BIM BH3 peptide to cross the BBB.

In conclusion, we have demonstrated with our proof-of-concept experiments that abiotic peptide macrocycles can exhibit significantly enhanced penetration of the brain. While synthetic peptide macrocycles have been engineered as successful inhibitors of protein-protein interactions, especially for cancer therapeutics, they are just starting to be explored for crossing the BBB.<sup>14</sup> Here we show the first example of improving brain penetration solely through the introduction of an abiotic macrocycle. The mechanism of transport across the BBB and the role of linker placement remain to be elucidated. However, given the widespread interest in peptide macrocyclization, we expect this finding may be of immediate use to the scientific community in designing therapeutics and imaging agents for central nervous system diseases.

## 5.3. Experimental

### 5.3.1. Materials

H-Rink Amide-ChemMatrix resin was obtained from PCAS BioMatrix Inc. (St-Jean-sur-Richelieu, Quebec, Canada). 1-[Bis(dimethylamino)methylene]-1*H*-1,2,3-triazolo[4,5-*b*]pyridinium-3-oxid-hexafluorophosphate (HATU), Fmoc-L-Arg(Pbf)-OH, Fmoc-L-Lys(Boc)-OH, Fmoc-L-Asp(tBu)-OH, Fmoc-L-Glu(tBu)-OH, Fmoc-L-Asn(Trt)-OH, Fmoc-L-Cys(Trt)-OH, Fmoc-L-Gly-OH, Fmoc-L-Ala-OH, Fmoc-L-Val-OH, Fmoc-L-Leu-OH, Fmoc-L-Phe-OH, Fmoc-L-Tyr(tBu)-OH, and Fmoc-L-Trp(Boc)-OH were purchased from Chem-Impex International (Wood Dale, IL). Peptide synthesis-grade *N,N*-dimethylformamide (DMF), CH<sub>2</sub>Cl<sub>2</sub>, diethyl ether, *t*-butanol and HPLC-grade acetonitrile were obtained from VWR International (Radnor, PA). Cy5.5-azide and 5-TAMRA azide were purchased from Lumiprobe Corporation (Hallandale Beach, FL). Decafluorobiphenyl was purchased from Oakwood Products, Inc. (Estill, SC). The LDH Assay kit was purchased from Promega (Madison, WI). The primary human astrocytes, astrocyte growth medium and endothelial cell growth medium were obtained from Lonza Bioscience (Walkersville, MD). The human brain microvascular pericytes and the pericyte medium were obtained from ScienCell Research Laboratories (Carlsbad, CA). The hCMEC/D3 human cerebral microvascular endothelial cells were from Cedarlane Labs (Burlington, ON, Canada). The human serum was from Valley Biomedical (Winchester, VA). All other reagents were purchased from Sigma-Aldrich (St. Louis, MO), water was deionized before use, and reactions were conducted in open-air on the benchtop.

### 5.3.2. Methods for LC-MS Analysis

For all experiments except for the proteolysis assays, LC-MS chromatograms and associated mass spectra were acquired using an Agilent 6520 ESI-Q-TOF mass spectrometer equipped with a C<sub>3</sub> Zorbax column. Mobile phases were: 0.1% formic acid in water (solvent A) and 0.1% formic acid in acetonitrile (solvent B). The following LC-MS method was used for characterization of all TP10 analogues and for the serum stability assay: Zorbax SB C3 column: 2.1 x 150 mm, 5 μm, 5% B from 0 to 2 min, linear ramp from 5% B to 65% B from 2 to 11 min, 65% B from 11 to 12 min and finally 3 min of post-time at 5% B for equilibration, flow rate: 0.8 mL/min. The following LC-MS method was used for characterization of all BIM BH3 analogues: Zorbax SB C3 column: 2.1 x 150 mm, 5 μm, 1% B from 0 to 2 min, linear ramp from 1% B to 61% B from 2 to 11 min, 61% B to 99% B from 11 to 12 min and finally 3 min of post-time at 1%

B for equilibration, flow rate: 0.8 mL/min. All data were processed using Agilent MassHunter software package. Y-axis in all chromatograms shown represents total ion current (TIC) unless noted. For the proteolysis assays, LC-MS chromatograms and associated mass spectra were acquired using an Agilent 6550 iFunnel Q-TOF mass spectrometer equipped with a Jupiter C<sub>4</sub> Phenomenex column. The following LC-MS method was used: Phenomenex Jupiter C<sub>4</sub>: 150 x 1.0 mm ID, 5  $\mu$ m, linear gradient from 1% B to 91% B over 16 min, flow rate: 0.1 mL/min.

### 5.3.3. General Method for Peptide Preparation

*Fast-flow Peptide Synthesis:* Peptides were synthesized on a 0.1-mmol scale using an automated flow peptide synthesizer.<sup>36</sup> A 200 mg portion of ChemMatrix Rink Amide HYR resin was loaded into a reactor maintained at 90 °C. All reagents were flowed at 80 mL/min with HPLC pumps through a stainless steel loop maintained at 90 °C before introduction into the reactor. For each coupling, 10 mL of a solution containing 0.2 M amino acid and 0.17 M HATU in DMF were mixed with 200  $\mu$ L diisopropylethylamine and delivered to the reactor. Fmoc removal was accomplished using 10.4 mL of 20% (v/v) piperidine. Between each step, DMF (15 mL) was used to wash out the reactor. Special coupling conditions were used for arginine, in which the flow rate was reduced to 40 mL/min and 10 mL of a solution containing 0.2 M Fmoc-L-Arg(Pbf)-OH and 0.17 M PyAOP in DMF were mixed with 200  $\mu$ L diisopropylethylamine and delivered to the reactor. For the TP10 analogues, 4-pentynoic acid was coupled in flow on the automated peptide synthesizer using the same conditions as standard amino acids. For the BIM BH3 analogues, the resin was incubated for 30 min at room temperature with 4-pentynoic acid (1 mmol) dissolved in 2.5 mL 0.4 M HATU in DMF with 500  $\mu$ L diisopropylethylamine. After completion of the synthesis, the resins were washed 3 times with DCM and dried under vacuum.

*Peptide Cleavage and Deprotection:* Each peptide was subjected to simultaneous global side-chain deprotection and cleavage from resin by treatment with 8 mL of 94% (v/v) trifluoroacetic acid (TFA), 2.5% (v/v) 1,2-ethanedithiol (EDT), 2.5% (v/v) water, and 1% (v/v) triisopropylsilane (TIPS) for 6 min at 60 °C. The TFA was evaporated by bubbling N<sub>2</sub> through the mixture until only an oil and the resin remained. Then ~35 mL of cold ether was added to precipitate and wash the peptide (chilled at -80°C). The crude product and resin were pelleted through centrifugation for three minutes at 4,000 rpm and the ether decanted. The ether precipitation and centrifugation was repeated two more times. After the third wash, the pellet was redissolved in 50% water and 50% acetonitrile containing 0.1% TFA, filtered through a fritted

syringe to remove the resin and lyophilized. In the re-synthesis of BIM BH3 analogue 4 for Cy5.5-labeled constructs, the crude peptide was redissolved in 70% water, 20% acetonitrile, and 10% DMF, which improved peptide recovery.

#### 5.3.4. Macrocyclization, Alkylation, and Fluorophore Labeling Procedures

*Macrocyclization of TP10 Analogues:* The crude TP10 peptides were dissolved in DMF, and stock solutions of decafluorobiphenyl in DMF and Tris in DMF were added such that the final concentration in the reaction vessel was 1 mM of a given TP10 analogue, 2 mM decafluorobiphenyl, and 30 mM Tris (Figure 5.13). After 5 h, DMF was removed by rotary evaporation to a final volume of 10 mL and the reaction was quenched by adding 90 mL of 85:15 water:acetonitrile containing 4% TFA. The crude reaction was purified by mass-directed semi-preparative reversed-phase HPLC (Agilent Zorbax SB C3 column: 9.4 x 250 mm, 5  $\mu$ m). Solvent A was water with 0.1% TFA additive and Solvent B was acetonitrile with 0.1% TFA additive. A linear gradient that changed at a rate of 0.5%/min was run from 20% B to 60% B. Using mass data about each fraction from the instrument, only pure fractions were pooled and lyophilized. The purity of the fraction pool was confirmed by LC-MS.

*Alkylation of TP10 Analogues:* The crude TP10 peptides were dissolved in a buffer of 6 M guanidine•HCl, 0.2 M sodium phosphate, 50 mM 2-bromoacetamide, and 20 mM *tris*(2-carboxyethyl)phosphine (TCEP)•HCl, pH 7.1 to a final concentration of 1 mM peptide. After one hour, the reaction was quenched by bringing the pH of the solution to 2 with 6 M HCl. The crude reaction was purified by mass-directed semi-preparative reversed-phase HPLC (Agilent Zorbax SB C3 column: 9.4 x 250 mm, 5  $\mu$ m). Solvent A was water with 0.1% TFA additive and Solvent B was acetonitrile with 0.1% TFA additive. A linear gradient that changed at a rate of 0.5%/min was run from 20% B to 60% B. Using mass data about each fraction from the instrument, only pure fractions were pooled and lyophilized. The purity of the fraction pool was confirmed by LC-MS.

*Procedure for Fluorophore Labeling of TP10 Analogues by azide/alkyne Huisgen Cycloaddition:* Purified TP10 constructs (0.5  $\mu$ mol) were each dissolved in 200  $\mu$ L 50:50 *t*-butanol:water in a 1.7 mL microcentrifuge tube. The following solutions were added to the microcentrifuge tube in order: 10  $\mu$ L of 50 mM 5-tetramethylrhodamine azide (5-TAMRA azide) in DMSO, 100  $\mu$ L of 500 mM Tris pH 8 in water, 50  $\mu$ L of 100 mM copper(II) sulfate in water,

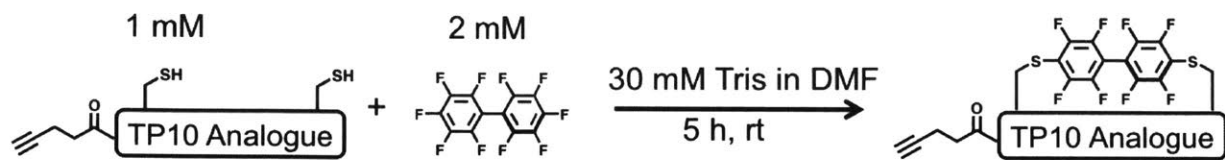


**Figure 5.13. Schematic of perfluoroaryl macrocyclization reaction.**

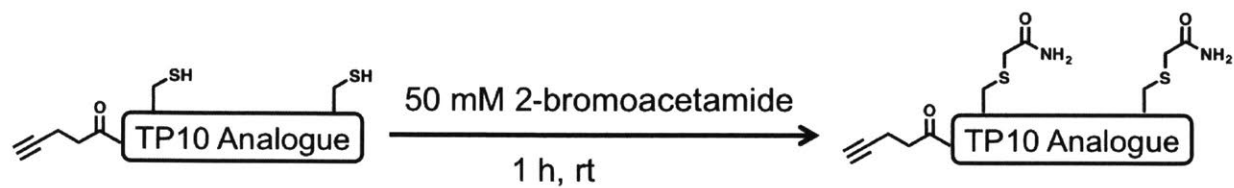


**Figure 5.14. Schematic of alkylation reaction.**

10  $\mu$ L of 10 mM Tris(benzyltriazolymethyl)amine (TBTA) in DMSO, 10  $\mu$ L of 100 mM TCEP•HCl in water, 100  $\mu$ L of 1 M ascorbic acid in water and 520  $\mu$ L 50:50 t-butanol:water. After one hour, the reaction was diluted with 9 mL of 85:15 water:acetonitrile containing 0.1% TFA, filtered and purified by mass-directed semi-preparative RP-HPLC (Agilent Zorbax SB C3 column: 9.4 x 250 mm, 5  $\mu$ m). Solvent A was water with 0.1% TFA additive and Solvent B was acetonitrile with 0.1% TFA additive. A linear gradient that changed at a rate of 0.5%/min was run from 20% B to 60% B. Using mass data about each fraction from the instrument, only pure fractions were pooled and lyophilized. The purity of the fraction pool was confirmed by LC-MS. For the Cy5.5 labeled versions of TP10 M13 and Q\*13, the same procedure was used, only the concentration of peptide was 1.5 mM and 15  $\mu$ L of 100 mM Cy5.5 azide in DMSO was added, instead of the 5-TAMRA azide.

*Purification of Crude BIM BH3 Peptides:* The crude BIM BH3 peptides were redissolved in 70% water and 30% acetonitrile containing 0.1% TFA, filtered through a 0.22  $\mu$ m nylon filter (the filter was rinsed with 1 mL 50% water and 50% acetonitrile) and purified by mass-directed semi-preparative reversed-phase HPLC (Agilent Zorbax SB C3 column: 9.4 x 250 mm, 5  $\mu$ m). Solvent A was water with 0.1% TFA additive and Solvent B was acetonitrile with 0.1% TFA additive. For the native BIM BH3 sequence, a linear gradient that changed at a rate of 0.5%/min was run from 15% B to 55% B. For the two analogues with cysteine substitutions, a linear gradient that changed at a rate of 0.5%/min was run from 30% B to 60% B. Using mass data about each fraction from the instrument, only pure fractions were pooled and lyophilized. The purity of the fraction pool was confirmed by LC-MS.

*Procedure for Macrocyclization of Purified BIM BH3 Peptides:* The purified, cysteine-containing BIM BH3 analogues were dissolved in DMF and a stock solution of decafluorobiphenyl in DMF was added such that the final concentration in the reaction vessel was 1 mM of a given BIM BH3 analogue and 2 mM decafluorobiphenyl. Diisopropylethylamine was added such that its final concentration in the reaction mixture was 50 mM. After 2 hours, the reaction mixture was diluted by a factor of two with water containing 0.1% TFA and filtered through a 0.22  $\mu$ m nylon filter. The filter was rinsed with 1 mL 50% water and 50% acetonitrile with no additive. The reaction mixture was then diluted to 30% organic components (DMF and acetonitrile) with water containing 0.1% TFA to prepare the sample for loading onto the HPLC column. The crude reaction was purified by mass-directed semi-preparative reversed-phase HPLC (Agilent Zorbax

SB C3 column: 9.4 x 250 mm, 5  $\mu$ m). Solvent A was water with 0.1% TFA additive and Solvent B was acetonitrile with 0.1% TFA additive. A linear gradient that changed at a rate of 0.5%/min was run from 30% B to 60% B. Using mass data about each fraction from the instrument, only pure fractions were pooled and lyophilized. The purity of the fraction pool was confirmed by LC-MS.

*Procedure for Alkylation of Pure BIM BH3 Peptides:* Initially, the same conditions were used to alkylate the purified, cysteine-containing BIM BH3 analogues as with the crude TP10 analogues. However, given poor recovery in the original conditions, we tested other conditions for the alkylation of BIM BH3 analogue 4 to ensure we had enough material for *in vivo* studies. BIM BH3 analogue 4 and 2-bromoacetamide were dissolved in 50% buffer containing 0.2 M sodium phosphate and 50 mM *tris*(2-carboxyethyl)phosphine (TCEP)•HCl, pH 8 and 50% DMF to a final concentration of 1 mM peptide and 50 mM 2-bromoacetamide. After one hour, the reaction was quenched by bringing the pH of the solution to 2 with 6 M HCl. The crude reaction was purified by mass-directed semi-preparative reversed-phase HPLC (Agilent Zorbax SB C3 column: 9.4 x 250 mm, 5  $\mu$ m). Solvent A was water with 0.1% TFA additive and Solvent B was acetonitrile with 0.1% TFA additive. A linear gradient that changed at a rate of 0.5%/min was run from 20% B to 60% B. Using mass data about each fraction from the instrument, only pure fractions were pooled and lyophilized. The purity of the fraction pool was confirmed by LC-MS.

*Procedure for Fluorophore Labeling of BIM BH3 Analogues by azide/alkyne Huisgen Cycloaddition:* Purified BIM BH3 analogues were labeled with 5-TAMRA azide using copper-catalyzed “click” chemistry. (see “Procedure for Fluorophore Labeling of TP10 Analogues by azide/alkyne Huisgen Cycloaddition”). For BIM BH3 wt, BIM BH3 Q\*4 and BIM BH3 Q\*9: After one hour, the reaction was diluted with 9 mL of water containing 0.1% TFA, filtered through a 0.22  $\mu$ m nylon filter (rinsed with 1 mL of 50:50 water:acetonitrile) and purified by mass-directed semi-preparative RP-HPLC (Agilent Zorbax SB C3 column: 9.4 x 250 mm, 5  $\mu$ m). Solvent A was water with 0.1% TFA additive and Solvent B was acetonitrile with 0.1% TFA additive. A linear gradient that changed at a rate of 0.5%/min was run from 25% B to 55% B. Using mass data about each fraction from the instrument, only pure fractions were pooled and lyophilized. The purity of the fraction pool was confirmed by LC-MS. For BIM BH3 M4 and BIM BH3 M9: After 1 h, the reaction was diluted with 1 mL of water containing 0.1% TFA, filtered through a 0.22  $\mu$ m nylon filter (rinsed with 1 mL of 50:50 water:acetonitrile) and purified by mass-directed semi-preparative

RP-HPLC (Agilent Zorbax SB C3 column: 9.4 x 250 mm, 5  $\mu$ m). Solvent A was water with 0.1% TFA additive and Solvent B was acetonitrile with 0.1% TFA additive. A linear gradient that changed at a rate of 0.5%/min was run from 35% B to 65% B. Using mass data about each fraction from the instrument, only pure fractions were pooled and lyophilized. The purity of the fraction pool was confirmed by LC-MS.

For the Cy5.5 labeled versions of BIM BH3 M4 and Q\*4, the same procedure was used only Cy5.5 azide in DMSO was added instead of 5-TAMRA azide. Also, a different linear gradient was used for purification, which changed at a rate of 0.5%/min and ran from 40% B to 70% B.

*Preparation of Hydrocarbon Cyclized BIM BH3 Peptide:* The peptide was synthesized using our standard fast-flow solid phase synthesis conditions with a 50 mg portion of ChemMatrix Rink Amide HYR resin. For each Fmoc-(*S*)-2-(4-pentenyl)Ala-OH residue and the residue immediately following, modified coupling conditions were utilized. For these residues, amino acid and HATU (150  $\mu$ mol) were dissolved together in 2 mL NMP. Next, 120  $\mu$ L of diisopropylethylamine was added to the vial and shaken to mix. The activated amino acid solution was flowed over the resin bed at a flow rate of 0.2 mL/min at a temperature of 90  $^{\circ}$ C. For the N-terminal isoleucine residue, the Fmoc protecting group was not removed prior to olefin metathesis. The olefin metathesis was carried out using a modified protocol from Kim *et al.*<sup>37</sup> Briefly, the peptidyl resin was swelled with 2 mL of DCE. The resin was treated with 1 mL of a 6 mM solution of Grubbs' first-generation catalyst in DCE under constant nitrogen bubbling at room temperature. After 2 hours, the reaction progress was assessed by removing a small portion of resin, subjecting the resin to cleavage, and analyzing the peptide by LC-MS. Given incomplete metathesis, the reaction was then allowed to proceed overnight. The resin was washed 3 times with DCE, then 3 times with DMF, and the Fmoc group was removed by treatment with 20% piperidine in DMF (2 x 4 minutes). Then, 4-pentynoic acid was coupled at room temperature (1 mmol in 2.5 mL of 0.4 M HATU with 500  $\mu$ L diisopropylethylamine). The peptide was cleaved using a cocktail of 95% (v/v) TFA, 2.5% (v/v) water, and 2.5% (v/v) TIPS for 6 min at 60  $^{\circ}$ C, triturated three times with ether, resuspended in 50% water and 50% acetonitrile, and lyophilized.

The crude, lyophilized hydrocarbon cyclized BIM BH3 peptide was redissolved in 70% water and 30% acetonitrile containing 0.1% TFA, filtered through a 0.22  $\mu$ m nylon filter and purified by mass-directed semi-preparative reversed-phase HPLC (Agilent Zorbax SB C3 column: 9.4 x 250 mm, 5  $\mu$ m). Solvent A was water with 0.1% TFA additive and Solvent B was acetonitrile



with 0.1% TFA additive. A linear gradient that changed at a rate of 0.5%/min was conducted from 25% B to 55% B. Using mass data about each fraction from the instrument, only pure fractions were pooled and lyophilized. The purity of the fraction pool was confirmed by LC-MS.

Finally, 5-TAMRA was conjugated the purified hydrocarbon cyclized BIM BH3 peptide using copper-catalyzed “click” chemistry. (see “Procedure for Fluorophore Labeling of TP10 Analogues by azide/alkyne Huisgen Cycloaddition”). Again, the reaction was purified by mass-directed semi-preparative RP-HPLC (Agilent Zorbax SB C3 column: 9.4 x 250 mm, 5  $\mu$ m). Solvent A was water with 0.1% TFA additive and Solvent B was acetonitrile with 0.1% TFA additive. A linear gradient that changed at a rate of 0.5%/min was run from 25% B to 55% B. Using mass data about each fraction from the instrument, only pure fractions were pooled and lyophilized. The purity of the fraction pool was confirmed by LC-MS.

### 5.3.5. Flow Cytometry Assays

*HeLa Flow Cytometry Experiment:* HeLa cells were maintained in DMEM supplemented with 10% (v/v) fetal bovine serum and 1% (v/v) Pen Strep at 37 °C and 5% CO<sub>2</sub>. Twelve hours before treatment, HeLa cells were plated at a density of 60,000 cells per well in a 24-well plate. 1 mM stocks of each of the peptides were prepared in DMSO. Concentration of the stocks was quantified by absorbance using a UV/Vis spectrophotometer and a 5-TAMRA extinction coefficient of  $\epsilon=54,124 \text{ M}^{-1}\text{cm}^{-1}$  at  $\lambda=552 \text{ nm}$  (determined experimentally by creating a standard curve of 5-TAMRA azide dissolved in DMSO/PBS). Then, each peptide was diluted to a final concentration of 2.5  $\mu$ M in serum-free DMEM. To treat the cells, the overnight growth media was aspirated from each well and 200  $\mu$ L of a given 2.5  $\mu$ M peptide stock was applied. Cells were incubated for 2 hours at 37 °C and 5% CO<sub>2</sub> with the peptide treatment, and then the treatment media was aspirated. Trypsin-EDTA 0.25 % (100  $\mu$ L) was added to the cells and incubated for 15 min at 37 °C and 5% CO<sub>2</sub>. To quench the trypsin, 400  $\mu$ L of phenol-red free DMEM supplemented with 10% (v/v) fetal bovine serum was added to each well. The dissociated cells in media were transferred to microcentrifuge tubes and spun at 500 rcf for 3 min. The supernatant was removed, the pellets were washed with 1 mL of phosphate-buffered saline (PBS), and the tube was spun again. The supernatant was again removed and the pellets were resuspended in 500  $\mu$ L PBS with 2% FBS (v/v) along with 1  $\mu$ L of 1 mg/mL propidium iodide in water. Flow cytometry analysis was carried out on a BD LSRII flow cytometer. Gates were applied to the data to ensure that only data from healthy, living cells were taken into account. Cells that were highly positive for

propidium iodide or had forward/side scatter readings that were sufficiently different from the main cell population were excluded. Each histogram contains at least 5,000 gated events (Figure 5.15).

*hCMEC/D3 Cell Flow Cytometry:* hCMEC/D3 cells were maintained in EGM-2 media with all included growth factors, cytokines, and supplements at 37 °C and 5% CO<sub>2</sub>. Twelve hours before treatment, hCMEC/D3 cells were plated at a density of 60,000 cells per well in a 24-well plate. The same 1 mM DMSO stocks of the peptides from the HeLa cell experiment were used. Each peptide was diluted to a final concentration of 2.5 μM in BBB-media (EGM-2 with 2% human serum without FBS or VEGF). To treat the cells, the overnight growth media was aspirated from each well and 200 μL of a given 2.5 μM peptide stock was applied. Cells were incubated for 2 hours at 37 °C and 5% CO<sub>2</sub> with the peptide treatment, and then the treatment media was aspirated. Trypsin-EDTA 0.25 % (200 μL) was added to the cells and incubated for 15 min at 37 °C and 5% CO<sub>2</sub>. To quench the trypsin, 800 μL of BBB media was added to each well. The dissociated cells in media were transferred to microcentrifuge tubes and spun at 500 rcf for 3 minutes. The supernatant was removed, the pellets were washed with 1 mL of PBS, and the tube was spun again. The supernatant was again removed and the pellets were resuspended in 500 μL PBS with 2% FBS (v/v) along with 1 μL of 1 mg/mL propidium iodide in water. Flow cytometry analysis was carried out on a BD LSRII flow cytometer. Gates were applied to the data to ensure that only data from healthy, living cells were taken into account. Cells that were highly positive for propidium iodide or had forward/side scatter readings that were sufficiently different from the main cell population were excluded. Each histogram contains at least 5,000 gated events (Figure 5.16).

### **5.3.6. Proteolysis Assay**

*Proteolysis Assay for Macrocyclic TP10 Analogues:* For each peptide, 10 μL of PBS, 0.1 μL of Proteinase K (0.005 mg/mL stock solution in PBS), and 1 μL of peptide (1 mM DMSO stock solution) were combined in a PCR tube. The resulting reaction mixture was capped and incubated at 37 °C for 2 hours. At each time point, 0.5 μL of the crude reaction was transferred to an LC-MS vial and quenched by addition of 39 μL of 50:50 water:acetonitrile. A 0.8 μL portion of the quenched reaction was injected onto an Agilent 6550 iFunnel Q-TOF MS. Time points were taken at t = 0 min, 30 min, 60 min, and 120 min. An extracted ion current (EIC) for the +4 charge state m/z was analyzed using the MassHunter software. The EIC peak was integrated and percent

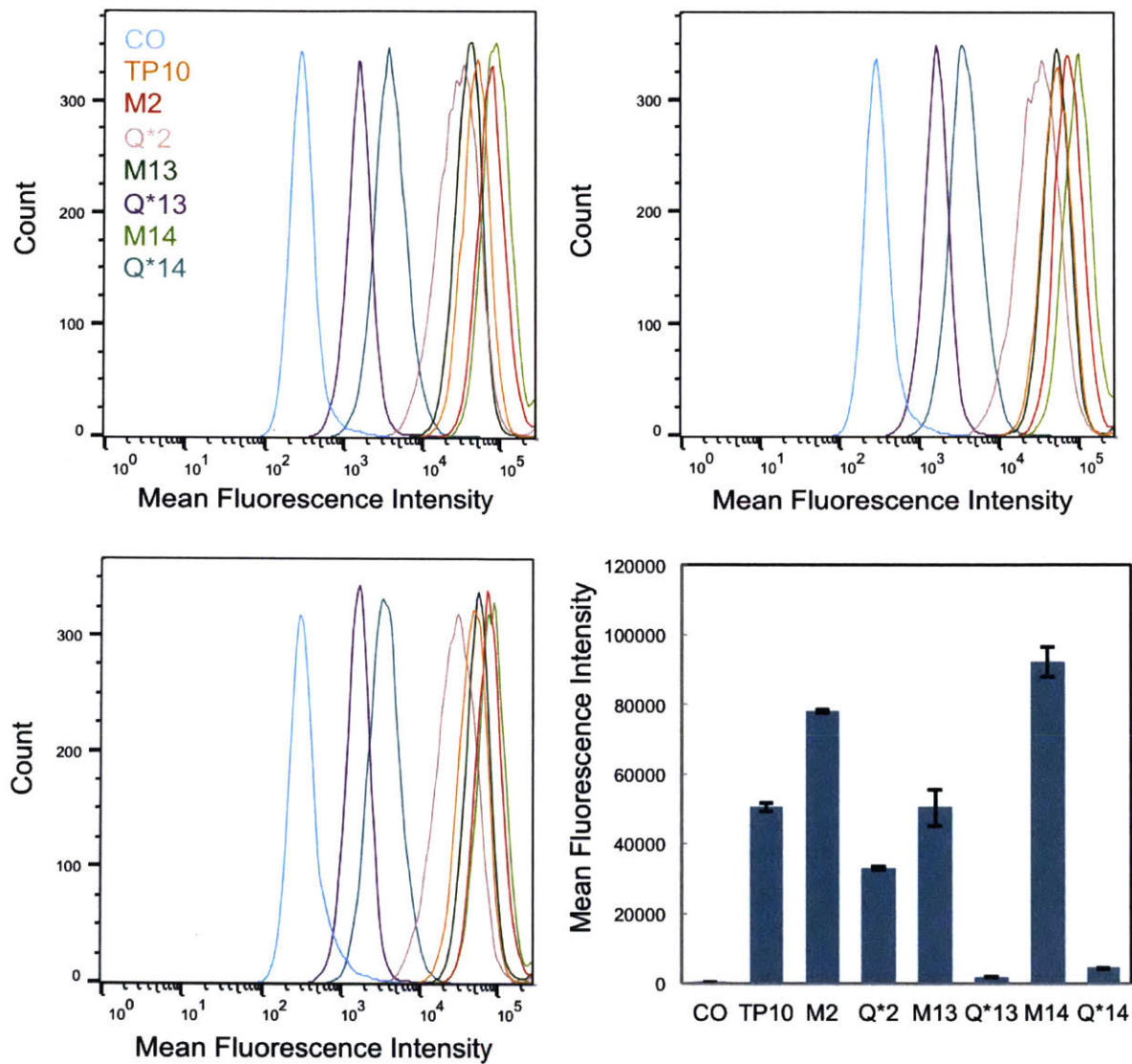


**Figure 5.15. Histograms from flow cytometry experiments with HeLa cells.** Histograms showing HeLa cells after treatment with each construct (n=3). The mean of the mean fluorescence intensities from the three experiments is displayed in Figure 5.2. CO is an untreated, cell-only control.

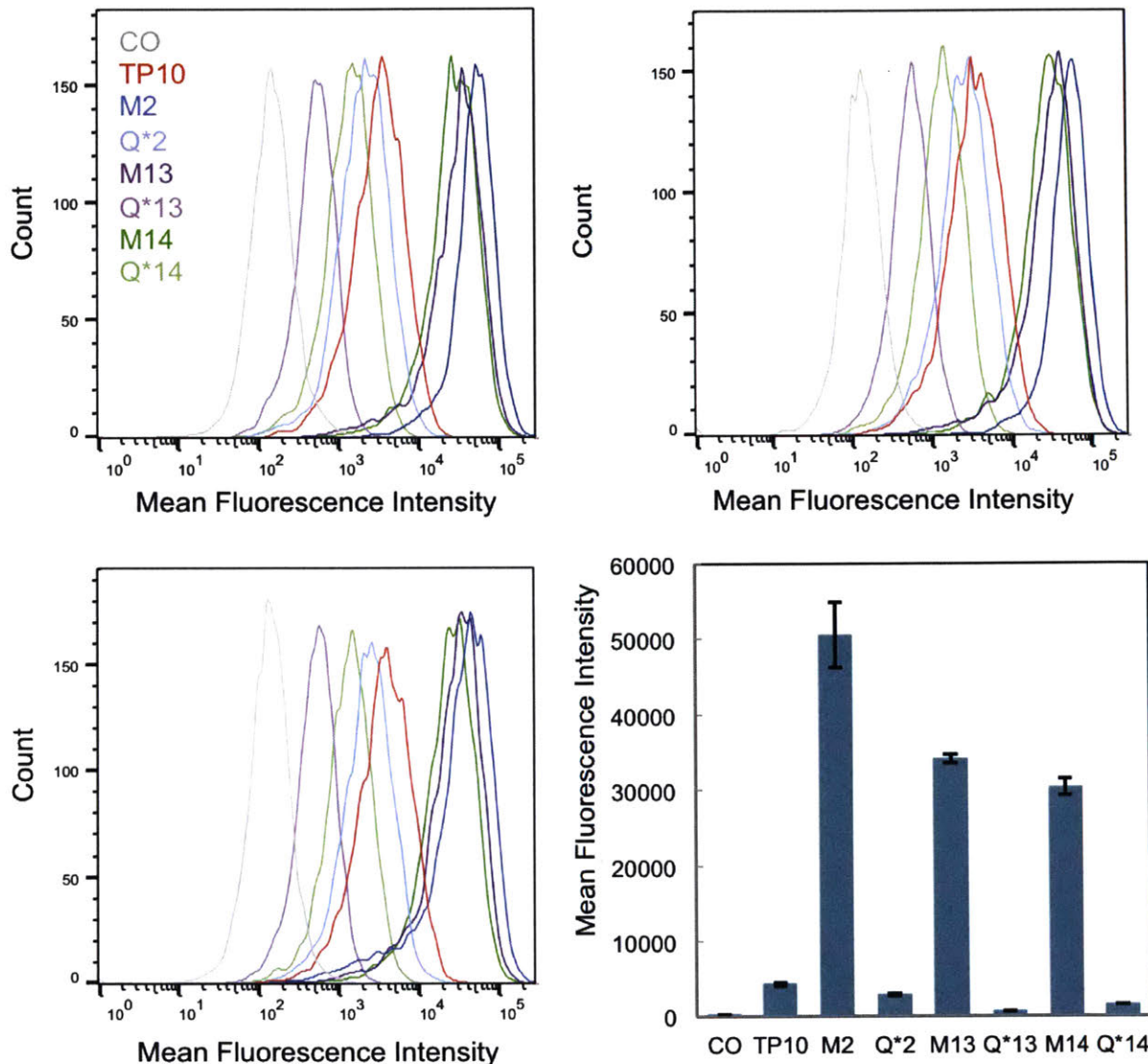


**Figure 5.16. Histograms from flow cytometry experiments with hCMEC/D3 brain endothelial cells.** Histograms showing hCMEC/D3 cells after treatment with each construct ( $n=3$ ). The mean of the mean fluorescence intensities from the three experiments is displayed in Figure 5.2. CO is an untreated, cell-only control.

peptide intact was determined by  $(EICT_1/EICT_0) * 100$  in which  $EICT_1$  is the peak integration at a given time point and  $EICT_0$  is the peak integration at time  $t = 0$  (Figure 5.3).

*Proteolysis Assay for Linear TP10 Analogues:* For each peptide, 10  $\mu$ L of PBS, 0.1  $\mu$ L of Proteinase K (0.05 mg/mL stock solution in PBS), and 1  $\mu$ L of peptide (1 mM DMSO stock solution) were combined in a PCR tube. The resulting reaction mixture was capped and incubated at room temperature for 2 hours. At each time point, 0.5  $\mu$ L of the crude reaction was transferred to a LC-MS vial and quenched by addition of 39  $\mu$ L of 50:50 water:acetonitrile. A 0.8  $\mu$ L portion of the quenched reaction was injected onto an Agilent 6550 iFunnel Q-TOF MS. Time points were taken at  $t = 0$  min, 20 min, 40 min, 60 min, and 120 min. An extracted ion current (EIC) for the +4 charge state  $m/z$  was analyzed using the MassHunter software. The EIC peak was integrated and percent peptide intact was determined by  $(EICT_1/EICT_0) * 100$  in which  $EICT_1$  is the peak integration at a given time point and  $EICT_0$  is the peak integration at time  $t = 0$ .

### 5.3.7. Lactate Dehydrogenase Assay

HeLa cells were maintained in DMEM supplemented with 10% (v/v) fetal bovine serum and 1% (v/v) Pen Strep at 37 °C and 5% CO<sub>2</sub>. Twelve hours before treatment, HeLa cells were plated at a density of 10,000 cells per well in a 96-well plate. Stocks (1 mM) of each of the peptides were prepared in DMSO. Concentration of the stocks was confirmed by absorbance using a UV/Vis spectrophotometer and a 5-TAMRA extinction coefficient of  $\epsilon=54,124 \text{ M}^{-1}\text{cm}^{-1}$  at  $\lambda=552$  nm. Each peptide was diluted to a final concentration of 10  $\mu$ M in serum-free DMEM. To treat the cells, the overnight growth media was aspirated from each well and a serial dilution was performed, such that the total volume in each well was 100  $\mu$ L and concentrations of 5  $\mu$ M, 2.5  $\mu$ M, and 1  $\mu$ M were evaluated. Additional wells included a DMSO control, to ensure the quantities of DMSO used to solubilize the peptide would not cause membrane leakage and two sets of cell only wells - one to serve as the negative control and the other to be frozen and thawed after incubation to serve as a positive control. Cells were incubated for 2 hours at 37 °C and 5% CO<sub>2</sub> and then the supernatant treatment media was transferred to another clear-bottom 96-well plate for the assay. The assay was performed using the CytoTox 96® Non-Radioactive Cytotoxicity Assay (Promega) according to the included technical bulletin. After completion of the assay, the final solution in each well was diluted 1:1 with PBS such that the measured absorbance was in the linear range of the instrument. The absorbance was measured on a BioTek Epoch Microplate

Spectrophotometer. Additional controls at this step included DMEM only and 5  $\mu$ M TAMRA-azide, to confirm that there was no background absorbance at 490 nm.

### **5.3.8. BBB Spheroid Assay**

Primary human astrocytes were cultured in AGM media with all included growth factors, cytokines, and supplements at 37 °C and 5% CO<sub>2</sub>. Astrocytes used in spheres were between passage number two and five. Human brain microvascular pericytes (HBVP) were cultured in pericyte medium containing 2% FBS, pericyte growth supplement and Pen Strep. HBVPs used in spheres were between passage number two and ten. hCMEC/D3 endothelial cells were maintained in EGM-2 with all included growth factors, cytokines, and supplements at 37 °C and 5% CO<sub>2</sub>. hCMEC/D3 endothelial cells were between passage 27 and 32. All cells were grown in T75 tissue culture flasks. For co-culture conditions for spheroid formation and functional assays, spheroids were maintained in BBB-media (EGM-2 with 2% human serum without FBS or VEGF) at 37 °C and 5% CO<sub>2</sub>.

Sterile 1% agarose (w/v) was transferred into a tissue culture hood and 50  $\mu$ L of the solution was dispensed into each well of a 96-well plate and allowed to cool and solidify. Primary human astrocytes, HBVPs, and hCMEC/D3 cells were treated with trypsin-EDTA 0.25% and incubated for 15 minutes at 37°C and 5% CO<sub>2</sub>. The trypsin in each flask was quenched with BBB-media. Each cell type was counted with a hemocytometer and 1000 cells of each cell type were seeded onto the 96-well plate containing the solidified agarose in a 1:1:1 ratio to a final volume of 100  $\mu$ L. Cells were incubated in a humidified incubator at 37 °C and 5% CO<sub>2</sub> for 48 hours, in order to allow the cells to assemble into multicellular BBB spheroids.

Microcentrifuge tubes containing a 5  $\mu$ M solution of each peptide analogue in BBB-media were prepared. Five to ten multicellular BBB spheroids were added to each tube. Spheroids were incubated for 3 hours at 37 °C on a rotator. The spheres were then removed and washed three times with PBS, fixed in 3.7% formaldehyde, and transferred into Nunc Lab-Tek II thin-glass 8-well chambered coverglass (Thermo Scientific). The spheroids were imaged using a confocal microscope under a 20x objective. Z-slices captured through each spheroid (up to 100  $\mu$ m depth) were analyzed using the ZEN imaging software (blue edition; 2012 version). In order to quantify the mean fluorescence intensity, the image at a depth of 88  $\mu$ m in the z-plane was used. The mean fluorescence of a 100  $\mu$ m circle centered on the center of the sphere in the XY-plane was quantified using ImageJ (Figure 5.6).

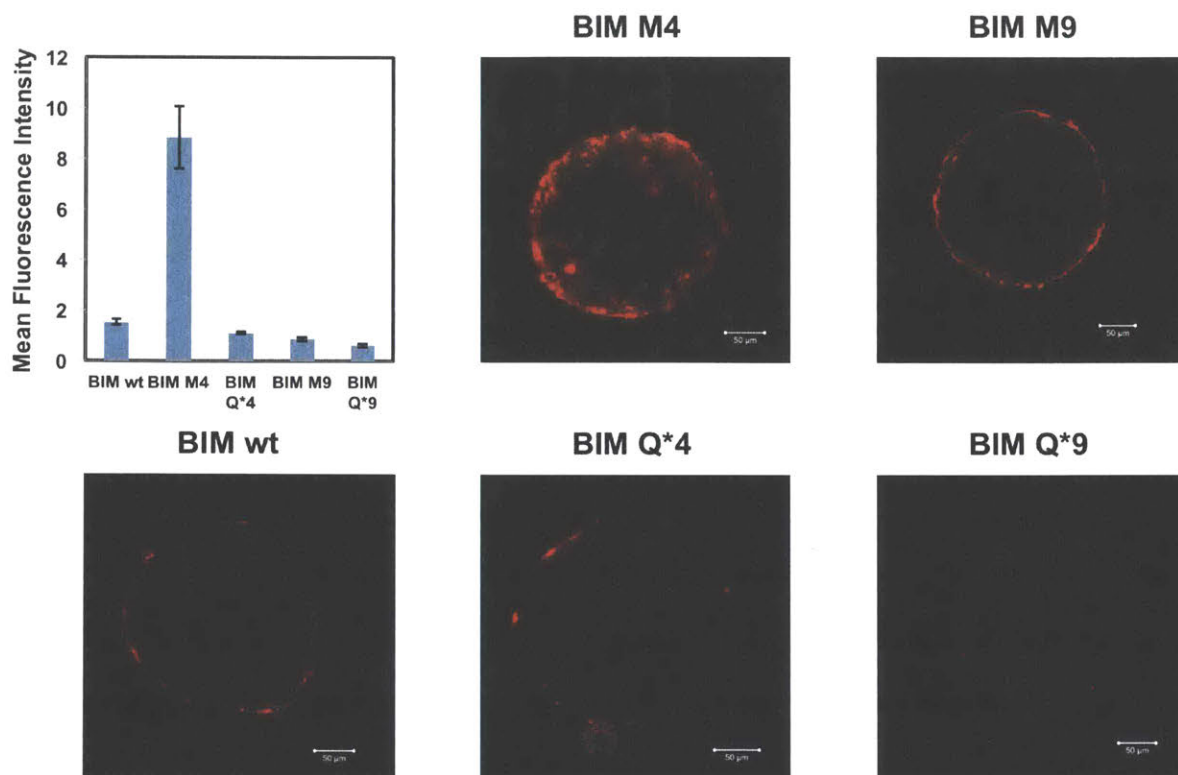


**Figure 5.17. Confocal images of representative spheres treated with BIM BH3 analogues.** The confocal microscopy images display a representative spheroid after incubation in a solution of BBB media with 5 μM of each BIM BH3 analogue. The images show fluorescence (5-TAMRA) and are at a z-depth of 85 μm into the core of the sphere. The plot (also Figure 5.11B) shows quantification of the mean fluorescence intensity in the core of the sphere for all BIM BH3 analogues (n=6).

### 5.3.9. Serum Stability Assay

PBS (95  $\mu\text{L}$ ), mouse serum (5  $\mu\text{L}$ ), and peptide solution (0.5  $\mu\text{L}$  of a 10 mM DMSO stock solutions of Cy5.5-TP10 M13 and Cy5.5-TP10 Q\*13 quantified by mass) were combined in a 0.7 mL microcentrifuge tube. The resulting mixture was capped and incubated at 37 °C for 24 hours. At each time point, 5  $\mu\text{L}$  of the solution was transferred to a different 0.7 mL microcentrifuge tube, flash frozen in liquid  $\text{N}_2$ , and lyophilized. Upon drying, the samples were redissolved in 30  $\mu\text{L}$  of 50:50 water:acetonitrile containing 0.1% TFA, transferred to an LC-MS vial, and 1  $\mu\text{L}$  was injected onto the Agilent 6520 (Figure 5.18, 5.19). Time points were taken at  $t = 0$  h, 1.5 h, 3 h, 6 h, 12 h, and 24 h. An extracted ion current (EIC) for the +5 charge state  $m/z$  was analyzed using the MassHunter software. The EIC peak was integrated and the fraction of peptide intact was determined by  $\text{EIC}_{t_1}/\text{EIC}_{t_0}$  in which  $\text{EIC}_{t_1}$  is the peak integration at a given time point and  $\text{EIC}_{t_0}$  is the peak integration at time  $t = 0$ .

### 5.3.10. *In Vivo* Imaging System Analysis

The lyophilized Cy5.5-TP10 M13, Cy5.5-TP10 Q\*13, Cy5.5-BIM M4, and Cy5.5-BIM Q\*4 powders were dissolved to a final concentration of 2 mM in DMSO by mass. Each peptide was then diluted to a concentration of 100  $\mu\text{M}$  in a solution of 50:50 polyethylene glycol (PEG)-300:0.9% sodium chloride (v/v) irrigation solution. A 100  $\mu\text{L}$  dose of each peptide solution was administered intravenously via the tail vein into healthy 8-week old female nude mice. After 4 hours, 100  $\mu\text{L}$  of 50 mg/mL tetramethylrhodamine isothiocyanate-labeled dextran (155 kDa) in 0.9% sodium chloride was injected via the tail vein. Mice were sacrificed 30 min later by cervical dislocation. The brain, heart, lungs, kidneys, spleen, and liver were excised from each mouse, frozen on dry ice and imaged using an *In Vivo* Imaging System (Perkin Elmer) at an excitation of 640 nm (Figure 5.7A, Figure 5.8, Figure 5.11C, and Figure 5.20). Using Living Image software, regions of interest were drawn around each organ and the total radiant efficiency of Cy5.5 from each organ was quantified (Figure 5.9).

*IVIS Study of TP10 Constructs 24 hours after treatment with lower concentration:* The lyophilized Cy5.5-TP10 M13 and Cy5.5-TP10 Q\*13 powders were dissolved to a final concentration of 2 mM in DMSO by mass. Each peptide was then diluted to a concentration of 10  $\mu\text{M}$  in a solution of 50:50 polyethylene glycol (PEG)-300:0.9% sodium chloride irrigation solution. A 100  $\mu\text{L}$  dose of each 10  $\mu\text{M}$  peptide solution was administered intravenously via the tail vein into healthy 8-week old female nude mice. The mice were sacrificed 24 hours after



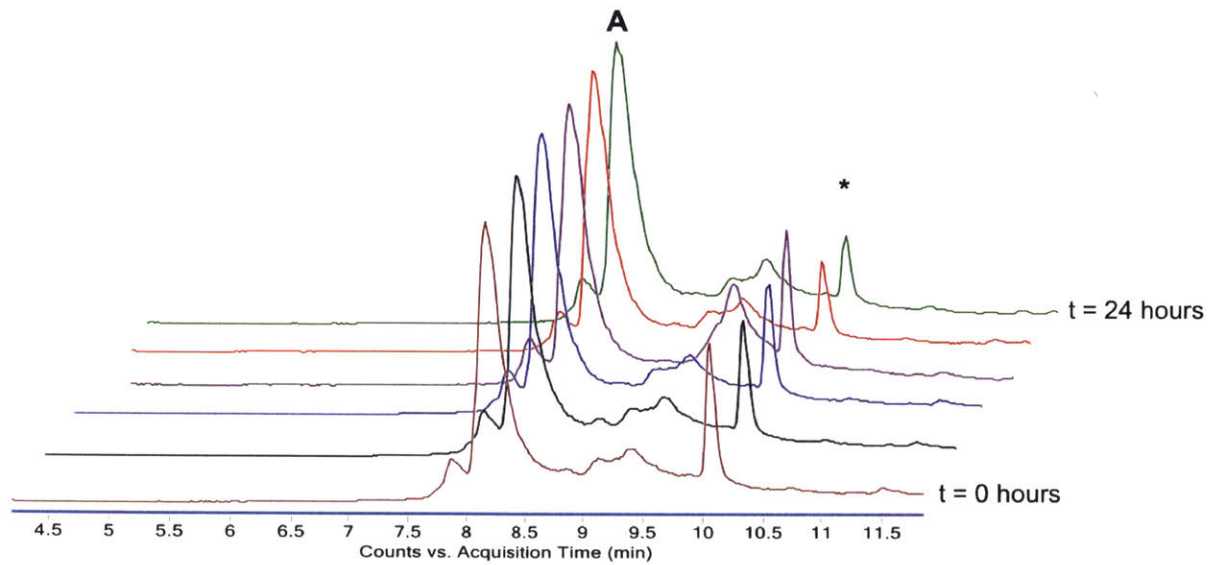


**Figure 5.18. Total ion current (TIC) chromatograms of the serum stability assay with peptide TP10 M13.** One representative trial. A = albumin \* = Cy5.5-TP10 M13

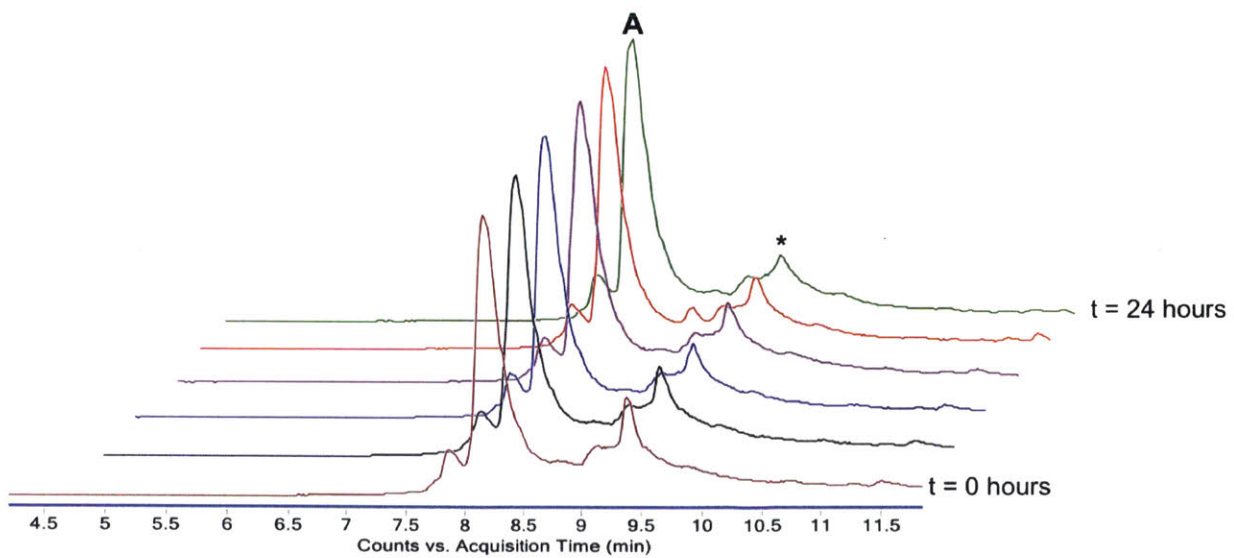


**Figure 5.19. Total ion current (TIC) chromatograms of the serum stability assay with peptide TP10 Q\*13.** One representative trial. A = albumin \* = Cy5.5-TP10 Q\*13

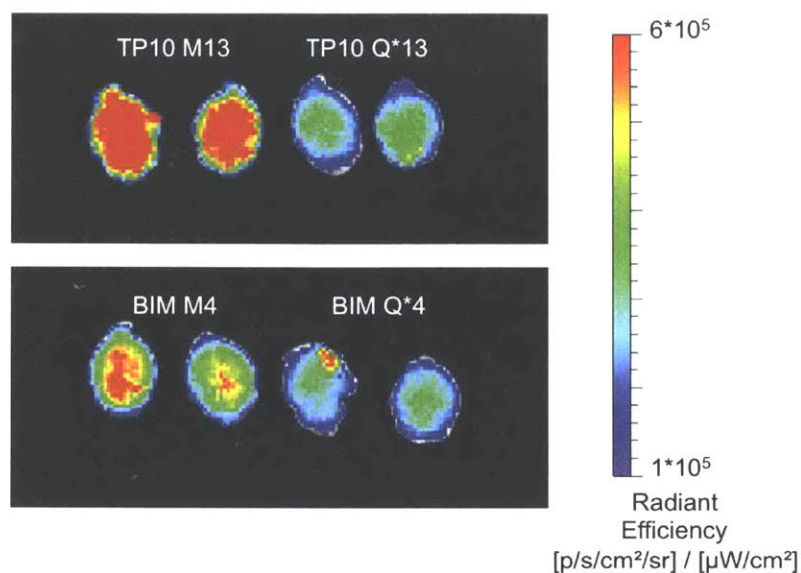


**Figure 5.20. IVIS images of mouse brains.** Cy5.5 radiant efficiency of each set of brains from mice treated with Cy5.5-labeled versions of TP10 M13, TP10 Q\*13, BIM M4, and BIM Q\*4. For imaging, the excitation wavelength was at 640 nm and the emission was monitored through the Cy5.5 filter on the instrument. One brain from each group is presented in Figure 5.7A and 5.11C. The bright spot on the left brain in the BIM Q\*4 group is due to a small amount of spleen that was frozen to the brain. The organs were all frozen next to each other and removal of the spleen risked damage to the brain.

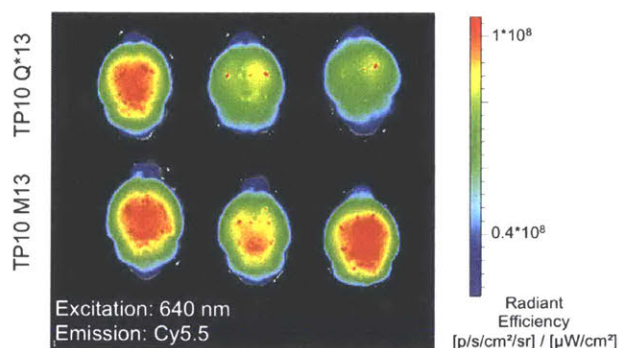


**Figure 5.21. IVIS Images of TP10 analogues at lower concentration.** Three brains treated with Cy5.5-TP10 Q\*13 (top) and three brains treated with Cy5.5-TP10 M13 (bottom) after excitation at 640 nm to image Cy5.5.

treatment (by CO<sub>2</sub> asphyxiation). Brains were excised and immediately imaged using an *In Vivo* Imaging System (Perkin Elmer)(Figure 5.21).

#### **5.3.11. Confocal Microscopy of *Ex Vivo* Brain Slices**

After imaging the frozen brains with the IVIS instrument, cryosections (30 μm) of the brains were obtained using a Microm HM 550 cryostat. Brain slices were fixed in 3.7% formaldehyde for 10 min, stained with Hoechst dye (1:1000 in PBS), mounted with a coverslip in VectaShield Antifade mounting media and imaged under a confocal microscope (63x oil-immersion objective). Tile scans (2x2) and z-slices were merged to generate a 2D maximum intensity projection using ZEN imaging software (black edition; 2012 version).

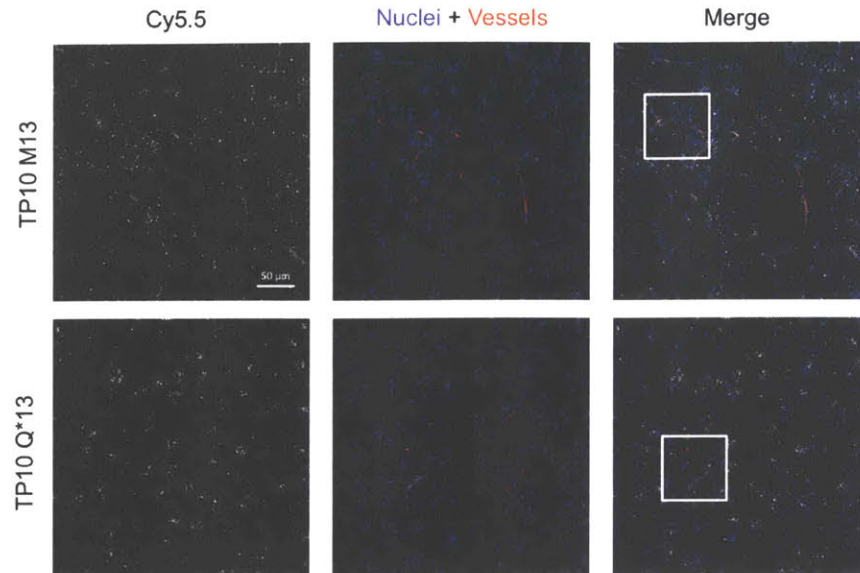


**Figure 5.22. Confocal images of brain slices after treatment with TP10 analogues.** Images of brain slices after treatment with Cy5.5-TP10 M13 (top) and with Cy5.5-TP10 Q\*13 (bottom) (nuclei – Hoechst – blue, dextran – TRITC – red, peptide – Cy5.5 – white). The left panel is only the Cy5.5 channel, the middle panel is a merge showing Hoescht for identification of nuclei and tetramethylrhodamine-labeled dextran in the vessels, and the right panel is a merge of all three channels. The square selections in each image are enlarged and shown in Figure 5.7B.

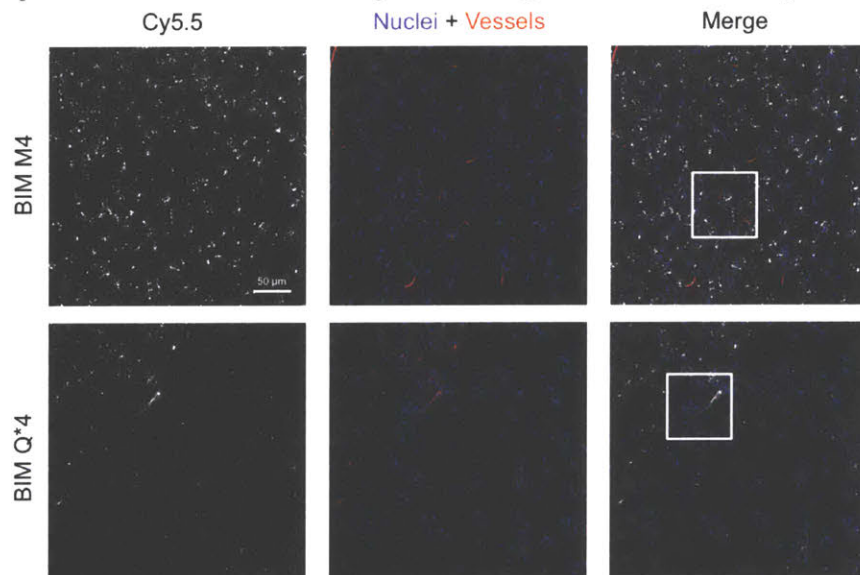


**Figure 5.23. Confocal images of brain slices after treatment with BIM analogues.** Images of brain slices after treatment with Cy5.5-BIM M4 (top) and with Cy5.5-BIM Q\*4 (bottom). The left panel is only the Cy5.5 channel, the middle panel is a merge showing Hoescht for identification of nuclei and tetramethylrhodamine-labeled dextran in the vessels, and the right panel is a merge of all three channels. The square box is the area that has been enlarged and displayed in Figure 5.11D.

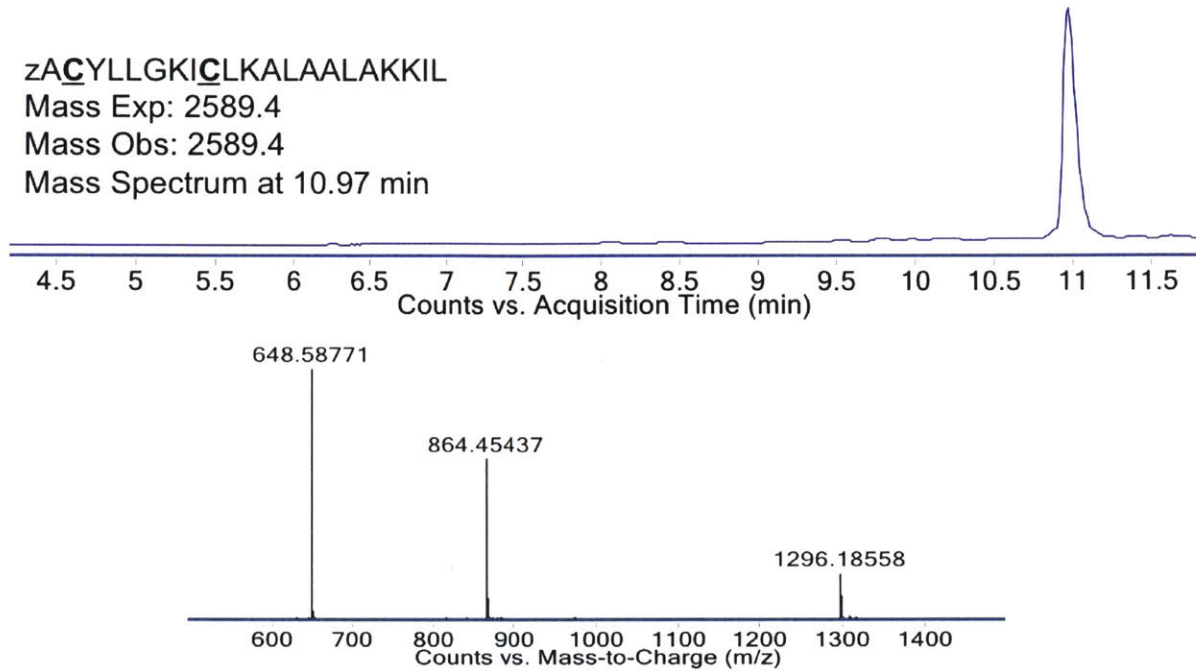
#### **5.4. Acknowledgments**

This work was supported by the National Institutes of Health (NIH; R01GM110535) and the Sontag Foundation Distinguished Scientist Award (to B.L.P.) C.M.F. is supported by the David H. Koch Graduate Fellowship Fund. J.M.W. is supported by the National Science Foundation Graduate Research Fellowship under Grant No. 1122374. C.-F.C. is supported by the Canadian Institute of Health Research Fellowship. The authors acknowledge the Swanson Biotechnology Center Flow Cytometry Facility at the Koch Institute for the use of their flow cytometers, IVIS instrumentation, and advice. The authors also acknowledge Yarah Ghotmi for assistance in brain cryosections, Roscoe Wasserburg for assistance with tissue culture, and Alex Mijalis for assistance in the synthesis of the hydrocarbon-stapled BIM BH3 peptide.

## 5.5. Appendix of LC-MS Characterization

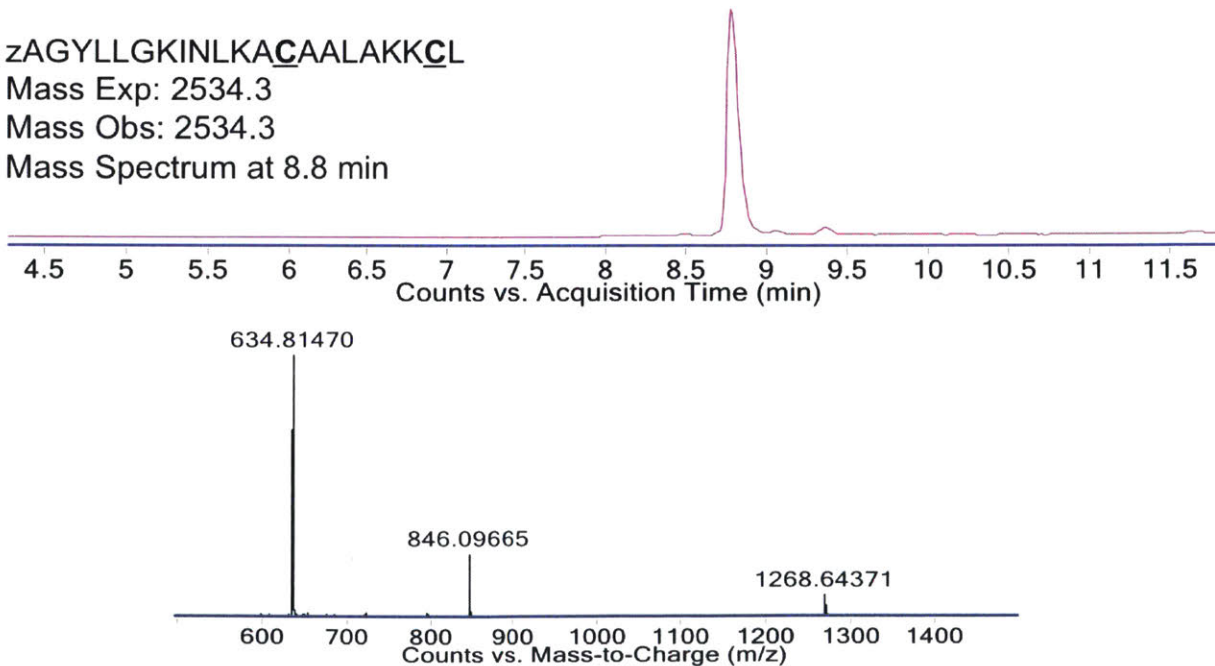
C = site of cyclization, *C* = site of alkylation, and z = 4-pentynoic acid

zACYLLGKICLKALAALAKKIL  
Mass Exp: 2589.4  
Mass Obs: 2589.4  
Mass Spectrum at 10.97 min



LC-MS characterization of purified TP10 M2. TIC and mass spectrum at peak maximum.

zAGYLLGKINLKCAALAKKCL  
Mass Exp: 2534.3  
Mass Obs: 2534.3  
Mass Spectrum at 8.8 min



LC-MS characterization of purified TP10 M13. TIC and mass spectrum at peak maximum.

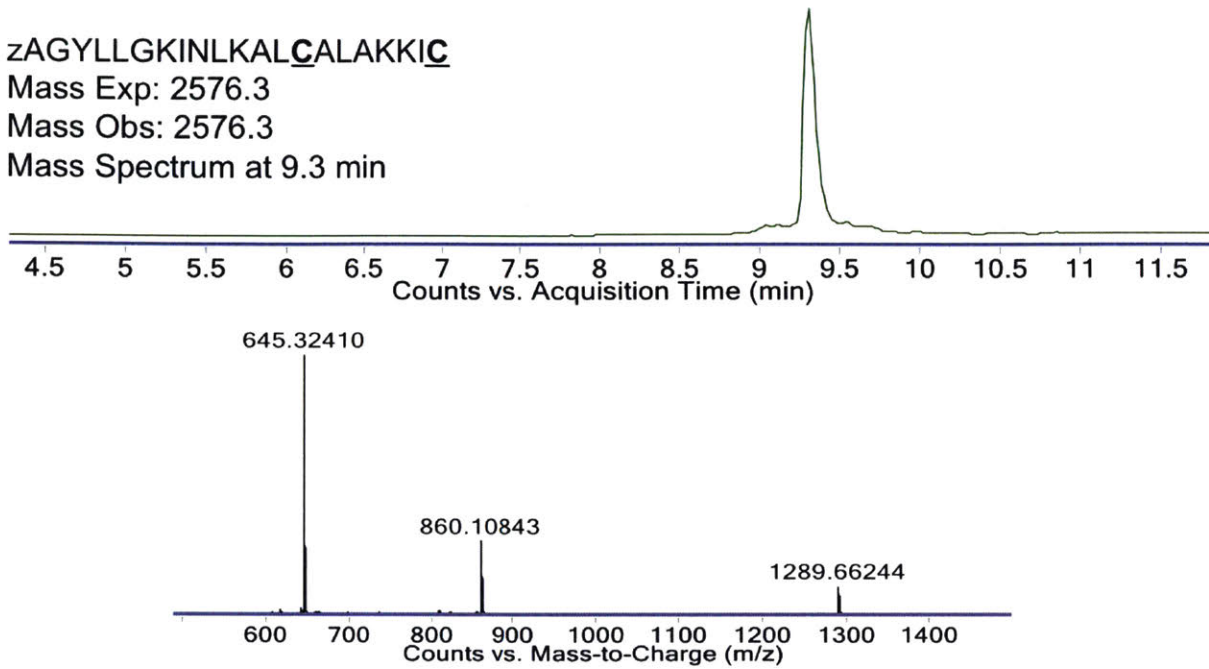


zAGYLLGKINLKALCALAKKIC

Mass Exp: 2576.3

Mass Obs: 2576.3

Mass Spectrum at 9.3 min



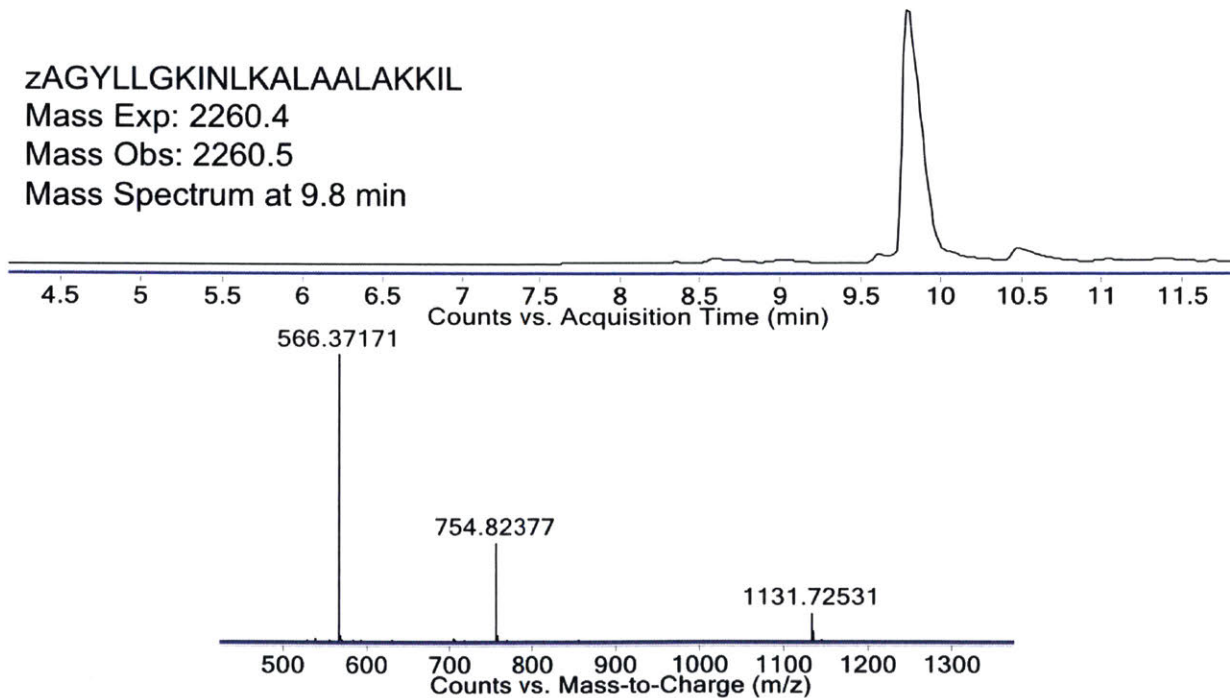
LC-MS characterization of purified TP10 M14. TIC and mass spectrum at peak maximum.

zAGYLLGKINLKALAALAKKIL

Mass Exp: 2260.4

Mass Obs: 2260.5

Mass Spectrum at 9.8 min



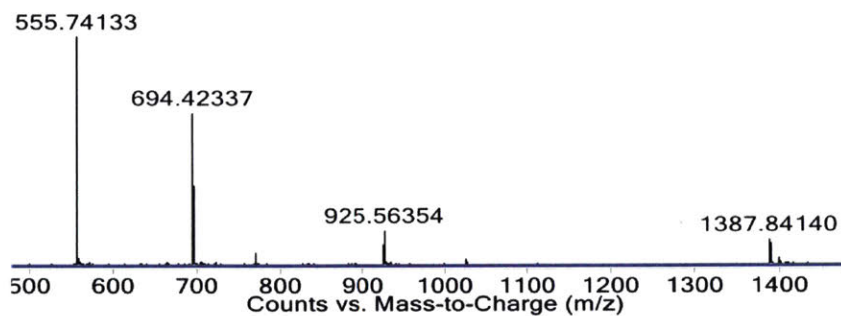
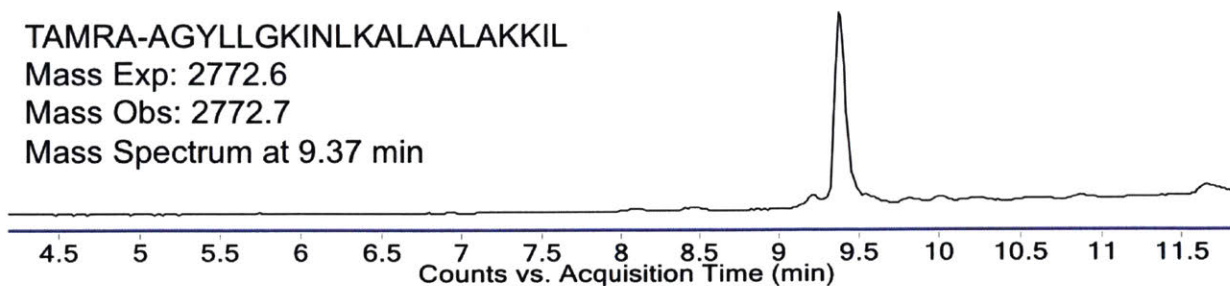
LC-MS characterization of purified TP10. TIC and mass spectrum at peak maximum.

TAMRA-AGYLLGKINLKALAALAKKIL

Mass Exp: 2772.6

Mass Obs: 2772.7

Mass Spectrum at 9.37 min



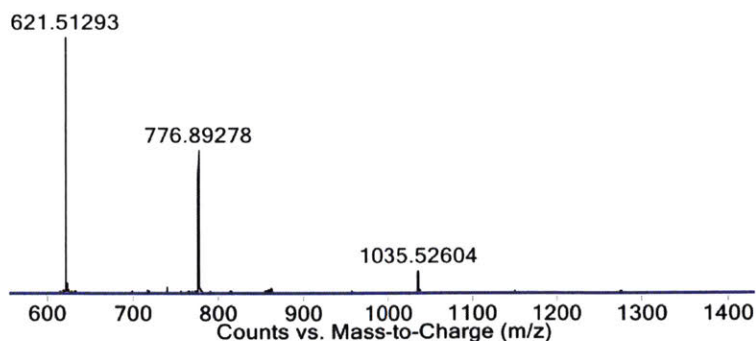
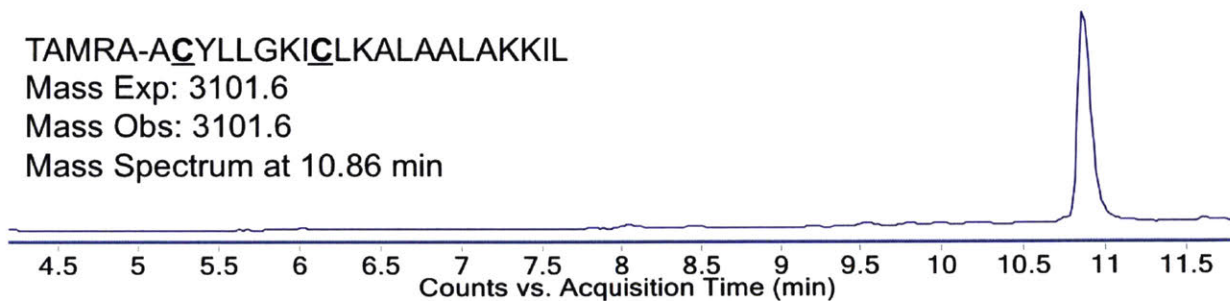
LC-MS characterization of purified TAMRA-TP10. TIC and mass spectrum at peak maximum.

TAMRA-AGYLLGKINLKALAALAKKIL

Mass Exp: 3101.6

Mass Obs: 3101.6

Mass Spectrum at 10.86 min



LC-MS characterization of purified TAMRA-TP10 M2. TIC and mass spectrum at peak maximum.

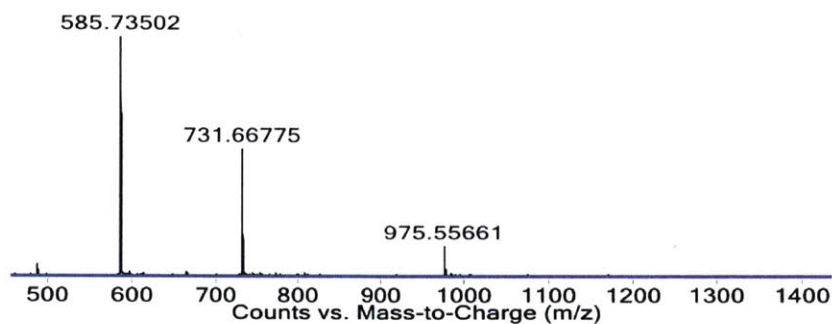
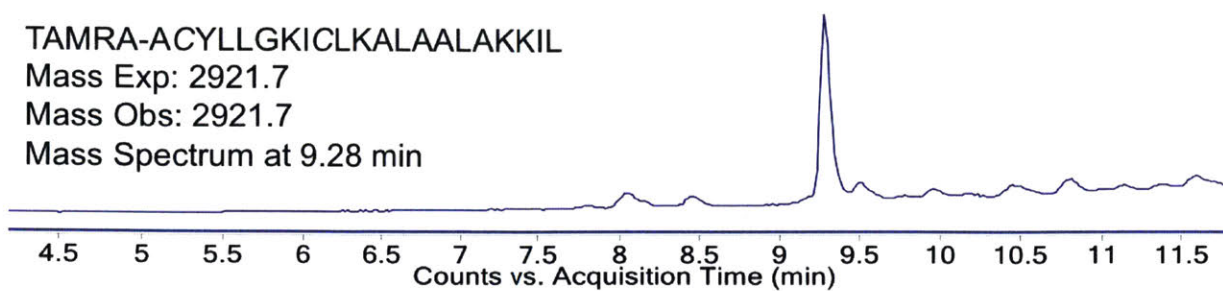


TAMRA-ACYLLGKIKLKALAALAKKIL

Mass Exp: 2921.7

Mass Obs: 2921.7

Mass Spectrum at 9.28 min



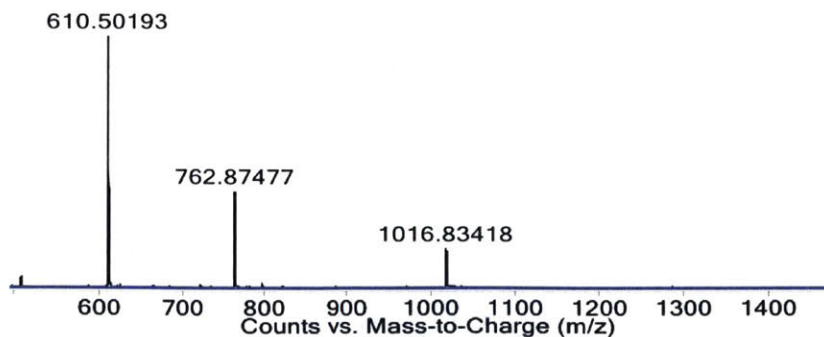
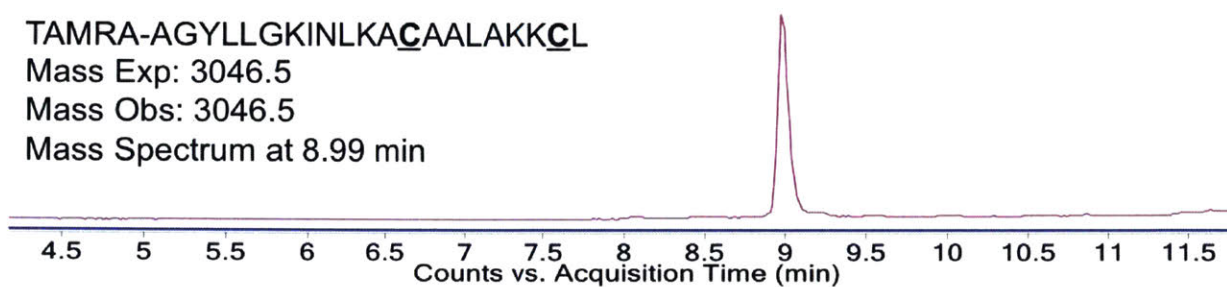
LC-MS characterization of purified TAMRA-TP10 Q\*2. TIC and mass spectrum at peak maximum.

TAMRA-AGYLLGKINLKACAALAKKCL

Mass Exp: 3046.5

Mass Obs: 3046.5

Mass Spectrum at 8.99 min



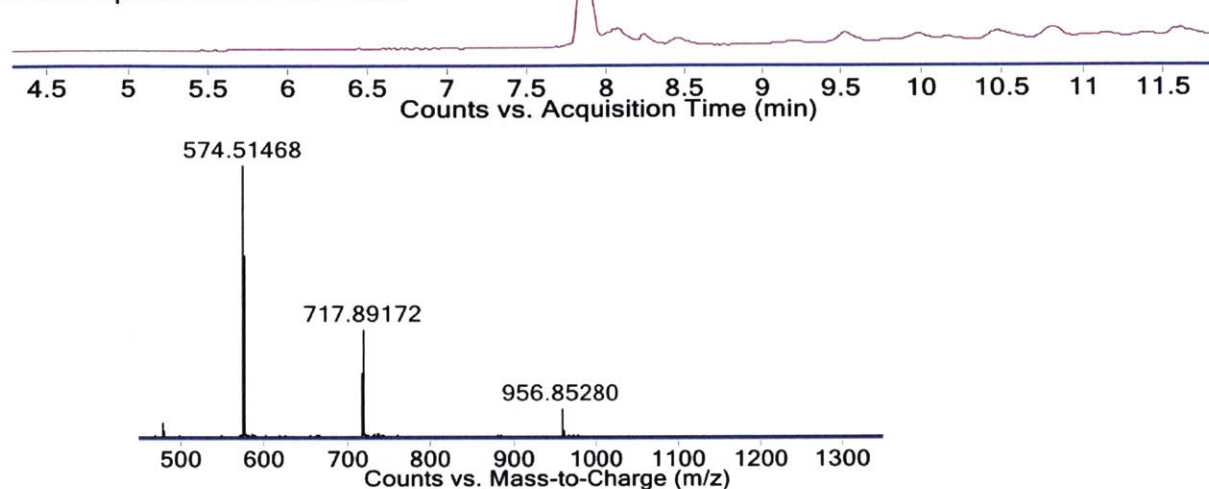
LC-MS characterization of purified TAMRA-TP10 M13. TIC and mass spectrum at peak maximum.

TAMRA-AGYLLGKINLKACAALAKKCL

Mass Exp: 2866.6

Mass Obs: 2866.6

Mass Spectrum at 7.84 min



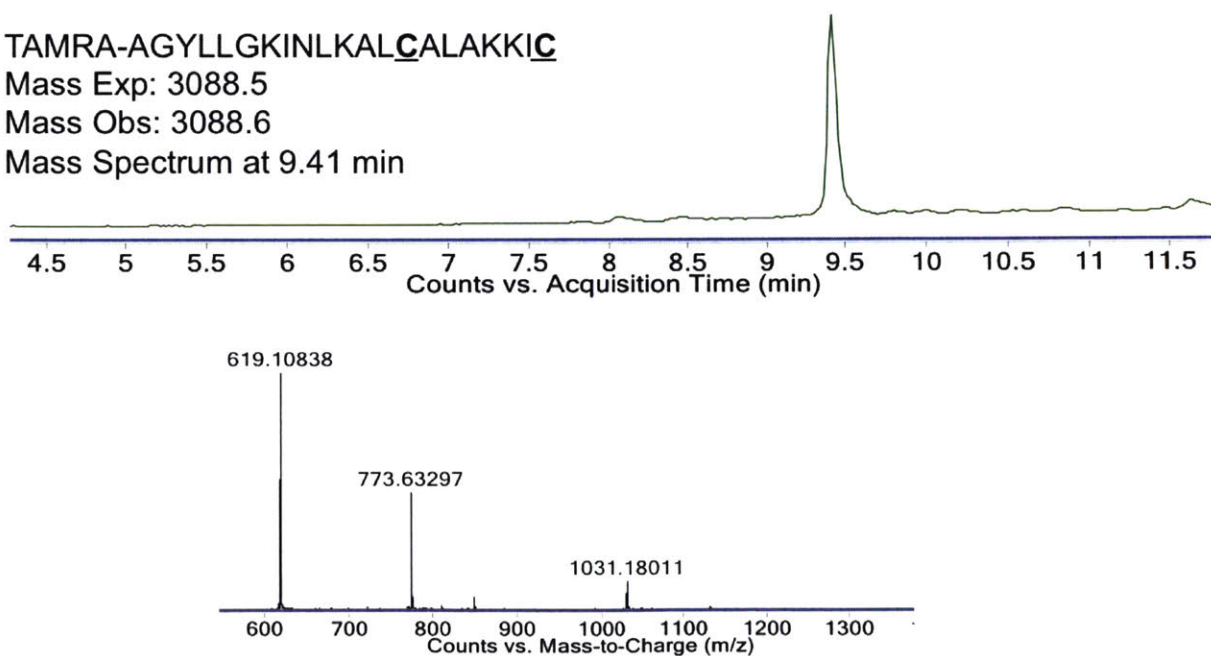
LC-MS characterization of purified TAMRA-TP10 Q\*13. TIC and mass spectrum at peak maximum.

TAMRA-AGYLLGKINLKALCALAKKIC

Mass Exp: 3088.5

Mass Obs: 3088.6

Mass Spectrum at 9.41 min



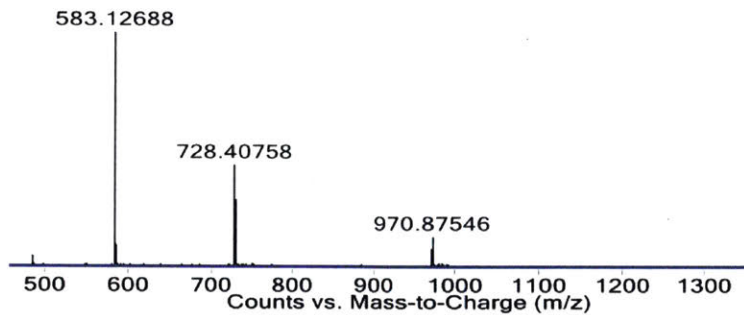
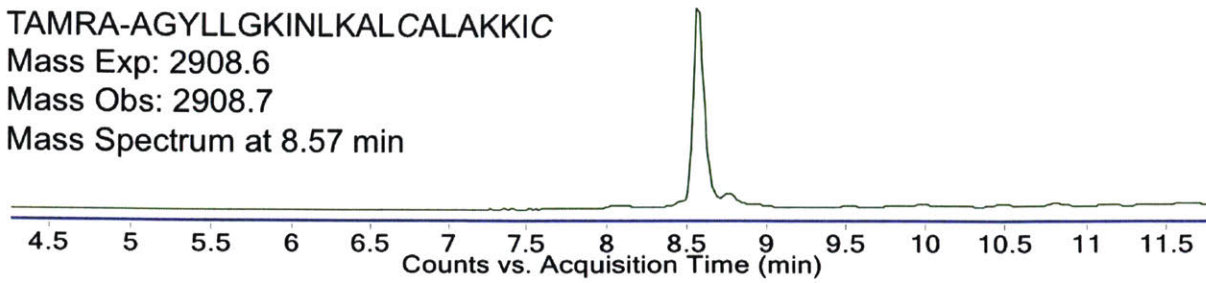
LC-MS characterization of purified TAMRA-TP10 M14. TIC and mass spectrum at peak maximum.

TAMRA-AGYLLGKINLKALCALAKKIC

Mass Exp: 2908.6

Mass Obs: 2908.7

Mass Spectrum at 8.57 min



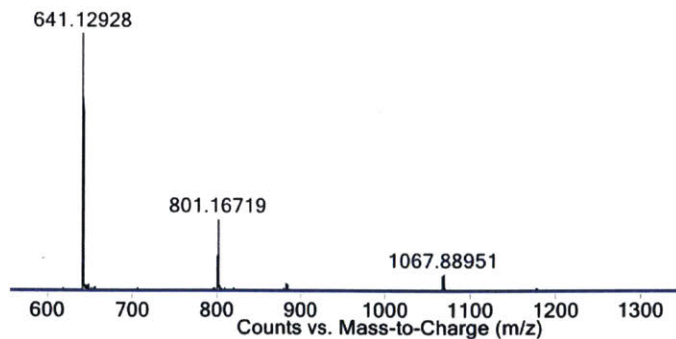
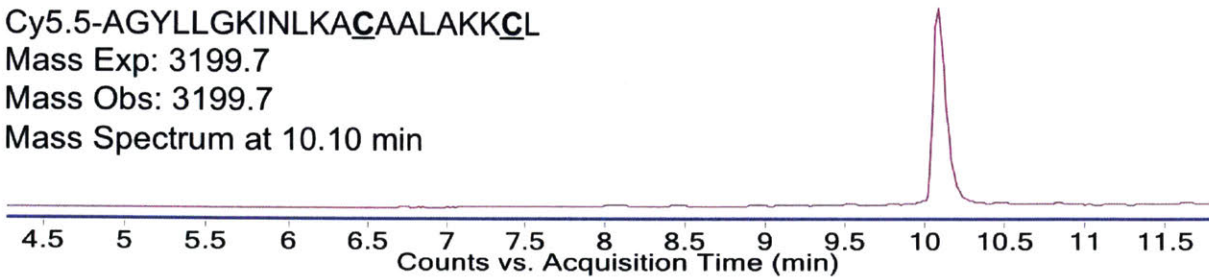
LC-MS characterization of purified TAMRA-TP10 Q\*14. TIC and mass spectrum at peak maximum.

Cy5.5-AGYLLGKINLKACAALAKKCL

Mass Exp: 3199.7

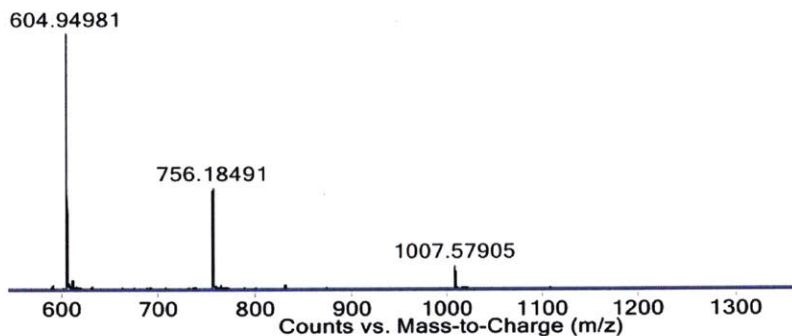
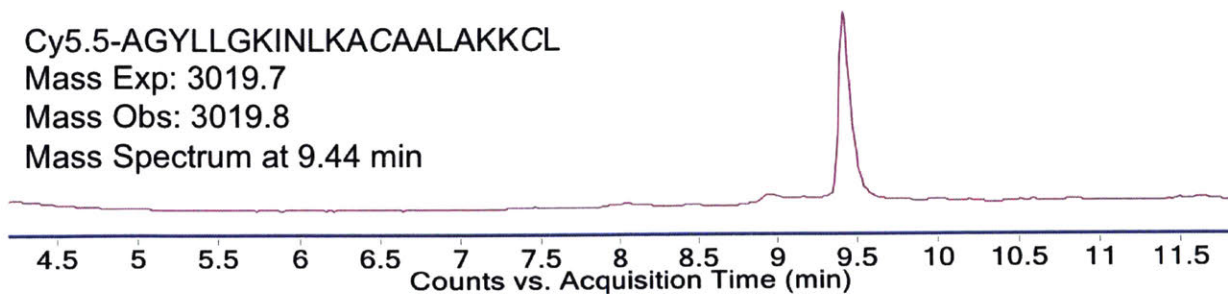
Mass Obs: 3199.7

Mass Spectrum at 10.10 min



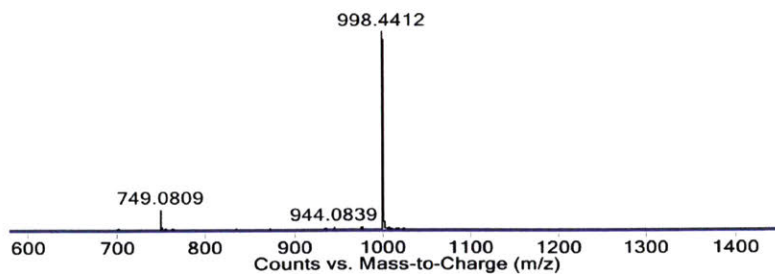
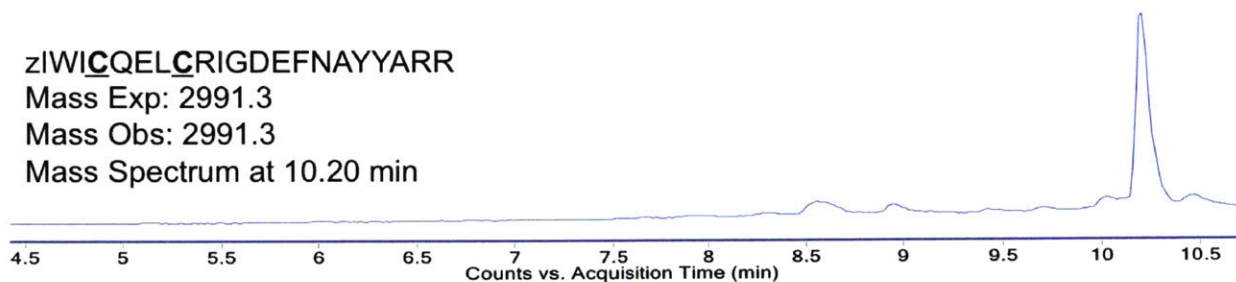
LC-MS characterization of purified Cy5.5-TP10 M13. TIC and mass spectrum at peak maximum.

Cy5.5-AGYLLGKINLKACAALAKKCL  
Mass Exp: 3019.7  
Mass Obs: 3019.8  
Mass Spectrum at 9.44 min

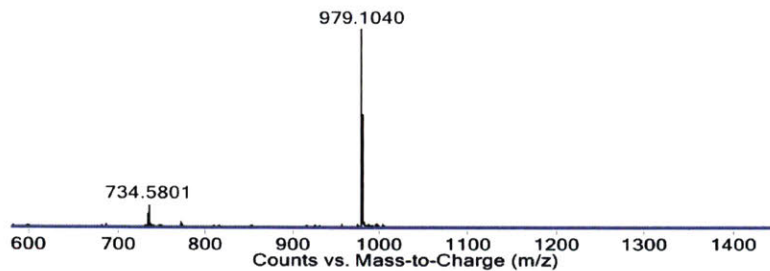
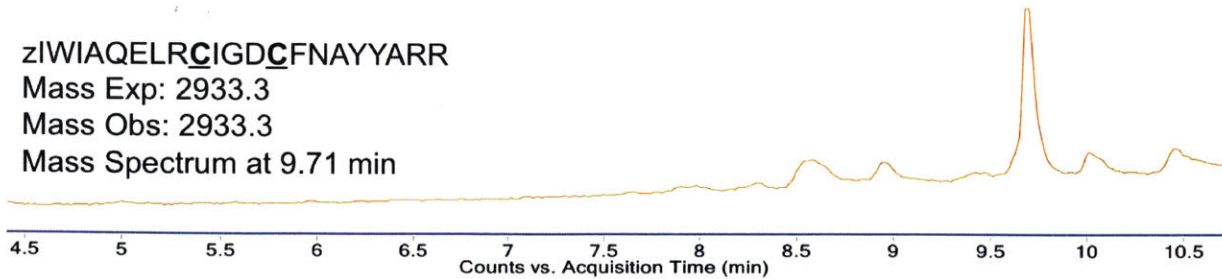


LC-MS characterization of purified Cy5.5-TP10 Q\*13. TIC and mass spectrum at peak maximum.

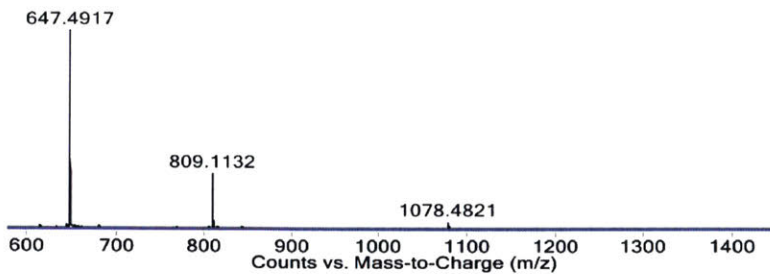
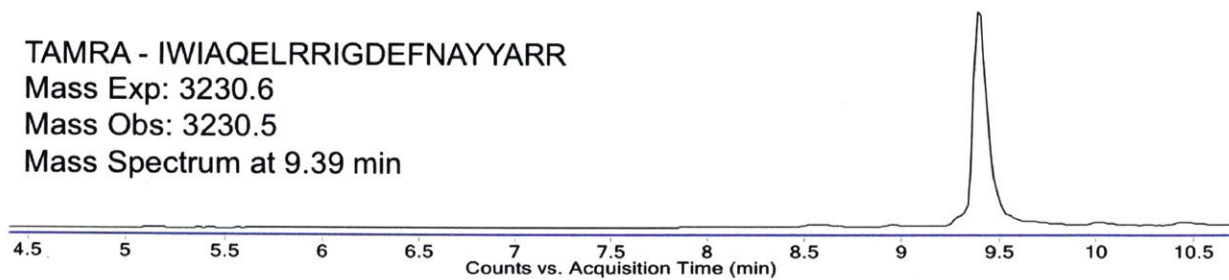
zIWICQELCRIGDEFNAYYARR  
Mass Exp: 2991.3  
Mass Obs: 2991.3  
Mass Spectrum at 10.20 min



LC-MS characterization of purified BIM BH3 M4. TIC and mass spectrum at peak maximum.



LC-MS characterization of purified BIM BH3 M9. TIC and mass spectrum at peak maximum.



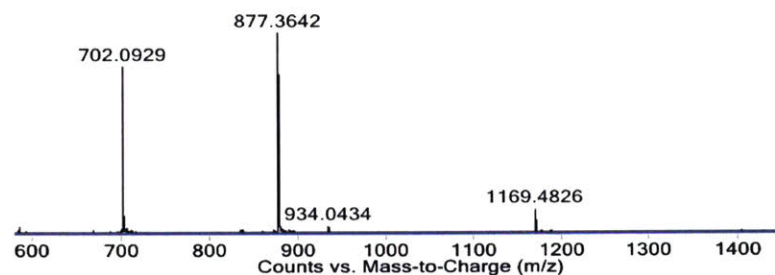
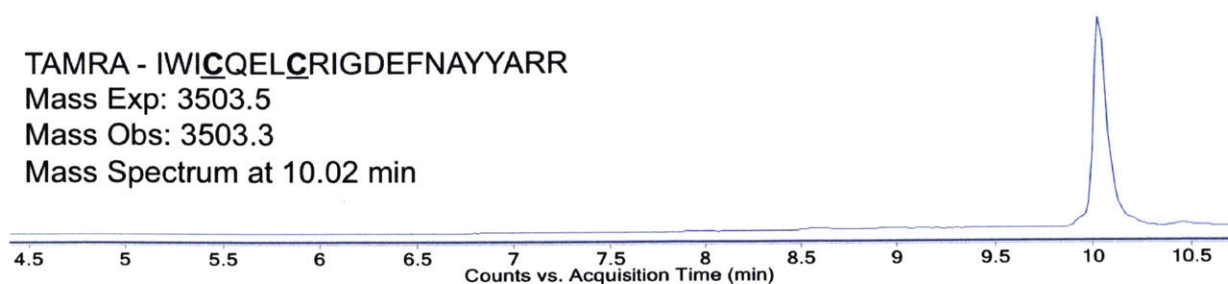
LC-MS characterization of purified BIM BH3. TIC and mass spectrum at peak maximum.

TAMRA - IWICQELCRIGDEFNAYYARR

Mass Exp: 3503.5

Mass Obs: 3503.3

Mass Spectrum at 10.02 min



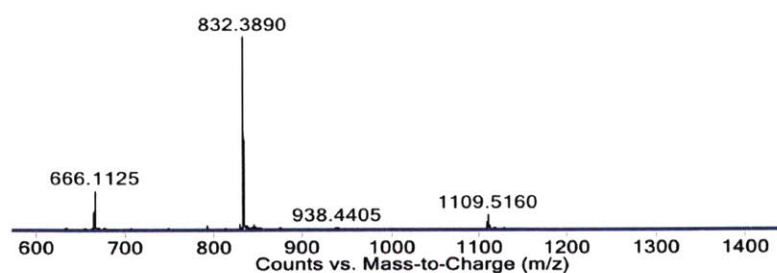
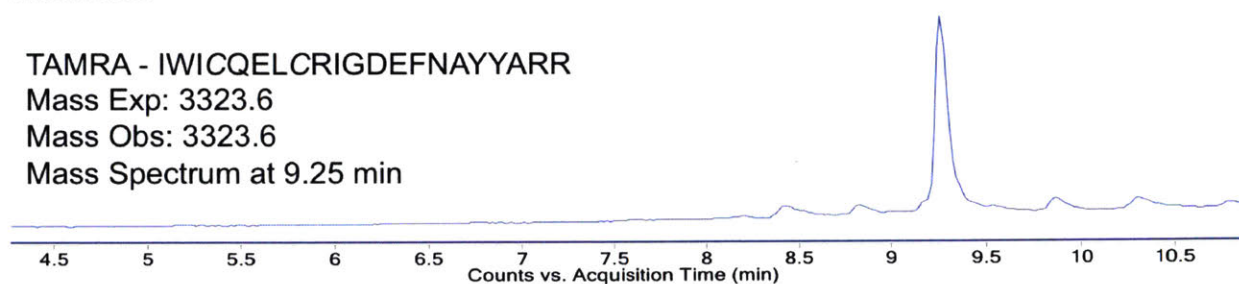
LC-MS characterization of purified TAMRA-BIM BH3 M4. TIC and mass spectrum at peak maximum.

TAMRA - IWICQELCRIGDEFNAYYARR

Mass Exp: 3323.6

Mass Obs: 3323.6

Mass Spectrum at 9.25 min



LC-MS characterization of purified TAMRA-BIM BH3 Q\*4. TIC and mass spectrum at peak maximum.

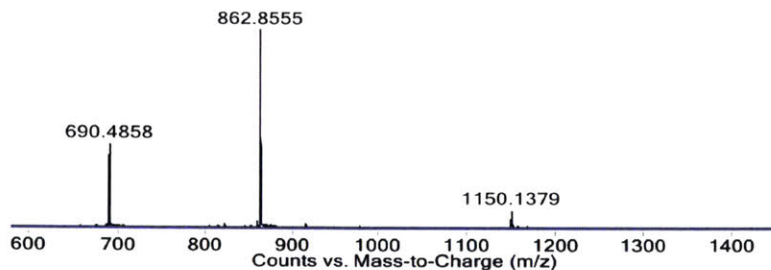
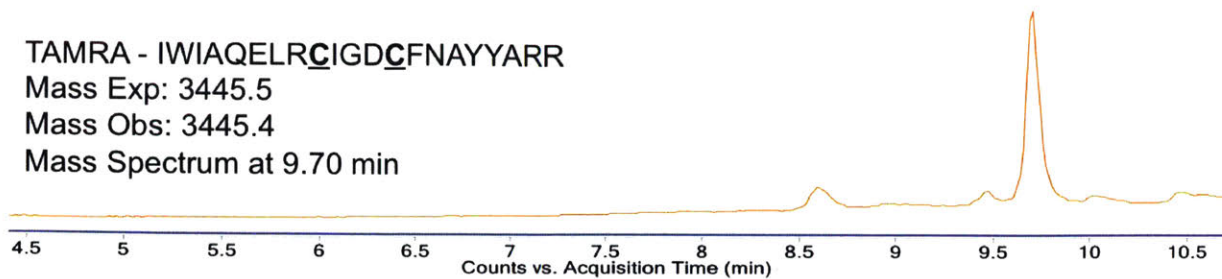


TAMRA - IWIAQELRCIGDCFNAYYARR

Mass Exp: 3445.5

Mass Obs: 3445.4

Mass Spectrum at 9.70 min



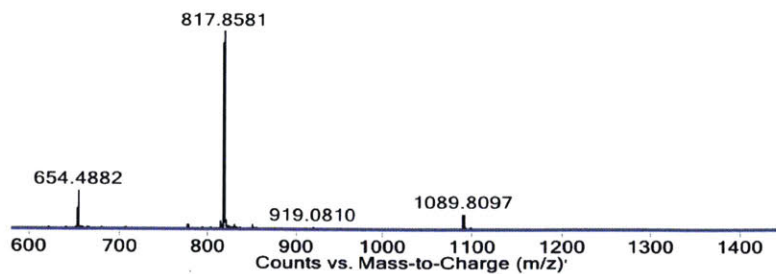
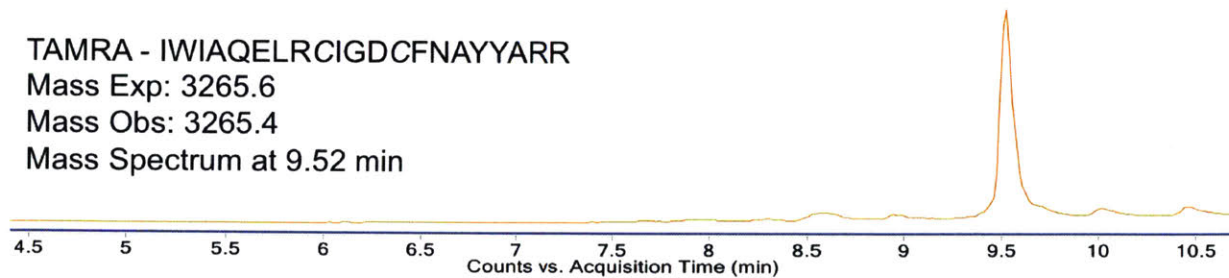
LC-MS characterization of purified TAMRA-BIM BH3 M9. TIC and mass spectrum at peak maximum.

TAMRA - IWIAQELRCIGDCFNAYYARR

Mass Exp: 3265.6

Mass Obs: 3265.4

Mass Spectrum at 9.52 min



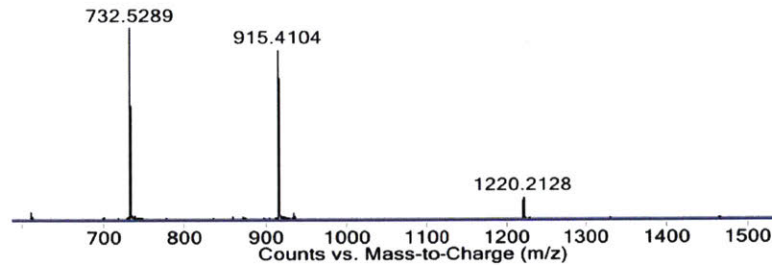
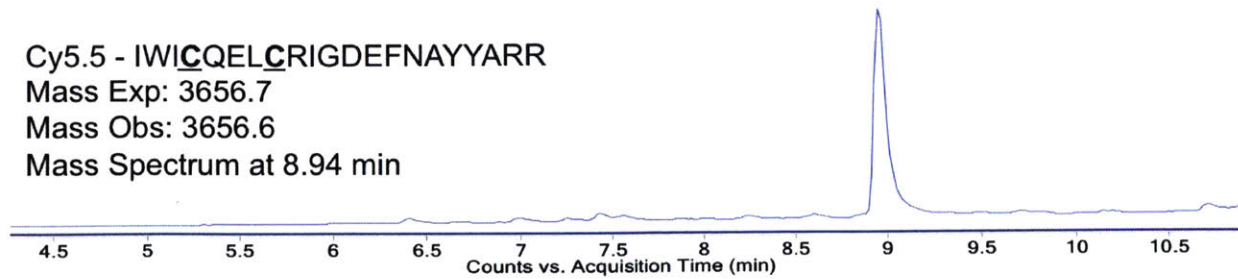
LC-MS characterization of purified TAMRA-BIM BH3 Q\*9. TIC and mass spectrum at peak maximum.

Cy5.5 - IWICQELCRIGDEFNAYYARR

Mass Exp: 3656.7

Mass Obs: 3656.6

Mass Spectrum at 8.94 min



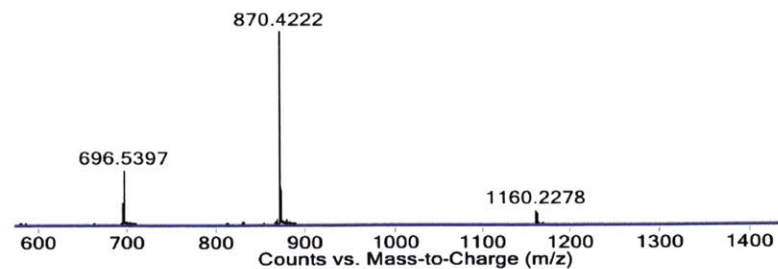
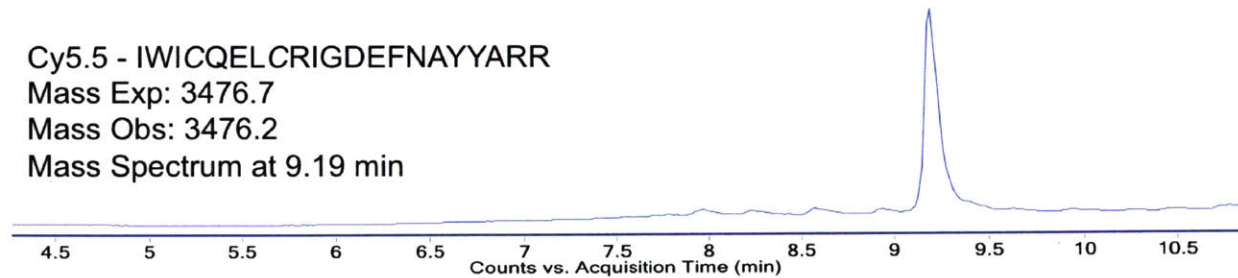
LC-MS characterization of purified Cy5.5-BIM BH3 M4. TIC and mass spectrum at peak maximum.

Cy5.5 - IWICQELCRIGDEFNAYYARR

Mass Exp: 3476.7

Mass Obs: 3476.2

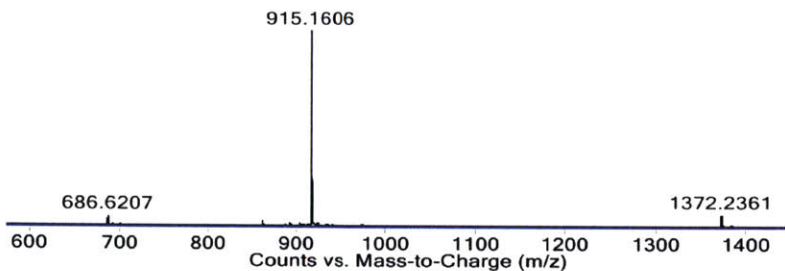
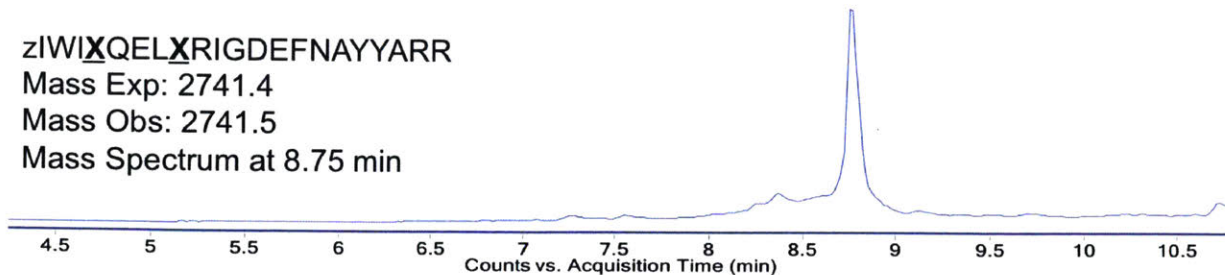
Mass Spectrum at 9.19 min



LC-MS characterization of purified Cy5.5-BIM BH3 Q\*4. TIC and mass spectrum at peak maximum.

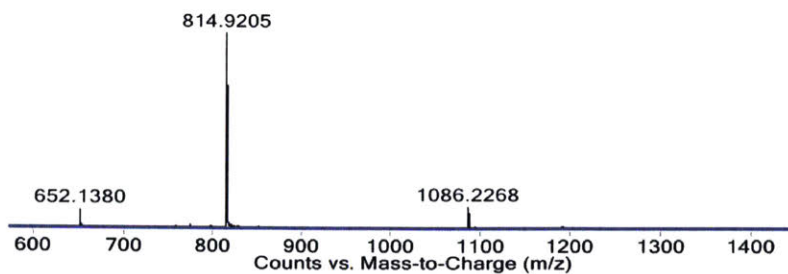
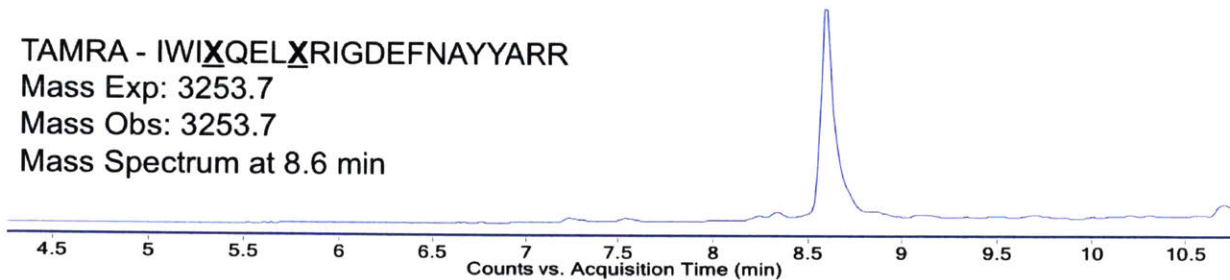


zIWIXQELXRIGDEFNAYYARR  
Mass Exp: 2741.4  
Mass Obs: 2741.5  
Mass Spectrum at 8.75 min



LC-MS characterization of purified BIM BH3 HC4. TIC and mass spectrum at peak maximum.

TAMRA - IWIXQELXRIGDEFNAYYARR  
Mass Exp: 3253.7  
Mass Obs: 3253.7  
Mass Spectrum at 8.6 min



LC-MS characterization of purified TAMRA-BIM BH3 HC4. TIC and mass spectrum at peak maximum.

## 5.6. References

- (1) Deeken, J. F.; Löscher, W. The Blood-Brain Barrier and Cancer: Transporters, Treatment, and Trojan Horses. *Clin. Cancer Res. Off. J. Am. Assoc. Cancer Res.* **2007**, *13* (6), 1663–1674.
- (2) Calvo, P.; Gouritin, B.; Villarroya, H.; Eclancher, F.; Giannavola, C.; Klein, C.; Andreux, J. P.; Couvreur, P. Quantification and Localization of PEGylated Polycyanoacrylate Nanoparticles in Brain and Spinal Cord during Experimental Allergic Encephalomyelitis in the Rat. *Eur. J. Neurosci.* **2002**, *15* (8), 1317–1326.
- (3) Chen, Y.; Liu, L. Modern Methods for Delivery of Drugs across the Blood–brain Barrier. *Adv. Drug Deliv. Rev.* **2012**, *64* (7), 640–665.
- (4) Nau, R.; Sörgel, F.; Eiffert, H. Penetration of Drugs through the Blood-Cerebrospinal Fluid/Blood-Brain Barrier for Treatment of Central Nervous System Infections. *Clin. Microbiol. Rev.* **2010**, *23* (4), 858–883.
- (5) Löscher, W.; Potschka, H. Drug Resistance in Brain Diseases and the Role of Drug Efflux Transporters. *Nat. Rev. Neurosci.* **2005**, *6* (8), 591–602.
- (6) Abbott, N. J.; Revest, P. A. Control of Brain Endothelial Permeability. *Cerebrovasc. Brain Metab. Rev.* **1991**, *3* (1), 39–72.
- (7) Sanovich, E.; Bartus, R. T.; Friden, P. M.; Dean, R. L.; Le, H. Q.; Brightman, M. W. Pathway across Blood-Brain Barrier Opened by the Bradykinin Agonist, RMP-7. *Brain Res.* **1995**, *705* (1–2), 125–135.
- (8) Sheikov, N.; McDannold, N.; Vykhodtseva, N.; Jolesz, F.; Hynynen, K. Cellular Mechanisms of the Blood-Brain Barrier Opening Induced by Ultrasound in Presence of Microbubbles. *Ultrasound Med. Biol.* **2004**, *30* (7), 979–989.
- (9) Oller-Salvia, B.; Sánchez-Navarro, M.; Giralt, E.; Teixidó, M. Blood–brain Barrier Shuttle Peptides: An Emerging Paradigm for Brain Delivery. *Chem. Soc. Rev.* **2016**, *45* (17), 4690–4707.
- (10) Kumagai, A. K.; Eisenberg, J. B.; Pardridge, W. M. Absorptive-Mediated Endocytosis of Cationized Albumin and a Beta-Endorphin-Cationized Albumin Chimeric Peptide by Isolated Brain Capillaries. Model System of Blood-Brain Barrier Transport. *J. Biol. Chem.* **1987**, *262* (31), 15214–15219.
- (11) Friden, P. M.; Walus, L. R.; Musso, G. F.; Taylor, M. A.; Malfroy, B.; Starzyk, R. M. Anti-Transferrin Receptor Antibody and Antibody-Drug Conjugates Cross the Blood-Brain Barrier. *Proc. Natl. Acad. Sci. U. S. A.* **1991**, *88* (11), 4771–4775.
- (12) Schwarze, S. R.; Ho, A.; Vocero-Akbani, A.; Dowdy, S. F. In Vivo Protein Transduction: Delivery of a Biologically Active Protein into the Mouse. *Science* **1999**, *285* (5433), 1569–1572.
- (13) Kumar, P.; Wu, H.; McBride, J. L.; Jung, K.-E.; Hee Kim, M.; Davidson, B. L.; Kyung Lee, S.; Shankar, P.; Manjunath, N. Transvascular Delivery of Small Interfering RNA to the Central Nervous System. *Nature* **2007**, *448* (7149), 39–43.
- (14) Oller-Salvia, B.; Sánchez-Navarro, M.; Ciudad, S.; Guiu, M.; Arranz-Gibert, P.; Garcia, C.; Gomis, R. R.; Cecchelli, R.; García, J.; Giralt, E.; et al. MiniAp-4: A Venom-Inspired Peptidomimetic for Brain Delivery. *Angew. Chem. Int. Ed Engl.* **2016**, *55* (2), 572–575.
- (15) Brown, S. P.; Smith, A. B. Peptide/Protein Stapling and Unstapling: Introduction of s-Tetrazine, Photochemical Release, and Regeneration of the Peptide/Protein. *J. Am. Chem. Soc.* **2015**, *137* (12), 4034–4037.

- (16) Kalhor-Monfared, S.; Jafari, M. R.; Patterson, J. T.; Kitov, P. I.; Dwyer, J. J.; Nuss, J. M.; Derda, R. Rapid Biocompatible Macrocyclization of Peptides with Decafluoro-Diphenylsulfone. *Chem. Sci.* **2016**, *7* (6), 3785–3790.
- (17) Schafmeister, C. E.; Po, J.; Verdine, G. L. An All-Hydrocarbon Cross-Linking System for Enhancing the Helicity and Metabolic Stability of Peptides. *J. Am. Chem. Soc.* **2000**, *122* (24), 5891–5892.
- (18) Blackwell, H. E.; Grubbs, R. H. Highly Efficient Synthesis of Covalently Cross-Linked Peptide Helices by Ring-Closing Metathesis. *Angew. Chem. Int. Ed.* **1998**, *37* (23), 3281–3284.
- (19) Botti, P.; Pallin, T. D.; Tam, J. P. Cyclic Peptides from Linear Unprotected Peptide Precursors through Thiazolidine Formation. *J. Am. Chem. Soc.* **1996**, *118* (42), 10018–10024.
- (20) Lau, Y. H.; de Andrade, P.; McKenzie, G. J.; Venkitaraman, A. R.; Spring, D. R. Linear Aliphatic Dialkynes as Alternative Linkers for Double-Click Stapling of P53-Derived Peptides. *ChemBioChem* **2014**, *15* (18), 2680–2683.
- (21) White, C. J.; Yudin, A. K. Contemporary Strategies for Peptide Macrocyclization. *Nat. Chem.* **2011**, *3* (7), 509–524.
- (22) Walensky, L. D.; Kung, A. L.; Escher, I.; Malia, T. J.; Barbuto, S.; Wright, R. D.; Wagner, G.; Verdine, G. L.; Korsmeyer, S. J. Activation of Apoptosis in Vivo by a Hydrocarbon-Stapled BH3 Helix. *Science* **2004**, *305* (5689), 1466–1470.
- (23) Chang, Y. S.; Graves, B.; Guerlavais, V.; Tovar, C.; Packman, K.; To, K.-H.; Olson, K. A.; Kesavan, K.; Gangurde, P.; Mukherjee, A.; et al. Stapled  $\alpha$ -helical Peptide Drug Development: A Potent Dual Inhibitor of MDM2 and MDMX for P53-Dependent Cancer Therapy. *Proc. Natl. Acad. Sci.* **2013**, *110* (36), E3445–E3454.
- (24) Lautrette, G.; Touti, F.; Lee, H. G.; Dai, P.; Pentelute, B. L. Nitrogen Arylation for Macrocyclization of Unprotected Peptides. *J. Am. Chem. Soc.* **2016**, *138* (27), 8340–8343.
- (25) Grossmann, T. N.; Yeh, J. T.-H.; Bowman, B. R.; Chu, Q.; Moellering, R. E.; Verdine, G. L. Inhibition of Oncogenic Wnt Signaling through Direct Targeting of  $\beta$ -Catenin. *Proc. Natl. Acad. Sci.* **2012**, *109* (44), 17942–17947.
- (26) Spokoyny, A. M.; Zou, Y.; Ling, J. J.; Yu, H.; Lin, Y.-S.; Pentelute, B. L. A Perfluoroaryl-Cysteine SNAr Chemistry Approach to Unprotected Peptide Stapling. *J. Am. Chem. Soc.* **2013**, *135* (16), 5946–5949.
- (27) Zou, Y.; Spokoyny, A. M.; Zhang, C.; Simon, M. D.; Yu, H.; Lin, Y.-S.; Pentelute, B. L. Convergent Diversity-Oriented Side-Chain Macrocyclization Scan for Unprotected Polypeptides. *Org. Biomol. Chem.* **2013**, *12* (4), 566–573.
- (28) Islam, M. Z.; Ariyama, H.; Alam, J. M.; Yamazaki, M. Entry of Cell-Penetrating Peptide Transportan 10 into a Single Vesicle by Translocating Across Lipid Membrane and Its Induced Pores. *Biochemistry (Mosc.)* **2014**, *53* (2), 386–396.
- (29) Fanghänel, S.; Wadhvani, P.; Strandberg, E.; Verdurmen, W. P. R.; Bürck, J.; Ehni, S.; Mykhailiuk, P. K.; Afonin, S.; Gerthsen, D.; Komarov, I. V.; et al. Structure Analysis and Conformational Transitions of the Cell Penetrating Peptide Transportan 10 in the Membrane-Bound State. *PLOS ONE* **2014**, *9* (6), e99653.
- (30) Weksler, B. B.; Subileau, E. A.; Perrière, N.; Charneau, P.; Holloway, K.; Leveque, M.; Tricoire-Leignel, H.; Nicotra, A.; Bourdoulous, S.; Turowski, P.; et al. Blood-Brain Barrier-Specific Properties of a Human Adult Brain Endothelial Cell Line. *FASEB J.* **2005**.

- (31) Vu, K.; Weksler, B.; Romero, I.; Couraud, P.-O.; Gelli, A. Immortalized Human Brain Endothelial Cell Line HCMEC/D3 as a Model of the Blood-Brain Barrier Facilitates In Vitro Studies of Central Nervous System Infection by *Cryptococcus Neoformans*. *Eukaryot. Cell* **2009**, *8* (11), 1803–1807.
- (32) Urich, E.; Patsch, C.; Aigner, S.; Graf, M.; Iacone, R.; Freskgård, P.-O. Multicellular Self-Assembled Spheroidal Model of the Blood Brain Barrier. *Sci. Rep.* **2013**, *3*.
- (33) Abbott, N. J.; Rönnbäck, L.; Hansson, E. Astrocyte–endothelial Interactions at the Blood–brain Barrier. *Nat. Rev. Neurosci.* **2006**, *7* (1), 41–53.
- (34) Cho, C.-F.; Wolfe, J. M.; Fadzen, C. M.; Calligaris, D.; Hornburg, K.; Chiocca, E. A.; Agar, N. Y. R.; Pentelute, B. L.; Lawler, S. E. Blood-Brain-Barrier Spheroids as an in Vitro Screening Platform for Brain-Penetrating Agents. *Nat. Commun.* **2017**, *8*, 15623.
- (35) Bird, G. H.; Mazzola, E.; Opoku-Nsiah, K.; Lammert, M. A.; Godes, M.; Neuberg, D. S.; Walensky, L. D. Biophysical Determinants for Cellular Uptake of Hydrocarbon-Stapled Peptide Helices. *Nat. Chem. Biol.* **2016**, *12* (10), 845–852.
- (36) Mijalis, A. J.; Thomas III, D. A.; Simon, M. D.; Adamo, A.; Beaumont, R.; Jensen, K. F.; Pentelute, B. L. A Fully Automated Flow-Based Approach for Accelerated Peptide Synthesis. *Nat. Chem. Biol.* **2017**, *13* (5), 464–466.
- (37) Kim, Y.-W.; Grossmann, T. N.; Verdine, G. L. Synthesis of All-Hydrocarbon Stapled  $\alpha$ -Helical Peptides by Ring-Closing Olefin Metathesis. *Nat. Protoc.* **2011**, *6* (6), 761–771.

## **Chapter 6: A Pt(IV) Prodrug – Perfluoroaryl Macrocyclic Peptide Conjugate with Improved Stability and Brain Distribution**

The work presented in this chapter has been submitted for publication:

Fadzen, C.M.,\* Zhou, W.,\* Wolfe, J.M., Cho, C-F., Chiocca, E.A., Lawler, S.E., Yilmaz, O.H., Lippard, S.J., & Pentelute, B.L. “A Pt(IV) Prodrug – Perfluoroaryl Macrocyclic Peptide Conjugate with Improved Stability and Brain Distribution”

\*: denotes authors contributed equally

## 6.1. Introduction

Glioblastoma (GBM) is the most common primary malignant brain tumor. Even with the current standard of care, which involves maximal safe surgical resection followed by radiation concurrent with temozolomide, the median survival from time of diagnosis is fifteen months.<sup>1</sup> Radical resection of the primary mass is not curative because of infiltrating tumor cells present throughout the whole brain. These infiltrating cells enable recurrence of the disease.<sup>2</sup> Although many experimental drugs have been tested in clinical trials for GBM over the past few decades, none have changed disease progression in any meaningful way. One limitation in the development of new drugs is poor drug delivery across the blood-brain tumor barrier (BBTB).<sup>3-5</sup>

Platinum-based chemotherapeutics such as cisplatin, carboplatin, and oxaliplatin are widely used for the treatment of malignancies.<sup>6</sup> Cisplatin for example, is a platinum(II) with two ammonia ligands and two chloride ligands. The mechanism of action for cisplatin involves exchange of a chloride ligand for water, followed by preferential platination of the nucleophilic N7 atom of a purine nucleobase. Another ligand substitution can occur with a nearby guanine base forming a DNA cross-link.<sup>6,7</sup> The cells are arrested at the G2/M transition of the cell cycle in an attempt to repair the DNA lesion. If DNA repair is unsuccessful, the cells initiate apoptosis. The platinum-based chemotherapeutics also react with off-target nucleophiles, which can lead to significant toxic side effects such as nephrotoxicity.<sup>8</sup>

One solution to mitigate off-target toxicity and improve the therapeutic index of platinum(II) chemotherapeutics is administering them as Pt(IV) prodrugs. The Pt(II) center of cisplatin is oxidized to Pt(IV) with the addition of two axial ligands. Upon internalization into cells, the Pt(IV) prodrug is reduced and enables the *in situ* generation of the native Pt(II) species inside a cancer cell. Unfortunately, premature reduction in the bloodstream can often limit the clinical utility of Pt(IV) prodrugs. Work to increase serum stability has focused on using the additional ligands to improve affinity for human serum albumin.<sup>9</sup>

Bioactive functional groups can be appended to the Pt(IV) center through the axial ligands.<sup>10-14</sup> For example, the Pt(IV) prodrug can be functionalized symmetrically with ligands containing carboxylates. These can be used to attach peptides to the Pt(IV) prodrugs that improve cellular uptake or target the drug to a particular cell type.<sup>11,12</sup> In fact, the Pt(IV) ligands could potentially be leveraged to attach a peptide that improves uptake into GBM.

For recurrent GBM, carboplatin has been a part of several clinical trials either as a single-agent or in conjunction with other chemotherapies with limited modulation of disease prognosis.<sup>15-17</sup> We posit that the BBTB may be one reason for the limited efficacy observed with platinum(II) therapeutics in GBM. To begin to address this challenge, we propose the preparation of conjugates between Pt(IV) prodrugs and perfluoroaryl macrocyclic peptides. We have recently shown that perfluoroaryl macrocyclic peptides have increased uptake into brain endothelial cells, have increased stability in mouse serum, and can improve the delivery of a small molecule organic dye across the blood-brain barrier.<sup>18</sup> These studies suggest that macrocyclic peptides could improve the delivery of Pt(IV) prodrugs to the brain.

Here we show the synthesis of a Pt(IV) prodrug – perfluoroaryl macrocyclic peptide conjugate (PtIV-M13) with efficacy against patient-derived glioma cells (GCs), improved serum stability, and improved brain uptake *in vivo*. First, we describe the synthesis of PtIV-M13 and demonstrate that the Pt(IV) prodrug is compatible with perfluoroaryl-cysteine S<sub>N</sub>Ar chemistry. Next, we perform *in vitro* experiments illustrating the efficacy of the conjugate against two glioma lines. Finally, we assess the pharmacokinetics and biodistribution of the conjugate after tail vein injection in mice. The amount of platinum in the brain after treatment with PtIV-M13 is 15-fold greater than cisplatin at five hours. This work highlights the potential of Pt(IV)-macrocyclic peptide conjugates represent a unique and promising approach for GBM therapy.

## 6.2. Results and Discussion

Pt(IV) prodrug synthesis began with the oxidation of cisplatin (**1**) to **2** with hydrogen peroxide in water (Scheme 1).<sup>9</sup> Reaction with succinic anhydride in dimethylformamide allowed the generation of asymmetric Pt complex **3**, as well as the symmetric disuccinate. From the reaction mixture, symmetric disuccinate is removed by acetone as the disuccinate is soluble in acetone and the asymmetric monosuccinate is not. Finally, complex **3** was reacted with *n*-butyl isocyanate to afford the final asymmetric Pt(IV) prodrug **4**, which has a single carboxylate for subsequent functionalization. The single carboxylate can be used for attachment to a peptide on resin. Pt(IV) prodrug **4** was characterized by <sup>1</sup>H-NMR spectroscopy, electrospray ionization mass spectrometry, and elemental analysis.

For conjugation, we chose the peptide TP10 M13 since it exhibited the highest uptake into the brain in previous work.<sup>18</sup> TP10 containing two cysteine residues for cyclization was prepared by automated fast-flow peptide synthesis.<sup>19</sup> Additionally, a linear control sequence (TP10 L13) was synthesized in which serine residues were substituted for cysteine (Figure 1A). Prodrug **4** was coupled to the N-terminus of each resin-bound peptide using standard active ester chemistry. The prodrug-peptide conjugates were cleaved from the resin with trifluoroacetic acid and purified by reversed-phase high-performance liquid chromatography (RP-HPLC). Next, the cysteine residues of the prodrug-peptide conjugate were cyclized using decafluorobiphenyl. The product (PtIV-M13) was characterized by liquid chromatography-mass spectrometry (LC-MS) (Figure 1C). No reduction of the prodrug was observed during the perfluoroaryl cyclization reaction, despite the presence of two unprotected thiols.

The cytotoxicity of the PtIV-M13 conjugate was evaluated against patient-derived glioma cells (GCs).<sup>20,21</sup> To evaluate the *in vitro* efficacy of the conjugate, G9 neurospheres were treated with PtIV-M13, prodrug **4**, and cisplatin for 80 hours. After treatment, the potency of the compounds was assessed by the CellTiter-Glo luminescent cell viability assay (Figure 2). The assay involves lysis of the cells and quantitation of the amount of ATP present, which is directly proportional to the number of living cells in culture. The IC<sub>50</sub> of PtIV-M13 conjugate against the G9 cells was determined to be  $4.51 \pm 0.22 \mu\text{M}$ , which is similar to cisplatin at  $4.34 \pm 0.66 \mu\text{M}$ . However, prodrug **4** was not potent, perhaps due to an inability to enter cells (Figure 2A). As a result, in the follow-up *in vitro* experiment with another GC line, PtIV-L13 was used as a control instead as this should have similar properties to the PtIV-M13, only without the perfluoroaryl. The



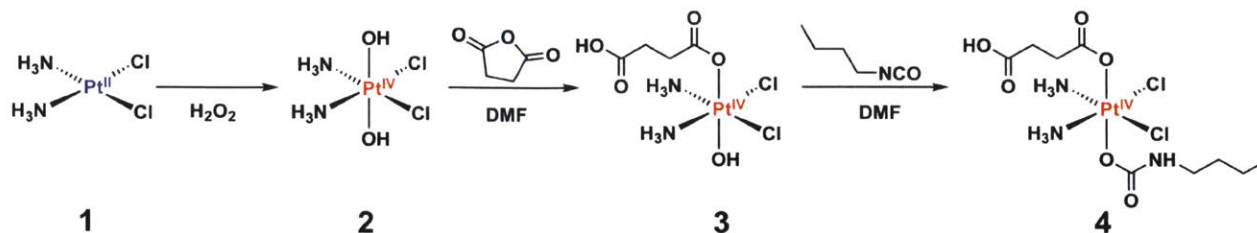


Figure 6.1. Synthetic Route for Preparing 4 from Cisplatin.

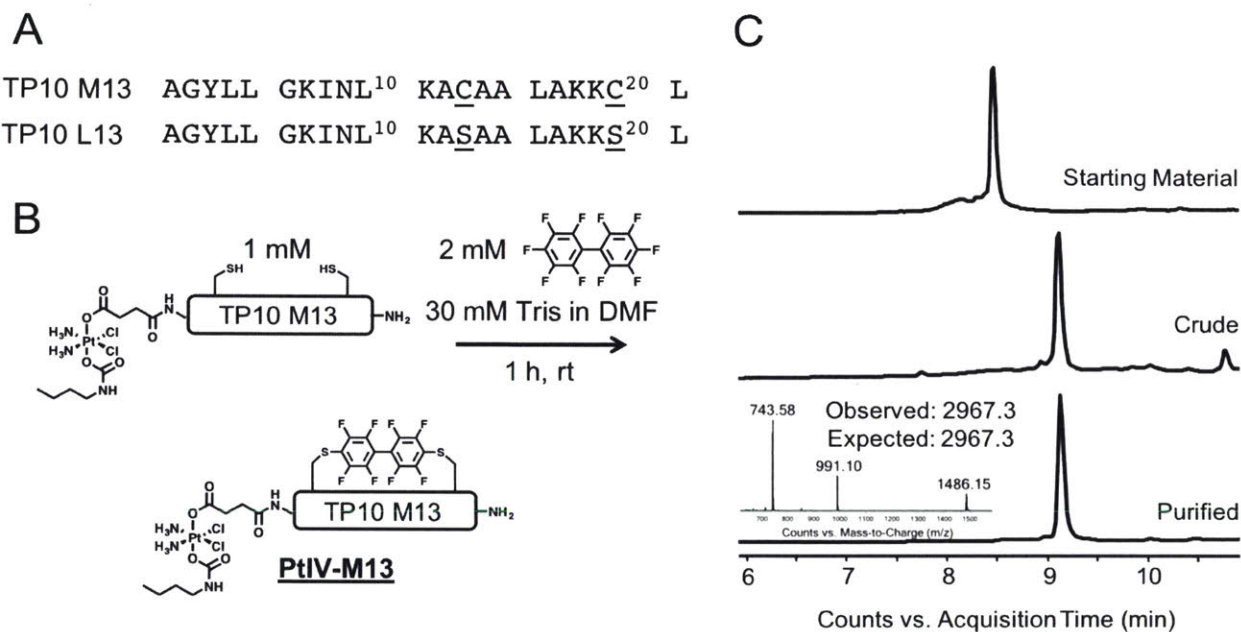
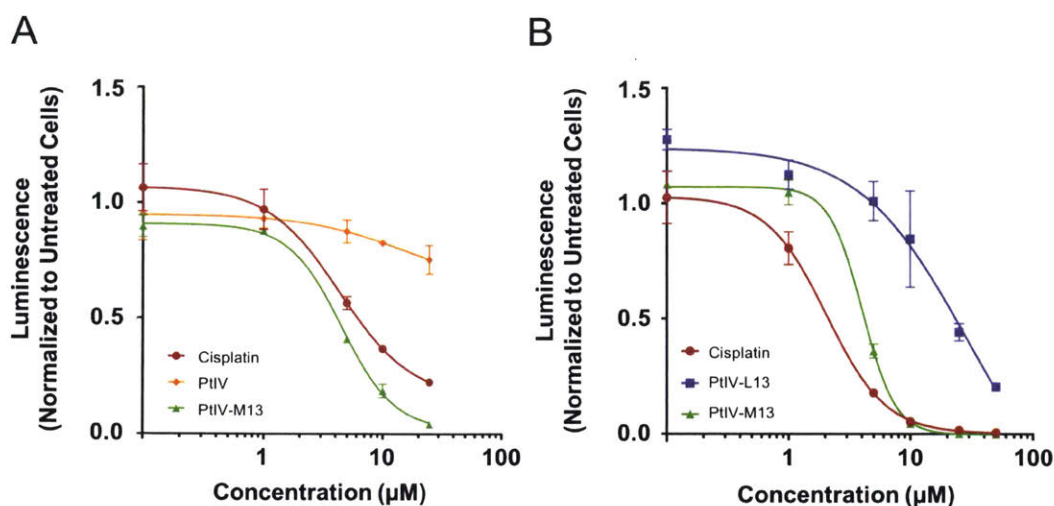
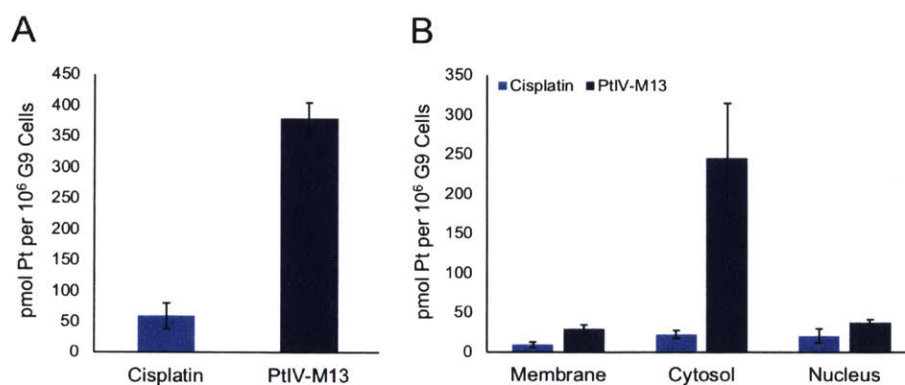


Figure 6.2. Synthesis and purification of PtIV-M13. (A) The amino acid sequences of TP10 M13 and the linear control TP10 L13. (B) Perfluoroaryl cyclization of Pt(IV)-prodrug functionalized peptide. Incubating a peptide with an N-terminal Pt(IV) prodrug and two free thiols (1 mM) with 2 mM decafluorobiphenyl in the presence of base for one hour yields the macrocyclic PtIV-M13. (C) LC-MS analysis of the starting material, crude reaction, and purified material after reversed-phase high-performance liquid chromatography. All chromatograms are total ion currents (TIC). The observed molecular weight of the final conjugate is consistent with intact Pt(IV) prodrug.



**Figure 6.3. PtIV-M13 has similar efficacy to cisplatin against patient-derived glioma initiating cells.** (A) G9 neurospheres were treated with cisplatin, PtIV-M13, and prodrug 4 (PtIV). After 80 hours, cell viability was measured by the CellTiter Glo assay. The data are shown in terms of luminescence normalized to untreated cells. The error bars are the standard deviation of three replicates. (B) G30 neurospheres were treated with cisplatin, PtIV-M13, and the linear control PtIV-L13. After 72 hours, cell viability was measured by the CellTiter Glo assay. The data are shown in terms of luminescence normalized to untreated cells. The error bars are the standard deviation of three replicates.



**Figure 6.4. *In vitro* characterization of the PtIV-M13 conjugate compared with cisplatin.** (A) G9 GCs were treated with 5 µM of cisplatin or the PtIV-M13 conjugate for 5 hours. The whole cell concentration of platinum was then evaluated by GFAAS. The error bars represent the standard deviation of three replicate wells. (B) G9 GSCs were treated with 5 µM of cisplatin or the PtIV-M13 conjugate for 5 hours. The cells were fractionated into different components and the amount of platinum was quantified by GFAAS. The error bars represent the standard deviation of three different wells treated with the compound.

same experiment was repeated on G30 GCs. The PtIV-M13 conjugate had similar potency of 4.04  $\mu\text{M}$ . The linear control conjugate PtIV-L13 was not as potent, with an  $\text{IC}_{50}$  of 28.75  $\mu\text{M}$ , suggesting that the perfluoroaryl macrocycle helps improve the potency of the prodrug-peptide conjugate (Figure 2B).

To further characterize the *in vitro* effects of the conjugate, we investigated the cellular uptake and cellular localization of PtIV-M13. G9 GSCs were treated with 5  $\mu\text{M}$  of cisplatin or the PtIV-M13 conjugate for 5 hours. The whole cell concentration of platinum was then evaluated by graphite furnace atomic absorption spectroscopy (GFAAS). The amount of platinum in the cells after treatment with the PtIV-M13 conjugate was six times greater than with cisplatin, suggesting the PtIV-M13 conjugate has superior uptake into cells (Figure 3A). The subcellular distribution was examined by fractionating the different cellular components. Most of the platinum from PtIV-M13 is present in the cytosol. The amount of nuclear platinum is relatively similar between the PtIV-M13 conjugate and cisplatin (Figure 3B).

Finally, to evaluate PtIV-M13 *in vivo*, we performed pharmacokinetic and biodistribution studies in healthy mice. For pharmacokinetics, 100  $\mu\text{L}$  of a 100  $\mu\text{M}$  solution of PtIV-M13 or PtIV-L13 dissolved in saline (corresponding to a dose of  $\sim 2.5$  mg/kg) were injected into the tail veins of mice. The brain and a blood sample were isolated at 1, 2.5, and 5 hours. A portion of the brain was dissolved in nitric acid and the amount of platinum in the brain and serum were quantified by GFAAS. For both PtIV-M13 and PtIV-L13, the serum concentration decreased over time and the brain distribution increased over time (Figure 4A). Although the read-out is platinum, platinum(II) is rapidly cleared by the kidney, suggesting that the majority of the quantified platinum in the serum comes from intact conjugates. Therefore, the results indicate that PtIV-M13 is more stable in serum and has more brain uptake than its linear control.

To study the biodistribution, 100  $\mu\text{L}$  of a 100  $\mu\text{M}$  solution of PtIV-M13, PtIV-L13, or cisplatin dissolved in normal saline were injected into the tail vein of mice. After five hours, the mice were sacrificed and the brain, heart, lungs, kidney, spleen and liver were removed. The amount of platinum in each organ was measured by dissolving a portion of the respective organ in nitric acid and then quantifying the amount of platinum by GFAAS (supporting information). The brains of the mice treated with the PtIV-M13 conjugate exhibited a 15-fold increase in the amount of platinum compared with cisplatin, suggesting the perfluoroaryl macrocycle improves the amount of drug that reaches the brain (Figure 4B).

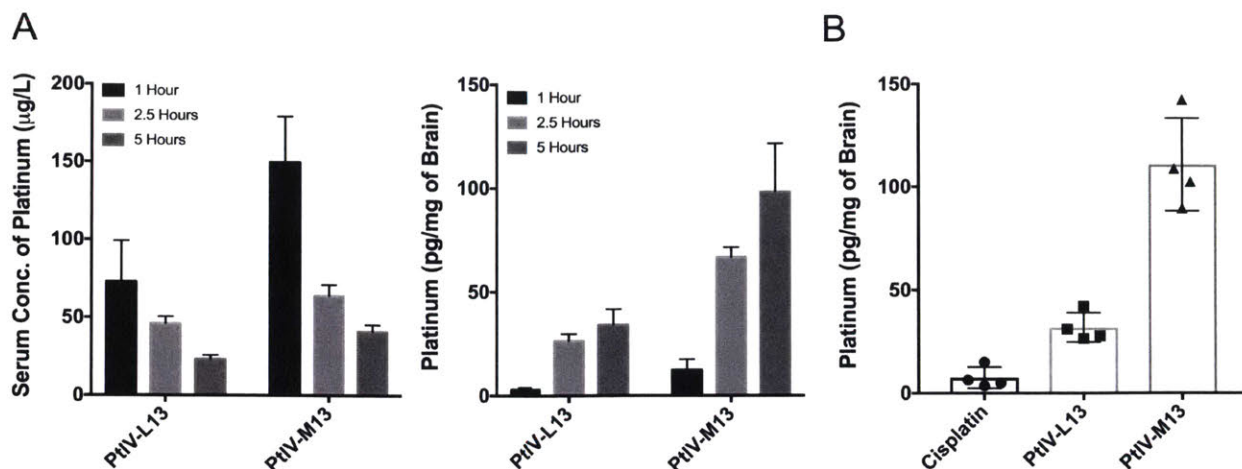


**Figure 6.5. PtIV-M13 conjugate improves platinum stability and distribution of platinum to the brain.** (A) The left plot is the concentration of platinum in serum at 1, 2.5, and 5 hours after treatment with either PtIV-M13 or the linear control PtIV-L13 ( $n = 3$  animals for each time point). The error bars are the standard deviation from three different animals injected with the compound. The right plot is the brain concentration of platinum at 1, 2.5, and 5 hours after treatment with either PtIV-M13 or the linear control PtIV-L13 ( $n = 3$  animals for each time point). The error bars are the standard deviation from three different animals injected with the compound. (B) The concentration of platinum in the brain of mice 5 hours after treatment with either PtIV-M13, PtIV-L13, or cisplatin ( $n = 4$  animals for each treatment group). The results are significant with a  $p$ -value of less than 0.0001 by a One-Way ANOVA test. After treatment with PtIV-M13, the amount of platinum in the brain at 5 hours is 15-fold greater than cisplatin.

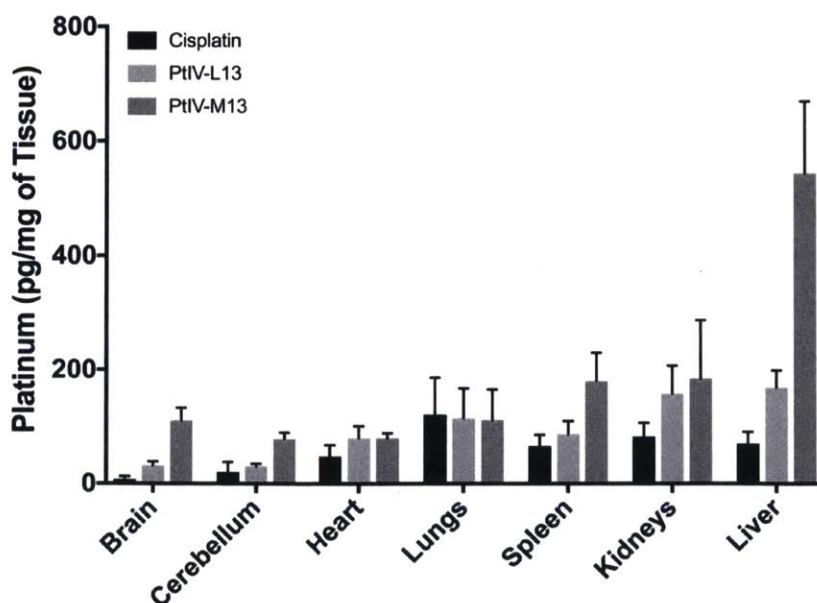


**Figure 6.6. The perfluoroaryl moiety increases distribution to the brain, cerebellum, spleen and liver.** The concentration of platinum in each organ after treatment with either PtIV-M13, PtIV-L13, or cisplatin ( $n = 4$  animals for each treatment group).

In conclusion, covalent attachment of a Pt(IV) prodrug to a brain penetrant perfluoroaryl macrocyclic peptide increases the *in vivo* stability of the prodrug and increases the distribution of platinum to the brain. The PtIV-M13. conjugate is the first compound to combine the benefits of oxidized platinum prodrugs with perfluoroaryl macrocyclic peptides. The observed efficacy against patient-derived, glioma cells is promising, and future work will focus on whether or not conjugates of this nature will be efficacious against GBM *in vivo*. However, we expect that this work will be of immediate use to those working in therapeutic development for oncology. Given the devastating nature of GBM, any maverick chemical approaches such as perfluoroaryl peptide-linked platinum prodrugs, will be helpful to broadening the scope of therapeutics available.

## 6.3. Experimental

### 6.3.1. Materials and Instrumentation

H-Rink Amide-ChemMatrix resin was obtained from PCAS BioMatrix Inc. (St-Jean-sur-Richelieu, Quebec, Canada). 1-[Bis(dimethylamino)methylene]-1H-1,2,3-triazolo[4,5-b]pyridinium-3-oxid-hexafluorophosphate (HATU), Fmoc-L-Arg(Pbf)-OH, Fmoc-L-His(Trt)-OH, Fmoc-L-Lys(Boc)-OH, Fmoc-L-Asp(tBu)-OH, Fmoc-L-Glu(tBu)-OH, Fmoc-L-Ser(tBu)-OH, Fmoc-L-Thr(tBu)-OH, Fmoc-L-Asn(Trt)-OH, Fmoc-L-Gln(Trt)-OH, Fmoc-L-Cys(Trt)-OH, Fmoc-L-Gly-OH, Fmoc-L-Ala-OH, Fmoc-L-Val-OH, Fmoc-L-Leu-OH, Fmoc-L-Ile-OH, Fmoc-L-Met-OH, Fmoc-L-Phe-OH, Fmoc-L-Pro-OH, Fmoc-L-Tyr(tBu)-OH, and Fmoc-L-Trp(Boc)-OH were purchased from Chem-Impex International (Wood Dale, IL). Peptide synthesis-grade N,N-dimethylformamide (DMF), CH<sub>2</sub>Cl<sub>2</sub>, diethyl ether, *t*-butanol and HPLC-grade acetonitrile were obtained from VWR International (Radnor, PA). Decafluorobiphenyl was purchased from Oakwood Products, Inc. (Estill, SC). Glioma stem cell lines G9 and G30 were previously described. The neurobasal media and GlutaMax, B-27, EGF, and FGF supplements were all obtained from Thermo Fisher Scientific (Waltham, MA). The G9 cells were transduced with copepod GFP using pCDH from Systems Biosciences (Mountain View, CA) and the G30 cells were transduced with Firefly luciferase using LPP-hLUC from GeneCopoeia (Rockville, MD). The CellTiter-Glo Luminescent Cell Viability Assay was obtained from Promega (Madison, WI). Athymic mice were obtained from Envigo (South Easton, MA). All other reagents were purchased from Sigma-Aldrich (St. Louis, MO), Strem (Newburyport, MA) or Alfa Aesar (Tewksbury, MA), water was deionized before use, and reactions were conducted in open-air on the benchtop. Deuterated solvents were purchased from Cambridge Isotope Laboratories (Andover, MA). <sup>1</sup>H NMR spectra were recorded on a Varian Inova 500 NMR spectrometer with an Oxford Instruments Ltd. Superconducting magnet in the Massachusetts Institute of Technology Department of Chemistry Instrumentation Facility (MIT DCIF). Electrospray ionization mass spectrometry (ESI-MS) of the small molecules was performed on an Agilent Technologies 1100 series liquid chromatography/MS instrument. Graphite furnace atomic absorption spectroscopic (GFAAS) measurements were taken on a Perkin Elmer AAnalyst 600 spectrometer.

### 6.3.2. Method for LC-MS Analysis

The following method was used on an Agilent 6520 ESI-Q-TOF mass spectrometer equipped with a C<sub>3</sub> Zorbax column (300SB C3, 2.1 x 150 mm, 5 μm) for characterization of all



peptides and peptide-prodrug conjugates. Mobile phases were: 0.1% formic acid in water (solvent A) and 0.1% formic acid in acetonitrile (solvent B). **Method:** 1% B from 0 to 2 min, linear ramp from 1% B to 61% B from 2 to 11 min, 61% B to 99% B from 11 to 12 min and finally 3 min of post-time at 1% B for equilibration, flow rate: 0.8 mL/min.

### 6.3.3. Synthesis of Pt(IV) Prodrug

*Synthesis of cis,cis,trans-[Pt(NH<sub>3</sub>)<sub>2</sub>Cl<sub>2</sub>(OH)<sub>2</sub>]<sup>2-</sup>:* To a 250 mL round bottom flask, cisplatin (600 mg, 2 mmol) and H<sub>2</sub>O<sub>2</sub> (20 mL, 30 wt% in H<sub>2</sub>O) was added. The reaction mixture was stirred at 50 °C for 2 h. Then, the reaction was heated to 100 °C for 30 min. A clear solution was generated. The reaction was cooled to RT and then left at 4 °C for 24 h. The product precipitated as yellow crystals and was isolated by centrifuge. The product was washed by 10 mL of EtOH twice and by 10 mL of Et<sub>2</sub>O twice. The yellow product was vacuum dried. (Yield: 535 mg, 80%)

*Synthesis of cis,cis,trans-[Pt(NH<sub>3</sub>)<sub>2</sub>Cl<sub>2</sub>(O<sub>2</sub>CCH<sub>2</sub>CH<sub>2</sub>COOH)(OH)]<sup>9-</sup>:* The *cis,cis,trans*-[Pt(NH<sub>3</sub>)<sub>2</sub>Cl<sub>2</sub>(OH)<sub>2</sub>] (100 mg, 0.30 mmol) and succinic anhydride (28 mg, 0.28 mmol) was stirred in 10 mL of dry DMF overnight. The insoluble material was removed by filtration and the solvent was removed under vacuum. 10 mL acetone was added to the reaction to precipitate a yellow solid. The solid was isolated by centrifuge and washed with 10 mL acetone three times and dried *in vacuo*. <sup>1</sup>H NMR (500 MHz, DMSO-*d*<sub>6</sub>) δ 5.87 (m, 6H, NH<sub>3</sub>), 2.32 (m, 4H, CH<sub>2</sub>). ESI MS: (MeOH + 0.1% TFA): *m/z* = 435.0 [M+H]<sup>+</sup>.

*Synthesis of cis,cis,trans-[Pt(NH<sub>3</sub>)<sub>2</sub>Cl<sub>2</sub>(O<sub>2</sub>CCH<sub>2</sub>CH<sub>2</sub>COOH)(*n*-Butyl Carbamate)]:* To a solution of *cis,cis,trans*-[Pt(NH<sub>3</sub>)<sub>2</sub>Cl<sub>2</sub>(O<sub>2</sub>CCH<sub>2</sub>CH<sub>2</sub>COOH)(OH)] (328 mg, 0.76 mmol) in 20 mL of DMF, *n*-butyl isocyanate (150 mg, 1.52 mmol) was added and the reaction was stirred at room temperature for 24 h. Then, a filtration was applied to remove the insoluble precipitates. The solvent was removed and the yellow solid was washed by acetone (10 mL\*2) and Et<sub>2</sub>O (10 mL\*2) and dried under vacuum to generate the pale yellow product (Yield: 372 mg, 92%). <sup>1</sup>H NMR (500 MHz, DMSO-*d*<sub>6</sub>) δ 12.09 (s, 1H, OH), 6.61 (m, 6H, NH<sub>3</sub>), 6.54 (t, 1H, NH), 2.88 (m, 2H, CH<sub>2</sub>), 2.47 (t, 2H, CH<sub>2</sub>), 2.36 (m, 2H, CH<sub>2</sub>), 1.23~1.32 (m, 4H, CH<sub>2</sub>), 0.84 (t, 3H, CH<sub>3</sub>). ESI MS: (MeOH + 0.1% TFA): *m/z* = 534.0 [M-H]<sup>+</sup>. Elemental Analysis calculated for C<sub>9</sub>H<sub>21</sub>Cl<sub>2</sub>N<sub>3</sub>O<sub>6</sub>Pt+2/3DMSO: C, 21.20%; H, 4.31%; N, 7.18%; found: C, 21.58%; H, 4.10%; N, 7.50%.

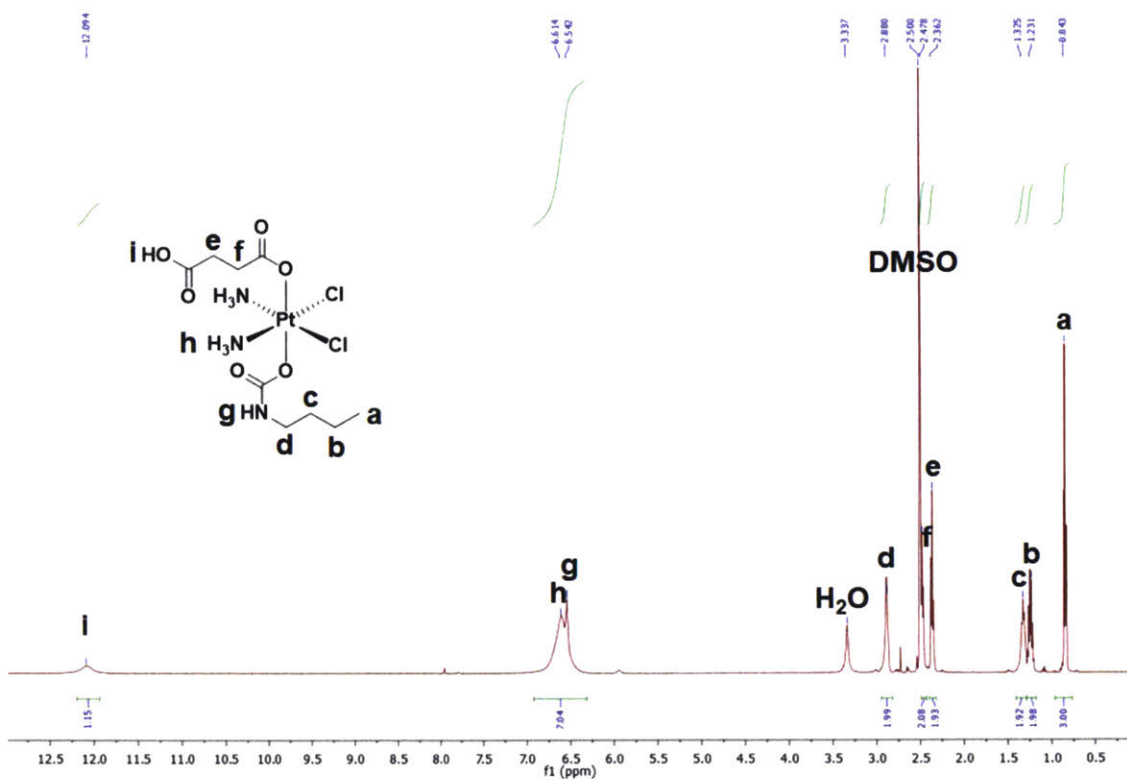


Figure 6.7. <sup>1</sup>H-NMR Analysis of prodrug 4.



#### 6.3.4. General Method for Peptide Preparation

*Fast-flow Peptide Synthesis:* Peptides were synthesized on a 0.1-mmol scale using an automated flow peptide synthesizer.<sup>19</sup> A 200 mg portion of ChemMatrix Rink Amide HYR resin was loaded into a reactor maintained at 90 °C. All reagents were flowed at 80 mL/min with HPLC pumps through a stainless-steel loop maintained at 90 °C before introduction into the reactor. For each coupling, 10 mL of a solution containing 0.2 M amino acid and 0.17 M HATU in DMF were mixed with 200 µL diisopropylethylamine and delivered to the reactor. Fmoc removal was accomplished using 10.4 mL of 20% (v/v) piperidine. Between each step, DMF (15 mL) was used to wash out the reactor. After completion of the synthesis, the resins were washed 3 times with DCM and dried under vacuum. A 100 mg portion of the peptidyl resin was transferred to a 3 mL Torviq fritted syringe and subsequently swelled in DMF. Prodrug **4** (50 mg, 94 µmol, ~ 4 equivalents with respect to theoretical loading of resin) was dissolved in 625 µL of 0.4 M HATU in a scintillation vial. 50 µL of diisopropylethylamine was added to the vial. The vial was briefly sonicated and the coupling solution was transferred to the fritted syringe containing the peptidyl resin, after draining the DMF from the resin. The syringe was capped and mixed on a nutating mixer for one hour. Following the one hour incubation, the coupling solution was removed from the resin and the resin was washed 5 times with DMF, 5 times with DCM and dried under vacuum.

*Peptide Cleavage and Deprotection:* Each peptide was subjected to simultaneous global side-chain deprotection and cleavage from resin by treatment with 4 mL of 94% (v/v) trifluoroacetic acid (TFA), 2.5% (v/v) water, and 2.5% (v/v) triisopropylsilane (TIPS) for 2 hr at room temperature. Note: with PtIV-L13, some reduction of the prodrug was observed upon cleavage. We hypothesize this is due to TIPS in the cleavage cocktail with a peptide that has fewer trityl-protected residues than PtIV-M13. For general use, researchers may want to omit TIPS from their cleavage cocktail. After cleavage, the TFA was evaporated by bubbling N<sub>2</sub> through the mixture until only an oil and the resin remained. Then ~35 mL of cold ether was added to precipitate and wash the peptide (chilled at -80°C). The crude product and resin were pelleted through centrifugation for 3 min at 4,000 rpm and the ether decanted. The ether precipitation and centrifugation was repeated two more times. After the third wash, the pellet was redissolved in 50% water and 50% acetonitrile containing 0.1% TFA and lyophilized.

Sequence: (PtIV)-AGYLLGKINLKSAALAKKSL-NH<sub>2</sub>  
Mass Expected: 2642.3  
Mass Observed: 2641.4

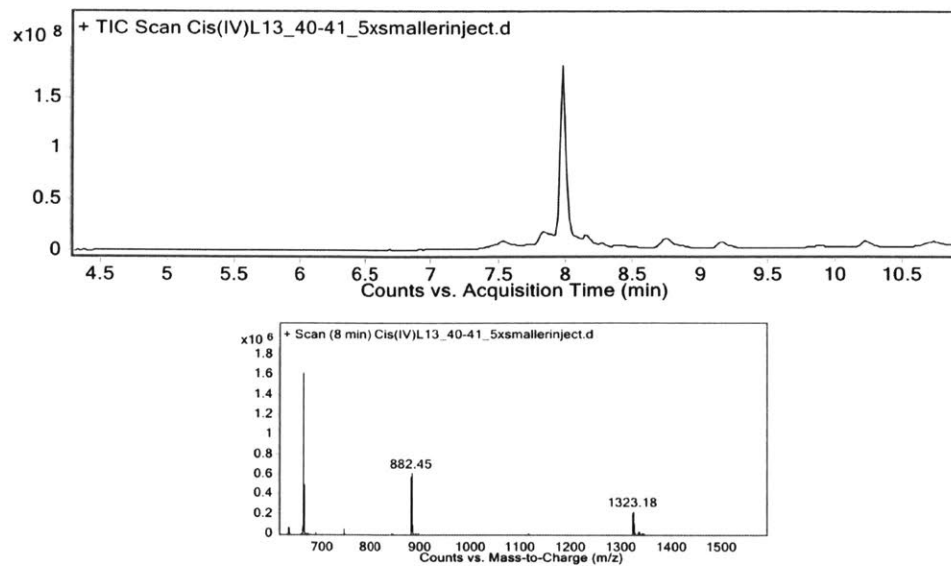


**Figure 6.8. LC-MS Analysis of PtIV-L13.**

Sequence: (PtIV)-AGYLLGKINLKACAALAKKCL-NH<sub>2</sub>  
Mass Expected: 2673.3  
Mass Observed: 2673.3

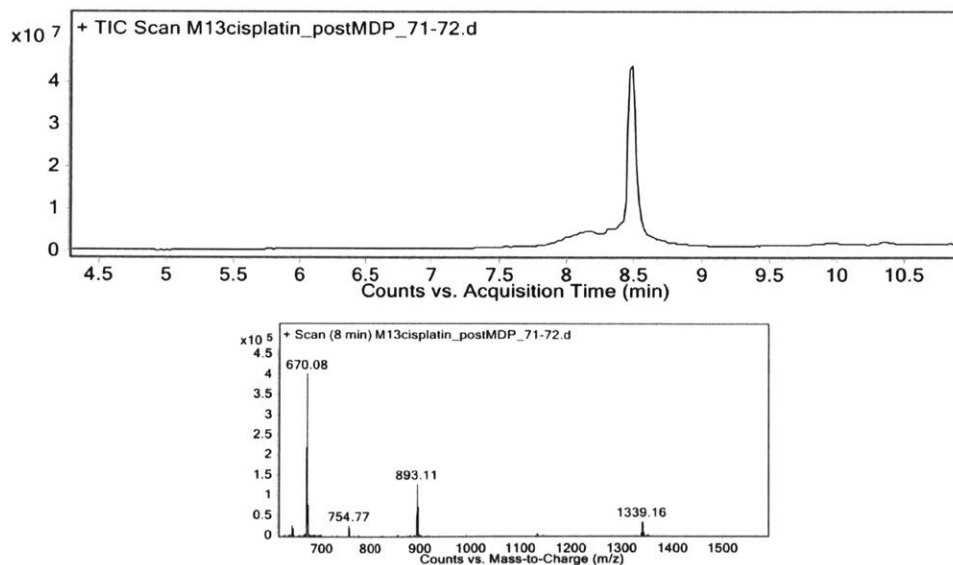


**Figure 6.9. LC-MS Analysis of PtIV-M13 prior to macrocyclization.**

*Peptide Purification:* After lyophilization, the peptides were redissolved in water and acetonitrile containing 0.1% TFA, filtered through a 0.22  $\mu\text{m}$  nylon filter and purified by mass-directed semi-preparative reversed-phase HPLC. Solvent A was water containing 0.1% TFA and Solvent B was acetonitrile containing 0.1% TFA. A linear gradient that changed at a rate of 0.5%/min was used from 15% Solvent B to 55% Solvent B over 80 min. The peptides were purified on an Agilent Zorbax SB C3 column: 9.4 x 250 mm, 5  $\mu\text{m}$ . Using mass data about each fraction from the instrument, only pure fractions were pooled and lyophilized. The purity of the fraction pool was confirmed by LC-MS (Figure 6.8, 6.9).

### **6.3.5. Macrocyclization Procedure for PtIV-M13**

The purified, pre-cyclization PtIV-M13 peptide was dissolved in DMF, and stock solutions of decafluorobiphenyl in DMF and Tris in DMF were added such that the final concentration in the reaction vessel was 1 mM of peptide, 2 mM decafluorobiphenyl, and 30 mM Tris. After 1 h, the reaction was quenched by diluting the reaction by a factor of ten with 85:15 water:acetonitrile containing 2% TFA. The crude reaction was purified by mass-directed semi-preparative reversed-phase HPLC (Agilent Zorbax SB C3 column: 9.4 x 250 mm, 5  $\mu\text{m}$ ). Solvent A was water containing 0.1% TFA and Solvent B was acetonitrile containing 0.1% TFA. A linear gradient that changed at a rate of 0.5%/min was run from 20% B to 60% B. Using mass data about each fraction from the instrument, only pure fractions were pooled and lyophilized. The purity of the fraction pool was confirmed by LC-MS (Figure 6.10).

### **6.3.6. Cytotoxicity Assays**

G9 and G30 cells were maintained in neurobasal media supplemented with 2% (v/v) B-27 Supplement (50X), 1% (v/v) GlutaMAX, 1% (v/v) Pen Strep and 20  $\mu\text{L}$  each of 20 ng/mL EFG and FGF for each 500 mL of media at 37  $^{\circ}\text{C}$  and 5%  $\text{CO}_2$ .<sup>21,23</sup> For routine passage of the cells, the cells and media were transferred from a T-75 tissue culture flask to a 15 mL conical tube. The tube was spun at 500 rcf for 3 min. The supernatant media was aspirated and 2 mL of StemPro Accutase were used to resuspend the cells. The cells were left in Accutase for 10 min at room temperature. The Accutase was quenched with 8 mL of media and then the desired amount of cell suspension was transferred to a new flask.

G9 Cytotoxicity Assay: 20 h before treatment, G9 cells were plated at a density of 10,000 cells per well in a 96-well plate (100  $\mu\text{L}$ /well). Note: the cells must be incubated with Accutase prior to counting to disrupt the spheres and generate a single cell suspension. 2.5 mM stocks of



PtIV-M13 and prodrug **4** were prepared in DMSO, and a 2.5 mM stock of cisplatin was prepared in PBS. Concentration of the stocks was determined by graphite furnace atomic absorption spectroscopy (GFAAS). Treatment media stocks were prepared by serial dilution with the supplemented neurobasal media such that there were treatment wells with concentrations of 150, 75, 30, 15, 3, and 0.3  $\mu\text{M}$ . To treat the cells, 50  $\mu\text{L}$  of each treatment media stock was added to the overnight growth media, such that the final volume in the well was 150  $\mu\text{L}$  and the final treatment concentrations were 50, 25, 10, 5, 1, and 0.1  $\mu\text{M}$  respectively. Cells were incubated for 80 h at 37  $^{\circ}\text{C}$  and 5%  $\text{CO}_2$  with the peptide treatment. At 80 h, the plate was removed from the incubator and the cells were allowed to equilibrate to room temperature. Then, 130  $\mu\text{L}$  of CellTiter-Glo reagent was added to each well. The plate was incubated for 10 min away from light. After incubation, 10  $\mu\text{L}$  from each well was transferred to a new plate and each well in the new plate was diluted with 90  $\mu\text{L}$  of PBS. The luminescence was read on a Perkin Elmer 1450 MicroBeta TriLux Microplate Scintillation and Luminescence Counter. The luminescence of each sample was normalized to untreated control wells and the data were plotted in GraphPad Prism.

G30 Cytotoxicity Assay: 20 h before treatment, G30 cells were plated at a density of 10,000 cells per well in a 96-well plate (100  $\mu\text{L}$ /well). Note: the cells must be incubated with Accutase prior to counting to disrupt the spheres and generate a single cell suspension. 2.5 mM stocks of PtIV-M13 and PtIV-L13 were prepared in DMSO, and a 2.5 mM stock of cisplatin was prepared in PBS. Concentration of the stocks was determined by graphite furnace atomic absorption spectroscopy (GFAAS). Treatment media stocks were prepared by serial dilution with the supplemented neurobasal media such that there were treatment wells with concentrations of 150, 75, 30, 15, 3, and 0.3  $\mu\text{M}$ . To treat the cells, 50  $\mu\text{L}$  of each treatment media stock was added to the overnight growth media, such that the final volume in the well was 150  $\mu\text{L}$  and the final treatment concentrations were 50, 25, 10, 5, 1, and 0.1  $\mu\text{M}$  respectively. Cells were incubated for 72 h at 37  $^{\circ}\text{C}$  and 5%  $\text{CO}_2$  with the peptide treatment. At 80 h, the plate was removed from the incubator and the cells were allowed to equilibrate to room temperature. Then, 130  $\mu\text{L}$  of CellTiter-Glo reagent was added to each well. The plate was incubated for 10 min away from light. After incubation, 10  $\mu\text{L}$  from each well was transferred to a new plate and each well in the new plate was diluted with 90  $\mu\text{L}$  of PBS. The luminescence was read on a Perkin Elmer 1450 MicroBeta TriLux Microplate Scintillation and Luminescence Counter. The luminescence of each sample was normalized to untreated control wells and the data were plotted in GraphPad Prism.

### 6.3.7. Cell Uptake Assays

*Whole Cell Uptake Assay:* 12 h before treatment, G9 cells were plated at a density of 300,000 cells per well in a 6-well plate (2.5 mL/well). The 2.5 mM stock of PtIV-M13 in DMSO and the 2.5 mM stock of cisplatin in PBS were used to prepare 30  $\mu$ M treatment solutions in supplemented neurobasal media. 0.5 mL of treatment media was added to each well such that the final treatment concentration was 5  $\mu$ M. The cells were incubated for 6 h at 37 °C and 5% CO<sub>2</sub>. Each well of cells was transferred to its own 15 mL conical tube and centrifuged at 500 ref for 3 min. The media was aspirated and the cells were treated with Accutase (1 mL) for 10 min at room temperature. After quenching the Accutase with 4 mL of PBS and the cells were counted with a hemocytometer. The cells were centrifuged, the PBS aspirated, and then the cells were resuspended in 5 mL of PBS. This PBS wash was repeated one additional time and then the amount of platinum was quantified by GFAAS.

*Cellular Distribution Assay:* 12 h before treatment, G9 cells were plated at a density of 370,000 cells per well in a 6-well plate (2 mL/well). The 2.5 mM stock of PtIV-M13 in DMSO and the 2.5 mM stock of cisplatin in PBS were used to prepare 15  $\mu$ M treatment solutions in supplemented neurobasal media. 1 mL of treatment media was added to each well such that the final treatment concentration was 5  $\mu$ M. The cells were incubated for 6 h at 37 °C and 5% CO<sub>2</sub>. Each well of cells was transferred to its own 15 mL conical tube and centrifuged at 500 ref for 3 min. The media was aspirated and the cells were treated with Accutase (1 mL) for 10 min at room temperature. After quenching the Accutase with 4 mL of PBS and the cells were counted with a hemocytometer. The cells were centrifuged, the PBS aspirated, and then the cells were resuspended in 5 mL of PBS. This PBS wash was repeated one additional time and then the cytoplasm, nucleus, and membrane fractions were isolated using the Thermo Scientific NE-PER Nuclear and Cytoplasmic Extraction kit. The platinum content in the cytoplasm, nucleus, and membrane was analyzed by GFAAS.

### 6.3.8. DNA Platination Assay

12 h before treatment, G9 cells were plated at a density of 2,000,000 cells per well in a 6-well plate (2 mL/well). 4  $\mu$ L of either the 2.5 mM stock of PtIV-M13 in DMSO or the 2.5 mM stock of cisplatin in PBS were added to a given well such that the final treatment concentration was 5  $\mu$ M. The cells were incubated for 22 h at 37 °C and 5% CO<sub>2</sub>. Each well of cells was transferred to its own 15 mL conical tube and centrifuged at 500 ref for 3 min. The media was

aspirated and the cells were treated with Accutase (1 mL) for 10 min at room temperature. After quenching the Accutase with 4 mL of PBS and the cells were counted with a hemocytometer. The cells were centrifuged, the PBS aspirated, and then the cells were resuspended in 5 mL of PBS. This PBS wash was repeated one additional time and the cell pellet was suspended in DNAzol (1 mL, genomic DNA isolation reagent, MRC). The DNA was precipitated with pure ethanol (0.5 mL), washed with 75% ethanol (0.75 mL x 3), and redissolved in 1 mL of 8 mM NaOH. The DNA concentration was determined by UV-Vis spectroscopy and the platinum content was quantified by GFAAS (Figure 6.11).

### **6.3.9. *In Vivo* Pharmacokinetics**

PtIV-M13 and PtIV-L13 powders were dissolved to a final concentration of 10 mM in DMSO (determined by GFAAS). Each peptide was then diluted to a concentration of 100  $\mu$ M in 0.9% sodium chloride (v/v) irrigation solution. A 100  $\mu$ L dose of each peptide solution was administered intravenously via the tail vein into healthy 5-6-week old athymic, female nude mice. At 1, 2.5 and 5 hours, the mice were sacrificed by cervical dislocation, blood was collected periorbitally, and the brains were excised and frozen on dry ice immediately. The blood samples were allowed to coagulate at room temperature for 30 to 60 min. The blood was subsequently spun at 2,500 rcf for 10 min at 4 °C. The serum was collected with a pipette and frozen in a -20 °C freezer for storage. The concentration of platinum in each serum sample was determined by GFAAS. Additionally, a small portion of each brain was dissolved in 500  $\mu$ L of nitric acid and the amount of platinum was quantified by GFAAS.

### **6.3.10. *In Vivo* Biodistribution**

PtIV-M13 and PtIV-L13 powders were dissolved to a final concentration of 10 mM in DMSO and cisplatin was dissolved to a final concentration of 5 mM in PBS (determined by GFAAS). Each compound was then diluted to a concentration of 100  $\mu$ M in 0.9% sodium chloride (v/v) irrigation solution. For the cisplatin sample, DMSO was added such that the % DMSO matched the peptide solutions. A 100  $\mu$ L dose of each treatment was administered intravenously via the tail vein into healthy 6-8-week old athymic, female nude mice. At 5 hours, the mice were sacrificed by cervical dislocation and the brain, brainstem/cerebellum, heart, lungs, spleen, liver, and kidneys were excised and frozen on dry ice immediately. A small portion of each organ was dissolved in 500  $\mu$ L of nitric acid and the amount of platinum was quantified by GFAAS.

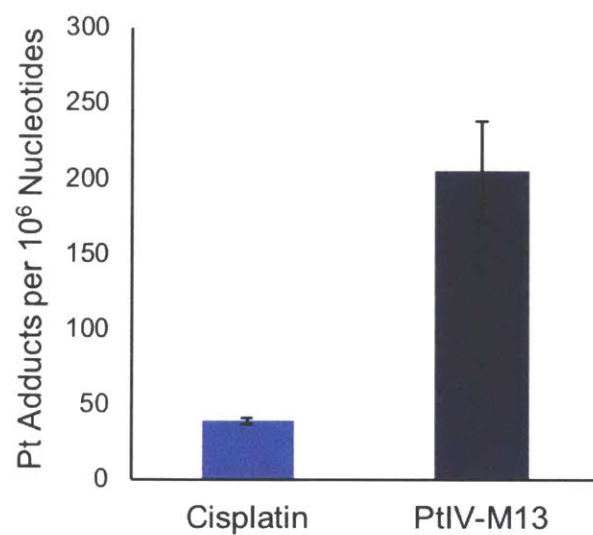


**Figure 6.11. DNA Platination Assay.** DNA was isolated from G9 cells after treatment with either cisplatin or PtIV-M13. The error bars are the standard deviation of triplicate experiments.



#### **6.4. Acknowledgments**

This work was supported by grant CA034992 to S.J.L., CA034992, AG045144, CA211184 to Ö.H.Y, and the Sontag Foundation Distinguished Scientist Award (to B.L.P.) C.M.F. is supported by the David H. Koch Graduate Fellowship Fund and by the Eunice Kennedy Shriver National Institute of Child Health and Human Development of the National Institutes of Health under award number F30HD093358. J.M.W. is supported by the National Science Foundation Graduate Research Fellowship under Grant No. 1122374. C.-F.C. is supported by the Canadian Institute of Health Research Fellowship.

## 6.5. References

- (1) Stupp, R.; Mason, W. P.; van den Bent, M. J.; Weller, M.; Fisher, B.; Taphoorn, M. J. B.; Belanger, K.; Brandes, A. A.; Marosi, C.; Bogdahn, U.; et al. Radiotherapy plus Concomitant and Adjuvant Temozolomide for Glioblastoma. *N. Engl. J. Med.* **2005**, *352* (10), 987–996.
- (2) Wong, E. T.; Hess, K. R.; Gleason, M. J.; Jaeckle, K. A.; Kyritsis, A. P.; Prados, M. D.; Levin, V. A.; Yung, W. K. A. Outcomes and Prognostic Factors in Recurrent Glioma Patients Enrolled Onto Phase II Clinical Trials. *J. Clin. Oncol.* **1999**, *17* (8), 2572–2572.
- (3) Sarin, H.; Kanevsky, A. S.; Wu, H.; Brimacombe, K. R.; Fung, S. H.; Sousa, A. A.; Auh, S.; Wilson, C. M.; Sharma, K.; Aronova, M. A.; et al. Effective Transvascular Delivery of Nanoparticles across the Blood-Brain Tumor Barrier into Malignant Glioma Cells. *J. Transl. Med.* **2008**, *6*, 80.
- (4) van Tellingen, O.; Yetkin-Arik, B.; de Gooijer, M. C.; Wesseling, P.; Wurdinger, T.; de Vries, H. E. Overcoming the Blood–brain Tumor Barrier for Effective Glioblastoma Treatment. *Drug Resist. Updat.* **2015**, *19*, 1–12.
- (5) Neuwelt, E.; Abbott, N. J.; Abrey, L.; Banks, W. A.; Blakley, B.; Davis, T.; Engelhardt, B.; Grammas, P.; Nedergaard, M.; Nutt, J.; et al. Strategies to Advance Translational Research into Brain Barriers. *Lancet Neurol.* **2008**, *7* (1), 84–96.
- (6) Wang, D.; Lippard, S. J. Cellular Processing of Platinum Anticancer Drugs. *Nat. Rev. Drug Discov.* **2005**, *4* (4), 307–320.
- (7) Blommaert, F. A.; van Dijk-Knijnenburg, H. C. M.; Dijt, F. J.; den Engelse, L.; Baan, R. A.; Berends, F.; Fichtinger-Schepman, A. M. J. Formation of DNA Adducts by the Anticancer Drug Carboplatin: Different Nucleotide Sequence Preferences in Vitro and in Cells. *Biochemistry (Mosc.)* **1995**, *34* (26), 8474–8480.
- (8) Miller, R. P.; Tadagavadi, R. K.; Ramesh, G.; Reeves, W. B. Mechanisms of Cisplatin Nephrotoxicity. *Toxins* **2010**, *2* (11), 2490–2518.
- (9) Zheng, Y.-R.; Suntharalingam, K.; Johnstone, T. C.; Yoo, H.; Lin, W.; Brooks, J. G.; Lippard, S. J. Pt(IV) Prodrugs Designed to Bind Non-Covalently to Human Serum Albumin for Drug Delivery. *J. Am. Chem. Soc.* **2014**, *136* (24), 8790–8798.
- (10) Dhar, S.; Gu, F. X.; Langer, R.; Farokhzad, O. C.; Lippard, S. J. Targeted Delivery of Cisplatin to Prostate Cancer Cells by Aptamer Functionalized Pt(IV) Prodrug-PLGA-PEG Nanoparticles. *Proc. Natl. Acad. Sci.* **2008**, *105* (45), 17356–17361.
- (11) Abramkin, S.; M. Valiahdi, S.; A. Jakupec, M.; Galanski, M.; Metzler-Nolte, N.; K. Keppler, B. Solid-Phase Synthesis of Oxaliplatin – TAT Peptide Bioconjugates. *Dalton Trans.* **2012**, *41* (10), 3001–3005.
- (12) Mukhopadhyay, S.; Barnés, C. M.; Haskel, A.; Short, S. M.; Barnes, K. R.; Lippard, S. J. Conjugated Platinum(IV)–Peptide Complexes for Targeting Angiogenic Tumor Vasculature. *Bioconjug. Chem.* **2008**, *19* (1), 39–49.
- (13) Wong, D. Y. Q.; Yeo, C. H. F.; Ang, W. H. Immuno-Chemotherapeutic Platinum(IV) Prodrugs of Cisplatin as Multimodal Anticancer Agents. *Angew. Chem. Int. Ed Engl.* **2014**, *53* (26), 6752–6756.
- (14) Gaviglio, L.; Gross, A.; Metzler-Nolte, N.; Ravera, M. Synthesis and in Vitro Cytotoxicity of Cis , Cis , Trans -Diamminedichloridodisuccinatoplatinum( Iv )– Peptide Bioconjugates. *Metallomics* **2012**, *4* (3), 260–266.
- (15) Yung, W. K.; Mechtler, L.; Gleason, M. J. Intravenous Carboplatin for Recurrent Malignant Glioma: A Phase II Study. *J. Clin. Oncol.* **1991**, *9* (5), 860–864.

- (16) Reardon, D. A.; Desjardins, A.; Peters, K. B.; Gururangan, S.; Sampson, J. H.; McLendon, R. E.; Herndon, J. E.; Bulusu, A.; Threatt, S.; Friedman, A. H.; et al. Phase II Study of Carboplatin, Irinotecan, and Bevacizumab for Bevacizumab Naïve, Recurrent Glioblastoma. *J. Neurooncol.* **2012**, *107* (1), 155–164.
- (17) Francesconi, A. B.; Dupre, S.; Matos, M.; Martin, D.; Hughes, B. G.; Wyld, D. K.; Lickliter, J. D. Carboplatin and Etoposide Combined with Bevacizumab for the Treatment of Recurrent Glioblastoma Multiforme. *J. Clin. Neurosci.* **2010**, *17* (8), 970–974.
- (18) Fadzen, C. M.; Wolfe, J. M.; Cho, C.-F.; Chiocca, E. A.; Lawler, S. E.; Pentelute, B. L. Perfluoroarene-Based Peptide Macrocycles to Enhance Penetration Across the Blood–Brain Barrier. *J. Am. Chem. Soc.* **2017**, *139* (44), 15628–15631.
- (19) Mijalis, A. J.; Thomas III, D. A.; Simon, M. D.; Adamo, A.; Beaumont, R.; Jensen, K. F.; Pentelute, B. L. A Fully Automated Flow-Based Approach for Accelerated Peptide Synthesis. *Nat. Chem. Biol.* **2017**, *13* (5), 464–466.
- (20) Berger, G.; Grauwet, K.; Zhang, H.; Hussey, A. M.; Nowicki, M. O.; Wang, D. I.; Chiocca, E. A.; Lawler, S. E.; Lippard, S. J. Anticancer Activity of Osmium(VI) Nitrido Complexes in Patient-Derived Glioblastoma Initiating Cells and in Vivo Mouse Models. *Cancer Lett.* **2018**, *416*, 138–148.
- (21) Williams, S. P.; Nowicki, M. O.; Liu, F.; Press, R.; Godlewski, J.; Abdel-Rasoul, M.; Kaur, B.; Fernandez, S. A.; Chiocca, E. A.; Lawler, S. E. Indirubins Decrease Glioma Invasion by Blocking Migratory Phenotypes in Both the Tumor and Stromal Endothelial Cell Compartments. *Cancer Res.* **2011**, *71* (16), 5374–5380.
- (22) Alderden, R. A.; Hall, M. D.; Hambley, T. W. The Discovery and Development of Cisplatin. *J. Chem. Educ.* **2006**, *83* (5), 728.
- (23) Mao, P.; Joshi, K.; Li, J.; Kim, S.-H.; Li, P.; Santana-Santos, L.; Luthra, S.; Chandran, U. R.; Benos, P. V.; Smith, L.; et al. Mesenchymal Glioma Stem Cells Are Maintained by Activated Glycolytic Metabolism Involving Aldehyde Dehydrogenase 1A3. *Proc. Natl. Acad. Sci. U. S. A.* **2013**, *110* (21), 8644–8649.